Next generation (hybrid) battery materials at the water/energy/recycling nexus

Dissertation
zur Erlangung des Grades
der Doktorin der Naturwissenschaften
der Naturwissenschaftlich-Technischen Fakultät
der Universität des Saarlandes

vorgelegt von

STEFANIE ARNOLD

aus Maulbronn

Saarbrücken, April 2023

ACKNOWLEDGMENT

ACKNOWLEDGMENT

Dank ihrer wissenschaftlichen Diskussionen und hilfreichen Kommentare konnte ich meinen Blick auf die Welt der Wissenschaft erweitern. Es war eine hervorragende Gelegenheit, mit diesen großartigen WissenschaftlerInnen weltweit Kontakte zu knüpfen und zusammenzuarbeiten.

Für ihre persönliche Unterstützung und Motivation während meiner Promotion geht nicht zuletzt ein riesiges Dankeschön auch an meine Freunde und Familie außerhalb des INMs sowie der Universität des Saarlandes

TABLE OF CONTENT

TABLE OF CONTENT

ZUSAMMENFASSUNG

Der Übergang zu einer groß angelegten Nutzung erneuerbarer Energien erfordert eine umweltfreundliche Energiespeichertechnologie. Insbesondere für die elektrochemische Energiespeicherung ist es unerlässlich, Elektrodenmaterialien mit höherer Leistung, besserer Wiederverwertbarkeit und verbesserter Umweltfreundlichkeit zu entwickeln. Solche Materialien und Technologien der nächsten Generation ermöglichen nicht nur eine verbesserte Energiespeicherung, sondern auch die elektrochemische Entsalzung zur Erzeugung von sauberem Trinkwasser oder die Rückgewinnung wertvoller Elemente wie Lithium-Ionen.

Im Rahmen dieser Arbeit werden neuartige (hybride) Materialien an der Schnittstelle zwischen Energie, Wasser und Recycling entwickelt. Sorgfältiges Materialdesign und -optimierung ermöglichen eine verbesserte elektrochemische Leistung von Interkalations-, Legierungs- und Umwandlungselektroden für Lithium-Ionen- und Natrium-Ionen-Batterieelektroden. Die Vertreter der großen 2D-Materialfamilie MXene beispielsweise liefern Hochleistungselektroden, wenn sie mit SnO_2 oder Sb kombiniert werden oder wenn ihr Zwischenschichtabstand sorgfältig angepasst wird. Ihre 2D-Natur ermöglicht auch einen neuen Ansatz für ein einfaches Elektrodenrecycling. Die nächste Generation der Wasseraufbereitung wird erforscht, indem zum ersten Mal ein Legierungsmaterial (Sb), Kobalthydroxid Hohlwürfel und Meerwasserbatterien eingesetzt werden. Die selektive Lithiumextraktion wird durch die Kombination einer Redox-Flow-Batterie mit einer Li-selektiven Keramikmembran demonstriert, um Lithiumionen direkt aus (synthetischem) Meerwasser zu gewinnen.

ABSTRACT

Transitioning toward large-scale utilization of renewable energy necessitates environmentally friendly energy storage technology. Especially for electrochemical energy storage, it is imperative to develop electrode materials with higher performance, better recyclability, and improved environmental friendliness. Such next-generation materials and technologies not only allow for enhanced energy storage but also enable electrochemical desalination to generate clean, potable water or recover precious elements, such as lithium ions.

This thesis develops novel (hybrid) materials for the energy/water/recycling nexus. Careful material design and optimization enable improved electrochemical performance of intercalation, alloying, and conversion electrodes for lithium-ion and sodium-ion battery electrodes. For example, members of the large 2D material family MXene yield high-performance electrodes when hybridized with SnO_2 or Sb, or when their interlayer space is carefully adjusted. Their 2D nature allows also a new approach to facile electrode recycling. Next-generation water remediation is explored by adopting, for the first time, an alloying material (Sb), hollow-cube cobalt hydroxide, and seawater batteries. Selective lithium extraction is demonstrated by combining a redox flow battery with a Li-selective ceramic membrane to harvest lithium ions directly from (synthetic) seawater.

1   INTRODUCTION AND MOTIVATION

In recent years, renewable energy storage has become an increasingly important issue due to politically set targets and standards. Due to rising living standards and the rapid growth of the world's population, today's society has a steadily increasing demand for electrical energy in various sectors. In 2022, the total amount of electricity produced by renewable energy sources such as solar, wind, hydro, and biomass was about 244 TWh, about 49.5% of the total net electricity generation.[1] Also, the increasing electrification leads to an ever-increasing quest for electricity supply independent of conditions (dark periods, no wind). Due to the renewable energies and the dependence of the production on external environmental influences, the topic of high-performance energy storage systems also plays a serious role at this point to supply energy flexibly at any time of day or night and independent of weather conditions. Energy storage technologies can generally be divided into thermomechanical and mechanical energy storage, electrical energy storage, electrochemical energy storage, chemical energy storage, and thermal energy storage. Batteries, which store energy through different redox potentials in electrochemical cells, are the second largest global energy storage technology after thermal storage.[2]

Electrochemical storage includes accumulators (rechargeable) and batteries, where storage takes the form of electrical charge carriers that are taken up and released through reduction and oxidation processes at two electrodes connected to an electrolyte. Lithium-ion-based technology has played an increasingly important role as an energy storage system from its initial introduction in the 70s to commercial availability in 1991 and beyond.[3] Primary battery materials used today include lithium nickel manganese cobalt oxide (NMC), lithium manganese oxide (LMO), lithium iron phosphate (LFP) as cathode materials, and graphite and lithium titanate (LTO) as anode materials, all of which are based on an intercalation process of lithium ions into the host structure. Owing to the high energy density and power density, the lithium-ion battery (LIB) plays a major role but is still under constant development and update.[4] The specific storage energy (Wh kg^{-1}) with the established electrode systems has practically tripled in the last 10 years. Due to raw materials like cobalt, on which many electrode materials in LIBs are based, combined with their mining in politically and ecologically sensitive areas and the steadily rising price of the increasingly scarce lithium sources, energy storage technologies beyond lithium are of great interest.[5] [6]

Owing sodium-ion technology offers a promising alternative due to its comparable intercalation chemistry of Na-ions compared to Li-ions, its high availability as one of the elements most abundant in the earth's crust as well as the resulting cost efficiency. In addition, the electrode materials do not require cobalt as several electrode materials of Li-counterpart. Due to the larger ion radius and so far lower energy and power density compared to LIB, sodium-ion batteries (NIBs) play increasingly

important roles in the field of stationary energy storage.[7] Owning the similar behavior of LIB and NIB technology, some findings of the advanced LIB technology could be applied to the NIB technology, which is expected to save time. However, sodium's electrochemical behavior differs from lithium's in several ways, such as higher reactivity, larger ionic radius, phase stability, transport properties, and formation of SEI, which can significantly affect the electrochemical performance.[8] In addition to research applications for the rapidly growing field of solid-state battery design, where the liquid or gel electrolyte is replaced by solid material, research is also continuing on various levels of electrode material composition for use in both LIBs and NIBs.

Conversion materials and alloying materials in general, offer a promising approach to provide higher capacities for energy storage devices since the intercalation of the ions is not limited to the existing sites of the host structure but reversible conversion reactions of the electrode materials into lithium-rich phases occur.[9, 10] However, due to large volume changes, high voltage hysteresis, and the associated shortened cycle stability, there are technical hurdles with these electrode materials which have so far prevented their commercial application.[11] A promising laboratory-scale method for successfully utilizing the capacity of the conversion and alloying materials is to combine them into a composite material. Embedding the materials in a stable, conductive matrix can improve the electrical conductivity, enable highly efficient ion-electron transport properties, and rapid charge-discharge rate of the composite/hybrid materials.[12] Carbon hybrid materials, which are the most popular combined materials for electrodes because they are inexpensive and abundant, also shorten the diffusion paths for ions and electrolytes through unique structures such as reticulated, hollow, porous, and vertically aligned nanocomposites.[13, 14] However, hybrids with the use of 2D materials are also very popular which provide structural stability since the volume of the 2D nanomaterial changes only minimally during alkali metal transport. A composite/hybrid structure of a conversion/alloying material can thus maintain the structure after cycling, even when subjected to volume expansion, while the composite/hybrid serves as a conductive additive, a protective layer, and a buffer for strong volume expansion.

The use of hybrid materials is not limited to energy storage in LIB and NIB technology. However, it can also be successfully used, for example, as an electrode material in a seawater battery, which generally enables the storage of electrochemical energy through the combination of a sodation/desodation anode and an electrolysis cathode, requiring only pure seawater as the electrolyte.[15] By enabling the seawater battery to be used as an energy storage device and a successful desalination device, the prospect for sustainable, environmentally friendly, performance-oriented, and cost-effective applications at the interface between energy and water is evident. Specifically, vital access to clean water has also become a growing concern in recent years due to the ever-growing economy and

human population.[16] Although about 71% of the earth's surface is water, most is saltwater and thereby not directly suitable for use as drinking water.[17] In addition to seawater batteries, capacitive deionization offers an energy-efficient electrochemical desalination method compared to typical desalination technologies such as reverse osmosis, multi-stage flash distillation, or electrodialysis.[18] Capacitive deionization describes a process for the separation of ions from an aqueous solution in which, with the aid of an applied electrical field, ions in an aqueous medium can be adsorbed and stored in different electrode materials.[19]

After the successful use of the electrode materials and the batteries, the end of life of the individual parts will also be reached at some point. Their whereabouts must be discussed extensively to ensure this is done as efficiently and environmentally friendly. Due to the constantly new openings of giga factories and the increase in electric cars, a large return of used battery modules can be expected in a few years. One possibility is the recycling of individual materials, whereby expensive battery materials used in large quantities in electric cars can be recycled and reprocessed through simple washing steps, thus offering the chance for a second-life battery.[20, 21] On another level, lithium, which plays a central role in the energy transition and has thus become a key industrial and strategic element in electromobility, can be recycled. In addition to the limited reserves, the environmental protection aspect and the sustainability concept also play a significant role in increasing production numbers. In the future, a certain percentage of the freshly produced battery must be made of recycled material. A promising technology for recovering lithium species from spent batteries must consider economic and ecological aspects. In this context, particularly interesting are ion-selective electrochemical methods that yield highly enriched LiCl, which can be returned to the cycle of energy storage technologies. In summary, this work reports different (hybrid) materials and their application at the interface of energy, water, and recycling.

2 THEORETICAL BACKGROUND

2.1 Electrochemical energy storage systems

Electrochemical energy storage (EES) is essential for implementing sustainable energy technologies.[22-24] With the society striving for renewable energy, various technologies ranging from solar cells, wind tubes, biomass, hydropower, and geothermal energy are already been well established and under growth to provide future energy demand in a renewable manner. In order to flexibly provide this generated electricity to consumers, reliable and efficient energy storage systems are needed. In the Ragone diagram (**Figure 1**), different energy storage technologies are compared according to their specific power and energy.[25] Supercapacitors, for example, can provide energy in a matter of seconds (high power density), have an extended lifetime, and are highly efficient and maintenance-free.[26] The drawbacks of supercapacitors with their considerably higher self-discharge rate than batteries or the low voltages resulting in a lower amount of energy stored per unit mass compared to electrochemical batteries.[27] This is about 3 Wh kg^{-1} to 5 Wh kg^{-1} for a supercapacitor than 30 Wh kg^{-1} to 40 Wh kg^{-1} of a battery. Further, the energy density is commonly only about a fifth to a tenth of a battery.[28] On the other hand, fuel cells offer a high energy density but require a long time (several hours) to charge and discharge, limiting their practical application, for example, in the automotive industry.[29] Lithium-ion (and post-lithium-ion) energy storage systems offer a compromise between energy density and power density and thus provide an attractive choice for a wide range of applications due to its availability and well-established supply chain and market presence, the current battery of choice for mobility.[30]
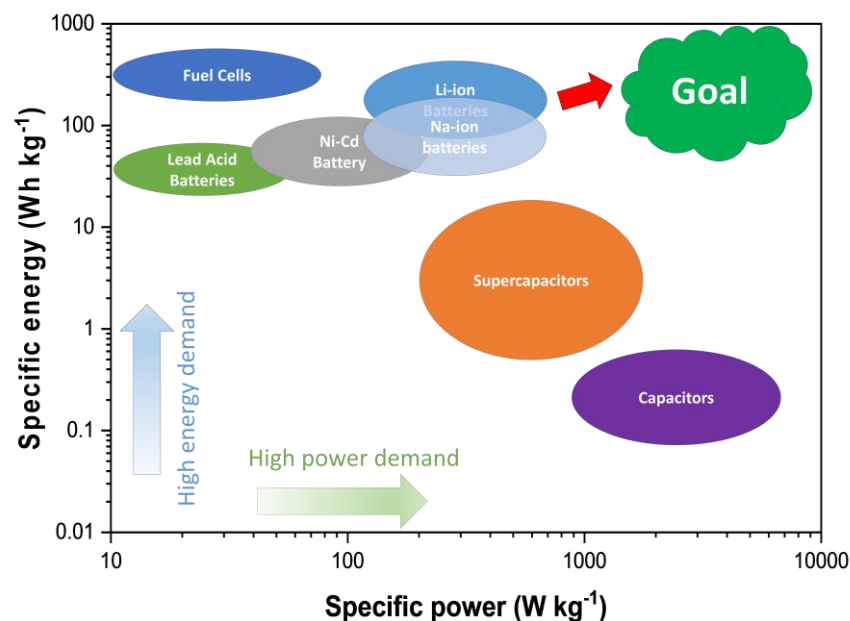
Figure 1: Ragone plot for different energy storage systems.[25]

2.2 Batteries

Batteries can store electrochemical energy in a reversible or non-reversible manner, known in the field as rechargeable or non-rechargeable batteries, respectively. Due to a difference in the electrode chemistry on the cathode versus anode side, they provide a voltage source to drive the electric current in circuits. The functioning of batteries is based on the electrical charge processes in liquids or solids, whereby the electrical charge is delivered. In the late 18th century, Alessandro Volta explored converting chemical energy into electrical energy, leading to the first functional battery in 1800.[31] Strictly speaking, the term battery means an interconnection (usually series connection) of several cells. A cell is the basic, smallest electrochemical current-producing unit of a battery, consisting of two electrodes, an electrolyte, the separator, and the housing. One can further distinguish between the technologies of primary and secondary batteries.[32] The term primary element refers to a galvanic element whose stored energy can be extracted as electrical energy. This process is not reversible, and batteries have to be discarded after the expiration of their lifetime. Primary batteries include, for example, alkaline LIBs, zinc-carbon batteries (Leclanché), alkaline zinc-manganese dioxide cells, and metal-air-depolarized batteries.[33] In contrast, secondary elements can be recharged with electric current, and the redox processes for electrical energy storage can occur reversibly. Examples of this type of technology include lead-acid batteries, Nickel-cadmium, nickel-metal hydride, LIBs and alkaline manganese dioxide-zinc.[33]

2.2.1 The lithium-ion battery (LIB)

The concept of lithium-ion batteries (LIBs), which is based on the formation of lithium compounds through the storage of lithium ions, was first presented in a conference lecture by Chilton Jr. and Cook at the fall meeting of the Electrochemical Society in Boston in 1962.[34] Until the first commercially available secondary LIBs by Sony in 1991, the initial proposals were further developed by various scientists such as Armand,[35] Goodenough,[36] and Lazzari & Scrosati.[37-39] A Nobel Prize for the development of the LIB was awarded to Goodenough, Whittingham, and Yoshino in 2019. These state-of-the-art LIBs typically feature a negative graphite electrode and a lithium-containing transition metal oxide (e.g., LiFePO$_4$ (LFP), LiMn$_2$O$_4$ (LMO), or LiCoO$_2$ (LCO)) positive electrode. LIBs are more compact, powerful, and flexible than other secondary battery types. Since its introduction, the LIB has revolutionized the battery market with high storage capability, stable performance, high power density, high energy density, high output voltage, and relatively long cycle life.[40, 41] To date, the research efforts aim to improve further safety, power, energy density, and battery lifetime. The main focus of the future battery research is on improving electrode materials and electrolyte systems. A drawback LIBs need to suffer from is the limit of the relative abundance of lithium and the resulting high cost. This is why energy storage systems beyond lithium are of high interest.

2.2.2 The sodium-ion battery (NIB)

Sodium-ion batteries (NIBs) were initially studied in parallel with LIBs in the 1970s and 1980s,[42] with LIBs emerging as the favorite due to their properties. Initially and until beyond commercialization, this technology has received significantly more attention. However, due to the steadily increasing demand for batteries and the continuous quest for sustainable energy storage in various sectors of society, there is a constant search for promising alternative energy storage devices. This is additionally driven by the simultaneous shortage of natural lithium resources and their shortage in supply, which consequently leads to a significant price increase for LIBs.[6]

Sodium is one of the most abundant elements in the earth's crust (for example, as NaCl in seawater) and the second lightest alkali metal after lithium.[43] On this basis, the sodium-ion battery could present a cheaper and more sustainable alternative for energy storage.[44] The redox potential of sodium (E_0 (Na^+/Na) = -2.71 V vs. standard hydrogen electrode) is only 0.3 V higher than that of lithium. Therefore, it is expected that there should not be a large drop in energy density compared to LIB technology ((E_0 (Li^+/Li) = -3.04 V vs. standard hydrogen electrode).[43] This allows, in principle, a straightforward technological implementation into battery technology similar to LIB. Since Na and Li ions have similar intercalation chemistry, much of the existing LIB research could be transferred to NIBs. In contrast, NIB manufacturing could be easily implemented into existing industrial practices. In addition, sodium-ion batteries, unlike most common LIBs, do not require rare or critical raw materials such as cobalt, nickel, and manganese.[45] Therefore, NIBs are expected to offer the possibility of cheaper production costs by combining already established knowledge gained from LIB with high natural abundance and inexpensive raw materials.[46] In addition to NIB technology being more environmentally friendly and more socially responsible to manufacture, copper current collectors required for LIB can be replaced by lighter and cheaper aluminum.[46, 47] NIBs are also less flammable and therefore safer, and score points for their cycle life and temperature resistance.[48]

Good power density also ensures good fast-charging capability and speed of energy delivery. Due to this fact, combined with the resulting price reduction and the more environmentally friendly and simpler production, NIBs are a promising and cheaper alternative to LIBs. However, the limited operating lifetime of sodium-ion batteries to date has prevented their widespread use. Also, the fact that sodium ions are about three times heavier than lithium ions means that NIBs would have to be significantly heavier for the same performance. Due to the higher ionic weight, Na^+ ions also move much slower in the electrolyte. Also the energy density of NIBs is sometimes lower than that of their LIB counterparts since about ten percent of the power is lost due to the 0.3 V lower cell voltage.[49, 50] As a result, comparable NIBs would currently not only be significantly heavier but also considerably

larger, limiting their use in everyday applications (portable electronic devices, electromobility) whereas stationary systems for energy storage can make perfect use of this technology.[51]

Tremendous research efforts are invested in optimizing NIB technology. For example, the Chinese battery manufacturer CATL (Contemporary Amperex Technology) has even announced the production of NIBs for mobile use in 2023. CATL is relying on an analogue of Prussian blue, Prussian white, as the positive electrode material while hard carbon serves as the negative electrode.[52] Compared to Prussian blue (iron hexacyanoferrate (II/III)), which is mainly known for its use as an inorganic color pigment that gives jeans their characteristic blue color, Prussian white has some iron atoms replaced by sodium atoms. Therefore, Prussian white cathodes exhibit high-speed rate kinetics for sodium ion insertion/de-insertion at relatively high potentials.[53]

2.2.3 Concept and mechanism

Batteries can store chemical energy and convert it into electrical energy through electrochemical processes. This process is based on the exchange of electrons between two redox pairs due to simultaneous spontaneous reduction and oxidation reactions at the electrode.[54] Classically, the electrochemical full cell consists of an anode and a cathode material. These two are separated by a microporous membrane (separator), which is permeable to electrolyte and Li^+/Na^+ ions but prevents a short circuit by introducing a physical barrier.

Figure 2 displays the working principle of a typical alkali-ion battery full cell by the example of a secondary sodium-ion battery system and corresponding characteristic electrode materials (Prussian white as a cathode and hard carbon as an anode). The charge carriers (Na^+ ions) are located in the electrolyte surrounding the electrodes, which usually consists of an inorganic dissolved salt (dissociated lithium/sodium conducting salt, depending on the battery) in an organic solvent. The charge storage mechanism of the sodium-ion battery is based on the migration of sodium ions back and forth between the electrodes during charging and discharging, accomplished by their intercalation/deintercalation in the host structures/materials. Due to a gradient between the two electrodes' chemical potentials, ions' diffusion in the electrolyte from the anode to the cathode occurs in the cell. This leads to a discharge of the battery whereby the electrons, as the carrier of electricity, simultaneously flow from the cathode via an external electrical connection (cable connection) to the anode (aluminum as a current collector). When the cell is charged, this process is reversed, so sodium ions diffuse from the cathode through the electrolyte and the separator to the anode by applying an external voltage as a driving force. A redox reaction takes place at the electrodes, which is divided into two half-reactions. During discharge, oxidation at the anode releases electrons that cause reduction at the cathode after passing through the external circuit.[55]
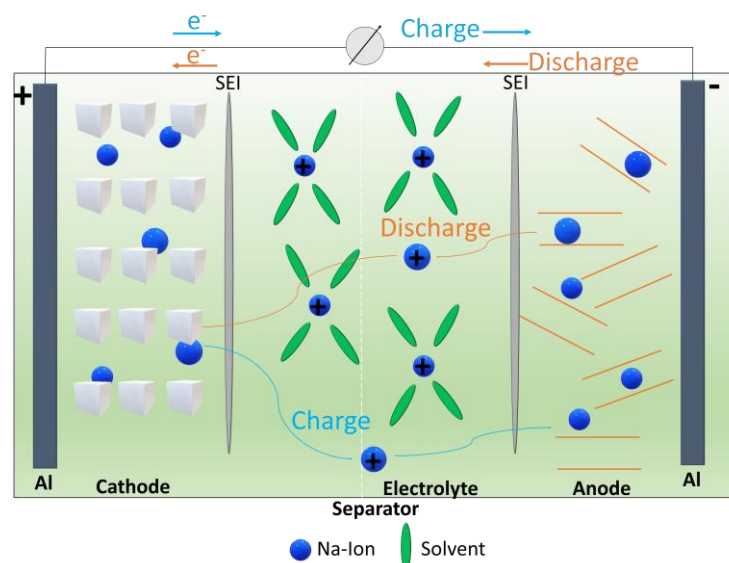
Figure 2: Working principle of alkaline ion batteries by an example of a sodium-ion battery.

During charging, ions removed from the cathode are reversibly incorporated into the host lattice of an anode (e.g., hard carbon; **Figure 2**) compound, known as intercalation. The carbon lattice of the electrode is reduced during intercalation. During discharge, the reverse process takes place. In this process, the Na^+ ions migrate from the anode back to the cathode and return to their original state. In deintercalation, the electrons migrate from the negatively charged electrode to the positively charged electrode via an external electrical connection.[37, 55] A sodium-ion battery can store and release electrical energy, while the energy released by the redox reaction can be used to do electrical work.[56] The overall reaction in a NIB anode is given by the following equation:

$$NaC_x \underset{Charge}{\overset{Discharge}{\rightleftharpoons}} xC + Na^+ + e^- \tag{I}$$
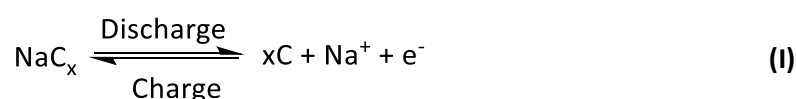
2.2.3.1 Solid-electrolyte interphase (SEI)

The solid-electrolyte interphase (SEI) is a passivation layer formed by electrolyte reduction at the anode of the alkali-ion battery.[57] This layer protects the active electrode material from direct electrolyte contact and, therefore, from further electrolyte reduction while still allowing Li^+/Na^+ transport.[58] If continuous contact between electrode and electrolyte occurs, more and more parts of the electrolyte/electrode would slowly decompose further. In the course of the battery lifetime, further layers are naturally built up on the SEI by chemical processes.[59]

Once the SEI is formed well, the layer should demonstrate high ion conductivity and negligible electronic conductivity. Optimally the SEI layer should be strong and flexible to accommodate volume changes (varies strongly during the process) of the electrode material during electrochemical cycling providing a uniform thick surface.[59] Chemically, an optimal SEI should preferably consist of stable components before metastable compounds to limit lithium/sodium losses to the first cycles and achieve full capacity.[60, 61] Simultaneously, the SEI layer should be as non-dissolvable as possible since lower capacity retention is expected due to continuous rebuild and repair.[62] Too thick SEI layers lead to a decrease in the battery cell capacity since some of the lithium ions dissociated in solutions are bound from the electrolyte, which consequently can no longer participate in the electrochemical reactions.[63]

If the SEI layer is too thick, the alkaline ion diffusion is also slowed, the current transport resistance increases, and the ohmic resistance is significantly higher. In addition, the morphology and elemental composition of the SEI layer have a crucial impact on dendrite growth.[64] A dendrite describes a characteristic tree-like structure of crystals that grow when the molten metal solidifies. In the battery context, dendritic growth is attributed to the depletion of ions near the anode interface at current densities higher than the limiting current density.[65] Lithium dendrite growth in batteries not only causes capacity fading and a limited lifetime, it also causes severe safety concerns.[66] To achieve stable and reversible cycling performance an option is to design and control the improved growth of the SEI layer. This can be done for example by adding electrolyte additives that have lower reductive stability and therefore protect the electrolyte from decomposition.[67]

2.2.4 Components and active materials

2.2.4.1 Cathode

Cathode materials refer to the electrochemically active material in the positive electrode, each undergoing a redox reaction during charging and discharging (reduction while discharging and oxidation during the charging process). In contrast to the anode materials, the cathode materials should preferably have a high potential, while a high energy density is possible due to the large potential differences.[68] Extensive study of optimized electrode materials led to layered oxide $LiCoO_2$ (LCO) as cathode material in the first commercialized LIB that was able to lithiate and delithiate reversibly and stably.[36, 68] In subsequent years, other materials such as olivine-structured $LiFePO_4$ (LFP), layer-structured $LiNi_xMn_yCo_{(1-x-y)}O_2$ (NMC), spinel-structured $LiMn_2O_4$ (LMO), and olivine-type $LiMnPO_4$ and many more have been investigated.[69] Since then, LCO and NMC have been widely and successfully used as cathode materials in commercial batteries,[70] where the future focus is to increase energy density and reduce costs, and mainly to promote eco-friendly alternatives.

In NIBs, oxides such as $NaMO_2$ (M=V, Vr, Ni, Co, and others) are frequently used in layered structures as cathode materials.[71] The difficulty here compared to lithium metal oxides is that the oxygen is often not very strongly bound in the electrode, and the electrolyte can be oxidized quickly by the electrode material. In addition, many of the metals used, such as nickel and cobalt, are critical and scarce.[71] A promising alternative seems to be materials such as phosphates with an olivine structure ($NaFePO_4$).[72-74] Also successfully used are three-dimensional framework structures, polyanionic compounds, sodium superionic conductors (NASICON), and many other materials.[71, 75-77] Prussian blue and its analogues are very popular in LIBs and promising materials for NIB cathodes due to their high working potential, high theoretical capacity, ease method of synthesis, and low toxicity. Prussian white, the completely reduced and sodium-containing form of Prussian blue, can deliver two electrons per formula mass, raising the theoretical capacity to 170 mAh g^{-1}.[78-81] In addition, bypassing the need for a reactive sodium-loaded anode in cell assembly could significantly ameliorate the manufacturability of commercial batteries.[79]

2.2.4.2 Anode (Intercalation, alloying, conversion)

A good anode material is an electrochemically active material used in the negative electrode with a low redox potential leading to high full-cell voltage. This is aimed to be combined with a high specific discharge capacity while donating alkali ions and electrons. In the early stages of lithium battery technology, lithium foil was initially used as the anode material, which has the highest theoretical capacity of 3860 mAh g^{-1} by batteries that rely on Li-ion storage.[37, 82] However, due to the high reactivity and the increased dendrite formation with the associated short circuits, thermal runaway, and short lifetimes, multiple alternatives have been explored.[37] **Figure 3A** presents various cathode and anode materials for LIBs along with their essential properties (energy density, environmental friendliness, safety). By using intercalation materials such as lithium titanate ($Li_4Ti_5O_{12}$, LTO), dendrite formation can be prevented or significantly reduced. However, LTO has disadvantages with a high redox potential of 1.55 V vs. Li$^+$/Li as well as a low theoretical capacity of 175 mAh g^{-1}.[83-85] Graphite has been categorized as a very important anode active material in state-of-the-art LIBs due to its environmental friendliness, natural occurrence, safety, low cycling life, low cost, theoretical capacity of 372 mAh g^{-1}, and as a low Li-ion intercalation potential below 0.3 V vs. Li$^+$/Li.[60, 86, 87] In general, the anode materials should have high power and energy density and a long lifetime, while also being cost-effective. However, graphite does not play a significant role in NIBs. Due to their twice as large ionic radius when comparing to Li, complicated intercalation between the tight graphite layers, intercalation of sodium ions into graphite is not preferred. In addition, the formation of stable sodium-hydrocarbon bonds is lacking due to the higher redox potential and also the generally slower kinetics with simultaneously significantly higher energy requirements for storage, leads to unfavorable conditions.[6, 38, 87, 88]
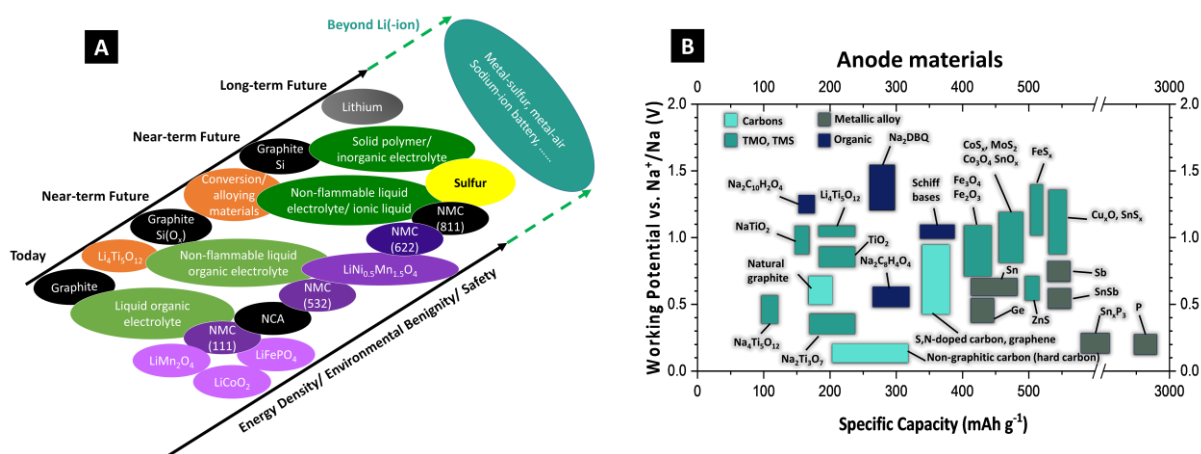
Figure 3: Overview of the established electrode materials for LIB and NIB A) Representation of different established cathode and anode materials for LIBs characterizing their important properties (energy density, environmental friendliness, safety) Adapted with permission.[89] Copyright 2018, Elsevier. B) Illustration of theoretical capacities of various anode materials for application in NIBs in a capacity vs. potential plot. Adapted with permission.[15] Copyright 2022, John Wiley and Sons.

In recent years, the application of carbonaceous anode materials, which are abundant, inexpensive, non-toxic, and offer high safety for NIB has played a significant role. From the beginning of NIB research the focus was on hard carbon, which in 2000 already had a high reversible capacity of 300 mAh g^{-1}, but the cycling ability was not satisfying for practical applications.[90] From 2010 on, the search for a suitable anode material intensified, starting from the adoption of promising LIB materials for NIB. Many metals/alloys, metal oxides, metal sulfides, metal phosphides, and carbonaceous materials, such as expanded graphite, carbon nanotubes, graphene, and hard carbon, were investigated.[55] **Figure 3B** overviews various established and researched NIB anode materials.

Due to the rapidly increasing performance requirements of the battery industry, carbon materials and intercalation materials with low-rate capability, limited space for ion intercalation, and moderate specific capacity must be replaced by next-generation electrodes. Thus, anode materials based on different reaction mechanisms with alkaline ions are developed in further research operations with the possibility of higher specific capacities. Electrode materials can be grouped into three categories according to the nature of their electrochemical reaction with alkaline ions (**Figure 4**) and their comparisons regarding important parameters for electrochemical application (**Figure 5**). The subdivision of the electrode material categories is valid for negative and positive electrode materials, respectively.
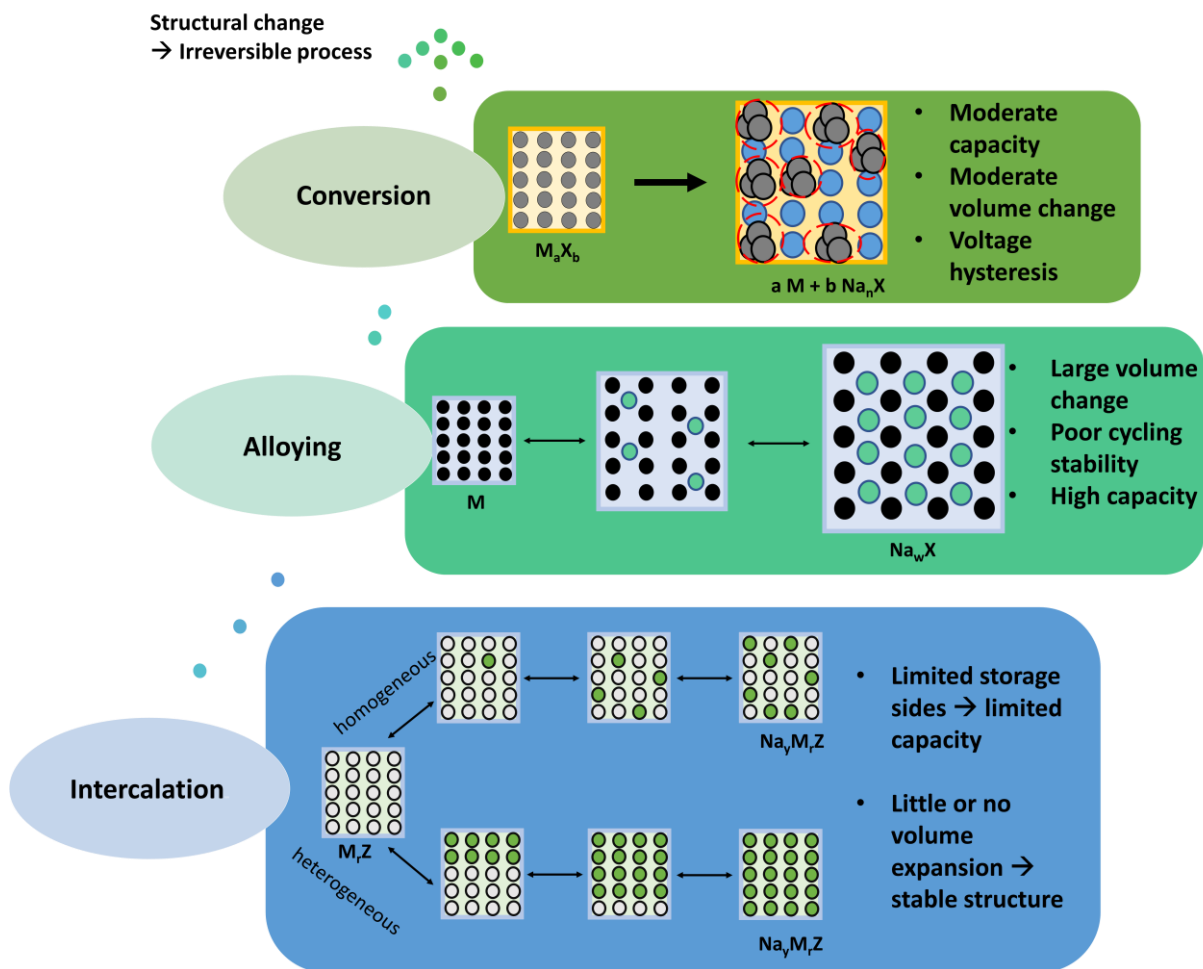
Figure 4: Schematic diagram of different charge storage mechanisms of electrode materials in alkaline ion batteries as an example of NIBs.

Intercalation-type materials show electrochemical activity while intercalating Li or Na ions between existing layers or free lattice sites of a host material. During the intercalation process, the active material accepts electrons while causing a simultaneous reduction of the active material lattice.[6] This reaction mechanism results in a limited stability range since the active material backbone is not changed while ion conductivity and electron conductivity are combined.[91, 92] However, the large volume expansion/contraction associated with the introduction/extraction of alkaline ions into the host structure can severely damage the electrode texture, resulting in possible loss of electrical contact and subsequent rapid capacity degradation.[93]
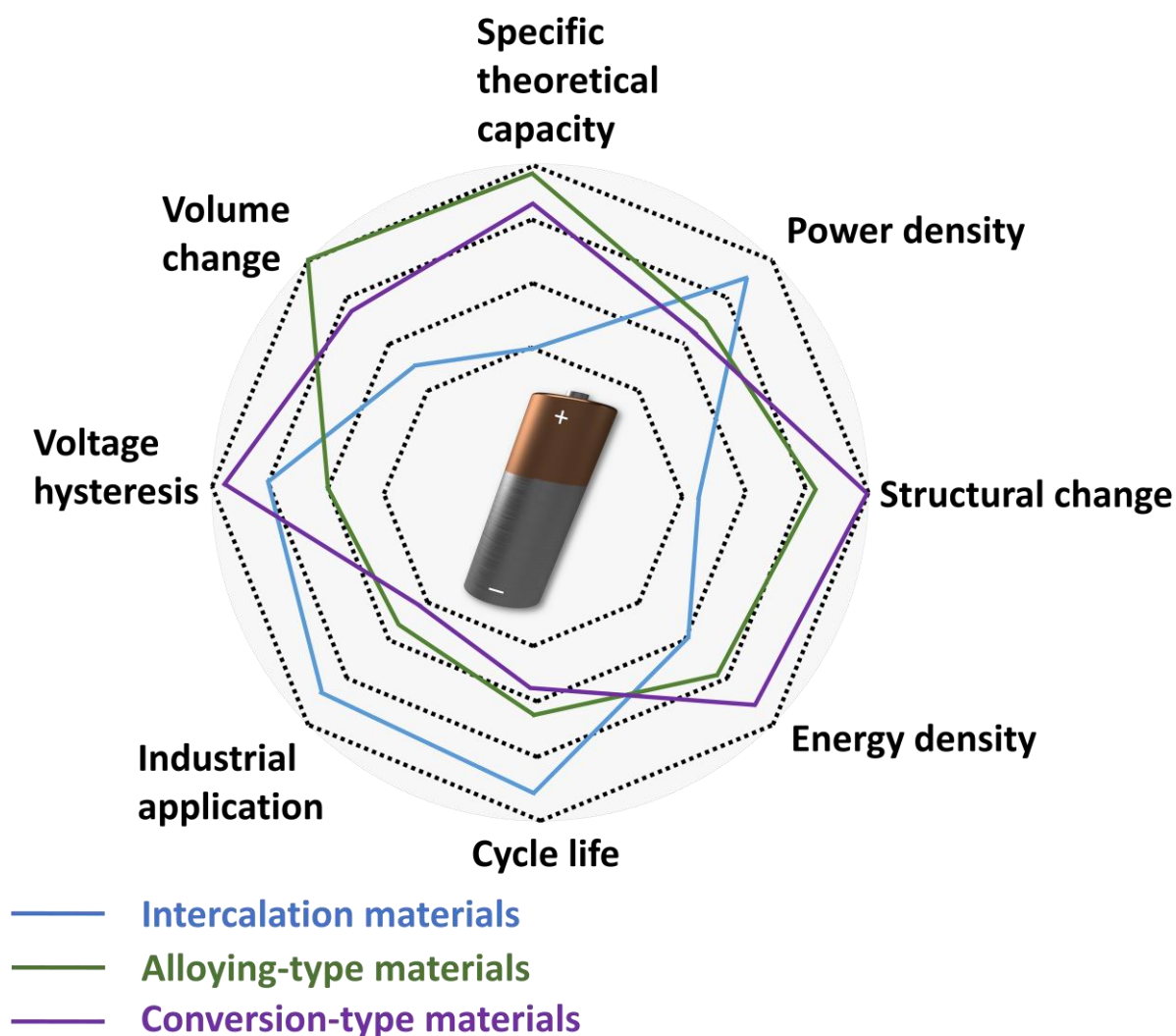
Figure 5: Comparison of different parameters for intercalation, alloying, and conversion type materials.

Alloying materials form Li/Na-rich intermetallic compounds during ion introduction. Group IVA and VA elements of the periodic table, such as Si, Ge, Sn, P, Sb, and Bi, can alloy with Li and Na to form alkali-ion-rich alloy phases. High theoretical alkali ion storage capacity between 660-4200 mAh g^{-1} calculated for lithium alloying formation $Li_{22}Si_5$/$Li_{15}Si_4$ (4200 mAh g^{-1}, 3579 mAh g^{-1}),[94, 95] $Li_{22}Ge_5$/$Li_{15}Ge_4$ (1623 mAh g^{-1}, 1384 mAh g^{-1}),[96] $Li_{22}Sn_5$ (990 mAh g^{-1}),[97] Li_3P (2596 mAh g^{-1}),[98] and Li_3Sb (660 mAh g^{-1}).[97] For sodium alloying compounds with respective theoretical capacities like NaSi (954 mAh g^{-1}),[99] NaGe (369 mAh g^{-1}),[100] $Na_{15}Sn_4$ (847 mAh g^{-1}),[97] Na_3P(2596 mAh g^{-1}),[101] and Na_3Sb (660 mAh g^{-1})[97] can be formed. The alloying reactions to produce the above alloy chemistry often take place at low potentials and are therefore considered for the negative electrode material. In addition, the working potentials of alloying-based electrode materials are suitable for application as an anode in LIB and NIB, while only

slightly extending the scanned potential range compared to those in typical insertion anodes (i.e., hard carbon and typical Ti-based compounds).

Although alloy-based materials admittedly have several advantages, this class of materials also has to contend with problems that have so far kept them from practical application.[102, 103] A major disadvantage of alloy materials in energy storage applications is the considerable loss of capacity during charge, and discharge cycles. The reason for this can be due to the huge volume change, over the course of cycling, which can lead to aggregation and subsequent pulverization of the active component of the electrode. As a result, the electrical contact is weakened, and the conductivity is reduced, slowing the reaction kinetics. In addition, the SEI layers on the surface must constantly reshape themselves due to the volume change during charging and discharging, which creates the risk of an excessively thick SEI layer on the electrode. This increasingly thick layer can act as an insulating layer, which also slows down charge transfer process, possibly leading to a strong capacity decline.[104, 105] Often, in addition, a low initial Coulombic efficiency can be observed during cycling, that is resulted from unstable, quick and easy dissolving SEI films. Furthermore, another critical point is raised by intrinsic low electron diffusion coefficients of these type of materials, limiting their cycle lifetime and provided capacities at high rates.[106, 107]

The third category pertains to conversion materials, where a phase transformation conversion occurs during the electrochemical process. This group of materials is distinguished by minimum binary transition metal compounds like metal oxides, phosphides, sulfides, or fluorides which form metallic nanoparticles inside a matrix when reacting with alkali ions.[108] In general, the redox potential increases with the ionicity of metal to oxide, sulfide, phosphide, and fluoride bonds resulting in a lower redox potential for oxides, sulfides, and phosphides. Therefore, they are suitable for negative electrodes. Fluorides show high redox potential with a possible application as the positive electrode.[109, 110] Generally, a conversion-type material completely transforms its structure during the cycle, creating new compounds with entirely new properties. Promisingly, the stored energy can be significantly increased while the battery weight can be reduced. However, as with all other materials, there are major drawbacks such as large voltage hysteresis and low energy efficiency during charging and discharging processes, which has hampered the commercial application of conversion materials so far.[111, 112] Therefore, improvements of the class of high capacity alloying and conversion-type materials are of high research interest in the state-of-the-art literature.

2.2.4.2.1   MXene

2D materials exhibit many fascinating properties not found in their bulk counterparts and therefore promise a wide range of applications from photocatalysts,[113-115] electrocatalysts,[113-115] senors,[116-118] biomedical applications, [119-121] to the fields of water remediation[122, 123] and energy storage[124-126]. MXenes are a relatively new class of 2D layered transition metal carbides, nitrides, and/or carbonitrides with combined properties such as good electronic conductivity, flexibility, and hydrophilicity.[127] The synthesis of the MXene structures is generally achieved by liquid etching the A-layers from the bulk MAX phases, which are distinguished as ternary carbides or nitrides with the general chemical formula of $M_{n+1}AX_n$ (M corresponds to an early transition material such as Ti, Mo, or Nb; A is an A group IIIA or IVA element such as Al, Ge, P; X represents carbon and/or nitrogen and n=1, 2, 3, 4).[128] The unit cells have nearly close-packed layers of M_6X octahedra intercalated between the A-element layers, with the X atoms occupying the octahedral sites between the M atoms.[129] Thereby, the M_6X octahedral are linked to each other via edge-sharing.[130] Since the M-X bonds (ionic and covalent bonding's) are much stronger than the M-A (metallic) bonds. It is possible with the use of a strong etchant like HF to etch the A-layer out of the compound resulting in the 2D MXene structure $M_{n+1}X_n$.[127, 131] Through the process of etching out the A-layer, the MXene is always terminated with surface functional groups, such as hydroxyl (-OH), oxygen (=O), and/or fluorine (-F), completing the general formula of $M_{n+1}X_nT_z$ (T_z=surface functional groups).[132, 133] In **Figure 6,** an overview of different compositions of MAX and MXene phases with possible surface terminations and intercalated ions information is presented.

Figure 6: Periodic table showing compositions of MAX and MXenes with corresponding surface terminations and intercalated ions specification.

Due to the wide range of combinations of elements and synthesis conditions, a vast spectrum of chemical and physical properties with potential for various applications can be obtained. Since its discovery in 2011, $Ti_3C_2T_z$ MXene has been the most common and best-explored MXene structure combining high electrical conductivity (up to 24,000 S cm^{-1} for $Ti_3C_2T_z$),[134, 135] tunable surface functionality,[135, 136] liquid-phase processability[137] and outstanding mechanical properties.[135, 138] One way to control the properties of MXene materials is to regulate the number of layers in the crystals and the film thickness. Single-layer and few-layer MXenes have advantageous properties, such as a low ion diffusion barrier, a low open-circuit voltage, and a high specific surface area.[139] Single-layer and few-layer MXenes can be explored via various preparation methods, including HF etching, molten salt etching, electrochemical etching method, chemical vapor deposition, self-assembly, and template-assisted growth.[139]

Among various two-dimensional conductive structures that have improved the mechanical properties of the different electrode systems, MXenes have attracted great interest in the field of energy storage or electrochemical desalination with their ability to host a variety of ions and molecules through intercalation. Due to the large pseudocapacitance of MXenes,[140] which exceeds the energy storage capacity of most other capacitive materials, MXene materials provide a nearly ideal intercalation material with rapid ion insertion between layers. After the fabrication of free-standing and binder-free electrodes, a high capacitance of >300 F cm^{-3} could be obtained in aqueous lithium or sodium sulfate media while successfully intercalating larger ions, such as ionic liquids or organic salts.[141, 142]

For example, Srimuk et al. 2016 employed the highly capacitive and reversible intercalation and deintercalation of MXenes for successful application as electrode materials for water desalination via CDI.[143] With the ion intercalation mechanism between the two-dimensional nanolamellar, stable performance for 30 cycles with a salt adsorption capacity of 13±2 mg g^{-1} while applying a cell voltage of 1.2 V and a 5 mM saline solution was achieved.[143] During the following years, the MXene and combined hybrid materials were widely explored in their application as cathode and anode materials for capacitive deionization in different salt concentrations and ion species.[144-147]

Fast energy storage benefits from the properties of tunable materials and scalable synthesis. MXenes can exhibit high capacitance (especially volumetric capacitance) along with metal-like conductivity, making them promising active materials for developing supercapacitors with high power and energy density. The first report of MXene as a supercapacitor electrode dates back to 2013 when Lukatskaya et al. showed an improved performance in basic solutions, such as KOH and NaOH combined with free-standing binder-free $Ti_3C_2T_z$ electrodes.[148] Due to the high flexibility, a volumetric capacitance of up to 350 F cm^{-3} could be obtained.[148] Due to environmental sustainability and safety aspects, the MXene etching was driven towards LiF/HCl or completely fluoride-free etching, leading towards new insights

for supercapacitor electrode materials.[149, 150] Li et al. successfully synthesized $Ti_3C_2T_z$ powder with 92 mass% purity via a 27.5 M NaOH treatment at 270 °C. The resulting F-free $Ti_3C_2T_z$ film electrodes in 1 M H_2SO_4 deliver a gravimetric capacity of 314 F g^{-1} and volumetric capacitance of 511 F cm^{-3} at 2 mV s^{-1}.[151] Thereby H_2SO_4 at time identifies the most promising electrolyte for MXene with extended voltage window of 1 V.[152,153] Overall aqueous electrolytes are extremely attractive in terms of environmental friendliness and cost. However, the possible voltage window is limited to 1.2 V due to the electrolysis of water, which limits the energy density of the supercapacitor cells enormously. Therefore, organic electrolytes for supercapacitor application are explored. For example, Dall' Agnese et al. reported in 2016 that EMIM-TFSI (1-ethyl-3-methylimidazolium bis(trifluoromethylsulfonyl)imide) in acetonitrile as an organic electrolyte, which boosted the electrochemical performance of the MXene/CNT materials to 85 F g^{-1} and 245 F cm^{-3} at 2 mV s^{-1}.[154] Further Liang et al. reported pre-intercalated Mxene with increased interlayer spacing of ≈2.2 nm while delivering a large 257 F g^{-1} (1428 mF cm^{-2} and 492 F cm^{-3}) in neat EMIM-TFSI electrolyte leading to high energy density.[155] These conditions also make the application of different MXene materials optimal for use in LIBs and NIBs. Initially, the material was used without further modification as an electrode material. In 2012, for example, layered Ti_2C-based materials achieved a capacity of 110 mAh g^{-1} at 1C and 80 cycles as LIB anode material,[156] and $Ti_3C_2T_z$ achieved an increased intercalation capacity of 124 mAh g^{-1} at 1C after intercalation of dimethyl sulfoxide.[157] $Ti_3C_2T_z$ nanosheets can host Na-Ions in their lattice reversible via a two-phase transition and solid-solution reaction in sequence while delivering a long-term capacity of 69 mAh g^{-1} after 1000 cycles at 0.2 A g^{-1}.[158]

The intrinsic performance of MXene has so far been generally limited to the intercalation mechanism.[159] Accordingly, the resulting discharge capacity is also limited to lower values than alloy or conversion materials.[160] This is why over the past few years, it has become increasingly attractive to use the versatile MXene materials in combination with other electrode materials (mostly alloying- or conversion-type materials) with their complementary properties to improve the cycling behavior. The combination is expected to enhance the capacity of the MXenes while enhancing the structural stability of alloying/conversion hybrid and composites due to the minimal volume change of 2D materials during alkali-metal transport. Therefore, the occurring agglomeration, high volume expansion, and possible subsequent electrode pulverization can be avoided or reduced to improve long cycling life. Various promising anode materials for LIB/NIB which have been successfully processed with Mxene include Si, SiO, SiO_2, Sn, SnO_2 carbon filler, metal oxide, phosphorus, metal sulfide, and layered double hydroxide.[161-167]

Chen et al., for example, reported a nanosized SnO_2/MXene composite for application as anode material in NIBs which delivers a Na-storage capacity of 414 mAh g^{-1}, proper rate capability (300 mAh g^-

[1] at 0.2 A g^{-1}) and stable cycling performance (79% capacity retention after 100 cycles).[168] 2021 reported Liang et al. chemically-confined mesoporous γ-Fe$_2$O$_3$ nanospheres with Ti$_3$C$_2$T$_z$ MXene. The mesoporous γ-Fe$_2$O$_3$ nanosphere, composed of nanocrystalline subunits, is encased by Ti$_3$C$_2$T$_z$ MXene, which can effectively mitigate the volume change of the γ-Fe$_2$O$_3$ nanosphere as a shield and ensure a fast electron flow, resulting in a high-performance electrode for LIB. The Fe$_2$O$_3$@Ti$_3$C$_2$T$_z$ anode provides a reversible capacity of 1060 mAh g^{-1} at 0.5 A g^{-1} after 400 cycles. MXene composites also play a major role in combination with alloying-type materials. For example, Meng et al. used a black phosphorus quantum dot/ Ti$_3$C$_2$T$_z$ MXene nanosheet composite for application in electrochemical lithium and sodium ion storage which delivers a high capacity of 910 mAh g^{-1} at 0.1 A g^{-1}.[169] The work of Arnold et al. benefitted from the high electrical conductivity as well as the buffering of the volume change of the MXenes. Showing that through the optimized combination of antimony and MXene in a homogeneous distribution with optimal electrochemical addressability of all components, a specific capacity of 450 mAh g^{-1} at 0.1 A g^{-1} and 365 mAh g^{-1} at 4 A g^{-1}, with a capacity retention of 96% after 100 cycles was obtained.[170]

MXene structures, due to their excellent tunability and favorable properties, offer the possibility of various applications. In particular, for energy storage, electrochemical performance can be increased by MXene, significantly contributing to improved conductivity or serving as a buffer volume of alloying or conversion materials while contributing to capacity and being electrochemically active.

2.2.4.2.2   Antimony

Antimony is a silvery-white, lustrous, brittle semimetal that can also be found in nature in elemental form. More commonly, the mineral stibnite (Sb$_2$S$_3$) can be found, also called antimonite, which is used for industrial extraction of the pure element. Due to its high theoretical capacity of 660 mAh g^{-1}, high specific capacity, and easy antimony (Sb) availability, it is a promising anode candidate for high-energy alkali ion batteries.[171-173] Sb-based anodes are advantageous in terms of electronic conductivity due to the intrinsic electrical conductivity of antimony and the ease of fabrication of nanostructured electrodes, which are essential for facilitating sluggish electrochemical kinetics mainly in NIBs and potassium-ion batteries. Antimony with a relatively low alloying potential while forming Na$_3$Sb/ Li$_3$Sb and K$_3$Sb and low stacking density of puckered-layer structure is beneficial for ion diffusion and release of structural stress.

Nevertheless, the vast volumetric change (~ 400%) during the alloying and de-alloying process can lead to tremendous stress in the electrode, which leads to possible pulverization of the electrode material and the loss of the electrochemical conductive path, resulting in poor electrochemical performance. As anode material in alkali-ion batteries, crystalline antimony first reacts with the alkali metal (AM) to

form various amorphous AM$_x$Sb compounds. AMSb reacts with an additional alkali metal in the next step and forms crystalline cubic and hexagonal (which stabilizes at the end) AM$_3$Sb (**Figure 7**, **Equation (II)**). In the reverse reaction, the AM$_3$Sb alloy converts back to elemental antimony, which is then present in an amorphous form.

Alkali metal (AM) insertion

$$Sb \text{ (crystalline)} + AM^+ + e^- \longrightarrow AM_xSb \text{ (amorphous)}$$

$$AM_xSb \text{ (mono)} + 2\,AM^+ + 2e^- \longrightarrow AM_3Sb_{hex} / AM_3Sb_{cub} \text{ (crystalline)} \longrightarrow AM_3Sb_{hex}$$

De-sodiation

$$AM_3Sb_{hex} \text{ (crystalline)} \longrightarrow Sb \text{ (amorphous)} + AM^+ + e^-$$

Equation (II): Reaction equation of antimony with different alkaline ions and corresponding electrochemical process.

The volume change that occurs negatively influences the loss of the electrical paths and the SEI formation. Due to the constant expansion and contraction of the electrode composite, the SEI is also affected and repeatedly rearranged in each cycle, which can lead to the formation of a very thick SEI on the one hand and to constantly occurring side reactions on the other. This leads to a slowed-down reaction kinetics which strongly influences the electrochemical performance. In application, bulk antimony often results in capacity fading in the first cycles due to extensive volume extension. Darwiche et al. reported less than 20 cycles with stable cycling performance as a NIB anode.[174]

Relatively easy developments of electrolyte systems or improvements in electrode preparation may strongly influence the impact on electrochemical performance. For example, using SEI-forming fluoroethylene carbonate as an electrolyte additive in NIB develops good cycling performance for Na/Sb system compared to Li/Sb.[174] Thus, initial capacities of over 660 mAh g^{-1} can be obtained for Li/Sb systems that are fully lost after 140 cycles. For NIBs, however, stable capacities of 576 mAh g^{-1} at C/2 over 160 cycles have been reported. Further works have demonstrated the importance of choosing the right carbon additive, which not only improves the conductivity in the electrode but also serves as a buffering agent for volume changes during cycling. Pfeifer et al. reported that nanoscale carbon with round shape particles provides the best percolation in the electrode since the agglomerated Sb particles are homogeneously covered, and the applied current can be better distributed to all active material particles, resulting in improved high conductivity and superior rate performance.[175] In this way, an optimal composition of antimony nanoparticles with onion-like carbon was obtained, resulting

in electrochemical performance values of $490\,\mathrm{mAh\,g^{-1}}$ at $0.1\,\mathrm{A\,g^{-1}}$ and $300\,\mathrm{mAh\,g^{-1}}$ at $8\,\mathrm{A\,g^{-1}}$ (normalized to antimony including the carbon additive).
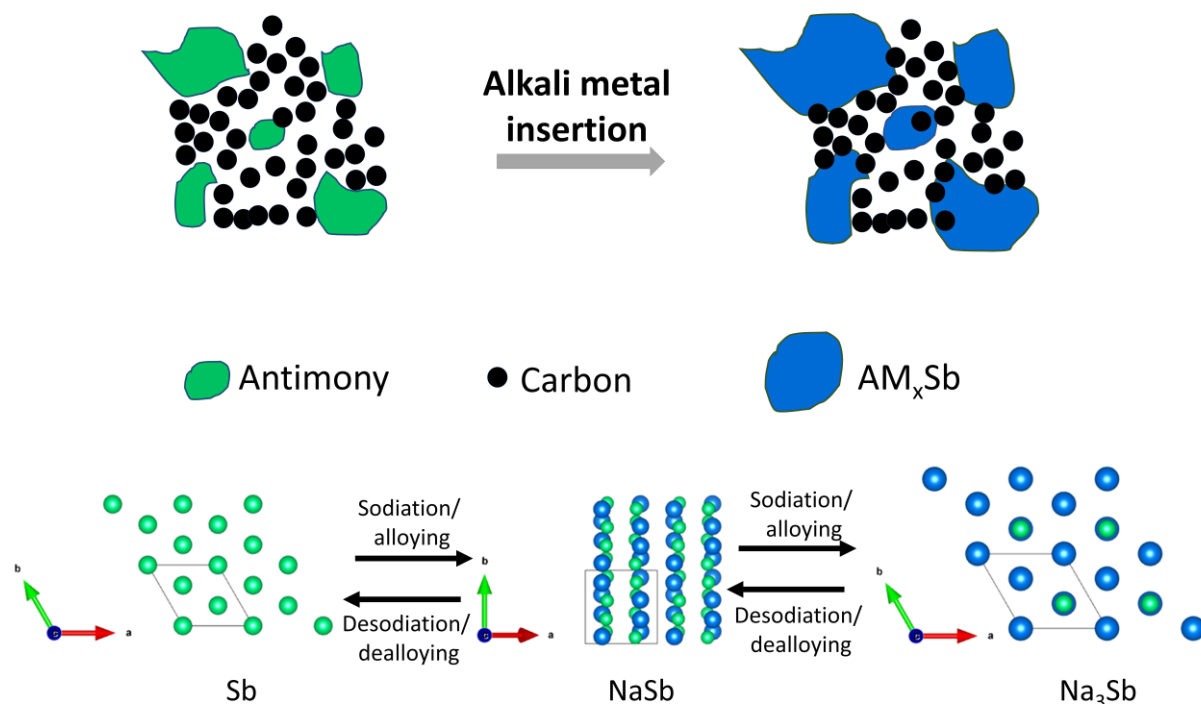
Figure 7: Representation of the mechanism and volume expansion of antimony alloying reaction during the electrochemical process, including a schematic drawing of sodiation/desodiation of antimony showing the crystal structures.

Novel designs of antimony nanostructures allow for counteracting the problem of substantial volume changes by shortening the alkali metal ion transport path and relieving stress-strain while the approach is limited.[176-179] To benefit from the promising antimony system, mostly approach of composite or hybrid formation is used, whereby the antimony particles are integrated into a composite of mostly carbon, thus maintaining the contact between the antimony particles and carbon during the charging and discharging process and additionally buffering the volume expansion.[171, 173, 176, 180, 181] The versatile antimony system is not only limited to elemental antimony. However, it offers the possibility of using other compound materials such as intermetallic antimony-based materials like Cu_2Sb, $SnSb$, or $TiSnSb$ or antimony chalcogenides like antimony oxides, antimony sulfides, antimony selenides, or antimony oxychlorides and many more.[173, 182]

Forming Sb-based intermetallic compounds leads to an improved electrochemical performance by having either only the antimony or both (or >2) of the components electrochemically active and stabilized by a matrix of the other metal during the charging and discharging process.[183, 184] For example, when applying SbSn nano-arrays as NIB anode, it delivered a capacity of $521\,\mathrm{mAh\,g^{-1}}$ at 5C

with a corresponding capacity retention of 82% after 800 cycles at 2C.[185] He et al. reported for intermetallic Cu_2Sb coated with amorphous carbon a reversible de-lithiation capacity of 477 mAh g^{-1} at 1C with capacity retention of 87%.[186]

Antimony chalcogenides (antimony oxides, sulfide, and selenide) react in a conversion-alloying mechanism mainly based on antimony reaction with favorable properties as anode materials for alkali-ion batteries. The conversion reaction products can contribute to electrochemical performance while forming a matrix preventing massive volume changes and agglomerations of antimony and stabilizing the electrode.[187, 188] With carboxy methyl cellulose and fumaric acid binder, Sb_2O_3 served as anode material in LIB with 611 mAh g^{-1} at 0.2 A g^{-1} after 200 cycles. Further, amorphous Sb_2S_3-embedded in the conductive graphite matrix exhibit stable 656 mAh g^{-1} at 1 A g^{-1} for 100 cycles when serving as NIB anode material.[189] Different morphologies of antimony oxychlorides, such as $Sb_4O_5Cl_2$ nanoparticles, $Sb_8O_{11}Cl_2$ nanoribbons, and nanowires, can provide an option to be applied as anode material in alkali ion batteries. While pure antimony oxychloride as NIB anode material often needs better morphology regulations, a composite with $Sb_4O_5Cl_2$ particles and graphene aerogel can result in an improved electrochemical performance with 400 mAh g^{-1} at^{-1}at 0.03 A g^{-1} after 50 cycles.[190-192]

2.2.4.2.3 Hybrids/composites

Hybrid or composites consist of two or more types of materials forming a matrix. Composite materials usually have two or more constituents with significantly different physical or chemical properties. Faradaic charge storage materials often suffer from low electric conductivity, while introducing a conductive additive by physical admixing in the context of composite formation overcomes the drawback.[193, 194] Hybrid nanomaterials, basically a subgroup of composite materials, are formed by combining an inorganic and organic material, often at the nanometer or molecular level, through a synthesis process.[194, 195] Hybrid materials are often obtained via an in-situ synthesis approach. At the same time, individual reaction components beforehand are deposited or synthesized from precursors leading to a final hybrid material.[196] Through the last years, tremendous efforts have been made to develop suitable hybrid materials by applying the nanoscopic blending of a redox-active component with carbon.[197] Redox-active materials are used in hybrid materials for battery applications, which offer a faster charge/discharge rate than non-hybrid materials.

In addition to improving electrical conductivities, and exhibiting highly efficient ion-electron transport properties and faster charge/discharge rates, hybrid materials also exhibit additional benefits for energy storage and conversion application. Carbon hybrid materials, the most popular combined materials for electrodes since they are cost-efficient and abundant, also shorten diffusion paths for ions and electrolytes through unique structures such as reticulated, hollow, porous, and vertically

aligned nanocomposites when well-designed. It is essential that reaction spaces in composites are available for the electrolyte but also feature sufficient electrical contact with other particles. This is typically achieved by adding conductive carbon and grinding it with the active material to create an electrically conductive percolation structure that permeates the composite.[71]
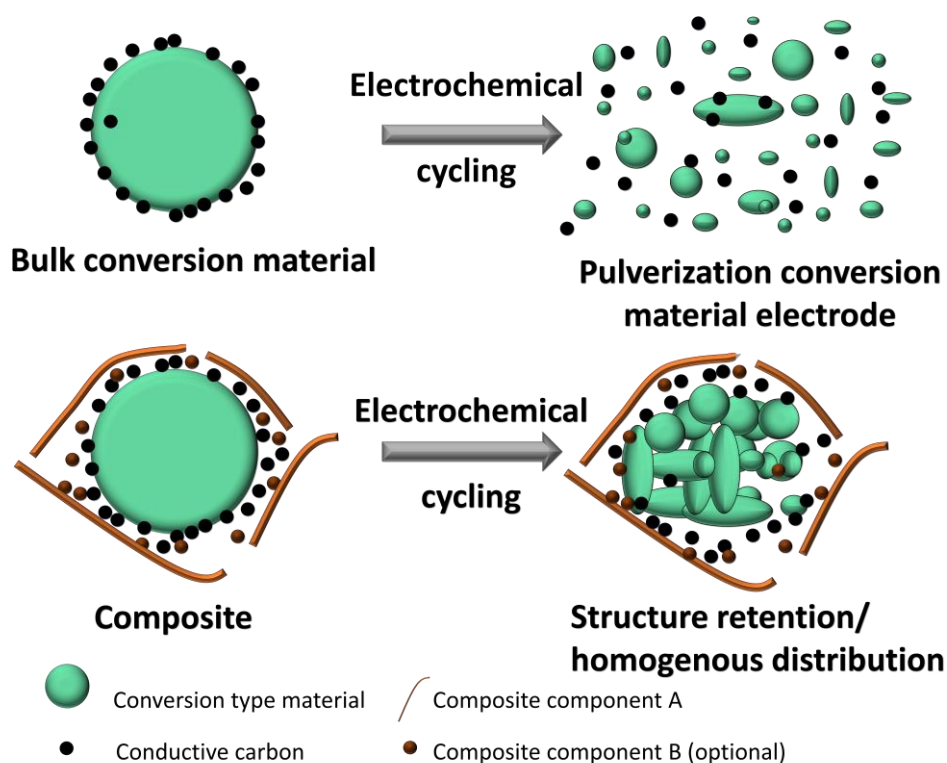
Figure 8: Schematic overview of comparison bulk conversion material and composite material after cycling (adapted and modified from Ref. [198])

Figure 8 compares bulk conversion and composite material after cycling. In the bulk material a pulverization of the electrode materials occurs due to the volume expansion, leading to quick capacity fading. In contrast, a composite/hybrid structure can be preserved after cycling even after exposure to volume expansion since the composite/hybrid provides a protective layer and buffers extensive volume expansion. The hybrid formation is not limited to carbon compounds. However, it can be further extended to 2D materials, which offer advanced structural stability since the volume change of the 2D nanomaterials during alkali metal transport/intercalation is only small (<<10% volume expansion/contraction).[126, 141, 199-201]

2D transition metal oxides and chalcogenides, for example, offer fast ion transport, abundant ion storage sites, and minimal volume change during charge-discharge cycles leading to improved electrochemical behavior.[199] At this point, for example, the class of MXenes, which stands out with their united properties such as good electronic conductivity, flexibility, and hydrophilicity while

inducing insignificant volume variation during Li$^+$ insertion.[131, 141, 202-204] In addition to acting as a conductive additive or a buffer for volume change during cycling, MXenes also have a reversible part in energy storage via an intercalation process.[205, 206]

2.2.4.3 Carbon conductive additive

A large portion of the electrochemically active materials has inherently low electronic conductivity. Thus, conductive additives like conductive carbons often need to be added during electrode formulation. A large specific surface area (~65 m^2 g^{-1}) and graphitic structure characterize such carbons. Usually, the conductive additive has a proportion of about 1-5 mass % based on the total mass of the solid in the slurry.[37] The conductive additive builds up a conductive network and thus improves the electrode's electrical conductivity, thermal conductivity, and electrical percolation. Conductive carbon additives speed up the charging and discharging process, which is crucial to optimize the cell's power density and specific power.[207, 208] The conductive additive can improve the cell's stability by absorbing and retaining the electrolyte to promote contact between ions and active material. Therefore, materials with large surface area, low mass, chemical inertness, and mostly graphitic structure, such as acetylene black and carbon black, carbon nanotubes, or porous carbon, are particularly suitable as conductive additives.[209] Especially in high-capacity electrode materials such as alloy or conversion systems, conductive carbon is considered to play an additional important role, namely buffering the volume change during the charging and discharging process.[210] In this way, aggregation of particles can be reduced, additional diffusion pathways are provided, and the electrode can be protected from possible subsequent pulverization, which would otherwise lead to poorer electrochemical behavior.[171, 207, 210, 211]

2.2.4.4 Binder

Apart from the electrochemically active materials, which are being intensively researched, the mostly electrochemical inactive binder is also an important component of batteries, as it ensures the connection between different components in the electrode like the active material, conductive additive, and the current collector providing mechanical flexibility. In the optimum case, the amount of binder in the electrode is kept low at 3-5 mass% as these polymeric materials often act as insulators and inhibit the charge transfer. In application, binder systems should be inert to the processes inside the battery and the electrode formulation process. High thermal, chemical, electrochemical, and mechanical stabilities are therefore required.[212] Mechanical stability, subdivided into flexibility tensile, elasticity, strength, hardness, and adhesive strength, characterizes the most important parameters.[213] An enhanced design of the flexible polymer binder is expected to reduce electrode decomposition during cycling, especially for materials with a large volume change, being highly electrochemical stable

for the whole potential window of electrode cycling and providing improved electrochemical performance via good interfacial properties.[214, 215]
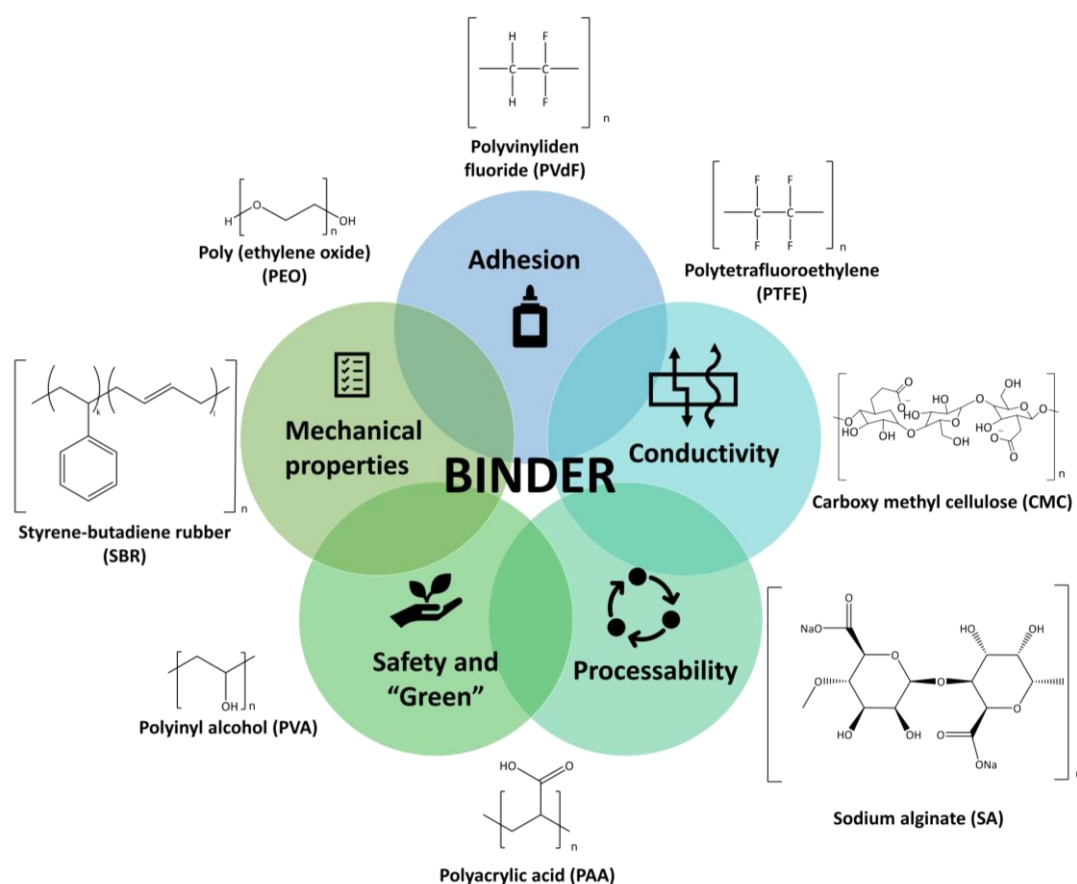
Figure 9: Overview of required properties of optimal binder system for electrode preparation with the corresponding chemical structure of typically deployed polymers.

Generally, the choice of the binder has a significant influence on the battery cost, lifetime, and the avoidance of organic solvents.[216] During the last years of battery research, several binder systems have been established, among which polyvinylidene fluoride (PVdF) stands out, and has also been commercialized in the LIB industry. One advantage of the PVdF binder is the low number of functional groups, which means that few unwanted side reactions are to be expected. However, PVdF systems are also criticized for instability due to side reactions of the fluorine groups, especially with sodium or unstable or too thick formation of the SEI layer.[217, 218] **Figure 9** summarizes the beneficial properties of improved binder systems in combination with chemical structures of recently employed polymer binders for energy storage, mainly in organic media.

In addition to the active material and the often-used polymer binder, the solvent is also vital for the slurry preparation, as it dissolves the polymer and thus guarantees a homogeneous distribution.

However, the solvent content should be kept as low as possible since this must be removed again after electrode preparation (especially coating) to create no side reactions in the electrochemical cell. In recent years, more effort has been put into developing environmentally friendly systems which include solubility in water instead of using toxic N-methyl-2-pyrrolidone (NMP) with high toxicity. The environmental impact of NMP, coupled with the fact that NMP can cause cancer and excessive NMP exposure can be linked to respiratory difficulties and severe health complications, highlighting the need for alternatives.[219] In addition, NMP is expensive and has been added to the restricted substances list by the European Commission in 2018, while in total, 47% of the process energy in LIB manufacturing is consumed in the electrode drying process for evaporation and recovery of NMP.[220, 221] Along with the minimization of the negative environmental impact, the cost, and safety for binder removal in the context of the electrode material recycling can be significantly improved when using an optional solvent system, especially water-based systems.[220]

If organic solvents are mandatory for electrode processability, systems with reduced environmental hazards and lower costs can still be employed. Several works show that with dimethyl sulfoxide (DMSO), an equivalent and less toxic and cost-effective alternative can be found without changing the conventional electrode process.[222, 223] By using electrode slurries with comparable rheological behavior, similar viscosity values, and wettability on the current collector when comparing to NMP, very reproducible and similar cycling performances can be obtained.[222] Some water-based examples are carboxy methyl cellulose (CMC), sodium alginate (SA), and polyacrylic acid (PAA), which exhibit more hydroxyl and/or carboxylate groups and therefore be able to build van der Waals forces that lead to higher tensile strength and flexibility.[224] The binder carboxy methyl cellulose, for example, is marketed as a particularly environmentally friendly and green binder mostly applied in anode materials with high capacity.[216] The fact of water-solubility allows working with aqueous pastes.

Over the last few years, wet slurry processing has been established throughout the industry without fully understanding the slurry properties, drying mechanisms, and electrode characteristics. However, with the increasing number of battery productions, it is imperative to keep an eye on the cost reduction of electrode production.[225] Opportunities lie in the reduction of inactive components and the development of solvent-free processing. This is usually done in a dry mixture of various powders, consisting of the active material, conductive additive, and binder. These are printed directly onto the current conductor and form independent electrodes with controllable electrode thickness and density by calendaring or hot rolling.[226, 227] By eliminating the drying process, it is possible to work at room temperature and low pressure, which means that less energy is required and the process is less time-consuming. At the same time, the microstructures of the resulting electrodes are easier to control due to the simplified process.

2.2.4.5 Electrolyte

The main role of an electrolyte in an electrochemical cell is to provide ionic conduction between the electrodes to ensure the electroneutrality of the two half-cells during both the charging and discharging of the cell. The electrolyte (solution) provides the ions, which are transported by the action of the applied electric field. The most typical electrolyte nowadays consists of salt solutions in solvents, with new concepts like the solid electrolyte setup and polymer electrolytes. An ideal electrolyte is characterized by a high level of chemical, and electrochemical stability (high electrochemical stability window), chemical inertness to avoid side reactions, high operating temperature range, low flammability, low costs, and environmentally friendly characteristics. The properties of the salt and the solvent strongly influence the electrochemical behavior, while the viscosity contributes to the fast ion conduction. Very fundamentally, the choice of electrolyte also determines the formation of the SEI, which characterizes a passivation layer at the surface of the anode material and is a direct consequence of the lack of stability of all organic electrolytes at very low potentials, which get reduced. It follows that the choice of electrolyte significantly affects the lifetime of an electrochemical cell, as well as the specific power and energy, and consequently plays a vital role in the electrochemical system.[43]

2.2.4.5.1 Salts

The most commonly used inorganic electrolyte salts require several properties suitable for use. These include good solubility in the electrolyte solvent, thermal stability, formation of a stable SEI layer, passivation of the current collector, and stability against hydrolysis.[228-232] **Figure 10** shows an overview of different lithium and sodium salts with their molecular structures. For LIBs, lithium hexafluorophosphate ($LiPF_6$) has emerged over several decades as the most suitable salt demonstrating a balance of the discussed properties. Sodium salts can often be chosen as equivalents, generally having a higher melting point than lithium salts, making it easier to remove moisture harmful to electrochemical applications compared to their Li equivalents, while the larger thermal stability present is also of benefit in terms of safety-related aspects required for application. In contrast to LIBs in which the PF_6 ion dominates application, they show serious safety issues, especially at higher temperatures and in the presence of humidity, suffering hydrolysis. For NIBs, sodium perchlorate ($NaClO_4$) has emerged as the most commonly used salt, likely due to a combination of previous experience and cost reasons.[232, 233] However, analogous to the LIB technology, $NaPF_6$ salts are the second most successfully used electrolyte salts for NIB.[234, 235] Further non-toxic electrolyte salts for NIB are sodium tetrafluoroborate ($NaBF_4$) and sodium trifluoromethanesulfonimide (NaTFSI) among others.[236]
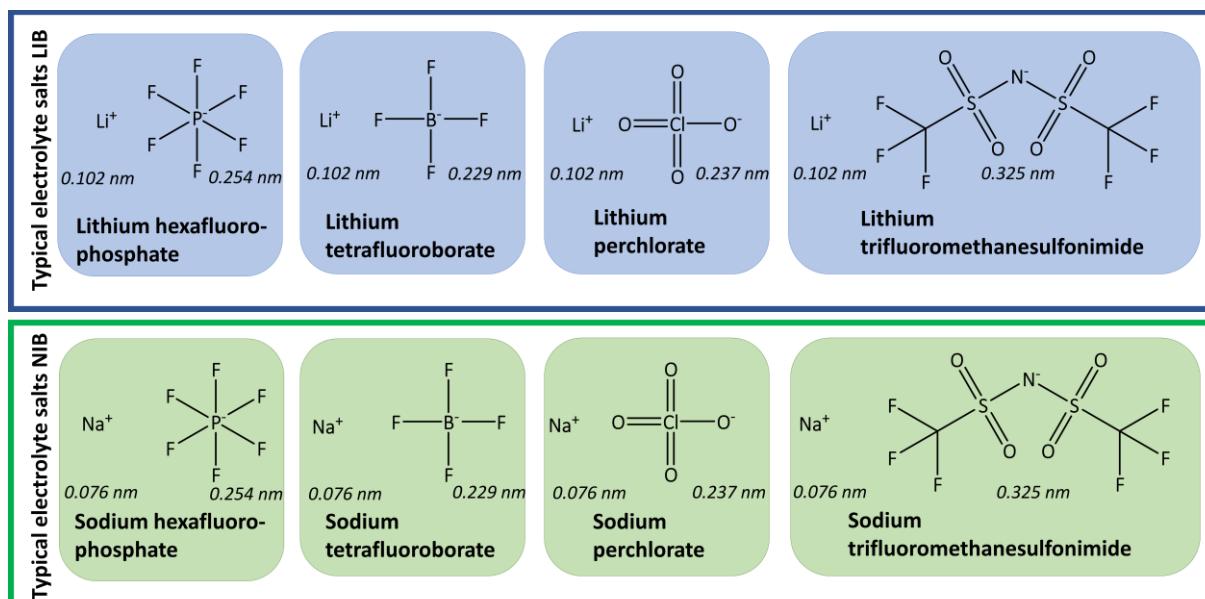
Figure 10: Chemical structures of different electrolyte salts for LIB and NIB.

2.2.4.5.2 Organic solvents

Organic solvents should exhibit high chemical and electrochemical stability while being suitable for applying a wide operating temperature range and high flame retardancy.[229, 230, 237] **Figure 11** shows electrolyte solvents with corresponding chemical structures. Organic esters and carbonates have been widely used as solvents for alkali-ion batteries and have been established until today.
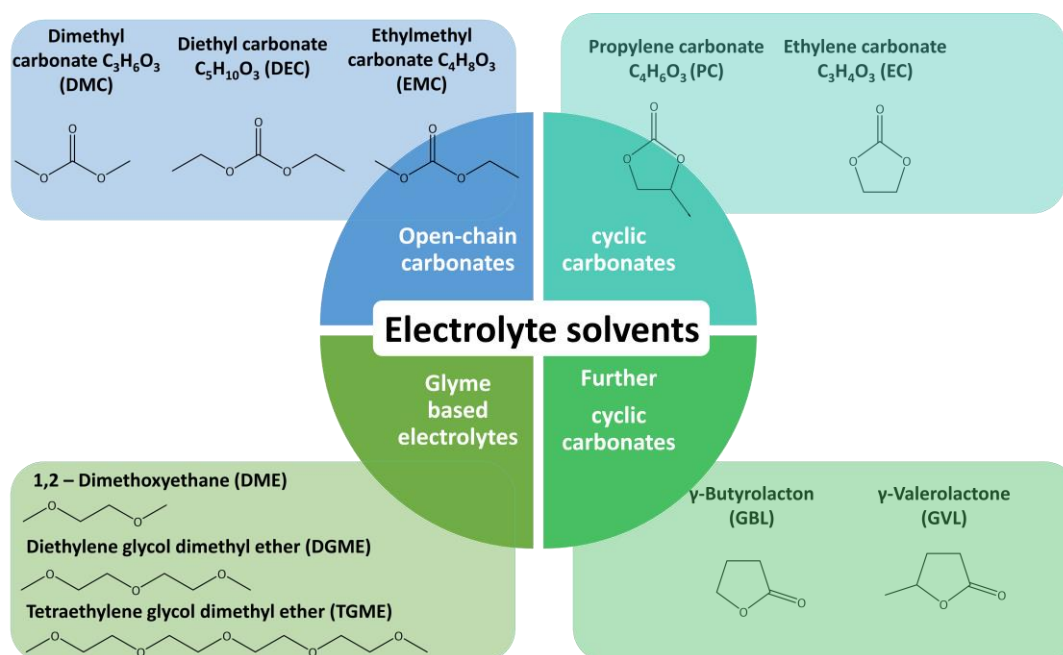
Figure 11: Overview of established electrolyte solvents with chemical structures for LIB and NIB.

Most frequently, carbonates, such as open-chain carbonates, include ethylmethyl carbonate $C_4H_8O_3$ (EMC), diethyl carbonate $C_5H_{10}O_3$ (DEC), and dimethyl carbonate $C_3H_6O_3$ (DMC) or cyclic carbonates like ethylene carbonate $C_3H_4O_3$ (EC) and propylene carbonate $C_4H_6O_3$ (PC) are applied.[72, 238, 239] Open-chain carbonates are known for their low viscosity and moderate dipole moments, and cyclic carbonates feature higher viscosity and high dipole moments.

Cyclic carbonates are often mixed with open-chain carbonates in electrolyte solutions.[240] Despite possible issues on fertility expected for glymes with lower chain lengths but with more straightforward and more environmentally friendly production routes, glyme-based electrolyte solvents, especially with longer chain lengths, are characterized by higher safety, lower flammability, improved cell performances, and economic impact and are emerging as an alternative to carbonate solvents.[241] For Na^+ storage, it was reported that ether-based electrolytes, especially bis(2-methoxyethyl) ether (diglyme), show superior electrochemical performance and thus represent a promising alternative to state-of-the-art literature.[187, 242, 243] Glyme-based electrolytes are a good alternative in LIBs by stabilizing the lithium metal anode, suppressing the lithium dendrite growth, and forming a more robust SEI layer.[244-246]

Further, carbonates like γ-butyrolactone (GBL) have also been used as a pure electrolyte system, providing higher boiling points, low freezing points, a high dielectric constant, and a low viscosity.[247-249] Further reports of combining with ionic liquids as GBL can significantly improve conductivity are outlined.[250] A significant disadvantage of GBL is that the solvent quickly decomposes on the surface of the negative electrode, mainly forming butylate and cyclic alkoxy-β-keto ester lithium salt, thus forming an SEI layer with very high resistance, leading to the deterioration of battery performance.[251] The same applies to the property-related γ-valerolactone (GVL).[252, 253] This problem can be somewhat counteracted by adding electrolyte additives in small quantities to the electrolyte solution.

2.2.4.5.3 Electrolyte additives

Often the obtained electrolyte formulations still need that specific last step to show a perfect performance. At this point, electrolyte additives which are solid or liquid compounds, are added in small amounts (i.e., 2-10 vol%) to the electrolyte solution. In most cases, electrolyte additives increase safety, adjust physical properties such as electrical conductivity or viscosity, or significantly improve SEI or cathode electrolyte interphase (CEI) formation. **Figure 12** displays the most commonly used additives for NIB and LIB electrolytes.
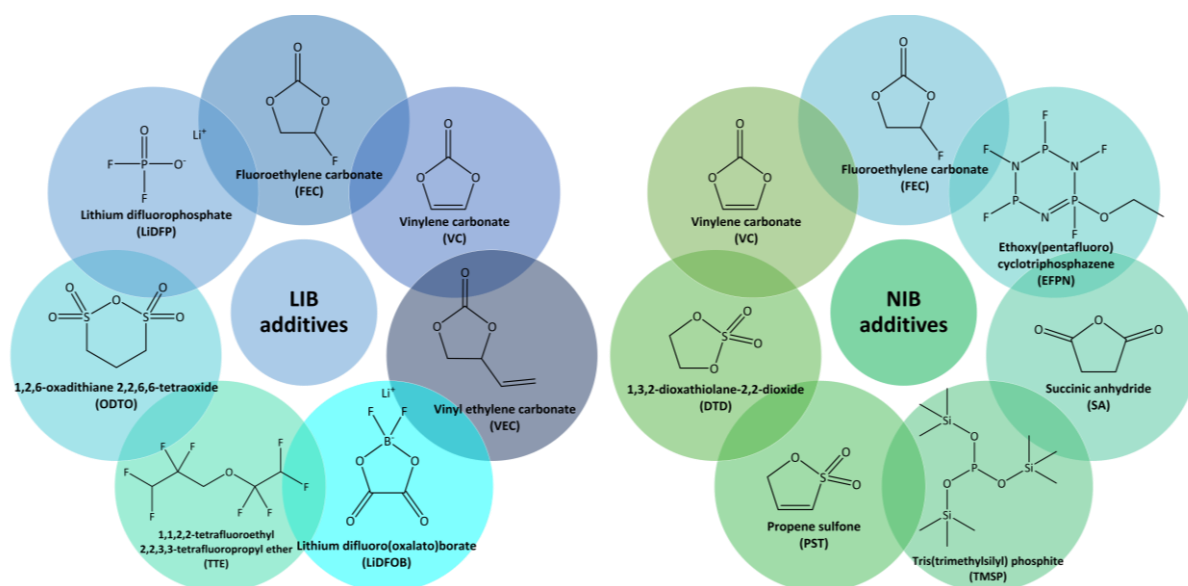
Figure 12: Overview of different electrolyte additives with the chemical structures for LIB and NIB.

The concept of additives capitalized off of a higher reduction potential than the electrolyte solvents used. Thus the decomposition/reduction of the solvents is reduced, and the SEI layer consists mainly of additive products.[254] For NIB, in addition to the reasons already mentioned for the need to use additives, it can also counteract the corroding that occurs with metallic sodium anode systems when organic electrolytes are used. Originally, vinylene carbonate (VC) was reported as one of the most promising additives in LIBs, reducing graphite anodes at a higher potential than 1 V vs. Li$^+$/Li.[255] However, NIB is also reported to be successfully used with hard carbon electrodes in ether-based electrolytes, which can positively influence storage performance.[256] Fluoroethylene carbonate (FEC) is an additive for NIBs, often used in literature as it improves the stability of the cells.[257, 258] Adding FEC can increase the stability of the formed SEI layer on top of the sodium metal electrode.[259] On the other hand, it also prevents the decomposition of the typically used solvents (EC/DMC) to by-products such as ethylene glycol bis-(methyl carbonate) since FEC has a higher oxidation potential than EC and DMC.[259]

Practically, during the electrochemical characterization, a first reduction potential of FEC at 0.7 V vs. Na$^+$/Na is obtained. A high-quality SEI layer is formed on the electrode, which can increase the electrochemical stability. The exact nature of the formed compound is still under debate. At the same time, it can be assumed that a polymer layer is formed during FEC reduction.[260, 261] This polymeric layer on top of the sodium metal can protect the electrode and guarantee reliable three-electrode measurements using a metallic sodium counter and reference electrode. Adding FEC may not only significantly improve the SEI properties of the working electrode, as reported in detail in the state-of-the-art literature[174, 257, 262], but also significantly protects the elemental sodium electrode against any

side reactions with the electrolyte.[175, 263] FEC is also used very successfully in LIB electrolytes as an additive,[264-266] but its effectiveness as a high voltage additive is still controversial, and FEC is still accused of causing dissolution of transition metals from the cathode while depositing at the anode.[267]

Lithium difluorophosphate (LiDFP) has proven to be very effective in suppressing cross-talk and improves the Coulombic efficiency and cycle lifetime, and reduces parasitic heat flow.[267-269] Other established LIB additives are, for example, 1,2,6-oxadithiane 2,2,6,6-tetraoxide (ODTO), further C-F bond additives like 1,1,2,2-tetrafluoroethyl 2,2,3,3-tetrafluoropropyl ether (TTE) or lithium borate based additives like lithium difluoro(oxalate)borate (LiDFOB). This should improve the CEI properties at higher potentials and higher temperatures and stabilize the high capacity of spinel materials.[254, 270-273] Vinyl ethylene carbonate, which has electron-rich double bonds compared to VC, has improved chemical properties because the compound is less reactive towards other double bonds.[274] For NIB, many of the practices already researched also related to electrolyte technology were once again taken over from LIB technology. In addition to FEC and VC, sulfur-containing additives like propene sulfone (PST) and 1,3,2-dioxathiolane-2,2-dioxide (DTD), and tris(trimethylsilyl) phosphite (TMSP) or the flame retardant additives ethoxy(pentafluoro)cyclotriphosphazene (EFPN) or succinic anhydride (SA), have shown a positive effect on the electrochemical performance.[275-279]

2.2.4.6 Separator

The separator is an electrically insulating and ionically conductive film utilized to avoid physical contact between the negative and positive electrodes and, therefore, a short-circuit of the electrochemical cell.[280] The separator generally consists of a microporous membrane consisting of cellulose fibers, glass fibers, or polymers permeable to electrolyte and alkali ions.[281] Commercially, microporous polymer membranes made of polyolefins such as polyethylene (PE), polypropylene (PP), and their blends (PE-PP) are commonly used. An optimal separator ideally features infinite electronic but zero ionic resistance while being mechanically stable and temperature stable during the battery lifetime.[282] Porosity, mean pore size, tortuosity, permeability, and wettability are additional important to consider.[282]

Further types of separators include non-woven mats made of fiber materials such as PVdF and celluloses with high porosity and low cost or glass fibers such as borosilicate microfibers with high porosity, excellent wettability, and thermal stability.[283-285] Another possibility for a thermal stable (zero shrinkage) separator with excellent wettability is offered by nanoscale inorganic particles such as Al_2O_3, MgO, or SiO_2 mixed with a small number of polymeric binders.[285]

2.2.4.7 Current collector

Electrons released (invested) during the electrochemical process (intercalation and extraction of alkali metal ions) are practically discharged (charged) using a current collector. The current collector consists of aluminum or copper, depending on the applied potential strength, used electrolyte, and alkali metal so that no undesirable reactions can occur with the alkali metal or the electrolyte.[286] Aluminum offers a cost-effective alternative to copper in NIBs because it does not form alloys with sodium.[42] Stable electrochemical performance combined with enhanced power handling was reported when using sputtered sub-µm aluminum layers as a current collector.[287] For LIB anodes, aluminum is an unsuitable current collector, as aluminum reacts with lithium ions at lower potentials of 0.6 V vs. Li$^+$/Li, forming alloying products.[288] When going to higher potentials, aluminum must be used as a current collector since starting from a potential of 3.2 V vs. Li$^+$/Li, copper starts to dissolve, thus would not be applicable for cathode material coatings.[229]

2.2.5 Key parameters for batteries

2.2.5.1 Battery capacity and Faradays' law

Capacity is usually defined as the charge storage capacity of an electrochemical energy storage device. It describes the amount of electrical charge Q stored or delivered by the cell or battery. The typical capacity unit is usually expressed in ampere-hours (Ah) and can be normalized to the volume or mass (Ah cm^{-3} or Ah g^{-1}) to give volumetric or specific capacity. The capacity depends on the active material's type/quantity/morphology, the respective charge/discharge current, the final discharge voltage, and the temperature.[37] By specifying the capacity, it is possible to calculate how long a certain current or how much current can be drawn over a certain time.

Faraday's law gives a quantitative relationship between the amount of charge flowing and the chemical conversion at the electrodes.[289] Faraday's law describes the limit of charge storage, resulting in the so-called theoretical capacity of the material. Therefore, to electrolytically deposit any amount of material n of a z valent ion, the charge Q is required.

$$Q = I * t = F * n * z$$

(III)

In this equation, n characterizes the maximum amount of insertable or extractable charge carriers with valence number z, I the electric current, t the time, and F the Faraday constant, composed of the Avogadro constant N_A and the elementary charge e_0.

$$F = e_0 * N_A$$

(IV)

The molar mass is the charge needed to deposit one mole of a monovalent ion. From $m = M * n$ with the molar mass M follows the maximum capacity a material with molecular mass M can theoretically achieve:

$$Q_{th} = \frac{m * z * F}{M}$$

(V)

Thus, the charge required to deposit a given mass of the substance by electrolysis can be determined.[236, 290]

2.2.5.2 Rate capability and C-rate

$$[C] = \frac{I}{Q} = \frac{1}{t}$$

(VI)

Currents are often specified as C-rates. The C-rate of a battery describes the charge or discharge current relative to the theoretical capacity of the material. In practical applications, theoretical capacity is not achieved due to polarization effects or capacity losses caused by material defects or side reactions. If the theoretical capacity is divided by one hour, the obtained current will correspond to a C rate of 1C. A coefficient of 1C indicates that a battery is completely charged or discharged within 1 h. For new systems, which lack the theoretical capacity information, C-rates are often not suitable. These systems are distinguished by the comparison of the specific currents and current density.

2.2.5.3 Coulombic efficiency (CE)

Coulombic efficiency (CE) is the relative ratio of the amount of charge ($Q_{discharge}$) that can be extracted from the battery to the total inserted charge (Q_{charge}) within a full cycle. The Coulombic efficiency characterizes the charge efficiency of the electron transfer and is expressed as a percentage (%). It is favored if the standard potential of the cell at the beginning of the charging process corresponds to the lower end-of-charge voltage during the subsequent discharge. Normally, the value of the Coulombic efficiency is reduced by irreversible charge losses, such as SEI formation and aging effects. Therefore, it remains below 100%. Commercially applied LIBs provide a CE, which commonly exceeds 99%.

$$n_c = \frac{Q_{discharge}}{Q_{charge}} * 100\%$$

(VII)

2.2.5.4 Cycling stability, capacity retention, and cycle life

Charging and discharging a battery in a certain voltage range with a particular current is called galvanostatic cycling. To evaluate the cell performance, the charge/discharge capacity is recorded as a function of the number of cycles. In general, a safely decreasing capacity value is expected during

cycling, which is strongly dependent on applied cycling conditions (charge/discharge rate, voltage range, electrode material, as well as its mechanism, temperature, electrolyte stability, etc.). One of the main objectives for optimizing battery cells is their lifetime. The cycle life of a rechargeable battery, for which cycle stability is a key parameter, is defined by the number of charge or discharge cycles until the capacity is reduced to a certain amount of the nominal capacity (typically 50% to 80% capacity retention).[291, 292] The cycling stability of LIBs is mainly characterized by the SEI layer, as long as the electrochemical stability of the applied salt and solvent is appropriate.[62, 291, 293] The capacity retention is therefore also an important metric to evaluate the battery performance, especially to define the longevity of real devices, with describing the ratio of the delivered capacity in a specific cycle compared to the initial discharge capacity.[294]

2.2.5.5 Electrochemical signature

There exist well-established methods to characterize energy storage processes. For example, characterization via cyclic voltammetry (CV) and galvanostatic cycling with potential limitation (GCPL) provides access to a variety of properties such as capacity, capacitance, operating voltage, cell kinetics, rate stability, redox reactions, cyclability and equivalent series resistance (ESR).

Information about the reduction and oxidation processes, as well as electron transfer-initiated chemical reactions, can be obtained with the CV technique.[295] From a starting potential, preferably currentless, CV begins with a triangular voltage with a speed of potential change of $v = d\varphi$dt between working electrode and counter electrode (**Figure 13A**). Usually, the maximum upper and lower limits of this triangle voltage are defined by the redox pair as well as the employed electrolyte solvent so that optimally all redox reactions of the electrode material can be recorded without triggering a decomposition reaction of different cell components.[296] Practically, a current flow is generated by applying a voltage ramp $v = \frac{dU}{dt}$ on the cell. A current flow is generated by the applied voltage resulting in a plot consisting of the current between the counter electrode and the working electrode as a function of the applied potential (**Figure 13B**). After reaching a certain target potential, the potential is ramped in the reverse direction to return to a defined potential or the initial state. Peaks seen in a cyclic voltammogram commonly signal the charge transfer (Faradaic redox potential) between the electrode and the redox-active species at a certain potential whereby a current occurs as soon as the applied voltage reaches or exceeds the redox potential.
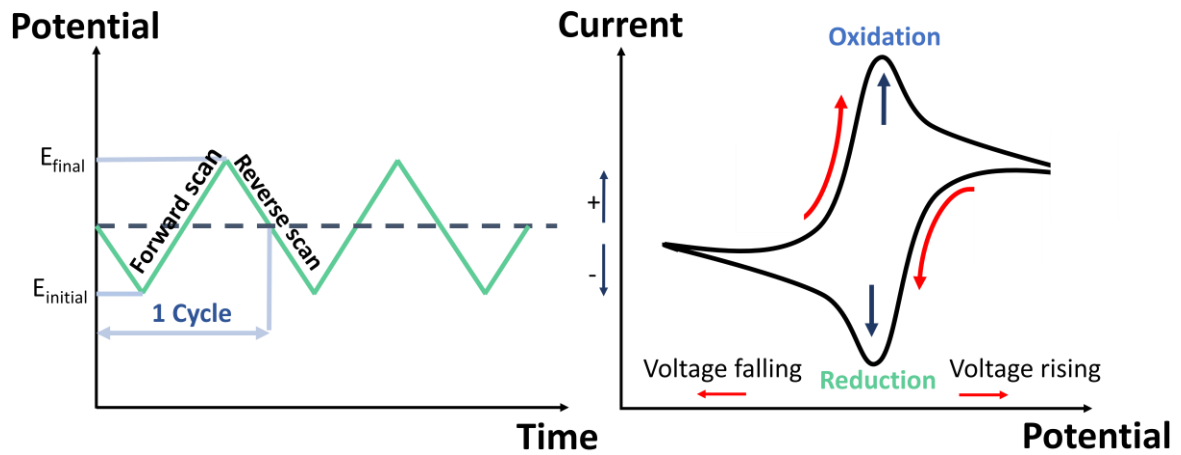
Figure 13: Potential-time excitation signal of CV experiment and typical voltammogram.

Galvanostatic cycling with potential limitation studies the behavior of battery calls upon cycling while applying a constant external charge/discharge current between the working and counter electrode (**Figure 14**). The constant current pulses lead to potential changes inside the battery. The potential limitation is needed to avoid irreversible processes such as electrolyte decomposition. The obtained potential is evaluated as a function of time in a certain voltage range to obtain information about the electrode processes and their changes. In addition, information about the amount of charge used during a discharge and charge cycle is obtained. Usually, this factor is related to the mass of the active material and referred to as specific capacity. Overall GCPL technique is the test that most closely resembles how a battery is mostly used in real-world practice (i.e., it is charged up and then discharged, usually at relatively constant rates).
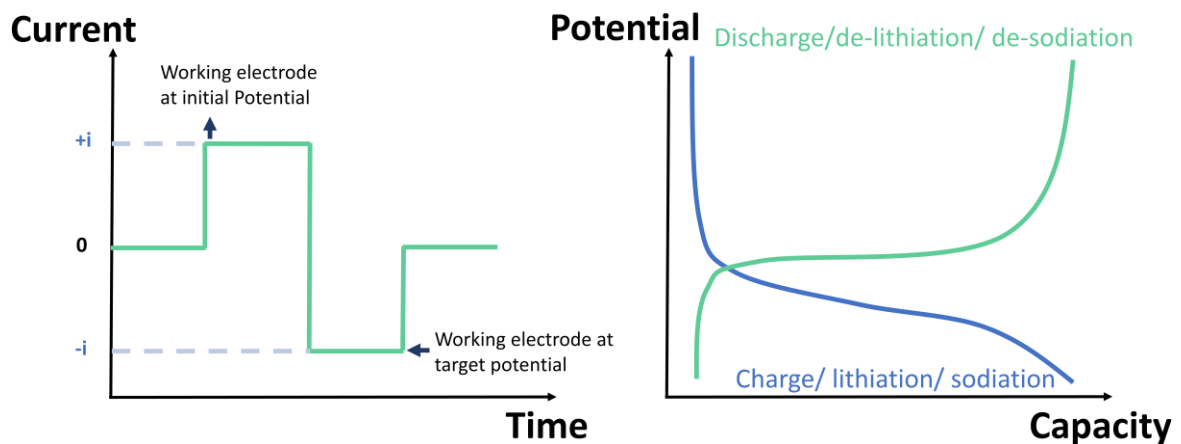
Figure 14: The change of the current with time in GCPL and typical charge and discharge curve in the GCPL experiment.

2.3 Seawater batteries

The global shift toward greater sustainability and time-sensitive pressures for more renewable energy use is steadily driving the development of promising new materials and technologies, continuous improvement, and creative redesign.[297, 298] Because of their versatile advantages, interesting energy storage systems beyond lithium have attracted much attention and have been studied scientifically more frequently in recent years.[299-302] One such post-lithium or beyond-lithium technology relates to NIB (**chapter 2.2.2**), which technology has seen a steady increase in interest since 2011, especially since sodium is one of the most abundant elements in the earth's crust, offers similar intercalation chemistry to LIBs, and manifests the potential for low-cost energy storage systems.[42, 43] A battery form that also relies on sodium ion transport is the seawater battery, which can simultaneously store energy and desalinate water due to its unique configuration (operation principle is displayed in **Figure 15**). Sodium-rich seawater, which occupies about two-thirds of the earth and has a sodium concentration of about 470 mM, is a nearly inexhaustible source of sodium ions and presents the electrolyte in seawater batteries.[303]

The first primary, non-rechargeable seawater battery was developed as early as 1943.[304] In 2014, the research field was revived and focused on secondary (rechargeable) seawater batteries.[305, 306] Rechargeable aqueous NIBs are an environmentally friendly and promising method of storing electrochemical energy, with seawater circulating as a low-cost electrolyte in the electrochemical cell. Seawater electrolytes eliminate or reduce many safety problems that organic electrolytes can cause.[6] Conventional seawater batteries provide electrochemical energy storage through a combination of a sodiation/de-sodation anode and an electrolysis cathode. This concept requires an open cell architecture to ensure a constant supply of fresh seawater as catholyte during the cell operation. The major components of a seawater battery are electrode materials (cathode and anode), electrolytes (anolyte, catholyte), current collectors, (ceramic) membranes, electrocatalysts, and common cell types.

A typical rechargeable seawater battery consists of two electrode compartments, one of which can be with an organic electrolyte side, and the other compartment usually contains an aqueous electrolyte. The cell compartments are separated by a solid diffusion membrane (such as the widely-used sodium superionic conductor (NASICON)) to ensure selective ion flow (**Figure 15A**). The organic part resembles a typical NIB cell, which can contain an elemental sodium anode. When seawater cells come in contact with seawater, free and abundant sodium ions in the catholyte can migrate to the anodic compartment during the charging process. They are finally stored as elemental sodium metal. On the cathode side, the oxygen evolution reaction (OER, $4OH^- \leftrightarrow O_2 + 2H_2O + 4e^-$ E = 0.77 V vs. SHE) leads to a theoretical

cell voltage of 3.48 V.[305] During the subsequent discharge, sodium ions are again released and delivered to seawater, accompanying the oxygen reduction reaction (ORR) at the cathodic compartment. Since introducing rechargeable seawater batteries in 2014,[306] most studies have optimized performance, including cathode and anode materials, catholyte and anolyte, and cell structure. The dual function of seawater batteries at the critical interface between water and energy research can help to simultaneously store intermittently available renewable energy and provide clean drinking water for residential areas and agriculture. The possibility of significantly increasing the technological desalination of seawater will also considerably advance the large-scale production of green hydrogen.
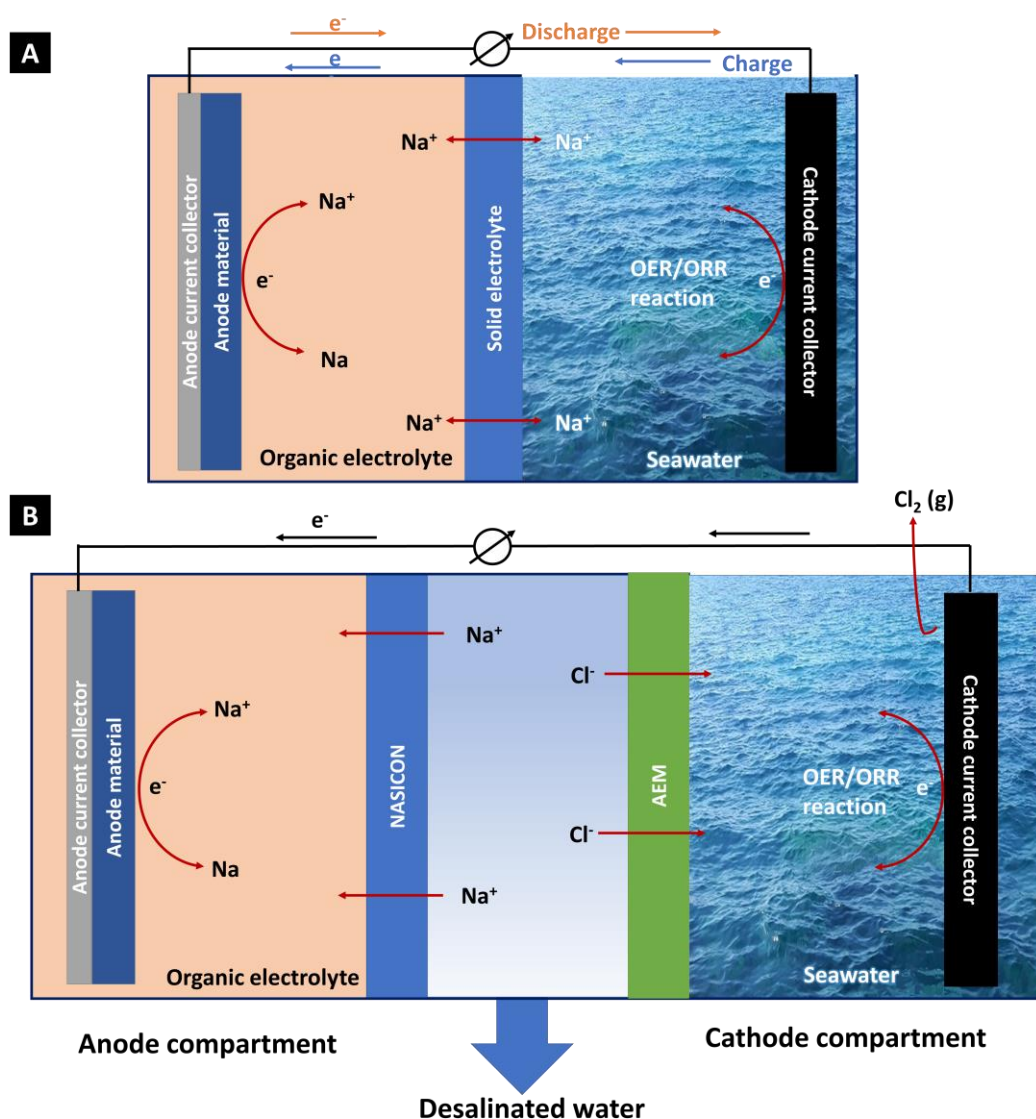
Figure 15: Schematical representation of the working principle of a seawater battery A) for energy storage purposes and B) for water desalination. Copyright 2022, Wiley.[15]

2.4 Electrochemical water treatment

Water is one of the resources that humanity needs to live, along with food, energy, and medicine. Due to the ever-increasing population, the progress of climate change, and the accompanying deterioration of environmental conditions, obtaining clean potable water has become a severe problem of the 21st century, especially in arid regions.[307] The worldwide oceans account for about 97% of the Earth's water, which has, in principle, the great potential to be the drinking, agricultural, and industrial water resources, while naturally, it contains a specific amount of salts. Researchers have been developing various desalination methods for many years to address the problem of drinking water out of salt-containing liquid media. These methods can be divided into membrane-based processes like reverse osmosis[308] or thermal processes like multi-effect distillation[309] or multistage flash distillation.[310] So far, reverse osmosis technology is the most widespread application, while plants require high energy consumption of 2-5 kWh m^{-3}.[311, 312] Another steadily growing research area is electrochemical desalination methods such as electrodialysis,[313] desalination fuel cells,[314, 315] desalination batteries[316, 317] or capacitive deionization.[318]

2.4.1 Capacitive deionization (CDI)

Besides suitable electrochemical desalination technologies mentioned above, capacitive deionization (CDI) is a highly energy-efficient method.[319, 320] The concept of CDI is based on an ion flow immobilized at the liquid/solid interface of nanoporous carbon by reversible ion electrosorption.[321] The first generation CDI cell consisted of two nanoporous carbon electrodes and a separator (open channel or porous dielectric material) that prevents the two electrodes from short-circuiting.[318] **Figure 16** provides a schematic drawing of a first-generation CDI cell. The constant electrical voltage or current applied to the cell creates a potential gradient whereby the salt ions present in the feed water migrate into the electrical double layer of the electrode material, thus removing salt from the effluent water stream by ionic electrosorption.[318, 322] During the subsequent discharge process, the electro adsorbed ions are rereleased and, the previously invested charge can be recovered unlikely other mostly desalination methods like thermal distillation, reverse osmosis or electrodialysis. Due to the use of typically aqueous media, the applied voltage is typically at a maximum of 1.2 V to satisfy the overpotential determinations of the water splitting. Although the origins of CDI date back about 60 years, it is only in the last decade that this method has gained importance and scientific progress.[323, 324] In particular, research has been conducted to develop new high-performance electrode systems for the CDI cell,[325-330] to design new cell configurations,[331-335], and to characterize better and elucidate the underlying mechanisms of ion adsorption. Furthermore, supporting computer-based studies to simulate different interactions were studied to advance the technology further.[336-338]

Co-ions and counter-ions would occupy the carbon electrodes and their corresponding nanopores during the electrochemical process.[339, 340] This means that the electrode pores are populated with ions of positive as well as negative charge, respectively. By applying an external current and the resulting polarization of the electrodes, co-ions are released from the electrochemical double layer to the same extent as counter ions are attracted (named co-ion effect). CDI technology is thus mainly limited to low molar concentrations since perm-selective ion removal only starts when the co-ion population is exhausted at higher charge states.[341, 342] In some cases, conditions can be changed by using pore diameters well below 1 nm.[343] An important exception, except for water molecules, is that the pores are empty in the uncharged state if they are smaller than the size of the hydrated ions.[344] Furthermore, the EDL that forms in carbon is limited to a charge storage capacity of about 0.1 F m^{-2}.[345, 346] With the storage mechanism via the electrical double layer of the nanoporous electrode, the desalination capacity achieves rather low values (ca. 10-30 mg$_{NaCl}$ g$_{electrode}^{-1}$)[347] and effective remediation in brackish water with low to medium salinity.[348]

In 2012, Pasta et al. first used Faradaic materials (sodium manganese oxides and silver) to successfully desalinate sea water while thereby overcoming the typical desalination limitations of carbon-based materials.[317] Other possibilities besides using Faradaic material as both electrodes is the possibility of pairing proven carbon with charge-transfer electrodes. Using sodium manganese oxides to capture sodium and carbon to store chloride 2014, Lee et al. exhibit a desalination capacity of about 31 mg$_{NaCl}$ g$_{electrode}^{-1}$.[349] So far, two different kinds of Faradaic materials have been successfully employed as electrodes for desalination. The first type relates to intercalation materials distinguished by ion intercalation into a host structure, such as sodium manganese oxides,[350] nickel hexacyanoferrate[351], or titanium disulfide.[352] On the other hand, analogous to the development of electrode materials for primary energy storage, high-performance conversion type electrode materials like silver[353] or bismuth[354] can also be introduced, which show desalination capacities between 85-115 mg$_{NaCl}$ g$_{electrode}^{-1}$.[355-357]
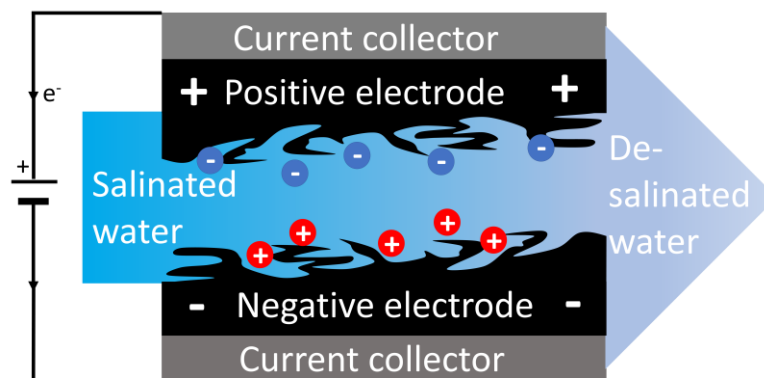
Figure 16: Structure of a typical first-generation CDI cell.

2.4.2 Membrane-based capacitive deionization (MCDI)

Membrane capacitive deionization (MCDI) is a modification of the original CDI technology. Like in a CDI cell, an electrical potential difference is applied to an aqueous solution. However, the electrode pair is additionally shielded with one or two ion exchange membranes on the surface so that more selective ion uptake (cation or anion uptake) can take place.[358] The first attempts to incorporate a charge barrier into the system to block co-ions and improve desalination was pioneered by Andelman and Walker in 2004.[359] In 2006, Lee et al. reported a 19% increase in desalination efficiency in wastewater desalination with his developed MCDI in which an anion exchange membrane (AEM) and a cation exchange membrane (CEM) were placed on the anode and cathode surfaces, respectively.[360]

Figure 17 a schematic drawing of a typical MCDI is displayed. The use of additional ion exchange membranes has several advantages. For example, the co-ions, which would otherwise always leave the electrode when a counter-ion is adsorbed during the cell charging process, can no longer leave the electrode area, thereby increasing the efficiency of the salt removal process.[358] On the other hand, the counter-ions released when the reverse voltage is applied can be flushed entirely directly from the electrode region, which can increase the driving force of the electrode for subsequent cycles.[361] An additional advantage of MCDI is the prevention of co-ion adsorption in the electrode and the ability to reverse the voltage during the desorption process, which can significantly improve the kinetics and adsorption capacity of MCDI.[362, 363] By preventing ions from leaving the electrode region, the interparticle porosity (electrode pore space) is available as a reservoir for salt ion storage, increasing the porous electrode's total ion storage capacity.[364]

As a sodium-ion-removal electrode, the experience with NIB electrode materials could significantly bring high-performance systems into the field. However, most of the high-capacity materials studied for battery research are not suitable for direct contact with aqueous media, or the expected oxidation and reduction reactions occur outside the stability range of water, making their direct use in CDI challenging. To lift the requirement to expose the electrode to the feedwater stream, for example, the concept of membrane-based CDI can support shielding one or both electrodes from direct contact to flowing through an aqueous medium. Considering the advantages mentioned above for various applications, the MCDI reduces the loss of desalination capacity and the additional energy consumption.[365] In particular, the MCDI offers the prospect of lower energy consumption than, for example, reverse osmosis, mainly for desalination of low-concentration brines.[340, 363, 366]
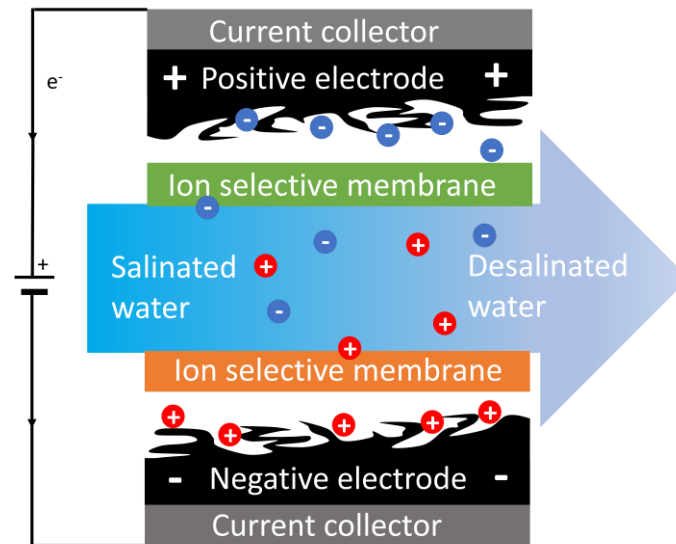
Figure 17: Schematic overview of an MCDI cell showing flow channel, ion-selective membranes as well as electrode materials.

Membranes that were initially mainly used for this technology consisted of polymers with functional groups serving as a fixes charge on the polymer backbones.[367, 368] In this way, the membranes can be designed very specifically by, for example, fixing the cation charge so that anions can be easily transported between the backbone. This characterizes the so-called anion exchange membrane. On the other hand, cations can be transported between the backbone if an anionic charge has been anchored to the membrane beforehand, leading to a cation exchange membrane. The ion transport through the specific membranes is related to the electrostatic interactions of the bound charge groups and the transported ions.[369-371] While in some studies it is assumed that polymer-based ion-selective membranes have partially limited ion permeability, the class of ceramic superionic conductors (NASICON), lithium superionic conductor (LISICON), which has already been extensively investigated in the field of battery research, seawater batteries, and fuel cells,[303, 372, 373] offers a promising alternative also with a focus on the use in electrochemical water desalination. Owing to its crystal structures, Na^+ or Li^+ ions can hop directly from one lattice site to another, resulting in high ionic conductivity and high selective ion permeability for specific ions (NASICON→ Na^+ ions and LISICON→ Li^+ ions).[374]

2.4.2.1 Sodium superionic conductors (NASICON)

Besides using NASICON as electrode material or as a solid electrolyte in NIBs, NASICON also shows increasing interest in its application as a membrane in seawater batteries and desalination. Typically, NASICON represents a family of solids with the chemical formula $Na_{1+x}Zr_2P_{3-x}Si_xO_{12}$ (x= 0-3).[375] In a broader sense, however, it is also used with various similar compounds based on the NASICON structure, in which isovalent elements replace elements such as Na, Zr, and/or Si.[375] Hong investigated that solids of the general formula with 0<x<3 as one of the first by heating to a temperature of 1200 °C obtain a crystallization in a NASICON structure.[376] Rhombohedral symmetry, except in the interval 1.8<x<2.2, was exhibited with this structure while a small distortion to monoclinic symmetry occurs.[376] Later, Von Alpen et al. reported a different general NASICON formula of $Na_{1+x}Zr_{2-x/3}Si_xP_{3-x}O_{12}$ to obtain zirconia-free material while still resulting in multiple phase compositions.[377] Comparing the most common Hong-tape NASICON with the Alpen-type, it offers the advantage that it can be produced at lower temperatures (1250 °C; ≥1300 °C Alpen-type NASICON) while still achieving very high densification, which is extremely important for application in seawater batterie as well as some desalination mechanism in which the membrane also serves as a barrier between the aqueous media as well as some water sensitive electrode materials (e.g., elemental sodium). Go et al. recently presented a vA-NASICON ($Na_{3.1}Zr_{1.55}Si_{2.3}P_{0.7}O_{11}$) with promising and suitable properties in competition with the established Hong-type NASICON.[378] Due to the changed composition and the microstructure, lower grain boundary resistance and higher ionic conductivity can be obtained. NASICON are promising candidates for various electrochemical devices and media attributed to their high ion mobility and chemical stability. In general, NASICON-structured materials offer, by their suitable tunnel size for sodium ion migration in a 3D framework, the possibility of highly selective Na ion uptake with a combination of high structural stability and fast ionic conductivity (10^{-3} S cm^{-1}). Low thermal expansion behavior, stability in different media, and large surface area complete the portrait of the ceramic material.[375]

2.4.2.2 Lithium superionic conductor (LISICON)

Lithium superionic conductors (LISICON) characterize a family of solid ceramic compounds with the chemical formula of $Li_{2+2x}Zn_{1-x}GeO_4$.[379] The first discovery of the LISICON structure dates back to 1977 when the first structural investigation of $Li_{14}Zn(GeO_4)_4$ was also reported by Hong.[380] The underlying crystal structure consists of a network of $[Li_{11}Zn(GeO_4)_4]^{3-}$ and 3 loosely bound Li^+-Ions. Loose bonds of the lithium ions allow simplified ion transport without breaking strong bonds. Free ions occupy interstitial sites, which are close to each other and thus energetically favored. As with NASICON structures, a tunnel-like channel is formed through which lithium ions can selectively, rapidly, and easily diffuse. LISICON structures are also promising for wide application due to their relatively high ionic conductivity of about 10^{-6} S cm^{-1} at room temperature.[380-383]

In the following years, many LISICON-like materials were discovered and developed, increasing properties such as ionic conductivity ($Li_{(3+x)}Ge_xV_{(1-x)}O_4$; $Li_{(4-x)}Si_{(1-x)}P_xO_4$).[381, 384-386] Some of the advantages of LISICON for an electrochemical application are the possibility to use it in a wide electrochemical stability window and thermal stability, which allows safe use.[387] Other important features, especially for the use in LIBs, characterize the stability against chemical reactions with electrode material (mainly elemental lithium or lithium alloys) as well as the expansion coefficient during ion transport and ion storage (depending on the use as solid electrolyte or as electrode material).[387] When using LISICON as a membrane, mainly in an aqueous medium, the density of the obtained ceramic membrane plays a significant role in separating different compartments and allowing selective ion transport.

Furthermore, environmental compatibility, toxicity, and cost efficiency are generally essential. Recently Wang et al. reported the investigation of LISICON membranes ($LiGe_2(PO_4)_3$) in the context of lithium recovery from lithium-containing water.[388] A continuous and energy-efficient selective lithium recovery from an aqueous solution was obtained by combining a redox flow battery, a polymer membrane for anion exchange, and two lithium-selective ceramic LISICON membranes.[388]

2.4.3 Bi-electrolyte

In addition to many modification possibilities of the cell structures to provide the appropriate reaction space for each system, a bi-electrolyte system has also become established. The original form of the CDI was limited to the stable voltage window of water, which is 1.2 V. In this way, the resulting desalination capacity was limited accordingly. Furthermore, the selection of suitable sodium-extracting electrodes for efficient electrochemical desalination is limited by their compatibility with water and their redox potentials in the stability window of water. A variety of promising new materials could be used for electrochemical desalination, especially NIB anode materials, if the requirement to expose the electrode to feedwater flow was removed. Approaches to find a solution to this problem were initially to use a cell that was operated only in organic electrolyte. Porada et al. 2016 first reported widening the CDI voltage window to 2.5 V and conducted a study of experimental ion removal at voltages beyond the water electrolysis window, showing that higher salt adsorption is possible when using CDI in organic electrolytes.[389] However, to continue to drive the desalination of the predominantly aqueous saline solutions, the bi-electrolyte system was then proposed by Kim et al. in 2018.[390]

The bi-electrode concept makes it possible to divide the desalination cell into two different compartments, in which an aqueous atmosphere prevails in the central channel. **Figure 18** gives an overview of different setups of the bi-electrolyte cell. An organic electrolyte is used in the side channel. The compartments were separated by using a polymer-based ion exchange membrane. This way, with

an extension of the stable cell voltage to 2.4 V, an excellent desalination capacity of 63 mg$_{NaCl}$ g^{-1} and a charge efficiency of 95% were obtained. Thus, the choice of electrode materials is no longer limited to compatibility with water and the redox potential within the stable potential range of water. This opens the door for using many high-performance electrode materials, which have already successfully demonstrated Na$^+$ ion uptake capability, for example, in NIBs. Arnold et al. in 2021 reported a bi-electrolyte membrane capacitive deionization in which a typical alloying material (antimony) was used in 1 M NaClO$_4$ in EC/DMC + 5% FEC organic electrolyte.[391] Using a selective sodium permeable membrane (NASICON) to separate the organic from the aqueous flowing compartment, an optimized desalination capacity of 294 mg$_{NA gSb}^{-1}$ in a voltage range of -2 V to +2 V with a charge efficiency of 74% in 600 mM was achieved.[391]
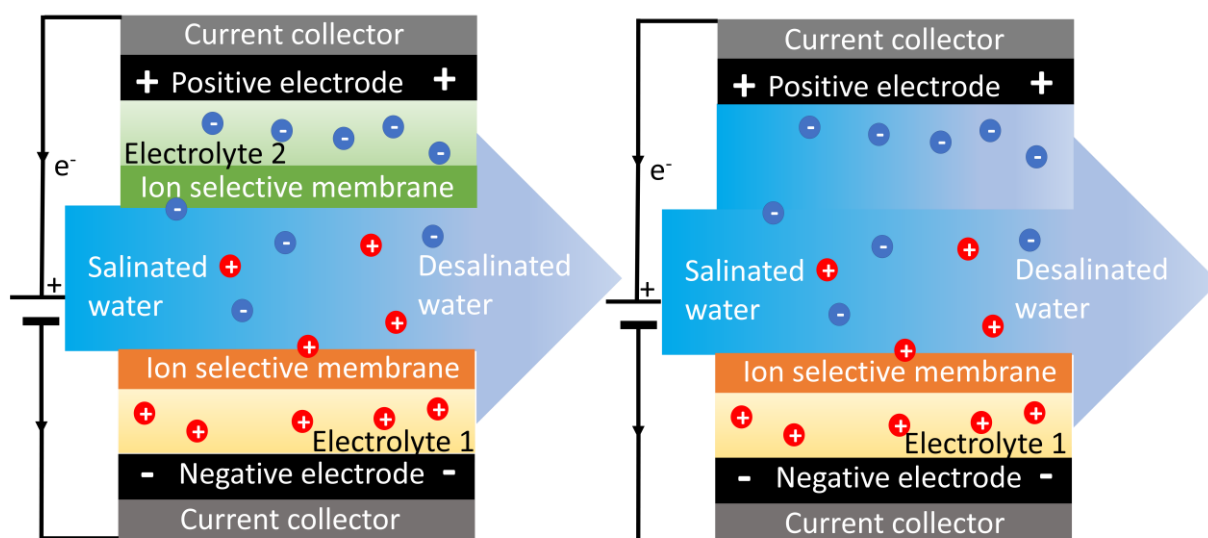
Figure 18: Overview of different types of bi-electrolyte Faradaic deionization cells. A) Two separated electrolyte compartments with different electrolytes in addition to the salinated water flow, B) one electrode can be operated in salinated water.

2.5 Recycling

All raw materials are found only in limited quantities on our planet. Only careful and fairer use of the earth's natural resources can help us sustainably protect our environment. In times of booming battery industry, it becomes increasingly important to have a recycling concept at hand for all the batteries that have come to their end of life and to design a sustainable concept. In addition, regulations ensure the obligation of battery recycling with set minimum recycling rates for individual battery materials, which are tightened over time. Furthermore, minimum values for the use of recyclates in the production of new batteries are prescribed. In the EU, the latest regulations call for about 73% of portable batteries to be collected by 2030 and minimum levels of cobalt (16%), lead (85%), lithium (6%), and nickel (6%) from manufacturing and consumer waste to be recycled in new batteries.[392, 393] Recycling makes waste that becomes unusable after a process is usable again and returns it to the economic cycle. In the best case, this is done multiple times. **Figure 19** presents an overview of the different recycling path of LIB components.
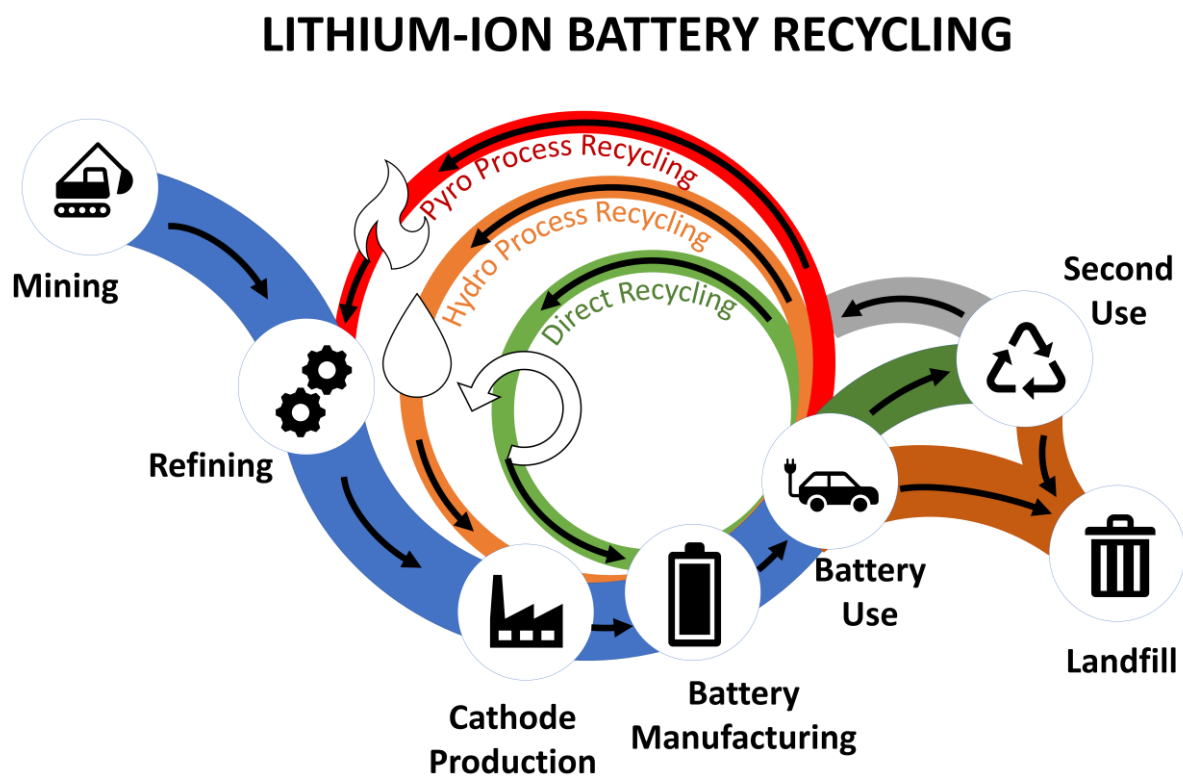
Figure 19: Overview of different recycling routes for LIBs components. Adapted with permission.[394] Copyright 2019, Argonne National Laboratory.

On the one hand, this can be done by reusing the material in its original form. However, it is also possible to recycle waste products through a chemical recycling process, in which the material is broken down into its basic components. In this way, responsible use of resources can be maintained, and a significant amount of CO_2 can be saved, significantly advancing battery research. The complexity of LIBs with different active and inactive material chemistries is an obstacle to the desire to introduce a robust recycling process for all types of LIBs. Therefore, the current state-of-the-art needs to be analyzed, improved, and adapted to upcoming cell chemistries and components. In addition, many recycling methods within the battery guidelines for different cell components have already been proposed and optimized.

2.5.1 Battery material recycling

Given sustainable development, the obligation to recycle certain shares, and the growing number of large-scale battery production factories, recycling spent batteries and valorizing the valuable components has never been more important. Since most of the battery (cathode) materials have a considerable percentage in the battery cell cost, finding a suitable way to recycle these materials or find a second-life application is becoming more attractive. Current recycling technologies, usually based on chemical leaching methods, have critical aspects such as massive consumption of various chemicals and secondary pollution and generally involve lengthy procedures. Therefore, developing cost-effective and environmentally friendly methods has been and continues to be necessary. In general, a distinction can be made between direct regeneration of the material and chemical processing (breaking down into different precursor compounds, oxidation, annealing, etc.). Often, however, all approaches require a relatively large amount of energy and costs in the form of chemicals to restore the materials' capacity. Therefore, the demand for improved methods is currently as high as ever.

The state-of-the-art literature already includes an approach to efficiently recycle $LiFePO_4$ (a widespread cathode material in commercial LIBs). Following a redox targeting-based approach of $LiFePO_4$ with $[Fe(CN)_6]^{3-}$, the material could be rapidly degraded to solid $FePO_4$ and soluble Li^+ ions in the electrolyte, where the $Fe(CN)_6]^{3-}$ is immediately regenerated in a connected oxygen flow cell.[395] At the same time, Li^+ ions are collected as LiOH. Highly pure LiOH and $FePO_4$ (<99.90%) could be obtained with a high Li removal efficiency (99.8%) without secondary contamination.[395] Other sustainable recovery processes of the individual elements have also been successfully carried out. By leaching with citric acid or tea waste, up to 99% of Co and 93% of Li were recovered from a $LiCoO_2$ cathode, whereby the citric acid can also be recycled.[396] Recently developed pyrometallurgical processes are well established for processing primary materials and can achieve high recovery yields concerning the metals cobalt, copper, and nickel, but they are challenging for lithium recovery.[397]

2.5.2 Lithium recycling

Exploiting lithium sources is expected to increase the metal's price due to increased electrification. In addition, there are geopolitical restrictions and social and ecological concerns, as the raw materials are often mined in politically unstable regions under questionable working conditions and using ecologically doubtful methods. In addition to the limited resources, environmental protection and the concept of sustainability are increasingly important in the overall consideration of raw material extraction. As an essential raw material and a strategic key element for electromobility, lithium requires research and profitability analysis of new recycling processes, especially for batteries. The anode material used in commercial LIBs is typically graphite.

In contrast, the cathode material often contains a considerable proportion of essential and scarce metals such as manganese, lithium, cobalt, and nickel. It thus also takes a larger overall percentage of the battery in terms of cost and mass. So far, hydro- and pyrometallurgical approaches dominate the recycling of cathode materials.[398-402] Occasionally, bioleaching, for example, by bacteria, is also reported.[403-405] A promising technology, both from an economic and an ecological point of view, that ties in with hydrometallurgical processes and enables lithium recovery represents ion-selective electrochemistry. Based on a desalination battery and technology, Pasta et al. proposed a new energy-efficient electrochemical method for recovering lithium from brines in 2012.[406] After wet chemical digestion, the obtained lithium-rich electrolyte was continuously pumped through the flow channel of the cell passing the two electrodes. By applying an external negative current (charging) to the cathode, lithium cations and chloride anions are selectively extracted from the solution by being captured by the electrode materials. In the subsequent discharging step, the ions can be mobilized again, resulting in a concentration of LiCl in the recovery solution (**Figure 20**).
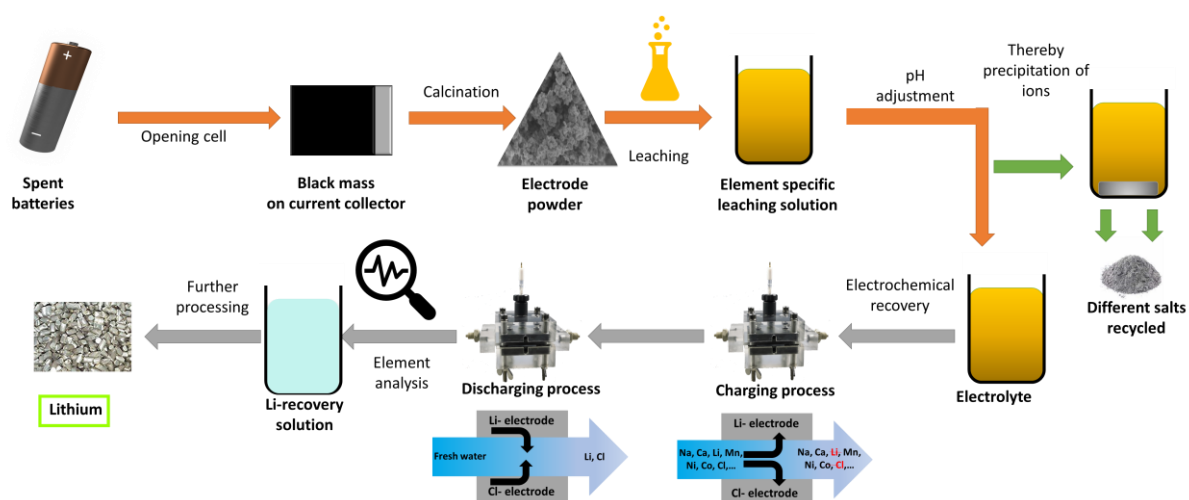
Figure 20: Compilation of the schematic sequence of an electrochemical recycling process of lithium on old used battery cells.

3 APPROACH AND OVERVIEW

Society's pursuit of renewable energy and environmentally friendly technologies has brought the battery industry a colossal mandate.[407-409] At the same time, it has increased the demands and requirements on these systems. LIBs are still one of the most important energy storage systems with high power density, large energy density, and high output voltage after their first commercialization by Sony in 1991.[3] However; alternative battery technologies are of great interest due to the ever-increasing demand for batteries and the expected sharp rise in price. No less important are the often precarious conditions of still mining some raw materials in politically and ecologically sensitive areas to extract electrode material for LIBs. The electrode materials are often limiting factors for a low lifetime, low energy density, and power density. Advanced electrode design often involves hybrid architecture (typically in conjunction with carbon), which leads to improved electrochemical performance due to the synergetic effects of carbon with the active material and other physical improvements of the electrode (electrical conductivity, buffering of volume change, etc.).

My work is motivated by the quest for next-generation electrode materials for electrochemical applications at the water/energy/recycling nexus. Thereby, the publications within my thesis work cluster in these three categories.

Segment 1: Energy nexus. Motivated by this, the present work explores hybrid materials for energy storage systems, including carbon and carbide hybrids. Carbon, usually in the form of carbon black, is the most common conductive additive. However, physical mixing to obtain (nano)composites is less potent in achieving a maximized performance than chemical co-synthesis (hybridization).[194] In this sense, **Section 4.1** explores nanohybrids of LTO and carbon onions toward LIB and NIB application. Compared to the bulk material, the hybridization of nanosized LTO with nanosized carbon enables improved rate stability and cycling stability. For lithium ion intercalation, LTO carbon onion hybrid electrodes achieve a specific capacity of 188 mAh g^{-1} at a specific current of 10 mA g^{-1}, which maintains 100 mAh g^{-1} at 1 A g^{-1} with a capacity retention of 96% after 400 cycles. Optimized hybrid material also shows improved electrochemical performance in NIBs with maximum capacity values of 102 mAh g^{-1} while retaining 96% of initial capacity after 500 cycles.

Carbon may be the most common conductive additive, but it is not the only promising material for hybridization strategies. Due to their unique physical and chemical natures, two-dimensional materials like MXenes are promising for forming interesting hybrids and heterostructures with other materials. MXenes alone also show good electrochemical addressability, but the capacity is limited to moderate values due to the limited storage sides for cations between the layers. **Section 4.2** shows the ability to significantly increase the interlayer spacing (1.75 nm) of $Ti_3C_2T_z$ MXenes by silica-pillaring. This design

resulted in a dramatically enhanced electrochemical performance, with superior capacities, rate capability (over 150 mAh g^{-1} at 1 A g^{-1}), and cycling stability (71% capacity retention after 500 cycles) compared to the non-pillared material. In addition, an in situ electrochemical dilatometry supported by further X-ray diffraction measurements showed the interplay between structural changes and electrochemical performance. Through this, silica-pillared Ti$_3$C$_2$T$_z$ MXene exhibits superior cycling performance with 314 mAh g^{-1} (at 0.2 mA g^{-1}) despite a larger volume change and a decrease in crystallinity was obtained, indicating an inhomogeneous expansion of the interlayers. Yet, the capacity remained limited by the predominance of ion intercalation as the charge storage mechanism.

To reach a capacity beyond the limitation of intercalation materials, one can hybridize MXene with conversion or alloying materials. In **Section 4.3**, antimony, a well-known alloying material with a theoretical capacity of 660 mAh g^{-1}, is combined with Ti$_3$C$_2$T$_z$ MXenes showing different morphologies and surface functional groups. Optimized synthesis protocol leads to materials with a high reversible capacity of 450 mAh g^{-1} at 0.1 A g^{-1} with a capacity retention of 96% after 100 cycles while also exhibiting high rate capability with 365 mAh g^{-1} at 4 A g^{-1}. This work illustrates the strong influence of the electrode material design on electrochemical performance. The best performance is not seen for the sample with the highest amount of antimony, the smallest particle size, or the largest interlayer distance of MXene. Instead, the best performance is seen for a homogeneous distribution of antimony and MXene particles.

Motivated by the promising results from MXene and an alloying material (Sb), my work explored the combination of MXene with a conversion material (SnO$_2$). While Sb is the 63rd most abundant element on Earth (crust; annual mining capacity about 147 kt [2018]),[410, 411] Sn is much more abundant (rank 45th; annual mining capacity 318 kt [2018]).[412] The challenge, like alloying materials, is for conversion materials to maintain a high charge storage capacity despite severe structural changes during cyclic charging and discharging. **Section 4.4** combines SnO$_2$ with MXenes as an anode material in LIB. Through the optimized composition of 1:1 (SnO$_2$:Ti$_3$C$_2$T$_z$), a stable de-lithiation capacity of 525 mAh g^{-1} for 700 cycles and high rate stability of 340 mAh g^{-1} at 8 A g^{-1} was achieved. At the same time, the reversibility and kinetics of the electrochemical reactions are due to the synergistic interaction between the tin oxide and MXenes, where the latter can act as a buffer for the conversion reaction as well as improve the charge transport properties in the electrode. In order to investigate the electrochemical mechanism of this material as well as to obtain further chemical, morphological and structural data of the system, XPS and STEM were used, among others.

Segment 2: Water nexus. NIBs are a promising LIB alternative, combining low cost, similar redox potential, and similar intercalation chemistry to lithium. Considering the abundance of sodium in seawater, NIB is an interesting model system for dual-use applications in electrochemical desalination.

Section 4.5 introduces seawater batteries as a unique energy storage system for the sustainable storage of renewable energy through the direct use of seawater as a source for converting electrical energy and chemical energy. Some technological challenges for seawater batteries, such as shortened lifetime, unsafe battery operation, low efficiencies, and low stabilities, have not yet been fully overcome. However, the advantages of seawater batteries offer a perspective for sustainable, environmentally friendly, performance-oriented, and cost-efficient applications at the interface between energy and water.

Seawater batteries, namely having one sodium ion removal electrode separated from seawater by a ceramic membrane, can also be translated to battery desalination. **Section 4.6** paired, for the first time, an Sb-based electrode (shielded by a sodium-selective ceramic membrane) with nanoporous carbon (capable of electrosorbing anions) to form an electrochemical desalination system. To this end, we developed a multi-channel bi-electrolyte cell. By optimizing the cell design, the application of a bi-electrolyte and using a selective sodium permeable membrane (NASICON) allows operating the system at ±2 V. At the same time, a desalination capacity of 294 $mg_{Na} \, g_{Sb}^{-1}$ could be achieved.

It is attractive to use a fast pseudocapacitive material to accomplish water desalination with a high rate and high capacity instead of a rather sluggish alloying process. **Section 4.7** reports cuboid cobalt hydroxide with a hollow architecture synthesized via template etching. The hollow structure allows rapid ion transport inside the material and thus keeps the electrode intact by mitigating volume expansion during cycling, as confirmed by in situ electrochemical dilatometry. Therefore the hollow electrode achieves an outstanding desalination capacity of 1176 $mg_{NaCl} \, g_{(Co(OH)2)}^{-1}$ with a high desalination rate of 3.3 $mg_{NaCl} \, g_{(Co(OH)2)}^{-1} \, min^{-1}$.

Segment 3: Recycling nexus. In the context of diminishing Li resources for energy storage and the continuously increasing demands for batteries, which at present mostly rely on LIB technology, it is also indispensable to extract lithium from aqueous media. For the challenge of accessing the enormous amount of lithium from low-concentrated sources, which has been a huge challenge so far, a redox flow battery for continuous and energy-efficient recovery from aqueous solutions is reported in **Section 4.8**. Using A green redox par and a solid-state lithium superionic conductor (LISICON) membrane for the selective uptake and release of Li^+, a technology has been proposed to extract dissolved lithium with a purity of 93.5% from simulated seawater.

The previous section dealt with ion recovery from artificial solutions (hydrometallurgical LIB recycling). Yet, avoiding the need to dissolve electrodes altogether and directly recycling LIB electrodes would be far more sustainable. The last part of my thesis, **Section 4.9**, therefore, focuses on the battery recycling of MXene. This unique 2D material allows assembly, disassembly, and re-assembly for a closed-loop

use/recycling/reuse process. This work also shows that the second life as an electrocatalytic material of oxidized MXene electrodes can be achieved. Specifically, free-standing MXene electrodes free of binder and conductive additives were used in the context of application in LIBs- and NIBs and underwent a direct recycling process. The electrode material exhibits good recyclability with capacity recovery rates above 90%. The spent end-of-life MXene materials were oxidized in the second step in controlled conditions to TiO_2/C materials, which have a great potential for application of second life in the field of batteries and further in electrochemical oxygen revolution, photocatalytic hydrogen evolution, or photodegradation.

Figure 21: Overview of the different segments of this thesis. All chapters refer to peer-reviewed publications.

4   RESULTS AND DISCUSSION

This thesis includes the following peer-reviewed research papers as subchapters of the results and discussion section

4.1   Hybrid anodes of lithium titanium oxide and carbon onions for lithium-ion and sodium-ion energy storage

4.2   In situ investigation of expansion during the lithiation of pillared MXenes with ultralarge interlayer distance

4.3   Design of high-performance antimony/MXene hybrid electrodes for sodium-ion batteries

4.4   Unravelling the electrochemical mechanism in tin oxide/MXene composites as highly reversible negative electrodes for lithium-ion batteries

4.5   Dual-use of seawater batteries for energy storage and water desalination

4.6   Antimony alloying electrode for high-performance sodium removal: how to use a battery material not stable in aqueous media for saline water remediation

4.7   Three-dimensional cobalt hydroxide hollow cube/vertical nanosheets with high desalination capacity and long-term performance stability

4.8   Redox flow battery for continuous and energy-effective lithium recovery from aqueous solution

4.9   Recycling and second life of MXene electrodes for lithium-ion batteries and sodium-ion batteries

4.1 Hybrid anodes of lithium titanium oxide and carbon onions for lithium-ion and sodium-ion energy storage

Hwirim Shim,[1,2] Stefanie Arnold,[1,2] Öznil Budak,[1,2]

Maike Ulbricht,[1,2] Pattarachai Srimuk[1] and Volker Presser[1,2]

[1]   INM - Leibniz Institute for New Materials, Campus D2.2, 66123 Saarbrücken, Germany

[2]   Department of Materials Science and Engineering, Saarland University, Campus D2.266123 Saarbrücken, Germany

Own Contribution:

Investigation, and writing – review & editing.

FULL PAPER

Hybrid Anodes of Lithium Titanium Oxide and Carbon Onions for Lithium-Ion and Sodium-Ion Energy Storage

Hwirim Shim, Stefanie Arnold, Öznil Budak, Maike Ulbricht, Pattarachai Srimuk, and Volker Presser*

This study demonstrates the hybridization of $Li_4Ti_5O_{12}$ (LTO) with different types of carbon onions synthesized from nanodiamonds. The carbon onions mixed with a $Li_4Ti_5O_x$ precursor for sol–gel synthesis. These hybrid materials are tested as anodes for both lithium-ion battery (LIB) and sodium-ion battery (SIB). Electrochemical characterization for LIB application is carried out using 1 M $LiPF_6$ in a 1:1 (by volume) ethylene carbonate and dimethyl carbonate as the electrolyte. For lithium-ion intercalation, LTO hybridized with carbon onions from the inert-gas route achieves an excellent electrochemical performance of 188 mAh g^{-1} at 10 mA g^{-1}, which maintains 100 mAh g^{-1} at 1 A g^{-1} and has a cycling stability of 96% of initial capacity after 400 cycles, thereby outperforming both neat LTO and LTO with onions obtained via vacuum treatment. The performance of the best-performing hybrid material (LTO with carbon onions from argon annealing) in an SIB is tested, using 1 M $NaClO_4$ in ethylene/dimethyl/fluoroethylene carbonate (19:19:2 by mass) as the electrolyte. A maximum capacity of 102 mAh g^{-1} for the SIB system is obtained, with a capacity retention of 96% after 500 cycles.

1. Introduction

The increased demand for energy storage applications in daily life necessitates the development of faster and more long-lasting energy storage devices. Lithium-ion batteries (LIBs) have been widely explored and implemented for mobile or stationary devices owing to their lightweight and high energy and power density.[1] Conventional LIBs use graphite as an anode due to its high theoretical capacity (372 mAh g^{-1}), good cycling stability,

and natural abundance.[2] However, graphite electrodes experience major safety issues, because their operation potential is near to the lithium electroplating potential of 0.1 V versus Li/Li$^+$, which leads to a high risk of penetrable dendrite formation.[3,4] An alternative to graphite anodes is lithium titanium oxide ($Li_4Ti_5O_{12}$, LTO), for which good structural stability during lithiation/delithiation and safety due to its high operation potential have been reported.[5] The theoretical capacity of LTO is 175 mAh g^{-1}, utilizing three Li$^+$ ions via Equation (1)[6]

$$Li_4Ti_5O_{12} + 3Li^+ + 3e^- \rightarrow Li_7Ti_5O_{12} \quad (1)$$
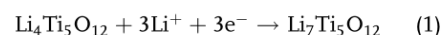
The operation potential of the LTO range of around 1.55 V versus Li/Li$^+$ for Li$^+$ intercalation and deintercalation prevents solid electrolyte interface (SEI) formation.[7,8] In addition, LTO exhibits minor to zero volume change during operation, yielding good cycling performance, and high coulombic efficiency.[7,9] However, LTO is known for its low Li$^+$ ion diffusion (10^{-13}–10^{-9} cm^2 s^{-1})[10] and low electrical conductivity of 10^{-8}–10^{-13} S cm^{-1}, which limits the achievable rate capability.[11–14] The performance of LTO can be enhanced by improving the intrinsic conductivity, which can be done by the introduction of oxygen deficiencies; however, this approach requires an extra step of thermal treatment of the active material.[15] Therefore, the mechanical or chemical implementation of carbon as a conductive additive is more preferred.[16] Much work has addressed the performance by forming nanocomposite or hybridizing conductive carbon materials to LTO. The former, nanocomposites, is the most common way of producing LTO-based electrodes, usually by the use of carbon black, carbon nanotubes, or graphene.[17–20] Hybrid materials can be obtained by methods, such as surface modification of LTO by carbon coating using carbon sources, such as sucrose, glucose, solvents, acids, or gases, which have resulted in enhanced electrochemical performance.[21–25] These works document the great importance of achieving a homogenous distribution of conductive and active material on a sub-100 nm length scale.[26] Therefore, the use of synthesis methods capable of yielding nanoscale hybridization is important, especially when using nanoscale carbon additive particles.

In addition to the ability to reversibly intercalate lithium, LTO has also been demonstrated to be suitable anode in sodium-ion

H. Shim, S. Arnold, Ö. Budak, M. Ulbricht, Dr. P. Srimuk, Prof. V. Presser
Program Division Energy Materials
INM—Leibniz Institute for New Materials
Saarbrücken 66123, Germany
E-mail: volker.presser@leibniz-inm.de

H. Shim, S. Arnold, Ö. Budak, M. Ulbricht, Prof. V. Presser
Department of Materials Science and Engineering
Saarland University
Saarbrücken 66123, Germany

The ORCID identification number(s) for the author(s) of this article can be found under https://doi.org/10.1002/ente.202000679.

RESULTS AND DISCUSSION

**ADVANCED
SCIENCE NEWS**
www.advancedsciencenews.com

Energy Technology
Generation, Conversion, Storage, Distribution
www.entechnol.de

batteries (SIBs).[27–34] Interest in SIBs is based on the high natural abundance of sodium and associated reduced costs.[33] The insertion–extraction potential of sodium into LTO is reported to be around 0.9 V versus Na/Na$^+$ without sodium metal plating on the electrode surface.[27,29,32]

The low intrinsic conductivity issue remains and possibly relates to the high overpotential or poor rate capability.[33,35] The theoretical Na$^+$ ion uptake capacity of LTO is also 175 mAh g^{-1}, assuming the insertion of three Na$^+$ ions, according to Equation (2)[27]

$$2Li_4Ti_5O_{12} + 6Na^+ + 6e^- \rightarrow Li_7Ti_5O_{12} + LiNa_6Ti_5O_{12} \qquad (2)$$
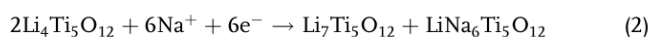
In this study, we explore hybrid materials composed of sol–gel-derived LTO and nanoscale carbon onions (OLC) for use as LIB and SIB anode material. To obtain carbon onions, we used thermal annealing of nanodiamond precursors in an inert atmosphere or under vacuum to yield carbon onions with a primary particle size of 5–10 nm.[36,37] We chose carbon onions, because the absence of inner porosity and the mesopore-dominate interparticle pore space allows a highly favorable nanoscale implementation of metal oxides.[38,39] The resulting hybrid materials were electrochemically surveyed for charge storage capacity, rate capability, and cycling stability for the reversible intercalation of lithium and sodium.

2. Experimental Section

2.1. Material Preparation

Two types of carbon onions were synthesized by thermal annealing of nanodiamond powder (ND; NaBond Technologies) at 1700 °C for 1 h under Ar atmosphere, noted OLCa, or at 1300 °C for 4 h under vacuum, labeled OLCv, using high-temperature graphite furnace (Carbolite).

For the synthesis of the hybrid LTO, we used sol–gel synthesis. Lithium ethoxide dissolved in tetrahydrofuran (LiOEt, THF; Sigma Aldrich) and titanium isopropoxide (TTIP; Sigma Aldrich) were used as lithium and titanium sources, respectively. LiOEt (4 mL) was added to 5 mL of THF with vigorous stirring; then, 1.48 mL of TTIP was added dropwise to the stirring solution. Subsequently, 0.45 g of oxalic acid was added, and then, the precursor solution was stirred for 2 h at 50 °C. Appropriate amounts of OLCa or OLCv powders were added by wet impregnation into prepared sol. The carbon content was 15 mass% of the final hybrid material. The impregnated mixtures were dried at 50 °C under vacuum for overnight, followed by further drying at 80 °C for 12 h.

In addition to LTO-carbon hybrids, we also synthesized neat LTO. The latter was prepared by following the same synthesis protocol but without the addition of carbon onions. The well-dried materials were then annealed at 700 °C for 2 h (heating rate 1 °C min^{-1}) under Ar atmosphere.

The resulting materials are named "LTO" = neat LTO, "LTO-OLCa" = LTO with the addition of argon-annealed carbon onions, and "LTO-OLCv" = LTO with the addition of vacuum-treated carbon onions.

2.2. Material Characterization

2.2.1. Structural Characterization

X-ray diffraction (XRD) was carried out in a D8 Discover Diffractometer (Bruker AXS) with a copper X-ray source (Cu-K$_\alpha$ radiation, 40 kV, 40 mA). We used a Göbel mirror with a 1 mm point focus and a 2D X-ray detector (VANTEC-500) for the measurements. The samples were placed on a sapphire single crystal and measured with the detector being placed at angles from 20θ to 80θ with a step width of 20θ and a measuring time of 1000 s per step.

The carbon content of the hybrid materials was determined with thermogravimetric analysis (TGA), performed with a TG-209-1 Libra (Netzsch). For each TGA measurement, the samples were heated to 1000 °C under synthetic air condition (80 vol% N$_2$, 20 vol% O$_2$) with a flow rate of 20 sccm at a heating rate of 5 °C min^{-1}.

Raman spectroscopy was performed with a Renishaw inVia Raman Microscope using an neodymium-doped yttrium aluminum garnet laser with an excitation wavelength of 532 nm and a power of about 0.5 mW at the focal point. The acquisition time for each spectrum was 30 s with ten accumulations to enhance the signal-to-noise ratio. Peak fitting of the measured spectra was accomplished, assuming two Voigt peaks for the D- and G-modes individually.

Transmission electron microscopy (TEM) was performed using a JEOL 2100F system at an operating voltage at 200 kV. Samples for TEM imaging were prepared by dispersion and tip-sonication of the hybrid materials in ethanol and subsequent drop-casting of the dispersion on a copper grid with a lacey carbon film.

Scanning electron microscopy (SEM) of the prepared electrodes was conducted with a JEOL JSM-7500F system at an acceleration voltage of 3 kV and an emission current of 10 μA. The energy-dispersive X-ray spectroscopy (EDX) was carried out using an X-Max-150 detector (Oxford Instruments) attached to the SEM system. The spectra were obtained at an acceleration voltage of 15 kV and an emission current of 10 μA. Before the spectral acquisition of each sample, calibration was conducted with a silicon wafer.

The porosity of the powder materials was analyzed by the use of nitrogen gas sorption at −196 °C with an Autosorb iQ system from Quantachrome (now: Anton-Paar). The powder samples were outgassed at 300 °C for 20 h before the measurement, and the recorded gas sorption isotherms along with the calculated Brunauer–Emmett–Teller (BET) surface area values are provided in Figure S1, Supporting Information.

2.2.2. Electrochemical Characterization

For the preparation of the anode, the synthesized LTO and the hybrid materials were mixed with polyvinylidene fluoride (PVDF; Alfa Aesar) binder with a 9:1 mass ratio without any further conductivity additive, followed by the addition of N-methyl-2-pyrrolidone (NMP; Sigma Aldrich) solvent. The mixed slurry was coated on a copper foil (25 μm, MTI) using a 200 μm doctor blade. The coated electrode was dried overnight in a fume hood at room temperature, then transferred to a vacuum oven, and dried

54

at 110 °C overnight. The dried coating was pressed in a hot roll press machine (MTI), and then punched to 10 mm discs using press punch (EL-CELL) for electrochemical benchmarking. The mass loadings of each electrode were 5.5 ± 0.4 mg cm^{-2} for neat LTO 3.7 ± 0.2 mg cm^{-2} for LTO-OLCa, and 3.7 ± 0.4 mg cm^{-2} for LTO-OLCv. The dry thickness of the prepared electrode was 36 µm for neat LTO and 39 µm for the two hybrid samples. The electrode density was 1.48 g cm^{-3} for neat LTO, 0.94 g cm^{-3} for LTO-OLCa, and 0.93 g cm^{-3} for LTO-OLCv.

For half-cell measurements, an LTO containing working electrode and lithium or a sodium disc counter and reference electrodes were assembled into CR2032 coin cells. We used a Whatman GF/F glass fiber separator and 1 M LiPF$_6$ salt in a mixture of ethylene carbonate and dimethyl carbonate (EC:DMC; 1:1 by volume, Sigma Aldrich) or 1 M NaClO$_4$ in a mixture of EC:DMC with 5 mass% fluoroethylene carbonate (FEC) as the electrolyte.[40]

Cyclic voltammetry was carried out with a Biologic VMP300 potentiostat/galvanostat and performed in a potential window from 1.0 to 2.8 V versus Li/Li$^+$ and 0.3 to 2.5 V versus Na/Na$^+$ at the scan rates of 0.1–10 mV s^{-1}. Electrochemical impedance spectroscopy (EIS) was measured at an applied AC voltage amplitude of 10 mV from the frequency range of 10^6–10^{-2} Hz. For quantifying the rate handling capability, galvanostatic charge/discharge with potential limitation (GCPL) measurement was carried out at an Arbin Battery Cycler in a potential range of 1.0–2.8 V versus Li/Li$^+$ and 0.3–2.5 V versus Na/Na$^+$ using specific currents ranging from 0.01 to 10 A g^{-1} and 0.025 to 5 A g^{-1}, respectively. The cycling stability was quantified using GCPL at a specific current of 0.1 A g^{-1} for both LIB and SIB testing. All the measurements were carried out in climate chambers (Binder) set to 25 ± 1 °C.

The specific capacity C_{sp} of the hybrid material was calculated by integration of the applied lithium or sodium extraction current I over the extraction time t accounting for the deintercalation step from 1.0 to 2.8 V versus Li/Li$^+$ and 0.3 to 2.5 V versus Na/Na$^+$, as in Equation (3)

$$C_{sp} = \frac{\int_{t_0}^{t} I dt}{m} \tag{3}$$

The specific capacity was normalized to the total mass of the hybrid material m in the electrode without the polymer binder.

3. Results and Discussion

3.1. Hybrid Material Synthesis

Figure 1A presents the schematic illustration of the LTO-OLC hybrid. The preparation of LTO sols and wet impregnation of two different types of carbon onions synthesized under different conditions lead to a synthesis of the hybrid material LTO-OLCa and LTO-OLCv by thermal annealing. As shown in TEM images (Figure 1B–D), LTO, LTO-OLCa, and LTO-OLCv show nanoscale crystalline domains related to lithium-titanium oxide. For better comparison, TEM images of carbon onions (OLCa and OLCv) are presented in Figure S2A,B, Supporting Information.

XRD was used to determine and study the crystal structure of the prepared pristine and hybrid materials. The data of all X-ray diffractograms (**Figure 2**A) match very well to cubic spinel lithium titanium oxide (LTO, PDF 49-0207, $a = 8.359$ Å). The measurement data are dominated by signals from the crystalline LTO phase, whereas the contribution of the incompletely graphitic carbon is mostly lost in the background; more information on the carbon structure can be inferred from the Raman spectra (later paragraph). We used Rietveld refinement to calculate the average coherence length (roughly corresponding with the domain size) of LTO (Table S1, Supporting Information). All sample materials, that is, LTO and the two types of LTO-carbon
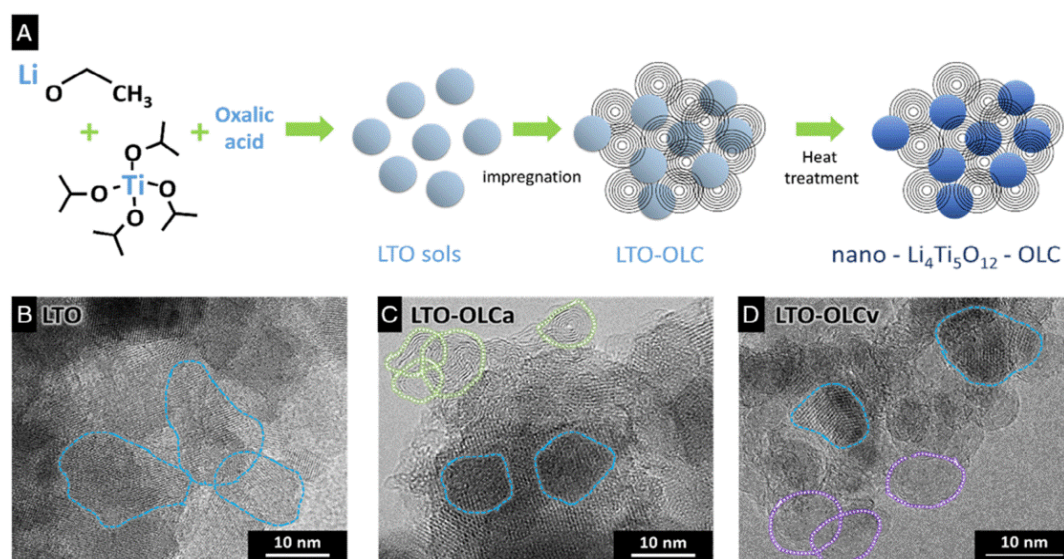
Figure 1. A) Schematic illustration of preparation for hybrid nano-LTO-OLC. The transmission micrograms of B) LTO, C) LTO-OLCa, and D) LTO-OLCv hybrid material. LTO domains are marked by blue dashed lines and carbon onions with C) green and D) purple dotted lines.

RESULTS AND DISCUSSION

**ADVANCED
SCIENCE NEWS**
www.advancedsciencenews.com

Energy Technology
Generation, Conversion, Storage, Distribution
www.entechnol.de
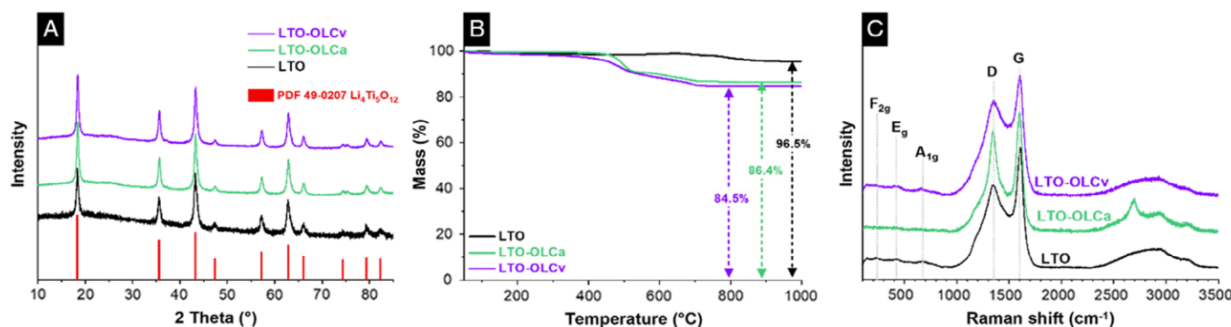
Figure 2. A) XRD patterns of LTO, LTO-OLCa, and LTO-OLCv. B) TGA of samples under synthetic air atmosphere for the characterization of the amount of carbon. C) Background-corrected Raman spectra of LTO, LTO-OLCa, and LTO-OLCv. All data were normalized to the intensity of the carbon G-mode as 100% and the intensity at $3500 \, cm^{-1}$ as 0%.

hybrids, have a highly comparable domain size of about $30 \pm 2 \, nm$ and a unit cell constant of $a = 8.366 \pm 0.002 \, Å$.

The carbon content of the synthesized LTO hybrid materials was determined by TGA (recorded in synthetic air) and elemental (CHNS/O) analysis. As displayed in Figure 2B, LTO without carbon onions showed 3.5 mass% carbon content, which is the carbon formed during the thermal annealing of the as-prepared oxide sols from the residual chains from metal alkoxide precursors. LTO-OLCa and LTO-OLCv showed 14 and 15.5 mass% carbon content, respectively. These data agree with the carbon amount introduced during the synthesis step, and the elemental analysis results in Table S2, Supporting Information.

We characterized the carbon structure of the samples with Raman spectroscopy. The resulting spectra are presented in Figure 2C for LTO and the hybrid materials, and in Figure S2D, Supporting Information, for carbon onions. For comparison, the peak position and full-width at half-maximum (FWHM) of each D- and G-modes and the I_D/I_G ratio by use of four Voigt peak fitting are provided in Table S3, Supporting Information. The individual deconvolution of the Voigt peak fitting is presented in Figure S3, Supporting Information. The Raman spectra of all carbon onions and hybrid materials show the characteristic D-mode and G-mode of incompletely graphitized carbon (nanocrystalline carbon) and the corresponding overtones.[41] Carbon onions synthesized under argon atmosphere and vacuum show very different Raman spectra in agreement with previous studies.[36,37] Specifically, we see narrower D- and G-modes in the case of OLCa (D-mode: $71 \, cm^{-1}$; G-mode: $70 \, cm^{-1}$) compared with OLCv (D-mode: $176 \, cm^{-1}$; G-mode: $90 \, cm^{-1}$); this aligns with the much lower synthesis temperature during vacuum annealing ($1300 \, °C$) compared with the thermal treatment in argon ($1700 \, °C$). Higher synthesis temperatures are known to result in a higher order of structural ordering of the carbon phase.[42]

In Figure 2C, at lower Raman shift, characteristic vibration bands at 243, 431, and $670 \, cm^{-1}$ for LTO are observed for LTO, LTO-OLCa, and LTO-OLCv.[43–45] At first, it may be surprising to see carbon-related Raman signals for the LTO sample where no carbon onions were introduced during the synthesis. Still, we see clearly, for LTO, a D-band at $1345 \, cm^{-1}$ and a G-band at $1607 \, cm^{-1}$. In addition, there is also the transpolyacetylene (TPA) peak in the range of $1150–1200 \, cm^{-1}$, which indicates the highly disordered nature of carbon.[41] This carbon

species is related to the carbonization of the metal alkoxide residues used for the synthesis. A small amount of carbon also aligns with the thermogram (Figure 2B), as indicated by the mass loss of about 3.5 mass% when heating above $600 \, °C$. The presence of incompletely graphitic carbon in LTO-OLCa and LTO-OLCv is associated mostly with the carbon onions type OLCa and OLCv, respectively. We can understand the Raman spectra of LTO-OLCv and LTO-OLCa as a superimposition of the carbon seen already in the LTO sample in addition to carbon from the carbon onion structure (Figure S3D,E, Supporting Information). LTO-OLCa, compared with the other materials, shows a shaper D-mode ($92 \, cm^{-1}$) and a sharper peak of the carbon-related combination and overtone modes between 2300 and $3400 \, cm^{-1}$. This suggests that the carbon network in LTO-OLCa, in general, possesses a higher degree of graphitic ordering compared with that of the other materials.

3.2. Lithium-Ion Intercalation Behavior and Performance

The synthesized LTO and hybrid materials were prepared to electrodes and tested with a CR2032 coin cell for electrochemical benchmarking of LIB systems. The SEM images of the prepared electrodes are found in Figure S4, Supporting Information. For an overview of the electrochemical performance, the prepared cells were first tested for cyclic voltammetry (CV) in the potential range of 1.0–2.8 V versus Li/Li$^+$ at various scan rates of 0.1–$10 \, mV \, s^{-1}$. The resulting cyclic voltammograms of LTO-OLCa are shown in **Figure 3**A, and voltammograms of LTO and LTO-OLCv are shown in Figure S5A,B, Supporting Information. For comparison, the cyclic voltammograms, which were normalized to the conducted scan rates, are also prepared and presented in Figure 3B for LTO-OLCa, and in Figure S5C,D, Supporting Information, for LTO and LTO-OLCv. In Figure 3A, the lithiation peak starts from 1.55 V versus Li/Li$^+$, and the delithiation peak at 1.6 V versus Li/Li$^+$. The peak separation is larger for faster scan rates due to the overpotential caused by kinetic limitation (Figure 3B).

For a better understanding of the charge transfer kinetics, we used Equation (4)[46–48]

$$i = av^b \tag{4}$$
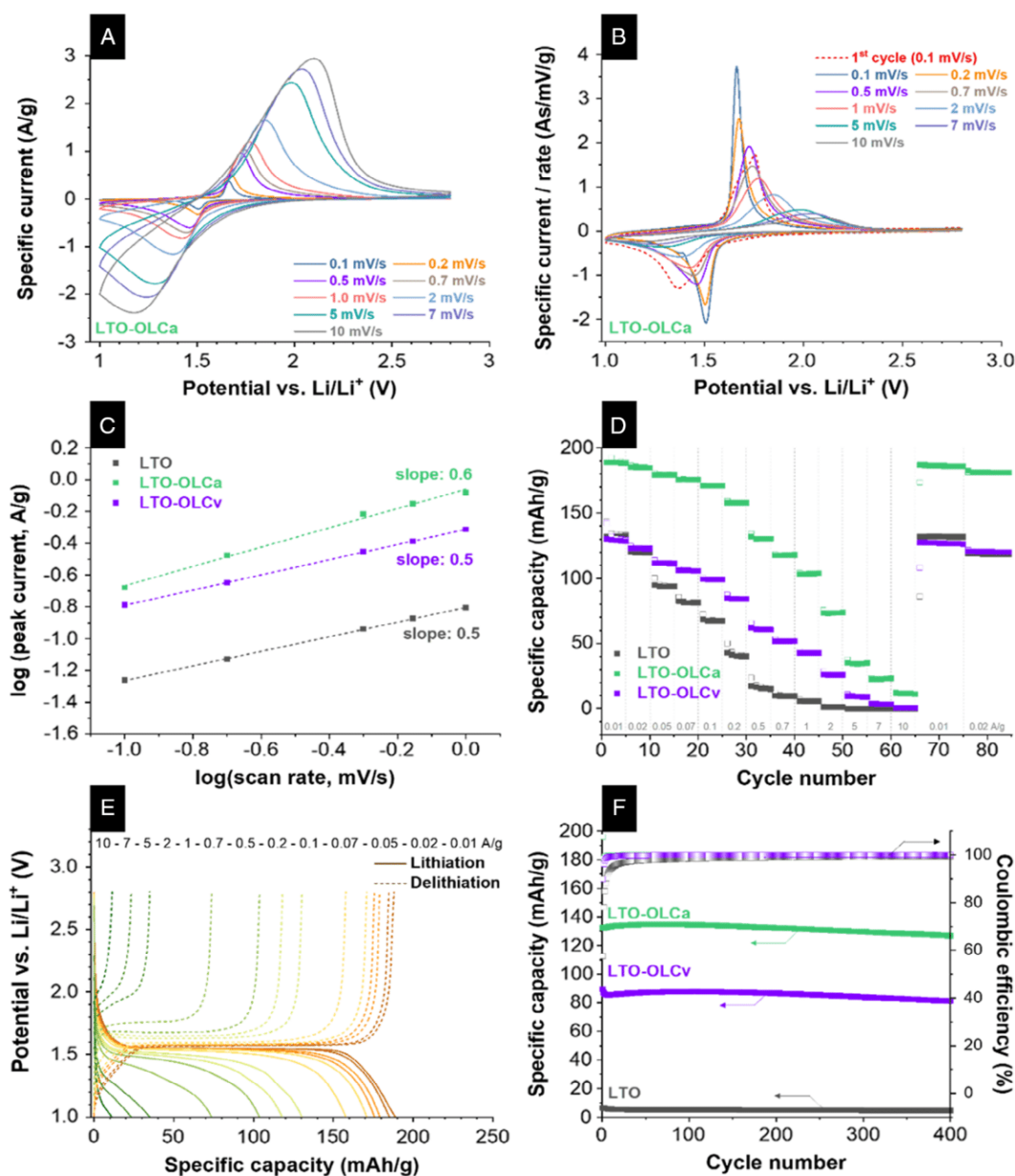
Figure 3. Lithium-ion intercalation behavior of LTO and LTO/carbon onion hybrid materials. A) Cyclic voltammograms recorded at 0.1–10 mV s^{-1} of LTO-OLCa and B) the cyclic voltammograms normalized to the recorded scan rate. C) Plot of log(*scan rate*) versus log(*peak current*) of the lithiation (cathodic) in the potential range of 1.0–2.8 V versus Li/Li$^+$ and the linear fitting of each sample. D) The lithiation and delithiation specific capacity of LTO, LTO-OLCa, and LTO-OLCv from galvanostatic charge/discharge cycling at different specific current for rate capability. E) Galvanostatic charge–discharge profiles of the fifth cycle at 0.01–10 A g^{-1} of sample LTO-OLCa between 1.0 and 2.8 V versus Li/Li$^+$. F) Galvanostatic charge/discharge cycling performance stability at a specific current of 0.1 A g^{-1} for LTO, LTO-OLCa, and LTO-OLCv.

where a and b are the variables, i is the peak specific current (A/g), and v is the scan rate (mV s^{-1}). From the obtained b value, the process kinetics fall between the boundary set by diffusion control ($b = 0.5$) or surface control ($b = 1$).[48] Figure 3C is obtained using CV data and the (shift-adjusted) peak currents of the hybrid materials at the scan rates of 0.1–1 mV s^{-1}. Thereby, we observed the b values of LTO (0.5),

LTO-OLCa (0.6), and LTO-OLCv (0.5). These values are all close to the ideal case of diffusion-controlled kinetics.

To further understand the behavior of the LTO-OLC hybrids, the electrochemical impedance was measured from the prepared cells before the CV measurement, and the corresponding Nyquist plot is shown in Figure S6, Supporting Information. The spectra before the CV of LTO-OLCa and

LTO-OLCv are similar, and the spectrum of LTO is shifted toward larger resistance values. To quantify the resistance dependency on the surface reaction or charge transfer, we used the equivalent circuit of $(R_s + CPE1/R_{int} + CPE2/(R_{ct} + W))$, as summarized in Table S4, Supporting Information. Therein, R_s stands for the electrolyte and cell component resistance, R_{int} stands for the film formation on the interface of electrode–electrolyte, and R_{ct} stands for the charge-transfer resistance; W demarks the Warburg impedance, and CPE is a constant phase element. The high-frequency region is known to represent the contributions of the electronic resistance of the cell.[49] The charge transfer resistance of LTO before the CV (3871 Ω) is higher than the hybrid LTO-OLCa (736 Ω) and LTO-OLCv (1607 Ω), which aligns with the superior rate capability of LTO-OLCa. The contribution of R_s is negligible for LTO-OLCa (4.6 Ω) and LTO-OLCv (2.2 Ω), but very high for LTO (84.0 Ω) before CV. The integrated semi-circles indicate the resistance of surface reactions, including the electrode–electrolyte interface and the ionic mobility at the surface of the electrode.[49,50]

The rate capability of the LTO-OLC hybrid materials was tested with the GCPL technique applying specific currents between 0.01 and 10 A g^{-1} at an operational potential of 1.0–2.8 V versus Li/Li$^+$ (Figure 3D). The highest specific capacity of 188 mAh g^{-1} was obtained from LTO-OLCa, with a coulombic efficiency of 92%, followed by $\approx$130 mAh g^{-1} for LTO and LTO-OLCv, with a coulombic efficiency of $\approx$92%. The coulombic efficiency of LTO-OLCa further increased to $\approx$100% by the third cycle and maintained over 98% during the rate capability testing sequence. As the applied specific current increases above 0.5 A g^{-1}, the specific capacity of LTO-OLCa decreased with a greater margin than at smaller specific currents. The specific capacity was 11 mAh g^{-1} at a specific current of 10 A g^{-1}, and the material recovered 98.9% of the initial capacity (corresponding with 186 mAh g^{-1}) when returning to a rate of 0.01 A g^{-1}.

The LTO and LTO-OLCa displayed the same initial capacity. LTO without carbon showed a low rate capability, enabling a charge storage of only 13 mAh g^{-1} at 0.7 A g^{-1}. Furthermore, LTO recovered 99% of the initial capacity, which corresponds with 127 mAh g^{-1} when returning to a rate of 0.01 mA g^{-1}. With only 3 mass% carbon content of the LTO electrode, the electron transfer might have enough time to establish the diffusion pathway at a low current of 0.01 mA g^{-1} to obtain the specific capacity of 130 mAh g^{-1}. However, at higher specific currents that require faster transport, the LTO only demonstrated inferior

rate capability. Although LTO-OLCv had the same initial capacity as the LTO, whereby LTO-OLCv showed better rate handling performance, which we ascribe to the higher carbon content of LTO-OLCv. Figure 3E shows the corresponding specific capacity and potential profile of LTO-OLCa. In good agreement with the cyclic voltammogram, the difference in the plateau between the lithiation and de-lithiation is small at low specific current (0.01–0.05 A g^{-1}). As the specific current increases, such a difference in lithiation and de-lithiation potential increases.

For comparison, the capacity and potential plot of LTO and LTO-OLCv are shown in Figure S5E,F, Supporting Information. We observed the same behavior of potential separation that the pristine LTO exhibits large potential separation already at 0.1 A g^{-1}, whereas LTO-OLCa and LTO-OLCv exhibit a large potential separation at 0.5 A g^{-1}. As the kinetic analysis suggests that diffusion is the limiting factor, the different rate handling performance (Figure 3D) must be the influence of the added OLC. Yet, the degree of graphitization carbon in LTO-OLCa is significantly better than LTO-OLCv (confirmed by Raman result, Table S3, Supporting Information). Also, the impedance data indicate better charge transport in LTO-OLCa compared with LTO-OLCv, which supports the higher lithium storage performance of LTO-OLCa. Thus, charge transfer in LTO-OLCa is faster than LTO-OLCv. The cycling performance of the LTO and LTO-OLC hybrid materials was carried out at 0.1 A g^{-1}, and the results are presented in Figure 3F, including their coulombic efficiencies. LTO-OLCa exhibits an initial capacity of 132 mAh g^{-1}, and 95.8% of the capacity remained after 400 cycles, losing only 0.013 mAh g^{-1} per cycle. Similarly, LTO-OLCv showed a slight decrease of 3 mAh g^{-1} after the initial capacity of 98 mAh g^{-1}, and then maintained 90.8% of the initial capacity.

Table 1 presents previously reported performance values of LTO/C composite and hybrid materials in comparison with data from this study. The best-performing material from our present study was LTO-OLCa material with a specific capacity of 184 mAh g^{-1} at 0.11C. The capacity retention is comparable to the state-of-the-art performance, which shows its potential as anode material for LIBs.

3.3. Sodium-Ion Intercalation Behavior and Performance

For testing the electrochemical performance for sodium-ion intercalation, we selected only LTO-OLCa due to its best

Table 1. Comparison of electrochemical performance of previously reported LTO materials with various synthesis methods and our LTO-OLCa hybrid material for LIBs.

Material	Synthesis	Specific capacity	Rate capability	Cycling stability	Reference
LTO-carbon onion	Sol–gel 700 °C, 2 h	184 mAh g^{-1} at 0.11 C	74 mAh g^{-1} at 11 C	95.8% after 400 cycles	This work
Li$_4$T$_5$O$_{12}$/C	Solid state 900 °C, 20 h	165 mAh g^{-1} at 0.2 C	–	–	[24]
Mesoporous Li$_4$T$_5$O$_{12}$/C	Self-assembly 700 °C, 2 h	144 mAh g^{-1} at 1 C	90 mAh g^{-1} at 5 C	90% after 500 cycles	[51]
Li$_4$T$_5$O$_{12}$/graphene oxide	Solid-state ball milling 500 °C, 4 h	170 mAh g^{-1} at 1 C	122 mAh g^{-1} at 30 C	94.8% after 300 cycles	[52]
Li$_4$T$_5$O$_{12}$-AC nanotubes	Electrospinning 800 °C, 3 h	120 mAh g^{-1} at 100 mA g^{-1}	84 mAh g^{-1} at 4 A g^{-1}	67% after 100 cycles	[17]
Li$_4$T$_5$O$_{12}$ porous monolith	Sol–gel, hydrothermal 700 °C, 2 h	165 mAh g^{-1} at 0.1 C	105 mAh g^{-1} at 30 C	98% after 500 cycles	[53]
Li$_4$T$_5$O$_{12}$ thin nanosheet	Hydrothermal, 600 °C, 3 h	168 mAh g^{-1} at 0.2 C	130 mAh g^{-1} at 64 C	96% after 400 cycles	[33]

performance and stability based on the LIB data. We prepared CR2032 coin cells using sodium metal as a counter and reference electrode for the electrochemical testing. Cyclic voltammetry was conducted in a potential range of 0.3–2.5 V versus Na/Na$^+$. **Figure** 4A presents the first and fifth voltammetric cycles at the scan rates of 0.1–10 mV s^{-1}. The first cycle shows sodiation peaks alongside the FEC redox activity starting from 0.6 V versus Na/Na$^+$, and the lowest current was observed at $\approx$0.3 V versus Na/Na$^+$ (Figure S7, Supporting Information). This can be ascribed to the structural change of the LTO spinel from

intercalating the larger sized Na$^+$ ions into the interstitial sites.[29] From the next cycle, the paired sodiation/desodiation peak is observed at 0.7 and 1.05 V versus Na/Na$^+$, and the peak separation is enhanced, as the scan rate increases; ΔV was 0.35 V at the initial scan rate of 0.1 mV s^{-1}, 0.65 V with 0.5 mV s^{-1}, and more than 0.9 V at 1 mV s^{-1}. The higher peak separation indicates the need for higher overpotential or energy to insert/extract Na$^+$ ion into or out of the structure.[20]

The sodiation regime from voltammetry starts to deteriorate above with a scan rate of 2 mV s^{-1}, and at 5 mV s^{-1} and higher
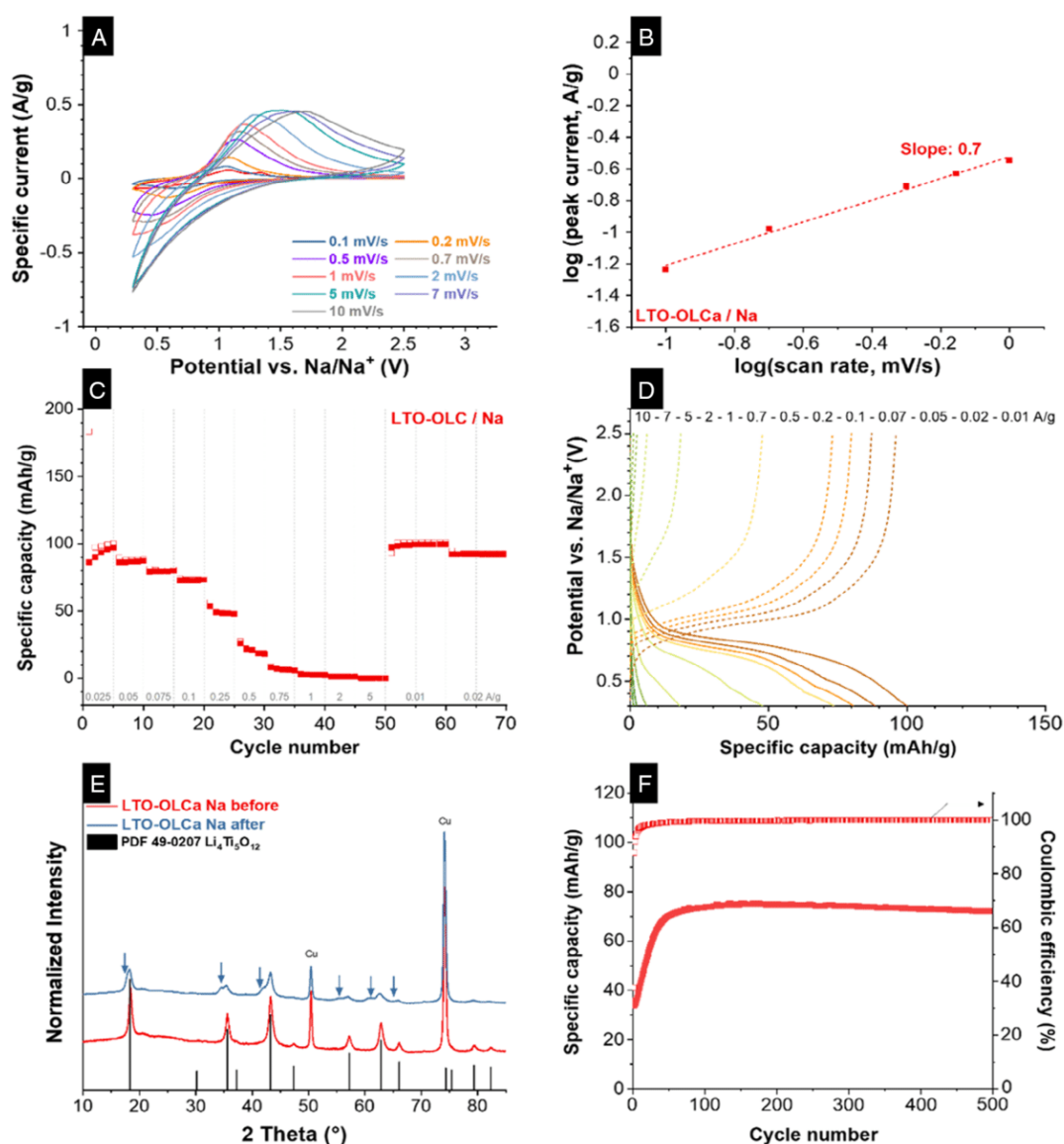
Figure 4. Sodium-ion intercalation performance of LTO-OLCa. A) Cyclic voltammograms recorded at 0.1–10 mV s^{-1} in the potential range of 0.3–2.5 V versus Na/Na$^+$. B) Plot of log(*scan rate*) versus log(*peak current*) of the sodiation (cathodic) in the potential range of 0.3–2.5 V versus Na/Na$^+$ and the linear fitting of LTO-OLCa. C) The sodiation and desodiation specific capacity of LTO-OLCa sample obtained from galvanostatic charge/discharge cycling at different specific current for rate capability. D) Galvanostatic charge–discharge profiles of the fifth cycle at 0.025–5 A g^{-1} of sample LTO-OLCa between 0.3 and 2.5 V versus Na/Na$^+$. E) The X-ray diffractograms of LTO-OLCa electrodes, before and after the galvanostatic charge–discharge process. F) Galvanostatic charge/discharge cycling performance stability at a specific current of 0.1 A g^{-1} for LTO-OLCa.

scan rates, the cyclic voltammograms do not show a further change in current reflex with changing scan rate. This implies that the insertion of Na$^+$ ion into the sites is kinetically hindered.[20] Just like for the Li-containing electrolyte, we calculated b values for SIB data (Figure 4B). The b value of LTO-OLCa tested against sodium was 0.7, which is higher than the values obtained from the lithium intercalation testing. The lowest peak current at 0.1 mV s^{-1} scan demonstrates a significant influence on the reconstruction of the LTO structure with sodiation. The b value of the sodium intercalation, excluding the peak current at 0.1 mV s^{-1}, was 0.6, which is close to the value found from LIB testing.

The GCPL of the LTO-OLCa hybrid material was tested in the specific current range of 0.025–5 A g^{-1} to quantify the rate capability. Figure 4C displays both sodiation and desodiation capacities of LTO-OLCa. The capacity values were normalized to the metal oxide mass for a better comparison with the literature. At 0.025 A g^{-1}, the initial desodiation capacity reaches 87 mAh g^{-1} at a low coulombic efficiency of 47%. Such a low coulombic efficiency might result from the irreversible sodiation in the first cycle and the side reactions regarding SEI formation.[54] However, the desodiation capacity increases slightly from the first cycle to the fifth, which may be due to the reconstruction of the LTO structure during the insertion/extraction of the sodium ions. Accordingly, the coulombic efficiency further enhances as the cell continues being tested. Above a specific current of 0.25 A g^{-1}, the capacity decreases severely, leading to no significant insertion/extraction capacity of Na$^+$ above 1 A g^{-1}. To distinguish the contribution of the carbon onion, an electrode of only carbon onion annealed in Ar (OLCa) was prepared and tested with GCPL at the same operational potential and specific current. The sodiation capacity values of OLCa are presented in Figure S8B, Supporting Information, with the highest capacity of 14 mAh g^{-1}; in addition, Figure S8A, Supporting Information, displays the capacity values of OLCa when used as an LIB anode. Figure 4D shows the corresponding potential profiles of the GCPL results at the fifth cycles of each applied specific currents tested in the potential range of 0.3–2.5 V versus Na/Na$^+$. At lower specific currents, the Na$^+$ insertion into LTO begins from 0.9 V versus Na/Na$^+$ to 0.6 V versus Na/Na$^+$ with the first slope, and then continues with a different slope to 0.3 V versus Na/Na$^+$. When comparing the GCPL result of LTO-OLCa between lithium-ion and sodium-ion cells, one can observe the difference between the slope of the plateau (Figure 3E and 4D) suggesting higher overpotential.

To characterize possible structural change that we suspect from the first voltammetric cycles and very low coulombic efficiency of GCPL at the first cycle, we carried out post-mortem XRD analysis of the tested electrodes. The diffractograms of the electrodes before and after GCPL testing are presented in Figure 4E. The diffractogram of LTO-OLCa before cycling matches the peak position of cubic LTO, which has $a = 8.366 \pm 0.002$ Å. In addition to the set of reflection peaks inherent to LTO, we also see the emergence of another set of the same number of reflections shifted toward larger d values (i.e., lower scattering angles) for the LTO-OLCa after cycling. We also see sharp and intense peaks relating to the current collector material (i.e., copper). After electrochemical testing, there is a significant increase in the unit cell dimension to $a = 8.4677$ Å and a decrease in the domain size to about 10 nm. We see double peaks for the main reflections of LTO-OLCa, which indicate the coexistence of a population of LTO domains with increased unit cell volume and one close to the initial value ($a = 8.3608$ Å). This phase also has a domain size of about 10 nm, and the mass ratio between both crystallographically distinct LTO phases is about 1:1 (46:54; i.e., there is slightly less expanded LTO). The presence of about 54 mass% of residual Na$_6$LiTi$_5$O$_{12}$ is in contrast to the full electrochemical desodiation treatment of the post-mortem electrode. In agreement with previous work, when inserting Na$^+$ into the LTO structure, Na$^+$ substitutes Li in the LTO lattice. Subsequently, Na$_6$LiTi$_5$O$_{12}$ heterogeneously emerges from the LTO phase.[55] Therefore, the inability to revert all of the sodiated materials to the initial crystal structure aligns with the reduced achievable charge storage capacity of about 100 mAh g^{-1} and the low initial coulombic efficiency of $\approx$50%. The disassembly of the cell was done after the desodiation step of the GCPL test; therefore, it is evident that the permanent transformation of the Na-containing phase occurs during the first cycles, as CV and GCPL profiles indicate.[34]

The size difference of Na$^+$ and Li$^+$ ions (ionic radius, Na$^+$ = 102 pm, Li$^+$ = 76 pm) is expected to trigger the poor rate performance of LTO as an anode in SIB than LIB. This size difference is initiated by the structural change, leading to more reduced cycling stability of the SIB.[29,33] Moreover, the dependency of SIB performance on the size of LTO was reported by Yu et al.,[30] which showed that smaller LTO particles enhance the rate and cycling performance of SIB. As our LTO-OLCa has a crystalline size of around 30 nm, the higher performance was expected. As presented in **Table 2**, the rate performance of LTO-OLCa in the SIB setup was not comparable to the

Table 2. Comparison of electrochemical performance of previously reported LTO materials with various synthesis methods and our LTO-OLCa hybrid material for SIBs, normalized to metal oxide mass. "rGO" means "reduced graphene oxide".

Material	Synthesis	Potential range	Specific capacity	Rate capability	Cycling stability	Reference
LTO-carbon onion	Sol–gel 700 °C, 2 h	2.5–0.3 V	97 mAh g^{-1} at 0.15 C	27 mAh g^{-1} at 2.8 C	95.6% after 500 cycles	This work
Li$_4$T$_5$O$_{12}$	Solid state 800 °C, 20 h	3.0–0.3 V	187 mAh g^{-1} at 0.1 C	–	–	[27]
Porous Li$_4$T$_5$O$_{12}$/C	Spray drying 950 °C, 24 h	3.0–0.5 V	155 mAh g^{-1} at 0.1 C	90 mAh g^{-1} at 5 C	95% after 20 cycles	[29]
Li$_4$T$_5$O$_{12}$/C nanowire	Hydrothermal 750 °C, 6 h	2.5–0.3 V	168 mAh g^{-1} at 0.2 C	38 mAh g^{-1} at 100 C	97% after 50 cycles	[31]
Li$_4$T$_5$O$_{12}$ porous monolith	Sol–gel, hydrothermal 700 °C, 2 h	1.5–0.5 V	127 mAh g^{-1} at 1 C	63 mAh g^{-1} at 30 C	70% after 100 cycles	[53]
Li$_4$T$_5$O$_{12}$ thin nanosheet	Hydrothermal, 600 °C, 3 h	2.5–0.5 V	170 mAh g^{-1} at 0.2 C	115 mAh g^{-1} at 30 C	92% after 150 cycles	[33]
Li$_4$T$_5$O$_{12}$–TiO$_2$/rGO aerogel	Hydrothermal 700 °C, 6 h	2.5–0.3 V	184 mAh g^{-1} at 0.5 C	77 mAh g^{-1} at 20 C	64% after 700 cycle	[56]

reported state of the art. Yet, around 96% capacity retention after 500 cycles compared with the maximum capacity is superior to the cycling performance in the reported literature, which reports very low counts of cycles. This suggests that the hybridization of LTO with carbon onion benefits the longevity of SIB (Figure 4F). Recently, Pfeifer et al. reported the importance of the appropriate selection of electrolytes for SIB application using sodium metal.[57] To enhance the performance and stability of hard carbon or sodium metal anodes for SIB, FEC was introduced to the electrolyte system additives.[54] Some have reported LTO as an anode for SIB using FEC-containing electrolytes, such as $NaClO_4$ in ethylene carbonate:diethyl carbonate:fluoroethylene carbonate (50:50:1 by volume)[58] or $NaClO_4$ in propylene carbonate:fluoroethylene carbonate (98:2 by volume),[31] which showed enhanced stability performance.

4. Conclusion

In conclusion, we synthesized nano-sized LTO and carbon onion hybrid materials and applied them, for the first time, as an anode in LIBs and SIBs. The LTO-OLCa successfully demonstrated its excellent performance with a high specific capacity of $188\,mAh\,g^{-1}$ and a favorable rate capability of $74\,mAh\,g^{-1}$ at $2\,A\,g^{-1}$, with 99% retention of its initial capacity after the testing to $10\,A\,g^{-1}$. The longevity test of LTO-OLCa yielded 95.8% of initial capacity, superior to both LTO synthesized without carbon onions with inferior performance, or LTO hybridized with OLCv, which only performed 91% recovery in both capacity and the retention for LIB. The LTO-OLCa, which had excellent performance in the LIB system, exhibited unsatisfactory performance when applied as anode for SIB with a specific capacity of only $102\,mAh\,g^{-1}$. Nevertheless, the longevity of LTO-OLCa with sodium showed 96% of the maximum capacity retention after 500 cycles using $1\,M\,NaClO_4$ in EC:DMC (1:1 by mass) containing 5 mass% FEC as the electrolyte. This work demonstrates carbon onion as a preferable hybridization substance. We believe that our LTO and carbon onion hybrid material has a potential for further improvement, for example, by the implementation of a different electrode design or a different electrolyte system to increase performance or longevity.

Supporting Information

Supporting Information is available from the Wiley Online Library or from the author.

Acknowledgements

Conflict of Interest

The authors declare no conflict of interest.

Keywords

[1] M. Armand, J. M. Tarascon, *Nature* **2008**, *451*, 652.
[2] J. Shim, K. A. Striebel, *J. Power Sources* **2003**, *119–121*, 955.
[3] R. Yazami, P. Touzain, *J. Power Sources* **1983**, *9*, 365.
[4] R. Yazami, *Electrochim. Acta* **1999**, *45*, 87.
[5] P. Cicconi, L. Postacchini, E. Pallotta, A. Monteriù, M. Prist, M. Bevilacqua, M. Germani, *J. Power Sources* **2019**, *436*, 226837.
[6] L. Kavan, M. Grätzel, *Solid State Lett.* **2002**, *5*, A39.
[7] T. Ohzuku, A. Ueda, N. Yamamoto, *J. Electrochem. Soc.* **1995**, *142*, 1431.
[8] S. S. Zhang, K. Xu, T. R. Jow, *J. Power Sources* **2004**, *130*, 281.
[9] W. J. H. Borghols, M. Wagemaker, U. Lafont, E. M. Kelder, F. M. Mulder, *J. Am. Chem. Soc.* **2009**, *131*, 17786.
[10] B.-N. Yun, H. L. Du, J.-Y. Hwang, H.-G. Jung, Y.-K. Sun, *J. Mater. Chem.* **2017**, *5*, 2802.
[11] K. Zaghib, M. Simoneau, M. Armand, M. Gauthier, *J. Power Sources* **1999**, *81–82*, 300.
[12] S. Bach, J. P. Pereira-Ramos, N. Baffier, *J. Power Sources* **1999**, *81–82*, 273.
[13] Y. H. Rho, K. Kanamura, *J. Solid State Chem.* **2004**, *177*, 2094.
[14] B. Yan, M. Li, X. Li, Z. Bai, J. Yang, D. Xiong, D. Li, *J. Mater. Chem. A* **2015**, *3*, 11773.
[15] M. Widmaier, K. Pfeifer, L. Bommer, V. Presser, *Batteries Supercaps* **2018**, *1*, 11.
[16] S. Fleischmann, A. Tolosa, V. Presser, *Chem. Eur. J.* **2018**, *24*, 12143.
[17] H. S. Choi, J. H. Im, T. Kim, J. H. Park, C. R. Park, *J. Mater. Chem.* **2012**, *22*, 16986.
[18] A. Nugroho, W. Chang, S. J. Kim, K. Y. Chung, J. Kim, *RSC Adv.* **2012**, *2*, 10805.
[19] H. Kim, K.-Y. Park, M.-Y. Cho, M.-H. Kim, J. Hong, S.-K. Jung, K. C. Roh, K. Kang, *ChemElectroChem* **2014**, *1*, 125.
[20] C. Chen, H. Xu, T. Zhou, Z. Guo, L. Chen, M. Yan, L. Mai, P. Hu, S. Cheng, Y. Huang, J. Xie, *Adv. Energy Mater.* **2016**, *6*, 1600322.
[21] L. Cheng, X.-L. Li, H.-J. Liu, H.-M. Xiong, P.-W. Zhang, Y.-Y. Xia, *J. Electrochem. Soc.* **2007**, *154*, A692.
[22] T. Yuan, X. Yu, R. Cai, Y. Zhou, Z. Shao, *J. Power Sources* **2010**, *195*, 4997.
[23] Y.-B. He, F. Ning, B. Li, Q.-S. Song, W. Lv, H. Du, D. Zhai, F. Su, Q.-H. Yang, F. Kang, *J. Power Sources* **2012**, *202*, 253.
[24] H.-G. Jung, S.-T. Myung, C. S. Yoon, S.-B. Son, K. H. Oh, K. Amine, B. Scrosati, Y.-K. Sun, *Energy Environ. Sci.* **2011**, *4*, 1345.
[25] H. Li, L. Shen, X. Zhang, J. Wang, P. Nie, Q. Che, B. Ding, *J. Power Sources* **2013**, *221*, 122.
[26] M. Widmaier, N. Jäckel, M. Zeiger, M. Abuzarli, C. Engel, L. Bommer, V. Presser, *Electrochim. Acta* **2017**, *247*, 1006.
[27] L. Zhao, H.-L. Pan, Y.-S. Hu, H. Li, L.-Q. Chen, *Chin. Phys. B* **2012**, *21*, 028201.
[28] Y. Wang, X. Yu, S. Xu, J. Bai, R. Xiao, Y. S. Hu, H. Li, X. Q. Yang, L. Chen, X. Huang, *Nat. Commun.* **2013**, *4*, 2365.

ADVANCED SCIENCE NEWS
www.advancedsciencenews.com

Energy Technology
Generation, Conversion, Storage, Distribution
www.entechnol.de

[29] Y. Sun, L. Zhao, H. Pan, X. Lu, L. Gu, Y.-S. Hu, H. Li, M. Armand, Y. Ikuhara, L. Chen, X. Huang, *Nat. Commun.* **2013**, *4*, 1870.

[30] X. Yu, H. Pan, W. Wan, C. Ma, J. Bai, Q. Meng, S. N. Ehrlich, Y.-S. Hu, X.-Q. Yang, *Nano Lett.* **2013**, *13*, 4721.

[31] K.-T. Kim, C.-Y. Yu, C. S. Yoon, S.-J. Kim, Y.-K. Sun, S.-T. Myung, *Nano Energy* **2015**, *12*, 725.

[32] M. Kitta, R. Kataoka, M. Kohyama, *Phys. Chem. Chem. Phys.* **2016**, *18*, 19888.

[33] X. Feng, H. Zou, H. Xiang, X. Guo, T. Zhou, Y. Wu, W. Xu, P. Yan, C. Wang, J.-G. Zhang, Y. Yu, *ACS Appl. Mater. Interfaces* **2016**, *8*, 16718.

[34] M. Kitta, R. Kataoka, S. Tanaka, N. Takeichi, M. Kohyama, *ACS Appl. Energy Mater.* **2019**, *2*, 4345.

[35] Y. Liu, J. Liu, M. Hou, L. Fan, Y. Wang, Y. Xia, *J. Mater. Chem. A* **2017**, *5*, 10902.

[36] M. Zeiger, N. Jäckel, M. Aslan, D. Weingarth, V. Presser, *Carbon* **2015**, *84*, 584.

[37] M. Zeiger, N. Jäckel, D. Weingarth, V. Presser, *Carbon* **2015**, *94*, 507.

[38] S. Fleischmann, A. Tolosa, M. Zeiger, B. Krüner, N. J. Peter, I. Grobelsek, A. Quade, A. Kruth, V. Presser, *J. Mater. Chem. A* **2017**, *5*, 2792.

[39] N. Jäckel, D. Weingarth, M. Zeiger, M. Aslan, I. Grobelsek, V. Presser, *J. Power Sources* **2014**, *272*, 1122.

[40] K. Pfeifer, S. Arnold, Ö. Budak, X. Luo, V. Presser, H. Ehrenberg, S. Dsoke, *J. Mater. Chem. A* **2020**, *8*, 6092.

[41] D. B. Schuepfer, F. Badaczewski, J. M. Guerra-Castro, D. M. Hofmann, C. Heiliger, B. Smarsly, P. J. Klar, *Carbon* **2020**, *161*, 359.

[42] G. A. Zickler, B. Smarsly, N. Gierlinger, H. Peterlik, O. Paris, *Carbon* **2006**, *44*, 3239.

[43] N. C. Saha, H. G. Tompkins, *J. Appl. Phys.* **1992**, *72*, 3072.

[44] Y. Tang, F. Huang, W. Zhao, Z. Liu, D. Wan, *J. Mater. Chem.* **2012**, *22*, 11257.

[45] C.-K. Lan, S.-I. Chuang, Q. Bao, Y.-T. Liao, J.-G. Duh, *J. Power Sources* **2015**, *275*, 660.

[46] S. Ardizzone, G. Fregonara, S. Trasatti, *Electrochim. Acta* **1990**, *35*, 263.

[47] M. Hillert, *Metall. Trans. A* **1975**, *6*, 5.

[48] M. Opitz, J. Yue, J. Wallauer, B. Smarsly, B. Roling, *Electrochim. Acta* **2015**, *168*, 125.

[49] J. Landesfeind, D. Pritzl, H. A. Gasteiger, *J. Electrochem. Soc.* **2017**, *164*, A1773.

[50] F. J. Günter, J. B. Habedank, D. Schreiner, T. Neuwirth, R. Gilles, G. Reinhart, *J. Electrochem. Soc.* **2018**, *165*, A3249.

[51] E. Kang, Y. S. Jung, G. H. Kim, J. Chun, U. Wiesner, A. C. Dillon, J. K. Kim, J. Lee, *Adv. Funct. Mater.* **2011**, *21*, 4349.

[52] Y. Shi, L. Wen, F. Li, H.-M. Cheng, *J. Power Sources* **2011**, *196*, 8610.

[53] G. Hasegawa, K. Kanamori, T. Kiyomura, H. Kurata, K. Nakanishi, T. Abe, *Adv. Energy Mater.* **2015**, *5*, 1400730.

[54] S. Komaba, T. Ishikawa, N. Yabuuchi, W. Murata, A. Ito, Y. Ohsawa, *ACS Appl. Mater. Interfaces* **2011**, *3*, 4165.

[55] M. Kitta, K. Kuratani, M. Tabuchi, N. Takeichi, T. Akita, T. Kiyobayashi, M. Kohyama, *Electrochim. Acta* **2014**, *148*, 175.

[56] Y. Tian, G. Xu, Z. Wu, J. Zhong, L. Yang, *RSC Adv.* **2017**, *7*, 52702.

[57] K. Pfeifer, S. Arnold, J. Becherer, C. Das, J. Maibach, H. Ehrenberg, S. Dsoke, *ChemSusChem* **2019**, *12*, 3312.

[58] L. Y. Yang, H. Z. Li, J. Liu, S. S. Tang, Y. K. Lu, S. T. Li, J. Min, N. Yan, M. Lei, *J. Mater. Chem.* **2015**, *3*, 24446.

Supplementary Information

Hybrid anodes of lithium titanium oxide and carbon onions for lithium-ion and sodium-ion energy storage

Hwirim Shim,[1,2] Stefanie Arnold,[1,2] Öznil Budak,[1,2]

Maike Ulbricht,[1,2] Pattarachai Srimuk,[1] Volker Presser[1,2,*]

[1] INM - Leibniz Institute for New Materials, 66123 Saarbrücken, Germany

[2] Department of Materials Science and Engineering, Saarland University, 66123 Saarbrücken, Germany

* Corresponding author's eMail: <u>volker.presser@leibniz-inm.de</u>

S1
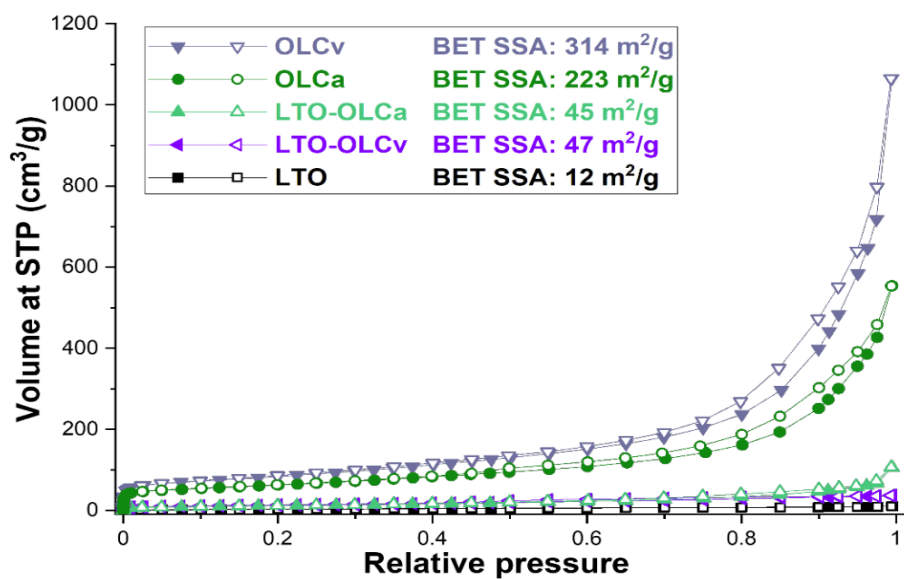
Fig. S1: Nitrogen gas sorption isotherms with volumes at standard-temperature-pressure (STP) as a function of relative pressure for LTO, OLCa, OLCv, LTO-OLCv, and LTO-OLCa powders.
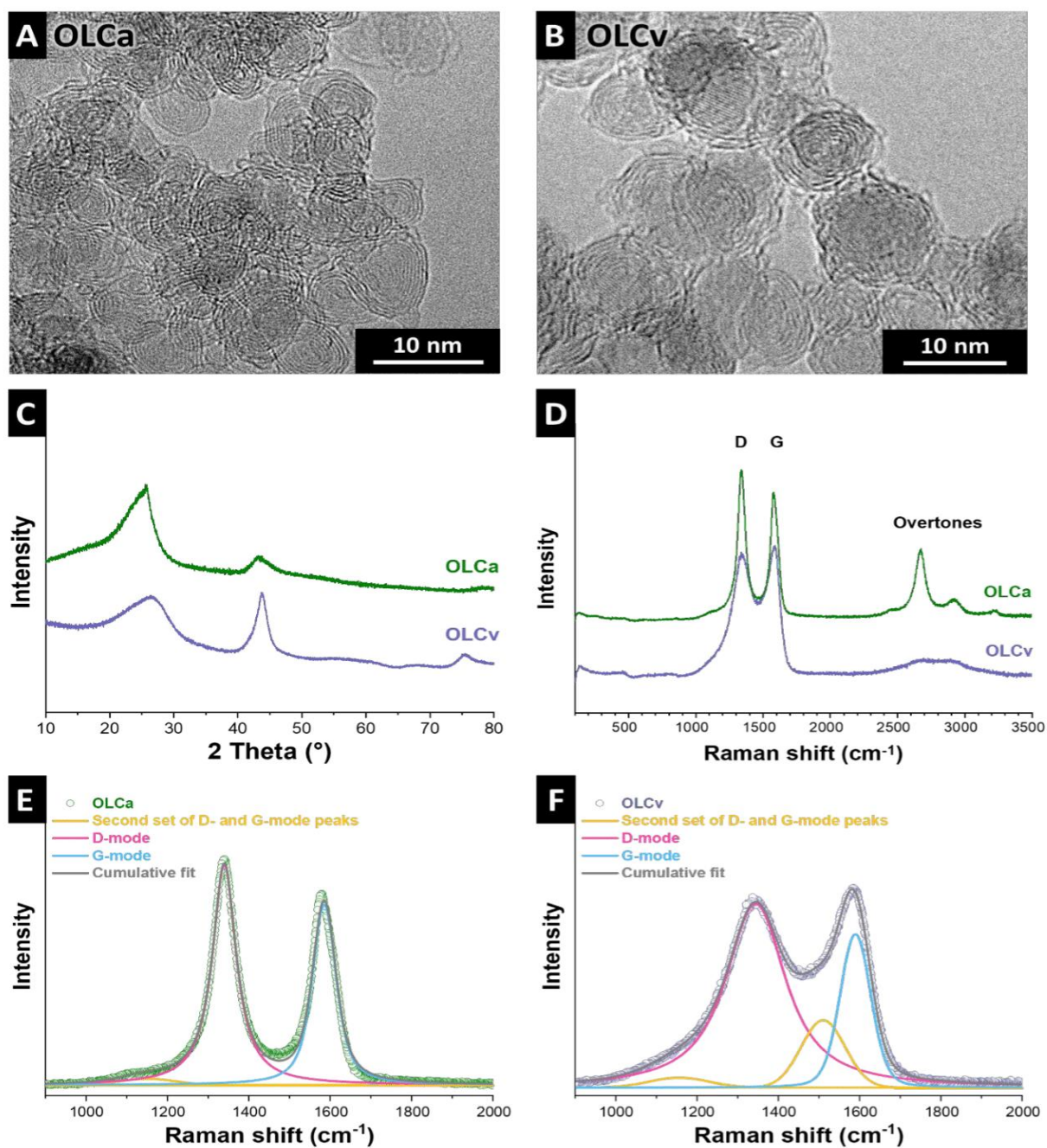
Fig. S2: The transmission micrograms of (A)OLCa and (B) OLCv. (C) X-ray diffractograms and (D) Raman spectra of OLCa and OLCv. D-mode and G-mode fitting of (E) OLCa, and (F) OLCv.
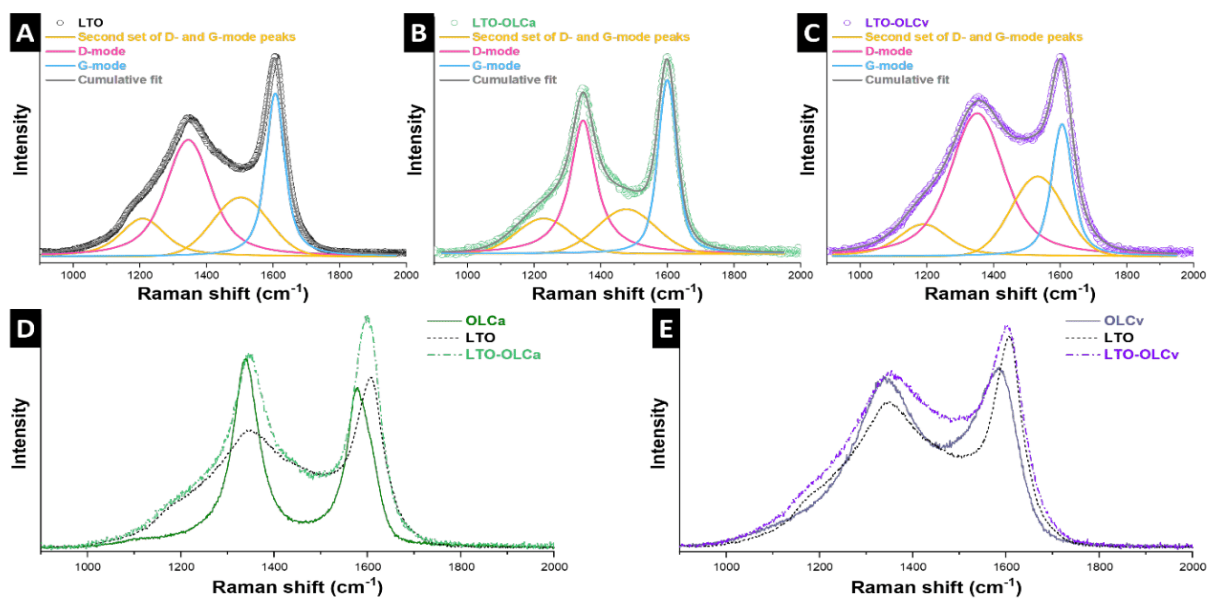
Fig. S3: Raman spectra: D- and G-mode peak fitting for (A) LTO, (B) LTO-OLCa, and (C) LTO-OLCv. Overlaid Raman spectra of (D) LTO, OLCa, and LTO-OLCa, and (E) LTO, OLCv, and LTO-OLCv; the relative intensities were adjusted to improve visibility of the individual carbon species.
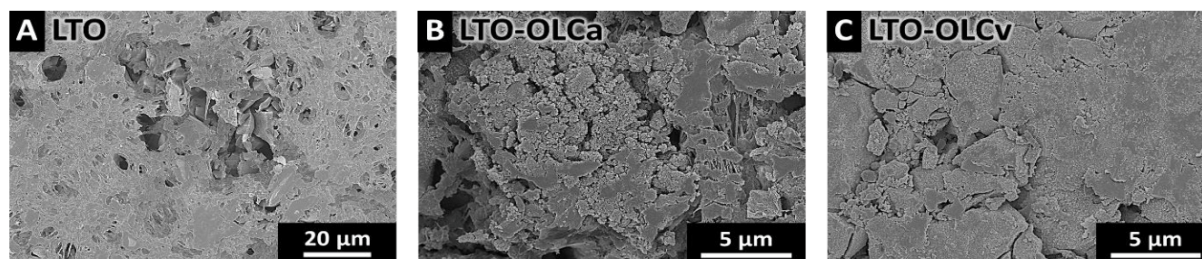
Fig. S4: Scanning electron micrographs of (A) LTO, (B) LTO-OLCa, and (C) LTO-OLCv electrodes.
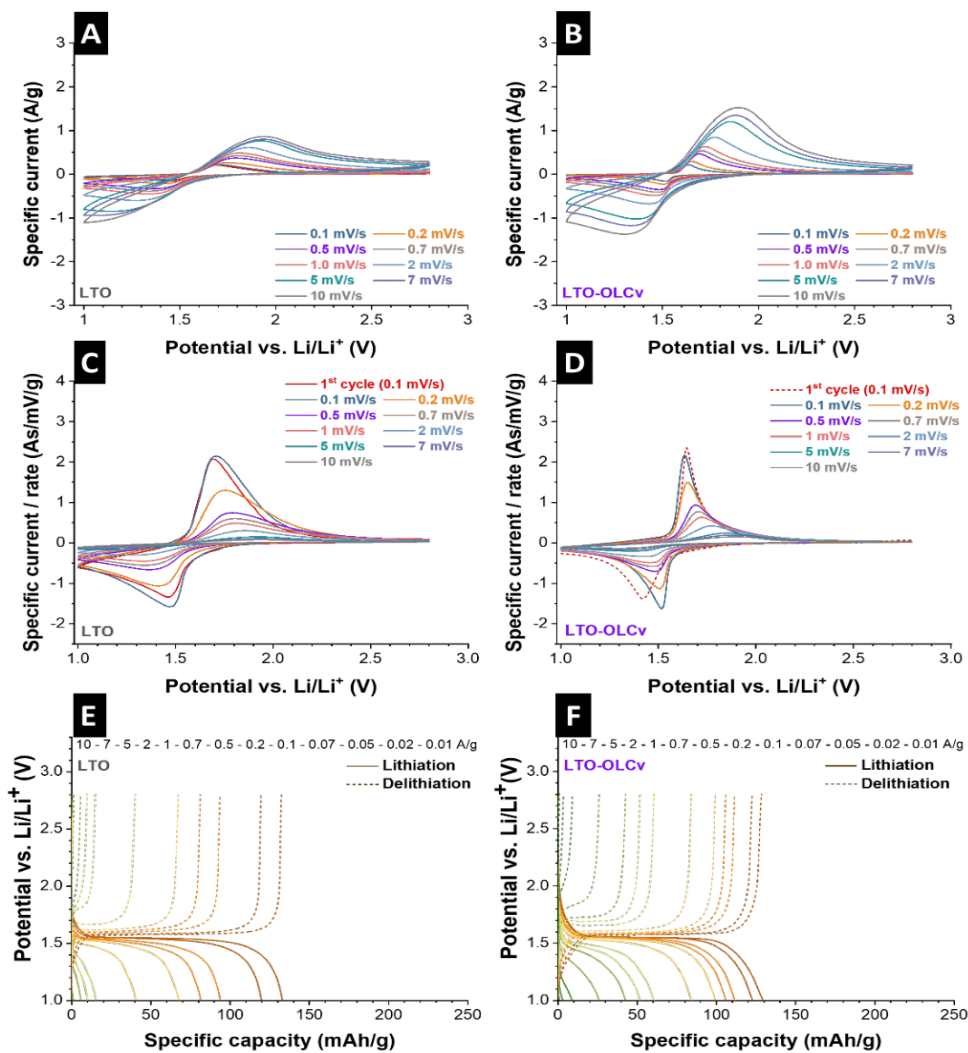
Fig. S5: (A-B) Cyclic voltammograms recorded at 0.1-10 mV/s for (A) LTO and (B) LTO-OLCv normalized by scan rates. (C-D) Cyclic voltammograms normalized by scan rates recorded at 0.1-10 mV/s and for (C) LTO and (D) LTO-OLCv. (E-F) Galvanostatic charge-discharge profiles of the 5th cycle at 0.01-10 A/g of samples (E) LTO and (F) LTO-OLCv.
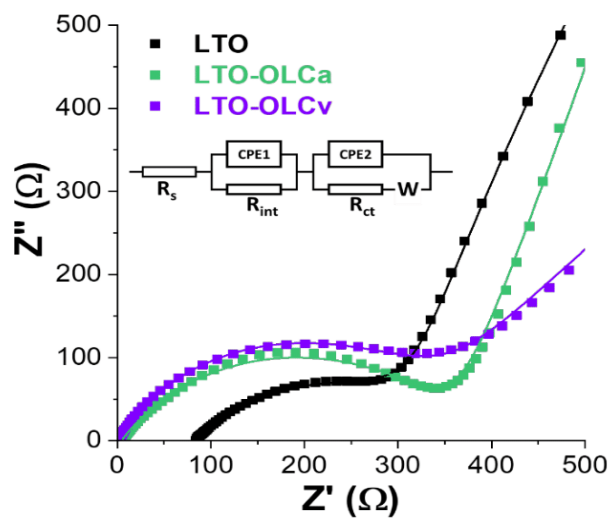
Fig. S6: Electrochemical impedance spectra of LTO, LTO-OLCa, and LTO-OLCv (dotted) and the fitting results (lined).
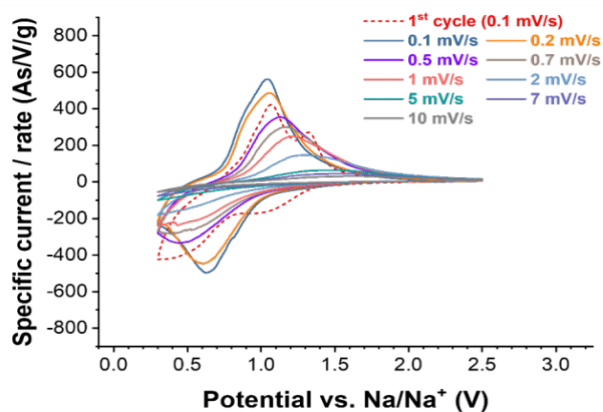
Fig. S7: Cyclic voltammograms displayed in Fig. 4a recorded at 0.1-10 mV/s for LTO-OLCa normalized by scan rates between 0.01-2.5 V vs. Na/Na⁺.
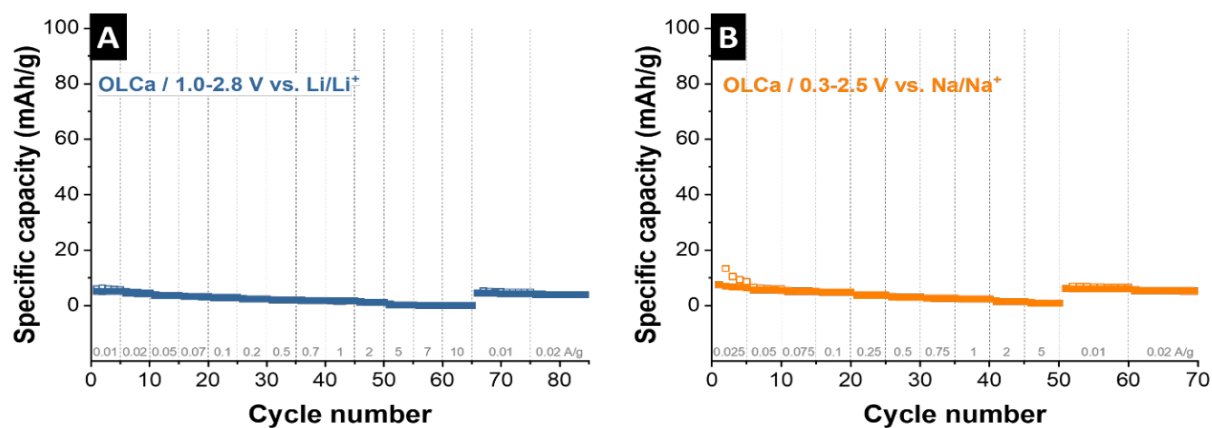
Fig. S8: (A) The lithiation and delithiation specific capacity of OLCa obtained from galvanostatic charge/discharge cycling at different specific current for rate capability in the range of 1.0-2.8 V vs. Li/Li$^+$. (B) The sodiation and desodiation specific capacity of OLCa obtained from galvanostatic charge/discharge cycling at different specific current for rate capability in the range of 0.3-2.5 V vs. Na/Na$^+$. Open symbols: charging; filled symbols: discharging.

Table S1: Crystal phases, lattice constants, and domain sizes obtained from Rietveld-fitting based on the X-ray diffractograms seen in Fig. 2.

Material	Crystal phase, space group, and PDF number	Fitted lattice parameters (Å)	Domain size (nm)
LTO	$Li_4Ti_5O_{12}$ cubic Fd-3m (PDF 49-0207)	a= 8.36384	30
LTO-OLCa	$Li_4Ti_5O_{12}$ cubic Fd-3m (PDF 49-0207)	a= 8.36655	31
LTO-OLCv	$Li_4Ti_5O_{12}$ cubic Fd-3m (PDF 49-0207)	a= 8.36577	30

Table S2: Results of the elemental analysis. All values in mass%. b.d.l.: below detection limit.

Material	C	H	N	S	O
OLCa	98.76±0.25	b.d.l.	b.d.l.	b.d.l.	1.90±0.48
OLCv	95.91±0.53	b.d.l.	1.67±0.01	b.d.l.	2.99±0.87
LTO	3.08±0.03	0.19±0.01	0.07±0.02	b.d.l.	20.53±0.28
LTO-OLCa	13.12±0.36	b.d.l.	0.15±0.06	b.d.l.	29.17±1.75
LTO-OLCv	13.72±0.25	0.21±0.02	0.22±0.04	b.d.l.	23.35±1.59

Table S3: Results of the carbon-related Raman peak analysis. Position and FWHM-values in units of cm^{-1}.

Material	D-mode		G-mode		I_D/I_G ratio
	position (cm^{-1})	FWHM (cm^{-1})	position (cm^{-1})	FWHM (cm^{-1})	
OLCa	1340	71	1585	70	1.3
OLCv	1344	176	1589	90	3.1
LTO	1345	162	1607	68	1.7
LTO-OLCa	1347	92	1600	67	1.3
LTO-OLCv	1351	193	1585	70	2.8

Table S4: Results of the R_s, R_{int}, and R_{ct} obtained by fitting the data in **Fig S6**.

Material	R_s (Ω)	CPE1 (F·s)	R_{int}(Ω)	CPE2 (F·s)	R_{ct}(Ω)	W
LTO	84.05	9.7e-05	247.3	5.5e-04	3871	1974
LTO-OLCa	4.6	6.0e-05	359.2	2.8e-03	736	1384
LTO-OLCv	2.2	3.4e-05	9333.5	1.1e-03	1607	911

4.2 In situ investigation of expansion during the lithiation of pillared MXenes with ultralarge interlayer distance

Philip A. Maughan,[1] Stefanie Arnold,[2,3] Yuan Zhang,[2,3]

Volker Presser,[2,3,4] Nuria Tapia-Ruiz,[5] and Nuno Bimbo[1,6]

[1] Department of Engineering, Lancaster University, Lancaster, LA1 4YW, United Kingdom

[2] INM - Leibniz Institute for New Materials, Campus D2.2, 66123 Saarbrücken, Germany

[3] Department of Materials Science and Engineering, Saarland University, Campus D2.266123 Saarbrücken, Germany

[4] Saarene Saarland Center for Energy Materials and Sustainability, Campus D4.2, 66123 Saarbrücken, Germany

[5] Department of Chemistry, Lancaster University, Lancaster, LA1 4YB, United Kingdom

[6] School of Chemistry, Highfield Campus, University of Southampton, Southampton, SO17 1BJ, United Kingdom

Citation:

Own Contribution:

Investigation, electrochemical measurements, data curation, visualization, writing-original draft, writing-review & editing.

Article

In Situ Investigation of Expansion during the Lithiation of Pillared MXenes with Ultralarge Interlayer Distance

Philip A. Maughan, Stefanie Arnold, Yuan Zhang, Volker Presser, Nuria Tapia-Ruiz, and Nuno Bimbo*

Read Online

ACCESS | Metrics & More | Article Recommendations | Supporting Information

ABSTRACT: Pillared $Ti_3C_2T_z$ MXene with a large interlayer spacing (1.75 nm) is shown to be promising for high-power Li-ion batteries. Pillaring dramatically enhances the electrochemical performance, with superior capacities, rate capability, and cycling stability compared to the nonpillared material. In particular, at a high rate of 1 A g^{-1}, the SiO_2-pillared MXene has a capacity over 4.2 times that of the nonpillared material. For the first time, we apply in situ electrochemical dilatometry to study the volume changes within the MXenes during (de)lithiation. The pillared MXene has superior performance despite larger volume changes compared to the nonpillared material. These results give key fundamental insights into the behavior of $Ti_3C_2T_z$ electrodes in organic Li electrolytes and demonstrate that MXene electrodes should be designed to maximize interlayer spacings and that MXenes can tolerate significant initial expansions. After 10 cycles, both MXenes show nearly reversible thickness changes after the charge−discharge process, explaining the stable long-term electrochemical performance.
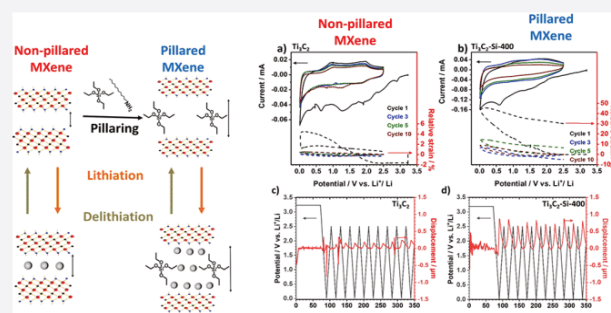
INTRODUCTION

MXenes are a family of two-dimensional materials first reported in 2011, which have shown promising performance in electrochemical energy storage applications such as metal-ion batteries and supercapacitors.[1−3] However, their electrochemical performance is highly dependent on the electrode architecture, with multilayered stacked MXene suffering from low capacities and poor rate capabilities and cycling stabilities.[4,5] This has increased the focus on developing porous MXenes with controlled and open architectures to enhance the electrochemical performance, such as flocculation, freeze drying, and pillaring.[6−8]

Pillaring introduces foreign species between the layers to act as pillars, allowing pore sizes to be tuned by pillar choice and heat treatment steps.[9] Recently, these techniques have been adapted to create porous MXenes for electrochemical applications, including metal-ion batteries, hybrid metal-ion capacitors, and supercapacitors.[10−18] For example, pillar species such as hexadecyl trimethylammonium bromide, SnS, and Sn cations have been utilized to enlarge the interlayer spacing and improve the performance of MXene electrodes in Li-ion batteries.[10,16−19] However, while it is well established that pillaring can significantly enhance the electrochemical performance, an in-depth understanding of the processes occurring in pillared structures during cycling is lacking.

In this work, we utilize in situ electrochemical dilatometry (eD) supported by X-ray diffraction (XRD) to rationalize the enhanced performance of silica-pillared $Ti_3C_2T_z$ MXene as a negative electrode for Li-ion batteries. In situ eD has previously been applied to MXene research to study the intercalation of various ions and molecules in several electrolyte systems such as ionic liquids[20,21] and aqueous Li, Na, and Mg systems.[22−24] However, this is the first time this technique has been applied to MXenes for organic Li-ion battery systems, and it can provide important information about the effect of pillars during (de)lithiation.

METHODS

The pillared $Ti_3C_2T_z$ MXene (Ti_3C_2-Si-400) was synthesized by using our previously reported pillaring method using tetraethylortho silicate as the silica source and dodecylamine (DDA) as the co-pillar amine (Figure 1a).[25] Full details of all synthesis and characterization methods can be found in the Experimental Section in the Supporting Information. The successful intercalation and pillaring of the synthesized $Ti_3C_2T_z$ MXene were confirmed by powder XRD (PXRD) data (Figure 1b and Supporting Information, Figure S1a), while scanning electron microscopy (SEM) confirmed the
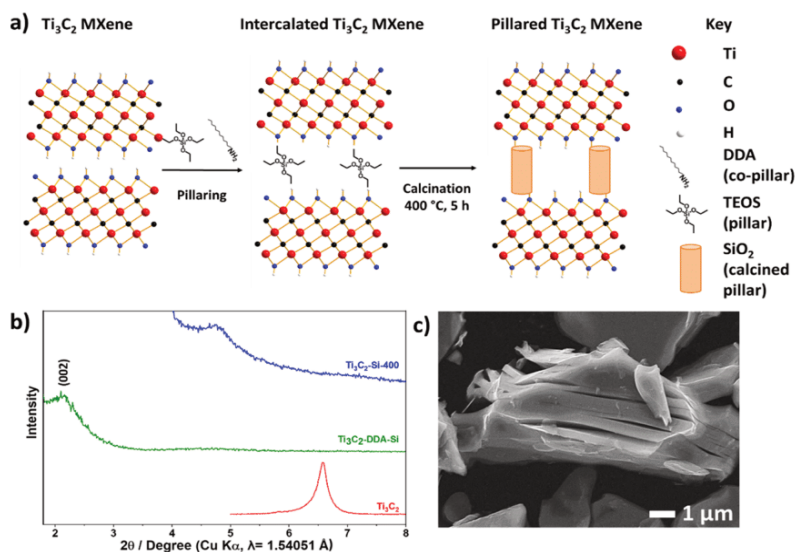
Figure 1. (a) Schematic illustration of the amine-assisted SiO_2 pillaring process used to create porous $Ti_3C_2T_z$ with an enlarged interlayer distance. (b) Low-angle ($1.8-8°$ 2θ) PXRD data demonstrating expanded interlayer spacing in the SiO_2-pillared MXene (Ti_3C_2-Si-400), intercalated MXene (Ti_3C_2-DDA-Si), and nonpillared MXene (Ti_3C_2). (c) SEM micrograph of the SiO_2-pillared MXene (Ti_3C_2-Si-400).

retention of the layered morphology (Figure 1c and Supporting Information, Figure S1b), which matches our previous report.[25] We note that our pillared structure is based on multilayered MXenes, and delamination was not attempted since delamination procedures can suffer from issues, such as low yield (52−60%), multiple steps, and low concentrations of delaminated nanosheets in solution.[26] One of the potential attractions of pillaring techniques is to allow full access of the MXene nanosheet layers in a stable electrode architecture using simple methods.

RESULTS AND DISCUSSION

Galvanostatic charge−discharge (GCD) experiments were used to investigate the performance of the pillared $Ti_3C_2T_z$ as a Li-ion battery electrode (Figure 2), with a specific current of 20 mA g^{-1} and a potential window of 0.01−3.0 V versus Li^+/Li. All further potentials in the article are referenced versus Li^+/Li. The voltage profiles of the pillared and nonpillared MXenes display similar features, with a linear region between 3.0 and 0.3 V, followed by a short plateau feature below 0.3 V. This signifies that the Li storage in $Ti_3C_2T_z$ is a two-stage process, as previously reported.[27] The first stage corresponds to Li^+ intercalation between $Ti_3C_2T_z$ nanosheets forming $Li_2Ti_3C_2T_z$ (theoretical capacity of 260 mA h g^{-1}), followed by Li^+ adsorption above the first intercalated layer, resulting in $Li_3Ti_3C_2T_z$, in the lower voltage region. An additional short plateau is observed on the initial discharge for both materials, which is commonly assigned to the solid electrolyte interphase (SEI) formation and irreversible reactions between Li and MXene surface groups.[27−29] Both materials also show typical linear charge profiles, with a small plateau around 1.5 V, resulting from Li deintercalation.

The pillared MXene has a significantly larger first discharge capacity (536 mA h g^{-1}) compared with the nonpillared (289 mA h g^{-1}) and a larger initial Coulombic efficiency (58% and 43%, respectively). The enhanced initial Coulombic efficiency can be explained by lower levels of Li trapping due to the enlarged interlayer spacings which would provide open Li

diffusion channels. Also, surface groups such as −OH, which have been reported to react irreversibly during lithiation, are likely to have already reacted with the co-pillars during the pillaring process. This would further reduce irreversible capacity losses during (de)lithiation.[27] For the second discharge cycle, the pillared $Ti_3C_2T_z$ shows capacities around 2.2 times greater than the nonpillared material (314 mA h g^{-1} and 142 mA h g^{-1}, respectively), likely as a result of the larger interlayer spacing facilitating greater ion accessibility to the MXene redox sites.

Significantly, the second discharge capacity (314 mA h g^{-1}) is considerably higher than expected based on monolayer lithium coverage, which is 235 mA h g^{-1} when accounting for the pillar mass (which is estimated to be 11 wt % based on the SEM−energy-dispersive system (EDS) analysis, Supporting Information, Figure S2), further implying that multilayer adsorption is contributing to the capacity. However, the full formation of a third lithium layer to form $Ti_3C_2O_2Li_3$ would give a capacity of around 350 mA h g^{-1}, which suggests that the third layer does not fully form. Xie et al. calculated that the extra adsorbed Li layer would be located around 2.8 Å above the Ti−O−Li lithium,[27] which requires an interlayer gallery space of at least 6 Å. This is less than the ca. 7 Å interlayer gallery space calculated from XRD data in our pillared MXene, demonstrating the feasibility of this charge storage mechanism, illustrated by the insets in Figure 2a,b. Note that the interlayer gallery space is defined as the free pore space between layers of a pillared material and is not equivalent to the d-spacing, which includes the sheet thickness. Our pillared $Ti_3C_2T_z$ has a d-spacing of 1.75 nm, as calculated from the (002) peak using the Bragg equation. An extra increase of 2.3 Å gallery space would be required for the adsorption of a further layer,[27] taking the total to at least 8.3 Å, which is larger than our spacings, revealing why further adsorption does not occur. Although the average interlayer gallery space was calculated to be 0.7 nm from XRD data using a monolayer $Ti_3C_2T_z$ thickness of just under 1 nm, in line with the method utilized by Luo et al.,[10] our previous work using transmission electron microscopy

RESULTS AND DISCUSSION
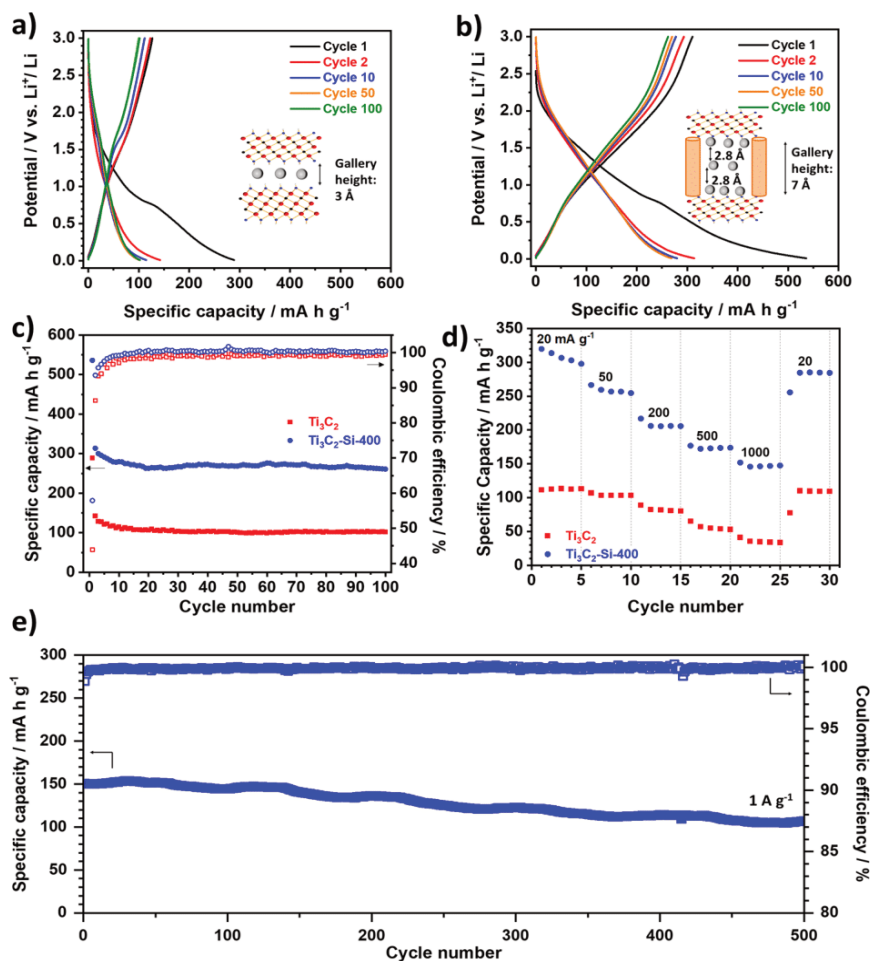
Figure 2. Galvanostatic data from half-cell tests against Li metal at 20 mA g^{-1} in the potential range 0.01−3.0 V using 1 M LiPF$_6$ in EC/DEC (1:1 mass ratio) as the electrolyte. Galvanostatic charge and discharge profiles for selected cycles for (a) nonpillared Ti$_3$C$_2$T$_z$ and (b) SiO$_2$-pillared Ti$_3$C$_2$T$_z$ (Ti$_3$C$_2$-Si-400). Insets illustrate the lithium layers (gray circles) in the respective MXene (blue rectangles) after lithiation (0.01 V). (c) Coulombic efficiency and discharge capacities of the pillared and nonpillared samples over 100 cycles. (d) Rate capability tests for the pillared and nonpillared MXene at rates of 20, 50, 200, 500, and 1000 mA g^{-1}. Five cycles are shown for each rate. (e) GCD data for SiO$_2$-pillared Ti$_3$C$_2$T$_z$ in a Li-ion half-cell tested for 500 cycles at a rate of 1 A g^{-1} in a potential window of 0.01−3.0 V.

revealed local variations in the gallery spacings across the pillared material,[25] with some areas having spacings less than 0.7 nm, explaining why a full extra adsorption layer was not formed.

The pillared MXene also showed improved capacity retention (83%, 262 mA h g^{-1}) compared with the nonpillared MXene (72%, 101 mA h g^{-1}) over 100 cycles (Figure 2c). The majority of the capacity fade occurred over the initial 15 cycles, with capacity retentions of 96% (pillared) and 91% (nonpillared) between cycles 15 and 100. These results demonstrate that the SiO$_2$ pillars significantly improve electrode stability during cycling.

The rate capability of the MXenes was investigated by cycling at specific currents of 20, 50, 200, 500, 1000, and 20 mA g^{-1}, with five cycles conducted at each specific current (Figure 2d). The pillared MXene outperformed the nonpillared material at all specific currents tested, with discharge capacities of 307, 260, 206, 173, 147, and 285 mA h g^{-1} at the respective rate compared to 113, 104, 82, 55, 35, and 109 mA h g^{-1}, respectively. Interestingly, the capacity enhancement is

more considerable at higher rates than lower ones, with an increase of 4.2 times that of the nonpillared Ti$_3$C$_2$T$_z$ observed at 1 A g^{-1}, compared with just 2.7 times at 20 mA g^{-1}. This demonstrates that the pillared architecture benefits the high rate performance in particular and implies that the enlarged interlayer distance increases the lithium storage capacity and creates channels that allow fast Li$^+$ ion diffusion through the structure. Cycling the pillared MXene at 1 A g^{-1} for a further 500 cycles after the rate capability tests resulted in a discharge capacity of 151 mA h g^{-1} (Figure 2e) with a capacity retention of 71%, which shows reasonable stability at high rates. The impressive high rate performance can be explained by the significant contribution of a surface-limited capacitive-like process to the charge storage, revealed by b-value analysis conducted on cyclic voltammetry (CV) data collected at multiple scan rates (Supporting Information, Figure S4a,b). At potentials above 0.5 V, the b-values are at least 0.85, consistent with most capacitive charge storage behavior. An ideal capacitor would display a b-value of 1, whereas an ideal diffusion-limited battery-like electrode would have b = 0.5.[30]
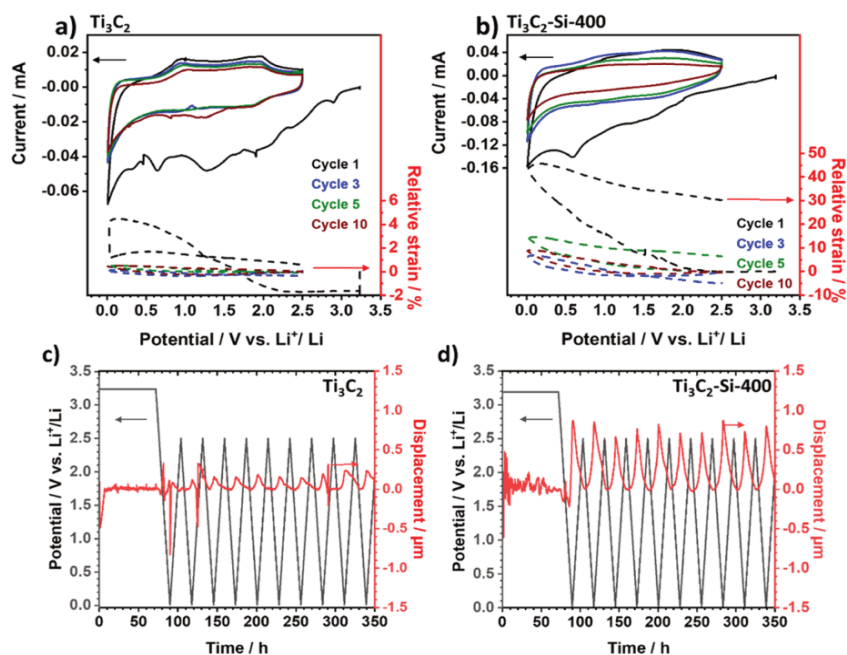
Figure 3. Cyclic voltammograms and corresponding in situ dilatometric measurements (electrode height change/initial height = strain) from half-cell setup vs. Li metal at 0.1 mV s^{-1} in the potential range 0.01−2.5 V for (a) nonpillared Ti$_3$C$_2$T$_z$ and (b) pillared MXene (Ti$_3$C$_2$-Si-400). The electrochemical response of the working electrode (continuous line) can be simultaneously tracked with the height change (dashed line). (c,d) Potential and relative height change vs time of MXene electrodes measured by in situ eD (c) for nonpillared Ti$_3$C$_2$T$_z$ (electrode thickness of 43 μm) and (d) for pillared MXene (Ti$_3$C$_2$-Si-400, electrode thickness of 26 μm). The artifacts which are unrelated to the electrode thickness response had been subtracted as background signals.

Furthermore, deconvolution of the capacitive and diffusion-limited charge storage processes, following the method described by Wang et al.,[31] revealed that at the scan rate of 5 mV s^{-1}, 78% of the total current was due to capacitive-like processes, demonstrating the importance of capacitive processes at high rates (Supporting Information, Figure S4c). A scan rate of 5 mV s^{-1} corresponds to a sweep time of 10 min, similar to the sweep time of 8 min for the GCD testing at 1 A g^{-1}. Even at the low scan rate of 0.2 mV s^{-1}, 43% of the total charge storage was a result of capacitive-like processes (Supporting Information, Figure S4d). As observed in previous studies of MXenes in organic Li-ion systems, the capacitive contribution to the charge storage increased with the increasing scan rate (Supporting Information, Figure S4d).[32,33] Further details on this analysis are given in the Experimental Section in the Supporting Information. This analysis uses a range of sweep rates, similar to other reported studies on pillared MXenes in organic electrolytes.[10,34]

To better understand the influence of interlayer gallery spacing on enhancing electrochemical lithium-ion storage, the volume change of pillared/nonpillared Ti$_3$C$_2$T$_z$ MXene during ion uptake and release was investigated by in situ eD, which can observe volume change and CV simultaneously. A scan rate of 0.1 mV s^{-1} was applied with a narrower potential window of 0.01−2.5 V to focus on expansion/contraction processes related directly to the (de)lithiation of the MXene. The CV shape for the pillared material closely matched with what was recorded in typical coin cells, with similar broad redox features, demonstrating that the cell used for in situ eD[35] does not change the electrochemical processes. Figure 3 shows the cyclic voltammogram in the dilatometry cell, and

Supporting Information, Figure S3 shows the comparison in a typical coin cell. The nonpillared material shows more pronounced redox peaks compared with the pillared MXene, which are very broad, as was observed in our previous work in a Na-ion system and supports the expanded nature of the MXene.[25,36] As expected from the GCD data, multiple irreversible reduction peaks are observed in the pillared material during the first discharge, with peaks at around 1.3 and 0.6 V attributed to the SEI formation and trapping of lithium-ions,[2] while lithiation of the conductive additive contributes to the peak at 0.01 V.[37,38] In the following delithiation sweep, two oxidation peaks were observed at 1.0 and 1.8 V, representing the extraction of lithium-ions, whose intensities continuously decrease slightly in the following cycles. For the nonpillared Ti$_3$C$_2$T$_z$, similar redox features occur, with pronounced reversible peaks at 1.8 and 1.0 V (reduction) and at 0.9 and 2.0 V (oxidation) throughout the cycling. The fact that the CV and load curves for the nonpillared and pillared MXenes display similar features with no extra redox peaks/plateaus present in the data for the pillared MXene strongly implies that the enhanced performance results from the enlarged interlayer spacing, rather than the electrochemical activity of the silica pillars. This is consistent with the results of our previous work on pillared Mo$_2$TiC$_2$, where ex situ X-ray photoelectron spectroscopy and nuclear magnetic resonance spectroscopy studies showed that the silica pillars in that system did not undergo lithiation during cycling.[15]

The unprocessed dilatometry data for the nonpillared MXene electrode reveal slight volume changes (∼0.5 μm) during the initial 72 h of stabilization time, which is related to

RESULTS AND DISCUSSION

the electrode wetting process (Figure 3c). A relatively large expansion (1.84 μm, 5.7% strain) occurs during the first discharging step, consistent with Li$^+$ intercalation (Figure 3a). At the end of the first lithiation sweep (0.01 V), a large jump is observed in the dilatometry data (Figure 3a). Comparison with the corresponding CV curve (Figure 3a) shows that while there is a large peak here, which likely results from a combination of Li$^+$ intercalation, lithiation of the carbon additive,[38] and changes in MXene termination groups, the magnitude of this jump is significantly larger than the corresponding CV peak. This implies that there is also significant contribution from device artifacts, which cannot be removed from the data in Figure 3a without losing physical meaning. However, it is clear that the contribution from artifacts is low overall and does not affect the conclusions that can be drawn from the data.

During delithiation, the expansion is only partially reversed, with a decrease in volume of ca. 1%. This demonstrates that Ti$_3$C$_2$T$_z$ remains in an expanded state even after delithiation, which is likely related to partial Li-trapping, changes in MXene surface chemistry, SEI formation, and solvent co-intercalation within the electrode layers. A similar pattern can be seen in the second cycle but with reduced amplitude of volume changes on charge/discharge while having a relative strain during the third cycle of −0.36%. Between cycles 3 and 10, the volume changes in the electrode appear to stabilize, with the magnitude of volume expansion on lithiation matching the magnitude of contraction on delithiation, so that the relative strain during the cycle tends toward zero. The pattern of expansion during lithiation and contraction during delithiation matches well with previous in situ XRD studies carried out on multilayered Ti-based MXenes, which supports our dilatometry data.[39]

Since the volume changes in the stabilization time are artifacts of the device, a background/baseline subtraction was used, as shown in Figure 3c,d. For the calculation of the relative and absolute expansion in Table 1, only the lithiation

Table 1. Comparison of the Displacement and Strain Measured Using In Situ Electrochemical Dilatometry for the Nonpillared (Ti$_3$C$_2$) and Pillared (Ti$_3$C$_2$-Si-400) MXenes[a]

cycle number	Ti$_3$C$_2$		Ti$_3$C$_2$-Si-400	
	displacement (μm)	relative strain (%)	displacement (μm)	relative strain (%)
cycle 1	0.08	0.10	1.02	3.91
cycle 3	0.15	0.35	0.69	2.69
cycle 5	0.18	0.41	0.82	3.14
cycle 10	0.23	0.53	0.80	3.07

[a]Background subtraction has been carried out to remove artifacts that are unrelated to the electrode shrinking and expansion and the data normalized by electrode thickness according to the method reported by Budak et al.[40] These values were calculated by referring to the height change between the start of the cycle (2.5 V) and the opposite end of the lithiation process (0.01 V).

process was considered in each case. During the cycles, the nonpillared MXene behaves as a low-strain material (<0.53% strain within the entire lithiation cycle). The expansion levels for this sample increase slightly continuously up to the 10th cycle. Since the GCD tests showed that the discharge capacity fades over these first 10 cycles, this may indicate the presence of irreversible side reactions, such as Li-trapping. This would

lead to a consistent expansion of the nonpillared material during cycling and explain the lower cycling stability for this material compared to the pillared MXene. The overall volume changes are very small for all cycles, which agree well with the stable cycling performance observed during the GCD tests after the initial few cycles.

Postmortem XRD recorded after two cycles of CV in custom-built polyether ether ketone cells of the nonpillared samples shows a slight shift in the (002) diffraction peak to lower angles (from 8.4° to 7.8° 2θ), supporting the small expansion observed in the dilatometry data (Supporting Information, Figure S5a,b).

For the pillared MXene (Figure 3b,d), a large initial expansion occurs over the first few hours under open-circuit potential, with a gradual relaxation toward a minimum level of ca. 1.6 μm lower compared to the initial volume over the remainder of the rest period.

As observed for the nonpillared MXene, a large expansion (~1.02 μm) occurs in the first lithiation cycle (Table 1). The initial contraction has a smaller magnitude compared to the initial expansion. This suggests that the pillars aid in keeping the MXene electrode expanded, allowing wide Li-diffusion pathways rather than fixing a constant interlayer spacing. The pillared electrode continues to expand and contract over the next few cycles with approximately constant absolute and relative expansion. After the first cycle, the strain decreases slightly in the short term, but when looking at the continuous change, consistent values of around 3−4% relative strain can be obtained for all cycles. This correlates with the electrode's stable performance during GCD cycling (Figure 2d). Simultaneously, slight capacity fading was observed over the first few cycles where the amplitude of contraction (delithiation) was consistently more minor than the previous expansion during lithiation, suggesting that small quantities of irreversible side processes, such as Li-trapping, were occurring, albeit significantly less than observed for the nonpillared material. Postmortem XRD on the pillared MXene after two cycles shows a loss of the (002) diffraction peak (Supporting Information, Figure S5d), suggesting that the expansions observed in the dilatometry arise from inhomogeneous changes in the interlayer spacing during the initial (de)-lithiation cycles. This early loss of observable diffraction peaks demonstrates the advantages of techniques such as in situ dilatometry to study the (de)lithiation processes, which does not rely on long-range order.

The nonpillared MXene undergoes more minor volume changes than the pillared counterpart, which may be explained by the significantly larger quantities of Li$^+$ intercalated into the structure (ca. 2.5 times) in the pillared electrode compared to the nonpillared. This implies that the key to unlocking high and persistent performance for MXenes is to engineer large interlayer spacings, which would avoid narrow interlayer spacings, limiting Li$^+$ storage capacity and diffusion. Large but reversible expansions do not seem to be detrimental to MXene performance. The pillared MXene undergoes large but consistent volume changes while displaying high cycling stability compared to the nonpillared MXene, where the expansion gradually increased in magnitude during cycling. This finding suggests that MXene architectures should be designed to minimize irreversible volume changes during cycling.

CONCLUSIONS

In conclusion, silica-pillared $Ti_3C_2T_z$ MXene with an ultralarge interlayer spacing displayed significantly enhanced performance as the negative electrode of a Li-ion battery. In particular, at the high rate of 1 A g^{-1}, the SiO_2-pillared MXene had a capacity over 4 times that of the nonpillared material (over 150 mA h g^{-1}) and retained over 71% of its initial capacity after 500 cycles. In situ dilatometry combined with XRD data revealed that the superior cycling performance occurred despite larger volume changes and a decrease in crystallinity, suggesting inhomogeneous interlayer expansion. During lithiation, a constant relative expansion of 3−4% in each cycle is obtained for the pillared MXene sample. In contrast, for the nonpillared MXene, a slightly increasing expansion is obtained with increasing cycle numbers. These results provide key insights into the design of MXene electrodes, demonstrating that large interlayer spacings and consistent volume changes, as provided by pillaring techniques, are key for high performance. This is the case even for large (3−4%) expansions, which are well tolerated by the pillared MXene.

ASSOCIATED CONTENT

ⓈⒾ Supporting Information

The Supporting Information is available free of charge at https://pubs.acs.org/doi/10.1021/acs.jpcc.1c05092.

Experimental methods for the synthesis and pillaring of MXenes; experimental details for the XRD characterization, SEM characterization, electrochemical characterization, dilatometry experiments, and ex situ XRD; X-ray diffractograms and SEM micrographs of the nonpillared $Ti_3C_2T_z$; SEM−EDS analysis for the pillared MXene; cyclic votammogram and capacitive contribution from CV data for the pillared MXene; and ex situ XRD and corresponding CV data for the pillared and nonpillared materials (PDF)

AUTHOR INFORMATION

Corresponding Author

Nuno Bimbo − *Department of Engineering, Lancaster University, Lancaster LA1 4YW, U.K.; School of Chemistry, Highfield Campus, University of Southampton, Southampton SO17 1BJ, U.K.;* ⓞ orcid.org/0000-0001-8740-8284; Email: N.Bimbo@soton.ac.uk

Authors

Philip A. Maughan − *Department of Engineering, Lancaster University, Lancaster LA1 4YW, U.K.*
Stefanie Arnold − *INM - Leibniz Institute for New Materials, Saarbrücken 66123, Germany; Department of Materials Science and Engineering, Saarland University, Saarbrücken 66123, Germany*
Yuan Zhang − *INM - Leibniz Institute for New Materials, Saarbrücken 66123, Germany; Department of Materials Science and Engineering, Saarland University, Saarbrücken 66123, Germany*
Volker Presser − *INM - Leibniz Institute for New Materials, Saarbrücken 66123, Germany; Department of Materials Science and Engineering, Saarland University, Saarbrücken 66123, Germany; Saarene Saarland Center for Energy Materials and Sustainability, Saarbrücken 66123, Germany;* ⓞ orcid.org/0000-0003-2181-0590

Nuria Tapia-Ruiz − *Department of Chemistry, Lancaster University, Lancaster LA1 4YB, U.K.;* ⓞ orcid.org/0000-0002-5005-7043

Complete contact information is available at: https://pubs.acs.org/10.1021/acs.jpcc.1c05092

Notes

The authors declare no competing financial interest.

REFERENCES

(1) Naguib, M.; Kurtoglu, M.; Presser, V.; Lu, J.; Niu, J.; Heon, M.; Hultman, L.; Gogotsi, Y.; Barsoum, M. W. Two-Dimensional Nanocrystals Produced by Exfoliation of Ti_3AlC_2. *Adv. Mater.* **2011**, *23*, 4248−4253.
(2) Tang, X.; Guo, X.; Wu, W.; Wang, G. 2D Metal Carbides and Nitrides (MXenes) as High-Performance Electrode Materials for Lithium-Based Batteries. *Adv. Energy Mater.* **2018**, *8*, 1801897.
(3) Anasori, B.; Lukatskaya, M. R.; Gogotsi, Y. 2D Metal Carbides and Nitrides (MXenes) for Energy Storage. *Nat. Rev. Mater.* **2017**, *2*, 16098.
(4) Naguib, M.; Mochalin, V. N.; Barsoum, M. W.; Gogotsi, Y. 25th Anniversary Article: MXenes: A New Family of Two-Dimensional Materials. *Adv. Mater.* **2014**, *26*, 992−1005.
(5) Greaves, M.; Barg, S.; Bissett, M. A. MXene-Based Anodes for Metal-Ion Batteries. *Batteries Supercaps* **2020**, *3*, 214−235.
(6) Bu, F.; Zagho, M. M.; Ibrahim, Y.; Ma, B.; Elzatahry, A.; Zhao, D. Porous MXenes: Synthesis, Structures, and Applications. *Nano Today*. Elsevier B.V. *30*, 2020, p 100803. DOI: 10.1016/j.nantod.2019.100803
(7) Bao, W.; Tang, X.; Guo, X.; Choi, S.; Wang, C.; Gogotsi, Y.; Wang, G. Porous Cryo-Dried MXene for Efficient Capacitive Deionization. *Joule* **2018**, *2*, 778−787.
(8) Zhang, S.; Huang, P.; Wang, J.; Zhuang, Z.; Zhang, Z.; Han, W.-Q. Fast and Universal Solution-Phase Flocculation Strategy for Scalable Synthesis of Various Few-Layered MXene Powders. *J. Phys. Chem. Lett.* **2020**, *11*, 1247−1254.
(9) Kloprogge, J. T. Synthesis of Smectites and Porous Pillared Clay Catalysts: A Review. *J. Porous Mater.* **1998**, *5*, 5−41.
(10) Luo, J.; Zhang, W.; Yuan, H.; Jin, C.; Zhang, L.; Huang, H.; Liang, C.; Xia, Y.; Zhang, J.; Gan, Y.; et al. Pillared Structure Design of MXene with Ultralarge Interlayer Spacing for High-Performance Lithium-Ion Capacitors. *ACS Nano* **2017**, *11*, 2459−2469.
(11) Luo, J.; Wang, C.; Wang, H.; Hu, X.; Matios, E.; Lu, X.; Zhang, W.; Tao, X.; Li, W. Pillared MXene with Ultralarge Interlayer Spacing as a Stable Matrix for High Performance Sodium Metal Anodes. *Adv. Funct. Mater.* **2019**, *29*, 1805946.
(12) Luo, J.; Zheng, J.; Nai, J.; Jin, C.; Yuan, H.; Sheng, O.; Liu, Y.; Fang, R.; Zhang, W.; Huang, H.; Gan, Y.; Xia, Y.; Liang, C.; Zhang, J.; Li, W.; Tao, X. Atomic Sulfur Covalently Engineered Interlayers of Ti$_3$C$_2$ MXene for Ultra-Fast Sodium-Ion Storage by Enhanced Pseudocapacitance. *Adv. Funct. Mater.* **2019**, *29*, 1808107.
(13) Tian, W.; VahidMohammadi, A.; Wang, Z.; Ouyang, L.; Beidaghi, M.; Hamedi, M. M. Layer-by-Layer Self-Assembly of Pillared Two-Dimensional Multilayers. *Nat. Commun.* **2019**, *10*, 2558.

(14) Maughan, P. A.; Tapia-Ruiz, N.; Bimbo, N. In-Situ Pillared MXene as a Viable Zinc-Ion Hybrid Capacitor. *Electrochim. Acta* **2020**, *341*, 136061.

(15) Maughan, P. A.; Bouscarrat, L.; Seymour, V. R.; Shao, S.; Haigh, S. J.; Dawson, R.; Tapia-Ruiz, N.; Bimbo, N. Pillared Mo 2 TiC 2 MXene for High-Power and Long-Life Lithium and Sodium-Ion Batteries. *Nanoscale Adv.* **2021**, *3*, 3145−3158.

(16) Zhang, S.; Ying, H.; Yuan, B.; Hu, R.; Han, W.-Q. Partial Atomic Tin Nanocomplex Pillared Few-Layered $Ti_3C_2T_x$ MXenes for Superior Lithium-Ion Storage. *Nano-Micro Lett.* **2020**, *12*, 78.

(17) Zhang, S.; Han, W.-Q. Recent Advances in MXenes and Their Composites in Lithium/Sodium Batteries from the Viewpoints of Components and Interlayer Engineering. *Phys. Chem. Chem. Phys.* **2020**, *22*, 16482−16526.

(18) Zhang, S.; Ying, H.; Huang, P.; Wang, J.; Zhang, Z.; Yang, T.; Han, W.-Q. Rational Design of Pillared $SnS/Ti_3C_2T_x$ MXene for Superior Lithium-Ion Storage. *ACS Nano* **2020**, *14*, 17665−17674.

(19) Liang, K.; Matsumoto, R. A.; Zhao, W.; Osti, N. C.; Popov, I.; Thapaliya, B. P.; Fleischmann, S.; Misra, S.; Prenger, K.; Tyagi, M.; et al. Engineering the Interlayer Spacing by Pre-Intercalation for High Performance Supercapacitor MXene Electrodes in Room Temperature Ionic Liquid. *Adv. Funct. Mater.* **2021**, *31*, 2104007.

(20) Xu, K.; Merlet, C.; Lin, Z.; Shao, H.; Taberna, P.-L.; Miao, L.; Jiang, J.; Zhu, J.; Simon, P. Effects of Functional Groups and Anion Size on the Charging Mechanisms in Layered Electrode Materials. *Energy Storage Mater.* **2020**, *33*, 460−469.

(21) Jäckel, N.; Krüner, B.; Van Aken, K. L.; Alhabeb, M.; Anasori, B.; Kaasik, F.; Gogotsi, Y.; Presser, V. Electrochemical in Situ Tracking of Volumetric Changes in Two-Dimensional Metal Carbides (MXenes) in Ionic Liquids. *ACS Appl. Mater. Interfaces* **2016**, *8*, 32089−32093.

(22) Come, J.; Black, J. M.; Lukatskaya, M. R.; Naguib, M.; Beidaghi, M.; Rondinone, A. J.; Kalinin, S. V.; Wesolowski, D. J.; Gogotsi, Y.; Balke, N. Controlling the Actuation Properties of MXene Paper Electrodes upon Cation Intercalation. *Nano Energy* **2015**, *17*, 27−35.

(23) Gao, Q.; Come, J.; Naguib, M.; Jesse, S.; Gogotsi, Y.; Balke, N. Synergetic Effects of K^+ and Mg^{2+} Ion Intercalation on the Electrochemical and Actuation Properties of the Two-Dimensional Ti3C2 MXene. *Faraday Discuss.* **2017**, *199*, 393−403.

(24) Torkamanzadeh, M.; Wang, L.; Zhang, Y.; Budak, Ö.; Srimuk, P.; Presser, V.; Budak, Ö.; Budak, Ö.; Srimuk, P.; Presser, V.; Presser, V. MXene/Activated-Carbon Hybrid Capacitive Deionization for Permselective Ion Removal at Low and High Salinity. *ACS Appl. Mater. Interfaces* **2020**, *12*, 26013−26025.

(25) Maughan, P. A.; Seymour, V. R.; Bernardo-Gavito, R.; Kelly, D. J.; Shao, S.; Tantisriyanurak, S.; Dawson, R.; Haigh, S. J.; Young, R. J.; Tapia-Ruiz, N.; et al. Porous Silica-Pillared MXenes with Controllable Interlayer Distances for Long-Life Na-Ion Batteries. *Langmuir* **2020**, *36*, 4370−4382.

(26) Shuck, C. E.; Sarycheva, A.; Anayee, M.; Levitt, A.; Zhu, Y.; Uzun, S.; Balitskiy, V.; Zahorodna, V.; Gogotsi, O.; Gogotsi, Y. Scalable Synthesis of Ti 3 C 2 T x MXene. *Adv. Eng. Mater.* **2020**, *22*, 1901241.

(27) Xie, Y.; Naguib, M.; Mochalin, V. N.; Barsoum, M. W.; Gogotsi, Y.; Yu, X.; Nam, K.-W.; Yang, X.-Q.; Kolesnikov, A. I.; Kent, P. R. C. Role of Surface Structure on Li-Ion Energy Storage Capacity of Two-Dimensional Transition-Metal Carbides. *J. Am. Chem. Soc.* **2014**, *136*, 6385−6394.

(28) Wang, Y.; Li, Y.; Qiu, Z.; Wu, X.; Zhou, P.; Zhou, T.; Zhao, J.; Miao, Z.; Zhou, J.; Zhuo, S. Fe3O4@Ti3C2 MXene Hybrids with Ultrahigh Volumetric Capacity as an Anode Material for Lithium-Ion Batteries. *J. Mater. Chem. A* **2018**, *6*, 11189−11197.

(29) Zhao, N.; Zhang, F.; Zhan, F.; Yi, D.; Yang, Y.; Cui, W.; Wang, X. Fe^{3+}-Stabilized $Ti_3C_2T_x$ MXene Enables Ultrastable Li-Ion Storage at Low Temperature. *J. Mater. Sci. Technol.* **2021**, *67*, 156−164.

(30) Augustyn, V.; Come, J.; Lowe, M. A.; Kim, J. W.; Taberna, P.-L.; Tolbert, S. H.; Abruña, H. D.; Simon, P.; Dunn, B. High-Rate Electrochemical Energy Storage through Li^+ Intercalation Pseudocapacitance. *Nat. Mater.* **2013**, *12*, 518−522.

(31) Wang, J.; Polleux, J.; Lim, J.; Dunn, B. Pseudocapacitive Contributions to Electrochemical Energy Storage in TiO_2 (Anatase) Nanoparticles. *J. Phys. Chem. C* **2007**, *111*, 14925−14931.

(32) Chao, H.; Qin, H.; Zhang, M.; Huang, Y.; Cao, L.; Guo, H.; Wang, K.; Teng, X.; Cheng, J.; Lu, Y.; et al. Boosting the Pseudocapacitive and High Mass-Loaded Lithium/Sodium Storage through Bonding Polyoxometalate Nanoparticles on MXene Nanosheets. *Adv. Funct. Mater.* **2021**, *31*, 2007636.

(33) Wan, L.; Chua, D. H. C.; Sun, H.; Chen, L.; Wang, K.; Lu, T.; Pan, L. Construction of Two-Dimensional Bimetal (Fe-Ti) Oxide/Carbon/MXene Architecture from Titanium Carbide MXene for Ultrahigh-Rate Lithium-Ion Storage. *J. Colloid Interface Sci.* **2021**, *588*, 147−156.

(34) Luo, J.; Fang, C.; Jin, C.; Yuan, H.; Sheng, O.; Fang, R.; Zhang, W.; Huang, H.; Gan, Y.; Xia, Y.; Liang, C.; Zhang, J.; Li, W.; Tao, X. Tunable Pseudocapacitance Storage of MXene by Cation Pillaring for High Performance Sodium-Ion Capacitors. *J. Mater. Chem. A* **2018**, *6*, 7794−7806.

(35) Hahn, M.; Barbieri, O.; Gallay, R.; Kötz, R. A Dilatometric Study of the Voltage Limitation of Carbonaceous Electrodes in Aprotic EDLC Type Electrolytes by Charge-Induced Strain. *Carbon* **2006**, *44*, 2523−2533.

(36) Cheng, R.; Hu, T.; Zhang, H.; Wang, C.; Hu, M.; Yang, J.; Cui, C.; Guang, T.; Li, C.; Shi, C.; et al. Understanding the Lithium Storage Mechanism of Ti3C2Tx MXene. *J. Phys. Chem. C* **2019**, *123*, 1099−1109.

(37) Sun, D.; Wang, M.; Li, Z.; Fan, G.; Fan, L.-Z.; Zhou, A. Two-Dimensional Ti3C2 as Anode Material for Li-Ion Batteries. *Electrochem. Commun.* **2014**, *47*, 80−83.

(38) Gnanamuthu, R.; Lee, C. W. Electrochemical Properties of Super P Carbon Black as an Anode Active Material for Lithium-Ion Batteries. *Mater. Chem. Phys.* **2011**, *130*, 831−834.

(39) Come, J.; Naguib, M.; Rozier, P.; Barsoum, M. W.; Gogotsi, Y.; Taberna, P.-L.; Morcrette, M.; Simon, P. A Non-Aqueous Asymmetric Cell with a Ti_2C-Based Two-Dimensional Negative Electrode. *J. Electrochem. Soc.* **2012**, *159*, A1368−A1373.

(40) Budak, Ö.; Geißler, M.; Becker, D.; Kruth, A.; Quade, A.; Haberkorn, R.; Kickelbick, G.; Etzold, B. J. M.; Presser, V. Carbide-Derived Niobium Pentoxide with Enhanced Charge Storage Capacity for Use as a Lithium-Ion Battery Electrode. *ACS Appl. Energy Mater.* **2020**, *3*, 4275−4285.

Supporting Information

In situ Investigation of Expansion during Lithiation
of Pillared MXene with Ultralarge Interlayer Distance

Philip A. Maughan,[1] Stefanie Arnold,[2,3] Yuan Zhang,[2,3] Volker Presser,[2,3,4] Nuria Tapia-Ruiz,[5] and Nuno Bimbo[1,6*]

[1] Department of Engineering, Lancaster University, Lancaster, LA1 4YW, United Kingdom
[2] INM - Leibniz Institute for New Materials, Saarbrücken, 66123, Germany
[3] Department of Materials Science and Engineering, Saarland University, 66123 Saarbrücken, Germany
[4] Saarene Saarland Center for Energy Materials and Sustainability, Campus D4.2, 66123 Saarbrücken, Germany
[5] Department of Chemistry, Lancaster University, Lancaster, LA1 4YB, United Kingdom
[6] School of Chemistry, Highfield Campus, University of Southampton, Southampton, SO17 1BJ, United Kingdom

[*] Corresponding author's email: N.Bimbo@soton.ac.uk

Table of Contents

Experimental methods
Materials

The following materials were used without any further purification: Ti_3AlC_2 (Carbon Ukraine Ltd), hydrochloric acid (37.5 mass%, Sigma Aldrich), tetraethylortho silicate (TEOS, 98% purity, Alfa Aesar), 1-dodecylamine (DDA, 97% purity, Alfa Aesar), N-Methyl-2-pyrrolidone (NMP, 99.5% purity, Alfa Aesar), PVDF (99.0% purity, Alfa Aesar), Super P carbon black (99% purity, Alfa Aesar), $LiPF_6$ in diethyl carbonate (DEC) and ethylene carbonate (EC) (1:1 by mass, 99% purity Gotion), copper foil (Tob New Energy).

Synthesis of $Ti_3C_2T_z$

To obtain the MXenes, 3 g of Ti_3AlC_2 were sieved through a -400 mesh sieve (pore size of 38 μm) and added over 10 min to a 6 M HCl solution with pre-dissolved LiF (7.5:1 F to Al ratio). This mixture was heated to 40 °C and left to etch for 48 h with magnetic stirring. The powder was re-dispersed in a 1 M HCl solution for 3 h at room temperature to remove any remaining impurities and to increase the number of -OH surface groups on the MXene.

Pillaring of $Ti_3C_2T_z$ samples

For the pillaring experiments, we applied our previously reported amine-assisted silica pillaring method.[1] Briefly, 0.5 g of the as-made $Ti_3C_2T_z$ MXene were added to a solution of dodecylamine (DDA) dissolved in TEOS in a MXene:DDA:TEOS molar ratio of 1:10:20 under argon. This was stirred in a sealed glass vial under argon at room temperature for 4 h. The black powder was then recovered by vacuum filtration, dried on filter paper under vacuum before being re-dispersed in de-ionized water (25 mL) overnight at room temperature (18 h). The intercalated product was then recovered by vacuum filtration and dried overnight at 60 °C. These samples were then calcined at 400 °C for 5 h under argon with a heating rate of 5 °C min^{-1}.

Characterization

The samples were characterized by X-ray diffraction (XRD) in a Smartlab diffractometer (Rigaku) using Cu-Kα radiation operating in reflection mode with Bragg-Brentano geometry to investigate the crystal structure. Prior to the XRD characterisation, all samples were dried in an oven at 80 °C for 18 h. The black powders were then ground and placed on a silica sample holder and pressed flat with a glass slide.

Scanning electron microscopy (SEM) was carried out in a JEOL JSM-7800F (JEOL), and energy-dispersive x-ray spectroscopy (EDX) was done in a X-Max50 (Oxford Instruments) using an accelerating voltage of 10 kV and a working distance of 10 mm, which were used to study the morphology and elemental composition. For the SEM and SEM-EDS studies, the dried powder samples were dry cast onto a carbon tape support, which was placed on to a copper stub for analysis. To minimize errors from the use of EDS for the estimation of the Si content, large flat particle surfaces were chosen for the EDS mapping.

Electrochemical characterization

To test the pillaring process's effect on the electrochemical performance, the pillared and un-pillared materials were tested in CR2032 coin cells with a half-cell configuration using lithium metal disks as the counter electrode and 1 M $LiPF_6$ in EC/DEC (1:1 mass ratio) as the electrolyte. The MXene was mixed with carbon black (Super P) as a conductive additive and PVDF as the binder in a 75:15:10 mass ratio, respectively. These were added to a few mL of NMP to make a slurry, which was then cast onto a Cu foil current collector, from which electrodes with a diameter of 16 mm were punched. The active mass weighting was around 3 mg cm^{-2}. Coin cells were constructed in an argon-filled glovebox (O_2 and H_2O levels < 0.1 ppm) using Whatman microglass fibre paper as the separator. The charge-discharge tests were carried out on a Neware battery cycler (Neware Battery Technologies Ltd.) at a current density of 20 mA g^{-1} in the voltage range of 0.01-3.0 V vs. Li$^+$/Li for 100 cycles. For rate capability tests, the cells were cycled at a specific current of 20 mA g^{-1} for one cycle to stabilise the cell followed by five cycles at each rate of 20, 50, 200, 500, 1000 mA g^{-1} before returning to 20 mA g^{-1}. Cyclic voltammetry (CV) measurements were conducted using an Ivium potentiostat (Ivium Technologies BV) with a scan rate of 0.2 mV s^{-1} for five cycles, followed by further cycles at 0.5, 2, 5 mV s^{-1} sweep rates in the voltage range of 0.01-3.0 V vs. Li$^+$/Li. The

S-3

final scan at each rate was used for the calculation of the *b*-values. The relationship between the current (*i*) and scan rate (*v*) is given by Equation (1):

$$i = av^b \qquad (1)$$

where *a* and *b* are fitting parameters.[2] A *b*-value of 0.5 corresponds to an ideal diffusion-limited (battery-like) charge storage process whereas a *b*-value of 1 indicates a perfect surface-limited (capacitive-like) process. To calculate the total contribution of capacitive-like processes to the charge storage, deconvolution of the total current into surface capacitive and diffusion controlled intercalation processes was carried out using the method described by Dunn et al, using the Equation (2-3).[3]

$$i(V, v) = k_1(V) + k_2(V)v^{1/2} \qquad (2)$$

$$i(V,v)/v^{1/2} = k_1(V)v^{1/2} + k_2(V) \qquad (3)$$

Here k_1 and k_2 are potential dependant constants, *i* is the current and is the *v* scan rate. The values for k_1 and k_2 were obtained using Equation (3) by plotting *i* against $v^{1/2}$ for each potential, where a linear fit has k_1 as the gradient and k_2 as the intercept. This was used to calculate the non-diffusion limited ($k_1.v$) and diffusion-limited ($k_2.v^{1/2}$) contributions at each potential for each scan rate studied. The non-diffusion limited contribution to the total charge is typically assumed to represent the capacitive charge. The total capacitive contribution to the charge storage for each scan rate was then calculated by integrating the area of a cyclic voltammogram for the total experimental current and the calculated capacitive current.

In situ dilatometry

The in situ dilatometry measurements (height change (strain) of the MXene electrodes during charging and discharging) were conducted by using an ECD-3-nano cell device from EL-CELL (setup adopting the design by Hahn et al.).[4] All cell parts were dried overnight at +80 °C and introduced into an argon-filled glovebox (MBraun Labmaster 130; O_2 and H_2O < 0.1 ppm). The cells were arranged in a two-electrode configuration for electrochemical measurement. The electrode discs were punched out of the electrode films with a diameter of 10 mm (0.785 cm^2) using a press punch (EL-CELL). Film thicknesses were measured inside the glovebox before cell assembly with a digital micrometer from HELIOS PREISSER. The lithium-ion cells contained an MXene electrode (pillared or nonpillared) as working electrode, followed by a fixed glass-ceramic separator so that only the thickness change of the working electrode was measured.

Circular punches lithium chips with a diameter of 11 mm as both counter and reference electrodes were placed on top of the separator. The investigated electrodes were compressed between the separator and a movable titanium plunger. The electrolyte, 1 M $LiPF_6$ salt in a mixture of ethylene carbonate and dimethyl carbonate (EC: DMC; 1:1 by volume, Sigma Aldrich) was filled by vacuum backfilling (approximately 0.5 mL). All electrochemical measurements were carried out at a climate chamber (Binder) with a constant temperature of +25±1 °C. Cyclic voltammetry (CV) measurements were carried out using a VMP3 multi-channel potentiostat/galvanostat from Bio-Logic.After a resting period and stabilization time of 72 h, cyclic voltammograms were recorded at 0.01 mV s^{-1} at voltages in the range of 0.1-2.5 V vs. Li^+/Li.

Ex-situ X-ray diffraction

For the ex-situ X-ray diffraction measurements, the MXene electrodes were cycled for two CV cycles and stopped in the de-lithiated state at 3.0 V vs. Li^+/Li. Cyclic voltammetry was carried out using a VMP3 multi-channel potentiostat/galvanostat from Bio-Logic. All electrochemical measurements were carried out in a climate chamber (Binder) with a constant temperature of +25±1 °C. All CV measurements were carried out with a scan rate of 0.1 mV s^{-1} in a potential window of 0.01-3.0 V vs. Li^+/Li. The cells were then transferred to an Ar-filled glovebox for disassembly. Prior to the XRD measurements, the electrodes were detached from the remaining parts and rinsed with DMC to remove remains of the salt of electrolyte. X-ray diffraction (XRD) measurements of the cycled electrodes were performed with a D8 Advance diffractometer (Bruker AXS) with a copper X-ray source (Cu-Kα (λ = 1.5406 Å), 40 kV, 40 mA). The samples were examined in the range 2θ, ranging from 3.50 ° to 79.02 ° and in steps of 0.02° 2θ.

S-5
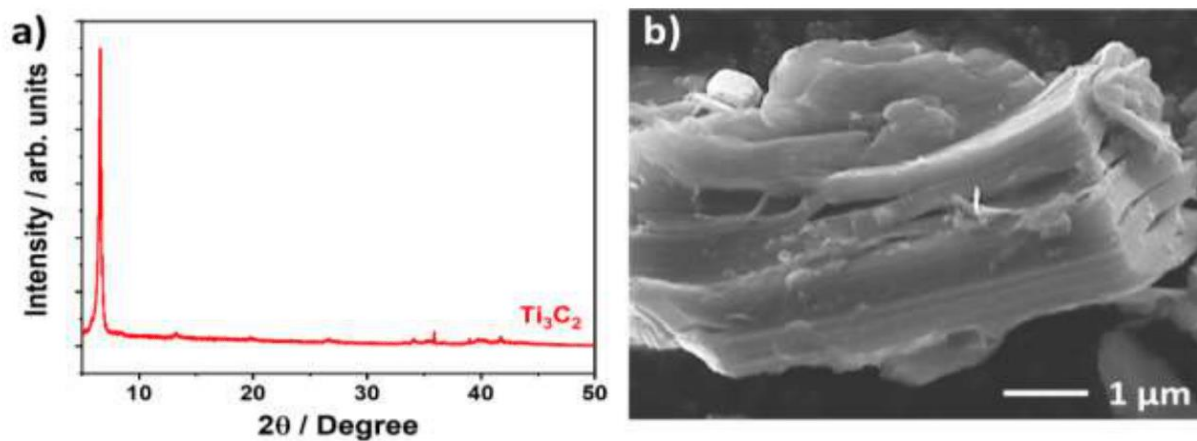
Figure S1. a) X-ray diffractogram of the as-synthesised nonpillared MXene. b) Scanning electron micrograph of the nonpillared MXene.
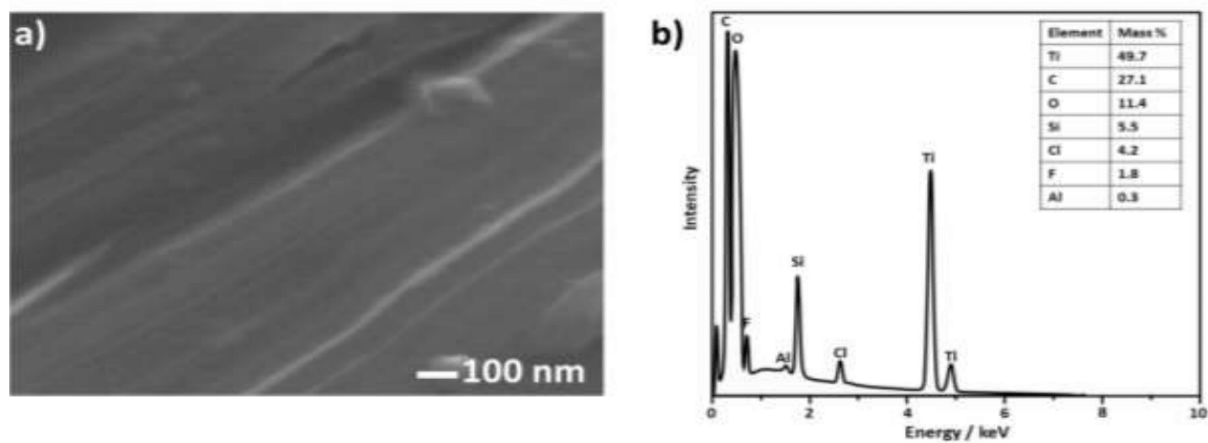
Figure S2. SEM-EDS analysis of the pillared MXene showing that the SiO_2 content is approximately 11 mass% in the pillared material. a) SEM of the analysed region. b) EDS spectrum.
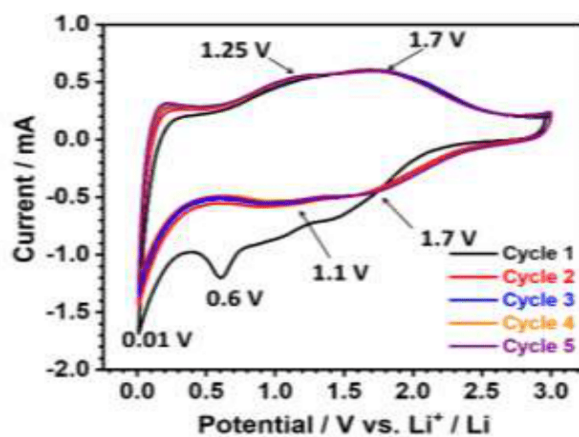
Figure S3. CV data from SiO$_2$-pillared Ti$_3$C$_2$T$_z$. Cells were run in a voltage window of 0.01-3 V vs. Li$^+$/Li using 1 M LiPF$_6$ in EC:DEC (1:1 mass ratio) as the electrolyte. First five cycles at a scan rate of 0.2 mV s^{-1}. The numbers and arrows highlight reaction peaks.
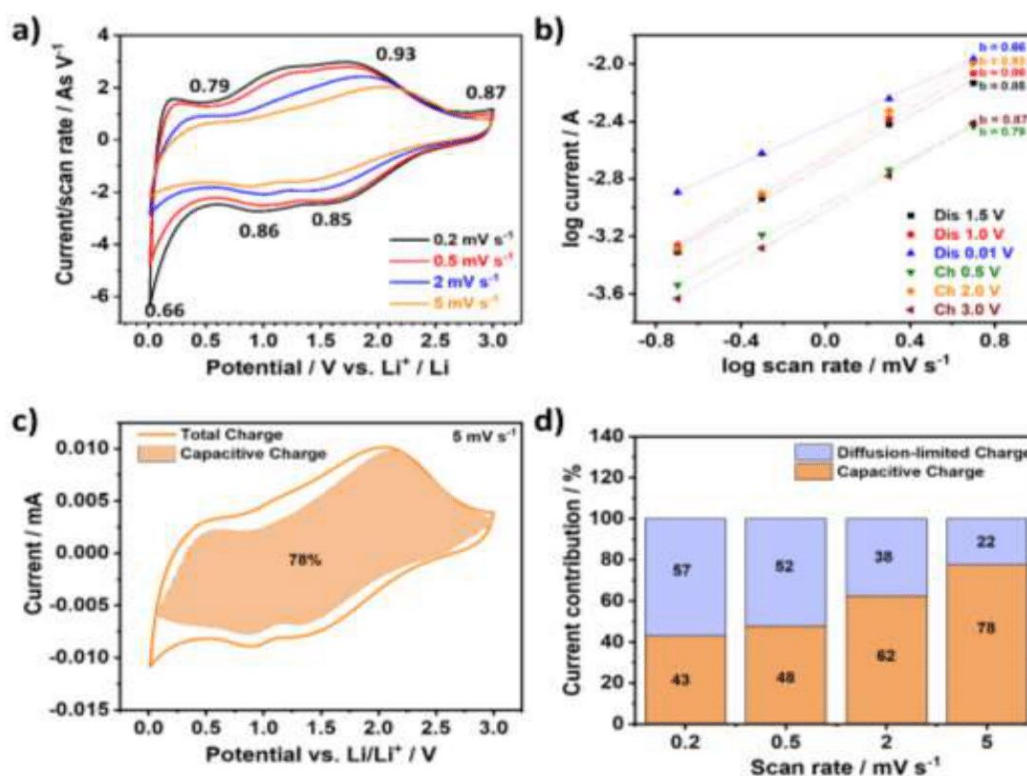
Figure S4. Capacitive contribution to charge storage from CV data for SiO_2-pillared $Ti_3C_2T_z$. Cells were run in a voltage window of 0.01-3 V vs. Li^+/Li using 1 M $LiPF_6$ in EC:DEC (1:1 mass ratio) as the electrolyte. **a)** Cyclic voltammograms when cycled at increasing rates of 0.2, 0.5, 2 and 5 mV s^{-1} in a voltage window of 0.01-3 V vs. Li^+/Li. Two cycles were carried out at each rate, with the second cycle being used for analysis. The numbers show *b*-value for the corresponding peak. **b)** Log current vs. log scan rate plots used to calculate each *b*-value shown in **a)**. R^2 values were greater than 0.999 in all cases, indicating a good fit. **c)** Cyclic voltammogram collected at a scan rate of 5 mV s^{-1} (10 min per sweep), with the capacitive contribution to the current shown by the dashed filled area. The total capacitive contribution to the charge storage at this rate was 78%, as shown by the label in the centre of the plot. **d)** Contribution of both diffusion-limited and capacitive current to the total charge storage at each scan rate: 0.2, 0.5, 2 and 5 mV s^{-1}.
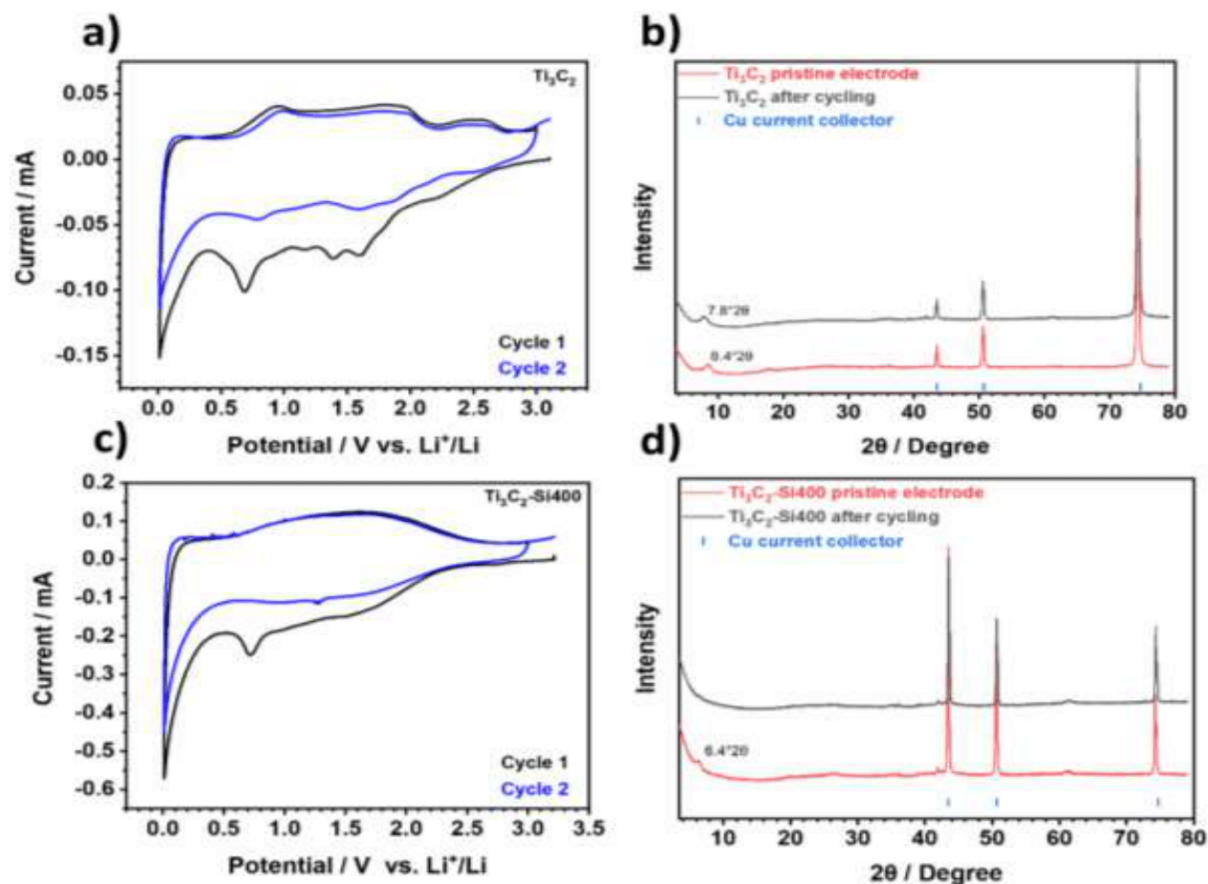
Figure S5. Cyclic voltammograms from half-cell setup at a scan rate of 0.1 mV s^{-1} in the voltage range from 0.01-3 V vs. Li$^+$/Li using 1 M LiPF$_6$ in EC:ED (1:1 mass ratio) as the electrolyte and corresponding post mortem XRD diffractograms. **a)** First and second cycle of cyclic voltammogram in PEEK cell for nonpillared Ti$_3$C$_2$T$_z$ **b)** Correlated post-mortem XRD measurements of cycled nonpillared Ti$_3$C$_2$T$_z$ electrode in comparison with the pristine electrode (both coated on copper foil) **c)** First and second cycle of cyclic voltammogram in PEEK cell for pillared MXene (Ti$_3$C$_2$-Si-400) **d)** Correlated post-mortem XRD measurements of cycled pillared MXene (Ti$_3$C$_2$-Si-400) electrode in comparison with the pristine electrode (both coated on copper foil).

References for the Supporting Information

1. Maughan, P. A. *et al.* Porous Silica-Pillared MXenes with Controllable Interlayer Distances for Long-Life Na-Ion Batteries. *Langmuir* **36**, 4370–4382 (2020).
2. Augustyn, V. *et al.* High-rate electrochemical energy storage through Li^+ intercalation pseudocapacitance. *Nat. Mater.* **12**, 518–522 (2013).
3. Wang, J., Polleux, J., Lim, J. & Dunn, B. Pseudocapacitive contributions to electrochemical energy storage in TiO_2 (anatase) nanoparticles. *J. Phys. Chem. C* **111**, 14925–14931 (2007).
4. Hahn, M., Barbieri, O., Gallay, R. & Kötz, R. A dilatometric study of the voltage limitation of carbonaceous electrodes in aprotic EDLC type electrolytes by charge-induced strain. *Carbon* **44**, 2523–2533 (2006).

4.3 Design of high-performance antimony/MXene hybrid electrodes for sodium-ion batteries

Stefanie Arnold,[1,2] Antonio Gentile,[3,4] Yunjie Li,[1,2] Qingsong Wang,[1,5]

Stefano Marchionna,[4] Riccardo Ruffo,[3,6*] and Volker Presser[1,2,7*]

[1] INM - Leibniz Institute for New Materials, Campus D2.2, 66123 Saarbrücken, Germany

[2] Department of Materials Science and Engineering, Saarland University, Campus D2.266123 Saarbrücken, Germany

[3] Dipartimento di Scienza dei Materiali, Università degli Studi di Milano Bicocca, Via Cozzi 55, 20125 Milano, Italy

[4] Ricerca sul Sistema Energetico- RSE S.p.A., Via R. Rubattino 54, 20134 Milano, Italy

[5] Institute of Nanotechnology, Karlsruhe Institute of Technology, Hermann-von-Helmholtz-Platz 1, 76344, Eggenstein-Leopoldshafen, Germany

[6] National Reference Center for Electrochemical Energy Storage (GISEL) - Consorzio Interuniversitario Nazionale per la Scienza e Tecnologia dei Materiali (INSTM), 50121 Firenze, Italy

[7] Saarene - Saarland Center for Energy Materials and Sustainability, Campus D4.2, 66123 Saarbrücken, Germany

Own Contribution:

Conceptualization, methodology, investigation, data curation, visualization, and writing – original draft.

Journal of Materials Chemistry A

PAPER

Design of high-performance antimony/MXene hybrid electrodes for sodium-ion batteries†

Stefanie Arnold, [ID] ab Antonio Gentile, [ID] cd Yunjie Li, [ID] ab Qingsong Wang, [ID] ae Stefano Marchionna, [ID] d Riccardo Ruffo [ID] *cf and Volker Presser [ID] *abg

Due to their versatile properties and excellent electrical conductivity, MXenes have become attractive materials for alkali metal-ion batteries. However, as the capacity is limited to lower values due to the intercalation mechanism, these materials can hardly keep up in the ever-fast-growing community of battery research. Antimony has a promisingly high theoretical sodiation capacity characterized by an alloying reaction. The main drawback of this type of battery material is related to the high volume changes during cycling, often leading to electrode cracking and pulverization, resulting in poor electrochemical performance. A synergistic effect of combing antimony and MXene can be expected to obtain an optimized electrochemical system to overcome capacity fading of antimony while taking advantage of MXene charge storage ability. In this work, variation of the synthesis parameters and material design strategy have been dedicated to achieving the optimized antimony/MXene hybrid electrodes for high-performance sodium-ion batteries. The optimized performance does not align with the highest amount of antimony, the smallest nanoparticles, or the largest interlayer distance of MXene but with the most homogeneous distribution of antimony and MXene while both components remain electrochemically addressable. As a result, the electrode with 40 mass% MXene, not previously expanded, etched with 5 mass% HF and 60% antimony synthesized on the surfaces of MXene emerged as the best electrode. We obtained a high reversible capacity of 450 mA h g^{-1} at 0.1 A g^{-1} with a capacity retention of around 96% after 100 cycles with this hybrid material. Besides the successful cycling stability, this material also exhibits high rate capability with a capacity of 365 mA h g^{-1} at 4 A g^{-1}. *In situ* XRD measurements and post mortem analysis were used to investigate the reaction mechanism.

1 Introduction

Their large energy density, high power density, and output voltage make lithium-ion batteries (LIBs) an essential

aINM – Leibniz Institute for New Materials, Campus D2.2, 66123 Saarbrücken, Germany. E-mail: volker.presser@leibniz-inm.de

bDepartment of Materials Science and Engineering, Saarland University, Campus D2.2, 66123 Saarbrücken, Germany

cDipartimento di Scienza dei Materiali, Università degli Studi di Milano Bicocca, Via Cozzi 55, 20125 Milano, Italy. E-mail: riccardo.ruffo@unimib.it

dRicerca sul Sistema Energetico-RSE S.p.A., Via R. Rubattino 54, 20134 Milano, Italy

eInstitute of Nanotechnology, Karlsruhe Institute of Technology, Hermann-von-Helmholtz-Platz 1, Eggenstein-Leopoldshafen, 76344, Germany

fNational Reference Center for Electrochemical Energy Storage (GISEL) – Consorzio Interuniversitario Nazionale per la Scienza e Tecnologia dei Materiali (INSTM), 50121 Firenze, Italy

gSaarene – Saarland Center for Energy Materials and Sustainability, Campus D4.2, 66123 Saarbrücken, Germany

† Electronic supplementary information (ESI) available: Supplementary X-ray diffraction patterns, supplementary scanning electron micrographs, particle size distribution of synthesized Sb particles, supplementary electrochemical characterization, and graphical illustration performance comparison of all obtained hybrid materials. See DOI: 10.1039/d2ta00542e

technology for electrochemical energy storage systems.[1] As a result of the increasing demand for batteries, scarcity of fossil resources of lithium, and the resulting rise in price, energy storage technologies beyond lithium are of high interest.[2,3] Sodium is one of the most abundant elements in the earth's crust. Thus, sodium-ion batteries (NIBs) offer cost-effective and sustainable energy storage compared to their LIB counterparts.[4] In recent years, extensive research efforts have been dedicated to NIB cathodes and anodes with high energy density, high power density, stable cycling performance, and good rate capability.[2,5,6] A particular challenge is the development of anodes that combine high capacity and long lifetime/high durability. Several studies focus on carbon-based materials as an alternative for graphite anodes, as they are used successfully in LIBs.[7,8] Hard carbon, the most widespread carbonaceous material in NIBs, can only achieve a capacity of up to 300 mA h g^{-1} because of pseudocapacitive Na$^+$-ion surface adsorption.[9–13] Other intercalation materials like Li$_4$Ti$_5$O$_{12}$,[14–16] TiO$_2$,[17] and Na$_2$Ti$_3$O$_7$ (ref. 18) are well known for their high structural stability, which enables high reversibility during sodiation and de-sodiation. Still, a major drawback is that the Na$^+$-ion intercalation enabled capacity is limited due to the

91

restricted number of storage sites.[19] This makes choosing high-capacity materials capable of forming sodium-rich intermetallic compounds through an alloying reaction extremely attractive, as demonstrated by extensive research on this topic published in the literature.[6,20–23] Sodium can form alloys with group 14 and 15 elements, such as Ge, Sn, Pb, P, and Sb. Intermetallic compounds such as $NaGe$,[24] $Na_{15}Sn_4$,[25] $Na_{15}Pb_4$,[26] Na_3P,[27] and Na_3Sb[28] are obtained which can realize a high sodium storage capacity. A major problem of alloying-based materials is the large volume change during sodiation and de-sodiation. This process causes possible aggregation, continuous reformation of the solid–electrolyte interphase (SEI), depletion of the electrolyte, and loss of the conductivity as well as slower kinetics which often leads to capacity fading.[20,21,29] This constitutes a major drawback since side reactions are constantly occurring during cycling, resulting in low Coulombic efficiency (CE). In addition, the inhomogeneous composition and thickness of the continuously restructured SEI can partly block charge transfer and cause typical rapid capacity fading.[30–34] With a high theoretical capacity of 660 mA h g^{-1}, a high specific capacity and the ease of availability of the material, antimony (Sb) represents a very common and promising anode material candidate for high energy NIBs.[1,35] Still, during the alloying reaction of antimony with sodium resulting in Na_3Sb compounds, this material suffers from high volume expansion ($\sim$300%) and contraction and slow reaction kinetics resulting in capacity fading and poor electrochemical performance.[20,35–37] Therefore, it is crucial to buffer the volume change sufficiently to mitigate pulverization and cracking of the electrode, while increasing the conductivity and improving the electrochemical performance.[21,38]

Besides the specific adaptations and variations of the binder and electrolytes, current work mainly presents two different approaches to counteract these problems. A promising path is to develop suitable carbon matrices, which act as a conductive additive and buffer the volume change occurring during sodiation and de-sodiation and provide additional diffusion pathways.[21,36,39–44] For example, Pfeifer et al. investigated the impact of carbon properties on antimony/carbon composite electrodes for NIBs by simple mechanical mixing only by considering the physical, chemical, and structural features of the carbon phase.[45] An alternative way is to develop suitable nanostructures/nanocomposites, which should improve the kinetics.[21] MXenes, a novel class of two-dimensional, inorganic layered transition metal carbides, nitrides, and carbonitrides, were discovered in 2011.[46] Among them, several MXenes are promising intercalation-type electrodes, for example, for LIBs and NIBs because of their distinctive physical and chemical properties.[47,48] Comparing 2D materials, MXenes stand out with their combined properties such as good electronic conductivity, hydrophilicity, and flexibility.[48,49] Furthermore, due to their low activation barrier for ion movement, they also represent an optimal candidate for NIBs.[50,51] Kajiyama et al. showed that the intercalation and deintercalation of the sodium-ions between $Ti_3C_2T_z$ sheets occur without any substantial structural change with a reversible capacity of around 100 mA h g^{-1} over 100 cycles at 0.02 A g^{-1}.[52] Gentile et al. showed different preparation routes of MXenes resulting in different structures,

compositions, properties, and morphologies and investigated their influence on the application of NIBs.[53] The optimized $Ti_3C_2T_z$ shows a capacity of 110 mA h g^{-1} at a specific current of 0.03 A g^{-1}.

Although MXene is an interesting electrode material, its intrinsic performance is commonly limited to the intercalation mechanism.[54] Accordingly, the resulting de-sodiation capacity is also limited to lower values than alloying or conversion type materials.[55] An attractive way to overcome this limitation is to combine MXene with other nanoparticles, either by forming nanocomposites or hybrids. This has been very successfully explored for different electrochemical applications, such as sensors,[56] photocatalysis,[57] and energy storage.[58] The list of nanomaterials used to enhance different types of MXenes is long and includes MnO_2,[59] MoS_2,[60] $NiCo_2S_4$,[61] NbS_2,[62] and TiO_2,[63] along with polymers (such as polyvinyl alcohol; ref. 64). Combining MXene and non-MXene materials extends to MXenes and alloying materials. Confining and synergizing materials like antimony with a high specific capacity and conductive MXene is promising to yield improved electrochemical performance and cycling stability. Combining the most common and best-explored MXene $Ti_3C_2T_z$ with antimony nanoparticles is expected to enhance the structural stability resulting in a long cycling life since there is a minimal volume change of the 2D nanomaterial during alkali metal transport. This includes NIBs[65] but also extends to other systems, such as potassium-ion batteries.[66,67] In addition, MXene nanosheets show excellent mechanical stability, compensating for significant volume changes during charging and discharging in nanomaterials like alloying materials during cycling.[68] This avoids or reduces agglomeration and the possible subsequent pulverization, which is also reflected in improved electrochemical behavior.

This work presents a guideline for designing an advanced hybrid antimony MXene compound for application in high-performance NIBs. We introduce two different routes for the hybrid material synthesis by variation of two different types of MXenes and compositions. In this way, different morphologies and compositions were obtained whose impact on the electrochemical performance in NIBs was studied. Finally, electrodes with an optimized synthesis protocol demonstrated stable and high-capacity electrochemical cycling stability and rate capability in NIBs.

2 Experimental

2.1 Materials synthesis

2.1.1 $Ti_3C_2T_z$ synthesis. The synthesis of the Ti_3AlC_2 MAX phase was done *via* spark plasma sintering and has been described in previous work.[53] In a typical synthesis, Ti/Al/TiC powders were mixed in an atomic ratio of 1/1/1.9 in a Turbula shaker (3D mixer TURBULA) for 24 h. The powders were rapidly heated to 1300 °C and pressed at 43 MPa between the pistons of the SPS for 5 min at an argon partial pressure of 300 mbar. The MAX phase disc produced was ground and sieved to obtain particles with a size below 50 μm.

10570 | J. Mater. Chem. A, 2022, 10, 10569–10585

This journal is © The Royal Society of Chemistry 2022

92

Two different $Ti_3C_2T_z$ MXenes were obtained in this work, referred to as MX_HF5 and MX_HF30. The synthesis of MX_HF5, treated with a 5 mass% solution of hydrofluoric acid (HF) proceeds as described below. In a polytetrafluoroethylene beaker, 2 g of Ti_3AlC_2 powder was stirred in 50 mL of 5 mass% HF in water for 24 h at room temperature. The powder was added slowly to the reaction solution within 2 min since the reaction between HF and the MAX phase leads to a strong evolution of H_2 in the solution. After 24 h, the solution was centrifuged for 15 min at 5000 rpm, and the subsequent precipitate was recovered from the supernatant, washed with MilliQ water, and centrifuged 5–6 times until the pH value of the solution was 6. The powder was finally dried under vacuum at 80 °C overnight.

For the synthesis of MX_HF30, treated with a 30 mass% hydrofluoric acid solution, the procedure is similar to the previous one, except for the treatment time. In a typical synthesis, 2 g of Ti_3AlC_2 powder was dispersed in 50 mL of 30 mass% HF in water under vigorous stirring at room temperature for 5 h. The hydrogen evolution is greater than the previous case, so the powder is added within 5 min. The washing and the drying procedure were the same as those of MX_HF5.

2.1.2 Antimony nanopowder synthesis. Antimony nanopowder synthesis was carried out using the protocol outlined in previous work[45,69] and the optimized synthesis route proposed in the literature.[93] To obtain high purity antimony, an excess of sodium borohydride ($NaBH_4$, 1.216 g, $\geq$98.0% purity, Sigma Aldrich) was suspended in 200 mL technical ethanol (>99.0% purity, Merck). Antimony chloride ($SbCl_3$, 2.244 g, $\geq$99.0% purity, Sigma Aldrich) was dissolved in 40 mL absolute ethanol (>99.9% purity, Sigma Aldrich). The $SbCl_3$ solution was added dropwise into the stirring solution of $NaBH_4$ in ethanol at room temperature using a syringe pump with a controlled dropping speed of 20 mL h^{-1}. The resultant black mixture was stirred for 1 h at room temperature and afterward sonicated for 10 min (P120H, Elmasonic). After sedimentation of the antimony particles, they were filtered under vacuum, and washed three times with ethanol and three times with deionized water. Antimony particles were dried in an oven at +80 °C for 4 h.

2.1.3 Synthesis of antimony–MXene hybrids. Two different routes were used to obtain the antimony MXene hybrids. In route A, the previously synthesized MXenes were first expanded. For successful expansion, 100 mg of $Ti_3C_2T_z$ (etched with 5 mass% HF or 30 mass% HF) was embedded in 40 mL of degassed Milli-Q water together with 4 mL of tetramethylammonium hydroxide (TMAOH, 1 M in water, Sigma Aldrich) over 12 h. The supernatant solution was decanted, and the solid was washed several times with Milli-Q water and centrifuged to remove the excess of TMAOH (each step of 30 min at 5000 rpm), which can be controlled by the change of the pH value (from 14 to 6). After the last washing step with water, the solvent was changed to ethanol and washed three times to eliminate the remaining water for subsequent synthesis of antimony. Then, 30 mL of ethanol was added to the powder, and the black suspension was treated in an ultrasonic bath (Emmi-40HC, EMAG) for 1 h. A specific amount of $NaBH_4$ (still the same

excess amount) was finally added with this reaction solution. The same synthesis process of antimony nanoparticles was performed equivalent to the process described above.

In synthesis route B, the synthesized 100 mg $Ti_3C_2T_z$ (etched with 5 mass% HF or 30 mass% HF) was soaked in a solution of $SbCl_3$ dissolved in 30 mL absolute ethanol for 12 h. To this suspension, a solution with an excess of $NaBH_4$ in 40 mL technical ethanol was dropped at a speed of 20 mL h^{-1} to reduce the Sb^{3+}-ions and form the elemental antimony particles.

2.2 Structural and chemical characterization

X-ray diffraction (XRD) measurements of the antimony hybrids were performed with three different systems. XRD-1: A D8 Advance diffractometer (Bruker AXS, Germany) with a copper X-ray source (Cu-K$_{\alpha}$, λ = 1.5406 Å, 40 kV, 40 mA). The samples were examined in the range of 3.5° to 80° 2θ and with 0.033 s per step. XRD-2: A D8 Discover diffractometer (Bruker AXS, Germany) with a copper X-ray source (Cu-K$_{\alpha}$, λ = 1.5406 Å, 40 kV, 40 mA), a Göbel mirror and a 1 mm point focus as optics. With a VANTEC-500 (Bruker AXS) two-dimensional X-ray detector positioned at 17° 2θ, 37° 2θ, 57° 2θ, and 97° 2θ with a measurement time of 1000 s per step, five frames were recorded. The third system (XRD-3) is outlined in Section 2.4.2. Unless noted, all presented XRD patterns are related to measurements that were carried out by using XRD-1.

The sample morphology was characterized with a field emission scanning electron microscope using a Zeiss Gemini 500 instrument (Carl Zeiss) at an acceleration voltage of 1 kV. The samples were fixed on a steel sample holder by using copper adhesive tape and analyzed without the aid of an additional, conductive sputter coating.

Transmission electron microscopy and selected area electron diffraction investigations were carried out using a JEOL 2011 instrument operated at 200 kV. The sample was dispersed in ethanol through sonication for 5 min and drop-casted onto a copper grid with a lacy carbon film.

2.3 Electrode materials and preparation

Pure MXene working electrodes were obtained with a ratio of 90 mass% MXene, and 10 mass% carboxymethyl cellulose (CMC, degree of substitution = 0.7, molecular weight = 250 000 g mol^{-1}, Sigma Aldrich) dissolved in water and ethanol (1 : 1 mass ratio) following the subsequently described mixing steps. The Sb@ $Ti_3C_2T_z$/C electrodes were manufactured by mixing an active material of 80 mass% of the different synthesized antimony MXene hybrids (Sb@A_MX_HF5(6 : 4), Sb@A_MX_HF5(7 : 3), Sb@B_MX_HF5(6 : 4), Sb@B_MX_HF5(7 : 3), Sb@A_MX_HF30(6 : 4), Sb@A_MX_HF30(7 : 3), Sb@B_MX_HF30(6 : 4), and Sb@B_MX_HF30(7 : 3)) with 10 mass% conductive carbon additive (C-NERGY SUPER C65 conductive carbon black, Imerys Graphite & Carbon) and 10 mass% CMC as the binder from a 3 mass% aqueous solution according to the mixing steps described below.

First, the active material and carbon were mixed and carefully dry ground in a mortar. Afterward, the dry powder mixture was dry-mixed at 1000 rpm for 5 min in a SpeedMixer DAC 150

This journal is © The Royal Society of Chemistry 2022

J. Mater. Chem. A, 2022, **10**, 10569–10585 | **10571**

93

SP from Hauschild. Ethanol (99.0% purity, Merck) was added dropwise to the mixture until the slurry achieved suitable viscosity. This paste was again mixed at 1500 rpm for 5 min followed by 2500 rpm for 5 min. Finally, the CMC binder solution (3 mass% CMC in Milli-Q-water) was added, and the viscous electrode paste kept mixing at 800 rpm for 10 min. The suspension was stirred for 12 hours with a magnetic stirrer to obtain a homogeneous slurry. The subsequently obtained slurries were doctor-bladed on aluminum foil (thickness of 15 μm, Ranafoil, Toyo Aluminium), and used as a current collector, with a wet thickness of 200 μm. The electrode coatings were initially dried under ambient conditions overnight. Then, an extra vacuum drying step was conducted at +110 °C for 12 h to remove the remaining solvent. The packing density of the electrode was adjusted by dry-pressing within a rolling machine (HR01 hot rolling machine, MTI), and discs of 12 mm diameter (1.131 cm^2) were punched from the electrode sheet using a press-punch (EL-CELL) and applied as the working electrode.

For comparison to the hybrid active material, simple mechanical mixing (MM) of the active antimony material, MXene, conductive carbon, and the binder solution was conducted in analogy to the procedure reported for the hybrid Sb@MXene. These samples were prepared to recreate the composition of the related hybrid materials and are referred to as Sb + MX_HF5(6 : 4)_MM and Sb + MX_HF5(7 : 3)_MM. The ensuing electrode thickness of the dried electrodes was typically 25–35 μm with a material loading of 3.8 ± 0.5 mg cm^{-2}.

2.4 Cell preparation and electrochemical characterization

2.4.1 Electrochemical half-cells. Custom-built polyether ether ketone (PEEK) cells with spring-loaded titanium pistons were used for electrochemical testing in a non-aqueous electrolyte.[70] The cells were arranged in a three-electrode configuration for electrochemical measurements. The electrode discs were punched out of the electrode films with a diameter of 12 mm. In NIBs, sodium metal is conventionally used as the counter and the reference electrode.

All used cell parts were dried overnight at +120 °C and introduced into an argon-filled glovebox (MBraun Labmaster 130, O$_2$ < 0.1 ppm, H$_2$O < 0.1 ppm). Initially, the punched working electrode with a diameter of 12 mm was placed in the cell, followed by a 13 mm diameter vacuum dried compressed glass-fiber separator (GF/D, Whatman). The counter electrode was punched into circular plates with a diameter of 10 mm and placed on the separator. Before using metallic sodium, the oxidized surface was polished to obtain a smooth surface to avoid non-uniformity and impurities. The counter electrodes were pressed to a uniform thickness of approximately 1 mm. A copper foil current collector was placed on the backside of each counter electrode. The sodium reference electrode was placed on a compressed glass-fiber separator (GF/D, Whatman) with a diameter of 2 mm in a cavity close to the working electrode/counter electrode stack and brought into contact with a titanium wire. The electrolyte was vacuum backfilled with a syringe into the cells.

The preparation and handling of the electrolyte solvent and salt were conducted in an argon-filled glovebox. A 1 M sodium perchlorate (NaClO$_4$, >99% purity, Alfa Aesar) solution in a solvent mixture of ethylene carbonate (EC, ≥99% purity, Sigma Aldrich) and dimethyl carbonate (DMC, ≥99% purity, Sigma Aldrich) in a 1 : 1 mass ratio with the addition of 5 mass% fluoroethylene carbonate (FEC, 99% purity, Sigma Aldrich) was used as the electrolyte. FEC is commonly used as a NIB additive that improves the stability of the SEI, modifying the composition of the SEI layer and preventing the decomposition of EC and DMC.[71–75] The sodium salt for the electrolyte was dried under vacuum at +80 °C for 48 h before use.

Galvanostatic cycling with potential limitation, cyclic voltammetry, and rate performance measurements were carried out using a VMP3 multi-channel potentiostat/galvanostat (Bio-Logic) equipped with the EC-Lab software. All electrochemical measurements were carried out in a climate chamber (Binder) at a constant temperature of +25 ± 1 °C. Cyclic voltammetry was carried out with a scan rate of 0.1 mV s^{-1} in a potential window of 0.1–2.0 V *vs.* Na$^+$/Na. The galvanostatic charge/discharge cycles were performed in the voltage range of 0.1–2.0 V *vs.* Na$^+$/Na. For all long cycling tests in this work, a specific current of 0.1 A g^{-1} was used. The cycling of the cells was stopped after 100 cycles in the de-sodiated state to conduct post mortem XRD and SEM analysis. Rate performance measurements were conducted at different currents to get more information about the half-cell rate capability and stability at higher currents. The applied specific currents were 0.1 A g^{-1}, 0.2 A g^{-1}, 0.5 A g^{-1}, 1.0 A g^{-1}, 2.0 A g^{-1}, 4.0 A g^{-1}, 8.0 A g^{-1}, and (again) 0.1 A g^{-1}. All obtained values for the capacity in Sb/MXene *vs.* sodium cells are related to the respective active mass (*i.e.*, the total mass of the antimony–Ti$_3$C$_2$T$_z$ hybrid).

2.4.2 *In situ* XRD measurements. A customized coin cell of the type CR2032 with a Kapton window of ∅ 4 mm on each side was used for carrying out *in situ* XRD measurements on a STOE Stadi P diffractometer equipped with a Ga-jet X-ray source (Ga-K$_\beta$ radiation, λ = 1.20793 Å; XRD-3). To ensure the sufficient XRD diffraction signal, the electrodes used here had an areal loading of 4.6 mg cm^{-2} active material, which is higher than that used for the electrochemical testing. In addition, the electrode slurry was cast on top of a carbon paper to avoid the sharp reflections of the aluminum current collector to overlay relevant reflections of the Sb alloying reaction. Apart from that, assembling the cells was compliant with the procedure already presented in detail above. The XRD patterns were collected in the transmission mode in the 2θ range from 6° to 70° with a counting time of around 105 min. Galvanostatic cycling with a specific current of 0.1 A g^{-1} was performed with a potentiostat/galvanostat (SP 150, BioLogic) at the cut-off voltages of 0.1 V and 2.0 V *vs.* Na$^+$/Na.

3 Results and discussion

3.1 Material characterization

The main process of synthesizing the antimony hybrid material is illustrated in Fig. 1. Thereby antimony hybrids were prepared by two different routes. In route A, the synthesized MXenes

10572 | *J. Mater. Chem. A*, 2022, **10**, 10569–10585

This journal is © The Royal Society of Chemistry 2022

94
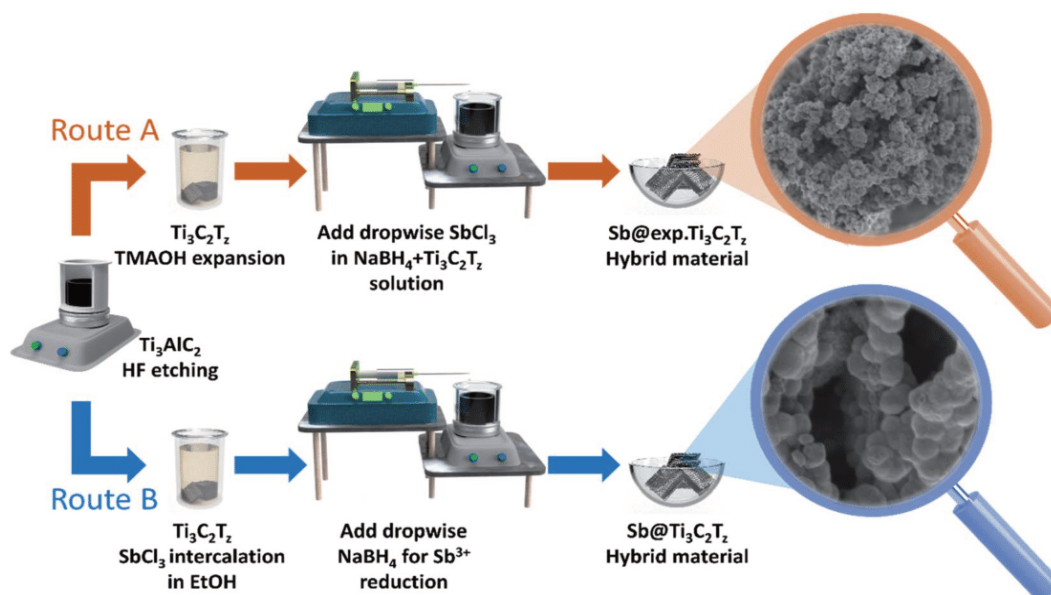
Fig. 1 Schematic illustration of the different synthesis routes of the antimony/MXene hybrids. Route A represents a previous expansion of the MXene layers before synthesizing the antimony/MXene hybrids while route B depicts intercalation of SbCl₃ in the MXene before subsequent antimony/MXene hybrid synthesis.

(etched with 5 mass% or 30 mass% hydrofluoric acid (HF)) were first expanded with the use of tetramethylammonium hydroxide (TMAOH) as the intercalant. In route B, the not-expanded MXene (etched with 5 mass% or 30 mass% HF) was soaked in the reaction solution of SbCl₃ in ethanol to possibly anchor the Sb³⁺ cations already on the surface and between the layers. In both cases, a co-precipitation method of synthesizing the antimony nanoparticle at the MXene is followed to obtain the antimony MXene hybrids. In this way, two hybrids with different compositions (Sb : Ti₃C₂Tz 70% : 30% and 60% : 40% by mass) were prepared for each type of MXene and each route, respectively.

All hybrids, the synthesized MXenes, and the expanded MXenes were characterized by X-ray diffraction (Fig. 2). The pure MXene phases (MX_HF5 and MX_HF30) each show well-defined diffraction peaks for the (002), (004), and (006) reflections which are indicative of the stacking sequence along the c-axis and the (110) distinct reflection, which characterizes the Ti–C order. The XRD pattern in Fig. 2A after expansion (A_MX_HF5) shows a strong (002) peak at 6.00° 2θ, compared to the initial value of (002)-Ti₃C₂Tz at 8.67° 2θ. The same observation can be made by looking at Fig. 2B where the (002) peak in pristine MXene (etched with 30 mass% HF) is found at 8.95° 2θ and undergoes a backshift to 5.89° 2θ after performing expansion/exfoliation (A_MX_HF30). This backshift of the (002) reflection is characterized by a significant increase in d-spacing along the c-axis, which corresponds to an increased value of 45% for the MXene etched with 5 mass% HF (MX_HF5) to the expanded MXene (A_MX_HF5) and a value of 51% for the MXene etched with 30 mass% HF (MX_HF30) to the expanded MXene (A_MX_HF30).

The XRD patterns of all hybrids where the MXene was etched with 5 mass% HF as reported in Fig. 2A and ESI, Fig. S1† show the

characteristic peaks of elemental antimony with the space group $R\bar{3}m$ (PDF: 00-035-0732). This indicates that the antimony particles were successfully synthesized. In the two hybrids where no prior expansion/exfoliation took place (Sb@B_MX_HF5(7 : 3) and Sb@B_MX_HF5(6 : 4)), the antimony reflections show a significantly higher intensity than the hybrids where MXenes were previously expanded using TMAOH (Sb@A_MX_HF5(7 : 3) and Sb@A_MX_HF5(6 : 4)). This may align with the facile distribution of antimony nanoparticles between the MXene layers when the interlayers were expanded by partial exfoliation beforehand. The shielding of Sb nanoparticles by the MXene layers and the lower dimensional level of the crystallographic coherence domains also decreases the corresponding signal detectable via X-ray diffraction. Comparing the MXene reflections, the reflections of the two compounds obtained by route B (Sb@B_MX_HF5(7 : 3) and Sb@B_MX_HF5(6 : 4)) show significantly less intensity than their counterparts obtained by the previous expansion of the MXene layers (Sb@A_MX_HF5(7 : 3) and Sb@A_MX_HF5(6 : 4)).

The low-intensity (002) reflections are shifted towards smaller scattering angles compared to the reflections of the bulk Ti₃C₂Tz. The samples Sb@B_MX_HF5(7 : 3) and Sb@B_MX_HF5(6 : 4) demonstrate that even without prior expansion of the MXene layers with TMAOH, there is a clear shift of bulk (002)-Ti₃C₂Tz from 8.67° 2θ to 6.83° 2θ and 6.72° 2θ, respectively. This is caused by the expansion of the MXene interlayer distance due to the Sb³⁺ intercalation. This can also be explained by the different reaction routes. Due to the previous expansion (route A), some antimony particles will enter between the layers of the MXene, and a large part of the surface of the MXene remains free, which can be well detected in the XRD pattern. In contrast, reaction route B yields antimony particles on the surface of the MXene. The latter forms

This journal is © The Royal Society of Chemistry 2022

J. Mater. Chem. A, 2022, **10**, 10569–10585 | **10573**

95
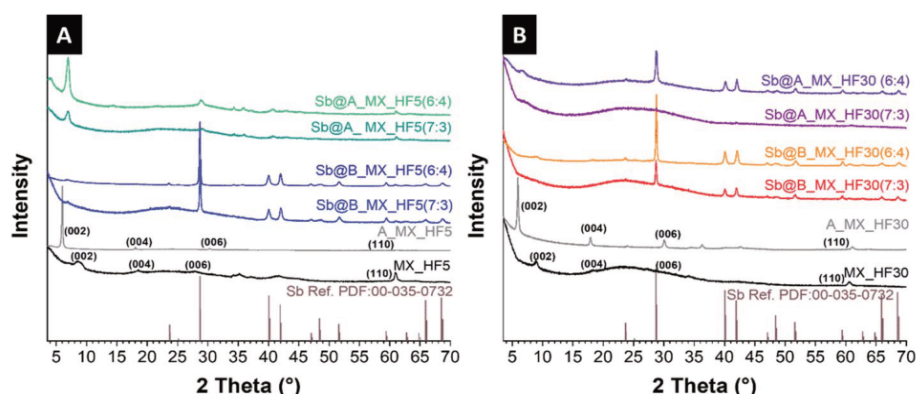
Fig. 2 X-ray diffractograms using Cu-Kα radiation for different compositions of the as-synthesized antimony MXene hybrid materials (A) with MXene etched with 5 mass% HF (B) with MXene etched with 30 mass% HF.

a layer around the MXene particles, which makes the Sb reflections more pronounced in the pattern.

For the antimony hybrid material synthesized based on MXene etched with 30 mass% HF (Fig. 2B), the observations agree with those for 5 mass% HF MXene. Only the reflection pattern of the hybrid with 40% expanded MXene, and 60% antimony (Sb@A_MX_30(6 : 4)) is conspicuous in which it shows pronounced reflections for the antimony particles compared to the compounds synthesized in the same way. A different morphology can explain this phenomenon compared to synthesis route B, where larger antimony particles are produced. The larger antimony particles which cannot be intercalated into the interlayers are therefore present in the hybrid. Generally, no TiO_2 reflections were detected, suggesting that the MXene layers are not oxidized or only limited MXene flakes are oxidized during the synthesis process but beyond the detection limit of XRD characterization.

The electron micrographs shown in Fig. 3 complement the findings gained from the X-ray diffractograms. While the bulk $Ti_3C_2T_z$ (5 mass% HF) presents the morphology of relative compact layers, the resulting antimony hybrid with 60% antimony shows that the $Ti_3C_2T_z$ particles are covered with partially agglomerated nanoparticles of antimony with a primary size of about 150–250 nm. A particle size distribution graph of the obtained antimony particles in different synthesis routes derived from SEM micrographs are provided in ESI, Fig. S2.† The remarkable difference in the two particle sizes and especially the agglomerated Sb nanoparticles of synthesis route B may be due to possible electrostatic adsorption of the Sb^{3+}-ions on the MXene layers.[65] Partially, the antimony particles are also located between the layers of the MXene. After the expansion of the bulk $Ti_3C_2T_z$ using TMAOH, the MXene layers look expanded and much thinner, and the particles look much smaller (Fig. 3C). Following synthesis route A, antimony particles were also synthesized on the surface of the MXene layers. In this route, significantly smaller primary particle sizes of 20–50 nm are formed, creating agglomerates. In addition, due to the smaller particle size, antimony particles and the formed agglomerates can diffuse into the expanded MXene layers.

Synthesis conditions can also explain these observations since in synthesis route A $NaBH_4$ was first added to the MXene suspension; therefore, the sodium-ions can be electrostatically adsorbed on the surface of the MXene.[76,77] Due to this, the remaining free areas on the surface are limited for Sb^{3+} adsorption, whereby these are diffused more efficiently between the layers. The differences in the particle size of the antimony particles can also be explained by the predominant concentration of antimony ions on the surface, which is significantly larger in route B, allowing seed crystals to form and fuse more easily into large particles and remain so after reduction. Under both conditions, we observe a well-developed homogeneity. Comparing the latter hybrids with $Ti_3C_2T_z$ etched with 30 mass% HF, similar conclusions are drawn except that this bulk MXene has a much more open structure from the beginning, which does not affect the antimony synthesis. Additional scanning electron micrographs of the different compositions are provided in ESI, Fig. S3–S6.†

Fig. 4 displays the results obtained by transmission electron microscopy, which verify the SEM findings. The synthesis route with the previous expansion of the MXene layers enables significantly smaller antimony particles in-between the expanded MXene. In contrast, in the synthesis route without prior expansion of the MXene layers, significantly larger particles are obtained, which adhere mainly agglomerates to the surface of the MXene particles. Specifically, antimony is mostly located between the MXene layers (Sb@A_MX_HF5(6 : 4)) which explains less pronounced reflections of elemental antimony in the X-ray diffractograms. The reflection planes of selected-area electron diffractograms (Fig. 4E and F) confirm the results obtained from XRD, with the clear evidence of elemental antimony with the space group $R\bar{3}m$ in Sb@A_MX_HF5(6 : 4) (Fig. 4E) and Sb@B_MX_HF5(6 : 4) (Fig. 4F).

3.2 Electrochemical characterization

To characterize the electrochemical performance of the Sb@$Ti_3C_2T_z$ hybrids as anodes for sodium-ion batteries, cyclic voltammetry profiles in the initial ten cycles were investigated at

10574 | J. Mater. Chem. A, 2022, 10, 10569–10585

This journal is © The Royal Society of Chemistry 2022

96
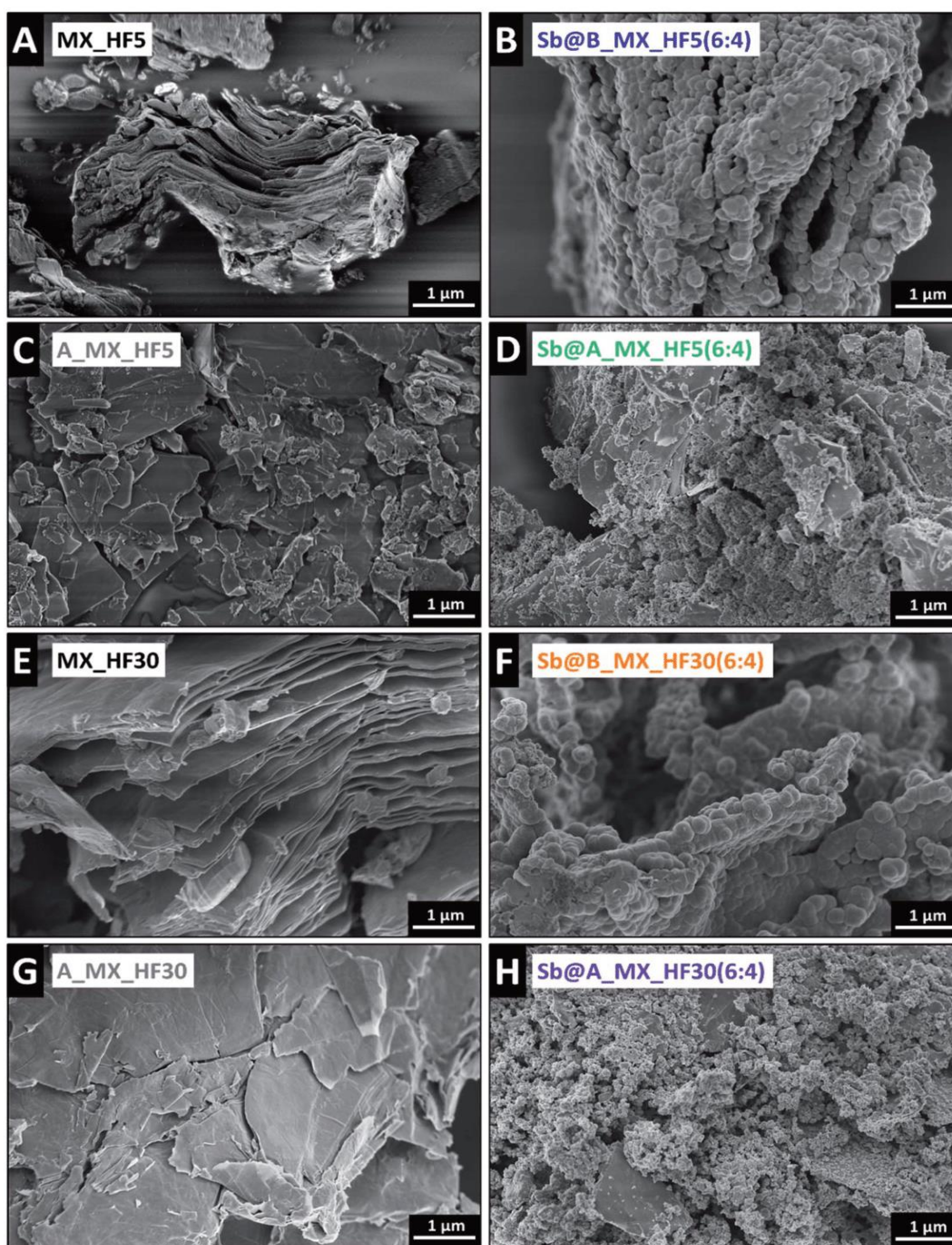
Fig. 3 Scanning electron micrograph of (A) as-synthesized $Ti_3C_2T_z$ etched with 5 mass% HF, (B) $Ti_3C_2T_z$ (5 mass% HF) hybrid with 60 mass% antimony, (C) TMAOH expanded $Ti_3C_2T_z$_HF5, (D) $Ti_3C_2T_z$_HF5 hybrid with 60 mass% antimony, (E) as-synthesized $Ti_3C_2T_z$ etched with 30 mass% HF, (F) $Ti_3C_2T_z$ (30 mass% HF) hybrid with 60 mass% antimony, (G) TMAOH expanded $Ti_3C_2T_z$_HF30 and (H) $Ti_3C_2T_z$_HF30 hybrid with 60 mass% antimony.

a scan rate of 0.1 mV s^{-1} between 0.1 V and 2.0 V *vs.* Na$^+$/Na and can be found in detail in ESI, Fig. S7.†

The third cycles of each of the eight antimony $Ti_3C_2T_z$ hybrid materials are shown comparatively in Fig. 5. After SEI formation, the typical peaks for the alloying reaction of antimony with

sodium occur mainly for all hybrids. Thus, the reduction peaks at around 0.7 V and 0.55 V (and 0.45 V) *vs.* Na$^+$/Na characterize the multistep transformation of antimony into hexagonal Na$_3$Sb. The complete reaction proceeds from elemental antimony to the formation of an amorphous Na$_x$Sb compound from
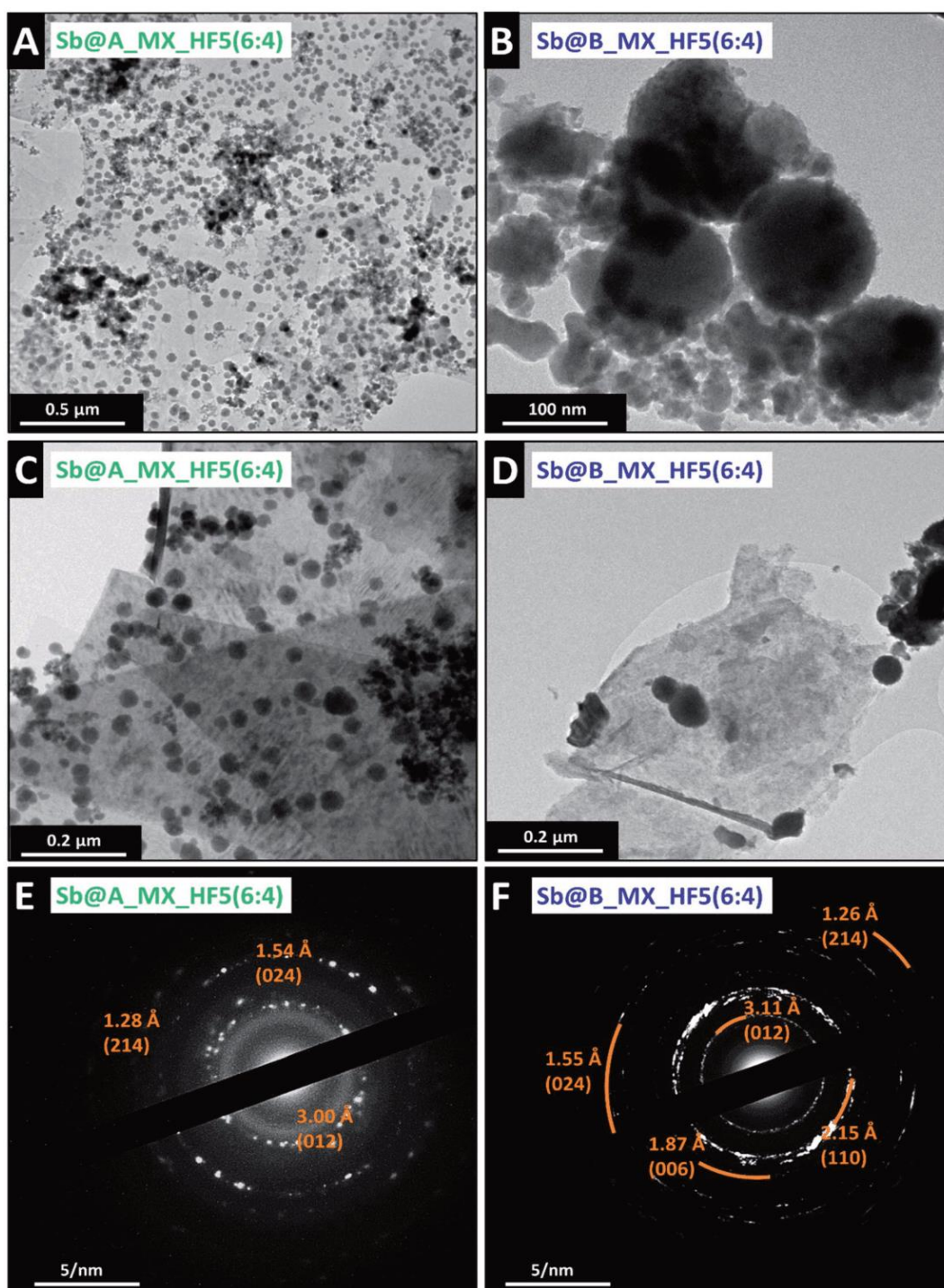
Fig. 4 Transmission electron micrographs of (A and C) TMAOH expanded $Ti_3C_2T_z$ (5 mass% HF) hybrid with 60 mass% antimony and (B and D) bulk $Ti_3C_2T_z$ (5 mass% HF) hybrid with 60 mass% antimony. Selected-area electron diffraction of (E) TMAOH expanded $Ti_3C_2T_z$ (5 mass% HF) hybrid with 60 mass% antimony, and (F) bulk $Ti_3C_2T_z$ (5 mass% HF) hybrid with 60 mass% antimony.

which NaSb is finally reacting further with sodium to crystalline Na_3Sb.[35,78] The oxidation peak in the subsequent de-sodiation scan at a potential of around 0.8 V *vs.* Na^+/Na characterizes the de-sodiation reaction of the Na_xSb alloy back to amorphous elemental antimony. Looking more closely at the performance of the hybrids with the MXene etched with 5 mass% HF, it is noticeable that in the hybrids synthesized in route A, the intensities of the oxidation and the reduction peaks are
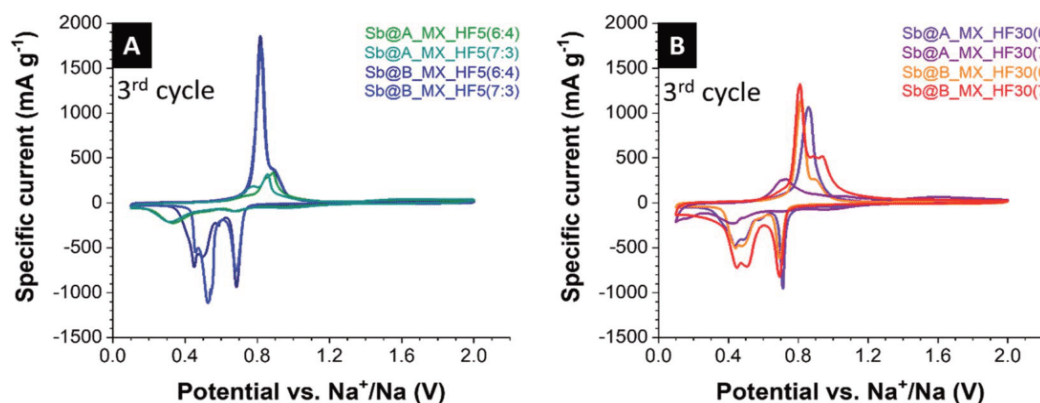
Fig. 5 Electrochemical characterization of the antimony MXene hybrids showing the 3rd cycles of the cyclic voltammograms at a scan rate of 0.1 mV s^{-1} in a potential range from 0.1 V to 2.0 V vs. Na$^+$/Na: (A) hybrids based on MX_HF5% (Sb@A_MX_HF5(6 : 4) and Sb@A_MX_HF5(7 : 3), and Sb@B_MX_HF5(6 : 4) and Sb@B_MX_HF5(7 : 3)). (B) Hybrids based on MX_HF30% (Sb@A_MX_HF30(6 : 4) and Sb@A_MX_HF30(7 : 3), and Sb@B_MX_HF30(6 : 4) and Sb@B_MX_HF30(7 : 3)).

significantly lower. In addition, the reduction and oxidation peaks are shifted to lower and higher potentials, respectively. This indicates that comparatively more antimony is electrochemically active and addressable in the hybrids in which the Sb^{3+}-ions have been previously intercalated (route B). This is consistent with the observations from the material characterization. The shift of the peaks probably indicates that the charge transfer process is more difficult for the samples with previously expanded MXene layers and intercalated antimony nanoparticles.[79]

Hybrids with MXene etched with 30 mass% HF still show the three reduction peaks and one oxidation peak. HF30 hybrids with 60% antimony show similar intensities of the peaks, whereas both HF30 hybrids with 70% antimony show significantly less of this signal. In contrast to Sb@B_MX_HF30(6 : 4), the oxidation peak of Sb@A_MX_HF30(6 : 4) is shifted towards a higher potential and has no shoulder. The oxidation peak of Sb@B_MX_HF30(7 : 3) has a very broad shoulder at a lower intensity of the main peak, and the peak at Sb@A_MX_HF30(7 : 3) is much broader and shifted towards smaller potential. The first reduction peak at 0.7 V vs. Na$^+$/Na is overlapping in three of the hybrid materials, whereas in the hybrid with expanded MXene and 70% antimony, the peak is very weak or not pronounced at all. In general, the redox peaks obtained for the hybrid with MXene etched with 30 mass% HF are broadened, indicating poorer kinetics due to the poorly conductive path of the large particles. There are also broadened peaks for the samples with non-expanded MXene, attributed to larger particle sizes. The same can be said for the subsequent reduction peaks at 0.55 V and 0.45 V vs. Na$^+$/Na. The cyclic voltammograms of pure Ti$_3$C$_2$-T$_z$_HF5 and Ti$_3$C$_2$T$_z$_HF30 anodes show a more pseudorectangular shape without obvious sodiation and de-sodiation peaks (ESI, Fig. S7 and S8†).[80]

The obtained reduction and oxidation peaks from cyclic voltammetry agree with the galvanostatic discharge and charge profiles tested at different specific currents in a voltage range between 0.1 and 2.0 V vs. Na$^+$/Na as shown in Fig. 6A and B.

Sb@A_MX_HF5(6 : 4) and Sb@B_MX_HF5(6 : 4) show different plateaus corresponding to the redox reactions associated with sodium alloying/de-alloying. This multistage process is visible for all electrodes and results in the formation of three pronounced plateaus which are consistent for antimony with observations in previous studies.[35,78] The initial sodiation curve of the Sb@B_MX_HF5(6 : 4) material (Fig. 6B) exhibits a long plateau at 0.5 V vs. Na$^+$/Na, which can, besides the alloying products, be assigned to the formation of SEI films on the electrode.[78] In contrast, the electrode with Sb@A_MX_HF5(6 : 4) (Fig. 6A) shows significantly more plateaus in the first cycle. This may indicate a different SEI formation process or the possibility of side reactions that may take place due to trace impurities from the expansion process using TMAOH. During the following cycles at higher specific currents, both compounds continuously show the plateaus reflecting the alloying reaction from crystalline antimony to amorphous Na$_x$Sb, then to cubic and hexagonal Na$_3$Sb mixtures and finally resulting in hexagonal Na$_3$Sb.[35]

The most significant difference between the two hybrids obtained with different synthesis routes is the potential drift of the galvanostatic curves. While the profiles of Sb@A_MX_HF5(6 : 4) have similar shapes during cycling, the charge plateaus of Sb@B_MX_HF5(6 : 4) shift clearly in the lower capacity direction while the discharge curve plateaus remain almost constant. This may indicate increasing overvoltage in the cell, but the capacity values seem to be unaffected. An explanation for the occurrence of this phenomenon can be, for example, the sluggish kinetics, inhomogeneities in the electrode, and undesirable side reactions for a change in the reaction mechanism, as shown by previous work on alloying electrodes.[1,20,69,81,82] Supplementary and detailed illustrations of the galvanostatic discharge and charge profiles of other hybrid materials synthesized in this work are presented in ESI, Fig. S9.†

The rate handling capability of the different antimony MXene hybrids was tested by galvanostatic charge/discharge with potential limitation, applying specific currents between

This journal is © The Royal Society of Chemistry 2022

J. Mater. Chem. A, 2022, 10, 10569–10585 | 10577

99

RESULTS AND DISCUSSION
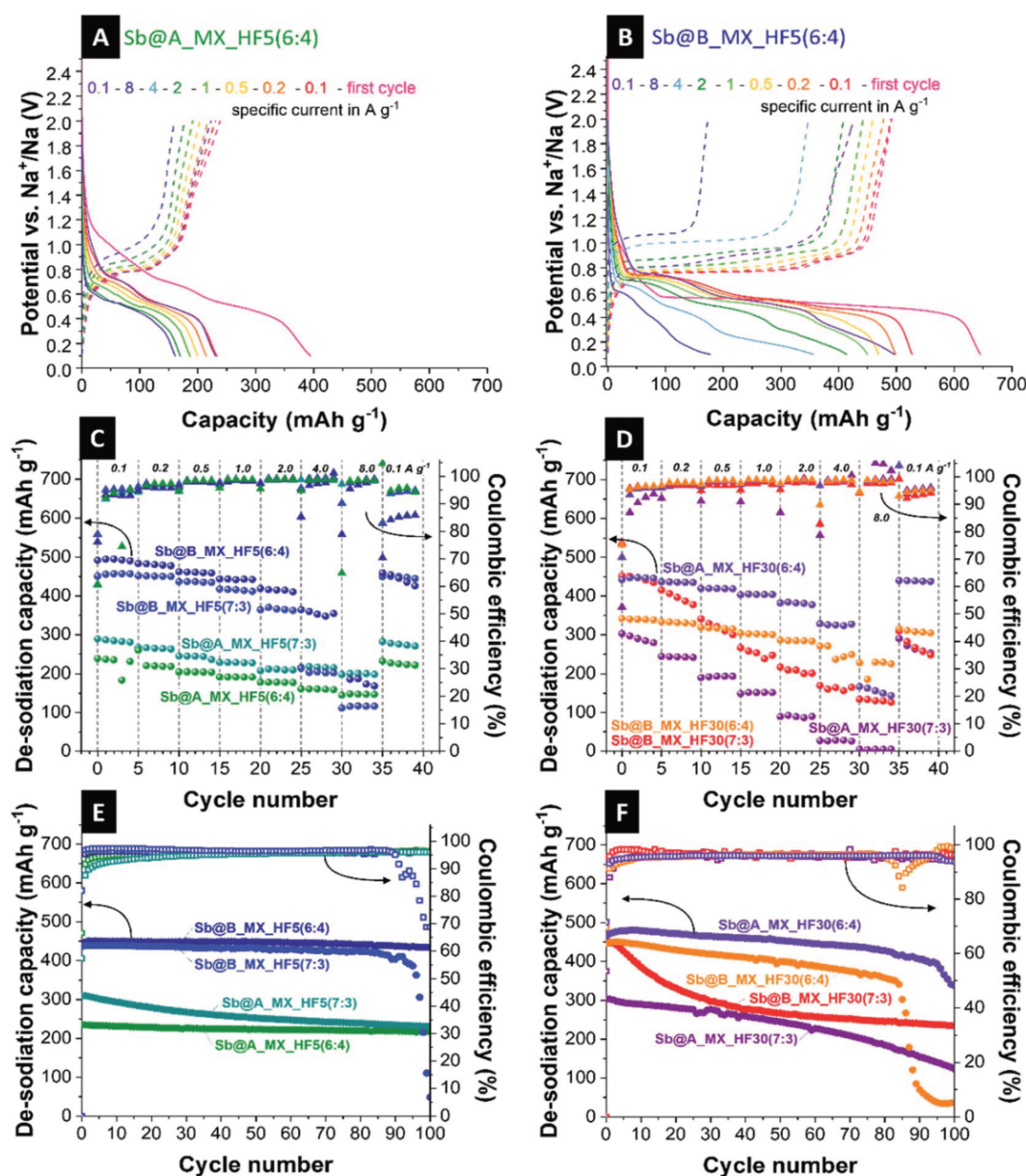
Fig. 6 Electrochemical performance of the antimony MXene hybrid electrodes. (A and B) Galvanostatic charge and discharge profiles at different applied specific currents of 0.1–8 A g^{-1} between 0.1 V and 2.0 V vs. Na$^+$/Na for (A) Sb@A_MX_HF5(6 : 4), and (B) Sb@B_MX_HF5(6 : 4). (C and D) Rate performance using galvanostatic charge/discharge cycling with the corresponding Coulombic efficiency values at different values for the specific current for (C) hybrids based on MX_HF5% (Sb@A_MX_HF5(6 : 4) and Sb@A_MX_HF5(7 : 3), and Sb@B_MX_HF5(6 : 4) and Sb@B_MX_HF5(7 : 3)), and (D) hybrids based on MX_HF30% (Sb@A_MX_HF30(6 : 4) and Sb@A_MX_HF30(7 : 3), and Sb@B_MX_HF30(6 : 4) and Sb@B_MX_HF30(7 : 3)). (E and F) Galvanostatic charge/discharge cycling stability at 0.1 A g^{-1} for (E) hybrids based on MX_HF5% (Sb@A_MX_HF5(6 : 4) and Sb@A_MX_HF5(7 : 3), and Sb@B_MX_HF5(6 : 4) and Sb@B_MX_HF5(7 : 3)), and (F) hybrids based on MX_HF5% (Sb@A_MX_HF30(6 : 4) and Sb@A_MX_HF30(7 : 3), and Sb@B_MX_HF30(6 : 4), and Sb@B_MX_HF30(7 : 3)).

0.1 and 8 A g^{-1} at an operational potential of 0.1–2.0 V vs. Na$^+$/Na. The obtained rate handling behavior with the corresponding Coulombic efficiency is given in Fig. 6C for compounds with the MXene etched with 5 mass% HF and in Fig. 6D for compounds with the MXene etched with 30 mass% HF. All four tested hybrid materials with MX_HF5 show the expected behavior of proportional decreasing de-sodiation capacity while

applying higher specific current and satisfying capacity retention between 93% and 100% after returning to the initial current. The hybrids with expanded MXene achieve stable and high electrochemical performance values even at 8 A g^{-1}, whereas the Sb@B_MX_HF5(7 : 3), and slightly later also Sb@B_MX_HF5(6 : 4), hybrid shows significant decreases in capacity at higher specific currents. This behavior can probably

Table 1 Overview of electrochemical performance and parameters of different A@MXene composites or hybrid materials. Data not available from literature references are donated as "n.a."

Identifier Fig. 9	Type of composite/hybrid	Composition composite	Total electrode composition	Potential	Preparation of A@MXene	Electrolyte	Normalization	Capacity/ mA h g⁻¹ at 0.1 A g⁻¹	Cycles	Ref.
a	MoS$_2$-nanosheet-decorated 2D titanium Carbide Ti$_3$C$_2$T$_z$	MoS$_2$: Ti$_3$C$_2$T$_z$ ~14% : 86%	AM : Acetylene black : PVdF, 80 : 10 : 10	0.01–3.0 V vs. Na$^+$/Na	Hydrothermal	1 M NaClO$_4$ in EC/PC (1 : 1 by volume) + 5 mass% (FEC)	n.a.	251 mA h g^{-1}	100	Wu et al.[86]
d	SnS nanoparticle-modified MXene (Ti$_3$C$_2$T$_z$) composites	SnS : Ti$_3$C$_2$T$_z$ ~35% : 65%	SnS/Ti$_3$C$_2$T$_z$ composites : Acetylene black : CMC, 70 : 20 : 10	0.01–3.0 V vs. Na$^+$/Na	Hydrothermal Annealing	1 M NaClO$_4$ in EC/DEC (1 : 1 by volume)	n.a.	413 mA h g^{-1}	50	Zhang et al.[87]
c	Ti$_3$C$_2$T$_z$ MXene decorated with Sb nanoparticles	Sb : Ti$_3$C$_2$T$_z$ ~24% : 76%	AM : SuperP : CMC : SBR, 80 : 10 : 5 : 5	0.01–3.0 V vs. Na$^+$/Na	In situ decoration of Ti$_3$C$_2$T$_z$ with Sb	1 M NaClO$_4$ in EC/PC (1 : 1 by volume) + 5 mass% (FEC)	n.a.	180 mA h g^{-1}	50	Chen et al.[65]
h	Black phosphorus/Ti$_3$C$_2$ MXene nanocomposite	BP : Ti$_3$C$_2$ ~66% : 33%	BP/Ti$_3$C$_2$ composite : acetylene black : PVdF, 70 : 20 : 10	0.01–3.0 V vs. Na$^+$/Na	Exfoliation with DMSO hydrothermal	1 M NaClO$_4$ in EC/PC (1 : 1 by volume)	n.a.	121 mA h g^{-1}	60	Li et al.[88]
f	Lattice-coupled Si/MXene	—	AM : acetylene black : CMC, 80 : 10 : 10	0.01–3.0 V vs. Na$^+$/Na	Exfoliation Annealing	1 M NaPF$_6$ EC DEC (1 : 1 by volume) + 5 mass% (FEC)	n.a.	185 mA h g^{-1}	—	Gou et al.[89]
b	2D-MXene/SnS$_2$ composites	SnS$_2$: MXene, ~17% : 83%	AM : acetylene black : CMC, 80 : 10 : 10	0.01–2.5 V vs. Na$^+$/Na	TBAOH exfoliation Mixing in solution	1 M NaClO$_4$ in EC/PC (1 : 1 by volume) + 5 mass% (FEC)	n.a.	322 mA h g^{-1}	200	Wu et al.[90]
e	Ultrasmall SnO$_2$ nanocrystals sandwiched into polypyrrole and Ti$_3$C$_2$T$_z$ MXene	P : SnO$_2$: Ti$_3$C$_2$, 4% : 42% : 55%	P–SnO$_2$/Ti$_3$C$_2$: Acetylene black : PVdF, 80 : 10 : 10	0.001–3.0 vs. Na$^+$/Na	Etching Sonication Hydrothermal	1.0 M NaClO$_4$ in DMC/DEC/EC (1 : 1 : 1 by volume)	n.a.	326 mA h g^{-1}	200	Ding et al.[91]
j	Sb$_2$O$_3$/MXene(Ti$_3$C$_2$T$_z$) hybrid anode	Sb$_2$O$_3$: MXene, ~79% : 21%	AM : Carbon black : CMC, 75 : 15 : 10	0.01–2.5 V vs. Na$^+$/Na	Etching Exfoliation Hydrolysis	1 M NaClO$_4$ in EC/PC (1 : 1 by volume) + 5 mass% (FEC)	Sb$_2$O$_3$	472 mA h g^{-1}	100	Guo et al.[92]
g	**Sb@B_MX_HF5(6 : 4)**	**Sb : MXene, ~60% : 40%**	**Sb@B_MX_HF5(6 : 4) : CB : CMC, 80 : 10 : 10**	**0.1–2.0 V vs. Na$^+$/Na**	**Soaking Hydrothermal**	**1 M NaClO$_4$ in EC/DMC (1 : 1 by mass) + 5 mass% (FEC)**	**Hybrid Sb@MXene**	**434 mA h g^{-1}**	**100**	**This work**

This journal is © The Royal Society of Chemistry 2022

J. Mater. Chem. A, 2022, **10**, 10569–10585 | **10579**

101

be explained due to a non-homogeneous distribution in the electrode. Thus, no optimal buffering of the large volume expansion during sodiation and de-sodiation can be created, leading to massive pulverization resulting in severe cracks in the electrode. This effect negatively affects the electrochemical performance.[21,38] Among the hybrids etched with the MXene with higher HF concentration (Sb@A_MX_HF30(6 : 4) and Sb@A_MX_HF30(7 : 3)), Sb@B_MX_HF30(6 : 4) shows similar stable values for the de-sodiation capacity, the corresponding CE, and the capacity retention between 92% and 99%. At the same time, the overall behavior of Sb@B_MX_HF30(7 : 3) is very unstable. The capacity continuously decreases, which is also reflected in a capacity retention of 69% after returning to 0.1 A g^{-1}. While MX_30% hybrids generally show less beneficial behavior than the MX_5% hybrids, Sb@A_MX_HF30(6 : 4) can provide stable performance up to a rate of 4 A g^{-1}. Detailed charge and discharge profiles, cycling stability studies, and rate performance of the pure MXene electrodes are given in ESI, Fig. S10.†

The cycling stability performance of the Sb@MXene anodes was investigated at a specific current of 0.1 A g^{-1} (Fig. 6E and F). Comparing the stability of the synthesized compounds, where the MXene was mechanically mixed with antimony nano-particles for electrode preparation (ESI, Fig. S11†), all hybrids show a significantly more stable capacity over 100 cycles. The stability curves in ESI, Fig. S11† show that the cells have satisfactory capacities with initial values of around 480 mA h g^{-1} for Sb + MX_HF5(6 : 4)_MM and 420 mA h g^{-1} for Sb + MX_HF5(7 : 3)_MM, respectively. Still, between the 50th and 80th cycle, a collapse of the cell performance occurs, depending on the amount of antimony. In this case, optimal buffering of the volume expansion of the antimony particles and maintenance of the conductive path seems not to have been ensured, which is why early pulverization of the electrode takes place.[21,36,38,39,42–44]

In contrast, the Sb@MXene hybrid shows a significantly improved electrochemical stability performance. Sb@B_MX_HF5(6 : 4) provides a high capacity of 450 mA h g^{-1} and also a high capacity retention of around 96% after 100 cycles. This hybrid combines an optimal distribution of antimony and MXene particles with an optimized content of MXene and antimony; thereby, facile electron transport is enabled. The layers of MXene buffer the volume changes of antimony, and the antimony particles provide excellent electrochemical addressability. The optimal amount of antimony for this hybrid type is 60% to achieve the maximum capacity with the highest possible stability. Our electrochemical data for the hybrid with MX_HF30 support this finding. Here, the two hybrid materials Sb@B_MX_HF30(6 : 4) and Sb@A_MX_HF30(6 : 4) show the most stable behavior at a higher capacity, although a slight degradation can already be observed over the 100 cycles.

The two samples Sb@B_MX_HF30(6 : 4) and Sb@A_MX_HF30(6 : 4) are suffering from a rapid loss of capacity after around 90 cycles. This effect may be caused by the nature of the electrode materials and the distribution of the relatively large MXenes and antimony particles in the electrode, whereby the volume change cannot be satisfactorily buffered. This finally leads to electrode pulverization. However, the Sb@B_MX_HF30(7 : 3) material already loses about one-third of its capacity after about 30 cycles. Sb@A_MX_HF30(7 : 3) shows a decent degradation and a significantly lower de-sodiation capacity right from the start. All Coulombic efficiency values for these compounds are comparable and achieve around 97%, a value that is influenced by the inherent mechanical instability of Na/Sb alloying, which is lower than the charge efficiencies of intercalation electrodes, where structural variations are minimal, but is still comparable to that of the best alloying/conversion electrodes. This stabilization of the Coulombic efficiency indicates a stabilization of the electrodes towards side reactions. However, the processes are still not fully reversible
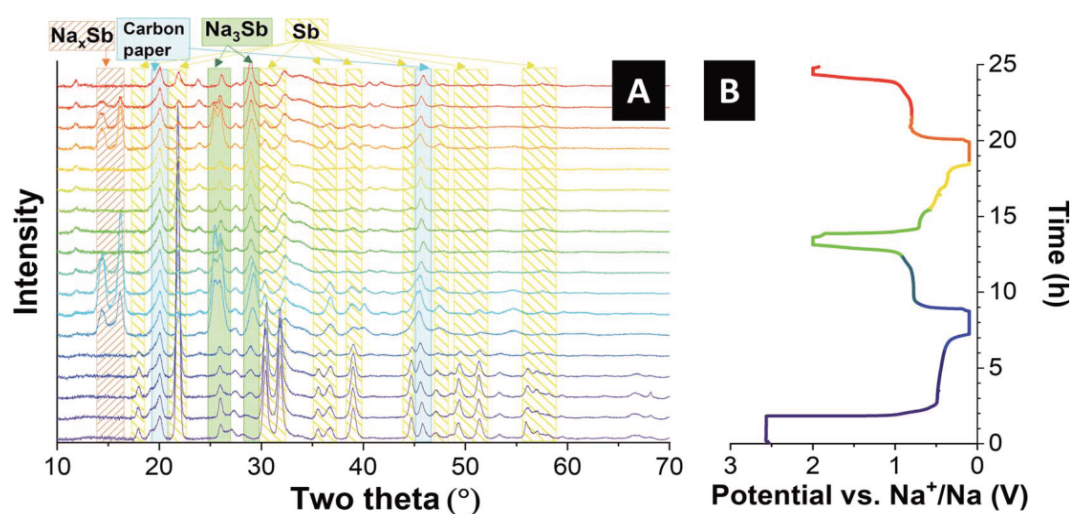
Fig. 7 (A) *In situ* X-ray diffractograms using a setup with Ga-K$_\beta$ radiation (XRD-3; $\lambda = 1.20793$ Å) for Sb@B_MX_HF5(6 : 4). The cell was operated at 0.1 A g^{-1} between 0.1 V and 2.0 V *vs.* Na$^+$/Na also showing the corresponding voltage profile (B).

10580 | *J. Mater. Chem. A*, 2022, 10, 10569–10585

This journal is © The Royal Society of Chemistry 2022

102

since, for rechargeable batteries, a Coulombic efficiency of about 100% is required for both the anode and the cathode in the cells. Nevertheless, these values can be challenging to obtain due to various types of losses such as SEI formation or aging processes.

Compared to other MXene composites and MXene hybrid systems (Table 1 and Fig. 9), the optimized materials in our work offer highly promising performance values (*e.g.*, 434 mA h g^{-1} after 100 cycles for Sb@B_MX_HF5(6 : 4)). This applies not just to Sb/MXene studies but also includes other studies on hybrids and nanocomposites involving MXene. For example, Ti$_3$C$_2$T$_z$ decorated with Sb nanoparticles reported by Chen *et al.*[65] provides nearly 2.5-times lower capacity (185 mA h g^{-1}) with lower cycling stability (50 cycles). The composite material studied by Meng *et al.*[83] was based on black phosphorus; while providing an excellent initial capacity of 1300 mA h g^{-1}, this value quickly dropped to ∼180 mA h g^{-1} after 5 cycles.

ESI, Fig. S13† compares all the systems listed in this work and the associated electrochemical performance. This compilation demonstrates the different performances when synthesis parameters are changed. All other materials have a significantly lower initial capacity than the best-performance material Sb@B_MX_HF5(6 : 4). An optimized Sb/MXene hybrid system is a promising approach to exploit the advantages of both groups of materials and to compensate for the disadvantages of both systems used individually, which ultimately leads to stable high cycling stability. However, a direct comparison with literature data is complicated by different experimental settings, such as
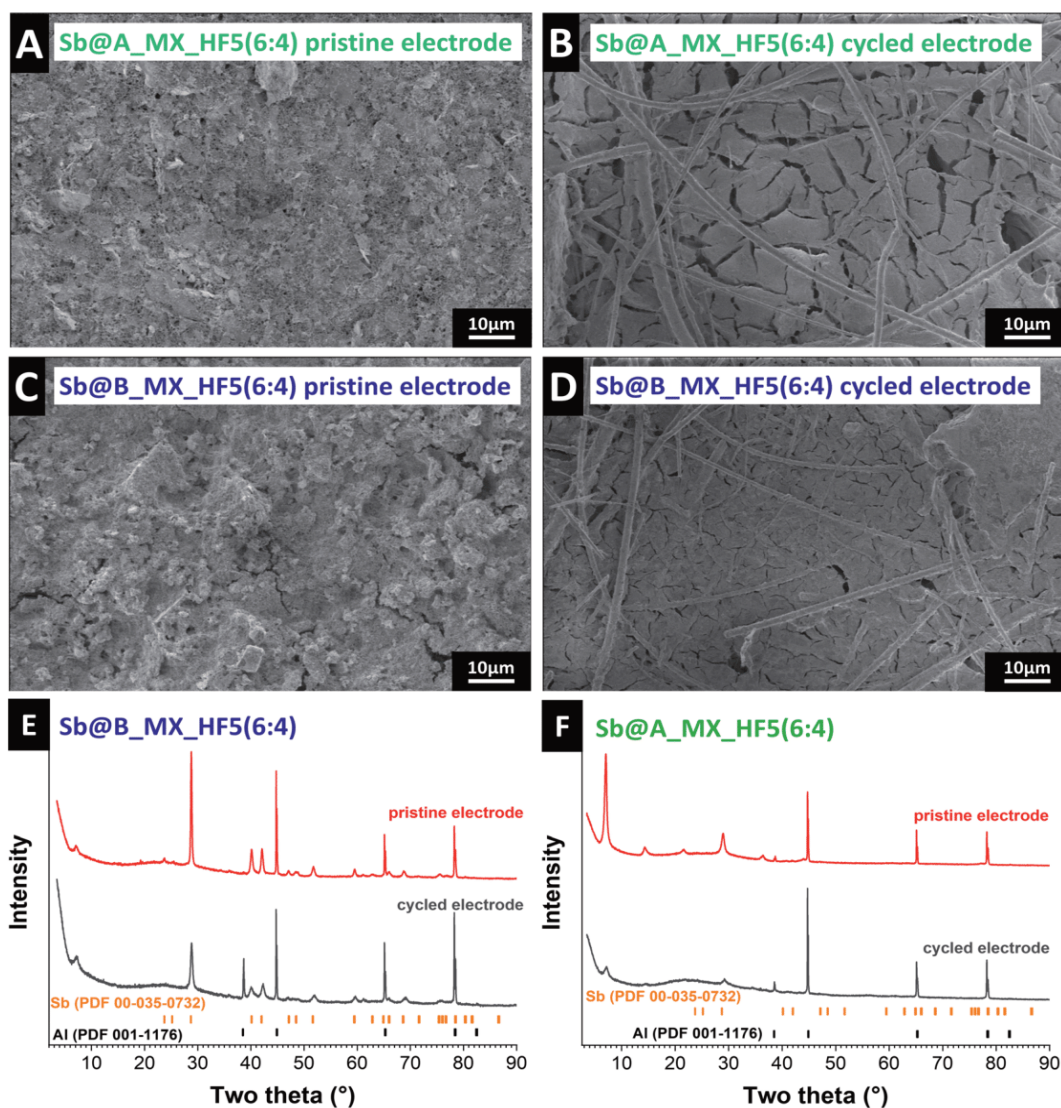
Fig. 8 Scanning electron micrographs of the (A) pristine Sb@A_MX_HF5(6 : 4) electrode, (B) cycled Sb@A_MX_HF5(6 : 4) electrode, (C) pristine Sb@B_MX_HF5(6 : 4) electrode, and (D) cycled Sb@B_MX_HF5(6 : 4) electrode. X-ray diffraction pattern of (E) pristine and cycled Sb@B_MX_HF5(6 : 4) electrodes, (F) pristine and cycled Sb@A_MX_HF5(6 : 4) electrodes.

electrolytes, cell setups, or normalization and real compositions.

3.3 *In situ* and post mortem characterization

To better characterize the sodiation and the de-sodiation mechanism of the Sb@MXene hybrid electrodes with sodium, the structural change of the anode material was investigated by *in situ* XRD measurements for five charge–discharge cycles. Fig. 7 shows *in situ* X-ray diffractograms of the best-performance Sb@B_MX_HF5(6 : 4). The reflections at 17.9° 2θ 21.8° 2θ, 30.5° 2θ, 31.8° 2θ, 35.6° 2θ, 36.7° 2θ, 39.0° 2θ, 44.8° 2θ, 47.0° 2θ, 49.3° 2θ, and 51.4° 2θ in the initial state of the Sb@MXene electrode correspond to the (003), (012), (104), (110), (015), (006), (202), (024), (107), (116), and (112) reflections, respectively, for crystalline trigonal antimony phase with hexagonal axes and the space group $R\bar{3}m$. The two reflections at 20.1° 2θ and 45.7° 2θ are assigned to the carbon paper used as a current collector. The last two reflections do not change in intensity and position during the complete charge and discharge process. In the first charging cycle, until a potential of about 0.4 V is reached, no significant difference in the XRD pattern is observed. Further reduction of the potential leads to the observation of two additional reflections at 14.43° 2θ and 16.24° 2θ indicating the formation of intermediate Na_xSb.[35,42,71,84,85] At the same time, the less and less intense reflections, especially for the reflection at 21.80° 2θ, which are due to the original crystalline antimony present, and the reduction of the amorphous pattern also indicates an alloying reaction with sodium. When the cell is charged further to a lower potential limit, two broader reflections are obtained at about 25° 2θ and 29° 2θ due to the formation of cubic-hexagonal Na_3Sb and the ultimate stabilization in hexagonal Na_3Sb.[35]

Our observations confirm the already elucidated mechanism of the alloying reaction of antimony with sodium in a multistep process resulting in a crystalline product. During cell discharge, the alloy reflections gradually weaken, and the intensity of the elemental antimony reflections gradually increases. At the same time, the intensity of the initially obtained antimony reflection is not restored. This indicates that the reactions cause some antimony to return back to amorphous antimony. In addition, from the first discharge cycle onwards, an additional, increasingly more prominent reflection becomes visible, which, apart from the formation of an SEI, can probably also refer to the formation of antimony oxide which forms a thin layer on the surface of the antimony electrode while cycling. An explanation for the very high and stable performance of Sb@B_MX_HF5(6 : 4) can be derived by comparing the main differences between the hybrids even after cycling. Leaving aside the influence of the different MXenes and focusing only on the two similar Sb@A_MX_HF5(6 : 4) and Sb@B_MX_HF5(6 : 4) hybrids, one can see in the pristine electrode (Fig. 8A and C) significantly larger particles and partly already cracks in Sb@B_MX_HF5(6 : 4). No such cracks are seen for the electrode made from Sb@A_MX_HF5(6 : 4).

Post-mortem analysis shows that the promising electrochemical performance of the Sb@B_MX_HF5(6 : 4) electrode
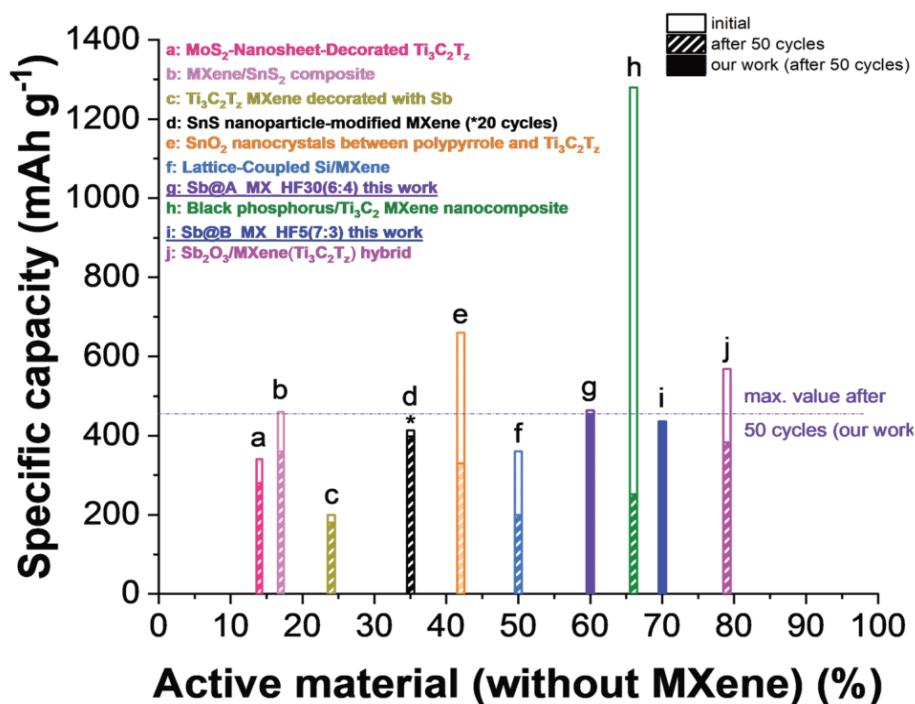
Fig. 9 Graphical illustration and overview of the initial specific capacities and values after 50 cycles of cycling at a specific current of 0.1 A g^{-1} for different A@MXene composites or hybrid materials of the state-of-the-art systems in comparison to the values obtained in this work. Data from ref. 65 and 86–92.

10582 | *J. Mater. Chem. A*, 2022, **10**, 10569–10585

This journal is © The Royal Society of Chemistry 2022

104

aligns with significantly fewer volume changes and fewer cracks of the electrodes. The best distribution of antimony particles, MXene layers, and conductive additive results in the best buffering of volume expansion, which is concluded in a good cycle and rate behavior. Optimized conductive paths allow homogeneous charge transfer on the surface of the antimony particles. Also seen in the electron micrographs is that the post mortem of the Sb@B_MX_HF5(6 : 4) electrode shows a homogeneous and flat electrode surface. It is suggested that this probably characterizes the SEI, which may have stabilized the electrochemical behavior compared to the other electrodes. Disordered parts and impurities could catalyze the chemical reactions, resulting in an improved SEI, better-buffering effects, and better interaction between the antimony material and MXene particles.[45]

The XRD patterns recorded *ex situ* (Fig. 8E and F) also confirm the statement of the reaction mechanism to Na_3Sb and a larger fraction of amorphous antimony while cycling. Due to this, the antimony reflections become less intense, and new reflections appear. Also, the diffraction pattern of the Sb@A_MX_HF5(6 : 4) electrode displays a different intensity of the (002) reflection before and after cycling. This effect may be caused by the strong reflection of the aluminum current collector, which is more visible after cycling due to the cracks in the electrode. Despite the difficulty in detecting antimony in-between the layers of the MXene, it was possible to confirm that the antimony particles always react as in the proposed reaction mechanism.

4 Conclusions

MXenes' unique properties, including their high electrical conductivity and accessible interlayer space, make them highly attractive for numerous electrochemical applications, including alkali metal-ion batteries. So far, based only on ion intercalation, the specific capacity remains limited and mandates the exploration of combinations of MXene with other materials, such as alloying electrode materials. Antimony is a very promising anode candidate, which reacts in an alloying reaction with sodium to form Na_3Sb delivering a high theoretical capacity of 660 mA h g^{-1}. Yet, the major drawback of alloying materials is their large change in the volume during charging and discharging, which often leads to electrode cracking, pulverization, and poor electrochemical performance. An appropriate matrix can mitigate such a drawback, and we demonstrate the benefits (and limitations) of MXene/Sb electrodes.

In our work, the influence of different types of MXenes, different synthesis routes, morphology, and different electrode compositions on electrochemical stability and longevity for use as an anode material in sodium-ion batteries was systematically investigated. The initial expansion of the MXene layers and the subsequent intercalation of the antimony nanoparticles in between the layers are disadvantageous properties of the hybrid electrodes as some parts of antimony seem not to be electrochemically accessible. The best performance is not triggered by the highest amount of antimony particles, the smallest nanoparticles, or the largest interlayer distance of the MXene but by the most homogeneous distribution of antimony and MXene

while both components remain electrochemically addressable. With the best hybrid material, we obtained electrodes with a specific capacity of 450 mA h g^{-1} at 0.1 A g^{-1} and 365 mA h g^{-1} at 4 A g^{-1}, with a capacity retention of around 96% after 100 cycles. In addition, the mechanism was investigated by *in situ* XRD and post mortem analysis, and an alloying reaction of antimony without side reactions was confirmed.

Author contributions

Stefanie Arnold: conceptualization, methodology, investigation, data curation, visualization, and writing – original draft. Antonio Gentile: conceptualization, investigation, data curation, and visualization. Yunjie Li: investigation, and writing – review & editing. Qingsong Wang: investigation, and writing – review & editing. Stefano Marchionna: resources, and writing – review & editing. Riccardo Ruffo: supervision, and writing – review & editing. Volker Presser: supervision, writing – review & editing, and funding acquisition.

Conflicts of interest

There are no conflicts to declare.

Acknowledgements

References

1 M. Li, J. Lu, Z. Chen and K. Amine, *Adv. Mater.*, 2018, **30**, 1800561.
2 D. Kundu, E. Talaie, V. Duffort and L. F. Nazar, *Angew. Chem., Int. Ed.*, 2015, **54**, 3431–3448.
3 J. M. Tarascon, *Nat. Chem.*, 2010, **2**, 510.
4 M. D. Slater, D. Kim, E. Lee and C. S. Johnson, *Adv. Funct. Mater.*, 2013, **23**, 947–958.
5 V. Palomares, P. Serras, I. Villaluenga, K. B. Hueso, J. Carretero-González and T. Rojo, *Energy Environ. Sci.*, 2012, **5**, 5884–5901.
6 M. Dahbi, N. Yabuuchi, K. Kubota, K. Tokiwa and S. Komaba, *Phys. Chem. Chem. Phys.*, 2014, **16**, 15007–15028.

This journal is © The Royal Society of Chemistry 2022

J. Mater. Chem. A, 2022, **10**, 10569–10585 | **10583**

7 H. Buqa, D. Goers, M. Holzapfel, M. E. Spahr and P. Novák, *J. Electrochem. Soc.*, 2005, **152**, A474.

8 B. Simon, S. Flandrois, K. Guerin, A. Fevrier-Bouvier, I. Teulat and P. Biensan, *J. Power Sources*, 1999, **81–82**, 312–316.

9 D. A. Stevens and J. R. Dahn, *J. Electrochem. Soc.*, 2001, **148**, A803.

10 Y. Li, S. Xu, X. Wu, J. Yu, Y. Wang, Y.-S. Hu, H. Li, L. Chen and X. Huang, *J. Mater. Chem. A*, 2015, **3**, 71–77.

11 S. Komaba, W. Murata, T. Ishikawa, N. Yabuuchi, T. Ozeki, T. Nakayama, A. Ogata, K. Gotoh and K. Fujiwara, *Adv. Funct. Mater.*, 2011, **21**, 3859–3867.

12 M. M. Doeff, Y. Ma, S. J. Visco and L. C. De Jonghe, *J. Electrochem. Soc.*, 1993, **140**, L169–L170.

13 S. Fleischmann, J. B. Mitchell, R. Wang, C. Zhan, D.-e. Jiang, V. Presser and V. Augustyn, *Chem. Rev.*, 2020, **120**, 6738–6782.

14 X. Yu, H. Pan, W. Wan, C. Ma, J. Bai, Q. Meng, S. N. Ehrlich, Y.-S. Hu and X.-Q. Yang, *Nano Lett.*, 2013, **13**, 4721–4727.

15 Y. Sun, L. Zhao, H. Pan, X. Lu, L. Gu, Y.-S. Hu, H. Li, M. Armand, Y. Ikuhara and L. Chen, *Nat. Commun.*, 2013, **4**, 1–10.

16 Z. Liang, P. Hui-Lin, H. Yong-Sheng, L. Hong and C. Li-Quan, *Chin. Phys. B*, 2012, **21**, 028201.

17 J. P. Huang, D. D. Yuan, H. Z. Zhang, Y. L. Cao, G. R. Li, H. X. Yang and X. P. Gao, *RSC Adv.*, 2013, **3**, 12593–12597.

18 P. Senguttuvan, G. Rousse, V. Seznec, J.-M. Tarascon and M. R. Palacín, *Chem. Mater.*, 2011, **23**, 4109–4111.

19 Y. Kim, K. H. Ha, S. M. Oh and K. T. Lee, *Chem. –Eur. J.*, 2014, **20**, 11980–11992.

20 M.-S. Balogun, Y. Luo, W. Qiu, P. Liu and Y. Tong, *Carbon*, 2016, **98**, 162–178.

21 M. Lao, Y. Zhang, W. Luo, Q. Yan, W. Sun and S. X. Dou, *Adv. Mater.*, 2017, **29**, 1700622.

22 E. Edison, S. Sreejith, C. T. Lim and S. Madhavi, *Sustainable Energy Fuels*, 2018, **2**, 2567–2582.

23 W. Brehm, J. R. Buchheim and P. Adelhelm, *Energy Technol.*, 2019, **7**, 1900389.

24 L. Baggetto, J. K. Keum, J. F. Browning and G. M. Veith, *Electrochem. Commun.*, 2013, **34**, 41–44.

25 H. Zhu, Z. Jia, Y. Chen, N. Weadock, J. Wan, O. Vaaland, X. Han, T. Li and L. Hu, *Nano Lett.*, 2013, **13**, 3093–3100.

26 L. D. Ellis, B. N. Wilkes, T. D. Hatchard and M. N. Obrovac, *J. Electrochem. Soc.*, 2014, **161**, A416–A421.

27 J. Qian, X. Wu, Y. Cao, X. Ai and H. Yang, *Angew. Chem., Int. Ed.*, 2013, **125**, 4731–4734.

28 M. He, K. Kravchyk, M. Walter and M. V. Kovalenko, *Nano Lett.*, 2014, **14**, 1255–1262.

29 J. B. Goodenough and Y. Kim, *Chem. Mater.*, 2010, **22**, 587–603.

30 L. Bodenes, A. Darwiche, L. Monconduit and H. Martinez, *J. Power Sources*, 2015, **273**, 14–24.

31 A. Darwiche, L. Bodenes, L. Madec, L. Monconduit and H. Martinez, *Electrochim. Acta*, 2016, **207**, 284–292.

32 L. Ji, M. Gu, Y. Shao, X. Li, M. H. Engelhard, B. W. Arey, W. Wang, Z. Nie, J. Xiao, C. Wang, J. G. Zhang and J. Liu, *Adv. Mater.*, 2014, **26**, 2901–2908.

33 S. Komaba, T. Ishikawa, N. Yabuuchi, W. Murata, A. Ito and Y. Ohsawa, *ACS Appl. Energy Mater.*, 2011, **3**, 4165–4168.

34 V. Winkler, G. Kilibarda, S. Schlabach, D. V. Szabó, T. Hanemann and M. Bruns, *J. Phys. Chem. C*, 2016, **120**, 24706–24714.

35 A. Darwiche, C. Marino, M. T. Sougrati, B. Fraisse, L. Stievano and L. Monconduit, *J. Am. Chem. Soc.*, 2012, **134**, 20805–20811.

36 H. Hou, M. Jing, Y. Yang, Y. Zhang, W. Song, X. Yang, J. Chen, Q. Chen and X. Ji, *J. Power Sources*, 2015, **284**, 227–235.

37 L. Wu, H. Lu, L. Xiao, X. Ai, H. Yang and Y. Cao, *J. Mater. Chem. A*, 2015, **3**, 5708–5713.

38 V. L. Chevrier and G. Ceder, *J. Electrochem. Soc.*, 2011, **158**, A1011.

39 M. Widmaier, N. Jäckel, M. Zeiger, M. Abuzarli, C. Engel, L. Bommer and V. Presser, *Electrochim. Acta*, 2017, **247**, 1006–1018.

40 M. Widmaier, K. Pfeifer, L. Bommer and V. Presser, *Batteries Supercaps*, 2018, **1**, 11–26.

41 C. Li, A. Sarapulova, K. Pfeifer and S. Dsoke, *ChemSusChem*, 2020, **13**, 986–995.

42 C. Cui, J. Xu, Y. Zhang, Z. Wei, M. Mao, X. Lian, S. Wang, C. Yang, X. Fan and J. Ma, *Nano Lett.*, 2018, **19**, 538–544.

43 L. Wu, X. Hu, J. Qian, F. Pei, F. Wu, R. Mao, X. Ai, H. Yang and Y. Cao, *Energy Environ. Sci.*, 2014, **7**, 323–328.

44 Y. Zhu, X. Han, Y. Xu, Y. Liu, S. Zheng, K. Xu, L. Hu and C. Wang, *ACS Nano*, 2013, **7**, 6378–6386.

45 K. Pfeifer, S. Arnold, Ö. Budak, X. Luo, V. Presser, H. Ehrenberg and S. Dsoke, *J. Mater. Chem. A*, 2020, **8**, 6092–6104.

46 M. Naguib, M. Kurtoglu, V. Presser, J. Lu, J. Niu, M. Heon, L. Hultman, Y. Gogotsi and M. W. Barsoum, *Adv. Mater.*, 2011, **23**, 4248–4253.

47 M. Naguib, J. Come, B. Dyatkin, V. Presser, P.-L. Taberna, P. Simon, M. W. Barsoum and Y. Gogotsi, *Electrochem. Commun.*, 2012, **16**, 61–64.

48 B. Anasori, M. R. Lukatskaya and Y. Gogotsi, *Nat. Rev. Mater.*, 2017, **2**, 16098.

49 M. Naguib, M. W. Barsoum and Y. Gogotsi, *Adv. Mater.*, 2021, **33**, 2103393.

50 E. Yang, H. Ji, J. Kim, H. Kim and Y. Jung, *Phys. Chem. Chem. Phys.*, 2015, **17**, 5000–5005.

51 D. Er, J. Li, M. Naguib, Y. Gogotsi and V. B. Shenoy, *ACS Appl. Energy Mater.*, 2014, **6**, 11173–11179.

52 S. Kajiyama, L. Szabova, K. Sodeyama, H. Iinuma, R. Morita, K. Gotoh, Y. Tateyama, M. Okubo and A. Yamada, *ACS Nano*, 2016, **10**, 3334–3341.

53 A. Gentile, C. Ferrara, S. Tosoni, M. Balordi, S. Marchionna, F. Cernuschi, M. H. Kim, H. W. Lee and R. Ruffo, *Small Methods*, 2020, **4**, 2000314.

54 M. K. Aslam, T. S. AlGarni, M. S. Javed, S. S. A. Shah, S. Hussain and M. Xu, *J. Energy Storage*, 2021, **37**, 102478.

55 M. K. Aslam, Y. Niu and M. Xu, *Adv. Energy Mater.*, 2020, **11**, 2000681.

56 H. Riazi, G. Taghizadeh and M. Soroush, *ACS Omega*, 2021, **6**, 11103–11112.

10584 | *J. Mater. Chem. A*, 2022, **10**, 10569–10585

This journal is © The Royal Society of Chemistry 2022

57 J. K. Im, E. J. Sohn, S. Kim, M. Jang, A. Son, K.-D. Zoh and Y. Yoon, *Chemosphere*, 2021, **270**, 129478.

58 A. Zhang, R. Liu, J. Tian, W. Huang and J. Liu, *Chem. –Eur. J.*, 2020, **26**, 6342–6359.

59 J. Zhou, J. Yu, L. Shi, Z. Wang, H. Liu, B. Yang, C. Li, C. Zhu and J. Xu, *Small*, 2018, **14**, 1803786.

60 K. Ma, H. Jiang, Y. Hu and C. Li, *Adv. Funct. Mater.*, 2018, **28**, 1804306.

61 J. Yu, J. Zhou, P. Yao, J. Huang, W. Sun, C. Zhu and J. Xu, *J. Power Sources*, 2019, **440**, 227150.

62 S. Husmann, M. Torkamanzadeh, K. Liang, A. Majed, C. Dun, J. J. Urban, M. Naguib and V. Presser, *Adv. Mater. Interfaces*, 2022, 2102185.

63 M. Naguib, O. Mashtalir, M. R. Lukatskaya, B. Dyatkin, C. Zhang, V. Presser, Y. Gogotsi and M. W. Barsoum, *Chem. Commun.*, 2014, **50**, 7420–7423.

64 Z. Ling, E. Ren Chang, M.-Q. Zhao, J. Yang, M. Giammarco James, J. Qiu, W. Barsoum Michel and Y. Gogotsi, *Proc. Natl. Acad. Sci. U. S. A.*, 2014, **111**, 16676–16681.

65 H. Chen, N. Chen, M. Zhang, M. Li, Y. Gao, C. Wang, G. Chen and F. Du, *Nanotechnol*, 2019, **30**, 134001.

66 X. Guo, H. Gao, S. Wang, G. Yang, X. Zhang, J. Zhang, H. Liu and G. Wang, *Nano Lett.*, 2022, **22**, 1225–1232.

67 H. Gao, X. Guo, S. Wang, F. Zhang, H. Liu and G. Wang, *EcoMat*, 2020, **2**, e12027.

68 F. Zhang, Z. Jia, C. Wang, A. Feng, K. Wang, T. Hou, J. Liu, Y. Zhang and G. Wu, *Energy*, 2020, **195**, 117047.

69 S. Arnold, L. Wang, Ö. Budak, M. Aslan, P. Srimuk and V. Presser, *J. Mater. Chem. A*, 2021, **9**, 585–596.

70 D. Weingarth, M. Zeiger, N. Jäckel, M. Aslan, G. Feng and V. Presser, *Adv. Energy Mater.*, 2014, **4**, 1400316.

71 J. Qian, Y. Chen, L. Wu, Y. Cao, X. Ai and H. Yang, *Chem. Commun.*, 2012, **48**, 7070–7072.

72 Y.-X. Wang, Y.-G. Lim, M.-S. Park, S.-L. Chou, J. H. Kim, H.-K. Liu, S.-X. Dou and Y.-J. Kim, *J. Mater. Chem. A*, 2014, **2**, 529–534.

73 A. Ponrouch, A. R. Goñi and M. R. Palacín, *Electrochem. Commun.*, 2013, **27**, 85–88.

74 A. Ponrouch, D. Monti, A. Boschin, B. Steen, P. Johansson and M. R. Palacín, *J. Mater. Chem. A*, 2015, **3**, 22–42.

75 V. Simone, L. Lecarme, L. Simonin and S. Martinet, *J. Electrochem. Soc.*, 2016, **164**, A145–A150.

76 A. Rozmysłowska-Wojciechowska, J. Mitrzak, A. Szuplewska, M. Chudy, J. Woźniak, M. Petrus, T. Wojciechowski, A. S. Vasilchenko and A. M. Jastrzębska, *Materials*, 2020, **13**, 2347.

77 G. R. Berdiyorov, *Appl. Surf. Sci.*, 2015, **359**, 153–157.

78 X. Zhou, Z. Dai, J. Bao and Y.-G. Guo, *J. Mater. Chem. A*, 2013, **1**, 13727–13731.

79 S. Pruneanu, E. Veress, I. Marian and L. Oniciu, *Mater. Sci.*, 1999, **34**, 2733–2739.

80 S. Fleischmann, Y. Zhang, X. Wang, P. T. Cummings, J. Wu, P. Simon, Y. Gogotsi, V. Presser and V. Augustyn, *Nat. Energy*, 2022, **7**, 222–228.

81 P. R. Abel, Y.-M. Lin, T. de Souza, C.-Y. Chou, A. Gupta, J. B. Goodenough, G. S. Hwang, A. Heller and C. B. Mullins, *J. Phys. Chem. C*, 2013, **117**, 18885–18890.

82 Y. Kim, Y. Park, A. Choi, N. S. Choi, J. Kim, J. Lee, J. H. Ryu, S. M. Oh and K. T. Lee, *Adv. Mater.*, 2013, **25**, 3045–3049.

83 R. Meng, J. Huang, Y. Feng, L. Zu, C. Peng, L. Zheng, L. Zheng, Z. Chen, G. Liu, B. Chen, Y. Mi and J. Yang, *Adv. Energy Mater.*, 2018, **8**, 1801514.

84 Q. Li, W. Zhang, J. Peng, W. Zhang, Z. Liang, J. Wu, J. Feng, H. Li and S. Huang, *ACS Nano*, 2021, **15**, 15104–15113.

85 X. Ou, C. Yang, X. Xiong, F. Zheng, Q. Pan, C. Jin, M. Liu and K. Huang, *Adv. Funct. Mater.*, 2017, **27**, 1606242.

86 Y. Wu, P. Nie, J. Jiang, B. Ding, H. Dou and X. Zhang, *ChemElectroChem*, 2017, **4**, 1560–1565.

87 Y. Zhang, B. Guo, L. Hu, Q. Xu, Y. Li, D. Liu and M. Xu, *J. Alloys Compd.*, 2018, **732**, 448–453.

88 H. Li, A. Liu, X. Ren, Y. Yang, L. Gao, M. Fan and T. Ma, *Nanoscale*, 2019, **11**, 19862–19869.

89 L. Gou, W. Jing, Y. Li, M. Wang, S. Hu, H. Wang and Y.-B. He, *ACS Appl. Energy Mater.*, 2021, **4**, 7268–7277.

90 Y. Wu, P. Nie, L. Wu, H. Dou and X. Zhang, *Chem. Eng. J.*, 2018, **334**, 932–938.

91 J. Ding, C. Tang, G. Zhu, F. He, A. Du, M. Wu and H. Zhang, *Mater. Chem. Front*, 2021, **5**, 825–833.

92 X. Guo, X. Xie, S. Choi, Y. Zhao, H. Liu, C. Wang, S. Chang and G. Wang, *J. Mater. Chem. A*, 2017, **5**, 12445–12452.

93 H. Hou, Y. Yang, Y. Zhu, M. Jing, C. Pan, L. Fang, W. Song, X. Yang and X. Ji, *Electrochim. Acta*, 2014, **146**, 328–334.

This journal is © The Royal Society of Chemistry 2022

J. Mater. Chem. A, 2022, **10**, 10569–10585 | **10585**

Supporting Information

Design of High-Performance Antimony /

MXene Hybrid Electrodes for Sodium-Ion Batteries

Stefanie Arnold,[1,2] Antonio Gentile,[3,4] Yunjie Li,[1,2] Qingsong Wang,[1,5]

Stefano Marchionna,[4] Riccardo Ruffo,[3,6]* and Volker Presser[1,2,7]*

[1]   INM - Leibniz Institute for New Materials, Campus D2.2, 66123 Saarbrücken, Germany

[2]   Department of Materials Science and Engineering, Saarland University, Campus D2.266123 Saarbrücken, Germany

[3]   Dipartimento di Scienza dei Materiali, Università degli Studi di Milano Bicocca, Via Cozzi 55, 20125 Milano, Italy

[4]   Ricerca sul Sistema Energetico- RSE S.p.A., Via R. Rubattino 54, 20134 Milano, Italy

[5]   Institute of Nanotechnology, Karlsruhe Institute of Technology, Hermann-von-Helmholtz-Platz 1, 76344, Eggenstein-Leopoldshafen, Germany

[6]   National Reference Center for Electrochemical Energy Storage (GISEL) - Consorzio Interuniversitario Nazionale per la Scienza e Tecnologia dei Materiali (INSTM), 50121 Firenze, Italy

[7]   Saarene - Saarland Center for Energy Materials and Sustainability, Campus D4.2, 66123 Saarbrücken, Germany

*   Corresponding author's E-Mail: VP: volker.presser@leibniz-inm.de; RR: riccardo.ruffo@unimib.it
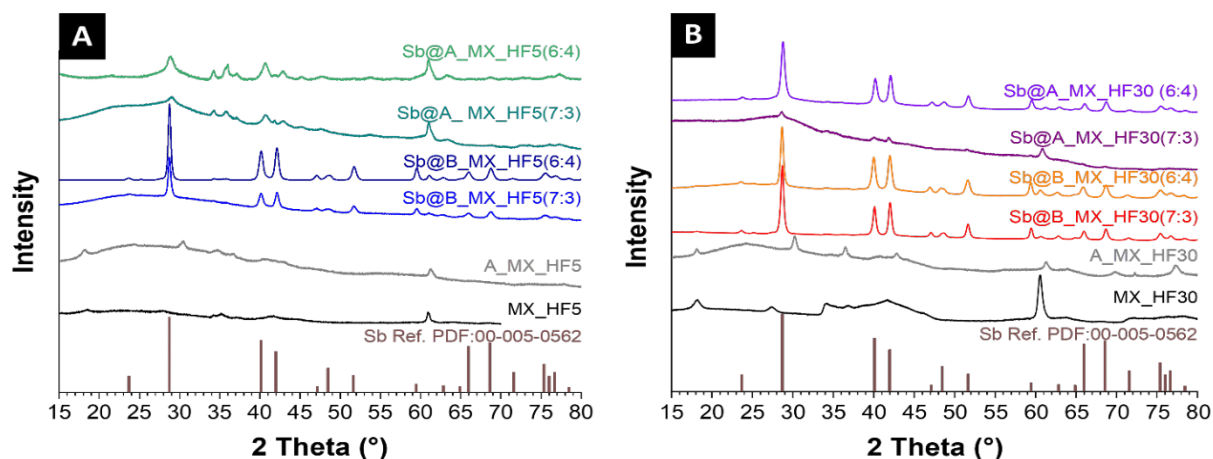
Figure S1: X-ray diffraction patterns of different Sb@Ti$_3$C$_2$T$_z$ hybrid materials (+pure Ti$_3$C$_2$T$_z$ and expanded Ti$_3$C$_2$T$_z$) by using the MXene etched with 5 mass% HF (**A**) and 30 mass% HF (**B**).
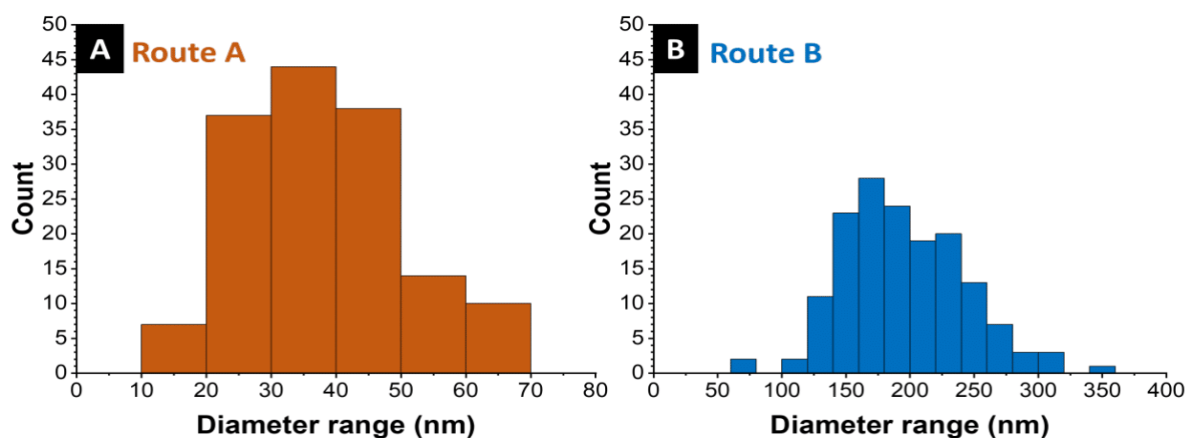
Figure S2: Particle size distribution derived from image analysis of scanning electron micrographs of 150 antimony particles synthesized via synthesis Route A (**A**) and via synthesis Route B (**B**).
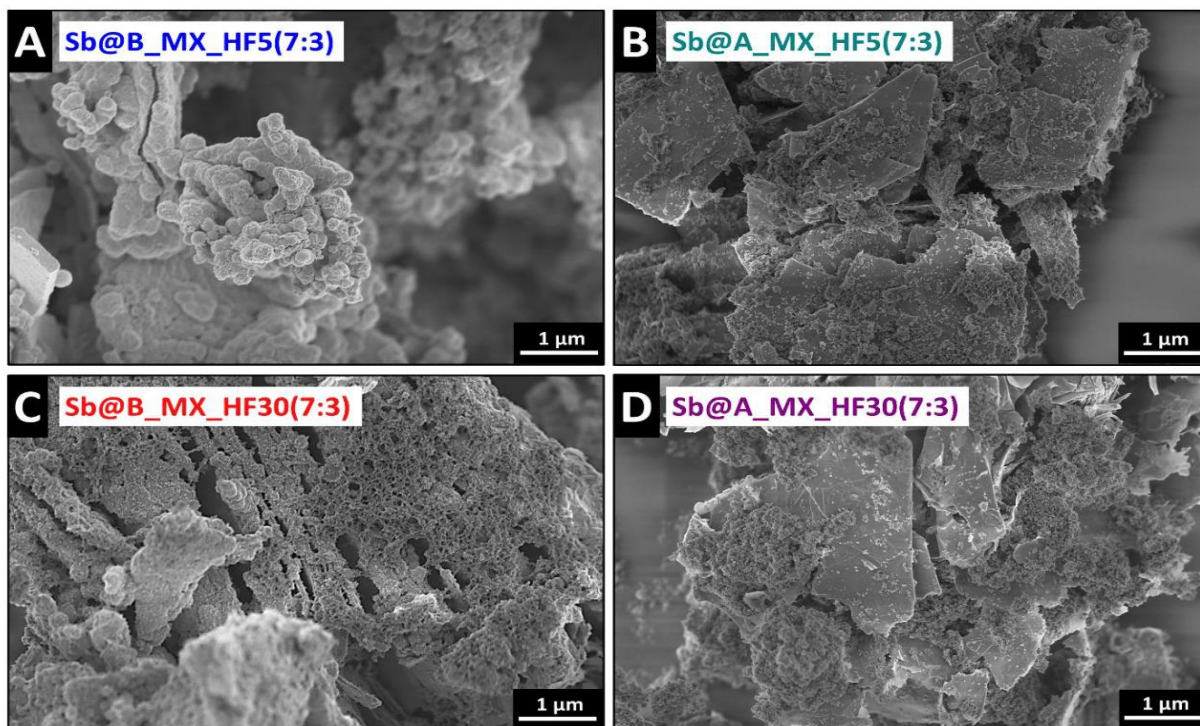
Figure S3: Scanning electron micrographs of (**A**) antimony Ti$_3$C$_2$T$_z$ (5 mass% HF) hybrid with a composition of 7:3 (**B**) antimony expanded Ti$_3$C$_2$T$_z$ (5 mass% HF) hybrid with a composition of 7:3 (**C**) antimony Ti$_3$C$_2$T$_z$ (30 mass% HF) hybrid with a composition of 7:3 (**D**) antimony expanded Ti$_3$C$_2$T$_z$ (30 mass% HF) hybrid with a composition of 7:3.
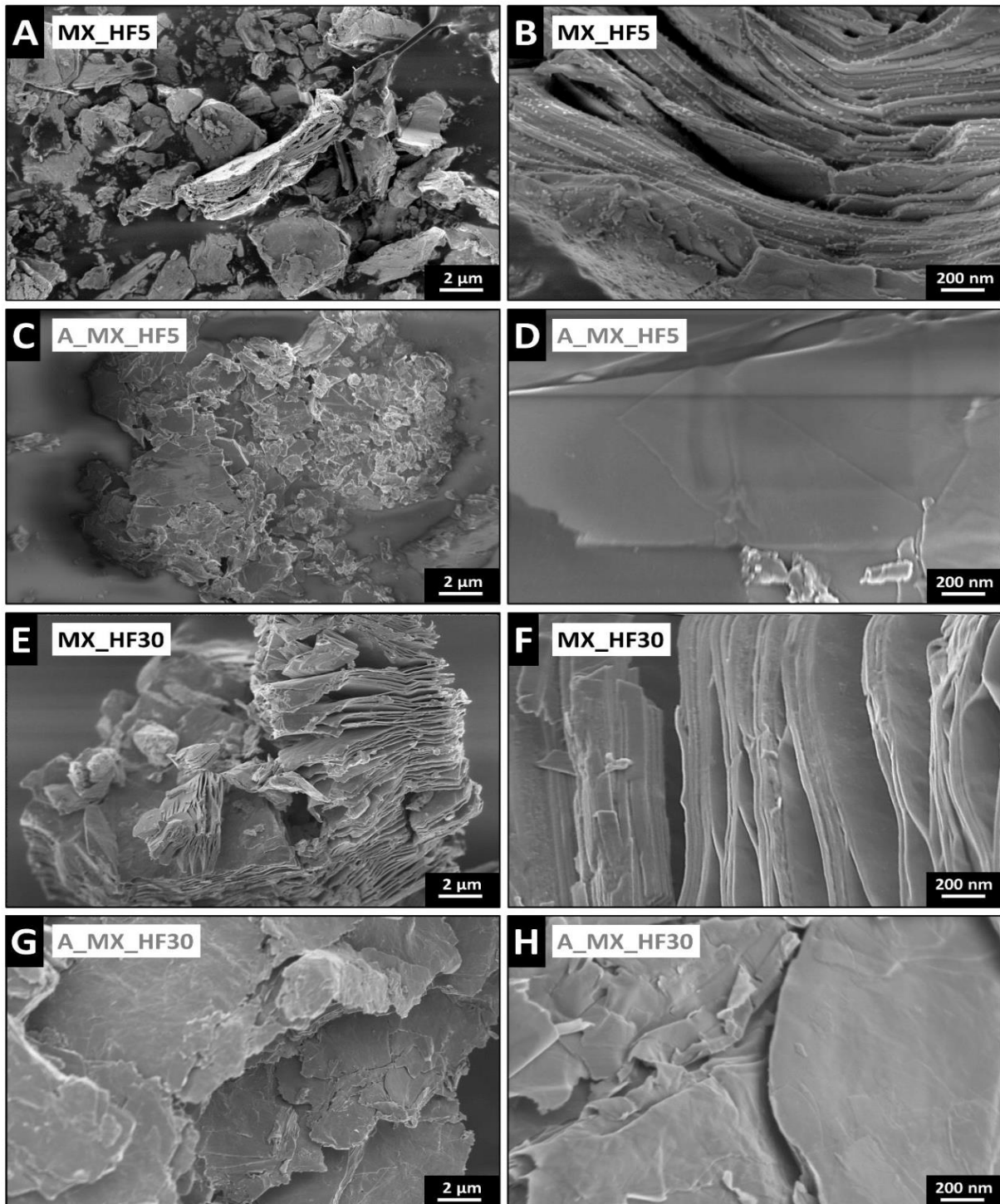
Figure S4: Material characterization of the different MXenes. Scanning electron micrographs of (**A-B**) $Ti_3C_2T_z$ (5 mass% HF), (**C-D**) with TMAOH expanded $Ti_3C_2T_z$ (5 mass% HF), (**E-F**) $Ti_3C_2T_z$ (30 mass% HF), (**G-H**) with TMAOH expanded $Ti_3C_2T_z$ (30 mass% HF).
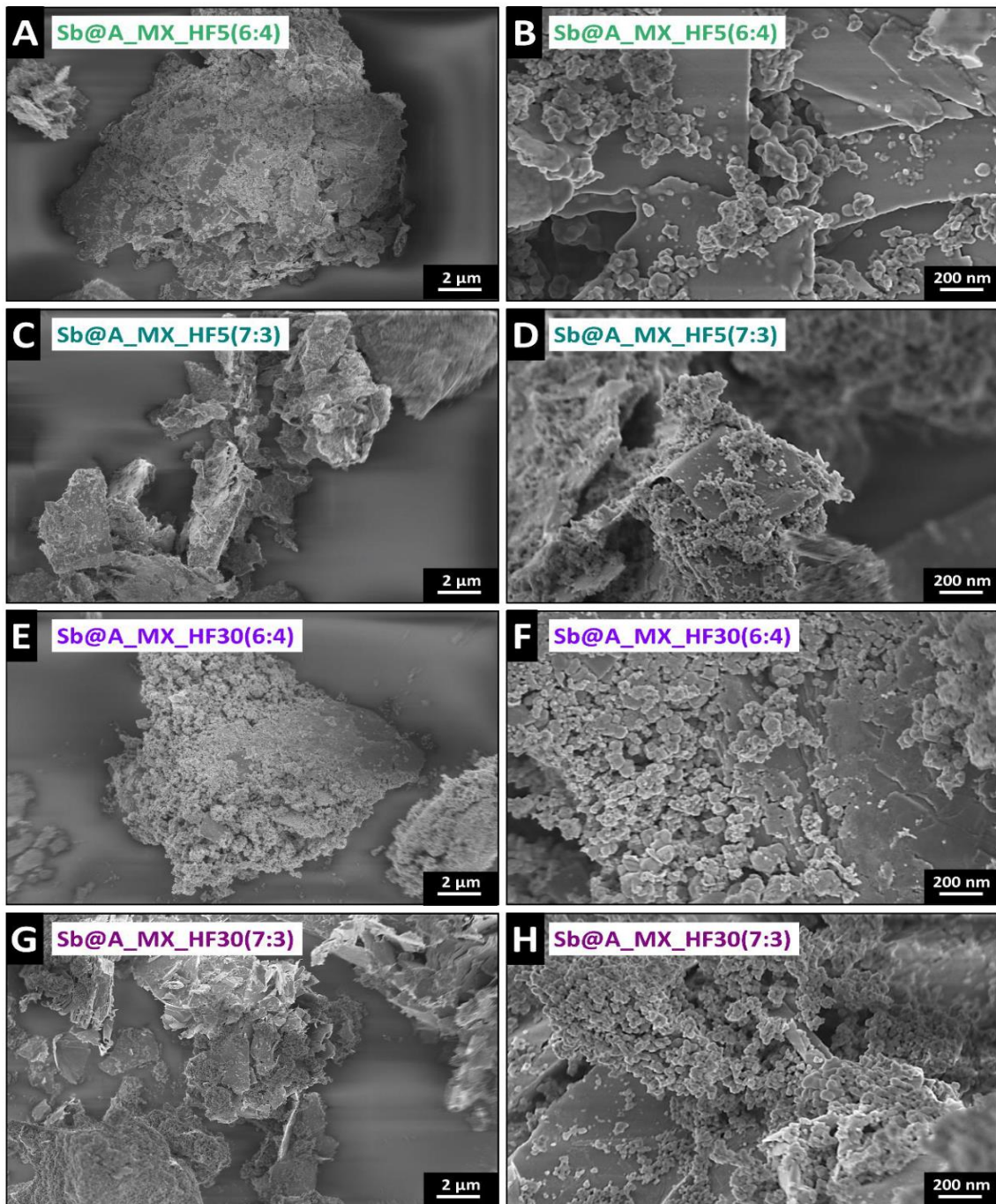
Figure S5: Material characterization of the different with TMAOH expanded MXene antimony hybrids. Scanning electron micrographs of (**A-B**) antimony expanded $Ti_3C_2T_z$ (5 mass% HF) hybrid with a composition of 6:4, (**C-D**) antimony expanded $Ti_3C_2T_z$ (5 mass% HF) hybrid with a composition of 7:3, (**E-F**) antimony expanded $Ti_3C_2T_z$ (30 mass% HF) hybrid with a composition of 6:4, (**G-H**) antimony expanded $Ti_3C_2T_z$ (30 mass% HF) hybrid with a composition of 7:3.
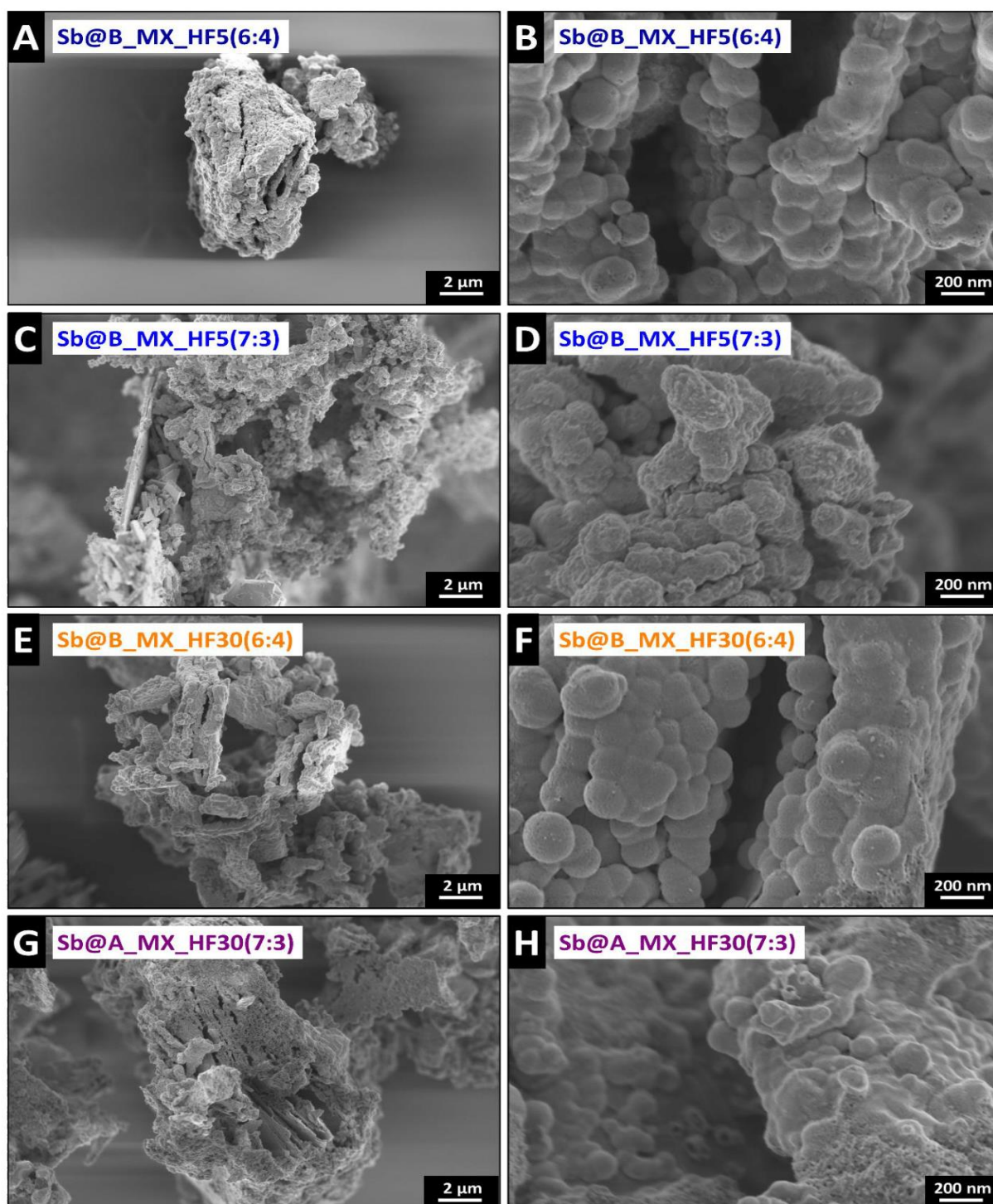
Figure S6: Material characterization of the different MXenes hybrids. Scanning electron micrographs of (**A-B**) antimony $Ti_3C_2T_z$ (5% mass% HF) hybrid with a composition of 6:4, (**C-D**) antimony $Ti_3C_2T_z$ (5% mass% HF) hybrid with a composition of 7:3, (**E-F**) antimony $Ti_3C_2T_z$ (30% mass% HF) hybrid with a composition of 6:4, (**G-H**) antimony $Ti_3C_2T_z$ (30% mass% HF) hybrid with a composition of 7:3.
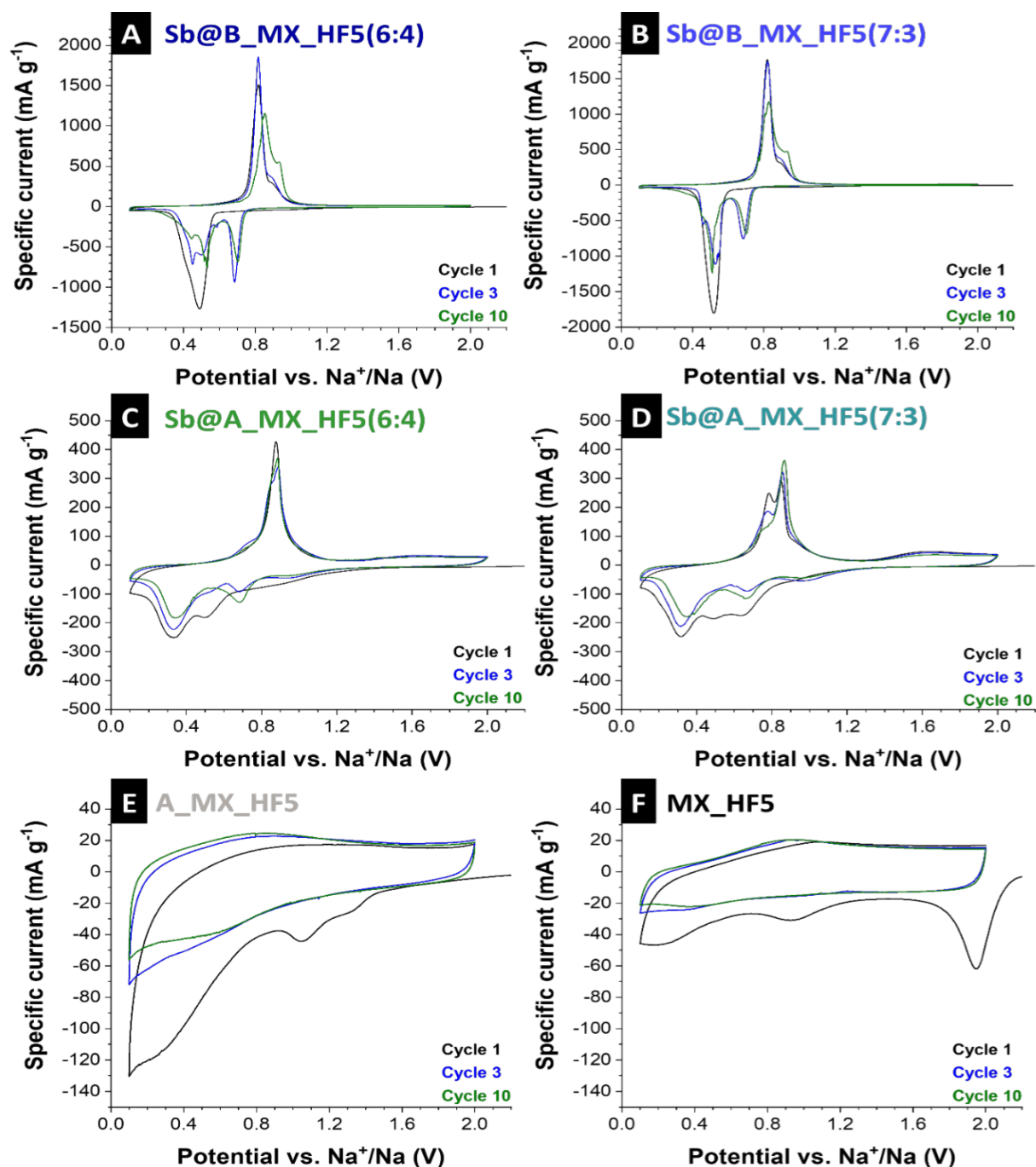
Figure S7: Cyclic voltammograms recorded at 0.1 mV s^{-1} in the potential range of 0.1-2.0 V vs. Na$^+$/Na for (**A**) antimony Ti$_3$C$_2$T$_z$ (5% mass% HF) hybrid with a composition of 6:4, (**B**) antimony Ti$_3$C$_2$T$_z$ (5% mass% HF) hybrid with a composition of 7:3, (**C**) antimony expanded Ti$_3$C$_2$T$_z$ (5% HF) hybrid with a composition of 6:4, (**D**) antimony expanded Ti$_3$C$_2$T$_z$ (5% mass% HF) hybrid with a composition of 7:3, (**E**) v Ti$_3$C$_2$T$_z$ (5% mass% HF), (**F**) not expanded Ti$_3$C$_2$T$_z$ (5% mass% HF).
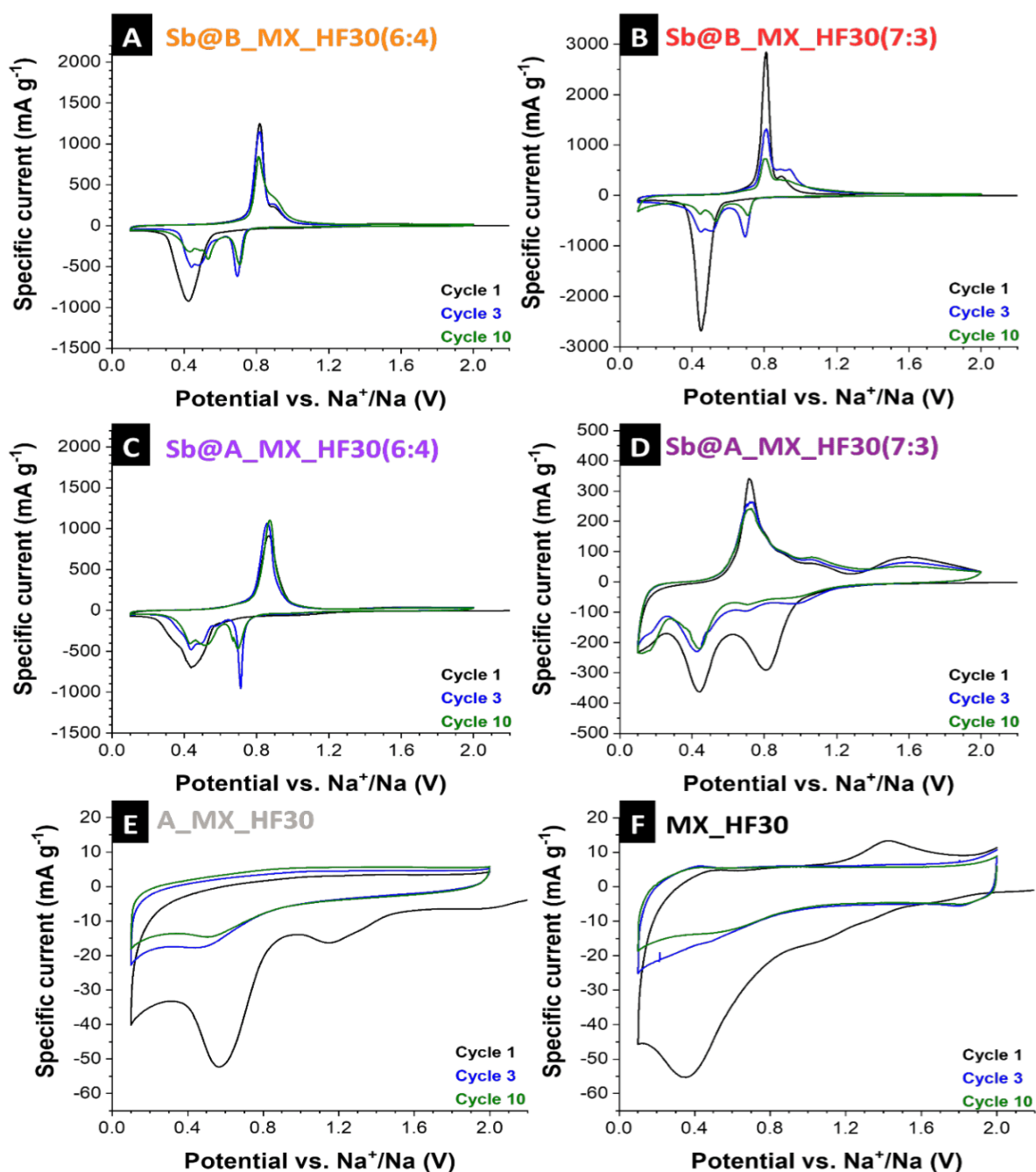
Figure S8: Cyclic voltammograms recorded at 0.1 mV s^{-1} in the potential range of 0.1-2.0 V vs. Na$^+$/Na for (**A**) antimony Ti$_3$C$_2$T$_z$ (30% mass% HF) hybrid with a composition of 6:4, (**B**) antimony Ti$_3$C$_2$T$_z$ (30% mass% HF) hybrid with a composition of 7:3, (**C**) antimony expanded Ti$_3$C$_2$T$_z$ (30% mass% HF) hybrid with a composition of 6:4, (**D**) antimony expanded Ti$_3$C$_2$T$_z$ (30% mass% HF) hybrid with a composition of 7:3, (**E**) expanded Ti$_3$C$_2$T$_z$ (30% mass% HF), (**F**) not expanded Ti$_3$C$_2$T$_z$ (30% mass% HF).
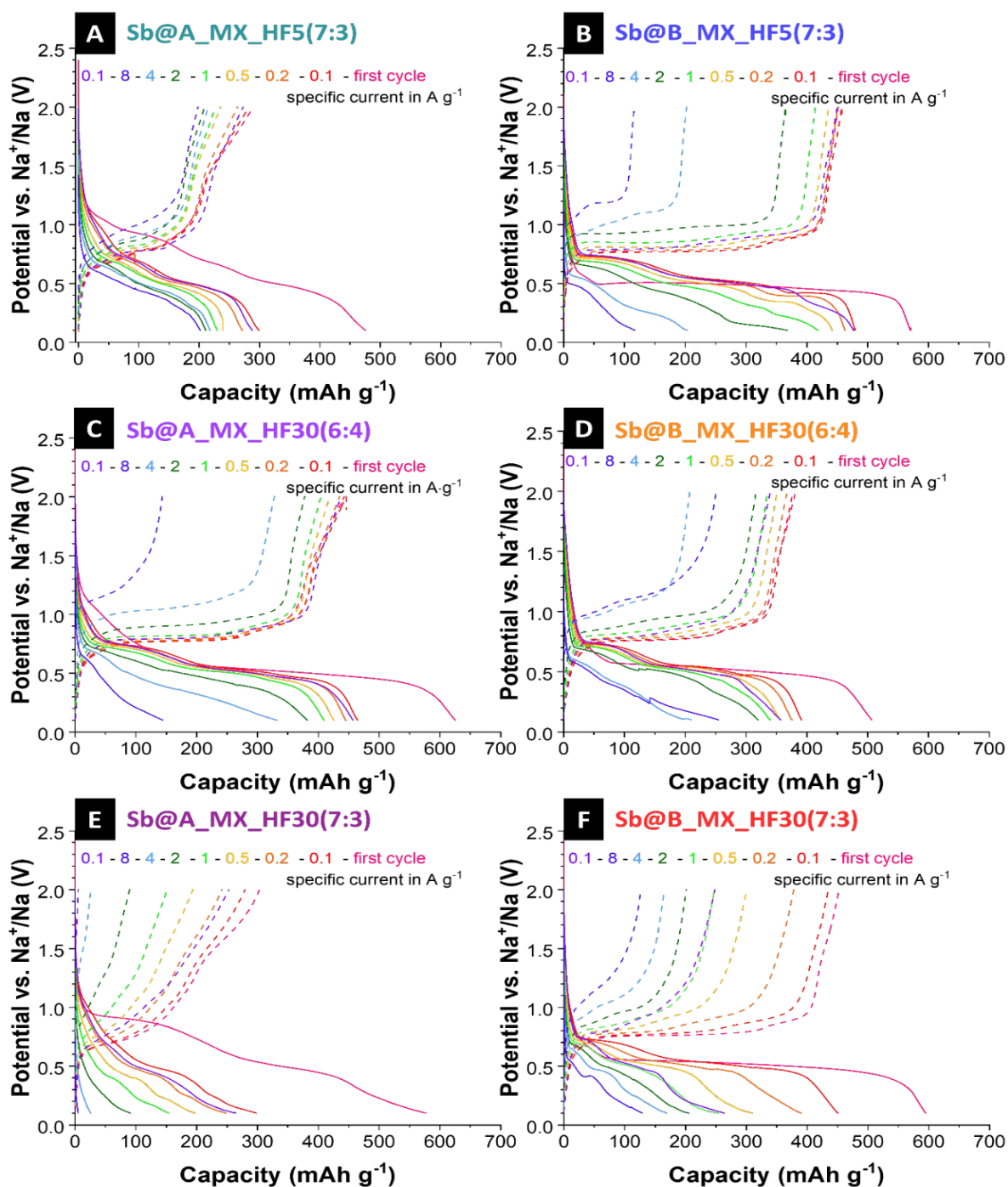
Figure S9: Galvanostatic charge and discharge profiles at different applied specific currents of 0.1-8 A g^{-1} between 1.0 V and 3.0 V *vs.* Na$^+$/Na of (**A**) Sb@A_MX_HF5(7:3), (**B**) Sb@B_MX_HF5(7:3), (**C**) Sb@A_MX_HF30(6:4), (**D**) Sb@B_MX_HF30(6:4), (**E**) Sb@A_MX_HF30(7:3), and (**F**) Sb@B_MX_HF30(7:3).
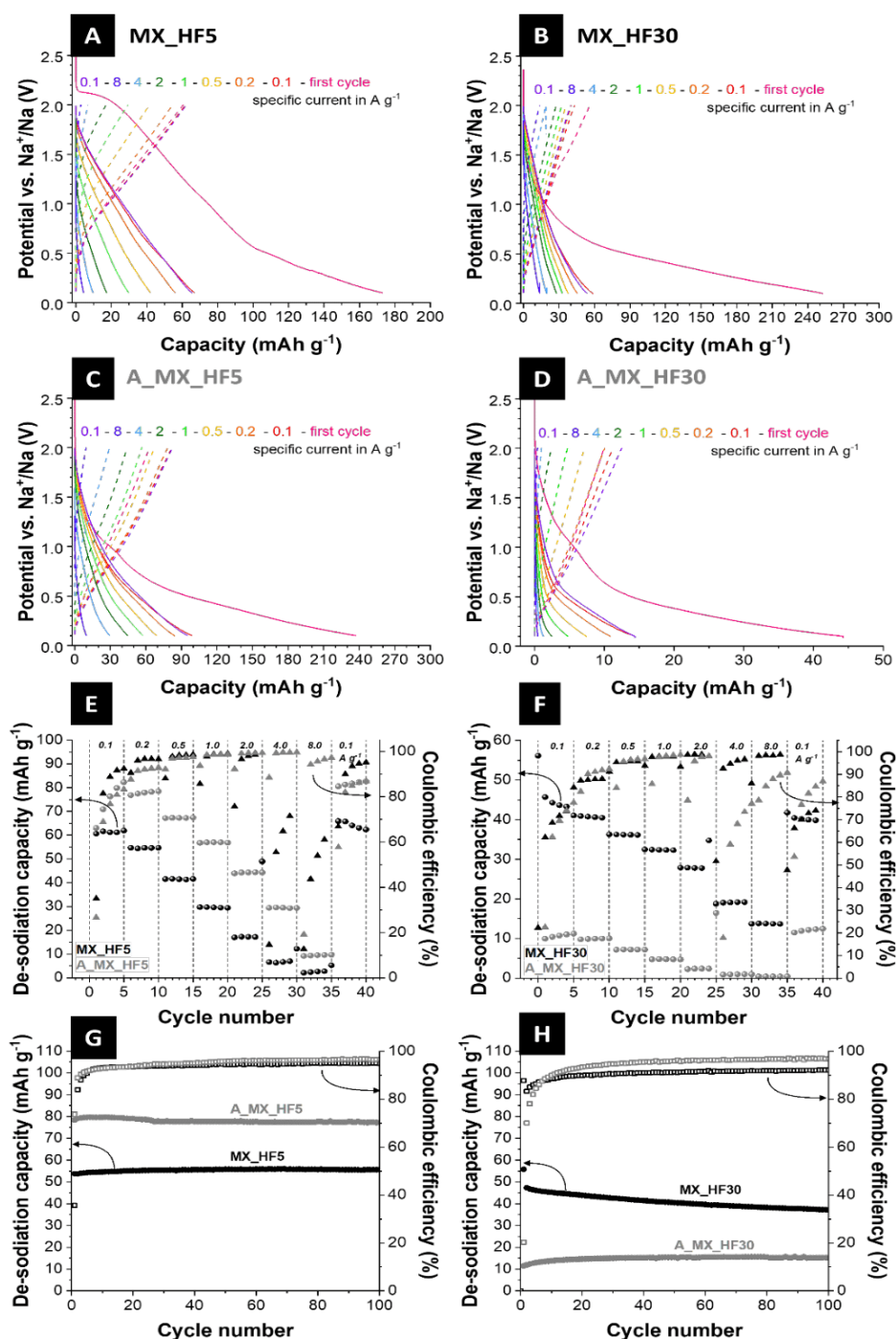
Figure S10: Electrochemical characterization of the non-expanded and expanded $Ti_3C_2T_z$, etched with 5 mass% HF. Galvanostatic charge and discharge profiles at rates of 0.1-8 A g^{-1} (1.0-3.0 V vs. Na^+/Na) of (**A**) MX_HF5, (**B**) MX_HF30, (**C**) A_MX_HF5, and (**D**) A_MX_HF30. Rate performance using galvanostatic charge/discharge cycling and Coulombic efficiency values at different rates for (**E**) MX_HF5 and A_ MX_HF5, (**F**) MX_HF30 and A_MX_HF30. Galvanostatic charge/discharge cycling stability and Coulombic efficiency values at a specific current of 0.1 A g^{-1} for (**G**) MX_HF5 and A_MX_HF5, (**H**) MX_HF30 and A_MX_HF30.
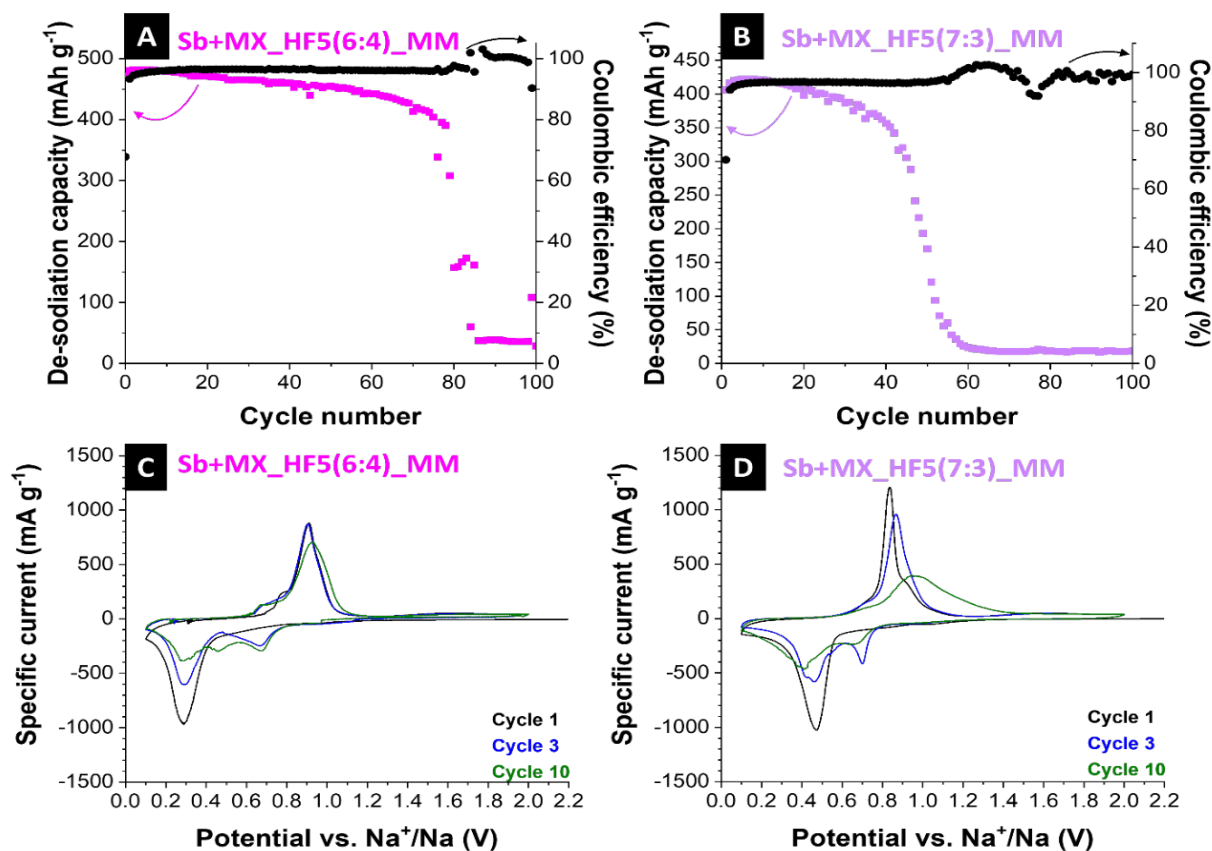
Figure S11: Galvanostatic charge/discharge cycling performance electrochemical stability with corresponding Coulombic efficiency values at a specific current of 0.1 A g^{-1} for (**A**) Sb+MX_HF5(6:4)_MM, and (**B**) Sb+MX_HF5(7:3)_MM. Cyclic voltammograms recorded at a rate of 0.1 mV s^{-1} in the potential range of 0.1-2.0 V vs. Na$^+$/Na for (**C**) Sb+MX_HF5(6:4)_MM, and (**D**) Sb+MX_HF5(7:3)_MM.
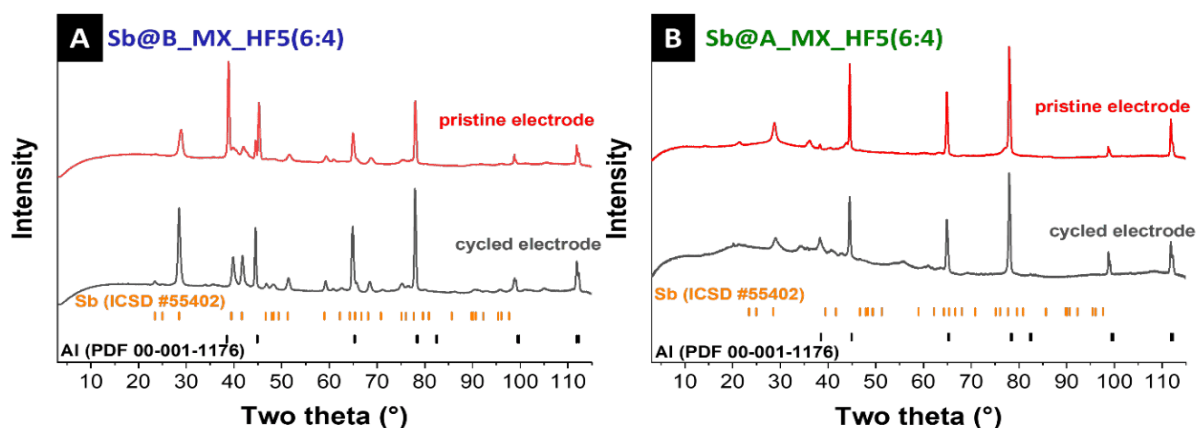
Figure S12: X-ray diffraction pattern of (**A**) pristine and post mortem Sb@B_MX_HF5(6:4) electrode (**B**) pristine and cycled Sb@A_MX_HF5(6:4) electrode. The diffraction patterns were recorded with the setup XRD-2 (see Experimental).
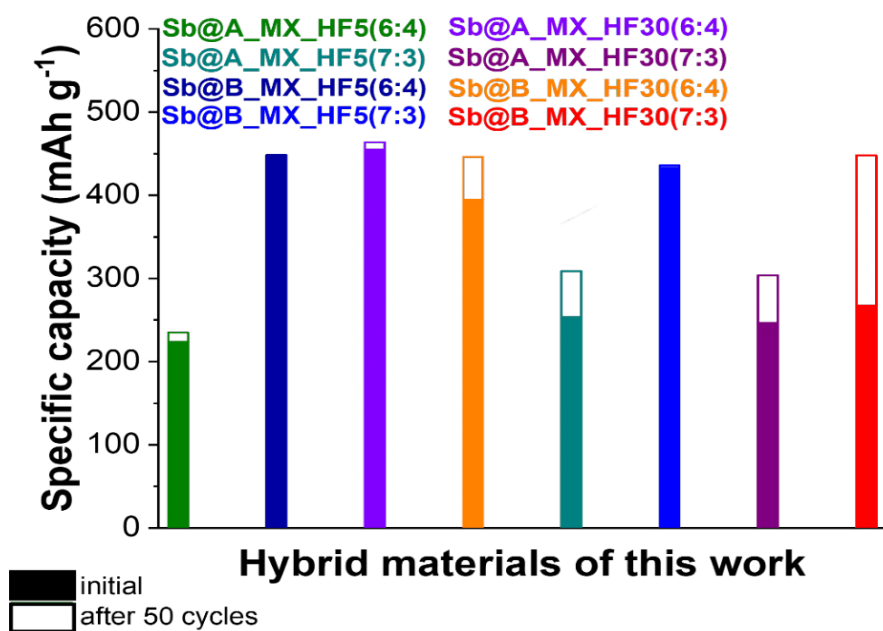
Figure S13: Graphical illustration and overview of initial specific capacities as well as values after 50 cycles of cycling at a specific current of 0.1 A g^{-1} of all hybrid antimony MXene hybrid materials produced in this work.

4.4 Unravelling the electrochemical mechanism in tin oxide/MXene composites as highly reversible negative electrodes for lithium-ion batteries

Antonio Gentile[1,~], Stefanie Arnold[2,3,~] Chiara Ferrara[4,5,6], Stefano Marchionna[1], Yushu Tang[7], Julia Maibach[7], Christian Kübel[7], Volker Presser[2,3,8,*,] and Riccardo Ruffo[4,5,6,*]

[1] Ricerca sul Sistema Energetico - RSE S.p.A., Via R. Rubattino 54 - 20134 Milano, Italy

[2] INM - Leibniz Institute for New Materials, Campus D2.2, 66123 Saarbrücken, Germany

[3] Department of Materials Science and Engineering, Saarland University, Campus D2.266123 Saarbrücken, Germany

[4] Dipartimento di Scienza dei Materiali, Università di Milano Bicocca, 20125 Milano, Italy

[5] National Reference Center for Electrochemical Energy Storage (GISEL) - Consorzio

[6] INSTM, Consorzio Interuniversitario per la Scienza e Tecnologia dei Materiali, I-50121 Firenze, Italy

[7] Institute of Nanotechnology, Helmholtz Institute Ulm & Karlsruhe Nano Micro Facility, Karlsruhe Institute of Technology, Hermann-von-Helmholtz Platz 1, 76344 Eggenstein-Leopoldshafen, Germany

[8] saarene - Saarland Center for Energy Materials and Sustainability, Campus D4.2, 66123 Saarbrücken, Germany

Own Contribution:

Conceptualization, investigation, data curation, visualization, writing – review & editing.
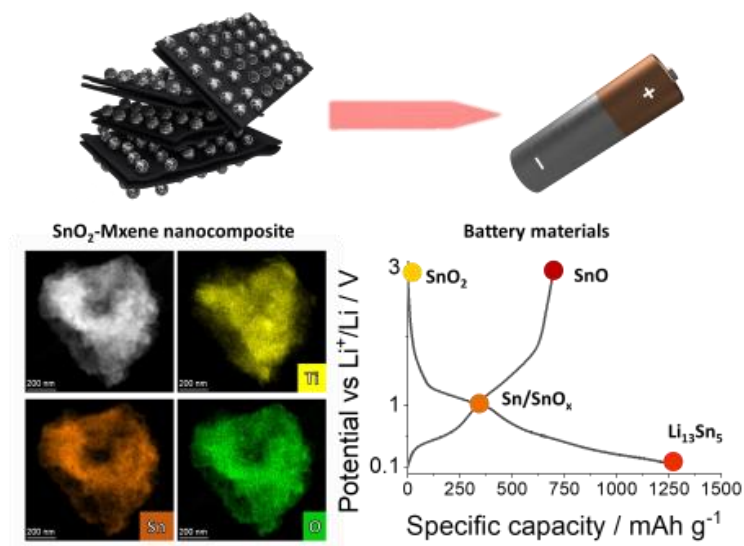
RESEARCH ARTICLE

Unraveling the Electrochemical Mechanism in Tin Oxide/MXene Nanocomposites as Highly Reversible Negative Electrodes for Lithium-Ion Batteries

Antonio Gentile, Stefanie Arnold, Chiara Ferrara, Stefano Marchionna, Yushu Tang, Julia Maibach, Christian Kübel, Volker Presser,* and Riccardo Ruffo*

Lithium-ion batteries are constantly developing as the demands for power and energy storage increase. One promising approach to designing high-performance lithium-ion batteries is using conversion/alloying materials, such as SnO_2. This class of materials does, in fact, present excellent performance and ease of preparation; however, it suffers from mechanical instabilities during cycling that impair its use. One way to overcome these problems is to prepare composites with bi-dimensional materials that stabilize them. Thus, over the past 10 years, two-dimensional materials with excellent transport properties (graphene, MXenes) have been developed that can be used synergistically with conversion materials to exploit both advantages. In this work, a 50/50 (by mass) $SnO_2/Ti_3C_2T_z$ nanocomposite is prepared and optimized as a negative electrode for lithium-ion batteries. The nanocomposite delivers over 500 mAh g^{-1} for 700 cycles at 0.1 A g^{-1} and demonstrates excellent rate capability, with 340 mAh g^{-1} at 8 A g^{-1}. These results are due to the synergistic behavior of the two components of the nanocomposite, as demonstrated by ex situ chemical, structural, and morphological analyses. This knowledge allows, for the first time, to formulate a reaction mechanism with lithium-ions that provides partial reversibility of the conversion reaction with the formation of SnO.

1. Introduction

Rechargeable lithium-ion batteries (LIBs) are experiencing unprecedented success primarily due to the growing market penetration of electric vehicles (EVs). LIBs are the only technology capable of powering EVs today and will likely remain so for the next decades.[1] However, to ensure better acceptance of the technology and to bridge the performance gap that remains with internal combustion engines, EV batteries must be even more efficient, safer, and less expensive than the current state-of-the-art. Cutting-edge LIB cells, called generation 3a, have gravimetric and volumetric energy densities of 250/300 mAh g^{-1} and 700 Wh L^{-1}, respectively, with charging times of about 20 min and lifetimes of 1000 cycles (80% capacity retention).[2] However, these performances seem difficult to overcome while maintaining the rocking chair operation principle that characterizes LIBs, based on the reversible

A. Gentile, S. Marchionna
Ricerca sul Sistema Energetico – RSE S.p.A.
Via R. Rubattino 54, Milano 20134 Italy
S. Arnold, V. Presser
INM – Leibniz Institute for New Materials
Campus D2.2, 66123 Saarbrücken, Germany
E-mail: volker.presser@leibniz-inm.de
S. Arnold, V. Presser
Department of Materials Science and Engineering
Saarland University
Campus D2.2, 66123 Saarbrücken, Germany

C. Ferrara, R. Ruffo
Dipartimento di Scienza dei Materiali
Università di Milano Bicocca
Milano 20125, Italy
E-mail: riccardo.ruffo@unimib.it
C. Ferrara, R. Ruffo
National Reference Center for Electrochemical Energy Storage (GISEL)
Via G. Giusti 9, Firenze 50121, Italy
C. Ferrara, R. Ruffo
INSTM
Consorzio Interuniversitario per la Scienza e Tecnologia dei Materiali
Via G. Giusti 9, Firenze 50121, Italy
Y. Tang, J. Maibach, C. Kübel
Institute of Nanotechnology
Helmholtz Institute Ulm & Karlsruhe Nano Micro Facility
Karlsruhe Institute of Technology
Hermann-von-Helmholtz Platz 1, 76344 Eggenstein-Leopoldshafen, Germany
V. Presser
Saarene – Saarland Center for Energy Materials and Sustainability
Campus D4.2, 66123 Saarbrücken, Germany

121

ion intercalation mechanisms at both electrodes. While it guarantees long lifetimes, it limits the specific energy, especially of the graphite-based negative electrode in almost all LIBs.

Moreover, already in generation 3a, a small quantity of conversion/alloying materials (5–7% of Si/SiO$_x$) have been introduced in the negative electrode to increase the specific capacity without compromising the mechanical integrity. To obtain superior performance for the next LIB generations, it is necessary to increase this quantity while simultaneously finding a way to contain the volume expansions inevitably associated with these compounds. Among different conversion/alloying materials, using SnO$_2$ or SnO$_x$ has several advantages, such as the easy preparation routes and the large availability of raw materials. For example, the use of SnO$_2$ as an anode in LIBs dates back to 1997 when Jeff Dahn's group demonstrated the conversion/alloying reaction mechanism related to the insertion of lithium in glassy or crystalline SnO$_x$:[3]

$$xLi^+ + SnO_{x/2} + xe^- \rightarrow x/2Li_2O + Sn \tag{1}$$

$$yLi^+ + Sn + ye^- \rightleftarrows Li_ySn \tag{2}$$
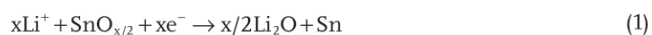
The mechanism can be described as an irreversible reduction of the oxide to metallic Sn with the formation of Li$_2$O (Equation (1)) followed by the reversible alloying/de-alloying reaction (Equation (2)).[4] The amount of irreversible and reversible capacities depends on the oxygen content in the SnO$_x$ and on the stoichiometry of the lithiated alloy, which in the case of tin, can be up to Li$_{4.4}$Sn. The approach was promising, and Fuji Film researchers were close to commercializing SnO$_x$-based electrodes able to provide 50% more capacity than carbon compounds.[5] Later, the Schleich Group published seminal works on thin film crystalline SnO$_2$ electrodes, confirming the conversion/alloying mechanism, and revealing the morphological evolution of the system during cycling.[6–8] It soon became clear that the limiting factor in the commercial application of these electrodes was the decrease of capacity during cycling due to the mechanical instability of the alloys and the volume expansion during the charge and discharge cycle, with loss of electric contact during cycling and electrode pulverization, a process defined as decrepitation.[9] Two main routes have been explored to overcome this issue, namely nanostructuring of electrodes to allow expansion and contraction of the active material,[10] and preparation of nanoscale composites, which in addition to buffering the volumetric changes, allow optimal electron distribution in the electrode bulk. In the former case, SnO$_2$ nanostructured fibers,[11] porous structures,[12,13] nanoparticles,[14,15] hollow nanostructures,[16,17] nanowires,[18–20] and nanotubes[21] have been prepared and characterized. Among the many composites investigated, however, the most interesting results were obtained with composites based on nanostructured carbons,[21–28] graphene,[29–35] metallic structures,[36] and biopolymers.[37] These works showed that nanostructured composites withstand a higher number of cycles, with performances often exceeding the theoretical limits calculated by combining the specific capacities of both SnO$_x$ (according to Equations (1) and (2)) and the secondary phase (carbon, graphene, etc.). In combination with experimental evidence previously obtained by utilizing Mössbauer spectroscopy,[38] this led to a revision of the electrochemical mechanism, attributing partial

reversibility to the conversion reaction (Equation (1)), which has been attributed to the oxidation reaction of freshly formed Sn by de-lithiation with Li$_2$O at the atomic scale. This is usually detected in differential capacity curves as belly-shaped peaks at potentials higher than 1 V.

Among the various two-dimensional conductive structures that can be used to improve the mechanical properties of conversion systems, MXenes have attracted interest in recent years. MXenes are a novel class of 2D layered transition metal carbides, nitrides, and/or carbonitrides with their combined properties such as good electronic conductivity, hydrophilicity, and flexibility.[39–41] In particular, the Ti$_3$C$_2$T$_z$ MXene phases have been recently used to produce composites with SnO$_2$ through different methods, such as self-assembly,[42] atomic layer deposition,[43] in situ quantum dots[44,45] or nanoparticle formation.[46,47] These works are characterized by performances that depend on the relative composition of the two phases, and which are concluded in a specific capacity range between 360[47] and 700 mAh g^{-1}.[43] The discrepancies are also related to the different cycling conditions and the different electrode charges. Despite these differences, in the charge and discharge profiles, there are common characteristics linked to the reaction potentials, which allow, through the differential capacity curves, to highlight the 3 main reactions, that is, the conversion of the oxide, the alloying of the tin and the intercalation in the MXene. Other common characteristics are the low Coulombic efficiencies in the first cycle, generally between 60%[46] and 75%.[45] At the same time, little information is available regarding the charge efficiency in the subsequent cycles, which does not exceed 98.5%.[44,47] Despite these promising results, the progress in using this material combination for high-performance batteries has been stalled. This is because of the limited understanding of the intricate interaction between the oxide nanoparticles and the MXene and of the reaction mechanism when used as an anode in LIB.

In the present study, we show the possibility of preparing Ti$_3$C$_2$T$_z$/SnO$_2$ nanocomposite with excellent energy storage properties thanks to the intimate contact between the two components. With the idea of preparing nanocomposite with excellent reversibility properties, we limited the amount of tin oxide to 50% of the total mass, even if this choice may limit the specific capacity of the system. Moreover, we investigated the reversibility of the conversion reaction, highlighting, for the first time, the presence of amorphous SnO in the de-lithiated electrodes and proposing a coherent mechanism to explain the electrochemical data.

2. Results and Discussion

2.1. Materials Preparation

MXenes are suitable materials for preparing nanocomposites, and several strategies have been reported.[48–51] In the present work, we prepared the desired nanocomposite following the procedure reported in **Figure 1**a. This synthesis was chosen both because it is capable of producing SnO$_2$ single-crystalline nanoparticles with dimensions on the order of a few nanometers,[52] and because it can be carried out easily in the
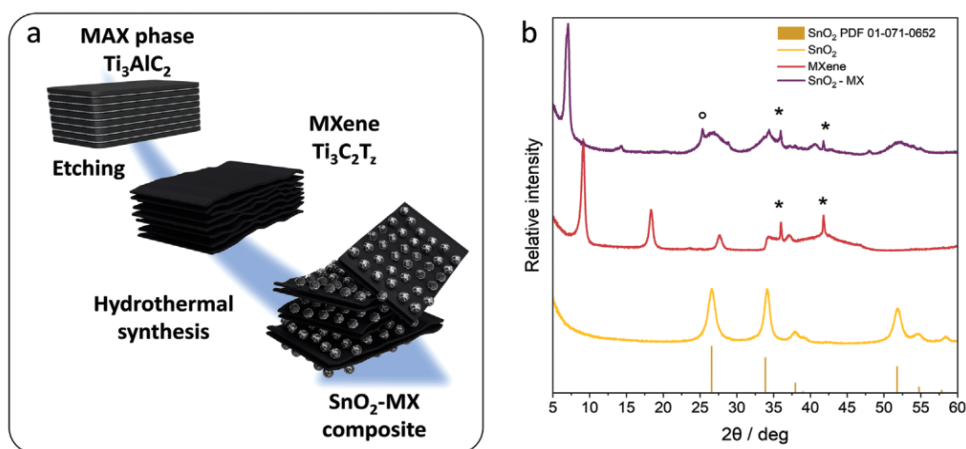
Figure 1. a) Scheme of the synthesis of the nanocomposite and b) X-ray diffractogram for the MXene (red), SnO$_2$ (yellow), and the nanocomposite (purple). Stars mark the TiC reflections; the circle marks the F-doped TiO$_2$ reflection.

presence of dispersed MXenes. The goal is to produce the nanoparticles directly on the surface of Ti$_3$C$_2$T$_z$ layers by promoting their exfoliation during HCl evolution and thus maximizing the interaction between the nanoparticles and the MXene layers. A higher amount of oxide would have led to unacceptable values of Coulombic efficiency, while a decrease in it would have made the specific capacity of the nanocomposite of little application interest. Aiming to characterize the nanocomposite, the two components, Ti$_3$C$_2$T$_z$ and SnO$_2$, have been carefully investigated to set the starting point for the subsequent analysis.

2.2. Materials Characterization

MXene was obtained by using HF-etching in high concentrations to obtain the well-known open-lamellae morphology.[53,54] The obtained MXene structure is confirmed by the X-ray diffraction (Figure 1b). The collected data for the MXene are similar to those previously reported and discussed by our group and generally compliant with diffraction data of MXenes obtained with solution etching.[51,55–58] The main features are the position of the (002) reflection at 9.1° 2θ related to the interlayer distance among the Ti$_3$C$_2$T$_z$ layers and the blurring of the bands in the 30–50° 2θ region associated with the high level of disorder due to the presence of stacking faults and the distribution of the interlayer distances. Characteristic reflections of TiO$_{2-x}$F$_x$ and TiC, as typical impurities for such type of synthesis, are also observed in the diffraction patterns.[55,59–61] Scanning electron micrographs in **Figure 2**a show that the MXene presents the characteristic layered structure and microstructure, as already reported when high concentrations of HF and/or fast etching kinetic are exploited.[53,55] This peculiar morphology was chosen because it was considered favorable for the intercalation of Sn ions during the immersion process in the tin chloride solutions and thus for the nucleation of the oxide on the surface of the lamellae. TEM investigations, reported in Figure 2b, and Figures S1 and S2 (Supporting Information), show the layered arrangement of the structure with extended disordered regions with variable interlayer distances, as also evidenced

by XRD. The EDX maps (Figure S1, Supporting Information) indicate the presence of Ti, C, F, and O compatible with the nominal MXene composition with mixed –F and –O terminations. Small traces of Al are also revealed but strongly localized and ascribable to AlF$_3$ and Al$_2$O$_3$ surface impurities, residues of the synthesis (Table S1, Supporting Information). O and F terminations are homogenously distributed, indicating the absence of clustering. From the selected area electron diffraction (SAED; Figure S2, Supporting Information) it is also possible to detect the presence of surface TiO$_2$ and/or TiO$_{2-x}$F$_{2x}$ nanoparticles, as already evidenced indirectly in our previous study.[55] SAED also confirms the presence of a high level of 2D disorder. From the analysis of the radial distribution function (RDF) patterns,[62,63] revealing the short-range structure, it is possible to detect the typical Ti–C (2.14 Å) and Ti–Ti (3.06 Å) distances expected for the parental MAX phase (comparison with the simulated data in Figure S2, Supporting Information) confirming that the etching procedure unalters the Ti$_3$C$_2$ skeleton. Moreover, the obtained bond distances agree with those derived from the X-ray absorption spectroscopy (XAS) analysis performed on the same sample by our group.[56] The additional peaks observed at 1.33 and 1.67 Å in the experimental RDF profile are ascribed to the O/F terminations interacting with trapped interlayer water molecules. This attribution is confirmed by the absence of such distances in the RDF profile of the MAX phase. The Ti–Ti bond distance is similar to the Ti–C distance, as already evidenced by XAS investigation, density functional theory (DFT), and pair distribution function (PDF) analysis.[56,64,65] The surface chemistry has been characterized through XPS analysis (**Figure 3**). Both –F and –O terminations are observed, confirming the energy-dispersive X-ray (EDX) results. Titanium is observed in several oxidation states associated with different coordination with C, O, and F.[55,61,66] The presence of surface TiO$_2$ is detected, again in agreement with previous observations.[66,67]

To compare the results of the nanocomposite with the pristine material, it is also relevant to determine the structure, stoichiometry, and morphology of the tin oxide powders obtained via hydrolysis of the tin chloride. The diffraction
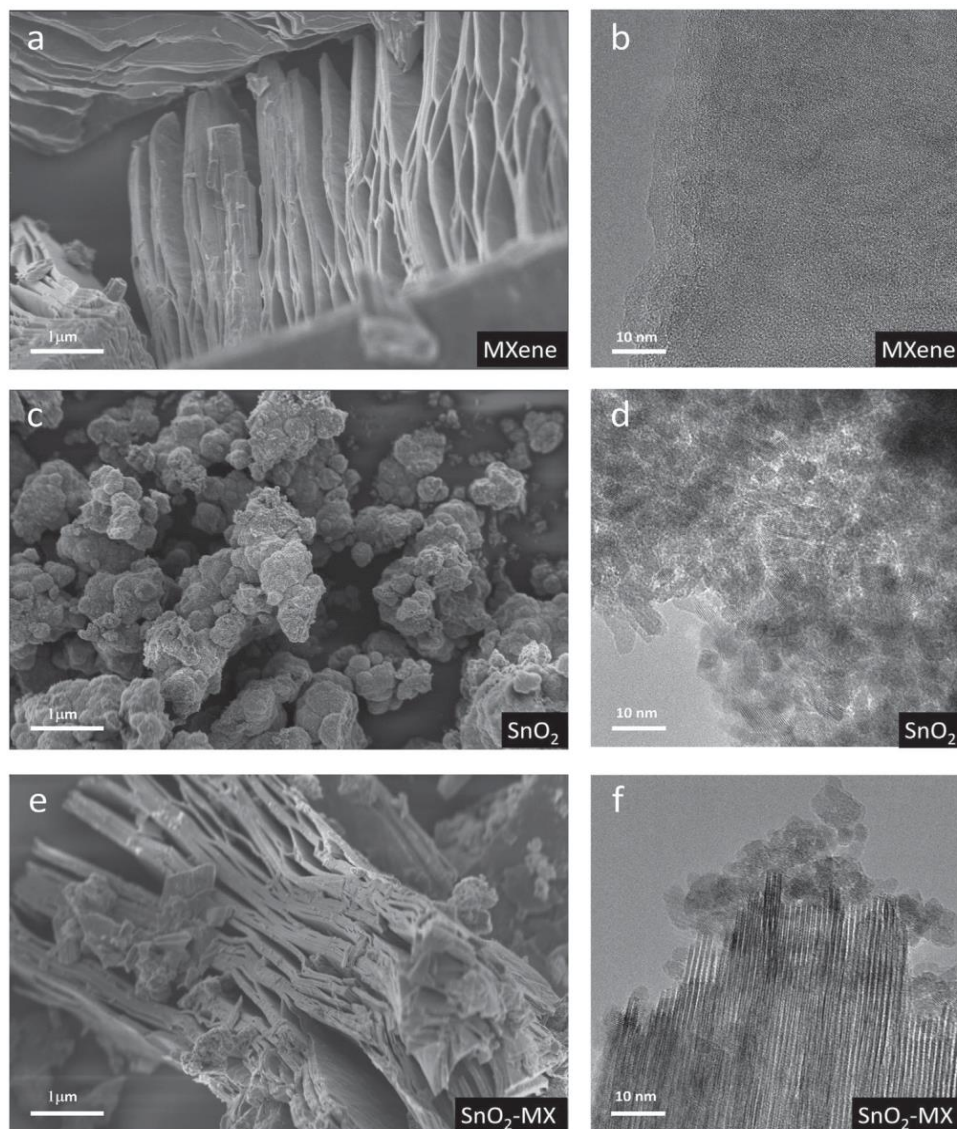
Figure 2. Scanning and transmission electron micrographs of a,b) MXene; c,d) SnO_2; e,f) SnO_2-MX nanocomposite.

pattern collected for the tin oxide powders (Figure 1b) is compatible with the cassiterite structure (PDF 01-071-0652), and the broadening of all reflections indicates that the powders are nanostructured; indeed, the size of the coherently scattering domains estimated from the two most intense XRD reflections is 8 ± 2 nm. This is also confirmed by the transmission electron microscopy (TEM) images (Figure 2d), revealing coherent crystalline domains of several nanometers, which tend to aggregate in secondary structures. Scanning electron micrographs (Figure 2c) reveal spherical agglomerates with a particle size of several hundred nanometers. The structural and morphological features can be further observed in TEM using diffraction (SAED) and energy dispersive X-ray spectroscopy (EDX), as represented in Figure S3 (Supporting Information), obtained on a single spherical agglomerate with a diameter of 350–400 nm. The diffraction pattern of such agglomerates reveals their

crystalline nature, with diffraction cones formed by many spots due to the random orientation of coherent crystalline domains. The surface chemistry has been investigated using XPS analysis, as reported in Figure 3. The analysis performed on the tin oxide powders suggests that the systems can be described as cassiterite SnO_2 and not as SnO, confirming XRD and TEM results.

The 50:50 nanocomposite, which represents the best compromise between higher specific capacity and reversibility of the electrochemical process, has been characterized by exploiting the same combination of techniques; results are reported in Figures 1–3. The X-ray diffractograms of the SnO_2-MX nanocomposite can be rationalized as the sum of the two components and indicates the successful synthesis of the nanocomposite (Figure 1b). Indeed, the main reflections of both the MXene and SnO_2 are still visible, indicating that the

124
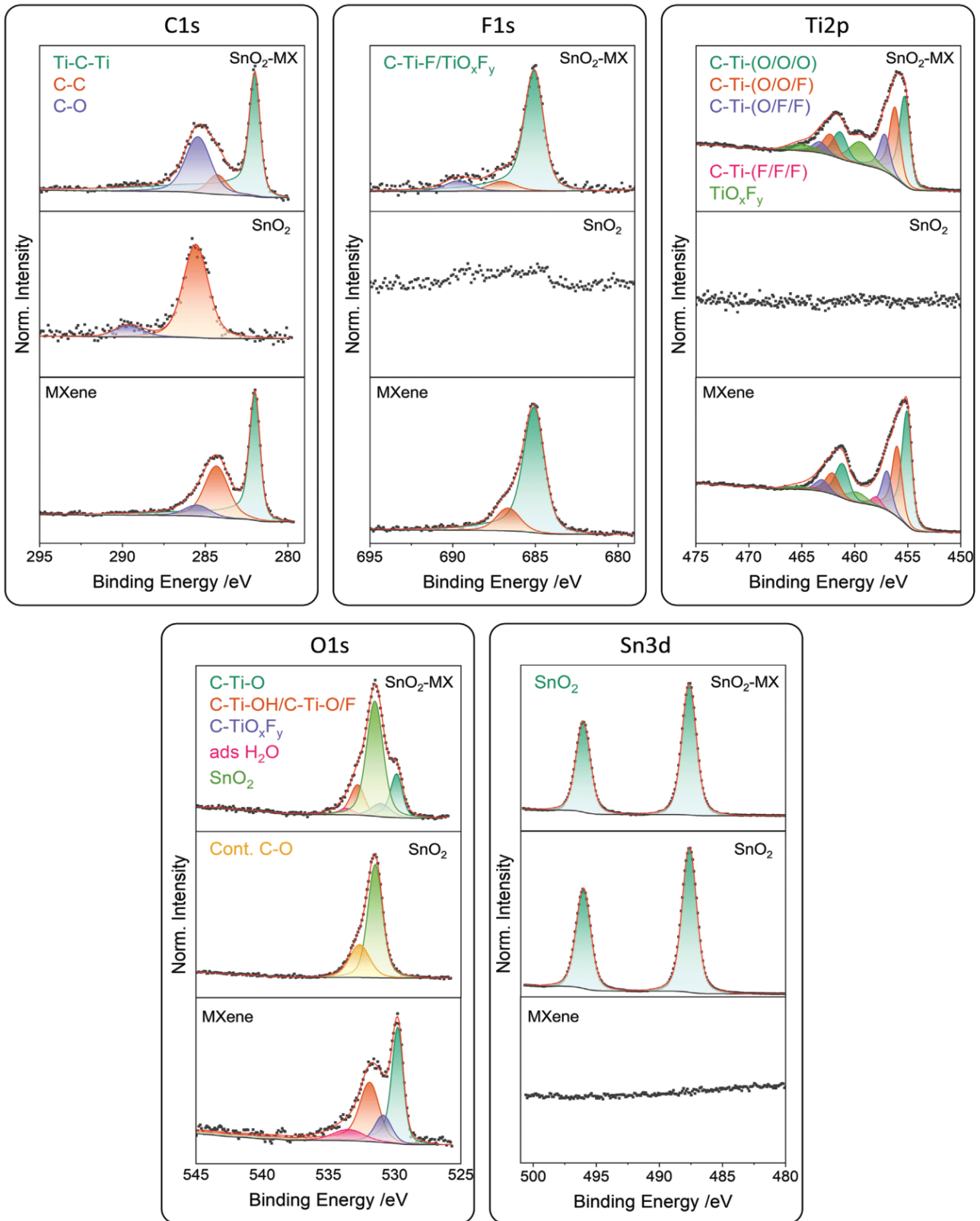
Figure 3. X-ray photoelectron spectra of the MXene, SnO_2, and the SnO_2-MX nanocomposite.

two structures are still present in the nanocomposite. At the same time, a significant shift at lower angles is observed for the 00l class of reflection of the MXene. In particular, the (002) reflection is downshifted to 6.9° 2θ, indicating a widening of the interlayer distance moving from 9.6 to 12.6 Å. This can be related to the intercalation of Sn ions within the layers and/or the trapping of water molecules during the synthesis. The reflections of TiC and TiO_2 impurities are still visible; the amount of doped TiO_2 seems to be slightly increased for the pure MXene. This can be attributed to the open lamellar structure, which exposes a larger surface of the MXene layers, which are more susceptible to oxidation. Finally, it can be observed that the reflections attributed to the SnO_2 in the nanocomposite are broader than in the pure compound suggesting the formation of smaller particles of tin oxides when nucleating on the MXene surface. Similar evidence comes from electron microscopy. The nanocomposite clearly shows the presence of the two structures, as highlighted in Figure 2e,f. The open accordion-like structure of the MXene is present and unaltered by the preparation of the nanocomposite. SnO_2 particles with different degrees of aggregation can be observed on the MXene blocks (large clusters) and within the lamellae (small clusters). It is thus evident that the synthesis does not compromise the structure of the MXene and the SnO_2 powder. The SAED patterns confirm that the bond distances related to the Ti_3C_2 skeleton and the SnO_2 systems are the same as for the pristine materials. The EDX maps confirm the two components' homogeneous distribution and fine dispersion (Figure S4, Supporting Information). The XPS data obtained for the nanocomposite reveal that no strong surface modification has been introduced (Figure 3). The spectral region of oxygen in the nanocomposite appears as the superimposition of the contributions from the O-terminations of the MXene and the oxygen anions in SnO_2. At the same time, other elemental spectra are unaffected after the assembling procedure.

These results thus confirm the successful preparation of the 50:50 SnO_2-MX nanocomposite; the two components are present and unaltered. The fine dispersion of the two components is obtained at the nanometric level with the SnO_2 particles anchored on the MXene layers' surfaces.

2.3. Electrochemical Performance

For the sake of clarity, before discussing the electrochemical characteristics of the nanocomposite, the behaviors of pristine materials will be discussed (Figure S5, Supporting Information). Charge and discharge profiles and the resulting differential capacity curves were obtained in 3-electrode cells in all 3 cases, while long cycling of the nanocomposite was performed in two-electrode coin cells.

In pure SnO_2, the charge/discharge profiles (Figure S5a, Supporting Information) agree with the literature and are related to the conversion/alloying processes widely discussed in the introduction. The first cycle cathodic capacity is 1595 mAh g^{-1}, slightly higher than the theoretical value obtained considering the conversion reaction and the fully alloying to $Li_{4.4}Sn$ (1493 mAh g^{-1}, 8.4 electrons per SnO_2 unit formula). The difference could be ascribed to the SEI

formation (starting below 1.3 V), also considering that the alloying reaction could be incomplete. The first cycle oxidation delivers 955 mAh g^{-1}, which corresponds to 5.4 electrons per unit formula, a value larger than the full de-lithiation of $Li_{4.4}Sn$ to Sn (782 mAh g^{-1}). Moreover, a not negligible part of such capacity (250 mAh g^{-1}) is obtained at a potential >1.2 V, implying the partial reversibility of the conversion reaction and/or the reoxidation of the freshly formed SEI. The cycling properties of the SnO_2-based electrodes are very poor, with a capacity retention of 18% after 20 cycles (Figure S5c, Supporting Information). The specific capacity trend evidences the decrepitation of the electrode during oxidation, the cathodic capacity at a given cycle is practically equal to the anodic capacity at the previous cycle. The differential capacity curves help to better analyze electrochemical behavior (Figure S5b, Supporting Information). No reduction processes are detected up to 1.6 V during the first lithiation, while below this threshold, according to recent in situ characterizations,[68] SnO_2 reacts to SnO and Li_2SnO_3. At around 1.0 V the main peak of the conversion reaction is observed, leading to the formation of metallic Sn and Li_2O. The further reduction peaks are attributed to the alloying between Sn and Li, with the following formation of intermediated phases such as LiSn, $Li_{2.6}Sn$, $Li_{3.5}Sn$, and $Li_{4.4}Sn$ (cut off at 0.01 V). During the reoxidation, the peaks at 0.45 and 0.62 V are the footprint of the de-alloying reaction. In comparison, a further oxidative process (belly-shaped peak at 1.27 V) is detected, probably due to the partial conversion of Sn to SnO_x.

In pristine MXene, the charge/discharge profile (Figure S5d, Supporting Information) shows the already observed features first reported by Naguib et al. in 2012.[69] Monotonic variation of the potential with the charge indicates a pseudocapacitive behavior during lithium-ion intercalation and de-intercalation. The specific cathodic and anodic capacities for the first cycle are 405 and 205 mAh g^{-1}, respectively, with a charge efficiency of 51%. The rate capability shows a good performance where the material can maintain a capacity from 120 mAh g^{-1} at 500 mA g^{-1} with excellent capacity retention of 99% after 70 cycles (Figure S5f, Supporting Information). The pseudocapacitive behavior is also seen in the differential capacity curves (Figure S5e, Supporting Information), which show a flat shape with little pronounced peaks after the first cycle which, instead, is characterized by the peaks of the SEI formation, the MXene stabilization, and the Li^+ intercalation.

The electrochemical characteristics of the nanocomposites are reported in **Figure 4**. During these characterizations, the lower cut-off voltage was increased to 0.1 V because of the slight irreversibility of MXene reduction below this threshold, thus maximizing the electrode lifetime. The potential profiles (Figure 4a) reflect the behaviors of both active materials, showing the two main SnO_2 conversion/alloying processes (the latter is not complete due to the higher cut-off voltage) with a monotonic variation of the potential due to pseudocapacitive intercalation in MXene. The specific capacities for the first cycle are 1230 ± 70 mAh g^{-1} and 695 ± 50 mAh g^{-1}, for the cathodic and the anodic scan, respectively, with a Coulombic efficiency of 56.5 ± 3.5% (data obtained with 4 different cells). The capacity profiles, the black curves in Figure 4b (first cycle) show in the cathodic process three main peaks related to the SEI

2202484 (6 of 13)
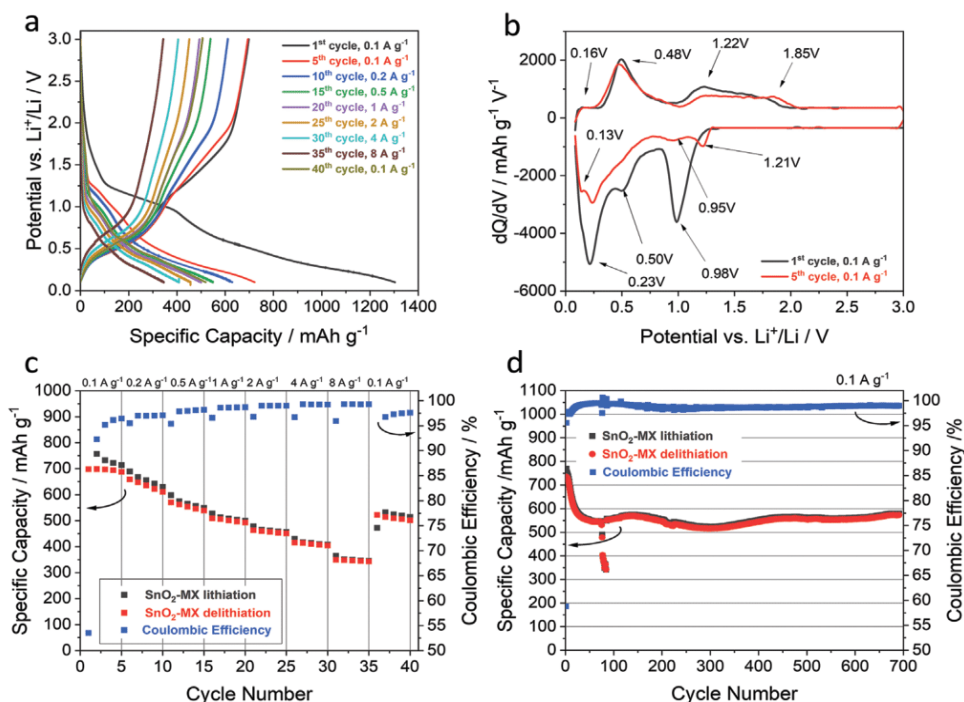
Figure 4. a) Charge–discharge profiles, b) differential capacity, c) rate capability test, and d) long-term stability test for SnO_2-MX nanocomposite as lithium-ion battery electrode.

formation, the conversion process, and the alloying of Sn with lithium. The first two processes happen at similar potentials and may be superimposed. During the successive oxidation, after the main process at 0.48 V (peak), which can be identified as the de-alloying reaction, a large amount of charge (around 300 mAh g^{-1}) is obtained at a potential higher than 1.0 V. This may be ascribed to the removing of lithium-ions from the MXene sheets; however, the presence of the peak at 1.22 V is not fully in agreement with the typical pseudocapacitive behavior of $Ti_3C_2T_x$, whose profile should be less pronounced.[70,71] Since the conversion reaction (Equation (1)) should occur during the initial cycles, analyzing the differential capacity in the 5th cycle reveals essential information about the mechanism. Here (red curve in Figure 4b), during the reduction of the nanocomposite, a clear contribution to the capacity is present at a potential >0.75 V, with two peaks at 1.21 and 0.95 V. In this zone, the MXene is electroactive due to the Li$^+$ intercalation in between the lamellae; however, the presence of the well-defined peak is an indication of a simultaneous phase transformation. The successive reoxidation shows a pseudocapacitive zone after the stable de-alloying reaction. In conclusion, the analysis of the differential capacity curves of the 5th cycle suggests the partial reversibility of the conversion reaction.

The three-electrode set-up was used to evaluate the kinetic performances of the nanocomposite/electrolyte interface (rate capability test) because the overvoltage at the Li$^+$/Li counter electrode can affect specific capacity values at the highest currents increasing the real cut-off voltages of the working electrode. In the rate capability test (Figure 4c), the nanocomposite shows excellent properties, being able to sustain 450 mAh g^{-1}

at 2 A g^{-1}, 400 mAh g^{-1} at 4 A g^{-1}, and 340 mAh g^{-1} at 8 A g^{-1}. These values correspond to C-rate values of around 5, 10, and 20 C for commercial LIB negative electrodes with 400 mAh g^{-1}. This remarkable performance is probably the result of the synergistic interaction between the two materials. The long-term stability test (Figure 4d), performed in a coin cell in the low current regime (100 mA g^{-1}), which is normally a critical condition because secondary/degradation reactions have more time to occur, reveals that the material needs 50 cycles to stabilize the electrochemical performances. This effect has already been observed in the literature due to the initial decrease in Sn grain size formed by the conversion reaction with the loss of active material.[72] Moreover, it has been proven that this results in a decrease of specific capacity until the Sn particles fall below a critical value that establishes greater reversibility in the conversion reaction, promoting the oxidation of more Sn to SnO by consuming Li_2O (see discussion in the next section). The tradeoff between Sn's fragmentation and the conversion reaction's reversibility is also the key to understanding the slow performance fluctuation observed from cycle 50 to cycle 700. In this cycle range, where the performance can be considered stable, an anodic capacity of 525 ± 25 mAh g^{-1} with a charge efficiency of 98.8 ± 0.3% is observed. This represents a promising result considering the low current used during cycling and the use of commercial, non-optimized electrolyte. The stability test at 100 mA g^{-1} lasted about 7700 h (over 320 days). Despite the long period and 700 cycles, the electrode showed no change in specific capacity from the stable values obtained after 50 cycles (100% capacity retention). In contrast, the first cycle capacity retention is 72%.

RESULTS AND DISCUSSION

2.4. Ex Situ Analysis of Cycled Electrodes

A detailed characterization of selected cycled electrodes has been performed to identify the electrochemical behavior's origin and explain the electrochemical reaction's mechanism. Detailed chemical (XPS, EDX), structural (SAED), and morphological (STEM) characterizations have been performed on cycled electrodes. XPS analysis has been carried out on electrodes collected from cells at the open-circuit voltage (OCV) and reduced to 1.0, 0.5, and 0.1 V. A further electrode was obtained after reoxidation to 3.0 V. Results are reported in **Figure 5**, and Figures S6 and S7 (Supporting Information). As demonstrated by our data, both nanocomposite components are electrochemically active. Indeed, both Ti and Sn regions
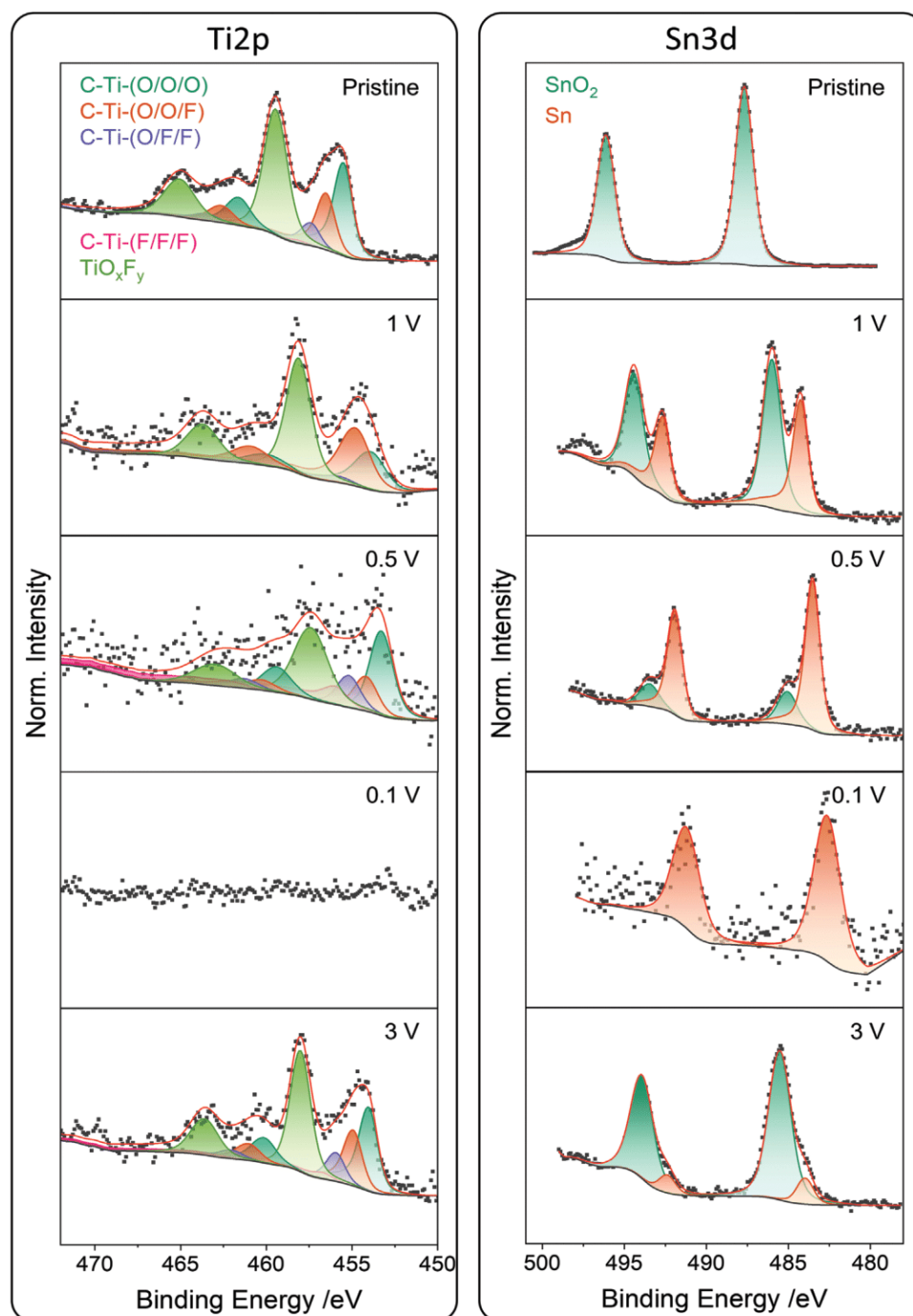
Figure 5. Ex situ Ti and Sn XPS spectra for electrodes cycled at different potentials.

(Figure 5) changed significantly upon cycling, but the two species behaved differently. The Ti region is characterized by different signals attributed to the different oxidation states and local coordination in the MXene phase, as already discussed in the first section. The evolution of this complex signal with lithiation is essentially a shift of all the components, attributed to the pseudocapacitive behavior of the MXene, already evidenced by a previous study.[55] Due to SEI formation, the Ti 2p intensity drops significantly for low potentials but recovers in the de-lithiated state, indicating a dynamic SEI or surface layer that could contribute to the pseudocapacitive effect. The reoxidized electrode presents a Ti spectrum similar to the pristine compound, highlighting the reversible behavior of the MXene components. Contrary, the Sn region presents sharp changes with the appearance of new peaks for the electrode cycled to 1.0 V. From the OCV to this potential, a small lithiation of the SnO_2 is expected, with the tin oxide behaving like an insertion system for a very small fraction of Li.[68] Below this potential, the reduction promotes the conversion reaction to Sn and Li_2O, attested by the appearance of the peak ascribed to metallic Sn (Figure 5).

Moreover, the contribution of Li_2O in the O 1s spectral region (Figure S6, Supporting Information) starts to appear at low energy (528.5 eV). These contributions (Sn and LiO_2) grow in intensity for the electrode reduced to 0.5 V and reach the highest intensities for the electrode reduced to 0.1 V. In this state, the component associated with Sn(IV) is not visible, suggesting the complete conversion of the tin oxide. Metallic Sn formed during the reduction can further lithiate at 0.1 V, forming various alloys. Based on the XPS results, it is impossible to distinguish among these different species as no suitable bulk-specific point of reference for the binding energy is present in the system. Although XPS is not the best tool to investigate alloying reactions, the Li 1s spectral region analysis provides information about the lithiation process, as further supported by STEM. A lithium peak (Figure S6, Supporting Information) appears at 1.0 V as the effect of the insertion reaction, and it shows the features of the characteristic Li^+ in oxides or fluorides. However, as the alloying reaction proceeds (spectrum obtained at 0.1 V), a not negligible contribution is present at lower binding energy, as observed from the clear shoulder at 54.5 eV. This low energy contribution is usually associated with the higher electronic density of lithium bonded with less electronegative atoms, such as metallic Sn.

The analysis of the XPS for the electrode cycled to 3.0 V helps to understand the oxidation mechanism. The electrode's primary component in the Sn 3d spectrum cycled to 3.0 V shifts back to higher binding energies. However, compared to the electrode cycled to 1.0 V, a shift in binding energy toward lower binding energies remains, indicating that the conversion reaction is only partly reversible and the reoxidation does not produce SnO_2 but SnO_x. Additionally, a small shoulder at lower binding energies shows either incomplete reversibility of the conversion process or incomplete de-alloying. The signal related to Li_2O in the O 1s region is not observed at 3.0 V anymore, indicating that the tin reoxidation mechanism occurs at the expense of the lithium oxide formed during the conversion reaction. Finally, incomplete oxidation to SnO_2 and or de-alloying is also supported by the remaining Li intensity

at 3.0 V (Figure S6, Supporting Information), which, however, could also be incorporated in the SEI as LiF or other electrolyte decomposition products. This is further supported by the F1s and P2p regions (Figure S7, Supporting Information), where the decomposition of the $LiPF_6$ electrolyte salt can be observed. Traces of Na (not reported) are also observed due to the CMC binder used to prepare the electrodes. Given the absence of spectral variations in the Na 1s signal, we can exclude the Na as electrochemically active in the explored conditions.

To further characterize the conversion reaction and its reversibility, electrodes in the fully reduced state (0.1 V) and reoxidized to 3.0 V have been analyzed through (S)TEM, EDX, and SAED; the vacuum transfer holder was used to avoid contact with air; results on representative portions of such electrodes are reported in **Figure 6** and Figure S8 (Supporting Information). The fully reduced sample is unstable under the high-energy electron beam of HR-TEM, which induces the growth of metallic lithium. The STEM images collected for the 0.1 V cycled sample reveal that the electrode is mechanically stable after the alloying reaction. The elemental maps (EDX) of Sn and Ti show the intimate contact between the two materials, with the two elements homogeneously distributed in the corresponding phases. SAED results show that the external part of the MXene lamellae is covered with LiF nanometric particles formed as SEI. At the same time, the Sn-rich phase is compatible with the crystalline $Li_{13}Sn_5$ alloy, a direct demonstration of the alloying reaction. At the cut-off voltage of 0.1 V, the total composition should be Li_3Sn with the equilibrium between the $Li_{13}Sn_5$ and the Li_7Sn_2 alloys.[73] This is in agreement with the phase observed by SAED, also considering that the two crystalline phases ($Li_{13}Sn_5$ and Li_7Sn_2) have very similar d-spacing. The analysis of the reoxidized electrode again highlights that the reaction does not involve a mechanical degradation of the nanocomposite, with the Ti and Sn EDX maps showing good homogeneity at the nanoscale level. The SAED analysis confirms the XPS results, indicating the conversion back to SnO. The analysis of the total diffraction data reveals that the conversion does not entirely restore the initial configuration as, together with SnO_2, it is possible to detect SnO in an amorphous state. On the contrary, the MXene component is stable and structurally unaltered by the reduction and oxidation reactions.

The electrochemical performance of our material is in line with SnO_2/MXene composites obtained with similar approaches (nanoparticles or other nanostructures on MXene sheets), as evident from **Table 1**. All the materials reported have low first-cycle charge efficiencies, require several cycles to reach stable performance, and show excellent lifetimes in half cells versus Li. However, as evident in the table, there is generally little attention to either the ratio of oxide to MXene or the Coulombic efficiency in subsequent cycles, which does not allow for a proper evaluation of the durability of full cells equipped with lithiated positive electrodes. In our case, these aspects have been carefully evaluated, and the 50/50 composition by mass was chosen as a compromise between increasing specific capacity and the reversibility of the electrochemical processes. The irreversible capacity value at the first cycle is an intrinsic characteristic of conversion materials related to oxide reduction. It often depends on the contact between the electrode surface and electrolyte, thus on the separator used and the type of cell.
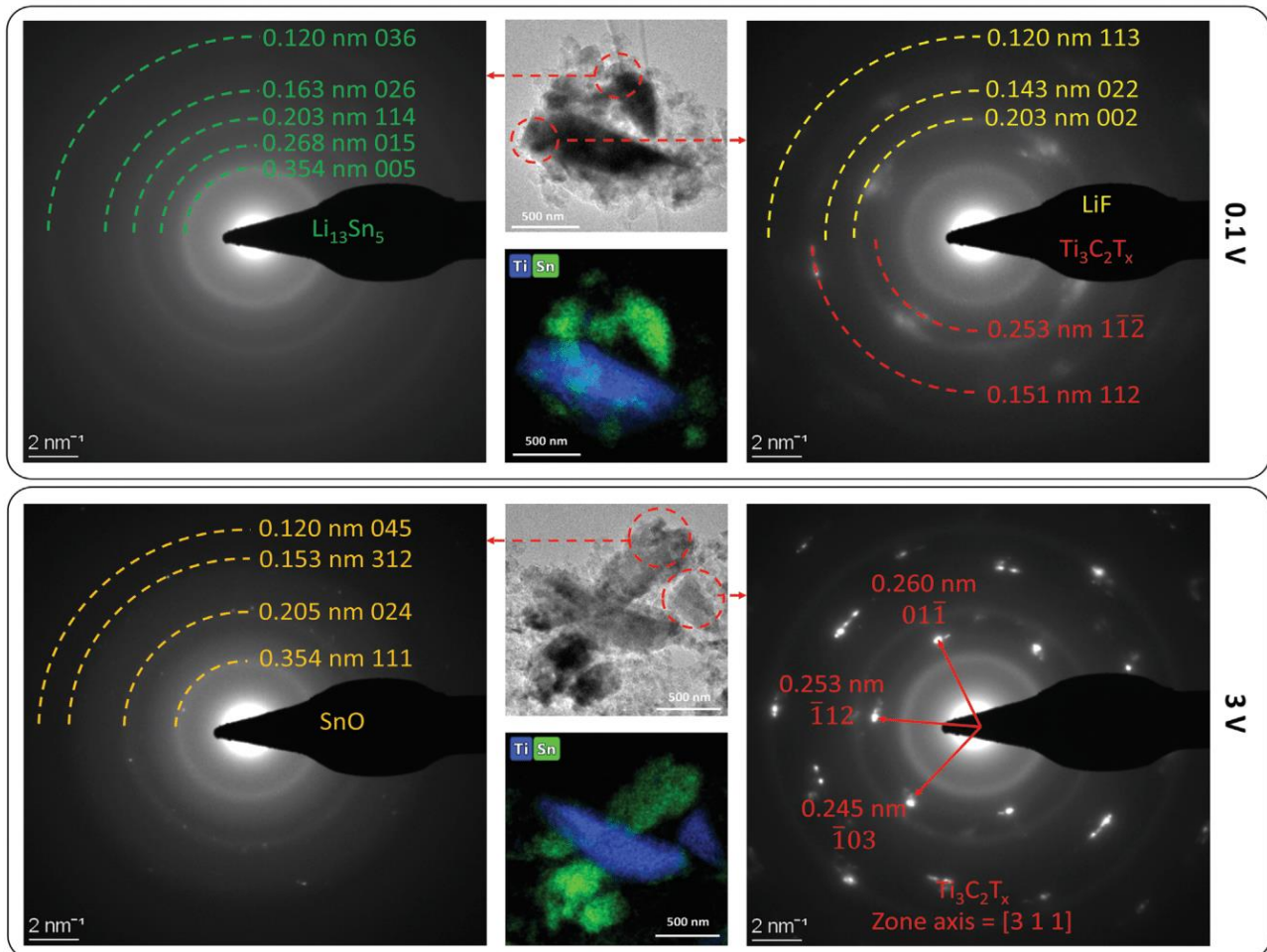
Figure 6. Ex situ STEM, EDS, SAED analysis for 0.1 and 3.0 V cycled electrodes.

In our case, we observed a marked increase from the custom-made cell to the coin cell. Methods to remedy this characteristic include chemical, and electrochemical pre-cycling, reductions by direct contact with lithium metal, or using sacrificial agents in the electrolyte.[74]

3. Conclusions

Exploiting the possibility of preparing SnO_2 nanoparticles in the presence of $Ti_3C_2T_z$ MXene, we successfully prepared a 50/50 mass% nanocomposite electrode able to provide an

Table 1. Comparison among the performances of different SnO_2/MXene composites. NR: not reported.

SnO_2[a] morphology	SnO_2 mass%	Anodic specific capacity 1st cycle [mAh g^{-1}]	Coulombic efficiency 1st cycle	Stable anodic specific capacity [mAh g^{-1}]	Coulombic efficiency	Number of cycles	Charge retention[b]	Ref.
TLs	NR	1041	71%	900	NR	50	100%	[42]
NWs	70%	1700	NR	700	NR	500	100%	[43]
QDs	NR	960	73%	697	98.5%	700	100%	[44]
QDs	NR	637	61%	506	NR	160	98%	[45]
NPs	NR	961	60%	900	NR	1000	100%	[46]
NPs	NR	350	35%	350	98%	300	100%	[47]
NPs	50%	695	56%	525	98.8%	700	100%	This work

[a]TL = thin layer; NWs = nanowires, QDs = quantum dots, NPs = nanoparticles; [b]Calculated after stabilization of the electrode.

Adv. Mater. Interfaces **2023**, 2202484

2202484 (10 of 13)

© 2023 The Authors. Advanced Materials Interfaces published by Wiley-VCH GmbH

anodic capacity of 525 mAh g^{-1} for hundreds of cycles at low current over 10 months in lithium-ion battery half cell configuration. The electrode also shows promising kinetic properties, sustaining at 8 A g^{-1} currents with a specific capacity of 340 mAh g^{-1}.

Due to the scarcity of chemical, morphological and structural data on such systems, we have used XPS and STEM to understand the electrode reactions better and elucidate the electrochemical mechanism. The results demonstrated that during the first cycle, the SnO_2 is converted to Sn first (Equation (1) in the Introduction) and Li_2O, while the formed Sn is then lithiated to the $Li_{13}Sn_5$ phase at a lower potential. Considering the amount of charge involved in the conversion reaction (711 mAh g^{-1}), in the alloying to Li_3Sn (533 mAh g^{-1}), and in MXene intercalation and stabilization (around 400 mAh g^{-1}), the total amount of charge at the first reduction of the 50–50% nanocomposite should be around 825 mAh g^{-1}. The excess of measured charge (417 mAh g^{-1}) could be due to the SEI formation or to the higher extension of the alloying reaction since, at the cut-off potential at 0.1 V, a higher amount of $Li_{3.5}Sn$ may also be formed.

During the de-lithiation, the alloying reaction is mechanically stabilized thanks to the presence of the MXene sheets and the intimate interaction between the nanoparticles and the layered structure. Moreover, the conversion reaction becomes partially reversible, with the formation of amorphous SnO consuming part of the Li_2O following Equation (3):

$$Sn + Li_2O \rightleftarrows SnO + 2e^- + 2Li^+ \qquad (3)$$

Considering the amount of charge involved in Equation (3), the alloying to $Li_{13}Sn_5$, and the MXene contribution (100 mAh g^{-1}), the stable capacity of the nanocomposite should be around 545 mAh g^{-1}. This value, again, is less than the measured specific capacity of the first 25 cycles and may be influenced by the extension of the alloy lithiation. However, it agrees with the observed stable charge capacity during cycling (525 mAh g^{-1}).

Considering the overall performance, our nanocomposite material showed a high specific capacity, excellent capacity retention, and excellent rate capability. The charge storage properties are achieved due to the presence of tin oxide, while the reversibility and kinetics of the electrochemical reactions are due to the synergistic interaction between tin oxide and MXene, the latter being able to both act as a buffer for the conversion reaction and to enhance the charge transport proprieties in the electrode.

4. Experimental Section

MXene Preparation: MXene was prepared from the corresponding MAX phase of Ti_3AlC_2 by chemical etching. The MAX precursor was obtained by spark plasma synthesis using a procedure already described in the previous work, where a complete structural and morphological characterization of the precursor can also be found. The etching was done following the synthetic method used in previous work.[55,75] The etching was performed using the following route: 500 mg of Ti_3AlC_2 (size <50 μm) was kept under stirring in a Teflon beaker containing an aqueous solution of hydrofluoric acid (HF) 30 mass% for 5 h at room temperature. The powder was recovered and washed by a series of centrifugation steps until the pH of the washing liquid was ≈6. The resulting product was dried for 12 h under a vacuum at 80 °C.

Nanocomposite Preparation: The SnO_2-MX nanocomposite synthesis was carried out by modifying a synthesis protocol of SnO_2 nanopowders proposed in the literature.[52] The synthetic scheme is shown in Figure 1. In a typical synthesis, 400 mg of $SnCl_4·5H_2O$ (Sigma-Aldrich, 98% purity) was dissolved in 40 mL of deionized water. 170 mg of MXenes ($Ti_3C_2T_z$) were soaked overnight in this solution to promote the pre-intercalation of Sn ions into the 2D structure. The obtained solution was sonicated for 1 h, then 4 g of urea (Sigma-Aldrich, >99% purity), 8 mL of fuming HCl, and water were added under stirring (total volume was 160 mL). The solution was transferred into a Teflon-lined stainless-steel autoclave of 200 mL. The autoclave was sealed and maintained at 140 °C for 24 h. Finally, it was cooled down to room temperature in ambient conditions. The resulting white product was retrieved by centrifugation and washed several times with MilliQ water and absolute ethanol to reach a pH of 7. The powders were dried in a vacuum at 50 °C for 4 h.

To further investigate the system, tin oxide has been prepared as a pure compound following the same procedure reported without adding the MXene.

X-Ray Diffraction: X-ray diffraction measurements of the MXene nanocomposites were performed with a D2 PHASER diffractometer (Bruker AXS) with a copper X-ray source (Cu-K$_\alpha$, λ = 1.5406 Å, 30 kV, 10 mA). The samples were measured in the range of 5 to 60 2θ deg and with 0.02 s per step.

Electron Microscopy: The morphology of the samples was characterized using Zeiss Gemini scanning electron microscope (SEM) equipped with a field emission source (FE-SEM). The electrons were accelerated using an electric potential of 1–5 kV for image acquisition. The samples were fixed on a steel sample holder using conductive carbon adhesive tapes. Scanning electron micrographs were analyzed using the ImageJ software.

The microstructure and elementary distribution of the samples were characterized by a probe-corrected Themis 300 transmission electron microscope (TEM; Thermo Fisher Scientific) equipped with a high-angle annular dark-field (HAADF) detector and a Super-X energy dispersive X-ray spectroscopy (EDX) detector. Selected area electron diffraction (SAED) was used to characterize the crystal structure of the samples. The measurements were carried out at an accelerating voltage of 300 kV. The pristine powder sample was dispersed on a TEM grid coated with holey carbon film. Samples of the cycled electrodes were scratched off using tweezers and dispersed on a TEM grid. The samples were transferred from a glove box into the TEM using a Gatan vacuum transfer holder (model number 648).

X-Ray Photoelectron Spectroscopy (XPS): XPS measurements were carried out using a K-Alpha spectrometer (Thermo Fisher Scientific), equipped with a micro-focused, monochromated Al Kα X-ray source (1486.7 eV) with 400- μm spot size. The data was recorded using a pass energy of 50 eV in the concentric hemispherical analyzer. To prevent sample charging during the analysis, the powder samples required K-α charge compensation system using a combination of both electrons and low-energy argon ions. Powder samples (MXene, SnO_2, SnO_2-MX nanocomposite) were measured as is and deposited directly on conductive copper tape. The electrodes were removed from the batteries at the desired state of charge and rinsed with DMC inside a glovebox to remove access electrolyte salts. To avoid reactions of the dried electrodes with air and moisture, the samples were transferred under Ar atmosphere to the spectrometer. Data acquisition and processing, using the Thermo Avantage software, as described in reference.[66] The binding energy was referenced to C-Ti component at 282 eV for the powder samples containing MXene and to the hydrocarbon peak at 285 eV for all other samples, while the overall binding energy scale was controlled using well-known photoelectron peaks of metallic Ag, Au, and Cu. Data fitting followed the proposed model for MXenes described in reference[66] using a smart background as implemented in the Thermo Avantage software.

Electrode Preparation: For the electrode preparation, a soft mixing method was used to preserve the morphology of the nanocomposites.

The 50/50_SnO$_2$-MX electrodes were manufactured by mixing the active material, conductive carbon, and carboxymethyl cellulose (CMC) in the ratio of 7:2:1. Firstly, the active material and carbon were mixed in a mortar. Afterward, the dry powder mix was dry-mixed at 1000 rpm for 5 min in a SpeedMixer DAC 150 SP from Hauschild. Milli Q water was added dropwise to the mixture until the slurry achieved suitable viscosity. This paste was again mixed at 1000 rpm for 5 min following 2500 rpm for 5 min. Finally, the CMC binder solution was added, and the viscous electrode paste kept mixing at 800 rpm for 10 min. The slurry was stirred for 12 h with a magnetic stirrer to obtain a homogeneous slurry. The slurry was spread with a doctor blade onto copper current collector foil (thickness of 9 μm, MTI) with an automatic coater (MTI Mini Cast Coater MSK-AFA-HC100), in a wet thickness of 200 μm. The electrode coatings were initially dried at room temperature overnight and in a vacuum at 110°C for 12 h to remove the remaining solvent. The electrode was dry-pressed with a rolling machine (HR01 rolling machine, MTI), and finally, discs of 12 mm diameter were punched, resulting in a mass loading of the active material of ≈1.5 mg cm^{-2}.

Electrochemical Characterization: Custom-built polyether ether ketone (PEEK) cells with spring-loaded titanium pistons were used for electrochemical tests.[76] After drying all cell parts at 120 °C for 14 h, the cells were assembled inside an Ar-filled glovebox (MBraun Labmaster 130; O$_2$; and H$_2$O < 0.1 ppm). The cells were arranged in a three-electrode configuration for electrochemical measurements, with the nanocomposites used as the working electrode and lithium metal as the counter and reference electrode. The electrolyte used was commercial LP30 (1 M LiPF$_6$ in ethylene carbonate and dimethyl carbonate (EC/DMC 50:50 by volume, Sigma-Aldrich)). All electrode potentials are reported versus the Li$^+$/Li standard couple.

All electrochemical measurements were carried out in a climate chamber (Binder) with a constant temperature of +25 ± 1 °C. Rate performance measurements were conducted at different currents, in the potential window 0.1–3.0 V, to get more information about the half-cell rate capability and stability at higher currents. The applied specific currents were 0.1, 0.2, 0.5, 1.0, 2.0, 4.0, 8.0 A g^{-1}, and (again) 0.1 A g^{-1}.

The long-term stability tests were performed at 0.1 A g^{-1}. Two-electrode coin cells (2032-type) were used for these tests because they provide better sealing than PEEK cells, considering that the long-term tests lasted about one year due to the relatively low current, which provides more realistic results. All values obtained for cell capacity refer to the respective total active mass of the nanocomposite.

The cells were tested in a climatic chamber from BINDER with a constant temperature kept at 25 ± 1 °C, and the instruments used for the electrochemical analyses were a multichannel Bio-Logic VMP3 and an Arbin Battery Cycler.

Supporting Information

Supporting Information is available from the Wiley Online Library or from the author.

Conflict of Interest

The authors declare no conflict of interest.

Data Availability Statement

The data that support the findings of this study are available from the corresponding author upon reasonable request.

[1] D. Castelvecchi, *Nature* **2021**, *596*, 336.
[2] E. Commission, *SET-Plan ACTION n°7 –Declaration of Intent "Become competitive in the global battery sector to drive e-mobility forward"*, https://setis.ec.europa.eu/implementing-actions/set-plan-documents_en, **2016**.
[3] I. A. Courtney, J. R. Dahn, *J. Electrochem. Soc.* **1997**, *144*, 2943.
[4] I. A. Courtney, J. R. Dahn, *J. Electrochem. Soc.* **1997**, *144*, 2045.
[5] Y. Idota, T. Kubota, A. Matsufuji, Y. Maekawa, T. Miyasaka, *Science* **1997**, *276*, 1395.
[6] T. Brousse, R. Retoux, U. Herterich, D. M. Schleich, *J. Electrochem. Soc.* **1998**, *145*, 1.
[7] T. Brousse, *Solid State Ionics* **1998**, *113–115*, 51.
[8] R. Retoux, T. Brousse, D. M. Schleich, *J. Electrochem. Soc.* **1999**, *146*, 2472.
[9] R. A. Huggins, W. D. Nix, *Ionics (Kiel)* **2000**, *6*, 57.
[10] L. F. Nazar, G. Goward, F. Leroux, M. Duncan, H. Huang, T. Kerr, J. Gaubicher, *Int. J. Inorg. Mater.* **2001**, *3*, 191.
[11] N. Li, C. R. Martin, B. Scrosati, *J. Power Sources* **2001**, *97–98*, 240.
[12] A. Yu, R. Frech, *J. Power Sources* **2002**, *104*, 97.
[13] J. C. Lytle, H. Yan, N. S. Ergang, W. H. Smyrl, A. Stein, *J. Mater. Chem.* **2004**, *14*, 1616.
[14] H.-J. Ahn, H.-C. Choi, K.-W. Park, S.-B. Kim, Y.-E. Sung, *J. Phys. Chem. B* **2004**, *108*, 9815.
[15] S. Han, B. Jang, T. Kim, S. M. Oh, T. Hyeon, *Adv. Funct. Mater.* **2005**, *15*, 1845.
[16] X. W. Lou, Y. Wang, C. Yuan, J. Y. Lee, L. A. Archer, *Adv. Mater.* **2006**, *18*, 2325.
[17] Z. Wang, D. Luan, F. Y. C. Boey, X. W. (David) Lou, *J. Am. Chem. Soc.* **2011**, *133*, 4738.
[18] M.-S. Park, G.-X. Wang, Y.-M. Kang, D. Wexler, S.-X. Dou, H.-K. Liu, *Angew. Chem., Int. Ed.* **2007**, *46*, 750.
[19] P. Meduri, C. Pendyala, V. Kumar, G. U. Sumanasekera, M. K. Sunkara, *Nano Lett.* **2009**, *9*, 612.
[20] J. Y. Huang, L. Zhong, C. M. Wang, J. P. Sullivan, W. Xu, L. Q. Zhang, S. X. Mao, N. S. Hudak, X. H. Liu, A. Subramanian, H. Fan, L. Qi, A. Kushima, J. Li, *Science* **2010**, *330*, 1515.

[21] L. Li, X. Yin, S. Liu, Y. Wang, L. Chen, T. Wang, *Electrochem. Commun.* **2010**, *12*, 1383.

[22] J. Fan, T. Wang, C. Yu, B. Tu, Z. Jiang, D. Zhao, *Adv. Mater.* **2004**, *16*, 1432.

[23] F. Su, X. S. Zhao, Y. Wang, J. Zeng, Z. Zhou, J. Y. Lee, *J. Phys. Chem. B* **2005**, *109*, 20200.

[24] Y. Wang, H. C. Zeng, J. Y. Lee, *Adv. Mater.* **2006**, *18*, 645.

[25] X. W. Lou, D. Deng, J. Y. Lee, L. A. Archer, *Chem. Mater.* **2008**, *20*, 6562.

[26] H.-X. Zhang, C. Feng, Y.-C. Zhai, K.-L. Jiang, Q.-Q. Li, S.-S. Fan, *Adv. Mater.* **2009**, *21*, 2299.

[27] J. S. Chen, Y. L. Cheah, Y. T. Chen, N. Jayaprakash, S. Madhavi, Y. H. Yang, X. W. Lou, *J. Phys. Chem. C* **2009**, *113*, 20504.

[28] J. Liang, C. Yuan, H. Li, K. Fan, Z. Wei, H. Sun, J. Ma, *Nano-Micro Lett.* **2018**, *10*, 21.

[29] J. Yao, X. Shen, B. Wang, H. Liu, G. Wang, *Electrochem. Commun.* **2009**, *11*, 1849.

[30] L.-S. Zhang, L.-Y. Jiang, H.-J. Yan, W. D. Wang, W. Wang, W.-G. Song, Y.-G. Guo, L.-J. Wan, *J. Mater. Chem.* **2010**, *20*, 5462.

[31] X. Wang, X. Zhou, K. Yao, J. Zhang, Z. Liu, *Carbon N Y* **2011**, *49*, 133.

[32] X. Zhou, L.-J. Wan, Y.-G. Guo, *Adv. Mater.* **2013**, *25*, 2152.

[33] D. Wang, J. Yang, X. Li, D. Geng, R. Li, M. Cai, T.-K. Sham, X. Sun, *Energy Environ. Sci.* **2013**, *6*, 2900.

[34] J. Sun, L. Xiao, S. Jiang, G. Li, Y. Huang, J. Geng, *Chem. Mater.* **2015**, *27*, 4594.

[35] K. Zhao, L. Zhang, R. Xia, Y. Dong, W. Xu, C. Niu, L. He, M. Yan, L. Qu, L. Mai, *Small* **2016**, *12*, 588.

[36] J. Deng, C. Yan, L. Yang, S. Baunack, S. Oswald, H. Wendrock, Y. Mei, O. G. Schmidt, *ACS Nano* **2013**, *7*, 6948.

[37] B. Jiang, Y. He, B. Li, S. Zhao, S. Wang, Y.-B. He, Z. Lin, *Angew. Chem., Int. Ed.* **2017**, *56*, 1869.

[38] I. A. Courtney, R. Dunlap, J. R. Dahn, *Electrochim. Acta* **1999**, *45*, 51.

[39] B. Anasori, M. R. Lukatskaya, Y. Gogotsi, *Nat. Rev. Mater.* **2017**, *2*, 16098.

[40] M. Naguib, M. Kurtoglu, V. Presser, J. Lu, J. Niu, M. Heon, L. Hultman, Y. Gogotsi, M. W. Barsoum, *Adv. Mater.* **2011**, *23*, 4248.

[41] M. Naguib, M. W. Barsoum, Y. Gogotsi, *Adv. Mater.* **2021**, *33*, 2103393.

[42] B. Ahmed, D. H. Anjum, Y. Gogotsi, H. N. Alshareef, *Nano Energy* **2017**, *34*, 249.

[43] Y.-T. Liu, P. Zhang, N. Sun, B. Anasori, Q.-Z. Zhu, H. Liu, Y. Gogotsi, B. Xu, *Adv. Mater.* **2018**, *30*, 1707334.

[44] J. Xiong, L. Pan, H. Wang, F. Du, Y. Chen, J. Yang, C. (John) Zhang, *Electrochim. Acta* **2018**, *268*, 503.

[45] L. Wang, Y. He, D. Liu, L. Liu, H. Chen, Q. Hu, X. Liu, A. Zhou, *J. Electrochem. Soc.* **2020**, *167*, 116522.

[46] C. Zhao, Z. Wei, J. Zhang, P. He, X. Huang, X. Duan, D. Jia, Y. Zhou, *J. Alloys Compd.* **2022**, *907*, 164428.

[47] F. Wang, Z. Wang, J. Zhu, H. Yang, X. Chen, L. Wang, C. Yang, *J. Mater. Sci.* **2017**, *52*, 3556.

[48] S. A. Jasim, J. M. Hadi, M. J. C. Opulencia, Y. S. Karim, A. B. Mahdi, M. M. Kadhim, D. O. Bokov, A. T. Jalil, Y. F. Mustafa, K. T. Falih, *J. Alloys Compd.* **2022**, *917*, 165404.

[49] L. Biswal, R. Mohanty, S. Nayak, K. Parida, *J. Environ. Chem. Eng.* **2022**, *10*, 107211.

[50] H. T. Das, T. E. Balaji, S. Dutta, N. Das, T. Maiyalagan, *Int. J. Energy Res.* **2022**, *46*, 8625.

[51] C. Ferrara, A. Gentile, S. Marchionna, R. Ruffo, *Curr. Opin. Electrochem.* **2021**, *29*, 100764.

[52] G. Xi, J. Ye, *Inorg. Chem.* **2010**, *49*, 2302.

[53] M. Alhabeb, K. Maleski, B. Anasori, P. Lelyukh, L. Clark, S. Sin, Y. Gogotsi, *Chem. Mater.* **2017**, *29*, 7633.

[54] M. Benchakar, L. Loupias, C. Garnero, T. Bilyk, C. Morais, C. Canaff, N. Guignard, S. Morisset, H. Pazniak, S. Hurand, P. Chartier, J. Pacaud, V. Mauchamp, M. W. Barsoum, A. Habrioux, S. Célérier, *Appl. Surf. Sci.* **2020**, *530*, 147209.

[55] A. Gentile, C. Ferrara, S. Tosoni, M. Balordi, S. Marchionna, F. Cernuschi, M. Kim, H. Lee, R. Ruffo, *Small Methods* **2020**, *4*, 2000314.

[56] C. Ferrara, A. Gentile, S. Marchionna, I. Quinzeni, M. Fracchia, P. Ghigna, S. Pollastri, C. Ritter, G. M. Vanacore, R. Ruffo, *Nano Lett.* **2021**, *21*, 8290.

[57] L. Verger, V. Natu, M. Carey, M. W. Barsoum, *Trends Chem.* **2019**, *1*, 656.

[58] R. M. Ronchi, J. T. Arantes, S. F. Santos, *Ceram. Int.* **2019**, *45*, 18167.

[59] R. B. Rakhi, B. Ahmed, M. N. Hedhili, D. H. Anjum, H. N. Alshareef, *Chem. Mater.* **2015**, *27*, 5314.

[60] M. Naguib, V. N. Mochalin, M. W. Barsoum, Y. Gogotsi, *Adv. Mater.* **2014**, *26*, 992.

[61] J. Halim, K. M. Cook, M. Naguib, P. Eklund, Y. Gogotsi, J. Rosen, M. W. Barsoum, *Appl. Surf. Sci.* **2016**, *362*, 406.

[62] D. J. H. Cockayne, *Annu. Rev. Mater. Res.* **2007**, *37*, 159.

[63] X. Mu, S. Neelamraju, W. Sigle, C. T. Koch, N. Totò, J. C. Schön, A. Bach, D. Fischer, M. Jansen, P. A. van Aken, *J. Appl. Crystallogr.* **2013**, *46*, 1105.

[64] Q. Tang, Z. Zhou, P. Shen, *J. Am. Chem. Soc.* **2012**, *134*, 16909.

[65] C. Shi, M. Beidaghi, M. Naguib, O. Mashtalir, Y. Gogotsi, S. J. L. Billinge, *Phys. Rev. Lett.* **2014**, *112*, 125501.

[66] V. Natu, M. Benchakar, C. Canaff, A. Habrioux, S. Célérier, M. W. Barsoum, *Matter* **2021**, *4*, 1224.

[67] J. Yang, M. Naguib, M. Ghidiu, L. M. Pan, J. Gu, J. Nanda, J. Halim, Y. Gogotsi, M. W. Barsoum, *J. Am. Ceram. Soc.* **2016**, *99*, 660.

[68] M. Mirolo, X. Wu, C. A. F. Vaz, P. Novák, M. El Kazzi, *ACS Appl. Mater. Interfaces* **2021**, *13*, 2547.

[69] M. Naguib, J. Come, B. Dyatkin, V. Presser, P.-L. Taberna, P. Simon, M. W. Barsoum, Y. Gogotsi, *Electrochem. Commun.* **2012**, *16*, 61.

[70] S. Fleischmann, J. B. Mitchell, R. Wang, C. Zhan, D. Jiang, V. Presser, V. Augustyn, *Chem. Rev.* **2020**, *120*, 6738.

[71] S. Fleischmann, Y. Zhang, X. Wang, P. T. Cummings, J. Wu, P. Simon, Y. Gogotsi, V. Presser, V. Augustyn, *Nat. Energy* **2022**, *7*, 222.

[72] P. Lian, X. Zhu, S. Liang, Z. Li, W. Yang, H. Wang, *Electrochim. Acta* **2011**, *56*, 4532.

[73] M. Winter, J. O. Besenhard, *Electrochim. Acta* **1999**, *45*, 31.

[74] V. Aravindan, Y. S. Lee, S. Madhavi, *Adv. Energy Mater.* **2017**, *7*, 1602607.

[75] S. Arnold, A. Gentile, Y. Li, Q. Wang, S. Marchionna, R. Ruffo, V. Presser, *J. Mater. Chem. A* **2022**, *10*, 10569.

[76] D. Weingarth, M. Zeiger, N. Jäckel, M. Aslan, G. Feng, V. Presser, *Adv. Energy Mater.* **2014**, *4*, 1400316.

**ADVANCED
MATERIALS
INTERFACES**

Supporting Information

Unraveling the Electrochemical Mechanism in Tin Oxide/ MXene Nanocomposites as Highly Reversible Negative Electrodes for Lithium-Ion Batteries

Antonio Gentile, Stefanie Arnold, Chiara Ferrara, Stefano Marchionna, Yushu Tang, Julia Maibach, Christian Kübel, Volker Presser,* and Riccardo Ruffo*

Supporting Information

Unraveling the electrochemical mechanism in tin oxide / MXene nanocomposites as highly reversible negative electrodes for lithium-ion batteries

Antonio Gentile, Stefanie Arnold, Chiara Ferrara, Stefano Marchionna, Yushu Tang, Julia Maibach, Christian Kübel, Volker Presser*, and Riccardo Ruffo*

A. Gentile and S. Arnold contributed equally

A. Gentile, S. Marchionna
Ricerca sul Sistema Energetico - RSE S.p.A., Via R. Rubattino 54, 20134, Milano, Italy.

S. Arnold, V. Presser
INM - Leibniz Institute for New Materials, Campus D2.2, 66123, Saarbrücken, Germany.
Department of Materials Science and Engineering, Saarland University, Campus D2.2, 66123, Saarbrücken, Germany.
E-mail: volker.presser@leibniz-inm.de

V. Presser
saarene - Saarland Center for Energy Materials and Sustainability, Campus D4.2, 66123 Saarbrücken, Germany.

C. Ferrara, R. Ruffo
Dipartimento di Scienza dei Materiali, Università di Milano Bicocca, 20125 Milano, Italy.
National Reference Center for Electrochemical Energy Storage (GISEL), Via G. Giusti 9, 50121 Firenze, Italy.
INSTM, Consorzio Interuniversitario per la Scienza e Tecnologia dei Materiali, Via G. Giusti 9, 50121 Firenze, Italy.
E-mail: riccardo.ruffo@unimib.it ·

Y. Tang, J. Maibach, C. Kübel
Institute of Nanotechnology, Helmholtz Institute Ulm & Karlsruhe NanoMicroFacility, Karlsruhe Institute of Technology, Hermann-von-Helmholtz Platz 1, 76344 Eggenstein-Leopoldshafen, Germany.

Table S1. EDX result related to Figure S1 image for the MXene sample.

Element	Atomic fraction[a] / %
C	29.8±4.7
O	13.5±3.4
F	9.9±2.5
Al	0.4±0.1
Ti	46.3±9.6

[a]random errors
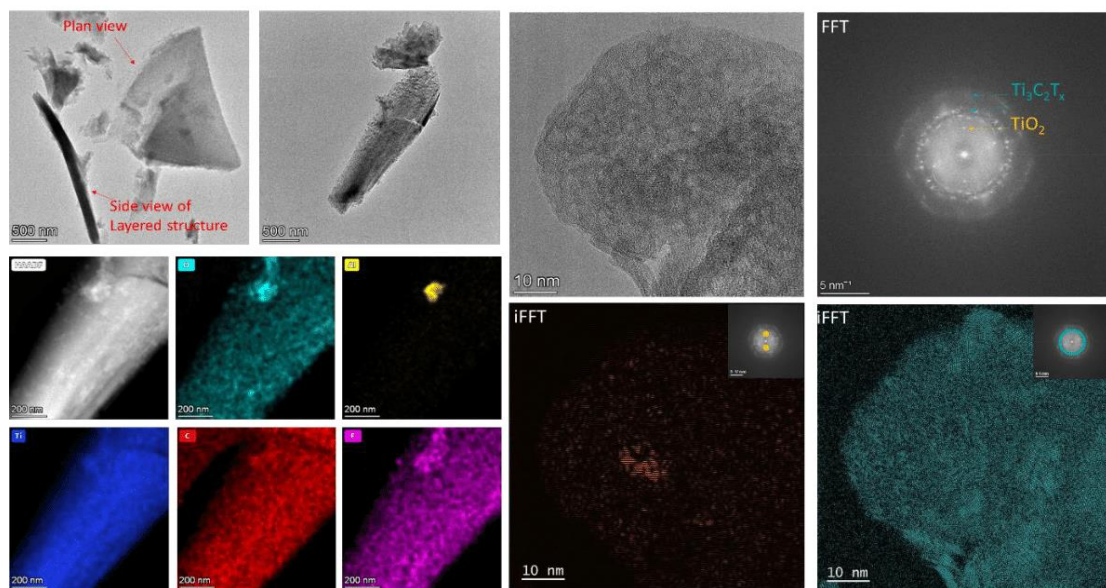
Figure S1. TEM, EDX, inverse FFT analysis for the pristine MXene.
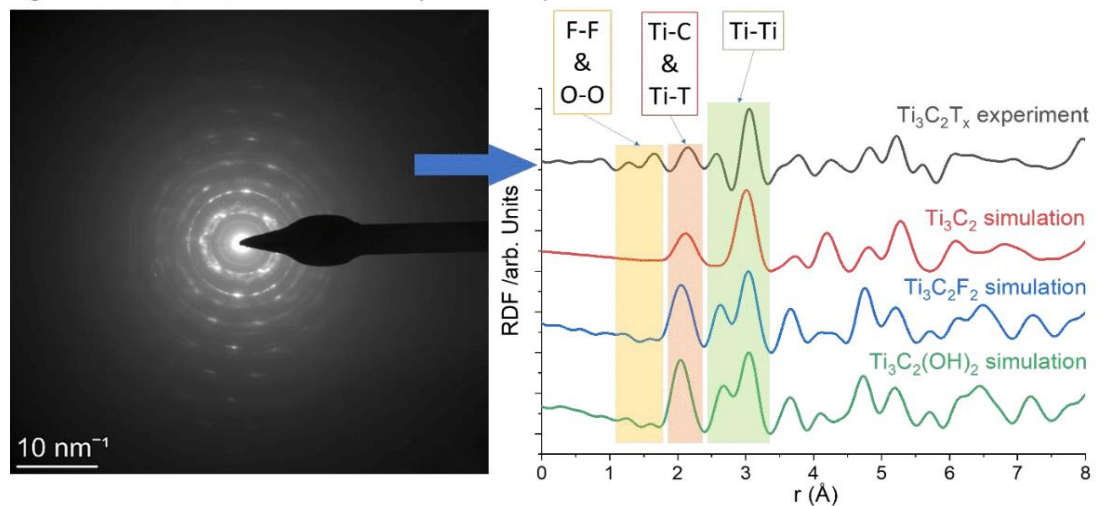
Figure S2. SAED and RDF for the MXene sample.
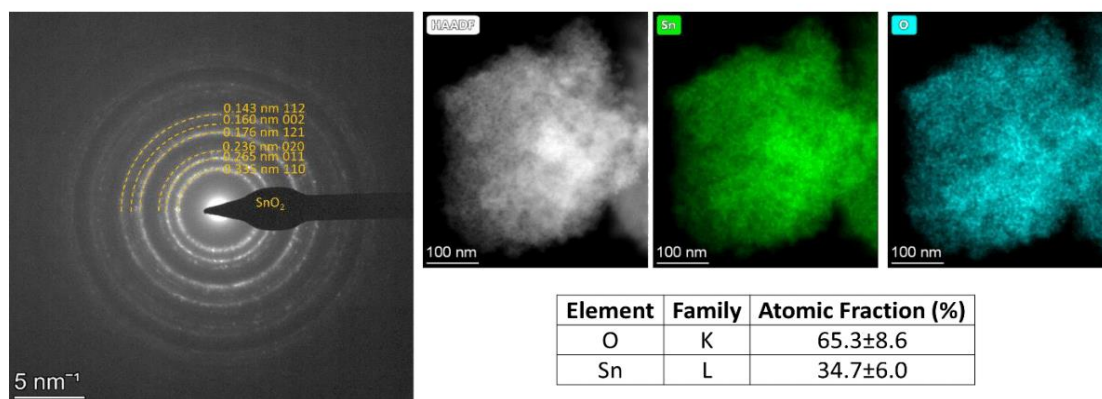
Figure S3. SAED and EDX for the SnO$_2$ sample.

Element	Family	Atomic Fraction (%)
O	K	65.3±8.6
Sn	L	34.7±6.0

S3
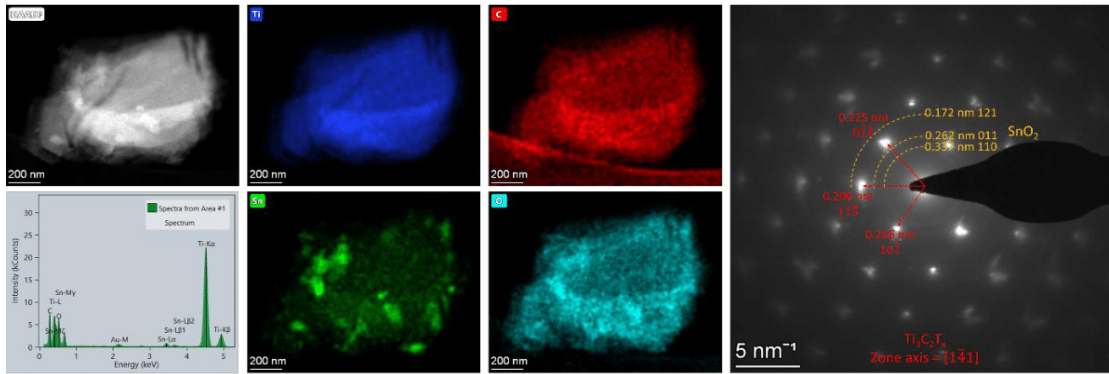
Figure S4. SAED and EDX maps for the MX-SnO$_2$ nanocomposite.

S4
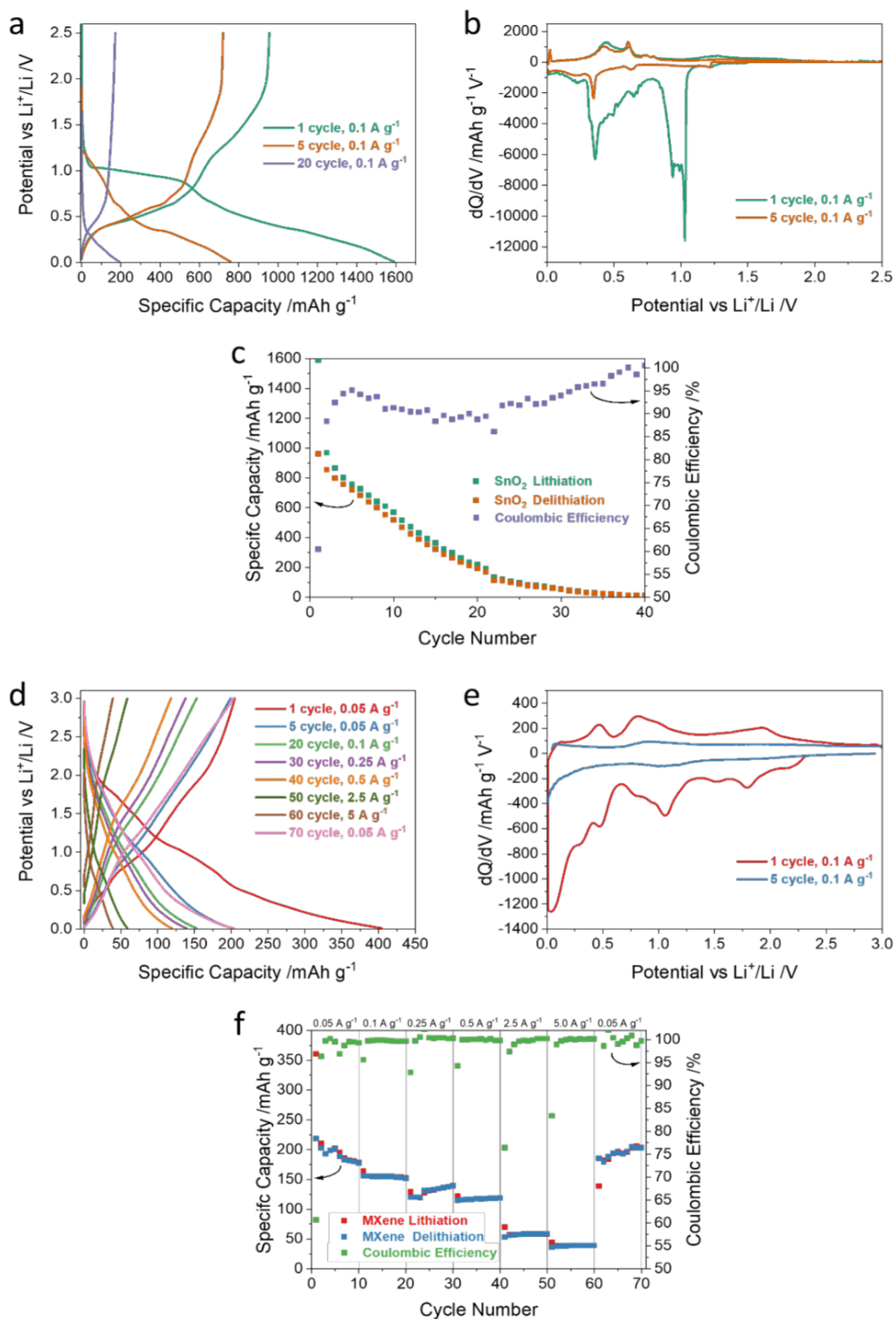
Figure S5. Charge-discharge profiles, differential capacity, capacity vs cycle numbers for **a-c)** SnO$_2$ nanoparticles and **d-f)** MXene.
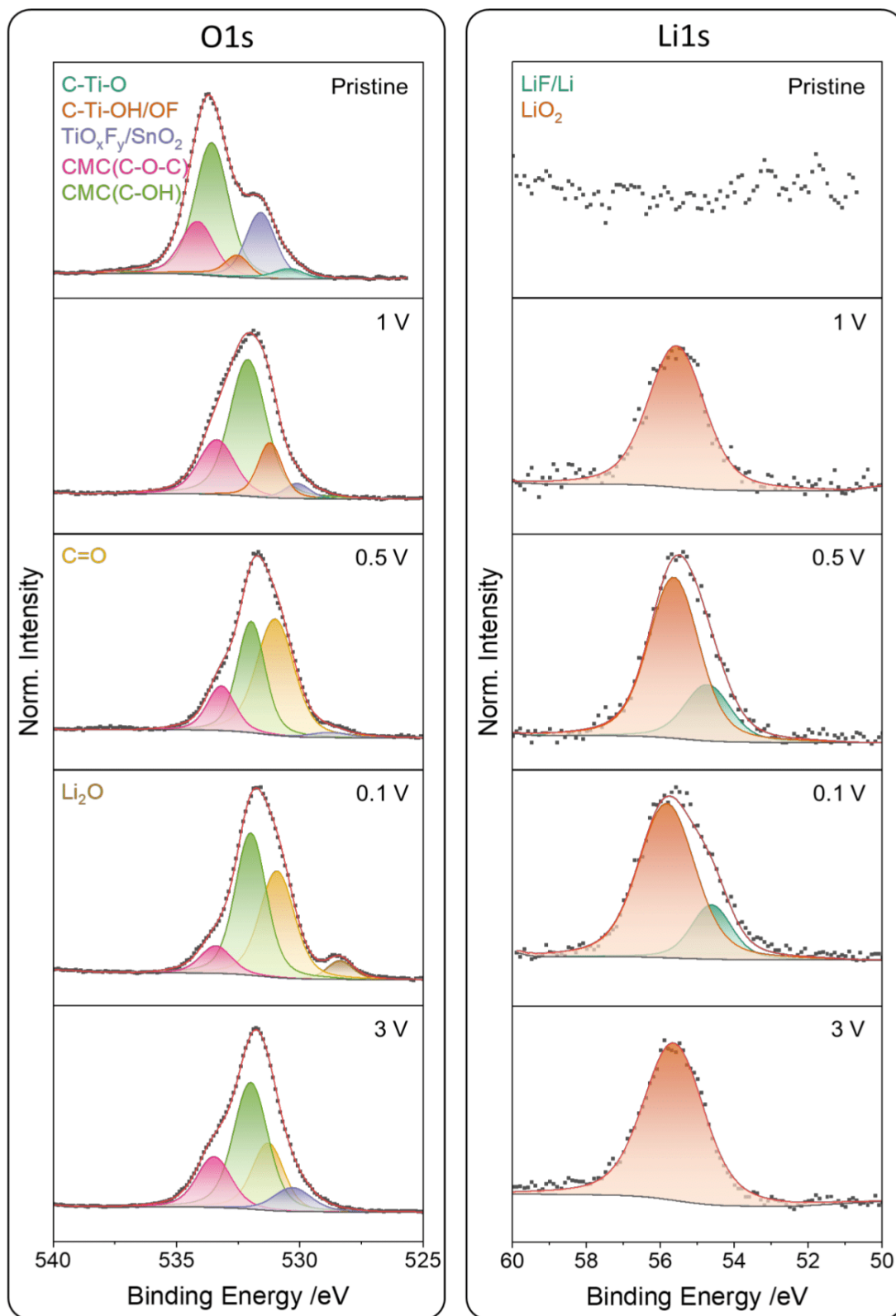
Figure S6. X-ray photoelectron spectra of O and Li at different potentials.
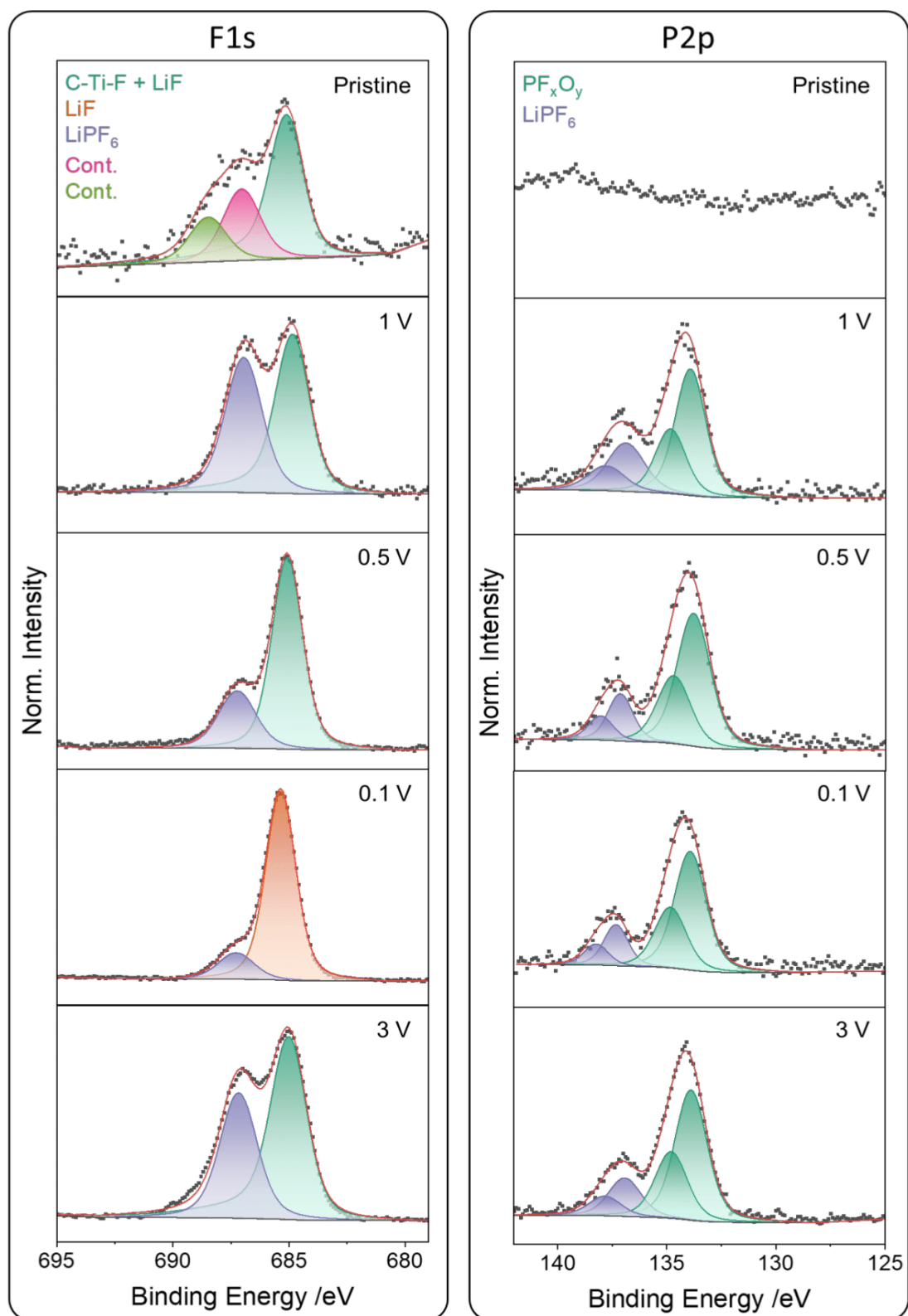
Figure S7. X-ray photoelectron spectra of F and P at different potentials.
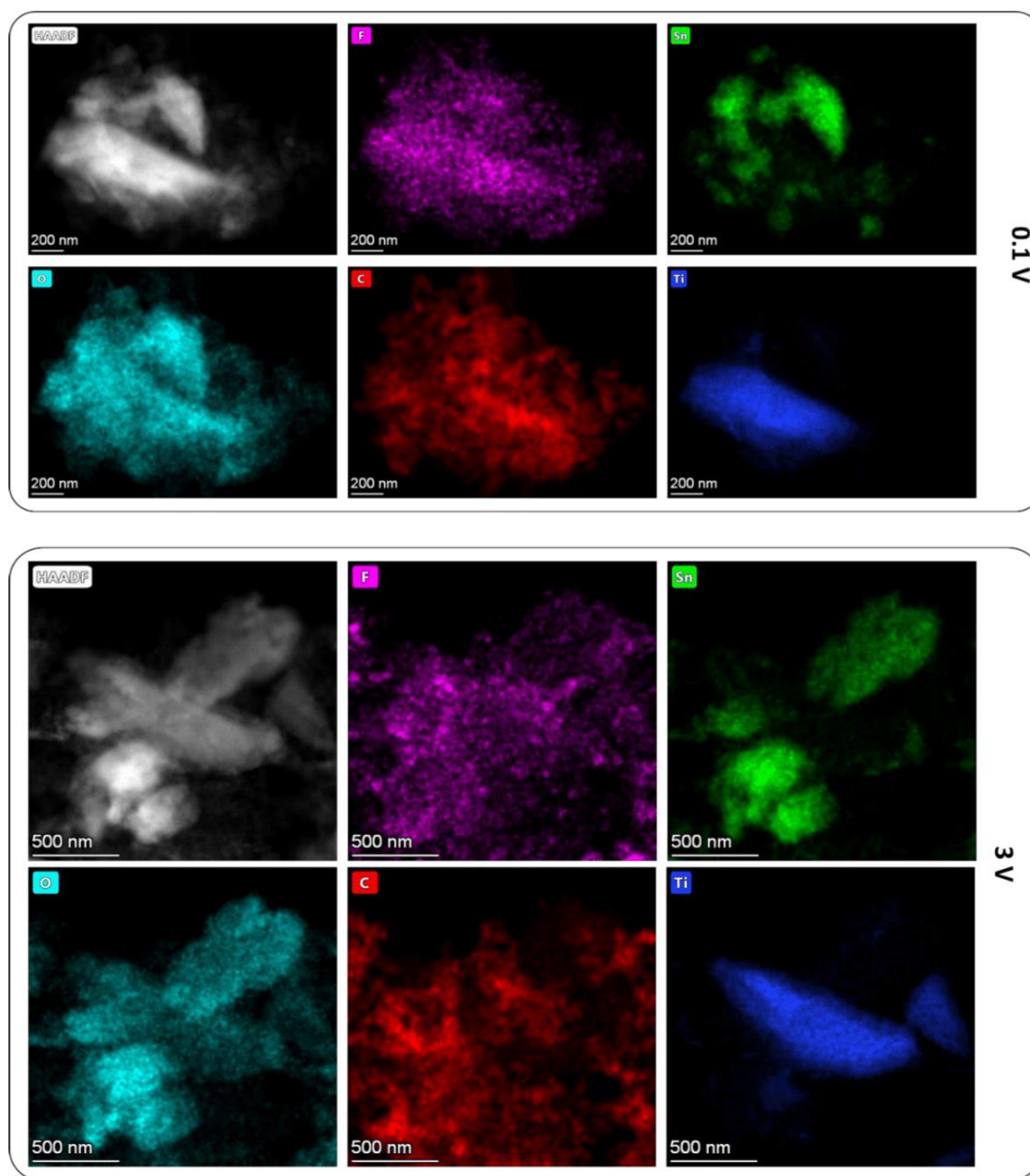
Figure S8. EDX maps for the MX-SnO_2 nanocomposite electrode electrochemically reduced to 0.1 V and re-oxidized to 3.0 V.

4.5 Dual-use of seawater batteries for energy Storage and water desalination

Stefanie Arnold,[1,2] Lei Wang[1,2] and Volker Presser[1,2,3*]

[1]   INM - Leibniz Institute for New Materials, 66123 Saarbrücken, Germany

[2]   Department of Materials Science and Engineering, Saarland University, 66123 Saarbrücken, Germany

[3]   Saarene - Saarland Center for Energy Materials and Sustainability, Campus D4.2, 66123 Saarbrücken, Germany

Own Contribution:

Conceptualization, validation, data curation, visualization, and writing – original draft
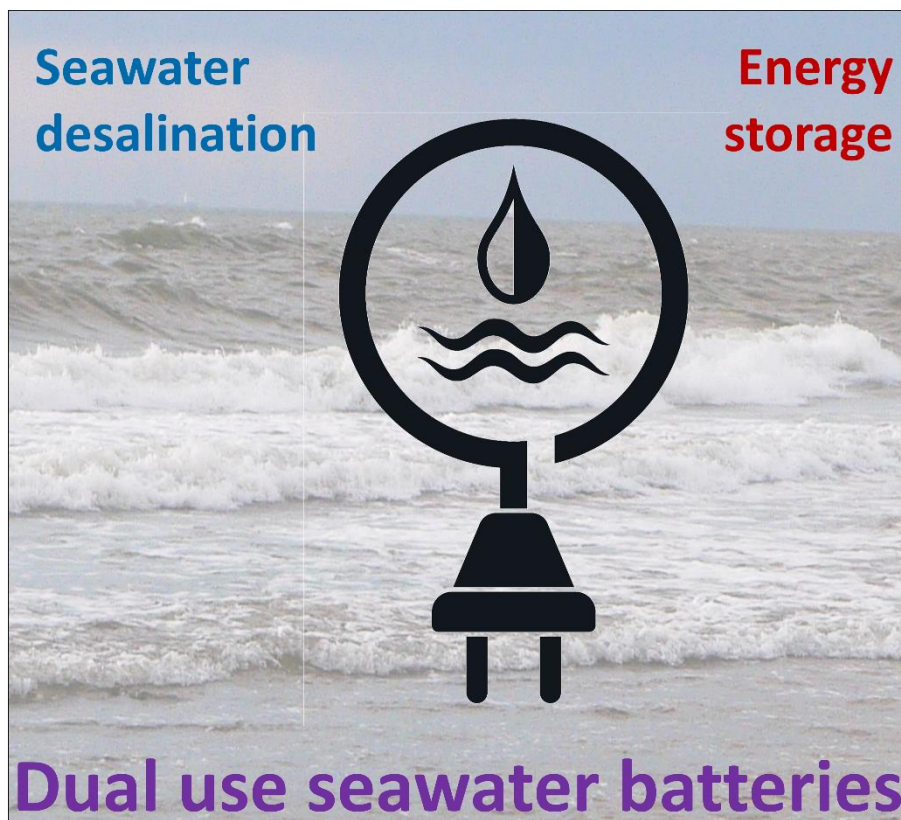
NANO · MICRO

small

Check for updates

Dual-Use of Seawater Batteries for Energy Storage and Water Desalination

Stefanie Arnold, Lei Wang, and Volker Presser*

Seawater batteries are unique energy storage systems for sustainable renewable energy storage by directly utilizing seawater as a source for converting electrical energy and chemical energy. This technology is a sustainable and cost-effective alternative to lithium-ion batteries, benefitting from seawater-abundant sodium as the charge-transfer ions. Research has significantly improved and revised the performance of this type of battery over the last few years. However, fundamental limitations of the technology remain to be overcome in future studies to make this method even more viable. Disadvantages include degradation of the anode materials or limited membrane stability in aqueous saltwater resulting in low electrochemical performance and low Coulombic efficiency. The use of seawater batteries exceeds the application for energy storage. The electrochemical immobilization of ions intrinsic to the operation of seawater batteries is also an effective mechanism for direct seawater desalination. The high charge/discharge efficiency and energy recovery make seawater batteries an attractive water remediation technology. Here, the seawater battery components and the parameters used to evaluate their energy storage and water desalination performances are reviewed. Approaches to overcoming stability issues and low voltage efficiency are also introduced. Finally, an overview of potential applications, particularly in desalination technology, is provided.

1. Introduction

The global shift toward sustainability has intensified the development of new materials and technologies, constant improvement, and creative redesign.[1,2] The large-scale implementation

S. Arnold, L. Wang, V. Presser
INM – Leibniz Institute for New Materials
Campus D22, 66123 Saarbrücken, Germany
E-mail: volker.presser@leibniz-inm.de
S. Arnold, L. Wang, V. Presser
Department of Materials Science and Engineering
Saarland University
Campus D22, 66123 Saarbrücken, Germany
V. Presser
Saarene – Saarland Center for Energy Materials and Sustainability
Campus C42, 66123 Saarbrücken, Germany

The ORCID identification number(s) for the author(s) of this article can be found under https://doi.org/10.1002/smll.202107913.

of renewable, green energy goes hand-in-hand with the digitalization of our power distribution grid and the rigorous use of energy storage technologies.[3] Electrochemical energy storage (EES) plays a crucial role in this context, from enabling mobile computing and communication to large-scale intermittent power storage.[4] The so-far best-researched lithium-ion batteries are known for their comparably high energy density, long shelf life, and high energy efficiency.[5] Accordingly, they have become an essential power source for consumer electronics, portable devices, and electric vehicles. However, lithium-ion batteries mainly face two issues. First, lithium is a limited resource on our planet, which induces a future hard limitation to lithium-ion battery technology proliferation.[6] This shortage has increased the global quest to explore alternative lithium sources, such as hydrothermal water, seawater, and mining water.[7–9] Second, lithium-ion batteries' high cost and safety issues make it hard to meet the continuously increasing demand for electronic devices, both portable electronic

devices and large-scale stationary devices.[5,10] The high cost comes from the limited availability and exceeding the demand for lithium, nickel, and cobalt (in addition to price fluctuations due to fluctuating trade markets).[11] The safety concern arises from the toxicity of cobalt and the flammable organic electrolytes. Interesting energy storage systems beyond lithium attract attention and have been explored in past years.[12,13]

Over the last years, several alternatives to lithium-ion batteries have been researched. In particular, the pure focus is placed on naturally occurring alkali metal ions such as sodium and potassium, which offers the possibility of low-cost energy storage systems.[14–16] Simultaneously, multivalent charge carriers such as Mg^{2+}, Zn^{2+}, Al^{3+}, and others are investigated, which theoretically transfer more than one electron, thus offering the possibility of a higher specific capacity and a higher energy density.[17–20] Especially sodium-ion batteries have received particular attention since 2011, as sodium is one of the most abundant elements on earth, offering the potential for low-cost energy storage systems.[21–24] Sodium is abundant in seawater and can be easily extracted from it. Another advantage is that Na-ion batteries do not require cobalt, which is still needed in Li-ion batteries. Most of the cobalt used today to make Li-ion batteries is mined in socially and environmentally challenged regions.[25,26] Thus, developing a promising

post-lithium energy storage technology with all its changes and optimizations represents an approach to the UN's Sustainable Development Goals (SDGs) claims. For example, direct contributions can be made to the areas outlined in the SDGs, which include the following indicators and measures: sustainable water management, sustainable consumption, production and development of communities, climate change mitigation, sustainable use of the oceans and terrestrial ecosystems, and affordable and clean energy. Sodium-ion-based and other beyond-lithium technologies can capitalize on know-how and materials available from decades of lithium-ion battery research and development.[27] In contrast, the Na-ion battery technology is still under development.[28,29] Researchers are working to increase its lifespan, shorten its charging time, and make batteries that deliver many watts of power.

Besides energy storage, sustainable water use is another vital part of sustainable development in the 21st century. According to the United Nations, ≈3 billion people currently have limited access to safe drinking water.[30] Two out of three humans will face water-stressed situations worldwide by 2050.[31] The oceans account for about 97% of the Earth's water, which has the great potential to be the drinking, agricultural, and industrial water resources. This particularly applies to the emerging global hydrogen economy, where seawater is an abundant source of water used for hydrogen production.[32] So far, various desalination technologies have been explored, which could be divided into thermal methods (i.e., multieffect distillation,[33] multistage flash distillation[34]), membrane-based processes (such as reverse osmosis[35]), and electrochemical methods (like electrodialysis,[36] capacitive deionization,[37] desalination batteries,[9,38] desalination fuel cells[39,40]), according to the mechanism. Reverse osmosis is dominant in desalination with an energy consumption of 3–5 kWh m^{-3}, which consumes more than 70% of the energy of the whole seawater desalination plants.[41,42] More energy-efficient technologies are required for large-scale seawater desalination.

A derivative of the rechargeable sodium-ion battery (NIB) is the rechargeable seawater battery, which could carry out simultaneous energy storage and desalination due to its unique configuration. Seawater, covering about two-thirds of our planet and a sodium concentration of around 470 mM, is a quasi-abundant resource of sodium ions.[43] The first commercial primary seawater batteries, which means cells that cannot be recharged, were developed in 1943.[44] The research field was re-energized with a focus on secondary (rechargeable) seawater batteries in 2014.[45,46] Aqueous rechargeable sodium-ion batteries are a promising and environmentally friendly way to store electrochemical energy by circulating seawater as a low-cost electrolyte; they eliminate many of the safety problems of organic electrolytes.[18]

A typical rechargeable seawater battery contains an organic electrolyte side and an aqueous electrolyte side, separated by the solid sodium diffusion membrane.[43] The organic parts resemble the typical NIB with elemental sodium as an anode. If the seawater battery is contacted with seawater, the catholyte's free and abundant sodium ions can migrate into the anode compartment during the charging process. They are ultimately stored as elemental sodium metal. At the cathode side, the oxygen evolution reaction

(OER, $4OH^- \leftrightarrow O_2 + 2 H_2O + 4e^-$ E = 0.77 V vs SHE) produces a theoretical cell voltage of 3.48 V.[45] The sodium ions are rereleased and transferred to the seawater during the subsequent discharge, and the dissolved oxygen is reduced (oxygen reduction reaction, ORR).

Since the rechargeable seawater batteries entered the market in 2014,[47] most works have optimized the performance, including the anode and cathode materials, anolyte and catholyte, and cell architecture.[45] However, there is a lack of systematic review that analyzes the relationship between the components of rechargeable seawater batteries, their application in desalination systems, and their performance. This may correlate with a separation between the energy storage and electrochemical water desalination communities; in our view, both communities are strongly linked and situated within the critical water/energy research nexus. The realization that batteries are electrochemical ion management/ion storage devices is a key to unlocking unseen synergy between the battery and desalination communities.[48] Dual functionality may help to address, at the same time, storing intermittently available renewable energy and providing clean, potable water to residential areas and agriculture. A growing amount of desalinated water will also significantly advance the large-scale production of green hydrogen.

We provide a review to meet the need for crossing disciplines and application areas along with sustainable electrochemical application and exemplify the synergy and dual-use application for the intriguing system of seawater batteries. This review introduces the component and properties of rechargeable seawater batteries and explores the possible reason for the demerits. Subsequently, we summarized the adopted approaches to overcome these drawbacks, including the materials design, cell-structure adjustment, and parameters optimization. Additionally, the applications of rechargeable seawater batteries are presented. Finally, the challenges faced by rechargeable seawater batteries and prospects for their further development are discussed.

2. Rechargeable Seawater Batteries

Conventional seawater batteries enable the storage of electrochemical energy by combining a sodiation/desodiation anode and an electrolysis cathode. This concept mandates an open-cell architecture to be able to constantly supply fresh seawater as the catholyte during the charge–discharge process. Based on the evaluation and continuous improvement of the cell parts, the electrochemical performance such as the stability, power, voltage efficiency, Coulombic efficiency, and other parameters of the resulting cell is then evaluated and reflects the current state of the art.

2.1. Rechargeable Seawater Battery Design and Components

To combine the individual components of a seawater battery into a functioning and efficient cell, it is necessary first to optimize and examine all the individual elements. The essential components of the seawater battery are electrode materials

(cathode and anode), electrolyte (anolyte, catholyte), current collector, ceramic solid electrolyte, electrocatalyst, and the general cell type. The following sections explain the requirements for the individual components, what needs to be considered and optimized, and the current research state.

2.1.1. Anode

A seawater battery basically consists of an anode in an organic electrolyte and a seawater cathode with a current collector. This design allows its use both as an energy storage system and for water desalination (**Figure 1**). A high-performance seawater battery needs an optimized anode compartment, including electrolyte and electrode material.[43,49–51] The cell's anode in the past consisted of an organic electrolyte and an electrode material used as a negative electrode. In addition to the ability to uptake

ions reversibly, anode materials and the associated anode compartments must fulfill several criteria. Apart from avoiding side reactions leading to cell swelling and failure, the anode material must combine good conductivity, a suitable electrochemical stability window at a low voltage range, and low cost and toxicity.[52] Elemental sodium is highly abundant and frequently used as an electrode material, with a very high theoretical capacity of 1166 mAh g^{-1}.[43,53–56] However, uncontrolled growth of sodium dendrites hinders safe battery operation, ruptures separators, and shortens the device lifetime while still exhibiting low Coulombic efficiency and battery performance.[57–61] Finally, light metals or alloy materials such as magnesium or aluminum promise access to a high theoretical specific capacity (Mg: 2200 mAh g^{-1}, Al: 2980 mAh g^{-1}) and can be considered as possible electrodes as well.[62,63]

The wealth of materials developed initially for high-performance electrodes of sodium-ion batteries can be capitalized on.
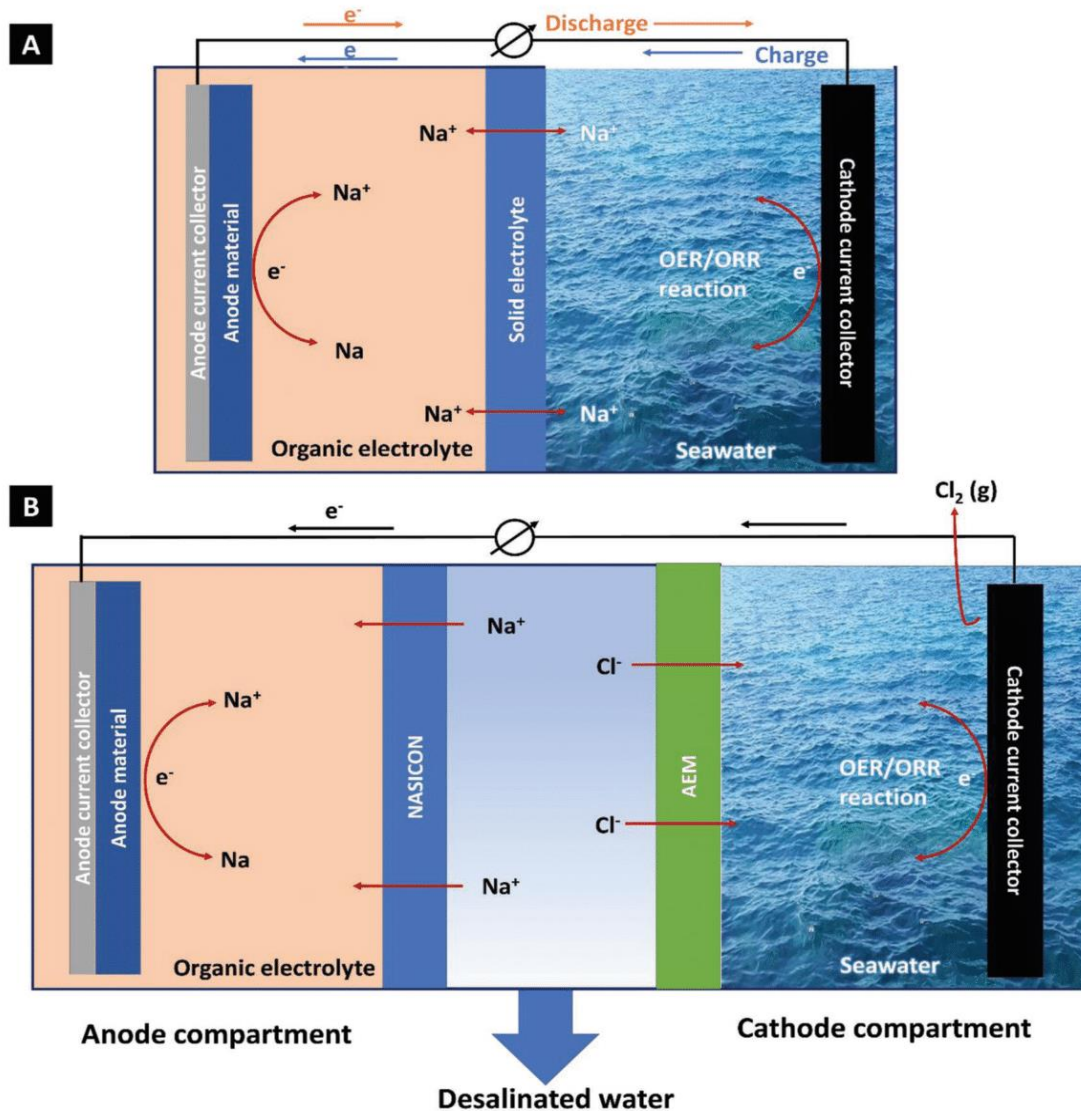
Figure 1. The operation principle of seawater battery A) for energy storage and B) for water desalination.
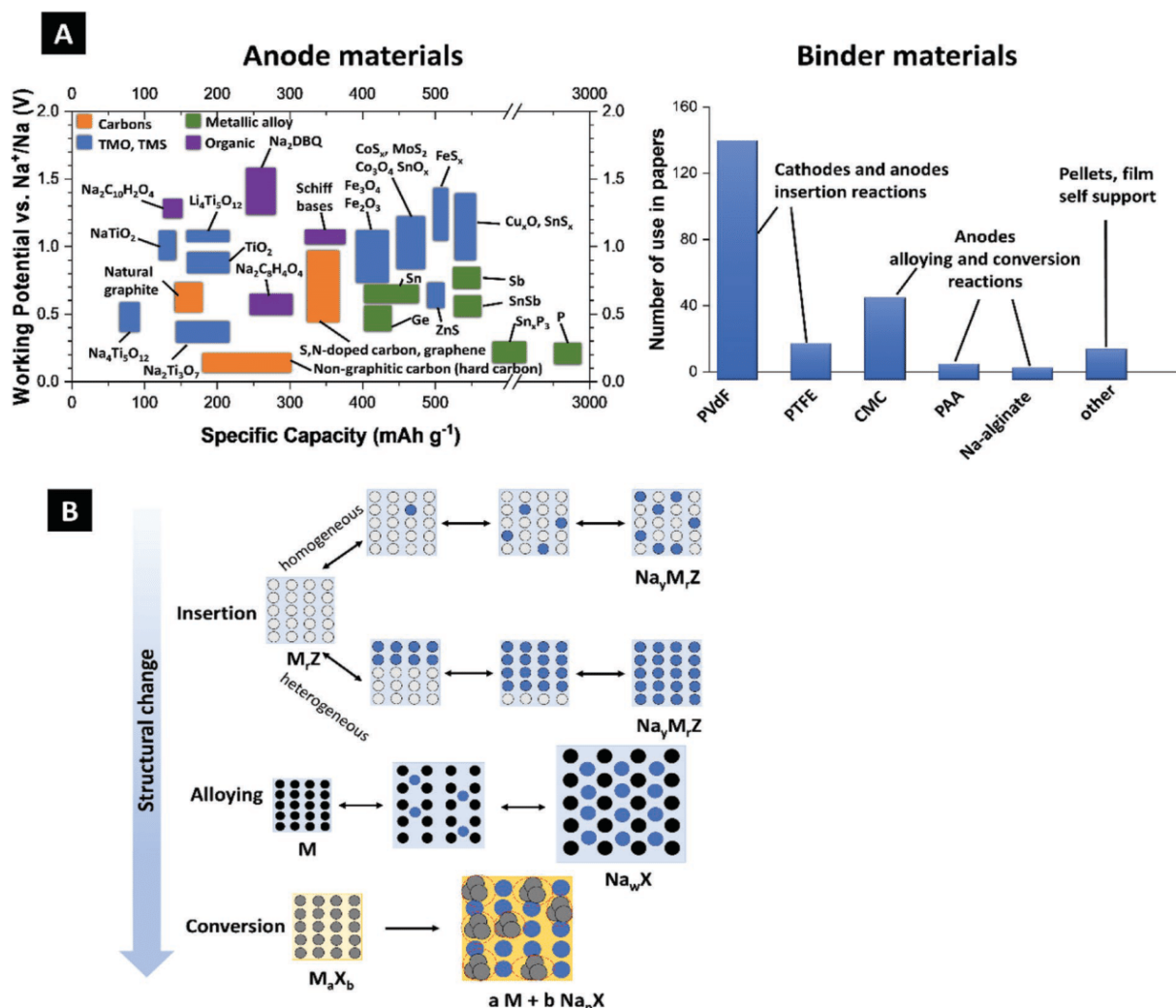
Figure 2. Overview of anode materials for sodium-ion batteries. A) Representation of the theoretical capacities of different anode materials and respective binder use in sodium-ion batteries. Adapted with permission.[214] Copyright 2017, Royal Society of Chemistry. B) Schematic representation of varying reaction mechanisms observed in electrode materials. Adapted with permission.[214] Copyright 2009, Royal Society of Chemistry. Abbreviation: PTFE = polytetrafluoro-ethylene, PVdF = polyvinylidene difluoride; CMC = carboxymethyl cellulose, PAA = polyacrylic acid, Na$_2$DBQ = disodium salt of 2,5-dihydroxy-1,4-benzoquinone.

Figure 2 schematically presents different reaction mechanisms of electrode materials and the expected theoretical capacities of these materials in sodium-ion batteries. Different types of anode materials interact with sodium in specific ways, including intercalation or conversion and alloying reactions. A commonly used intercalation material such as hard carbons can be adopted from its use in NIBs.[51,64–68] Other cation intercalation materials are TiO$_2$, Li$_4$Ti$_5$O$_{12}$, or Na$_2$Ti$_3$O$_7$, the associated theoretical capacities of 335, [69] 175,[70] and 177 mAh g^{-1},[71] respectively. Nevertheless, these values are moderate compared to large charge transfer capacities associated with processes such as alloying and conversion reactions.

Alloying materials form Na-rich intermetallic compounds through alloying reactions and promise high-capacity materials due to their specific reaction mechanism.[72] However, these materials have a significant volume expansion during

sodiation and desodiation, potentially leading to capacity fading.[73,74] The strong forces can break the electrode and damage the electrode material. Some approaches are already known to prevent this rapid loss of capacity. For example, the volume change can be buffered, and composites can maintain the conductive path in the electrode with carbon or other layer-like structures. Successful applications in seawater batteries include Sn–C[75] in an ionic liquid electrolyte or red phosphorous.[49]

Conversion-type materials accomplish reversible charge storage via a phase transformation.[76] The solid-state reactions result in new compounds with new properties. Conversion materials also exhibit a relatively large voltage hysteresis, providing low energy efficiency during charge/discharge cycling.[77,78] Conversion materials also suffer from a significant volume change during cycling.[79] As already reported material in a seawater

battery, Sb_2S_3 is a model material with a multistep conversion and alloying charge storage process.[80] In a seawater full-cell, the synthesized antimony sulfide nanoparticle aggregates provided a specific capacity of 470–485 mAh g^{-1} at a discharge voltage of about 1.9 V after 50–70 charging and discharging cycles (corresponding Coulombic efficiency: 83–88%).[81] By contrast, the initial discharge capacity was relatively low.[81]

Comparing the specific capacities by using alloying or conversion-based materials in contrast to intercalation anode materials, one obtains values about 4–5 times as high. Typical carbon materials in seawater batteries provide a capacity of about 100–200 mAh g^{-1}, which is much smaller than alternative systems, such as red phosphorus (900 mAh g^{-1}; **Table 1**).[49]

2.1.2. Cathode

The unique design of seawater batteries and the underlying electrochemical processes make it impossible to use common battery electrode materials found in sodium-ion batteries. Also, the wettability of the cathode current collector and seawater catholyte must be considered to improve the battery performance (voltage efficiency).[82] Since an electrocatalytic process is used, the cathode employs only seawater and a current collector. Referring to standard seawater data, the amount of salt in one liter of water reaches about 35 g.[83] In addition to the main component of sodium chloride, many other cations and anions are found in standard seawater, such as magnesium, calcium, potassium, sulfates, bicarbonates, and fluorides (**Figure 3**A).[83] The composition of seawater varies from place to place, depth to depth, and time to time, depending on the respective climate, conditions, and environment. Since there is no typical solid electrode in this system, a current collector is still required at this point. Electrons released from the anode part during deintercalation/dealloying are carried away via the current collector. The current collector also carries the cathode reactions (oxygen evolution reactions and oxygen reduction reactions) and is required for the associated charge transport. Compared to organic batteries with solid cathodes, the current collector requires special properties like the stability in saltwater, which is indispensable for their use in seawater batteries.[53,84] Besides high electronic conductivity and electrochemical and mechanical stability, other criteria such as large surface area, uniformly distributed transport area, and a low mass are also considered.

Copper and aluminum foils are typical current collectors in alkali metal batteries. Depending on the potential, it can be decided which current collector can be used without forming alloys and other byproducts by also considering the cost-effectiveness. Since these metals are usually not stable in the presence of NaCl and after application of a potential, carbon-based collectors are the most common in seawater batteries.[45] A seawater battery current collector offers sites for the cathode reactions and ensures the charge transport. This mandates a large interface surface area, good electrochemical stability, and high electrical conductivity. An attractive current collector material should also be cost-effective and, ideally, based on an environmentally friendly material. These requirements are, in large parts, met by carbon-based current collectors. Carbons are abundantly available and offer high corrosion resistance in seawater, predestined for use in the former primary seawater batteries with the ORR and HER (hydrogen evolution reaction).[85,86] Yet, the limited mechanical stability of carbon provides a limitation to its application.[47]

There are different carbon materials explored on the cathode side.[45] Carbon felts, which did not exhibit the previously explored weaknesses of carbon current collectors, showed mechanical stability, high flexibility, and conductivity.[64,84] Figure 3B–D shows scanning electron images of carbons commonly used as cathodes. Senthilkumar et al. investigated the cathode side porous carbon with defects and oxygen functional obtained from bio-organic waste (grapefruit peels).[87] The resulting materials provided efficient OER/ORR activities, a discharge capacity of 191–196 mAh g^{-1}, and 96–98% Coulombic efficiency over 100 cycles of the full-cell.

Zhang et al. used an electrolytic carbon sponge with an open design and a highly interconnected and macroporous framework.[84] The bifunctional electrocatalytic OER and ORR activities yielded a low charge–discharge voltage gap, high voltage efficiency, high-power density, and long-term cycling stability.[84] In another work by Park et al., activated carbon cloth was used as a current collector on the cathode side and compared to the performance of a low surface area carbon felt.[64] In addition to the OER/ORR electrolytic activity, the carbon cloth electrode provides electrical double-layer formation. The hybrid electrochemical process improved the voltage/energy efficiency (86%) and power performance (16 mA cm^{-2}) of high surface area carbon cloth as the current collector for seawater batteries.[64]

2.1.3. Ceramic Membranes

A sodium-ion-conducting membrane separates the anode and cathode compartments of seawater batteries. Such membrane materials are commonly employed as solid electrolytes in solid-state batteries.[88] The stability of the membrane against different types of liquid electrolytes has to be preserved to guarantee stability in organic and aqueous solutions. Essential for the application in an electrochemical system is applying a high current and stability in a relatively wide electrochemical potential window for the highest possible capacity without degrading parts of the cell.[89,90] In general, the solid electrolytes in seawater batteries also need to provide high sodium-ion conductivity, robust mechanical property, and ultralow porosity to avoid the penetration of electrolytes.

There are three main types of solid electrolytes that have the possibility of selective Na ion transport: ceramics, polymers, and inorganic composite.[91–94] Given the mechanical stability and effective separation of the organic/aqueous sides, inorganic compounds and ceramic membranes are commonly used as solid electrolytes in seawater batteries. The most often used membrane materials are the inorganic β''-Al_2O_3 or sodium superionic conductor (NASICON) because of the high ion mobility and chemical stability.[54,88] A general issue of ceramic membranes is their mechanical brittleness, which imposes specific considerations onto seawater battery design and scalability.

β''-Al_2O_3 is a layered fast ionic conductor closely related to the widely studied class of β-Al_2O_3 (**Figure 4**A). It consists of

Table 1. Comparison and summary of different parameters seawater battery in the state-of-the-art literature. CC: current collector.

Anode	Cathode/cathode current collector	Solid electrolyte	Liquid electrolyte	Mechanism	Cell setup	Capacity	Coulombic efficiency/voltage efficiency	Refs.
Prepatterned Cu/ Al current collector (anode-free)	Seawater carbon felt	NASICON $(Na_3Zr_2Si_2PO_{12})$	1 M NaOTf in DME	–	2465-type coin cells	n.a.	98%	[127]
Sodium with nickel mesh	Seawater Ag foil	NASICON $(Na_3Zr_2Si_2PO_{12})$	1 M $NaCF_3SO_3$ in TEGDME	OER/ORR	Seawater test cells (421Energy Co., Ltd)	n.a.	98.6–98.7% 90.3%	[111]
Hard carbon:Super-P carbon black:PVdF 8:1:1	Seawater carbon paper	1 mm thick β''-Al_2O_3 3 mm thick NASICON $(Na_3Zr_2Si_2PO_{12})$	1 M $NaCF_3SO_3$ in TEGDME	OER/ORR	Seawater cell in water was from (421Energy Co Ltd)	≈10 mAh g^{-1} ≈120 mAh g^{-1} at 0.05 mA cm^{-2}	91%	[88]
Activated carbon fiber coated with Na metal	Simulated seawater carbon felt Pt wire Ag/AgCl Ref	PE separator NASICON $(Na_3Zr_2Si_2PO_{12})$	1 M $NaCF_3SO_3$ in TEGDME	OER/ORR	Coin cells	20 mAh g^{-1} 0.6 mA (0.3 mA cm^{-2})	n.a.	[194]
Na metal attached to Ni taps	Air cathode S-rGO-CNT-Co powder coating with PVdF on carbon felt electrocatalyst	NASICON $(Na_3Zr_2Si_2PO_{12})$ PE separator	1 M $NaCF_3SO_3$ in TEGDME	OER/ORR	Pouch cells	n.a.	n.a.	[112]
Hard carbon:Super-P carbon black:PVdF 8:1:1 On Cu foil	Ti mesh carbon Carbon paper	0.8 mm-thick NASICON $(Na_3Zr_2Si_2PO_{12})$	1 M $NaCF_3SO_3$ in TEGDME	OER/ORR	–	296 mAh g^{-1} 0.025 mA cm^{-2}	98%	[129]
Na metal on stainless-steel CC	Seawater	NASICON membrane	1 M $NaCF_3SO_3$ in TEGDME		Seawater battery coin cells	37 mAh g^{-1} 0.5 mA cm^{-2}	Na-BP-DME 99.5% over 10 cycles	[52]
Al, Mg, and Zn	NiHCF crystals:carbon black:PVdF 7:2:1 on carbon cloth	–	Seawater	–	Two electrode cells	57 mAh g^{-1} At 1 A g^{-1}	n.a.	[55]
Na foil and Na/carbon composite on PAN-based carbon cloths	Seawater carbon felt	NASICON $(Na_3Zr_2Si_2PO_{12})$	1 M $NaCF_3SO_3$ in TEGDME		Coin cell seawater battery	40 mAh g^{-1} At 1 mA	98%	[218]
Na metal or hard carbon Ni tap CC	Seawater Ti mesh and a sheet of carbon paper	0.8 mm thick NASICON $(Na_3Zr_2Si_2PO_{12})$	1 M $NaCF_3SO_3$ in TEGDME	OER/ORR		190 mAh g^{-1} hard carbon 0.05 mA cm^{-2}	~96–98%	[87]
Using Na metal	Seawater heat-treated carbon felt	PE Hong-type NASICON $(Na_{1+x}Zr_2Si_xP_{3-x}O_{12}, x = 2)$	1 M $NaCF_3SO_3$ in TEGDME	OER/ORR	2465-coin-cell seawater battery	n.a.	n.a.	[56]
Pristine or graphene-coated Cu	Seawater carbon felt	1 mm thick NASICON $(Na_{1+x}Zr_2Si_xP_{3-x}O_{12}, x = 2)$	1 M NaOTF-DME		Modified 2465-type coin cell flow cell	n.a.	95%	[219]
Sn-C:Super-P carbon black:PVdF 8:1:1	Seawater carbon paper	NASICON $(Na_3Zr_2Si_2PO_{12})$	1 M solution of $NaClO_4$ in EC/DEC And sodium bis(trifluoromethanesulfonyl)imide (NaTFSI) and *N*-butyl-*N*-methyl-pyrrolidiniumbis(trifluoromethanesulfonyl)imide (Pyr14TFSI)		n.a.	~325 mAh g^{-1} Sn 312 mAh g^{-1} Sn 0.05 mA cm^{-2}	55% 1st cycle 91%	[75]
Sodium metal/carbon cloth composite	Pyridinic-N catalyst, in a carbon cloth CC	1 mm thick NASICON $(Na_3Zr_2Si_2PO_{12})$	1 M $NaCF_3SO_3$ in DME	OER/ORR	Coin cell anode Seawater flow battery tester	n.a.	n.a.	[169]

Table 1. Continued.

Anode	Cathode/cathode current collector	Solid electrolyte	Liquid electrolyte	Mechanism	Cell setup	Capacity	Coulombic efficiency/voltage efficiency	Refs.
Na metal or hard carbon:carbon black:Super-P:PVdF 8: 1:1 Ni taps CC	CMO nanoparticles: carbon black Super-P:PVdF 8:1:1 Air–electrode CMO catalyst	NASICON $(Na_{1+x} Zr_2 Si_x P_{3-x} O_{12}, x = 2)$	1 M $NaCF_3SO_3$ in TEGDME	OER/ORR	Pouch cell seawater	190 mAh g^{-1} hard carbon 0.01 mA cm^{-2}	>96% energy 85%	[68]
Na metal foil	Carbon felt catalyst and CC	0.8 mm thick NASICON $(Na_{1+x} Zr_2 Si_x P_{3-x} O_{12}, x = 2)$	1 M $NaCF_3SO_3$ in TEGDME	OER/ORR	Coin cell	n.a.	n.a.	[54]
Hard carbon:Super-P carbon black:PVdF 8:1:1	Seawater carbon paper	NASICON $(Na_3Zr_2Si_2PO_{12})$	1 M $NaClO_4$ in EC/PC 1 M $NaCF_3SO_3$ in TEGDME		Flowing-seawater cell	118 mAh g^{-1} 125 mAh g^{-1} 0.05 mA cm^{-2}).	n.a.	[67]
Na metal at Ni mesh	90 wt% PNC-electrocatalyst:PVdF 9:1 carbon felt CC	0.8 mm thick NASICON $(Na_3Zr_2Si_2PO_{12})$	1 M $NaCF_3SO_3$ i n TEGDME	OER/ORR	Pouch cell of seawater batteries	n.a.	n.a.	[166]
Sodium metal or hard carbon	P2-type $Na_{0.5}Co_{0.5}Mn_{0.5}O_2$ layered electrocatalyst:SP-carbon:PVdF 8:1:1 carbon felt CC	Celgard NASICON	1 M $NaCF_3SO_3$ in TEGDME	OER/ORR	Coin cell Flow cell tester	183 mA h g^{-1} at 0.1 mA	85% Coulombic efficiency 80% voltage efficiency	[66]
Hard carbon: SuperC45: CMC 8:1:1 On Cu foil	Seawater Carbon felt	NASICON $(Na_3Zr_2Si_2PO_{12})$	0.1 M NaFSI–0.6 M $Pyr_{13}FSI$–0.3 M $Pyr_{13}TFSI$ and 0.1 M NaFSI–0.6 M $Pyr_{13}FSI$–0.3 M $Pyr_{13}TFSI$ with 5 wt% EC 1 M $NaCF_3SO_3$ in TEGDME	OER/ORR	Coin cell	290 mA h g^{-1} hard carbon 1.0 C (= 300 mA g^{-1})	ILE-EC 98% energy efficiency (80.5%) 76.3% for the LE	[124]
Sodium or hard carbon:SuperP:PVdF 8:1:1 Ni mesh	Seawater NiHCF:SuperP:PVdF 8:1:1	0.8 mm thick NASICON	1 M $NaCF_3SO_3$ in TEGDME	OER/ORR	Pouch cell	56 mA h g^{-1} 20 mA h g^{-1}	95% to 98%	[65]
Sodium anode Hard carbon Ti mesh	Seawater activated carbon cloth (ACC) and carbon felt (CF; PAN-based, CNF)	PE 1 mm thick NASICON $(Na_{1+x}Zr_2Si_xP_{3-x}O_{12}, x = 2)$	1 M $NaCF_3SO_3$ in TEGDME	OER/ORR	Coin cell	16.2 mA cm^{-2}	energy efficiency of 78% ACC-seawater battery CF-seawater battery (60%)	[64]
Na metal or a-Sb_2S_3 electrode	Natural seawater air electrode	0.8 mm thick NASICON $(Na_{1+x}Zr_2Si_xP_{3-x}O_{12}, x = 2)$	1 M $NaClO_4$ dissolved in a mixture of EC/DEC (1:1) with 5 wt% FEC	OER/ORR	Seawater flow cells (421Energy Co., Ltd)	470–485 mA h g^{-1} 0.05 mA cm^{-2}	83–88%	[81]
Red phosphorus: SuperP:polyacrylic acid 7:1:2 Al foil CC Or Na	Natural seawater carbon felt	NASICON $(Na_3Zr_2Si_2PO_{12})$	1 M $NaClO_4$ in EC:DEC + 5%FEC	OER/ORR	Coin cell	900 mA h g^{-1} composite 200 mA g^{-1} composite	>92%	[49]
Na metal Stainless steel	Natural seawater Activated carbon cloth (ACC-5092-20, Kynol)	PE NASICON $(Na_3Zr_2Si_2PO_{12})$	1 M $NaCF_3SO_3$ in TEGDME	OER/ORR	Coin cell	n.a.	n.a.	[53]

Table 1. Continued.

Anode	Cathode/cathode current collector	Solid electrolyte	Liquid electrolyte	Mechanism	Cell setup	Capacity	Coulombic efficiency/voltage efficiency	Refs.
Liquid anodes (Na-BPs, Na-PYRs, and Na-BP-PYRs) and the red phosphorus Semiliquid anodes (P/C@Na-BP-PYRs and the P/C@LE)	0.47 M NaCl carbon fabric	NASICON ($Na_3Zr_2Si_2PO_{12}$)	LE: 1 M $NaPF_6$ in DEGDME	OER/ORR	2465-type seawater coin cells seawater flow cell testers	7.5 mAh cm^{-2} 0.5 mA cm^{-2}	n.a.	[124]

alumina blocks arranged in a spinel structure in between which the mobile sodium cations are postured in conductor planes.[95] β''-Al_2O_3 is characterized by a higher proportion of sodium ions than other compounds in this class, which can be explained by the structural arrangement of the conduction planes, which comprises a network of sodium ions in the stoichiometric compound.

Kim et al. compared β''-Al_2O_3 with a type of NASICON in a rechargeable seawater battery using a hard carbon anode and seawater as the catholyte.[88] It has been shown that protonated H_3O^+ species in β''-Al_2O_3 are allowed to pass through the conduction band into the anode compartment of the seawater battery, which in the end leads to not
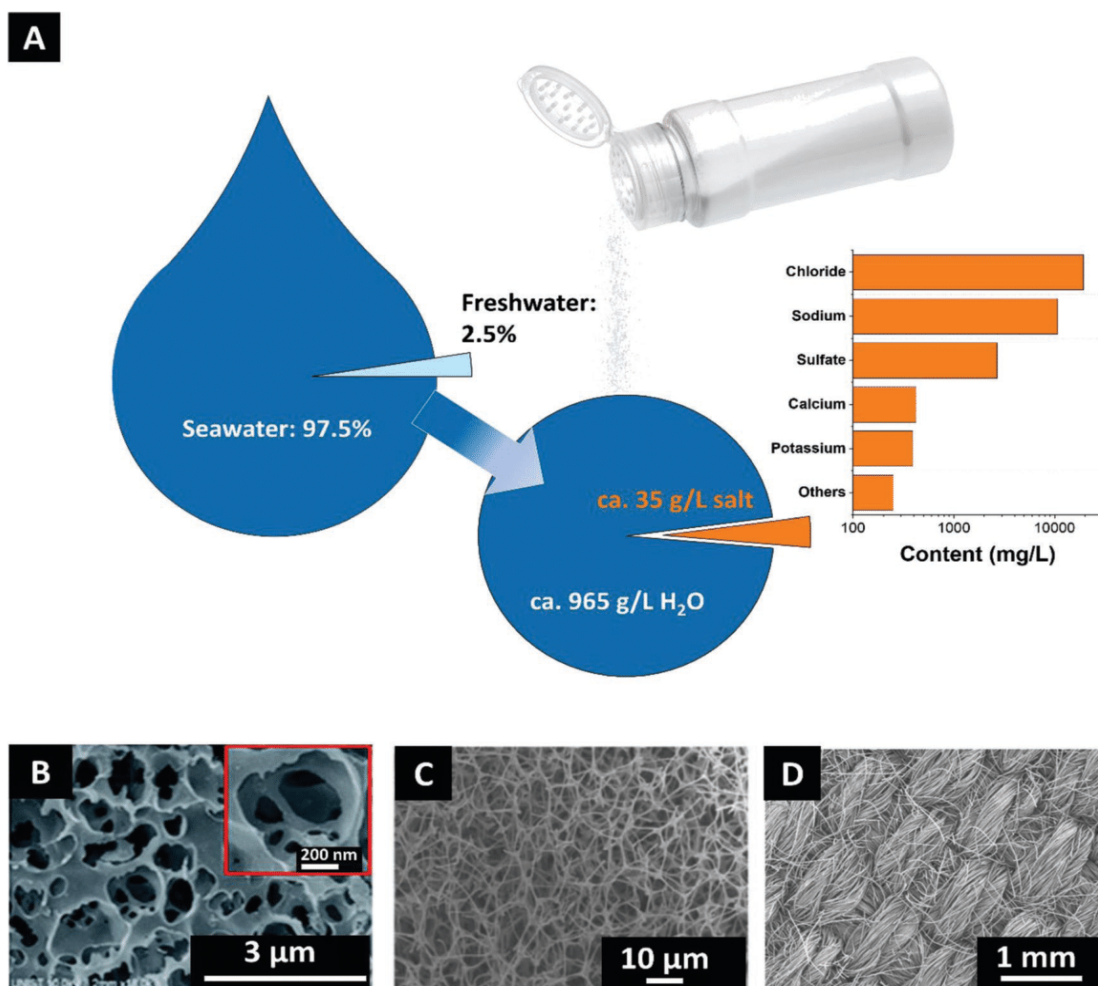
Figure 3. A) Main components and distribution of different ions in natural seawater. Scanning electron images of carbonaceous materials used as cathode current collector in seawater battery B) carbon felt, Reproduced with permission.[87] Copyright 2018, Elsevier, and C) carbon sponge. Reproduced with permission.[84] Copyright 2019, Elsevier, and D) carbon cloth. Reproduced with permission.[64] Copyright 2019, Elsevier.
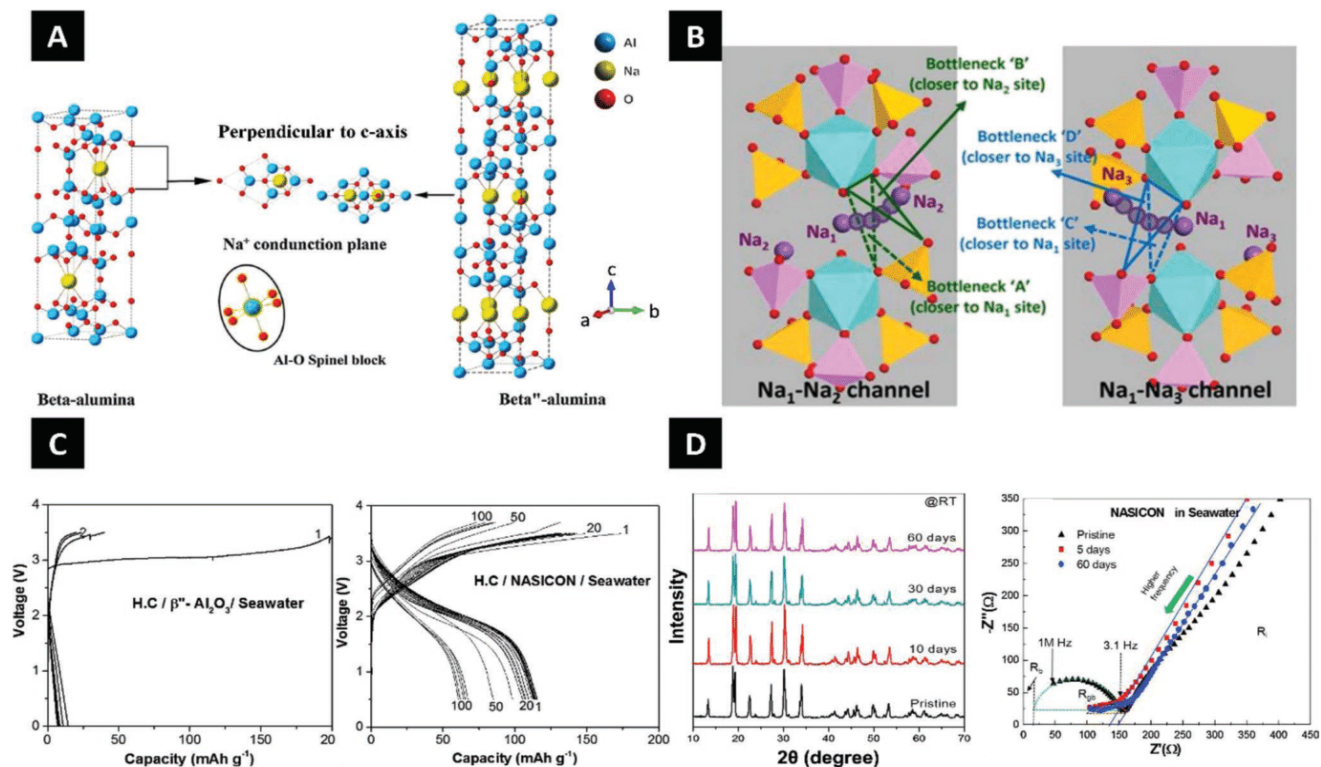
Figure 4. A) The structure of β-Al$_2$O$_3$ and β''-Al$_2$O$_3$. Reproduced with permission.[216] Copyright 2020, Elsevier. B) The structure of Na$_3$Zr$_2$Si$_2$PO$_{12}$. Reproduced with permission.[217] Copyright 2016, American Chemical Society. C) The performance of rechargeable seawater batteries with β''-Al$_2$O$_3$ (left) and NASICON (right) as the solid membrane. Reproduced with permission.[88] Copyright 2016, Elsevier. D) Structural changes of β''-Al$_2$O$_3$ and NASICON membranes during stability testing. Reproduced with persmission.[88] Copyright 2016, Elsevier.

satisfactory matched performance. NASICON-structured materials are desirable because they exhibit high structural stability and fast ionic conductivity (10^{-3} S cm^{-1}) because of their suitable tunnel size for sodium-ion migration in a 3D framework (Figure 4B).

In general, there are mainly two different NASICON types found for seawater batteries. The Hong-type NASICON (Na$_{1+x}$Zr$_2$Si$_x$P$_{3-x}$O$_{12}$) offers the advantage compared to the von Alpen-type (Na$_{1+x}$Zr$_{2-x/3}$Si$_x$P$_{3-x}$O$_{12-x/3}$) NASICON that it can be produced at lower temperatures (1250 °C), even compared to β-Al$_2$O$_3$ (≥1600 °C β-Al$_2$O$_3$, ≥1300 °C Alpen-type NASICON), and still achieves very high densification.[96,97] In some works, the density (≤78%) of the synthesized NASICON membranes only insufficiently prevents water from penetrating the membrane. For this reason, the remaining open pore channels are filled with epoxy resin.[90,98] A recent report by Go et al. reported that a vA-NASICON (Na$_{3.1}$Zr$_{1.55}$Si$_{2.3}$P$_{0.7}$O$_{11}$) has even better and more suitable properties compared to the Hong-type NASICON.[99] Due to the changed composition and the microstructure, higher ionic conductivity and a lower grain boundary resistance can be obtained. In addition to the higher bend strength, an improved voltage efficiency and higher power output for use in a seawater battery could be demonstrated in this way.[99]

NASICON structures are known for their use as materials in sodium-ion batteries, both as electrode material and solid electrolytes. Goodenough and Hing discovered this electrode material and showed the formula Na MMA(XO$_4$), where M and MA represent metals and X are silicon, phosphorus, or sulfur.[100,101] Due to the diverse use and the different structure of NASICON structures, a unique and targeted design is possible. Their open framework allows them to intercalate up to four sodium ions, making them a promising electrode material in sodium-ion batteries.[102] With their fast ionic diffusion, relatively high structural facile production/synthesis, stability in different solvents, and rich structural diversity, they are also attractive for seawater batteries. The catholyte, seawater, provides an ample supply of sodium ions to be transported across the NASICON membrane. Corrosion is inevitable even for NASICON, which provides much higher stability than β''-Al$_2$O$_3$ membranes (Figure 4C,D).

In the work of Kim et al., NASICON membranes were immersed in seawater for several days.[88] A slight change in the crystalline structure was observed due to changes in intensity ratios in the subsequent X-ray analysis, which was also reported in other publications.[103,104] A proposed mechanism can be attributed to a topotactic ion exchange between Na$^+$ and H$_3$O$^+$ ions at the surface of the NASICON grains.[103,104] Many factors influence this behavior, such as the applied current density, which at high rates (2 mA cm^{-2}) causes structural degradation with irreversible phase deformation and Na$^+$ extraction.[54] However, further detailed investigations need to be carried out

in the future to better understand this process (and membrane degeneration in general).

2.1.4. Liquid Electrolyte

Besides the solid electrolyte (membrane), a thorough selection of the liquid electrolyte is of defining importance. In sodium-ion batteries, an inorganic conductive salt dissolved in organic solvents is mainly used to guarantee ionic conductivity between the electrodes. The key points that apply here, such as a wide electrochemical stability window, thermal stability, or a low electronic conductivity, can only address the needs of the seawater battery to a minimal extent. However, this type of electrolyte shows relatively low stability at low potentials, so the Coulombic efficiency is generally low in the first cycles. The solid electrolyte interphase (SEI), the protective cover layer at the electrode surface, is also formed due to electrolyte decomposition.[105] The ideal liquid electrolyte would combine high ion mobility, high electrochemical stability, low cost, natural abundance, and low environmental impact.

The electrolyte stability and SEI formation are essential in seawater batteries' operation and stability. The SEI is a passivating and isolating boundary layer that, ideally, protects the active material from direct contact with the electrolyte.[105] The SEI prevents continuous and degradative reactions between the electrolyte and the electrode material depending on the applied potential and type of electrode material.[106] The SEI is formed during the first cycle because of the (initial) instability stability of organic electrolytes at low potentials.[107] Applying organic electrolytes leads to forming a solid and dense SEI at the anode and protects the electrolyte from further decomposition.[108] An ideal SEI should have a low electronic but high alkali-ion conductivity, an appropriate thickness, good flexibility, and uniform morphology.[109,110] If this layer is too thick, the cell's capacity will decrease. However, especially in the early stage of seawater battery research, an electrolyte adapted from the NIB was often used in the anode compartment; that was later revised and replaced because its properties could not lead to high performance in seawater batteries.

An organic electrolyte that has been one of the most successful in seawater batteries is a 1 M sodium trifluoromethanesulfonate ($NaCF_3SO_3$) solution in tetraethylene glycol dimethyl ether (TEGDME)[53,64,111,112] since the SEI layer seems beneficial with the TEGDME-based electrolyte.[67] A disadvantage for the anode section is the occurrence of side reactions with resulting gas evolution in this compartment during cycling. This causes a swelling of this cell section; therefore, the battery cell cannot run for a long time and in stable conditions but rather breaks down relatively quickly.[113] It is not an easy task to solve this problem due to the high reactivity of the commonly used metallic sodium anode. Thereby, achieving long performance stability remains a tall challenge. Lee et al. developed an alternative system using sodium-biphenyl-dimethoxyethane (Na-BP-DME) as a redox-active.[52] This approach allows the chemical and electrochemical stability of the anode side to be optimized, which ultimately represents a decisive advantage for practical applications. Compared with the conventional, nonaqueous

liquid electrolyte (NaTf-TEGDME), the Na-BP-DME anolyte showed enhanced chemical and electrochemical stability with better cycling stability and cost-effectiveness.

2.1.5. Electrocatalyst: Oxygen Evolution Reaction and Oxygen Reduction Reaction

Charging and discharging a seawater battery combines the concurrence of sodium-ion reactions (much common to NIBs) at the anode and an electrocatalytic reaction involving seawater at the cathode/catholyte side.[68,114] Due to the usually very open-structured design of the cathode in the seawater battery, this part is continuously exposed to the renewed inflow of oxygen from the environment. The battery cell takes advantage of this and uses this abundant gas directly to discharge as electricity. Due to the excess of (dissolved) oxygen, it actively participates in the redox reaction of the seawater catholyte, which leads to the well-known OER/ORR shown in Equations (1)–(3)

$$4OH^- \leftrightarrow O_2 + 2H_2O + 4e^- \text{ (ORR} \leftrightarrow \text{OER)} \tag{1}$$

$$4Na^+ + 4e^- \leftrightarrow 4Na \tag{2}$$

$$4Na + O_2 + 2H_2O \leftrightarrow 4NaOH \text{ pH dependent} \tag{3}$$

The facile reduction of oxygen dissolved in seawater carries the ORR process. During discharging, the stored chemical energy is converted to electricity, and charge-compensation is accomplished by transferring sodium ions from the anode compartment across the membrane (back) into the seawater. This two-electron reduction pathway process ($O_2 + H_2O + 2e^- \rightarrow HO_2^- + OH^-$) is kinetically advantageous but will cause a lower theoretical cell voltage of seawater batteries from 3.48 to 2.9 V with the pH of seawater at 8. This can be avoided by using the selective four-electron reduction pathway ($O_2 + 2H_2O + 4e^- \rightarrow 4OH^-$) electrocatalysts, which lead to a thermodynamically favored process (pH = 8) with more charge carriers.[45] This reaction plays a crucial role in the process, strongly linked to the resulting cell performance. An electrocatalyst can be used as a critical component to enhance the reaction kinetics, and the cathode current collector can be carefully chosen.

To develop an optimal catalyst for this complex system, the following criteria must be fulfilled: 1) high catalytic activity, (2) high pore volume with a large specific surface area, balancing ion transport, and electrode kinetics, 3) high density of accessible, active sites with a homogenous distribution to enable a low OER and high ORR potential, 4) (electro)chemical and mechanical stability to enable device longevity, 5) high and volumetric activity, and 6) cost-efficiency associated with available resources.[45] Electrocatalysts used in seawater batteries can be divided into nonprecious metal oxide-based electrocatalysts ($Co_xMn_{3-x}O_4$,[68] $Co_3V_2O_8$ [115]), carbon-based electrocatalysts (mostly doped carbon black, nanotubes, porous carbon, graphene, and nanofibers),[116–119] and hybrid or composite electrocatalysts (graphene–carbon nanotube-cobalt hybrid)[112] as an alternative to the usual precious-metal-based electrocatalysts (iridium oxide, ruthenium oxide, and Pt/C). Catalysts such as

iridium oxide and ruthenium oxide are well-known for providing an attractive OER performance.[120,121] Most commonly, Pt/C catalysts are being used as an accelerator for the ORR.[113] However, using such noble metal catalysts does not align with the cost sensitivity intrinsic to large-scale applications.[122]

2.1.6. Cell Design

Since operation with only one electrode compartment is not energy-efficient, operation in the aqueous medium for the anode and cathode sides is not promising. One of the reasons for this is that most high-capacity materials are not stable in aqueous media, and the potential window is limited to the stable range of water (1.2 V). The main seawater battery design can be divided into an organic anode compartment and a seawater cathode compartment. Larger systems are also being designed and successfully used for applications beyond energy storage. These systems are mostly built as dual-use systems; while water is desalinated during the charging process, the charge is stored during subsequent discharging. Therefore, at least one additional compartment is responsible for the desalination, besides the sodium collection compartment and another compartment. This extra compartment, which consists of the seawater and a current collector, is used in this additional application in the work of Bae et al. as a carbon capture compartment.[123] In this hybrid system, silver was used to form AgCl particles during the charging of the system and the resulting oxidation on the Ag electrode. For this purpose, Na-ions are brought into the anode compartment in the same step as already done in the well-known seawater battery. In addition, the water is desalinated. In the subsequent discharge process, the Na metal in the Na-compartment is oxidized to ions and made available to the carbon capture side. At the same time, the ORR takes place, generating electrical energy. The presence of Ca^{2+} in the seawater and the relaxed OH^- leads to the formation of $CaCO_3$ from the CO_2 gas.[123]

Seawater battery design also capitalizes on established concepts and components from other energy storage segments (lithium-ion and sodium-ion batteries). So far, a modified coin cell, shown in **Figure 5**A, has been used in most cases, mostly with a direct connection to a flow-type cell tester. The pouch cell is also being used more and more. Recently, new optimization attempts have emerged that employ a rectangular cell produces an improved charge–discharge performance (comparison illustrated in Figure 5B). With improved conductivity and efficiency in stacking, this cell should show enhanced competitive performance with other already published commercial battery systems.[124]

2.2. Criteria Evaluating the Performance of Seawater Battery

The individual parts of the seawater battery are combined in a complex structure and are fully functional, which optimally results in an environmentally friendly battery cell with good performance. The following sections outline the criteria for seawater battery performance. An illustrative graph is given in **Figure 6** showing the actual performance of the seawater battery as well as the future design goals considering different key points

2.2.1. Capacity

The capacity describes the charge storage capacity of an electrochemical energy storage device. The capacity indicates the amount of electrical charge Q that a battery can supply or store. Capacity is usually expressed in ampere-hours (Ah), and it is commonly normalized to mass (Ah g^{-1}) or volume (Ah cm^{-3}), thus forming the basis for the battery field naturalized nomenclature of mAh g^{-1}. This index is applied to describe the performance of alkaline metal batteries, as well as likewise for seawater batteries. The capacity also depends on the type/amount of active material, discharge current, discharge voltage, and temperature[125] and can be used to calculate how long a given current or how long a specific current, or how much current can be extracted over a specific time. The limit of electrochemical charge storage is the theoretical capacity of a material given by Faraday's law of electrolysis.[126] The theoretical capacity cannot be reached in practical applications due to polarization effects or losses due to side reactions or material defects. The overall capacity of the cell can only be as good as the weakest component of a battery. Hence, anode and cathode must provide the same capacity, resulting in a balanced and perfectly composed interaction. While a high capacity is desired, other criteria and parameters are also critical. Typical values of the capacities, which are reached in the state-of-the-art seawater batteries, range from 10 mAh g^{-1} (β''-Al_2O_3 membrane and hard carbon anode[88]) to 900 mAh g^{-1} (NASICON membrane and red phosphorus anode[49]), depending on the used electrode material, based on the reaction mechanism and the applied current.

2.2.2. Efficiency

Efficiency is a critical evaluation criterion that describes a particular system's performance, especially for electrochemical systems. Three parameters (Coulombic efficiency, energy efficiency, and voltage efficiency) are typically used in this context.

The Coulombic efficiency (CE) is the ratio of the amount of charge (Q) flowing through the cell during discharging and charging and will be expressed as a percentage. Optimally, the standard potential of the cell at the start of charging should correspond to the lower end-of-charge voltage at the subsequent discharge. The Coulombic efficiency is based on losses such as SEI formation and aging effects. Past works show a Coulombic efficiency in the range of 76–98%,[51,111,127] whereas commercial lithium-ion batteries typically show values above 99%.

Two more efficiency values are to be considered. First, the voltage efficiency (VE) represents the voltage ratio between charging and discharging, considering the internal resistance and different polarizations. Second, the energy efficiency (EE) is a derivative of the Coulombic efficiency and the voltage efficiency (EE = CE × VE).[128] Several conditions, such as the temperature, electrolyte conductivity, specific current, and the selection of the membrane/separator, influence the values of the efficiencies. In general, the efficiency of the seawater battery can be evaluated with all these three factors. Commonly, the Coulomb efficiency is taken as a comparative value to determine the capacity loss cycle by cycle, which is an essential parameter for predicting the remaining battery life.
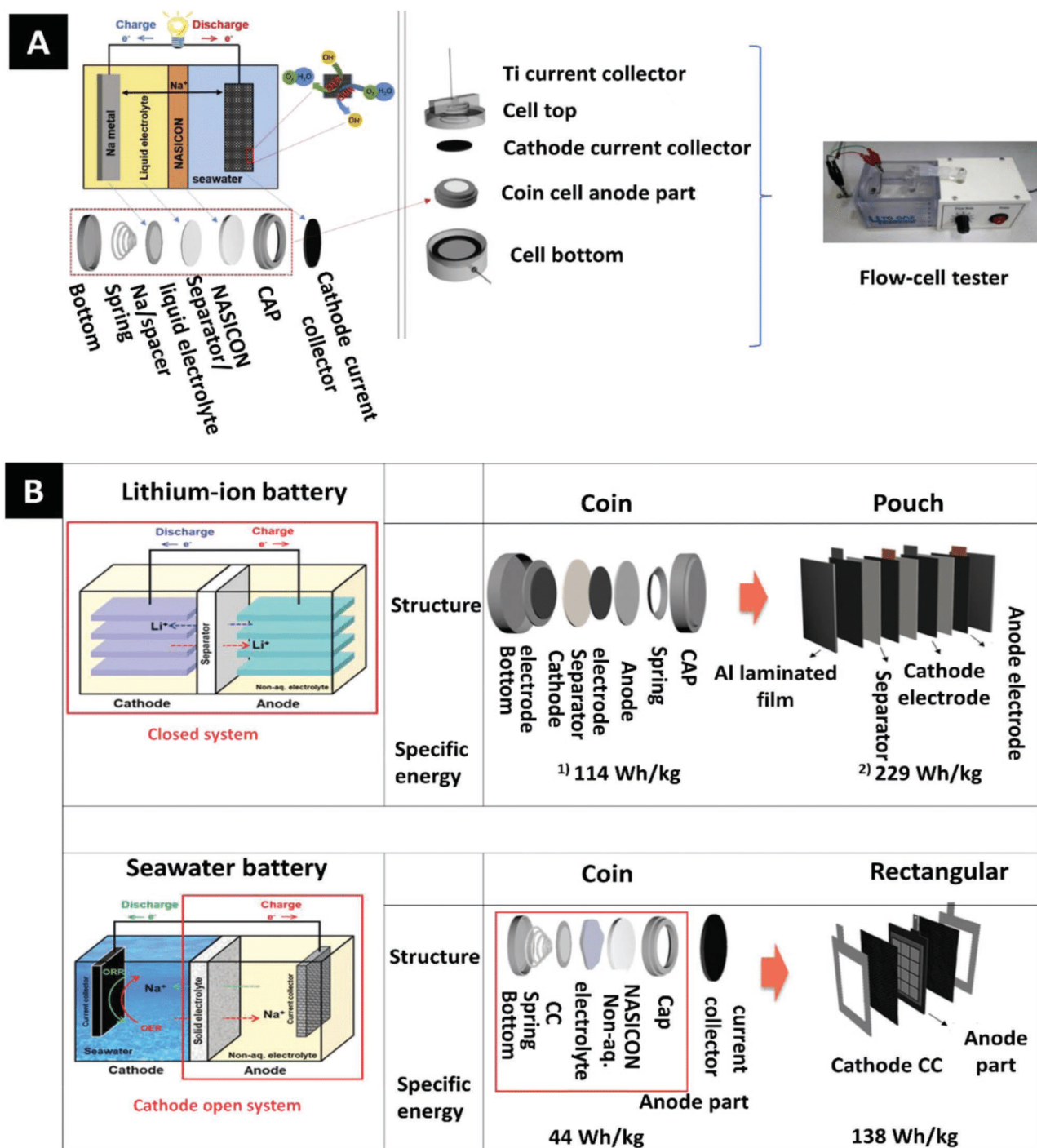
Figure 5. State-of-the-art seawater battery cell set up. A) Schematic diagram of the seawater battery (top) and the integrated cell components of the coin-type cell (bottom) and assembled coin-type cell with flow-cell tester adapted and modified with permission from.[82] Copyright 2018, Elsevier Note: (1) PD2450 rechargeable Li-ion battery, Routejade. (2) LG325134115 Li-ion polymer battery, LG chem. B) Scheme of the operating mechanism of a lithium-ion battery compared to a seawater battery and the corresponding unit cell adapted and modified with permission from.[124] Copyright 2020, John Wiley and Sons. CC = current collector.

2.2.3. Stability and Performance Longevity

In addition to the efficiency and capacity, which mainly characterize the instantaneous consumption of a state, the cell's

lifetime and stability are critical parameters for evaluating seawater batteries. In addition to all the other factors involved in the aging of battery cells and several side reactions, the stability of the solid electrolyte in the aqueous medium (NaCl solution)

**ADVANCED
SCIENCE NEWS**
www.advancedsciencenews.com

NANO · MICRO
small
www.small-journal.com
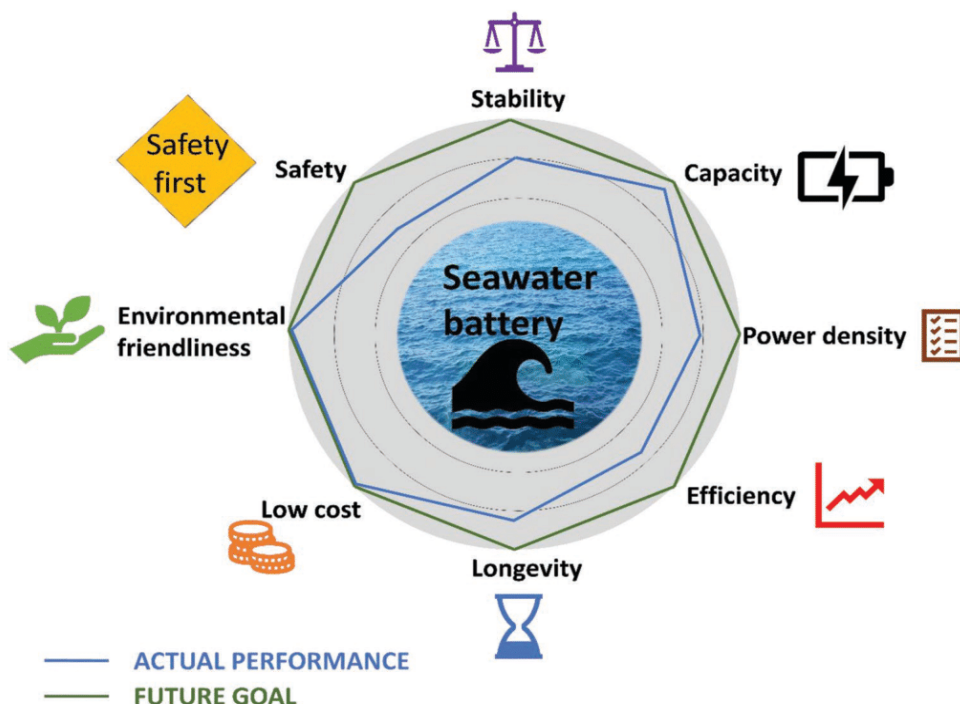
Figure 6. Parameters of designing a good performing seawater battery.

is a limiting factor. The cycle numbers typically reported for seawater batteries are 20–100 cycles[52,55,56,87,129] with satisfying capacity retention. Therefore, the aim is to reduce these limiting factors as far as possible to create batteries that are as long-lasting and stable as possible.

2.2.4. Safety and Environmental Friendliness

Seawater batteries present a particular issue as many device types employ both metallic sodium and water. A dangerous and unsafe action can also happen, for example, by forming Na dendrites, which can then cause a short circuit in the cell and trigger a simple ignition of the battery.[113]

An equally important aspect is the environmental friendliness of seawater batteries. There is the environmental hazard of some materials used as electrodes or even organic electrolytes. As common in the battery industry, polyvinylidene fluoride (PVdF) with N-methyl pyrrolidone (NMP) as its respective solvent is often used to prepare the electrode coating.[55,130–132] The environmental concerns of NMP are aggravated by health concerns, such as cancerogeneity and the cause of respiratory difficulties, and excessive mortality mandate to explore safer and greener alternatives.[133] As electrolytes are often adopted from the NIB community, the safety risks also apply to seawater batteries. So, the physical hazards associated with conventional $NaClO_4$ and carbonate-based electrolytes are well documented.[134,135] Sometimes, this can result in elevated temperature, large combustion enthalpy, and high flammability.[135]

It is also necessary to consider recycling after the cell has reached the end of its battery life. So far, no work proposes or applies the recycling of seawater battery components. While the metallic components may be straightforward to recycle and repurpose, issues arise with ceramic ion-exchange membranes. However, the ceramic membranes may well be the most cost-intense component; therefore, their recyclability may be highly desirable.

2.3. Limitations and Advantages of Present-Day Seawater Batteries

Due to the growing electrification and increased demand for renewable energy storage systems, exploring alternatives and substitutes to existing primary power sources is necessary. These include, among other things, that the lithium-ion batteries must consider increased prices due to the exhausted resources of Li and the concerns about geopolitical and environmental aspects. Additionally, the typical metal-ions batteries, like lithium-ion and sodium-ion batteries, the cathode accounts for 30% to 35% of the total costs (**Figure 7**A).[49]

Using natural seawater as the catholyte is highly cost attractive, abundantly available, and rich in sodium ions. Seawater can be circulated along the aqueous components to mitigate possible heat-buildup in large-scale modules.[43] So far, it is not common in the seawater battery community to present the material's rate stability, and only a few works provide such data.[51]

2.3.1. Issues at the Anode

On the anode side, if this is not an elementary anode, there are often simply degradation problems compared to those in
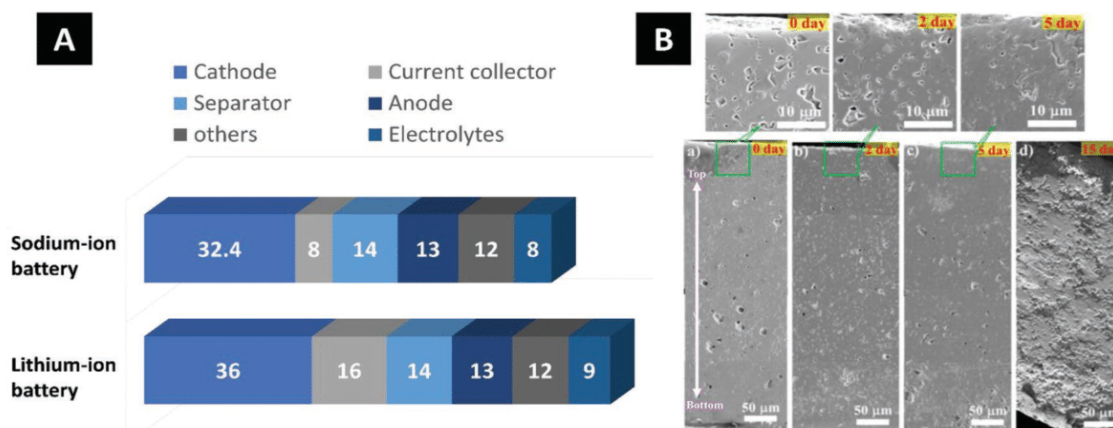
Figure 7. A) Comparison of cost contribution of each component for lithium- and sodium-ion battery system in percent. Reproduced with permission.[49] Copyright 2014, John Wiley and Sons. B) Scanning electron images of the polished surfaces of the Hong-type NASICON ceramic samples immersed in seawater at 80 °C for 0 d, 2 d, 5 d, and 15 d. Reproduced with persmission.[145] Copyright 2017, American Chemical Society.

a NIB.[136] One problem is the proper selection of the binder. Many systems have been adopted directly from the lithium-ion battery community without considering a seawater battery's unique (electro)chemical setting. The choice of the binder significantly influences the battery life, costs, and the avoidance of toxic organic solvents.[137] PVdF is a standard binder in lithium-ion batteries. Due to the low number of functional groups, it has the advantage of low reactivity, good adhesion properties, and electrochemical stability.[138] Still, PVdF binder can also cause system instability as other side reactions may occur. For example, using fluorinated binders leads to reductions that influence the cell reaction and reduce the capacity and performance of the cell.[139] Sodium in the presence of the PVdF binder may also destabilize the cell.[140] The decomposition of PVdF weakens the electrode, so individual particles may become detached and act as insulators. This results in lower efficiency and high capacitance loss.[141,142] The formation of SEI also has a significant influence on the cell's performance. PVdF, for example, has a significantly lower cycle performance as it continuously reduces carbonate solvents, resulting in a (too) thick or unstable SEI layer.[143]

A further problem known from sodium-ion batteries relates to using elemental sodium as an electrode. During electrochemical cycling, dendrites can occur, and uncontrolled growth of tree-like Na dendrites hinders safe battery operation and shortens lifetime while still exhibiting low Coulombic efficiency.[57–61] Therefore, limiting or avoiding the growth of sodium dendrites is crucial. The future of seawater battery electrode materials may well be with anode systems that do not require binders or elemental sodium, such as the redox-mediated red-phosphorous semiliquid anode system.[144]

2.3.2. Stability of the Membrane and Cathode in Saltwater

The selective sodium permeable membrane's stability is highly important for seawater batteries. Like the rarely used β''-Al$_2$O$_3$ membrane, NASICON also shows signs of aging after a certain period (Figure 7B), whereby different stresses build up inside the NASICON ceramic during the structural

degradation process and increased compressive stress can be observed. Likewise, investigations by Jung et al. have described the local compaction of NaCl at the surface, which can be related to a reaction of the chloride ions with the sodium species from the NASICON structure.[145] These exposed sodium sites get occupied by H_3O^+ ions in a subsequent reaction, which leads to volume changes and intense precipitation of NaCl.

Comparing the energy densities of different energy storage systems, the seawater battery with an energy density of mostly <150 Wh kg^{-1}[65] has been relatively moderate. In comparison, considering a commercial lithium-ion battery, a conventional battery can deliver up to four times the energy density (250–590 Wh kg^{-1}).[6,146] The reasons are complex but can be due to the low capacity, achieved mainly by limitations in the anode and cathode selection and the low working voltage. At least one compartment must continuously be operated in the aqueous medium. However, optimizing the cathode materials remains challenging since they have to be stable in the aqueous medium and resistant to side reactions concerning the OER and ORR.

Despite this knowledge and further studies on undesired side-reactions in OER/ORR on the cathode side, there is still a lack of a more profound understanding of performance failure, especially performance degradation. From the transfer from fuel cells, it could be assumed that the primary carbon material used as a cathode current collector can be oxidized by a corrosion reaction and thus rendered unusable/less efficient.[147–154] Another issue is scaling via the possible precipitation of $CaCO_3$ in primary seawater batteries.[155,156] This process may occur during the cell discharging via the ORR process in seawater.[53]

Activated carbon can be an environmentally friendly and (electro)chemically stable choice for the current collector at the cathode side. Past works show that it provides an increased voltage gap (0.6 to 1.42 V) and limited energy efficiency (64–83%).[53] The gradual increase in overvoltage and the recovery of voltage efficiency after replacement of the cathode suggests that the cathode is the leading cause of cell performance degradation and that there may be several degradation processes.[53] On the one hand, oxidation of the carbon

RESULTS AND DISCUSSION

**ADVANCED
SCIENCE NEWS**
www.advancedsciencenews.com

**NANO · MICRO
small**
www.small-journal.com

current collector surface probably occurs, leading to a gradual build-up of the impedance. On the other hand, structural damage to the cathode occurs after a critical running time of the cell.

2.4. Approaches to Improve Present-Day Seawater Battery Technology

2.4.1. Voltage Efficiency: Enhancing the Kinetics of ORR/OER

Increasing Concentration of Dissolved Oxygen: Since seawater batteries use seawater as catholyte, fresh reactants (water and oxygen) must be continuously supplied to the cathode current collector during cell operation.[45] If this is not the case, few to no reactants will be available, reactions will be slower and weaker, and the cell efficiency will be low. The concentration of dissolved oxygen in the catholyte can be increased to counteract this limiting factor by flowing seawater continuously through the cell compartment. Han et al. have compared the values of efficiency and overpotential with and without a continuous electrolyte flow. Without flowing the seawater, the charge and discharge voltage of the cell is slowly saturated with a voltage gap of 1.1 V between charging and discharging. By contrast, when the seawater is flowing, that difference decreases to 0.7 V. Thus, it also appears essential to have a continuous flow of seawater catholyte. This may partly be due to the facilitated diffusion of the reaction to the cathode current collector, resulting in reduced concentration polarization during the charge and discharge cycle.

Synthesis of a New Catalytical Electrode with High Catalytical Activity: To increase the efficiency, one can use a suitable bifunctional oxygen evolution reaction/oxygen reduction reaction electrocatalyst at the cathode. This approach could effectively reduce the side reactions (like other reactions of Cl_2 with the water) to OER/ORR at high overvoltages.[68] These side reactions depend on the applied current, the pH, and the local Cl^- concentration at the air cathode.[68] The large overpotentials that often occur in the charge and discharge cycles result from slow OER and ORR reaction kinetics. This yields a significant difference between the discharging and charging voltage profiles; the low voltage efficiency is accompanied by a low energy storage ability and insufficient cycling stability.[157–159]

These problems can be (partially) overcome with effective electrocatalyst systems, which allow the reaction to proceed faster. Mainly elements taken from general catalyst research, such as Pt, Ru, Pd, Au, and Ir, are used. Due to their comparatively high costs and scarce availability, they have not yet established themselves in large-scale industrial use.[147–154,157,159–161] Many studies have explored nonprecious metal oxides or heteroatom(s)-incorporated carbonaceous materials. Mixed spinel-type transition metal oxides based on Ni, Co, and/or Mn are promising. For example, Abirami et al. used cobalt manganese oxide with a spinel structure ($Co_xMn_{3-x}O_4$, CMO) as a seawater battery electrocatalyst without noble elements.[68] This catalyst accelerated the cathode reactions (OER/ORR) because of the large specific surface area with many electrocatalytically active sites by reducing the voltage gap and enhancing the voltage efficiency to a value of 85%.[68]

Further approaches are proposed to eliminate the efficiency problems by synthesizing completely new catalytic electrodes with high catalytic activity. For example, Liu et al. showed Mg-ion-based seawater batteries.[162] The porous heterostructure of the synthesized CoP/Co_2P provided a large specific surface area, abundant active interfaces, and enhanced active sites with accelerated charge transfer.[162] This enabled a high hydrogen evolution reaction activity, enhanced performance with good efficiency, and promising stability for Mg seawater batteries.[162]

Shin et al. proposed a new electrocatalyst that optimizes the kinetic of the seawater cathode OER/ORR process.[115] $Co_3V_2O_8$ with large active sites enabled an increased voltage efficiency of ≈76% by lowering the charge voltage from 3.88 to 3.76 V and increasing the discharge voltage from 2.80 to 2.87 V (compared to a cell without catalyst).[115] The resulting seawater battery provided promising cycling stability with voltage gaps of ≈0.95 V.[115]

Modifying the Carbon Current Collector at the Cathode Side: Side effects of carbon corrosion and scaling via $CaCO_3$ plague the cathode during the charging process. Preventing irreversible carbon corrosion at the cathode enables a higher voltage efficiency and better cycling stability.[53] This can be accomplished by using more corrosion-resistive carbons and catalyst materials.[163,164] For example, Tao et al. reported that inducing various defects and the resulting shift of charge in the subsequent electrochemical characterization makes it possible to increase the activity for electrocatalytic reactions (ORR, OER, and HER).[165]

The carbon current collector can also be modified by heteroatom doping. This can be explored to improve electrocatalytic activity. For example, Jeoung et al. fabricated PNCs (high surface area, nitrogen-doped carbon) and efficiently adjusted the porosity of PNCs by varying the transformation conditions.[166] The mesoporosity was crucial for controlling the electrocatalytic activity and the seawater battery performance. This distinct improvement made it possible also to obtain improved electrochemical properties (stable voltage gaps of <0.53 V at 0.01 mA cm^{-2} over 20 cycles),[166] thus highlighting the use of PNCs as a promising metal-free catalyst in the seawater battery.

Another effective method to improve the efficiency from several points of view was proposed by Suh et al., who used hydrophilic carbon electrodes on the one hand and a 3D hybrid (S-rGO-CNT-Co).[112] The uniform distribution of Co/CoO_x nanoparticles on the porous 3D graphene creates many active sites, resulting in good cycling stability and rate properties. The additional CNTs, with their high conductivity and stability, prevent rapid cell degradation due to electrode decomposition.

Hybridizing Catalytic Reaction: The optimized performance can also be enabled by hybridizing the catalytic reaction with other electrochemical processes or using other electrochemical processes as a substitute. No less attractive and effective is an approach in which the catalytic reaction is combined with another electrochemical process. Park et al. combined ion electrosorption via the formation of an electrical double-layer with the OER/ORR electrolytic activities in activated carbon cloth seawater batteries.[64] This lowered the voltage gap to 0.49 V, increased the voltage efficiency to 86%, and yielded increased power performance.[64] Kim et al. introduced a silver foil as a chloride ion capturing.[111] Silver's reversible Ag/AgCl reaction

with the Cl⁻-ions released from the seawater catholyte at 2.93 V versus Na⁺/Na (in the charge and discharge cycle, respectively) bypasses the typical OER/ORR reaction. This process significantly reduced the voltage gap and increased the voltage efficiency to about 90%.[111]

2.4.2. Stability

Eliminating Side Reactions: The problem of side reactions with a particular binder system and sodium is known from present-day NIB research and occurs in seawater batteries.[67] As a promising binder, sodium alginate is very stable, environmentally friendly, and supports the formation of a stable SEI.[167] The carboxymethyl cellulose binder, for example, is an environmentally friendly and green material. It is soluble in water, which allows the processing of aqueous pastes. However, due to the solubility in water, only an application in the anode compartment is possible since the electrode on the seawater side would dissolve otherwise. It is mainly used in anodes that have a high capacity.[137]

Using elemental sodium as electrode material leads to a high capacity. Still, the cell voltage is limited by the (electro)chemical stability window of water.[129,168] Some approaches to overcome this problem have been proposed in past works. For example, Tu et al. proposed a method with enhanced ORR/OER activities of seawater batteries using a cathode made from nitrogen-doped carbon cloth.[169] Abirami et al. presented work that used next to the CMO cathode catalyst also a hard carbon electrode as a sodium-free anode; their cell provided a discharge capacity of around 190 mAh g⁻¹$_{hard carbon}$ with an average voltage of about 2.7 V during 100 cycles (corresponding with an energy efficiency of 74–79%).[68] Kim et al. proposed a hard carbon anode separated by a ceramic membrane from a carbon paper as a current collector for the seawater cathode side.[88] The discharge capacity of the resulting seawater battery was 120 mAh g⁻¹ after the first cycle, with a resulting Coulombic efficiency of 91% after 20 cycles.[88]

Many attempts have been made to counteract the rapid and uncontrolled growth of the Na dendrites. For example, approaches from Li-ion battery chemistry have been adopted, such as adjusting the charge/discharge rate at the current collector, increasing surface tension to suppress the dendrite formation mechanically, or modifying the electrolyte concentration.[14,61,84,170–177] Other works explored using a NaPF₆/glyme electrolyte, an artificial Al₂O₃ SEI layer, various inorganic electrolytes, or sodiated carbon as a nucleation layer.[178–186] Using a low current density may further delay dendrite formation and increase the critical nucleation radius.[171,187–189] Kim et al. proposed controlling the growth of sodium dendrites rather than avoiding their occurrence altogether.[189] Thereby, enhanced performance stability resulted from a low number of sodium dendrite cores formed on the homogenous surface of a graphene-coated copper current collector.[189]

Optimizing of the Anode Compartment: The liquid electrolyte is of critical importance at the anode because it reduces the interfacial resistance between the anode and the ceramic membrane (which serves as the solid electrolyte); this is important to enabling stable cell performance and efficiency.[111] An electrolyte adopted from the NIB was often used in the anode compartment. Still, some studies showed that an ethylene carbonate/propylene carbonate(EC/PC) electrolyte could not provide sufficient cycling stability.[49,67,124] For example, Kim et al. showed for the EC/PC-based electrolyte the formation of a poorly conductive, thick SEI layer and the degradation of the PVdF.[67] Successful and high-performance electrolytes based on TEGDME have been developed, which show good cycle performance over 100 cycles and are successfully used in almost every present-day seawater battery.

The areal/absolute capacity of some anode electrode materials can be increased by employing a semisolid anolyte, which includes two redox mediators.[190] One of these mentioned anolytes would be, for example, sodium biphenyl, which has been successfully used in combination with a semiliquid negative electrode of red phosphorus for the realization of metal-free Na-seawater batteries. Remarkably, using the semiliquid electrode as a static anode, high area capacities of about 11 mAh cm⁻² in Na half cells and 15 mAh cm⁻² in Na seawater cells could be achieved at room temperature.[144] For sodium metal batteries, sodium biphenyl is an attractive and cost-efficient anolyte system, which prevents hydrogen evolution and suppresses sodium dendrite growth, thus increasing the capacity and providing performance stability.[191] Ionic liquids (ILs) may be a future choice for high-performance seawater batteries. For example, NaFSI salt in two ionic liquids (Pyr₁₃FSI and Pyr₁₃TFSI)) showed a very high (electro)chemical and thermal stability in combination with the well-known low vapor pressure of IL.[51] This was accomplished despite the small amount (5 mass%) of organic solvent (EC) added to facilitate and enable the formation of a stable SEI on the hard carbon anode. In contrast to the typical liquid electrolytes (i.e., organic solvents), ILs show a lower cell polarization resulting in higher energy efficiency.[51] Kim et al. used this electrode and anolyte to obtain a capacity of 290 mAh g⁻¹$_{hard carbon}$ with a Coulombic efficiency of 98% during 600 charge/discharge cycles at rates up 5.0C, and associated energy efficiency up to 80%.[51]

3. Dual-Use Application: Seawater Batteries for Energy Storage and Desalination

3.1. Energy Storage

3.1.1. Wearable Devices

Marine wearable devices like life jackets and wetsuits are usually equipped with lights to illuminate and locate drowning persons. Since the seawater battery utilizes the seawater as the catholyte, it is very suitable for marine wearable devices' power supply. Cho et al. put forward a novel design for marine life jackets.[192] It takes advantage of the properties of seawater batteries that generate electricity once the cathode current collector contacts the seawater. Therefore, when people fall into the water wearing the life jacket, the batteries will be activated and charge the in-built global positioning system.[43]

3.1.2. Marine Fundamental Facilities

Marine primary public facilities on the ocean, such as light buoys and water-quality monitoring stations, are commonly
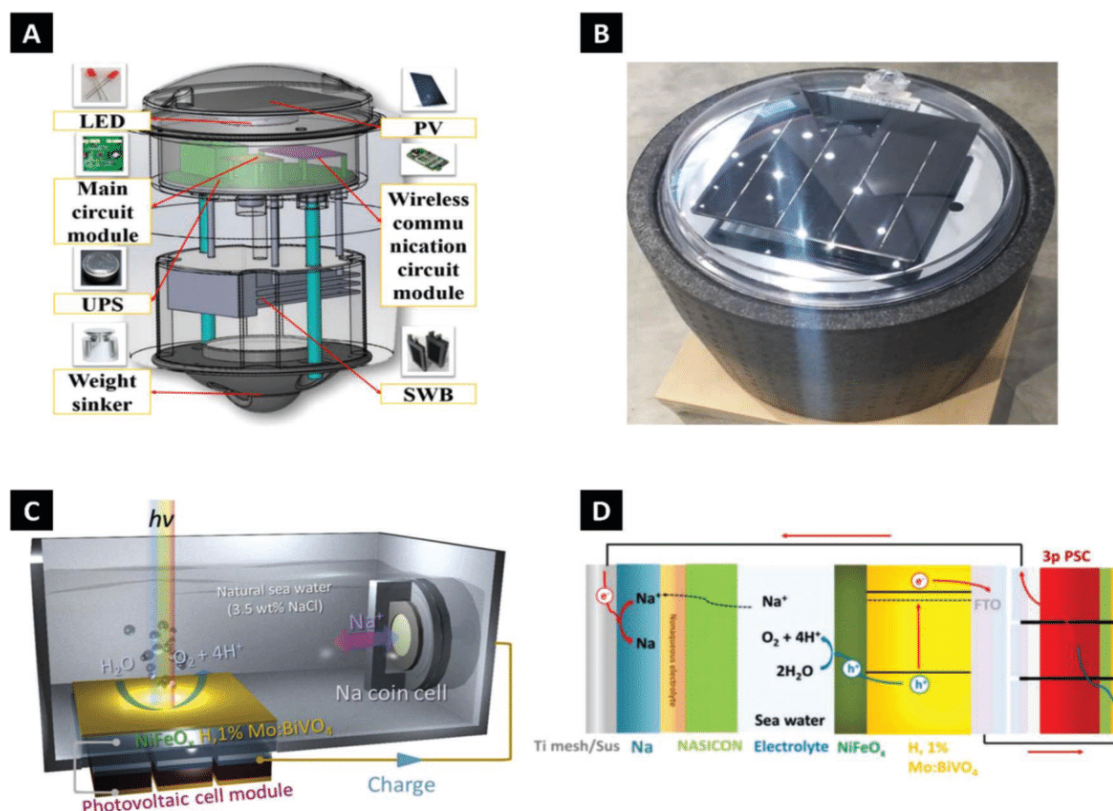
Figure 8. A) The conceptual diagram and B) optical photograph of seawater battery-based wireless buoy system. Reproduced under the terms of the Creative Commons Attribution 4.0 License.[192] Copyright 2021, the Author(s), Published by IEEE. C) Scheme image of unassisted solar-charging rechargeable seawater battery with $NiFeO_x/BiVO_4$ PE combined with PSC or c-Si PVs and D) the mechanism image of it with three pieces of PSC as the example. Reproduced with permission.[193] Copyright 2019, Elsevier.

powered by solar batteries assigned with energy storage systems like lithium-ion batteries or lead-acid batteries. Once these batteries have some leakage, the toxic component in the batteries will be released into the sea. Therefore, power with a long lifespan, low cost, and low/no environmental pollution are required. Recently, Kim et al. designed a wireless marine buoy system based on rechargeable seawater batteries.[124] The system comprised seawater batteries (energy storage), light-emitting diodes light, the main circuit module, an uninterruptible power supply, a wireless communication circuit module, and photovoltaic batteries (self-powered energy resource), as shown in **Figure** 8A,B. The state-of-charge (SOC) is monitored by Coulomb counting, and variance measurements detect the state-of-health. Through wireless communication, the position of marine buoys and the SOC information of the batteries can be obtained on a mobile phone.

3.1.3. Large-Scale Energy Storage

Apart from the small devices, rechargeable seawater batteries are also expected to serve as the energy storage systems for the solar, wind, or tidal power station installed near the ocean. Recently, Kim et al. designed a combined photoelectrode (PE)– photovoltaic (PV) device to accomplish the solar energy-driven rechargeable seawater batteries.[193] In the cell, $NiFeO_x/H$, 1% Mo:BiVO$_4$, and

a series-connection of crystalline silicon solar cells or lead halide perovskite solar cells were applied as the cathode, and the other components were adopted from conventional rechargeable seawater batteries (Figure 8C). Oxygen and hydrogen are obtained during the charging process on the cathode side, while on the anode side, the sodium ions precipitate as metallic sodium, as shown in Figure 8D. This setup provides an avenue to apply rechargeable seawater batteries independently as marine facilities' power supply without extra power.

3.2. Desalination and Water Purification

3.2.1. Cell Configurations and Performance Metrics

Due to the unique structure, containing both aqueous (seawater) electrolyte and organic electrolyte, it is easy to implement simultaneous water desalination and energy storage if the system of rechargeable seawater batteries is modified.

In 2018, Zhang et al. proposed a rechargeable seawater battery desalination system.[132] Unlike conventional seawater batteries, the system used stilled water as the catholyte and seawater as the feed water. Oxygen evolution reactions occur at the cathode part during the charging process, producing protons; sodium ions insert into the hard carbon anode. To keep the charge balance, Cl$^-$ and Na$^+$ in the seawater (middle channel)

will migrate through the anion exchange membrane (AEM) and the NASICON membrane, respectively. Thereby, HCl and desalinated water are produced during the charging process, and during the discharging process, the sodium anode is regenerated, and NaOH is formed (**Figure 9**A). Due to the high resistance partially caused by the AEM, there is a high overpotential for OER, resulting in the competition between OER and chloride evolution reactions ($2Cl^- - 2e^- \rightarrow Cl_2$, $E^0 = -1.36$ V vs SHE). Thereby, the partial migrated Cl^- could also be removed by CER.[194] After 10 cycles, the total ion concentration decreases from 34.9 to 31.9 g L^{-1}, with an average Coulombic efficiency of 92% and an energy efficiency of 76%. The relatively low-efficiency values could be due to the irreversible intercalation of Na^+ in the hard carbon[132] or the energy dissipation caused by sluggish ORR and OER reaction kinetics and the high resistance of the cell.[194]
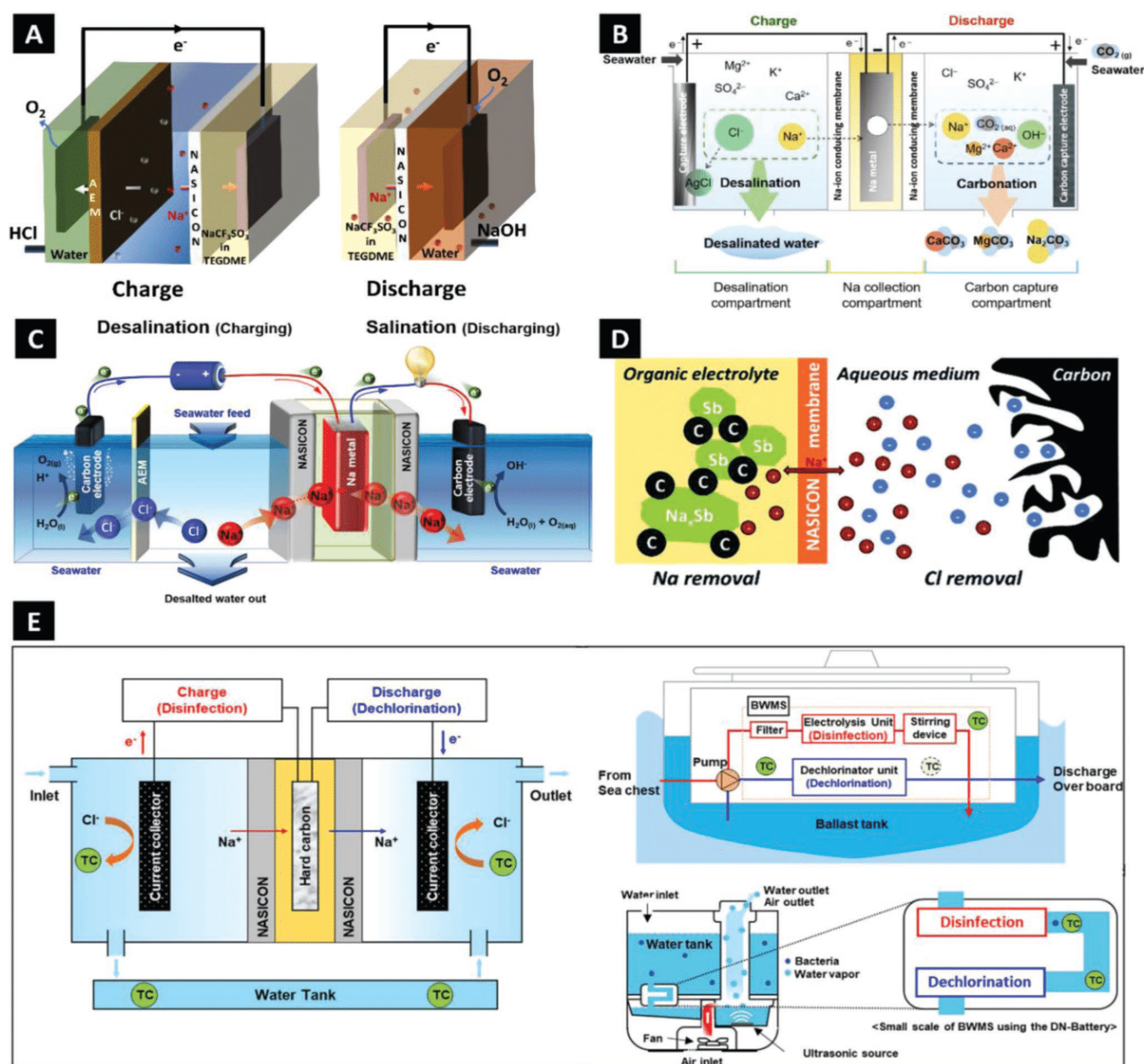
Figure 9. Schemes of different device technologies. A) Rechargeable seawater batteries desalination system with charging and discharging process, redesigned according to Figure 1 of ref. [132]. B) hybrid of desalination and carbon capture system based on rechargeable seawater batteries. Reproduced with permission.[123] Copyright 2019, Elsevier. C) Compartmentalized rechargeable seawater batteries desalination system. Reproduced with permission.[194] Copyright 2020, Elsevier. D) Desalination mechanism in bielectrolyte desalination cell. Reproduced with permission.[90] Copyright 2021, Royal Society of Chemistry. The schematic diagram E) of disinfection–dechlorination battery (left side), conventional electrochlorination and dechlorination of ballast water (right upper corner), and the disinfection–dechlorination battery used in a humidifier (right bottom corner). Reproduced with permission.[195] Copyright 2021, American Chemical Society.

Following works modified the basic rechargeable seawater desalination system mentioned before to optimize the system or add more functionalities. For instance, Bae et al. combined the seawater battery system with a CO_2 capture system (Figure 9B).[123] This system contains the desalination compartment and the carbon dioxide capture compartment. Silver was used as a Cl^- capture electrode instead of an OER catalytic electrode to compose the desalination parts with NASICON and Na metal, unlike the typical seawater battery system. This effectively reduces the overpotential and improves the voltage efficiency during the charging time caused by the sluggish kinetics of OER.[45] After the desalination process (system charging), the system is discharged with Na metal and porous carbon paper as the electrodes, where OH^- is generated and CO_2 is captured by the metal hydroxides, like $NaOH$, $Mg(OH)_2$, and $Ca(OH)_2$. Consequently, $CaCO_3$ or $MgCO_3$ are simultaneously generated as a by-product.

Arnold et al. used carbon cloth as the alternative to OER, for its low price compared to Ag (Figure 9D).[90] With antimony/C as the anode, the initial capacity of the cell was 714 mAh g^{-1} and the average desalination capacity was 294 mg_{Na} g^{-1}_{Sb} with a charge efficiency of around 74%. In 2020, Kim et al. improved the previous architecture of seawater batteries.[194] The cell contains independent desalination and salination parts (Figure 9C). This avoids disassembling cells between the charging and discharging process, which reduces the energy losses and enables a higher nominal cell potential of 3.46 V (pH 8.4) and a theoretical energy density of 4010 kWh kg^{-1}. After galvanostatic charging for 20 mAh, 77% of the salts are removed from the seawater.

Apart from desalinating water, rechargeable seawater batteries also can disinfect the water if a higher voltage is applied. Recently, Park et al. proposed a disinfection-dechlorination battery with a NASICON ceramic membrane, depicted on the left part of Figure 9E.[195] During the charging process, the Na^+ moves through the NASICON membrane and deposits on the anode; Cl^- or OH^- partake at a redox reaction at the cathode (Equations (4)–(7)). The produced HOCl, ClO^-, and Cl_2 could kill microbes in the water. The residual chloride base product will be oxidized into Cl^- during the discharging process. After charging the cell for 3 h, the reduction rate of microorganism, *Escherichia coli* (MG1655), reaches 100%, while 8 h is required to 100% remove another microorganism, *Enterococcus aquimarinus* (DSM17690). This new system avoids the extra dechlorination process of standard disinfection technologies based on chloride disinfectant.[196] However, the competitive OER reactions would reduce the energy efficiency of this system, which may be addressed by applying selective catalysts for chloride evolution reactions.[197] In addition, the authors also put forward two typical applications; one is in the ballast water treatment, and the other is to disinfect microorganisms in humidifiers, which are illustrated in the upper right corner and bottom right corner of Figure 9E

$$2H_2O \leftrightarrow O_2 + 4H^+ + 4e^- \quad E_0 = 3.49 \text{ V vs Na/Na}^+ (pH = 8.3) \quad (4)$$

$$Cl^- + H_2O \leftrightarrow ClO^- + 2H^+ + 2e^- \quad E_0 = 3.94 \text{ V vs Na/Na}^+ (pH = 8.3) \quad (5)$$

$$Cl^- + H_2O \leftrightarrow HOCl + H^+ + 2e^- \quad E_0 = 3.95 \text{ V vs Na/Na}^+ (pH = 8.3) \quad (6)$$

$$2Cl^- \leftrightarrow Cl_2 + 2e^- \quad E_0 = 4.07 \text{ V vs Na/Na}^+ (pH = 8.3) \quad (7)$$
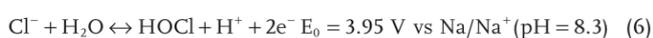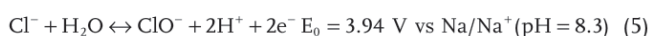
3.2.2. Desalination Performance and Energy Consumption

Seawater batteries provide a high desalination capacity compared to other electrochemical desalination technologies. This beneficial performance results from the extended voltage window and the possibility of using materials with higher capacity as anodes, such as Na metal (theoretical capacity, 1165 mAh g^{-1}),[47] red phosphorus (theoretical capacity, 2596 mAh g^{-1}).[124] Therefore, seawater batteries could remove 70–80% of salts from seawater, among which Na^+ and Cl^- dominate due to the selectivity of the NASICON membrane (**Table 2**).

Limited by the water-splitting voltage window, a relatively low voltage (generally <1.2 V) is applied in other electrochemical technologies, such as capacitive deionization,[37] and desalination batteries.[198] Consequently, materials with suitable potential range but relatively low capacity like carbon (5–30 mg_{NaCl} $g^{-1}_{electrode}$), some intercalation materials (50–100 mg g^{-1}), and some conversion materials (100–150 mg g^{-1}), are employed as the electrode, as shown in Table 2. Compared with the salt rejection rates of current seawater desalination technologies, such as reverse osmosis (RO) (≥99%),[199] multiple-effect distillation (MED) (almost 100%),[200] seawater batteries technology is not suitable to produce potable water, which requires the total dissolved solid lower than 500 mg L^{-1},[199] independently from the seawater. This is because seawater battery desalination generally removes sodium ions due to the selectivity of the NASICON membrane. However, it adapts desalinating the water with the salinity from low to hypersaline. Thereby, this technology could combine with some filtration technologies playing the role of pretreatment and the 2nd pass treatment to desalinate seawater; this technology could also replace some units or be added additionally in the current seawater desalination plants to reduce the energy consumption.

The energy consumption of seawater batteries must also be considered when assessing its application potential. The energy consumption of seawater batteries desalination depends on the amount of removed salt. The removal of 9% of all salt ions corresponded with an energy consumption of 4.7 kWh m^{-3}.[132] The energy consumption increased to 53.9 kWh m^{-3} when the salt removal increased to ≈75%.[201] **Table 3** shows the energy consumption of some industrial plants with various desalination technologies. As can be seen, the energy consumption of RO is ≈3–5 kWh m^{-3},[202] varying from the operation parameters, which is less than that of MED (5–58 kWh m^{-3})[203] and electrodialysis (ED; 3–20 kWh m^{-3}). These industrial plants also employ energy recovery devices to reduce the total energy consumption. Considering the energy recovery of seawater batteries desalination technologies (i.e., discharging process), the energy consumption could reduce to around 5 kWh m^{-3} with the energy recovery reaching 90% by declining the voltage gap during the cycling.[131]

Recently, Ligaray et al. used reverse osmosis models to evaluate the energy consumption of a new system where a seawater battery is applied to be the energy recovery component or the substitute of the first RO in the conventional RO design with the energy recovery devices after the first filtration for the energy recovery of 50% (**Figure 10**A).[201] Their modeling assumed the Coulombic efficiency of seawater batteries to be 100%. Consequently, compared with the standard RO system

Table 2. Desalination performance of seawater-battery-based system, carbon materials, and Faradaic materials used for desalination.

	Electrodes	Feedwater salinity [mg L^{-1}]	Feedwater volume [mL]	Desalination	Desalination capacity [mg g^{-1}]	Charge efficiency [%]	Energy consumption	Refs.
Seawater-battery based system	Sodium metal//carbon felt	33 460	3.4	77%	–	≈70% for Cl$^-$ ≈80% for Na$^+$	37 kT ion^{-1}	[194]
	Sodium metal//silver foil	34 000	–	97% for Na$^+$ 9% for Cl$^-$	–	–	–	[123]
	Hard carbon//Pt/C	34 910	10	9% after 10 cycles	–	–	4.7 Wh L^{-1}	[132]
	Antimony/C//carbon cloth	35 100	–	–	294	74	16 kT ion^{-1}	[90]
	Sodium metal coated on carbon cloth//carbon cloth	12 182.5	3.4	73%	–	–	–	[220]
Carbon materials	Carbon cloth//carbon cloth	58 400	–	–	30	≈90	20 kT ion^{-1}	[221]
	Activated carbon// activated carbon	292.5	–	–	13	86	–	[222]
	Activated carbon//activated carbon	35 100	–	–	12	63	–	[223]

	Electrodes	Feed water salinity [mg L^{-1}]	Volume of the feed water [mL]	Desalination	Desalination capacity [mg g^{-1}]	Charge efficiency [%]	Energy consumption	Refs.
Faradaic materials	Na$_{0.44}$MnO$_2$ //BiOCl	760	50	–	69	97.7	–	[224]
	Na$_{2-x}$Mn$_5$O$_{10}$/Ag/AgCl	34 800	≈0.3	25%	–	–	0.3 Wh L^{-1}	[38]
	VS$_2$-CNT//carbon cloth	35 100	–	–	15	>85	29 kT ion^{-1}	[225]
	NaNiHCF//NaFeHCF	34 465	0.6	40% for Na$^+$	60	–	0.3 Wh L^{-1}	[226]
	Iodide// activated carbon	35 100	–	–	69	64	1.6 Wh L^{-1}	[204]
	Bi/C// activated carbon	1000	50	–	113	–	–	[227]

for seawater desalination, which contains the ultrafiltration (UF), RO, and brackish water reverse osmosis (BWRO), using seawater batteries as the additional energy storage devices could save about 104 kWh m^{-3} energy by reducing the salt concentration from 61 200 mg L^{-1} to less than 20 000 mg L^{-1}. Applying seawater batteries instead of the first RO step (UF-SWB system, UF + SWB + BWRO), the seawater batteries could save 49–50 kWh m^{-3}; utilizing nanofiltration (NF) + seawater batteries (NF-SWB system, UF + NF + SWB + BWRO) together as the alternative of first RO, the seawater batteries can save 24 kWh m^{-3} and 1.1 kWh m^{-3} pump energy could be reduced. The net specific energy consumption (SEC) of the UF-SWB system and NF-SWB system are 1.35 and 2.1 kWh m^{-3}, respectively; these values are below what is needed for the net SEC of a standard 2nd-pass-RO system (2.8 kWh m^{-3}).

The energy consumption of the seawater battery system is relatively high compared with desalination batteries based on the intercalation materials[38] or redox electrolytes[204] (Table 2); this could be due to the high overpotential of the seawater battery system and the high resistance of NASICON membrane.[43] Another potential issue of the seawater battery system is the relatively low desalination rate (generally < 1 mg cm^{-2} h^{-1}), compared with other electrochemical technologies, for instance, flow electrode capacitive deionization (2–40 mg cm^{-2} h^{-1})[205–211]

Table 3. Comparison the performance of current industrial desalination technologies and seawater batteries.

	TDS[a] of feed water [mg L^{-1}]	TDS of product water [mg L^{-1}]	Water recovery [%]	Specific energy consumption [kWh m^{-3}]	Scale	Refs.
Reverse osmosis	40 070	183	46	4.8	Industrial application 16 800 m^3 day^{-1}	[228]
	35 000	174–214	30–50	1.89–2.04	Modeling	[229]
Electrodialysis	35 000	<500	50–60	16.21	Pilot test 30 m^3 day^{-1}	[230]
	35 000	450	41	6.6	Laboratory-scale experiments	[231]
Multieffect distillation	–	–	–	<5	Industrial application (10 000 t day^{-1})	[200]
Seawater batteries[b]	33 700	<200	–	1.35	Modeling	[201]

[a]TDS the abbreviation of total dissolved solid; [b]The results are modeled by RO analysis software where seawater batteries replace RO in the typical RO system.
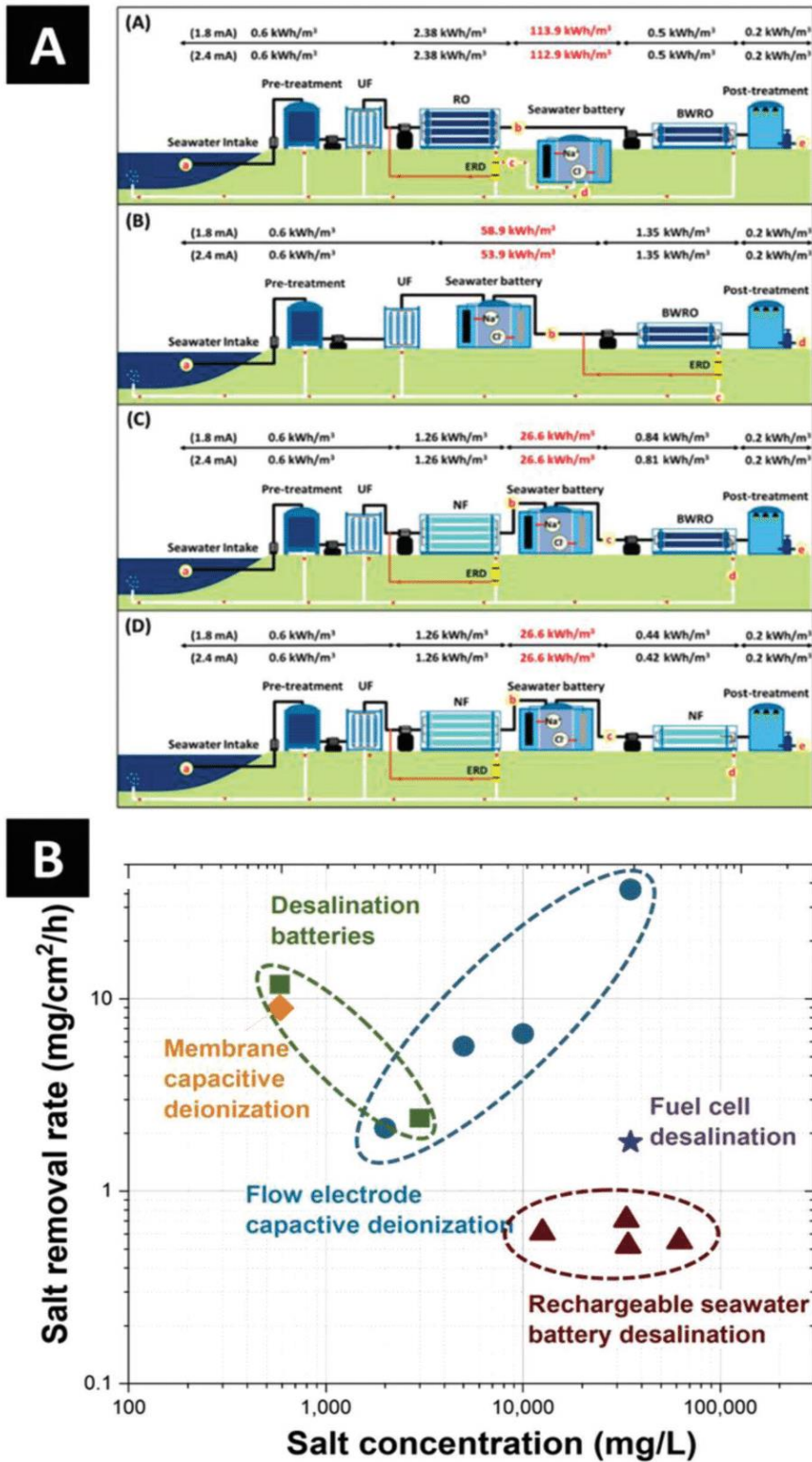
Figure 10. A) Proposed designs for rechargeable seawater battery desalination with various feed water. Reproduced with permission.[201] Copyright 2020, Elsevier. B) Average salt removal rate of different electrochemical desalination technologies. Data adapted from refs. [40,194,201,205–210,212].

164

and desalination batteries (1–10 mg cm^{-2} h^{-1}),[204,212] as shown in Figure 10B. This could be due to the relatively low ion diffusion rate of the NASICON membrane[94] and the sluggish kinetics rate of ORR and OER.[45] However, it should note that the salt removal rate also has a strong relationship with the operation parameters, like the voltage, current, and concentration of the feed water.[213]

4. Conclusions

Since expanding the rechargeable battery industry is indispensable when considering the growing demand for portable electronic devices and sizeable stationary energy storage systems, the seawater battery offers a promising alternative. So far, mainly used lithium-ion battery technology cannot be used as the sole power due to the exploitation of raw materials, the resulting prices increase, and other concerns about geopolitical and environmental aspects. Therefore, the seawater battery, which uses a very environmentally friendly and resource-saving raw material, namely natural seawater, as an almost inexhaustible ion source, provides the possibility of more environmentally friendly energy storage.

Simultaneously energy storage and desalination encourage seawater desalination batteries to be a good choice for replacing some seawater reverse osmosis components. Additionally, attributed to the high selectivity of the NASICON membrane, using seawater batteries to desalinate the water also means extracting sodium ions from seawater. In addition, using other ion-selective membranes would enable elemental harvesting within the context of lithium extraction. Alternatively, nonselective membranes would boost the performance in seawater because cations beyond sodium would be removed. Finally, the advantages of seawater batteries provide a perspective toward sustainable, environmentally friendly, performance-oriented, and cost-efficient applications at the energy/water nexus.

Seawater battery development has yet to overcome technological challenges. A shortened lifetime, prevented safe battery operation, low Coulombic/energy efficiency, and low stability result from the partial instability of the individual cell components such as the solid electrolyte membrane or the anode electrode, as well as side reactions and nonoptimized cell components. Extending seawater batteries for desalination from the laboratory scale to pilot plants also requires optimized system design and benchmarking in real-water applications. The low desalination rate and high voltage gap are significant obstacles. However, these challenges can be addressed by advances in materials science, battery chemistry, and process engineering. In addition, the successful use and application of present-day seawater batteries make us optimistic about the more widespread application of this technology and the positive impact on sustainable devices at the energy/water research nexus.

Conflict of Interest

The authors declare no conflict of interest.

[1] K. G. Cassman, P. Grassini, *Nat. Sustain.* **2020**, *3*, 262.
[2] S. Mitchell, R. Qin, N. Zheng, J. Pérez-Ramírez, *Nat. Nanotechnol.* **2021**, *16*, 129.
[3] J. D. Hunt, E. Byers, Y. Wada, S. Parkinson, D. E. Gernaat, S. Langan, D. P. van Vuuren, K. Riahi, *Nat. Commun.* **2020**, *11*, 947.
[4] C. S. Lai, G. Locatelli, *Energy* **2021**, *214*, 118954.
[5] K. Turcheniuk, D. Bondarev, V. Singhal, G. Yushin, *Nature* **2018**, *559*, 467.
[6] D. Larcher, J.-M. Tarascon, *Nat. Chem.* **2015**, *7*, 19.
[7] L. Wang, K. Frisella, P. Srimuk, O. Janka, G. Kickelbick, V. Presser, *Sustainable Energy Fuels* **2021**, *5*, 3124.
[8] M. Pasta, A. Battistel, F. La Mantia, *Energy Environ. Sci.* **2012**, *5*, 9487.
[9] P. Srimuk, X. Su, J. Yoon, D. Aurbach, V. Presser, *Nat. Rev. Mater.* **2020**, *5*, 517.
[10] K. Turcheniuk, D. Bondarev, G. G. Amatucci, G. Yushin, *Mater. Today* **2021**, *42*, 57.
[11] B. E. Murdock, K. E. Toghill, N. Tapia-Ruiz, *Adv. Energy Mater.* **2021**, *11*, 2102028.
[12] H. Pan, Y.-S. Hu, L. Chen, *Energy Environ. Sci.* **2013**, *6*, 2338.
[13] J. B. Goodenough, K.-S. Park, *J. Am. Chem. Soc.* **2013**, *135*, 1167.
[14] D. Lin, Y. Liu, Y. Cui, *Nat. Nanotechnol.* **2017**, *12*, 194.
[15] M. Ko, S. Chae, J. Ma, N. Kim, H.-W. Lee, Y. Cui, J. Cho, *Nat. Energy* **2016**, *1*, 16113.
[16] L. Lu, X. Han, J. Li, J. Hua, M. Ouyang, *J. Power Sources* **2013**, *226*, 272.
[17] J.-M. Tarascon, *Nat. Chem.* **2010**, *2*, 510.
[18] D. Kundu, E. Talaie, V. Duffort, L. F. Nazar, *Angew. Chem., Int. Ed.* **2015**, *54*, 3431.
[19] C. Vaalma, D. Buchholz, S. Passerini, *Curr. Opin. Electrochem.* **2018**, *9*, 41.
[20] T. Perveen, M. Siddiq, N. Shahzad, R. Ihsan, A. Ahmad, M. I. Shahzad, *Renewable Sustainable Energy Rev.* **2020**, *119*, 109549.
[21] R. Rajagopalan, Y. Tang, X. Ji, C. Jia, H. Wang, *Adv. Funct. Mater.* **2020**, *30*, 1909486.
[22] R. K. Guduru, J. C. Icaza, *Nanomaterials* **2016**, *6*, 41.
[23] T. Liu, X. Cheng, H. Yu, H. Zhu, N. Peng, R. Zheng, J. Zhang, M. Shui, Y. Cui, J. Shu, *Energy Storage Mater.* **2019**, *18*, 68.
[24] Y. Li, J. Fu, C. Zhong, T. Wu, Z. Chen, W. Hu, K. Amine, J. Lu, *Adv. Energy Mater.* **2019**, *9*, 1802605.
[25] A. Ebensperger, P. Maxwell, C. Moscoso, *Resour. Policy* **2005**, *30*, 218.
[26] S. Komaba, W. Murata, T. Ishikawa, N. Yabuuchi, T. N. Ozeki, *Adv. Funct. Mater.* **2011**, *21*, 3859.

[27] N. Tapia-Ruiz, A. R. Armstrong, H. Alptekin, M. A. Amores, H. Au, J. Barker, R. Boston, W. R. Brant, J. M. Brittain, Y. Chen, M. Chhowalla, Y.-S. Choi, S. I. R. Costa, M. Crespo Ribadeneyra, S. A. Cussen, E. J. Cussen, W. I. F. David, A. V. Desai, S. A. M. Dickson, E. I. Eweka, J. D. Forero-Saboya, C. P. Grey, J. M. Griffin, P. Gross, X. Hua, J. T. S. Irvine, P. Johansson, M. O. Jones, M. Karlsmo, E. Kendrick, et al., *J. Phys.: Energy* **2021**, *3*, 031503.

[28] K. Chayambuka, G. Mulder, D. L. Danilov, P. H. Notten, *Adv. Energy Mater.* **2018**, *8*, 1800079.

[29] C. Yang, S. Xin, L. Mai, Y. You, *Adv. Energy Mater.* **2021**, *11*, 2000974.

[30] UN Water, *Sustainable Development Goal 6 Synthesis Report on Water and Sanitation*, United Nations, New York **2018**.

[31] C. E. Cosgrove, W. J. Cosgrove, *The United Nations World Water Development Report No 4: The Dynamics of Global Water Futures: Driving Forces 2011–2050*, Vol. 2, UNESCO, Paris, France **2012**.

[32] J. Mohammed-Ibrahim, H. Moussab, *Mater. Sci. Energy Technol.* **2020**, *3*, 780.

[33] M. A. Al-Obaidi, G. Filippini, F. Manenti, I. M. Mujtaba, *Desalination* **2019**, *456*, 136.

[34] O. A. Hamed, M. A. K. Al-Sofi, M. Imam, G. M. Mustafa, K. Ba Mardouf, H. Al-Washmi, *Desalination* **2000**, *128*, 281.

[35] Y. J. Lim, K. Goh, M. Kurihara, R. Wang, *J. Membr. Sci.* **2021**, *629*, 119292.

[36] M. Sadrzadeh, T. Mohammadi, *Desalination* **2008**, *221*, 440.

[37] M. E. Suss, S. Porada, X. Sun, P. M. Biesheuvel, J. Yoon, V. Presser, *Energy Environ. Sci.* **2015**, *8*, 2296.

[38] M. Pasta, C. D. Wessells, Y. Cui, F. La Mantia, *Nano Lett.* **2012**, *12*, 839.

[39] M. E. Suss, Y. Zhang, I. Atlas, Y. Gendel, E. B. Ruck, V. Presser, *Electrochem. Commun.* **2022**, *136*, 107211.

[40] Y. Zhang, L. Wang, V. Presser, *Cell Rep. Phys. Sci.* **2021**, *2*, 100416.

[41] F. A. AlMarzooqi, A. A. Al Ghaferi, I. Saadat, N. Hilal, *Desalination* **2014**, *342*, 3.

[42] H. Nassrullah, S. F. Anis, R. Hashaikeh, N. Hilal, *Desalination* **2020**, *491*, 114569.

[43] S. M. Hwang, J.-S. Park, Y. Kim, W. Go, J. Han, Y. Kim, Y. Kim, *Adv. Mater.* **2019**, *31*, 1804936.

[44] I. C. Blake, *J. Electrochem. Soc.* **1952**, *99*, 202C.

[45] S. T. Senthilkumar, W. Go, J. Han, L. Pham Thi Thuy, K. Kishor, Y. Kim, Y. Kim, *J. Mater. Chem. A* **2019**, *7*, 22803.

[46] J.-K. Kim, F. Mueller, H. Kim, D. Bresser, J.-S. Park, D.-H. Lim, G.-T. Kim, S. Passerini, Y. Kim, *NPG Asia Mater.* **2014**, *6*, e144.

[47] J. K. Kim, E. Lee, H. Kim, C. Johnson, J. Cho, Y. Kim, *ChemElectroChem* **2014**, *2*, 328.

[48] M. E. Suss, V. Presser, *Joule* **2018**, *2*, 10.

[49] Y. Kim, K.-H. Ha, S. M. Oh, K. T. Lee, *Chem.–Eur. J.* **2014**, *20*, 11980.

[50] Y. Kim, J.-K. Kim, C. Vaalma, G. H. Bae, G.-T. Kim, S. Passerini, Y. Kim, *Carbon* **2018**, *129*, 564.

[51] Y. Kim, G. T. Kim, S. Jeong, X. W. Dou, C. X. Geng, Y. Kim, S. Passerini, *Energy Storage Mater.* **2019**, *16*, 56.

[52] S. Lee, I. Y. Cho, D. Kim, N. K. Park, J. Park, Y. Kim, S. J. Kang, Y. Kim, S. Y. Hong, *ChemSusChem* **2020**, *13*, 2220.

[53] W. Lee, J. Park, J. Park, S. J. Kang, Y. Choi, Y. Kim, *J. Mater. Chem. A* **2020**, *8*, 9185.

[54] C. Lee, T.-U. Wi, W. Go, M. F. Rahman, M. T. McDowell, Y. Kim, H.-W. Lee, *J. Mater. Chem. A* **2020**, *8*, 21804.

[55] Z. Le, W. Li, Q. Dang, C. Jing, W. Zhang, J. Chu, L. Tang, M. Hu, *J. Mater. Chem. A* **2021**, *9*, 8685.

[56] T.-U. Wi, C. Lee, M. F. Rahman, W. Go, S. H. Kim, D. Y. Hwang, S. K. Kwak, Y. Kim, H.-W. Lee, *Chem. Mater.* **2021**, *33*, 126.

[57] C. Yang, K. Fu, Y. Zhang, E. Hitz, L. Hu, *Adv. Mater.* **2017**, *29*, 1701169.

[58] W. Luo, Y. Zhang, S. Xu, J. Dai, E. Hitz, Y. Li, C. Yang, C. Chen, B. Liu, L. Hu, *Nano Lett.* **2017**, *17*, 3792.

[59] L. Lutz, D. Alves Dalla Corte, M. Tang, E. Salager, M. Deschamps, A. Grimaud, L. Johnson, P. G. Bruce, J.-M. Tarascon, *Chem. Mater.* **2017**, *29*, 6066.

[60] X. B. Cheng, R. Zhang, C. Z. Zhao, F. Wei, J. G. Zhang, Q. Zhang, *Adv. Sci.* **2016**, *3*, 1500213.

[61] M. D. Tikekar, S. Choudhury, Z. Tu, L. A. Archer, *Nat. Energy* **2016**, *1*, 16114.

[62] J. M. Bergthorson, Y. Yavor, J. Palecka, W. Georges, M. Soo, J. Vickery, S. Goroshin, D. L. Frost, A. J. Higgins, *Appl. Energy* **2017**, *186*, 13.

[63] M. A. Rahman, X. Wang, C. Wen, *J. Electrochem. Soc.* **2013**, *160*, A1759.

[64] J. Park, J.-S. Park, S. T. Senthilkumar, Y. Kim, *J. Power Sources* **2020**, *450*, 227600.

[65] S. T. Senthilkumar, M. Abirami, J. Kim, W. Go, S. M. Hwang, Y. Kim, *J. Power Sources* **2017**, *341*, 404.

[66] P. Manikandan, K. Kishor, J. Han, Y. Kim, *J. Mater. Chem. A* **2018**, *6*, 11012.

[67] H. Kim, J.-S. Park, S. H. Sahgong, S. Park, J.-K. Kim, Y. Kim, *J. Mater. Chem. A* **2014**, *2*, 19584.

[68] M. Abirami, S. M. Hwang, J. Yang, S. T. Senthilkumar, J. Kim, W.-S. Go, B. Senthilkumar, H.-K. Song, Y. Kim, *ACS Appl. Mater. Interfaces* **2016**, *8*, 32778.

[69] H. Xiong, M. D. Slater, M. Balasubramanian, C. S. Johnson, T. Rajh, *J. Phys. Chem. Lett.* **2011**, *2*, 2560.

[70] L. Y. Yang, H. Z. Li, J. Liu, S. S. Tang, Y. K. Lu, S. T. Li, J. Min, N. Yan, M. Lei, *J. Mater. Chem. A* **2015**, *3*, 24446.

[71] C. Wu, W. Hua, Z. Zhang, B. Zhong, Z. Yang, G. Feng, W. Xiang, Z. Wu, X. Guo, *Adv. Sci.* **2018**, *5*, 1800519.

[72] C. Bommier, X. Ji, *Isr. J. Chem.* **2015**, *55*, 486.

[73] M.-S. Balogun, Y. Luo, W. Qiu, P. Liu, Y. Tong, *Carbon* **2016**, *98*, 162.

[74] V. L. Chevrier, G. Ceder, *J. Electrochem. Soc.* **2011**, *158*, A1011.

[75] J. K. Kim, F. Mueller, H. Kim, S. Jeong, J. S. Park, S. Passerini, Y. Kim, *ChemSusChem* **2016**, *9*, 42.

[76] A. Kraytsberg, Y. Ein-Eli, *J. Solid State Electrochem.* **2017**, *21*, 1907.

[77] M. Fichtner, *Chem. Unserer Zeit* **2013**, *47*, 230.

[78] J. Wang, H. Tang, H. Wang, R. Yu, D. Wang, *Mater. Chem. Front.* **2017**, *1*, 414.

[79] H. Wang, S. Chen, C. Fu, Y. Ding, G. Liu, Y. Cao, Z. Chen, *ACS Mater. Lett.* **2021**, *3*, 956.

[80] H. Hou, M. Jing, Z. Huang, Y. Yang, Y. Zhang, J. Chen, Z. Wu, X. Ji, *ACS Appl. Mater. Interfaces* **2015**, *7*, 19362.

[81] S. M. Hwang, J. Kim, Y. Kim, Y. Kim, *J. Mater. Chem. A* **2016**, *4*, 17946.

[82] J. Han, S. M. Hwang, W. Go, S. T. Senthilkumar, D. Jeon, Y. Kim, *J. Power Sources* **2018**, *374*, 24.

[83] A. Cipollina, G. Micale, L. Rizzuti, *Seawater Desalination: Conventional And Renewable Energy Processes*, Springer-Verlag, Berlin, Heidelberg **2009**, Ch. 11, pp. 1–15.

[84] Y. Zhang, J.-S. Park, S. T. Senthilkumar, Y. Kim, *J. Power Sources* **2018**, *400*, 478.

[85] C. Min, P. Nie, H.-J. Song, Z. Zhang, K. Zhao, *Tribol. Int.* **2014**, *80*, 131.

[86] J.-H. Huh, S. H. Kim, J. H. Chu, S. Y. Kim, J. H. Kim, S.-Y. Kwon, *Nanoscale* **2014**, *6*, 4379.

[87] S. T. Senthilkumar, S. O. Park, J. Kim, S. M. Hwang, S. K. Kwak, Y. Kim, *J. Mater. Chem. A* **2017**, *5*, 14174.

[88] Y. Kim, H. Kim, S. Park, I. Seo, Y. Kim, *Electrochim. Acta* **2016**, *191*, 1.

[89] C. Zhang, D. He, J. Ma, W. Tang, T. D. Waite, *Electrochim. Acta* **2019**, *299*, 727.

[90] S. Arnold, L. Wang, Ö. Budak, M. Aslan, P. Srimuk, V. Presser, *J. Mater. Chem. A* **2021**, *9*, 585.

[91] J.-J. Kim, K. Yoon, I. Park, K. Kang, *Small Methods* **2017**, *1*, 1700219.

[92] J.-K. Kim, Y. J. Lim, H. Kim, G.-B. Cho, Y. Kim, *Energy Environ. Sci.* **2015**, *8*, 3589.

[93] C. Zhao, L. Liu, X. Qi, Y. Lu, F. Wu, J. Zhao, Y. Yu, Y. S. Hu, L. Chen, *Adv. Energy Mater.* **2018**, *8*, 1703012.

[94] Z. Zhang, Y. Shao, B. Lotsch, Y. Hu, H. Li, *Energy Environ. Sci.* **2018**, *11*, 1945.

[95] M. L. Wolf, J. R. Walker, C. R. A. Catlow, *Solid State Ionics* **1984**, *13*, 33.

[96] R. O. Fuentes, F. Figueiredo, F. M. B. Marques, J. I. Franco, *Ionics* **2002**, *8*, 383.

[97] A. Ahmad, T. Wheat, A. Kuriakose, J. Canaday, A. McDonald, *Solid State Ionics* **1987**, *24*, 89.

[98] J. Lee, P. Srimuk, R. L. Zornitta, M. Aslan, B. L. Mehdi, V. Presser, *ACS Sustainable Chem. Eng.* **2019**, *7*, 10132.

[99] W. Go, J. Kim, J. Pyo, J. B. Wolfenstine, Y. Kim, *ACS Appl. Mater. Interfaces* **2021**, *13*, 52727.

[100] J. B. Goodenough, H. Y. P. Hong, J. A. Kafalas, *Mater. Res. Bull.* **1976**, *11*, 203.

[101] H.-P. Hong, *Mater. Res. Bull.* **1976**, *11*, 173.

[102] N. Yabuuchi, K. Kubota, M. Dahbi, S. Komaba, *Chem. Rev.* **2014**, *114*, 11636.

[103] R. O. Fuentes, F. Figueiredo, F. M. B. Marques, J. I. Franco, *Solid State Ionics* **2001**, *139*, 309.

[104] P. Komorowski, S. Argyropoulos, R. Hancock, J. Gulens, P. Taylor, J. Canaday, A. Kuriakose, T. Wheat, A. Ahmad, *Solid State Ionics* **1991**, *48*, 295.

[105] E. Peled, *J. Electrochem. Soc.* **1979**, *126*, 2047.

[106] T. Famprikis, P. Canepa, J. A. Dawson, M. S. Islam, C. Masquelier, *Nat. Mater.* **2019**, *18*, 1278.

[107] J. B. Goodenough, Y. Kim, *Chem. Mater.* **2010**, *22*, 587.

[108] M. Widmaier, B. Krüner, N. Jäckel, M. Aslan, S. Fleischmann, C. Engel, V. Presser, *J. Electrochem. Soc.* **2016**, *163*, A2956.

[109] K. Pfeifer, S. Arnold, Ö. Budak, X. Luo, V. Presser, H. Ehrenberg, S. Dsoke, *J. Mater. Chem. A* **2020**, *8*, 6092.

[110] P. Verma, P. Maire, P. Novák, *Electrochim. Acta* **2010**, *55*, 6332.

[111] K. Kim, S. M. Hwang, J.-S. Park, J. Han, J. Kim, Y. Kim, *J. Power Sources* **2016**, *313*, 46.

[112] D. H. Suh, S. K. Park, P. Nakhanivej, Y. Kim, S. M. Hwang, H. S. Park, *J. Power Sources* **2017**, *372*, 31.

[113] B. Lee, E. Paek, D. Mitlin, S. W. Lee, *Chem. Rev.* **2019**, *119*, 5416.

[114] G. Kim, M. Oh, Y. Park, *Sci. Rep.* **2016**, *6*, 33400.

[115] K. H. Shin, J. Park, S. K. Park, P. Nakhanivej, S. M. Hwang, Y. Kim, H. S. Park, *J. Ind. Eng. Chem.* **2019**, *72*, 250.

[116] E. Yoo, H. Zhou, *ACS Nano* **2011**, *5*, 3020.

[117] Z. Zhao, M. Li, L. Zhang, L. Dai, Z. Xia, *Adv. Mater.* **2015**, *27*, 6834.

[118] S. Chen, J. Duan, M. Jaroniec, S. Z. Qiao, *Adv. Mater.* **2014**, *26*, 2925.

[119] L. Tao, Q. Wang, S. Dou, Z. Ma, J. Huo, S. Wang, L. Dai, *Chem. Commun.* **2016**, *52*, 2764.

[120] P. He, T. Zhang, J. Jiang, H. Zhou, *J. Phys. Chem. Lett.* **2016**, *7*, 1267.

[121] Y. Lee, J. Suntivich, K. J. May, E. E. Perry, Y. Shao-Horn, *J. Phys. Chem. Lett.* **2012**, *3*, 399.

[122] K. Kishor, S. Saha, M. K. Gupta, A. Bajpai, M. Chatterjee, S. Sivakumar, R. G. S. Pala, *ChemElectroChem* **2015**, *2*, 1839.

[123] H. Bae, J.-S. Park, S. T. Senthilkumar, S. M. Hwang, Y. Kim, *J. Power Sources* **2019**, *410–411*, 99.

[124] Y. Kim, A. M. Harzandi, J. Lee, Y. Choi, Y. Kim, *Adv. Sustainable Syst.* **2021**, *5*, 2000106.

[125] R. Korthauer, *Handbuch Lithium-Ionen-Batterien*, Springer Vieweg, Berlin, Heidelberg **2013**, pp. 271–273.

[126] M. Faraday, *Philos. Trans. R. Soc. London* **1834**, *124*, 77.

[127] J. Jung, D. Y. Hwang, I. Kristanto, S. K. Kwak, S. J. Kang, *J. Mater. Chem. A* **2019**, *7*, 9773.

[128] C. Menictas, M. Skyllas-Kazacos, T. M. Lim, *Advances in Batteries for Medium and Large-Scale Energy Storage: Types and Applications*, Elsevier, New York **2014**.

[129] S. Park, B. SenthilKumar, K. Kim, S. M. Hwang, Y. Kim, *J. Mater. Chem. A* **2016**, *4*, 7207.

[130] W. Wei, W. Zou, D. Yang, R. Zheng, R. Wang, H. Chen, *J. Mater. Chem. A* **2020**, *8*, 11811.

[131] M. Son, S. Park, N. Kim, A. T. Angeles, Y. Kim, K. H. Cho, *Adv. Sci.* **2021**, *8*, 2101289.

[132] Y. Zhang, S. T. Senthilkumar, J. Park, J. Park, Y. Kim, *Batteries Supercaps* **2018**, *1*, 6.

[133] K. Lee, N. Chromey, R. Culik, J. Barnes, P. Schneider, *Fundam. Appl. Toxicol.* **1987**, *9*, 222.

[134] Y. Yu, H. Che, X. Yang, Y. Deng, L. Li, Z.-F. Ma, *Electrochem. Commun.* **2020**, *110*, 106635.

[135] E. P. Roth, C. J. Orendorff, *Electrochem. Soc. Interface* **2012**, *21*, 45.

[136] Y. Fang, L. Xiao, Z. Chen, X. Ai, Y. Cao, H. Yang, *Electrochem. Energy Rev.* **2018**, *1*, 294.

[137] S.-L. Chou, J.-Z. Wang, H.-K. Liu, S.-X. Dou, *J. Phys. Chem. C* **2011**, *115*, 16220.

[138] D. Versaci, R. Nasi, U. Zubair, J. Amici, M. Sgroi, M. A. Dumitrescu, C. Francia, S. Bodoardo, N. Penazzi, *J. Solid State Electrochem.* **2017**, *21*, 3429.

[139] L. Fransson, T. Eriksson, K. Edström, T. Gustafsson, J. O. Thomas, *J. Power Sources* **2001**, *101*, 1.

[140] K. Pfeifer, S. Arnold, J. Becherer, C. Das, J. Maibach, H. Ehrenberg, S. Dsoke, *ChemSusChem* **2019**, *12*, 3312.

[141] T. Nakajima, H. Groult, *Fluorinated Materials for Energy Conversion*, Elsevier, New York **2005**.

[142] T. Nakajima, H. Groult, *Advanced Fluoride-Based Materials for Energy Conversion*, Elsevier, New York **2015**.

[143] C. C. Nguyen, T. Yoon, D. M. Seo, P. Guduru, B. L. Lucht, *ACS Appl. Mater. Interfaces* **2016**, *8*, 12211.

[144] Y. Kim, A. Varzi, A. Mariani, G.-T. Kim, Y. Kim, S. Passerini, *Adv. Energy Mater.* **2021**, *11*, 2102061.

[145] J.-I. Jung, D. Kim, H. Kim, Y. N. Jo, J. S. Park, Y. Kim, *ACS Appl. Mater. Interfaces* **2017**, *9*, 304.

[146] B. D. McCloskey, *J. Phys. Chem. Lett.* **2015**, *6*, 3592.

[147] S. Maass, F. Finsterwalder, G. Frank, R. Hartmann, C. Merten, *J. Power Sources* **2008**, *176*, 444.

[148] J. Park, H. Oh, T. Ha, Y. I. Lee, K. Min, *Appl. Energy* **2015**, *155*, 866.

[149] H.-S. Oh, J.-G. Oh, S. Haam, K. Arunabha, B. Roh, I. Hwang, H. Kim, *Electrochem. Commun.* **2008**, *10*, 1048.

[150] J. Wang, G. Yin, Y. Shao, S. Zhang, Z. Wang, Y. Gao, *J. Power Sources* **2007**, *171*, 331.

[151] B. Avasarala, R. Moore, P. Haldar, *Electrochim. Acta* **2010**, *55*, 4765.

[152] L. Roen, C. Paik, T. Jarvi, *Electrochem. Solid State Lett.* **2003**, *7*, A19.

[153] H. Tang, Z. Qi, M. Ramani, J. F. Elter, *J. Power Sources* **2006**, *158*, 1306.

[154] M. Cai, M. S. Ruthkosky, B. Merzougui, S. Swathirajan, M. P. Balogh, S. H. Oh, *J. Power Sources* **2006**, *160*, 977.

[155] L. Eifert, R. Banerjee, Z. Jusys, R. Zeis, *J. Electrochem. Soc.* **2018**, *165*, A2577.

[156] Ø. Hasvold, H. Henriksen, E. Melv, G. Citi, B. Ø. Johansen, T. Kjønigsen, R. Galetti, *J. Power Sources* **1997**, *65*, 253.

[157] H. Wang, B.-H. Chen, D.-J. Liu, *Adv. Mater.* **2021**, *33*, 2008023.

[158] A. K. Thakur, M. Majumder, S. P. Patole, K. Zaghib, M. V. Reddy, *Mater. Adv.* **2021**, *2*, 2457.

[159] B. Singh, A. Indra, *Mater. Today Energy* **2020**, *16*, 100404.

[160] T. Hashimoto, K. Hayashi, *Electrochim. Acta* **2015**, *182*, 809.

[161] S. Dong, X. Chen, S. Wang, L. Gu, L. Zhang, X. Wang, X. Zhou, Z. Liu, P. Han, Y. Duan, *ChemSusChem* **2012**, *5*, 1712.

[162] G. Liu, M. Wang, Y. Xu, X. Wang, X. Li, J. Liu, X. Cui, L. Jiang, *J. Power Sources* **2021**, *486*, 229351.

[163] S.-E. Jang, H. Kim, *J. Am. Chem. Soc.* **2010**, *132*, 14700.

[164] J.-G. Oh, W. H. Lee, H. Kim, *Int. J. Hydrogen Energy* **2012**, *37*, 2455.

[165] L. Tao, M. Qiao, R. Jin, Y. Li, Z. Xiao, Y. Wang, N. Zhang, C. Xie, Q. He, D. Jiang, *Angew. Chem., Int. Ed.* **2019**, *131*, 1031.

[166] S. Jeoung, S. H. Sahgong, J. H. Kim, S. M. Hwang, Y. Kim, H. R. Moon, *J. Mater. Chem. A* **2016**, *4*, 13468.

[167] B. Koo, H. Kim, Y. Cho, K. T. Lee, N. S. Choi, J. Cho, *Angew. Chem., Int. Ed.* **2012**, *124*, 8892.

[168] C. Kim, P. Srimuk, J. Lee, V. Presser, *Desalination* **2018**, *443*, 56.

[169] N. D. K. Tu, S. O. Park, J. Park, Y. Kim, S. K. Kwak, S. J. Kang, *ACS Appl. Energy Mater.* **2020**, *3*, 1602.

[170] G.-y. Zheng, S. Lee, Z. Liang, H. Lee, K. Yan, H. Yao, H. Wang, W. Li, Y. Cui, *Nat. Nanotechnol.* **2014**, *9*, 618.

[171] P. Bai, J. Li, F. R. Brushett, M. Z. Bazant, *Energy Environ. Sci.* **2016**, *9*, 3221.

[172] W. Li, H. Yao, K. Yan, G. Zheng, Z. Liang, Y.-M. Chiang, Y. Cui, *Nat. Commun.* **2015**, *6*, 7436.

[173] C.-P. Yang, Y.-X. Yin, S.-F. Zhang, N.-W. Li, Y.-G. Guo, *Nat. Commun.* **2015**, *6*, 8058.

[174] S. Liu, A. Wang, Q. Li, J. Wu, K. Chiou, J. Huang, J. Luo, *Joule* **2018**, *2*, 184.

[175] R. Zhang, X. R. Chen, X. Chen, X. B. Cheng, X. Q. Zhang, C. Yan, Q. Zhang, *Angew. Chem., Int. Ed.* **2017**, *129*, 7872.

[176] R. Xu, X. Q. Zhang, X. B. Cheng, H. J. Peng, C. Z. Zhao, C. Yan, J. Q. Huang, *Adv. Funct. Mater.* **2018**, *28*, 1705838.

[177] H. Lee, X. Ren, C. Niu, L. Yu, M. H. Engelhard, I. Cho, M. H. Ryou, H. S. Jin, H. T. Kim, J. Liu, *Adv. Funct. Mater.* **2017**, *27*, 1704391.

[178] Z. W. Seh, J. Sun, Y. Sun, Y. Cui, *ACS Cent. Sci.* **2015**, *1*, 449.

[179] Y. Zhao, L. V. Goncharova, A. Lushington, Q. Sun, H. Yadegari, B. Wang, W. Xiao, R. Li, X. Sun, *Adv. Mater.* **2017**, *29*, 1606663.

[180] A. P. Cohn, N. Muralidharan, R. Carter, K. Share, C. L. Pint, *Nano Lett.* **2017**, *17*, 1296.

[181] W. Zhou, Y. Li, S. Xin, J. B. Goodenough, *ACS Cent. Sci.* **2017**, *3*, 52.

[182] J. Song, G. Jeong, A.-J. Lee, J. H. Park, H. Kim, Y.-J. Kim, *ACS Appl. Mater. Interfaces* **2015**, *7*, 27206.

[183] D. Ruiz-Martinez, A. Kovacs, R. Gómez, *Energy Environ. Sci.* **2017**, *10*, 1936.

[184] Y. Zhao, L. V. Goncharova, Q. Zhang, P. Kaghazchi, Q. Sun, A. Lushington, B. Wang, R. Li, X. Sun, *Nano Lett.* **2017**, *17*, 5653.

[185] A. Wang, X. Hu, H. Tang, C. Zhang, S. Liu, Y. W. Yang, Q. H. Yang, J. Luo, *Angew. Chem., Int. Ed.* **2017**, *129*, 12083.

[186] S. Liu, S. Tang, X. Zhang, A. Wang, Q.-H. Yang, J. Luo, *Nano Lett.* **2017**, *17*, 5862.

[187] W. Xu, J. Wang, F. Ding, X. Chen, E. Nasybulin, Y. Zhang, J.-G. Zhang, *Energy Environ. Sci.* **2014**, *7*, 513.

[188] Y. Guo, H. Li, T. Zhai, *Adv. Mater.* **2017**, *29*, 1700007.

[189] D. H. Kim, H. Choi, D. Y. Hwang, J. Park, K. S. Kim, S. Ahn, Y. Kim, S. K. Kwak, Y.-J. Yu, S. J. Kang, *J. Mater. Chem. A* **2018**, *6*, 19672.

[190] D. Kim, J.-S. Park, W.-G. Lee, Y. Choi, Y. Kim, *J. Electrochem. Soc.* **2022**, *169*, 040508.

[191] Y. Kim, J. Jung, H. Yu, G.-T. Kim, D. Jeong, D. Bresser, S. J. Kang, Y. Kim, S. Passerini, *Adv. Funct. Mater.* **2020**, *30*, 2001249.

[192] J. Cho, M. W. Kim, Y. Kim, J.-S. Park, D.-H. Lee, Y. Kim, J. J. Kim, *IEEE Access* **2021**, *9*, 104104.

[193] J. H. Kim, S. M. Hwang, I. Hwang, J. Han, J. H. Kim, Y. H. Jo, K. Seo, Y. Kim, J. S. Lee, *iScience* **2019**, *19*, 232.

[194] N. Kim, J.-S. Park, A. M. Harzandi, K. Kishor, M. Ligaray, K. H. Cho, Y. Kim, *Desalination* **2020**, *495*, 114666.

[195] J.-S. Park, S. Kim, Y. Choi, A. M. Harzandi, Y. Kim, *ACS ES&T Water* **2021**, *1*, 2146.

[196] *Wastewater Technology Fact Sheet: Dechlorination*, United States Environmental Protection Agency, Washington, DC **2000**, p. EPA 832-F-00-022.

[197] T. Lim, G. Y. Jung, J. H. Kim, S. O. Park, J. Park, Y.-T. Kim, S. J. Kang, H. Y. Jeong, S. K. Kwak, S. H. Joo, *Nat. Commun.* **2020**, *11*, 412.

[198] F. Yu, L. Wang, Y. Wang, X. Shen, Y. Cheng, J. Ma, *J. Mater. Chem. A* **2019**, *7*, 15999.

[199] L. F. Greenlee, D. F. Lawler, B. D. Freeman, B. Marrot, P. Moulin, *Water Res.* **2009**, *43*, 2317.

[200] A. Ophir, A. Gendel, *Desalination* **2007**, *205*, 224.

[201] M. Ligaray, N. Kim, S. Park, J.-S. Park, J. Park, Y. Kim, K. H. Cho, *Chem. Eng. J.* **2020**, *395*, 125082.

[202] J. Kim, K. Park, D. R. Yang, S. Hong, *Appl. Energy* **2019**, *254*, 113652.

[203] R. Semiat, *Environ. Sci. Technol.* **2008**, *42*, 8193.

[204] J. Lee, P. Srimuk, S. Carpier, J. Choi, R. L. Zornitta, C. Kim, M. Aslan, V. Presser, *ChemSusChem* **2018**, *11*, 3460.

[205] J. Ma, C. He, D. He, C. Zhang, T. D. Waite, *Water Res.* **2018**, *144*, 296.

[206] K. B. Hatzell, M. C. Hatzell, K. M. Cook, M. Boota, G. M. Housel, A. McBride, E. C. Kumbur, Y. Gogotsi, *Environ. Sci. Technol.* **2015**, *49*, 3040.

[207] S. Yang, J. Choi, J.-g. Yeo, S.-i. Jeon, H.-r. Park, D. K. Kim, *Environ. Sci. Technol.* **2016**, *50*, 5892.

[208] F. Chen, J. Wang, C. Feng, J. Ma, T. David Waite, *Chem. Eng. J.* **2020**, *401*, 126111.

[209] S. Yang, S.-i. Jeon, H. Kim, J. Choi, J.-g. Yeo, H.-r. Park, D. K. Kim, *ACS Sustainable Chem. Eng.* **2016**, *4*, 4174.

[210] J. Chang, F. Duan, H. Cao, K. Tang, C. Su, Y. Li, *Desalination* **2019**, *468*, 114080.

[211] H.-r. Park, J. Choi, S. Yang, S. J. Kwak, S.-i. Jeon, M. H. Han, D. K. Kim, *RSC Adv.* **2016**, *6*, 69720.

[212] J. Lee, S. Kim, C. Kim, J. Yoon, *Energy Environ. Sci.* **2014**, *7*, 3683.

[213] L. Wang, S. Lin, *Water Res.* **2018**, *129*, 394.

[214] J.-Y. Hwang, S.-T. Myung, Y.-K. Sun, *Chem. Soc. Rev.* **2017**, *46*, 3529.

[215] M. R. Palacin, *Chem. Soc. Rev.* **2009**, *38*, 2565.

[216] S. Liang, Y. Yang, K. Li, X. Zhang, *J. Eur. Ceram. Soc.* **2020**, *40*, 4047.

[217] H. Park, K. Jung, M. Nezafati, C. S. Kim, B. Kang, *ACS Appl. Mater. Interfaces* **2016**, *8*, 27814.

[218] W. Go, M.-H. Kim, J. Park, C. H. Lim, S. H. Joo, Y. Kim, H.-W. Lee, *Nano Lett.* **2019**, *19*, 1504.

[219] H. Choi, D. Y. Hwang, J. Park, K. S. Kim, S. Ahn, Y. Kim, S. K. Kwak, Y.-J. Yu, S. J. Kang, *J. Mater. Chem. A* **2018**, *6*, 19672.

[220] S. Park, M. Ligaray, Y. Kim, K. Chon, M. Son, K. H. Cho, *Desalination* **2021**, *506*, 115018.

[221] C. Kim, J. Lee, P. Srimuk, M. Aslan, V. Presser, *ChemSusChem* **2017**, *10*, 4914.

[222] M. Aslan, M. Zeiger, N. Jäckel, I. Grobelsek, D. Weingarth, V. Presser, *J. Phys.: Condens. Matter* **2016**, *28*, 114003.

[223] Y. Zhang, P. Srimuk, M. Aslan, M. Gallei, V. Presser, *Desalination* **2020**, *479*, 114331.

[224] F. Chen, Y. Huang, L. Guo, L. Sun, Y. Wang, H. Y. Yang, *Energy Environ. Sci.* **2017**, *10*, 2081.

[225] P. Srimuk, J. Lee, A. Tolosa, C. Kim, M. Aslan, V. Presser, *Chem. Mater.* **2017**, *29*, 9964.

[226] J. Lee, S. Kim, J. Yoon, *ACS Omega* **2017**, *2*, 1653.

[227] W. Shi, X. Qian, M. Xue, W. Que, X. Gao, D. Zheng, W. Liu, F. Wu, J. Shen, X. Cao, *ACS Appl. Mater. Interfaces* **2021**, *13*, 21149.

[228] F. Reverberi, A. Gorenflo, *Desalination* **2007**, *203*, 100.

[229] J. Kim, K. Park, S. Hong, *J. Membr. Sci.* **2020**, *601*, 117889.

[230] T. Seto, L. Ehara, R. Komori, A. Yamaguchi, T. Miwa, *Desalination* **1978**, *25*, 1.

[231] M. Turek, *Desalination* **2003**, *153*, 371.

Stefanie Arnold is presently a Ph.D. student under the supervision of Prof. Volker Presser at the Department of Materials Science and Engineering, Saarland University, and the INM – Leibniz Institute for New Materials in Saarbrücken, Germany. A trained chemist, she received her bachelor's degree and her master's degree from the Karlsruhe Institute of Technology, Germany, in 2018 and 2020, respectively. Her research explores high-performance sodium-ion battery materials, novel technologies for battery recycling, and water remediation.

Lei Wang is a doctoral student under the supervision of Prof. Volker Presser at the Department of Materials Science and Engineering, Saarland University, and the INM – Leibniz Institute for New Materials in Saarbrücken, Germany. He received his bachelor's degree at Sun Yat-sen University, Guangzhou, China, in 2016 and his master's degree in Environmental Engineering at Tongji University, Shanghai, China, in 2019. His current research is related to ion separation and water desalination via electrochemical methods.

Volker Presser is professor for Energy Materials at Saarland University, Program Division Leader at the INM – Leibniz Institute for New Materials, and Managing Director of the Saarland Center for Energy Materials and Sustainability (saarene) in Saarbrücken (Germany). He obtained his Ph.D. from the Eberhard-Karls-University Tübingen (Germany) in 2009 and worked as a Humboldt Fellow and Research Assistant Professor in the team of Yury Gogotsi at Drexel University (2010–2012). His research focuses next-generation materials (incl. MXene and hybrid materials) for energy storage and water remediation (esp. lithium recovery and seawater desalination).

4.6 Antimony alloying electrode for high-performance sodium removal: how to use a battery material not stable in aqueous media for saline water remediation

Stefanie Arnold[1,2], Lei Wang[1,2], Öznil Budak[1,2], Mesut Aslan[1],
Pattarachai Srimuk[1] and Volker Presser[1,2]

[1] INM - Leibniz Institute for New Materials, 66123 Saarbrücken, Germany

[2] Department of Materials Science and Engineering, Saarland University, 66123 Saarbrücken, Germany

Citation:

Own Contribution:

Planning, investigation, electrochemical measurements, data curation, visualization, writing-original draft, writing-review & editing.

Journal of Materials Chemistry A

PAPER

Check for updates
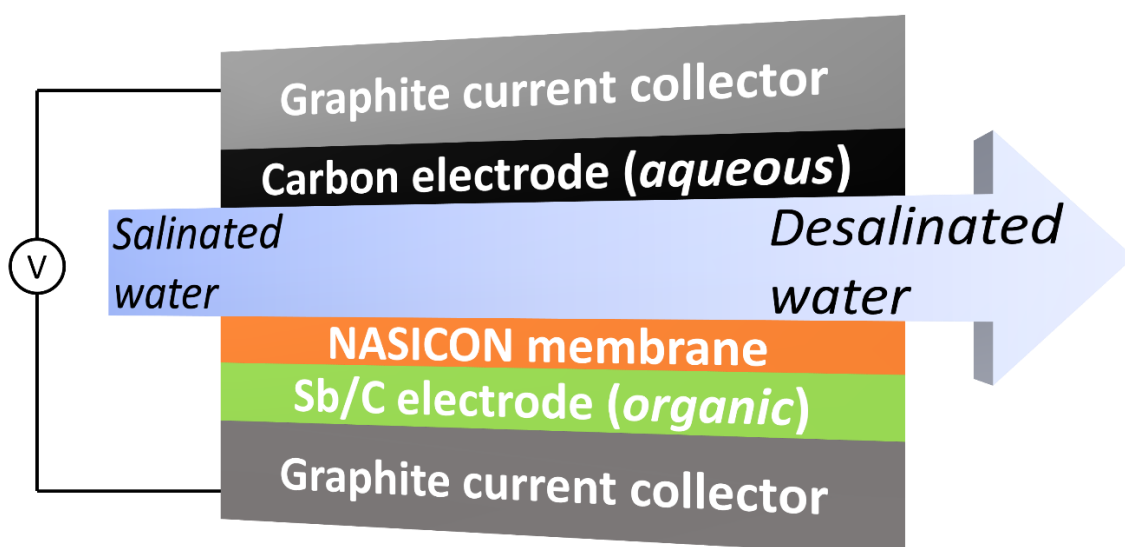
Antimony alloying electrode for high-performance sodium removal: how to use a battery material not stable in aqueous media for saline water remediation†

Stefanie Arnold, [ab] Lei Wang, [ab] Öznil Budak, [ab] Mesut Aslan,[a] Pattarachai Srimuk [a] and Volker Presser [*ab]

Capacitive deionization (CDI) is based on ion electrosorption and has emerged as a promising desalination technology, for example, to obtain drinking water from brackish water. As a next-generation technology, battery desalination uses faradaic processes and, thereby, enables higher desalination capacities and remediation of feed water with high molar strength such as seawater. However, the full use of a large capacity of charge transfer processes is limited by the voltage window of water and the need to use electrode materials non-reactive towards the water. Using our multi-channel bi-electrolyte cell, we now introduce for the first time an alloying electrode for sodium removal in the context of water desalination. Separated by a ceramic sodium superionic conductor (NASICON) membrane, the antimony/carbon composite electrode accomplished sodium removal while chlorine removal is enabled *via* ion electrosorption with nanoporous carbon (activated carbon cloth). In a sodium-ion battery half-cell setup, the antimony/carbon composite electrode reaches an initial capacity of 714 mA h g^{-1} at a specific current of 200 mA g^{-1}, which shows a slow but continuous degrading over the course of 80 cycles (426 mA h g^{-1} in 80th cycle). Our hybrid CDI cell provides a desalination capacity of an average of 294 mg$_{Na}$ g$_{Sb}^{-1}$ (748 mg$_{NaCl}$ g$_{Sb}^{-1}$) with a charge efficiency of *ca.* 74% in a 600 mM NaCl at a specific current of 200 mA g^{-1} and a voltage range of −2.0 V to +2.0 V.

1 Introduction

In the 21st century, due to the ever-increasing population and correspondingly the deterioration of the environment, obtaining clean potable water becomes a serious issue for sustaining livelihood, especially in arid regions.[1] Large-scale efforts have been invested in developing desalination technology to address this issue. From simple distillation, multi-stage flash distillation,[2] to reverse osmosis,[3,4] many methods have been studied. However, many of these methods are expensive and require high energy input. Among them, capacitive deionization (CDI) is considered as an energy-efficient technology, compared to the pressure or filtration-based desalination technology.[5] In CDI, ions are immobilized at the fluid/solid interface of nanoporous carbon by reversible ion-electrosorption.[6] A typical CDI cell employs a pair of nanoporous carbon electrodes and a separator (open channel or porous dielectric material), to prevent short-circuiting.[7] By applying a constant voltage or current, the salt ions present in feedwater migrate into the electrical double-layer (EDL) and, thus, remove salt from the water (ion-electrosorption). When the cell is discharged, the ions are released again, and the invested charge is recovered. The voltage applied to each electrode pair is typically around (slightly above) 1 V, depending on the overpotential of water splitting. Because of the low voltage, and because there is no need for other energy input such as high pressure or high temperature, CDI holds the promise of being a more energy-efficient method of desalinating water on a larger scale.[7]

However, uncharged carbon nanopores are populated by both co-ions and counter-ions, that is, ions with the same or opposite charge compared to the electrode.[8,9] Once the electrodes are polarized, co-ions will be released from the EDL at the same extent as counter-ion attraction takes place; only once the co-ion population has been depleted (at higher states-of-charge), permselective ion removal will be possible.[10] Thereby, CDI remains limited to low molar concentrations (with an initially low number of co-ions present in carbon nanopores).[11] This condition is only (partially) remedied when the pore

*a*INM – Leibniz Institute for New Materials, 66123 Saarbrücken, Germany. E-mail: volker.presser@leibniz-inm.de

*b*Department of Materials Science and Engineering, Saarland University, 66123 Saarbrücken, Germany

† Electronic supplementary information (ESI) available: chemical analysis data, supporting electrochemical characterization, schematic illustration of the cell operation, post mortem material characterization (SEM, XRD). See DOI: 10.1039/d0ta09806j

diameter significantly falls below 1 nm.[12] Also, the charge storage capacity intrinsically linked to EDL carbon electrodes is limited to about 0.1 F m^{-2} (typical values for the gravimetric capacitance of activated carbon is about 100–150 F g^{-1}).[13–15] Therefore, the desalination capacity of low-concentration brackish water with carbon electrodes is typically in the range of 10–30 mg$_{NaCl}$ g$_{electrode}$$^{-1}$ (~4–12 mg$_{Na}$ g$_{electrode}$$^{-1}$).[16]

To overcome the desalination limitations of carbon-based CDI, Pasta *et al.* introduced the concept of the desalination battery built of sodium manganese oxide and silver electrodes to deionize seawater.[17] Instead of using two faradaic electrodes, it is also possible to pair carbon with a charge-transfer electrode. For example, Lee *et al.* used sodium manganese oxide to capture sodium and carbon to electrosorb chloride.[18] By doing so, the authors achieved a desalination capacity of 31 mg$_{NaCl}$ g$_{electrode}$$^{-1}$ (~12 mg$_{Na}$ g$_{electrode}$$^{-1}$), while the carbon itself only provided 14 mg$_{NaCl}$ g$_{electrode}$$^{-1}$ (~6 mg$_{Na}$ g$_{electrode}$$^{-1}$).[18] Until now, mostly two kinds of faradaic materials have been applied for desalination: intercalation-type materials (*e.g.*, sodium manganese oxides,[19] nickel hexacyanoferrate,[20] titanium disulfide[21]) and conversion-type materials (*e.g.*, silver[22]), which show a desalination capacity of 85–115 mg$_{NaCl}$ g$_{electrode}$$^{-1}$ (up to about 22 mg$_{Na}$ g$_{electrode}$$^{-1}$).[23–27]

The selection of suitable sodium-removal electrode for electrochemical desalination is limited by their compatibility with water. Many new materials could be used for desalination, especially anode materials of sodium-ion batteries if the requirement to expose the electrode to the feedwater stream would be lifted. As a first step towards this goal, we introduced the use of organic solvent CDI in 2016 (ref. 28) and aqueous/organic bi-electrolyte CDI in 2018 (ref. 29). In the latter concept, a multi-channel system is used, and one of the electrodes, covered by an ion-exchange membrane, is operated in an organic electrolyte instead of an aqueous solution. Ion transfer into and out from the organic compartment is ensured by the ion-exchange membrane. Our initial design used a polymer-based ion-exchange membrane, so water cross-over was not fully eliminated. Still, the system allowed stable cell operation at voltages significantly above 1.2 V and resulting desalination capacities of up to 60 mg$_{NaCl}$ g$_{electrode}$$^{-1}$ (~24 mg$_{Na}$ g$_{electrode}$$^{-1}$; at 2.4 V cell voltage).

Research at the water/energy nexus between battery desalination and seawater batteries is a rapidly growing field for stationary applications.[30–33] Our present proof-of-concept now uses the bi-electrolyte concept and demonstrates the highly promising concept of combining a ceramic ion-exchange membrane (sodium superionic conductor: NASICON)[34] with antimony (Sb) as a high-performance sodium-alloy electrode material. Antimony offers a very high theoretical capacity of 660 mA h g^{-1} when assuming the formation of Na$_3$Sb.[35] However, it readily reacts with water and the electrode potential for the alloying reactions is far outside of the stability window of aqueous electrolytes. Therefore, one would never consider it for use in conventional desalination batteries. In previous work by Pfeifer *et al.*, the influence of different carbon additives in the antimony electrode on the electrical performance in sodium-ion batteries was investigated.[36] The highest capacity (620 mA h g^{-1})

and stability (capacity loss of 19% after 100 cycles) were shown by a composite mixture of 70 mass% nanoscale antimony with 20 mass% of carbon onions and 10% carboxymethyl cellulose binder.[36] The low alloying reaction potential, generally lower than 1.0 V *vs.* Na$^+$/Na, make alloy materials impossible to be adopted to conventional cells for electrochemical desalination because of the exposure to water.[37] Due to that reason, we chose this promising electrode material for use in the bi-electrolyte desalination concept. In this multi-channel cell, Sb and carbon electrodes were in organic and aqueous electrolyte, respectively. The two electrodes were separated by a Na$^+$ permeable membrane (NASICON). During the charging process, Na$^+$ in the organic electrolyte was captured by the alloying reaction between Sb and Na$^+$ in the organic compartment. To keep the charge neutrality in the organic compartment, Na$^+$ from feed water would diffuse into organic electrolytes resulting in desalination. The initial performance of this cell in 600 mM NaCl is about 495 mg$_{Na}$ g$_{Sb}$$^{-1}$ (excluding the first two preconditioning cycles), and the performance stabilizes at around 294 mg$_{Na}$ g$_{Sb}$$^{-1}$ with a charge efficiency of about 74% in aqueous 600 mM NaCl for 40 operating cycles.

2 Experimental

2.1 Materials synthesis

The synthesis of antimony nanopowder was carried out by optimizing a synthesis route given in the literature.[38] To obtain a high purity of antimony, an excess of sodium borohydride (NaBH$_4$, 1.216 g, ≥98.0% purity, Sigma Aldrich) was suspended in 400 mL technical ethanol (>99.0% purity, Merck). Antimony chloride (SbCl$_3$, 2.244 g, ≥99.0% purity, Sigma Aldrich) was dissolved in 100 mL absolute ethanol (>99.8% purity, Honeywell). The antimony chloride solution was added dropwise into the stirring solution of sodium borohydride in ethanol at room temperature within one hour. The resultant mixture was stirred for another hour at room temperature. To break up agglomerates, the reaction mixture was sonicated for 10 min after stirring (P120H, Elmasonic). After sedimentation of the antimony particles, they were filtered under vacuum, washed three times with ethanol and three times with deionized water. Antimony particles were dried in an oven at +80 °C for 4 h. NASICON powder with excess Na was synthesized in analogy to literature (*via* Na$_{3.3}$Zr$_2$Si$_2$PO$_{12}$)[39] by using a solid-state reaction. As the precursor, 26.80 g NH$_4$H$_2$PO$_4$ (98.0% purity, Alfa Aesar), 40.35 g Na$_2$CO$_3$ (100.0% purity, Alfa Aesar), 27.45 g SiO$_2$ (particle size <50 nm, Aerosil O × 50) and 56.00 g ZrO$_2$ (particle size 40 nm, Tosoh) were applied. They were homogenized in a tumbler mixer for first step dry with 10 mm zirconia balls for 1 h, and then for another 24 h as an ethanolic slurry (absolute ethanol) with 15 mass% solid content (without balls to avoid contamination). After evaporation of ethanol, the dry powder was calcinated in two steps: first, at +600 °C in the air for 4 h, followed by a second calcination step at +1150 °C in the air for 4 h. The calcinated powder was crushed by hand and dry milled with 10 mm diameter zirconia balls for 1 h in a tumbler mixer. After sieving, the powder was cold-isostatically pressed at 400 MPa in a cylindrical rubber mold to obtain a green body.

586 | *J. Mater. Chem. A*, 2021, **9**, 585–596

This journal is © The Royal Society of Chemistry 2021

172

The pressed body with a relative density of around 74% was sintered at +1100 °C for 10 h in an air atmosphere to obtain a NASICON cylinder with a relative density of 78%. Membrane discs of 0.5 ± 0.05 mm thickness and a diameter of 40 mm were cut using a saw with a diamond blade. The open pores in the membrane were filled with epoxy resin. More details about this synthesis procedure are given in previous work.[34]

2.2 Structural and chemical characterization

X-ray diffraction (XRD) measurements of the antimony and NASICON powder were performed with a D8 Discover diffractometer (Bruker AXS) with a copper X-ray source (Cu-Kα (λ = 1.5406 Å), 40 kV, 40 mA) and a Göbel mirror and a 1 mm point focus as optics. With a VANTEC-500 (Bruker AXS) two-dimensional X-ray detector positioned at 17° 2θ, 37° 2θ, 57° 2θ, and 97° 2θ with a measurement time of 1000 s per step, five frames were recorded.

Scanning electron microscope (SEM) images were recorded with a field emission scanning electron microscope (JEOL JSM-7500F) operating at an acceleration voltage of 3 kV. The samples were dispersed in ethanol, drop casted multiple times on the carbon film sticky tape on the steel sample holder. The samples were dried under vacuum for 30 min and analyzed without the aid of an additional, conductive sputter coating.

Raman spectroscopy was carried out with a Renishaw inVia Microscope equipped with a neodymium-doped yttrium aluminum garnet laser with an excitation wavelength of 532 nm and a laser power of approximately 0.05 mW, a 2400 mm^{-1} grating, and a 50× objective lens with a numeric aperture of 0.75. Three to four different spots of each sample were recorded with five accumulations and 30 s exposure time.

Elemental analysis (CHNS) was performed with a Vario Micro Cube system from Elementar. The samples were each weighed in tin boats with the same amount of WO_3 and pressed under air exclusion. The reduction temperature in the pipe represented +850 °C (combustion tube temperature: +1150 °C), and the device was calibrated through repeated measurements of sulfanilamide.

Quantitative analysis of elemental oxygen was performed by using a rapid OXY cube oxygen analyzer from Elementar at a pyrolysis temperature of +1450 °C. The samples were weight in silver boats and pressed under air exclusion. The system was calibrated by measurements of benzoic acid.

2.3 Electrode materials and preparation

The Sb/C electrodes were manufactured by mixing the active material of 70 mass% synthesized antimony nanopowder with 20 mass% carbon onions, produced from nanodiamond powder at a temperature of 1300 °C under vacuum (OLC1300-Va),[40] and 10 mass% carboxymethyl cellulose as binder from a 3 mass% aqueous solution (CMC, degree of substitution = 0.7, molecular weight = 250 000 g mol^{-1}, Sigma Aldrich), by hand mixing for 40 min. First, the active material and the carbon were mixed and ground dry in a mortar. After adding isopropanol, the suspension was kept grinding until the isopropanol is completely vaporized. In the next step, this was repeated with

ethanol. After that, the electrode material with a small amount of ethanol and water (ratio 1 : 1) kept stirring for 30 min. Finally, the CMC binder solution was added, and the electrode past kept stirring for another 1 hour. The suspension was stirred for several hours on a magnetic stirrer to obtain a homogeneous slurry. The obtained electrode slurries were doctor bladed on aluminum foil (Ranafoil, Toyo Aluminium), used as a current collector, with a thickness of 15 μm. The electrodes were initially dried at ambient conditions overnight. Then, they were dried further in a vacuum oven at +120 °C for 12 h. Subsequently, the electrodes were punched out with a 12 mm diameter and transferred into a vacuum oven. Finally, a vacuum drying step at +80 °C for 12 h was conducted to remove the remaining solvent. The resulting electrode thickness of the dried electrodes was 40–60 μm with a material loading of 1.4 ± 0.2 mg cm^{-2}.

To evaluate the performance of the carbon on the aqueous side, commercially available microporous activated carbon cloth (Kynol ACC-507-20) was investigated as a working electrode. These electrodes, showing thickness of 250 μm, were punched in 12 mm discs and can be operated as free-standing, binder-free electrodes. In aqueous half-cell setups, a free-standing oversized activated carbon powder electrode (YP-80F, Kuraray) function as a counter electrode. These electrodes were prepared by mixing 90 mass% of activated carbon and 10 mass% polytetrafluoroethylene (60 mass% dispersion in water, Sigma Aldrich) together with ethanol. The mixture was ground until a dough-like slurry was obtained, and then rolled to a thickness of about 600 μm. These electrodes were dried under vacuum at +80 °C and punched into circular plates with a diameter of 12 mm.

2.4 Cell preparation and electrochemical characterization

2.4.1 Electrochemical half-cells. For electrochemical testing in an aqueous or organic electrolyte, custom-built polyether ether ketone (PEEK) cells with spring-loaded titanium pistons were used.[41] The cells were arranged in a three-electrode configuration for electrochemical measurements. The electrode discs were punched out of the electrode films with a diameter of 12 mm (1.13 cm^2). In sodium-ion-batteries, an elemental sodium electrode is commonly used as a reference and counter electrode.

All cell parts were dried overnight at +80 °C and introduced into an argon-filled glovebox (MBraun Labmaster 130; O_2 and H_2O < 0.1 ppm). First, the 12 mm diameter working electrode was placed in the cell, followed by a 13 mm diameter vacuum dried compressed glass-fiber separator (GF/D, Whatman). The counter electrode was punched into circular plates with a diameter of 10 mm and placed on top of the separator. Before using sodium metal, the oxidized surface of sodium was removed to obtain a smooth surface to avoid inhomogeneity and impurities. The counter electrodes were pressed to a uniform thickness of approximately 1 mm. A copper foil current collector was placed on the backside of each counter electrode. The sodium reference electrode was placed on a 2 mm diameter compressed glass-fiber separator (GF/D,

This journal is © The Royal Society of Chemistry 2021

J. Mater. Chem. A, 2021, **9**, 585–596 | **587**

Whatman) in a cavity close to the working electrode/counter electrode stack and contacted with titanium wire. The other three holes were closed with PEEK-screws.

The cells were vacuum filled with the electrolyte. The preparation and handling of the electrolyte solvent and salt were conducted in an argon-filled glovebox (MBraun Labmaster 130, O_2, H_2O < 0.1 ppm). A 1 M sodium perchlorate (NaClO$_4$, >99% purity, Alfa Aesar) solution in a solvent mixture of ethylene carbonate (EC, ≥99% purity, Sigma Aldrich) and dimethyl carbonate (DMC, ≥99% purity, Sigma Aldrich) in a 1 : 1 mass ratio with the addition of 5 mass% fluoroethylene carbonate (FEC, 99% purity, Sigma Aldrich) was used as an electrolyte. FEC is an additive for sodium-ion batteries used to improve the stability by increasing the solid electrolyte interface (SEI) stability, modifying the composition of the SEI layer, and preventing the decomposition of EC and DMC because the oxidation potential of FEC is higher than those of EC and DMC.[42–46] The sodium salt for the electrolyte was dried under vacuum at +80 °C for 48 h. The electrolyte was examined *via* Karl-Fischer titration and was found to contain less than 25 ppm water.

For measurements in aqueous electrolyte, half-cells were prepared by using Kynol ACC-507-20 as a working electrode and YP-80F as the counter electrode, the electrodes were separated by a 13 mm diameter vacuum dried glass-fiber disc (GF/A, 210 μm thickness, Whatman) to avoid short-circuiting. We used aqueous 600 mM NaCl as the electrolyte. Graphite foil was used as a current collector, and the Ag/AgCl (3 M KCl $E_{0\ Ag/AgCl}$ = 0.210 V *vs.* normal hydrogen electrode) electrode was employed as a reference electrode.

To determine the electrochemical behavior and electrochemical stability window of aqueous electrolyte, an *S*-value test, according to Xu *et al.*[47] was conducted. The vertex potential started at 0 V and was increased with an incremental of 50 mV steps until the final potential of 1.2 V *vs.* Ag/AgCl was reached. These measurements were done with a scan rate of 1 mV s^{-1}. For *S*-value calculation, the data at the 4th cycle is selected so that the electrode is conditioned at every vertex potential. For positive potential window opening, the *S*-values obtained from cyclic voltammetry were calculated by applying the eqn (1):

$$S = \frac{Q_{pos}}{Q_{neg}} - 1 \qquad (1)$$

By integrating the positive and negative current *vs.* time of each cycle, the values for Q_{neg} and Q_{pos} are calculated.

Galvanostatic cycling with potential limitation (GCPL), cyclic voltammetry (CV), and performance measurements were carried out using a VMP3 multi-channel potentiostat/galvanostat from Bio-Logic. All obtained values for the capacity in Sb/C *vs.* sodium cells relate to the respective active mass (*i.e.*, the total mass of antimony). All electrochemical measurements were carried out at a climate chamber (Binder) with a constant temperature of +25 ± 1 °C. The galvanostatic charge/discharge cycling with potential limitation (GCPL) experiments was recorded at voltages in the range of 0.1–2.0 V *vs.* Na$^+$/Na. For all GCPLs in this work, a specific current of

200 mA g^{-1} was used. Rate performance measurements were conducted at different currents to get more information about the half-cell rate capability and stability at higher currents. The applied specific currents were 0.1 A g^{-1}, 0.2 A g^{-1}, 0.5 A g^{-1}, 1.0 A g^{-1}, 2.0 A g^{-1}, 4.0 A g^{-1}, 8.0 A g^{-1}, and (again) 0.1 A g^{-1}. All CV measurements were carried out with a scan rate of 0.1 mV s^{-1} in a potential window of 0.1–2.0 V *vs.* Na$^+$/Na.

2.4.2 Electrochemical desalination. For electrochemical desalination, a custom-built multi-channel concentration bi-electrolyte cell was used, following the design described by Lee *et al.*[48] This cell persists of two side channels out of acrylic glass and one middle channel through which the aqueous electrolyte can flow. The tightness of the cell is guaranteed by various silicon gaskets (600 μm thickness). Graphite blocks (5 × 5 cm^2, thickness: 10 mm) served as the current collector. First the 20 mm diameter Sb/C electrode (preparation see above; 7 ± 0.5 mg active material) was placed in the cell between the silicon gasket, followed by a 24 mm vacuum dried glass-fiber separator (GF/D from Whatman), on which 2 mL of the organic electrolyte (1 M NaClO$_4$ in EC/DMC + 5% FEC) was dropped. After that, the NASICON membrane (Ø = 40 mm, 300 μm thickness) was inserted, surrounded by the gasket, to separate the aqueous side from the organic side. After placing the flow channel, a porous separator (Ø = 24 mm, glass-fiber pre-filler, Millipore, 380 μm thickness), the activated carbon cloth electrodes (Ø = 24 mm; 160 ± 20 mg), followed by graphite current-collector, complete the cell setup. A picture of our desalination cell and the generalized operation process are depicted in Fig. 1.

Mass balancing between a carbon electrode and Sb/C electrode followed eqn (2):

$$m_{Sb/C}Q_{Sb/C} = m_C Q_C \qquad (2)$$

The feed solution with 600 mM NaCl was prepared by dissolving NaCl (≥99.5% purity, Sigma Aldrich) in deionized water (Milli-Q). Using a 10 L reservoir, this aqueous electrolyte was pumped at an average of 1.1 mL min^{-1} into one side channel of the cell by a peristaltic pump (Masterflex, L/S Series). The electrolyte tank was continuously flushed with nitrogen gas to remove dissolved oxygen. The electrochemical test was carried out using a VSP3 multi-channel potentiostat/galvanostat from Bio-Logic. The conductivity- and pH-modules (Metrohm) are controlled by the Tiamo software. All electrochemical measurements were carried out in a climate chamber (Binder) with a constant temperature of +25 ± 1 °C. The GCPL experiments were recorded in the range of ±2.0 V *vs.* antimony.

The desalination capacity is calculated with eqn (3):

$$\text{Desalination capacity} = \frac{vM_{NaCl}}{m_{total}} \int \Delta c \, dt \qquad (3)$$

where v stands for the flow rate (mL min^{-1}), M_{NaCl} is the molecular mass of NaCl (58.44 g mol^{-1}), m_{total} is the mass of the electrodes (g), Δc is the change of concentration of NaCl (mM), and t is the time over the adsorption step (min). Note: we also normalized the desalination performance just normalized to the mass of the Sb/C electrode and when only considering sodium to yield a value for the sodium-removal capacity.

588 | *J. Mater. Chem. A*, 2021, **9**, 585–596

This journal is © The Royal Society of Chemistry 2021

174
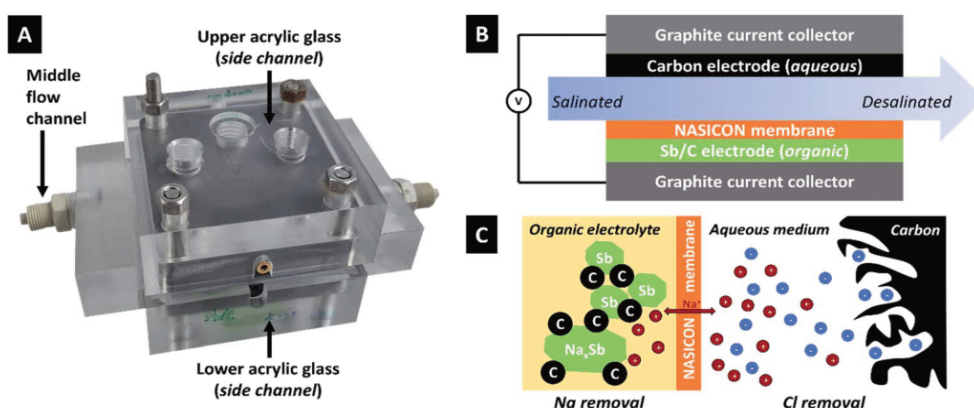
Fig. 1 (A) Photograph and (B) schematic drawing of the desalination cell used for this work. (C) Schematic drawing of the desalination mechanism.

3 Results and discussion

3.1 Working principle of the Sb/C *vs.* activated carbon cloth cell

We chose an optimized Sb/C composite electrode material based on our previous work which surveyed an array of different carbon additives; a detailed report on the structural, chemical, and porosity-related properties of the used carbon onion/antimony composite electrodes is found in ref. 36.

In this work, an Sb/C electrode is surrounded by an organic electrolyte and separated from the feedwater (aqueous 600 mM NaCl) by a ceramic cation-exchange membrane. During charging, 1 Sb atom reacts with (up to) 3 Na$^+$-ions in a multi-stage alloying process. Na$^+$ originates from the electrolyte solution on this side of the cell. This creates a concentration gradient of Na$^+$ during charging and a lack of these ions in the electrolyte. The saltwater on the other side of the cell is rich in Na$^+$ and the concentration gradient allows Na$^+$ to move through
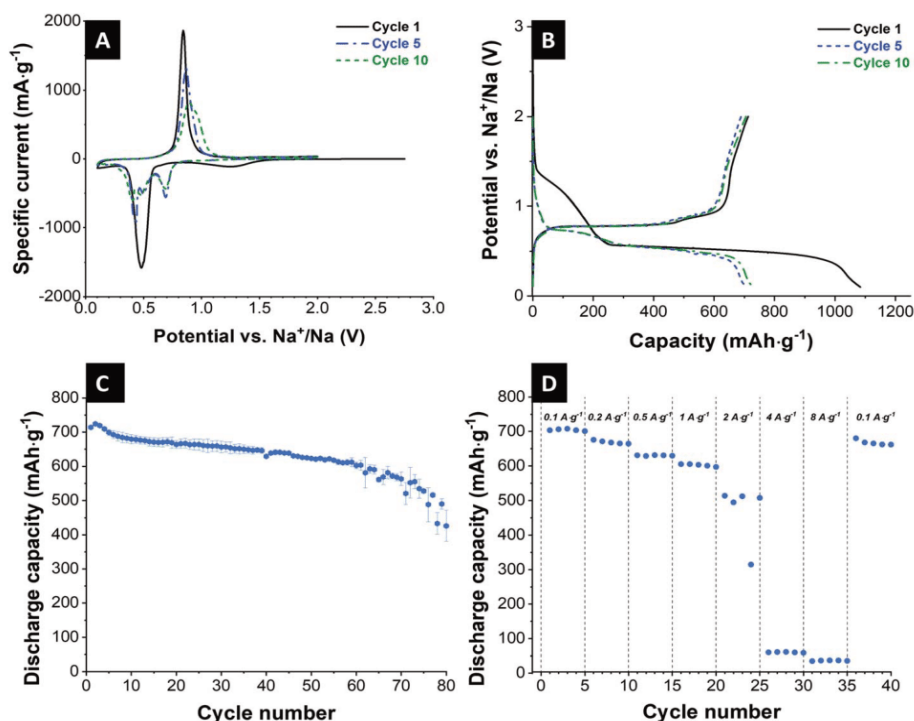
Fig. 2 Electrochemical performance of the Sb/C electrode. (A) 1st, 5th, and 10th cyclic voltammogram at a scanning rate of 0.1 mV s^{-1} from 0.1 V up to 2.0 V *vs.* Na$^+$/Na. (B) Galvanostatic charge and discharge profiles of the 1st, 5th, and 10th cycle at 200 mA g^{-1} between 0.1 V and 2.0 V *vs.* Na$^+$/Na. (C) Galvanostatic charge/discharge cycling performance electrochemical stability at a specific current of 200 mA g^{-1}. (D) Rate performance using galvanostatic charge/discharge cycling at different values for the specific current.
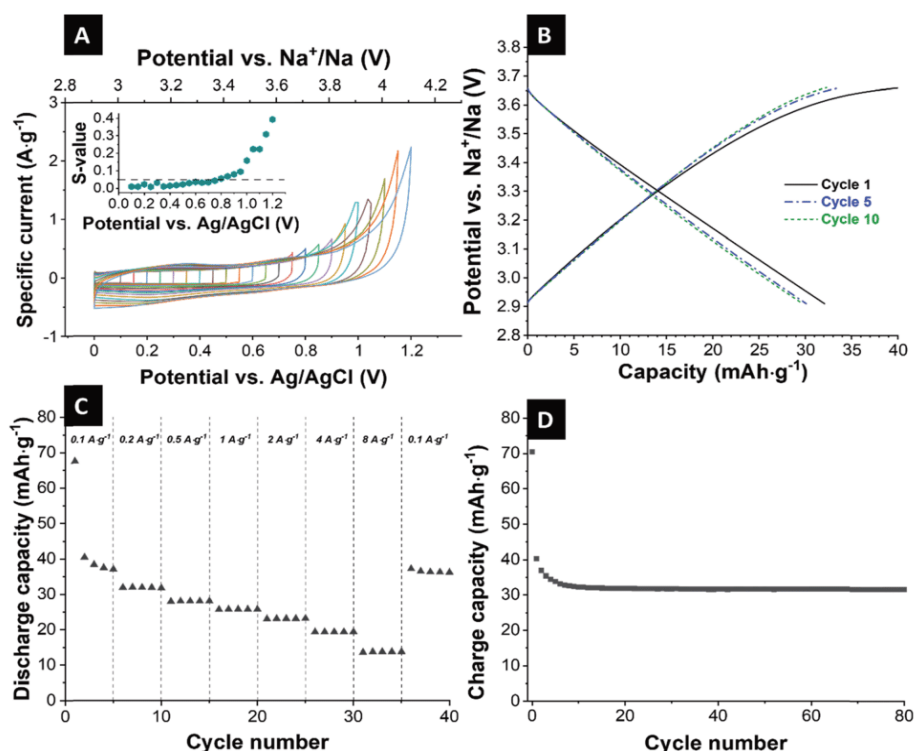
Fig. 3 Characterization of the activated carbon cloth electrode in 600 mM NaCl with an oversized activated carbon counter-electrode. (A) Voltammetric potential window opening experiments were recorded at a scan rate of 0.1 mV s^{-1} (inset: S-value vs. vertex voltage plot). (B) Galvanostatic charge−discharge profiles of the 1st, 5th, and 10th cycle at 200 mA g^{-1} of the activated carbon cloth electrode between 0 V and 0.75 V vs. Ag/AgCl, which corresponds with 2.91 V and 3.66 V vs. Na$^+$/Na. (C) Rate performance of the activated carbon cloth electrode from galvanostatic charge/discharge cycling at different values for the specific current. (D) Galvanostatic charge/discharge cycling performance electrochemical stability at a specific current of 200 mA g^{-1}.

the NASICON membrane, whereby sodium removal of the feedwater stream is accomplished. On the other side of the electrochemical desalination cell, chloride is removed from the saline solution via ion electrosorption at the fluid/solid interface. When discharging, the process would be reversed, and an increased amount of NaCl is released back into the effluent stream. Thereby, both the Sb and the carbon electrodes are both regenerated and ready for the next desalination cycle.

Data on the material characterization of antimony nanopowder and NASICON powder and membrane are given in ESI, Fig. S1 and S2.†

3.2 Electrochemical characterization

3.2.1 Electrochemical characterization of the Sb/C electrodes. Prior to desalination testing, we established the general electrochemical performance of the Sb/C electrodes in the organic electrolyte. Based on the investigations of Pfeifer et al.,[36] an electrode consisting of 70 mass% antimony and 20 mass% carbon onions were used as a working electrode. In the latter work, we compared different carbon additives, and we employ carbon onions because they showed the most promising electrochemical performance metrics.[36]

Cyclic voltammetry was carried out to characterize the redox behavior of the electrode material. Fig. 2A shows the typical CV

of the first, fifth, and tenth cycle at a scan rate of 0.1 mV s^{-1} between 0.1 V and 2.0 V vs. Na$^+$/Na. The redox peaks at around 1.2 V and 0.5 V vs. Na$^+$/Na in the first cycle correspond to the SEI formation and conversion of crystalline Sb to Na$_x$Sb, respectively.[49] The oxidation peak in the subsequent sodiation scan at a potential of 0.8 V vs. Na$^+$/Na characterize the de-sodiation reaction of Na$_x$Sb alloy back to elemental amorphous antimony. In the 5th and 10th cycles, there are additional reduction peaks at the potential of 0.7 V and 0.45 V vs. Na$^+$/Na. This is related to the reaction mechanism of the crystalline antimony, which reacts with the sodium to form amorphous compounds. NaSb further reacts with additional sodium to form crystalline Na$_3$Sb. Between the first and the following cycle, we can see key differences. The oxidation peak, resulting from the de-sodiation reaction of the alloy, is shifting from 0.74 V vs. Na$^+$/Na (1st cycle) over 0.87 V vs. Na$^+$/Na (5th cycle) to 0.91 V vs. Na$^+$/Na (10th cycle). These differences and the significant decrease in the current intensity after cycling can be attributed to the decomposition of the electrolyte, a change of reaction mechanism, and several changes in the involved structures.

The cycling stability of the Sb/C electrode was tested for 80 cycles at a specific current of 200 mA h g^{-1} in a voltage range between 0.1–2.0 V vs. Na$^+$/Na. The corresponding galvanostatic charge and discharge curves are displayed in Fig. 2B, which

590 | J. Mater. Chem. A, 2021, **9**, 585–596

This journal is © The Royal Society of Chemistry 2021

176
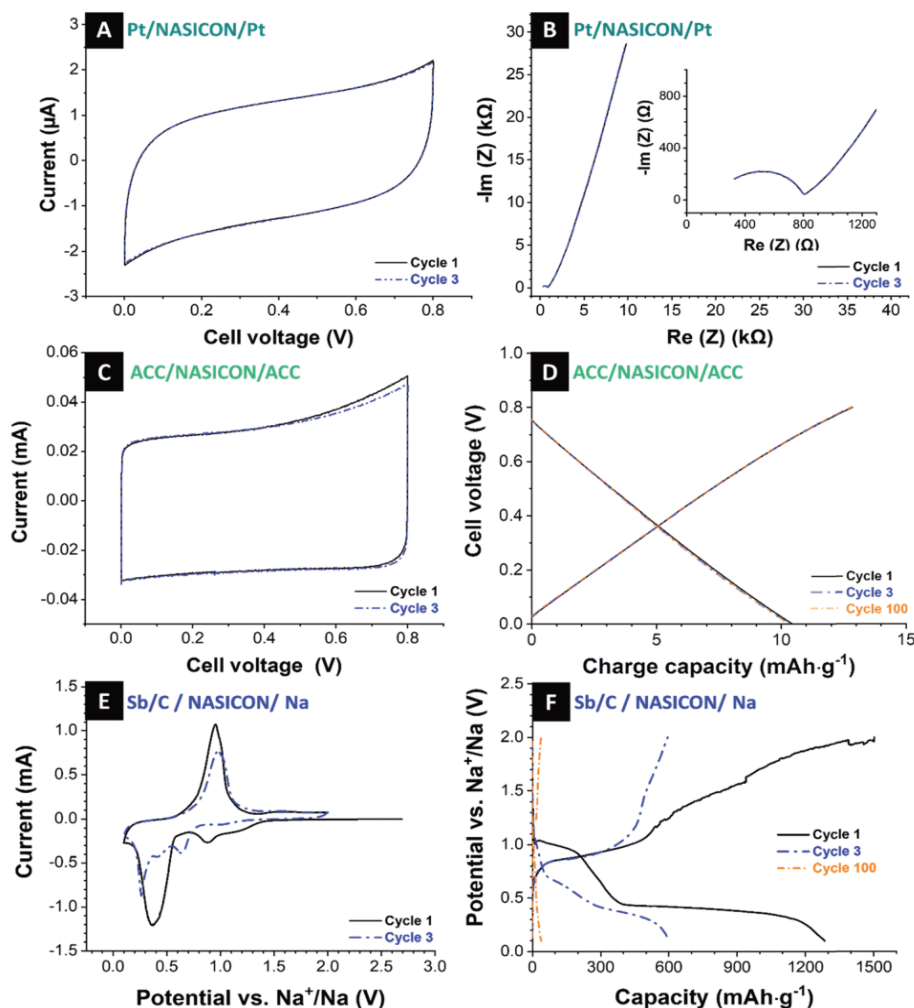
Fig. 4 (A and B) Electrochemical characterization of the platinum-sputtered NASICON membrane: (A) cyclic voltammograms recorded at 5 mV s^{-1} in the potential range of 0.0–0.8 V, (B) Nyquist plots. (C and D) Electrochemical characterization of activated carbon cloth with a NASICON separator: (C) cyclic voltammograms recorded at 0.1 mV s^{-1} in the potential range of 0.0–0.8 V, (D) galvanostatic charge and discharge curves of the 1st, 3rd, and 100th cycle. (E and F) Electrochemical characterization of the Sb/C electrode with a NASICON separator paired with a Na-disk counter electrode: (E) first and third cyclic voltammogram recorded with 0.1 mV s^{-1} within the potential range from 0.1 V up to 2.0 V vs. Na$^+$/Na, (F) galvanostatic charge and discharge curves of the 1st, 3rd, and 100th cycle.

show typical characteristics of the antimony electrodes.[38,49,50] The different plateaus correspond to the redox reactions associated with Na$^+$ alloying/de-alloying. The initial sodiation curve exhibits a long plateau at 0.4 V vs. Na$^+$/Na, which can, besides the alloying products, be assigned to the formation of SEI films on the electrode.[51] In the following cycles, it continuously shows the plateaus according to the alloying reaction from Sb to amorphous Na$_x$Sb to cubic and hexagonal Na$_3$Sb mixture to hexagonal Na$_3$Sb.[52] Subsequent to the 2nd cycle, there are no significant changes in the shape of the curves. Only a small loss of capacity is visible in the discharge curves. The results of these galvanostatic curves confirm the findings received from cyclic voltammetry.

The galvanostatic curves display a potential drift during the electrochemical measurements of the cell. The plateau of the charge curve shifts in the direction of lower capacity, while the

plateau of the discharge curve shifts partially in the direction of higher capacity. This characterizes an overvoltage in the cell, and the capacity is less affected compared to the plateau position (ESI, Fig. S3A†). The reasons for this shift may include low kinetics, inhomogeneities of the electrode, and undesired side reactions to a change in the reaction mechanism according to previous works on alloying electrodes.[38,53–55]

The cycling stability is depicted in Fig. 2C. The initial capacity has a value of 714 mA h g^{-1}. As usual for sodium-ion batteries, there is a small increase of the capacity over the course of the first cycles. The cells slowly degrade continuously over the course of the 80 cycles, especially toward the higher cycle numbers. The degradation occurred in all cells, but at different rates, which resulted in an increased error bar seen at higher cycle numbers in Fig. 2C. After 80 cycles, Sb/carbon

This journal is © The Royal Society of Chemistry 2021

J. Mater. Chem. A, 2021, **9**, 585–596 | **591**

177
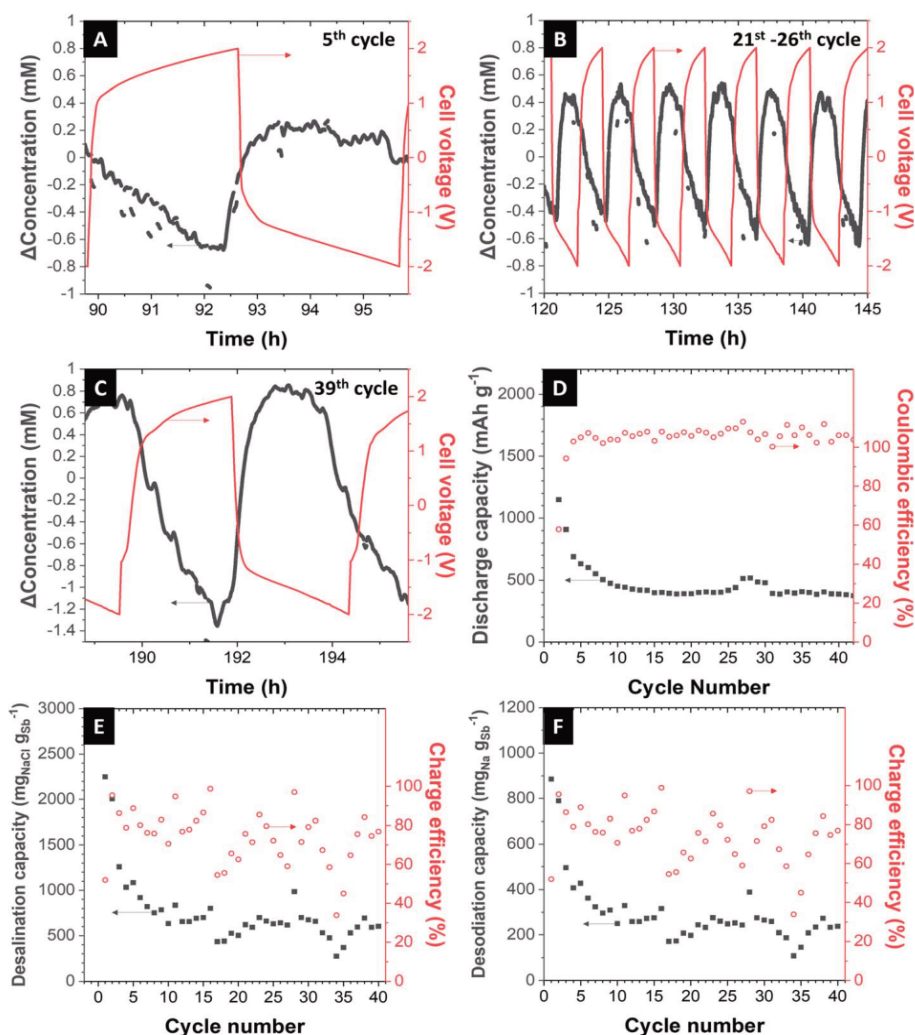
Fig. 5 Performance of the electrochemical desalination cell. (A−C) The change of concentration and voltage profile at the 5th cycle, 21st to 26th cycles and the 39th cycle. (D) The charge capacity and the corresponding values of the coulombic efficiency. (E) The desalination capacity ($mg_{NaCl}\ g_{Sb}^{-1}$) and charge efficiency. (F) The desalination capacity ($mg_{Na}\ g_{Sb}^{-1}$) and charge efficiency.

electrode reaches a capacity of 426 mA h g^{-1}, which corresponds to a value of 60% of the initial capacity.

The rate capability of these Sb/C electrodes is evaluated at a varying specific current from 0.1 A g^{-1} to 8 A g^{-1} (Fig. 2D). Up to a specific current of 1 A g^{-1}, the electrodes show stable electrochemical behavior with a capacity of higher than 600 mA h g^{-1} (0.1 A g^{-1}: 708 mA h g^{-1}; 0.2 A g^{-1}: 668 mA h g^{-1}; 0.5 A g^{-1}: 632 mA h g^{-1}; 1 A g^{-1}: 603 mA h g^{-1}). At a specific current of 2 A g^{-1} and higher, the cells lost most of their charge storage capacity. When the specific current is again reduced to 0.1 A g^{-1}, the cell nearly reaches its initial capacity but degrades toward the 5th cycle.

3.2.2 Electrochemical characterization of the activated carbon cloth electrodes. As a next step, we characterized the electrochemical behavior of the activated carbon cloth, which will be used on the aqueous side of our desalination cell. Using 600 mM NaCl electrolyte, we carried out S-value tests, cyclic voltammetry, galvanostatic cycling, cycling stability, and rate

capability benchmarking (Fig. 3). The electrochemical stability of aqueous electrolyte in the range of 2.9 V up to 4.1 V vs. Na⁺/Na was identified via the S-value test, where the criterion of dS/dV < 0.05 (5%) were applied.[47,56,57] The stable potential window for the activated carbon cloth is between 0 V and 0.75 V vs. Ag/AgCl; this potential window corresponds to values of 2.9 V and 3.7 V vs. Na⁺/Na. The measured cyclic voltammograms (Fig. 3A) at a scan rate of 0.1 mV s^{-1} show the typical ion-electrosorption behavior of carbon without any reduction and oxidation peaks within the identified stable potential region.

The obtained galvanostatic charge and discharge data (Fig. 3B) agree with the data from cyclic voltammetry. As expected for a nearly perfect electrical double-layer capacitor, the galvanostatic profiles show no plateaus, and the electrode delivers an initial capacity of 40 mA h g^{-1}. Over the next cycles, the capacity is stabilized at 32 mA h g^{-1} ($\approx$146 F g^{-1}) for 80 cycles (Fig. 3C).

Table 1 Overview of desalination capacities and charge efficiencies reported for different desalination systems and electrode materials. Not available data from literature references are donated as "n.a."

System	Electrode	Desalination capacity $mg_{NaCl}\ g_{electrode}^{-1}/mg_{Na}\ g_{electrode}^{-1}$	Charge efficiency (%)	Energy consumption	Cell voltage (V)	Electrolyte	Reference
Faradaic deionization	$Na_{2-x}Mn_5O_{10}/$ Ag/AgCl	n.a.	n.a.	0.29 W h L^{-1}	$\sim$0.55/ 0.19	600 mM NaCl	17
Capacitive deionization	Nanoporous carbon	7/3	$\sim$85%	n.a.	1.4/1.2 V	5 mM	69
Capacitive deionization	Nanoporous carbon	13/	86%	n.a.	1.2 V	1000 M NaCl	70
Faradaic deionization	Ti_3C_2-MXene	13 ± 2/5	n.a.	n.a.	1.2 V	5 mM NaCl	71
Faradaic deionization	$Bi/NaTi_2(PO_4)_3$	83/	n.a.	n.a.	0.75/ 0.55 V	600 M NaCl	25
Multi-channel membrane capacitive deionization	Activated carbon cloth	56/33	$\sim$82%	$\sim$20 kT	0.0/ −1.2 V	Side channel: 1000 M, middle channel: 5 mM	64
Membrane capacitive deionization (aqueous/organic bi-electrolyte)	Nanoporous carbon	64 ± 4/25 ± 2	95%.	14–27 kT	2.4 V	5 mM NaCl	29
Faradaic deionization	MoS_2-CNT	25/10	80%	24.6 kT	0.8/0.0 V	500 M NaCl	72
Hybrid capacitive deionization	$Na_4Mn_9O_{18}/$ nanoporous carbon	31/12	n.a.	n.a.	0.8/0.0 V	1000 M NaCl	18
Hybrid capacitive deionization (aqueous/organic bi-electrolyte)	**Sb–C/ nanoporous carbon**	**748 $mg_{NaCl}\ g_{Sb}^{-1}$, 294 $mg_{Na}\ g_{Sb}^{-1}$**	**74%**	**16 kT (0.0005 W h L^{-1})**	**+2.0/ −2.0 V**	**600 M NaCl**	**This work**

Fig. 3D shows the reversible capacities at various discharge/charge rates. The system retained a capacity of 36/32/27/24/23/19/14 mA h g^{-1} at a specific current of 0.1/0.2/0.5/1.0/2.0/4.0/8.0 A g^{-1}. During running different values of specific current, stable values for the capacities can be obtained, even for high currents of 8 A g^{-1}, which is the advantage of the ion-electrosorption. Only at the very first cycle, one can see that the cell needs one cycle for stabilization. When the specific current is returned to 0.1 A g^{-1}, the cell nearly reaches its initial capacity and shows good stability.

3.2.3 Electrochemical characterization of the NASICON membranes. As a next step, we only characterized the electrochemical behavior of ceramic NASICON membrane with a thickness of 950 μm. To this end, we assembled a solid-state cell by use of a platinum-sputtered NASICON electrode. The NASICON discs were sputtered with platinum to create blocking electrodes and then clamped well between the titanium pistons of the electrochemical cell, to ensure good surface contact and electrical conductivity. Cyclic voltammetry was conducted in a cell voltage range of 0.0–0.8 V. Fig. 4A presents the first and the third voltammetric cycle at a scan rate of 5 mV s^{-1}. Cyclic voltammograms at higher rates are provided in ESI, Fig. S4A.† These two cycles did not differ from each other. In the current *vs.* voltage profile, we see no anodic (oxidation) and cathodic (reduction) peaks. This means that there are no redox-active species, and no electrochemically reversible reactions are taking place.

Electrochemical impedance spectroscopy (EIS) at a voltage amplitude of 100 mV was conducted using a frequency sweep of 100 mHz to 1 MHz to characterize the NASICON membrane

conductivity. Fig. 4B shows the Nyquist plot with a semicircle in the medium-to-high frequency region. In the impedance spectra at high frequencies, the semicircle indicates the grain resistance of the membrane, whereas, at medium to low frequencies, the semicircle represents the grain boundary resistance. These resistors are characterized by a single semicircle as the total resistance of the membrane.[39,58] At low frequencies, the diffusion phenomena can be observed. Here, the near-straight line in the low-frequency range corresponds with the interface components (electrode polarization).[59]

Using these data, we can calculate the effective ionic conductivity. The latter is given by the theoretical intersections of the low-frequency ends of the semicircle with the Z' axis.

$$\kappa_{total} = \frac{1}{R\ \frac{A}{d}} \tag{4}$$

where κ indicates the total ion conductivity in Siemens per meter, R is the obtained resistance out of the EIS in Ω, d is the thickness of the electrode in cm, and A is the cross-sectional area of the sample in cm^{-2}. The resulting effective ionic conductivity for our NASICON sample was 0.17 mS cm^{-1}. The value is lower compared to the literature (10^{-5} to 10^{-3} mS cm^{-1}),[30,60,61] but usually higher sintering temperatures and thinner membranes are being used in other works. Thus, electrodes with sufficient conductivity for desalination were produced.

To characterize sodium transport across the ceramic NASICON membrane in an aqueous electrolyte, we paired the

NASICON disc with two activated carbon cloth electrodes in 600 mM NaCl electrolyte and sandwich on the NASICON membrane. The first and third cyclic voltammograms at a scan rate of 0.1 mV s^{-1} are given in Fig. 4C within a cell voltage of 0.0 V to 0.8 V. Cyclic voltammograms at higher rates are provided in ESI, Fig. S4B.† We see highly rectangular profiles, which are typical for an ideal electrical double-layer capacitor.[62] Additionally, the cell voltage of carbon cloth in the semi-solid cell is significantly lower than in a traditional cell. This is possibly due to the high contact resistance between carbon and NASICON interface as well as low ionic conductivity of the membrane.

The galvanostatic charge and discharge profiles of activated carbon cloth are shown in Fig. 4D. At a specific current of 200 mA g^{-1} within a voltage range of 0.0–0.8 V, there is a typical linear relation between charge and cell voltage in alignment with a nearly perfect capacitive behavior. There are no significant changes in charge/discharge capacity for 100 cycles (ESI, Fig. S5A and C†). However, considering the rate handling of carbon cloth (ESI, Fig. S5E†), the cell cannot provide fast charge/discharge as compared to the conventional cell with a glass fiber separator due to the fact that the sodium transport kinetics are much slower than that in glass fiber separator; a comparison thereof is shown in ESI, Fig. S3B.†

As in the next step, we used the Sb/C electrode as the working electrode and the pure sodium electrode as a counter electrode with the NASICON membrane as a separator. We used an organic electrolyte of 1 M NaClO$_4$ in EC/DMC + 5% FEC and a scan rate of 0.1 mV s^{-1} within the range from 0.1–2.0 V vs. Na$^+$/Na. The obtained cyclic voltammograms with the NASICON membrane (Fig. 4E) are similar to those with just a porous separator (Fig. 2A) with the characteristic peaks for the alloy reactions of antimony with sodium. This indicates that the comparatively thick NASICON electrode can transport Na$^+$ to the extent or at speed required for the alloy reactions to take place. Cyclic voltammograms at higher rates are provided in ESI, Fig. S4C.† Conspicuous is the broader shape of the obtained cyclic voltammograms with the NASICON membrane compared with the same cell setup with glass fiber separator. In general, the breadth of peaks depends on the limiting stage of processes like the velocity of mass or electron transfer and diffusion and chemical processes before or after electron transfer. So, in this current case, the broader peaks may be an indicator of lower transport rates of the ions in the cell because of the thick NASICON membrane.

Fig. 4F presents the galvanostatic charge and discharge profiles of Sb/C electrode vs. Na$^+$/Na with a NASICON membrane as the separator, at a specific current of 200 mA g^{-1} and a voltage range of 0.1–2.0 V. The initial charge curve exhibits the similar a long plateau at 0.4 V which represents the SEI formation. In addition, the discharge curve reaches beyond 1285 mA h g^{-1} of the corresponding charge curve. It seems that the sodium ions in the NASICON block the channels at times, and the cell cannot be discharged as easily. After the first cycle, this phenomenon is vanishing. During the next cycles, one sees the plateaus at 0.7–1.0 V during sodium-ion removal, which can be related to the reaction of Na$_3$Sb alloys back to crystalline

antimony. The observations from the galvanostatic charge and discharge curves are consistent with the information obtained from cyclic voltammetry.

The cycling stability is presented in ESI, Fig. S5B.† The performance is characterized by a continuous loss of capacity in each cycle. The cells exhibit a capacity of 643 mA h g^{-1} in the second cycle and show a capacity of about 453 mA h g^{-1} after only 10 cycles, which correspond to a loss of capacity of 30%. In the 50th cycle, the cells still reach a capacity of approximately 100 mA h g^{-1}, and after the 80 cycles, only a low capacity of 44 mA h g^{-1} is delivered, which corresponds to a total capacity loss of 93% over 80 cycles. The coulombic efficiency, shown in ESI, Fig. S5D,† shows constant values of 96–97%. Compared to the cell with porous separator, the rate capability shows a lower capacity and stability at all rates (ESI, Fig. S5F†) as the sodium ion diffusion through the element-specific channels of the NASICON membrane is limited by the thick membrane. Yet, the ceramic NASICON membrane works sufficiently well to provide the antimony electrode with a sufficient supply of sodium for the alloying reaction.

3.3 Desalination performance

Electrochemical desalination was performed in a desalination cell described elsewhere.[29,34] The Sb/C electrode was surrounded by 1 M NaClO$_4$ in EC/DMC + 5% FEC electrolyte and separated from the feedwater stream by a ceramic NASICON membrane with 300 μm thickness. Oversized activated carbon cloth is used as a counter electrode. As feedwater, aqueous 600 mM NaCl is fed to the cell with a peristaltic pump. To be sure that the electrolyte is oxygen-free, we constantly flushed the electrolyte with N$_2$ gas throughout the desalination experiment. As a specific current of 200 mA g^{-1} was applied to the cell with the cut-off cell voltage of ±2.0 V, the concentration profile behaves like in a regular capacitive deionization cell. In the first cycle, the concentration of NaCl has decreased with the amplitude of about 5 mM when the cell is charged. After 80 min of charging, the cell is rested for 2 min and discharged, one can see the increasing of NaCl concentration, indicating the de-sodiation of Sb/C electrode (Fig. 5A). After 40 cycles of operation, the amplitude of decreased NaCl concentration is significantly lower than that of the first cycle (Fig. 5B). This is due to the intrinsic mechanism of sodium-alloying in the Sb electrode. The charge capacity of our desalination cell is about 669 mA h g$_{Sb}^{-1}$ at the first cycle after conditioning cycles and decays to 360 mA h g$_{Sb}^{-1}$ after 40 cycles (Fig. 5C). The corresponding desalination capacity of the first cycle is 495 mg$_{Na}$ g$_{Sb}^{-1}$ and stabilizes at around 250 mg$_{Na}$ g$_{Sb}^{-1}$ (corresponds to 635 mg$_{NaCl}$ g$_{Sb}^{-1}$ and 1116 mg$_{Na}$ m$_{membrane}^{-2}$) with the charge efficiency of about 74% for 40 cycles (Fig. 5D).

Reasons for the low charge efficiency could be, among others, the side reactions (like oxidation of carbon or splitting of water), the imperfect shape, and properties of the NASICON membrane, which prevents the ions from being transported in the fastest and easiest way, which also results in poorer kinetics. These factors also will contribute towards the decay of performance seen during continued cell operation.

594 | J. Mater. Chem. A, 2021, **9**, 585–596

This journal is © The Royal Society of Chemistry 2021

In comparison to other systems (charge-transfer materials),[33] which successfully desalinate with different mechanisms like an ion electrosorption (3–27 mg_{NaCl} $g_{electrode}^{-1}$; 1–11 mg_{Na} $g_{electrode}^{-1}$),[63] insertion of different materials and redox couples (6–140 mg_{NaCl} $g_{electrode}^{-1}$; 2–55 mg_{Na} $g_{electrode}^{-1}$),[27] or conversion type (17–115 mg_{NaCl} $g_{electrode}^{-1}$; 7–22 mg_{Na} $g_{electrode}^{-1}$),[23,24] the system described in this work shows very promising values (Table 1).

For membrane capacitive deionization (MCDI), a value of 22 kT is often reported.[8,29] The first desalination battery achieved a value of 0.29 W h L^{-1} for energy consumption.[17] Kim *et al.* report for a multi-channel membrane capacitive deionization an energy consumption of 20 kT.[64] The energy consumption of the cell configuration in this work is calculated to be 16 kT or 39 kJ mol^{-1} $_{NaCl}$ after the first cycles. This value corresponds to the energy per processed water of 0.0005 W h L^{-1}, which is also comparable to traditional methods like reverse osmosis (0.5–2 W h L^{-1}),[65] multistage flash distillation (20–30 W h L^{-1}),[66] multi-effect distillation (15–20 W h L^{-1}),[67] freezing methods (6–8 W h L^{-1}).[68] Compared to other faradaic materials (including intercalation materials), conversion materials, redox electrolytes, and zinc–air desalination, alloying with the aid of NASICON deliver energy consumption lower than others. A direct comparison, however, is complicated by different experimental settings, such as flow rate, cell volume, and the extent of salt reduction.[27]

4 Conclusion

This study demonstrates a desalination cell by using antimony as a sodium-alloying material, which is a promising and high-performing electrode in sodium-ion batteries. By applying a bi-electrolyte system (organic and aqueous part), the cell can provide stable desalination performance at higher maximum cell voltage than the conventional capacitive deionization technology allows (1.0–1.2 V). In an optimized desalination cell configuration with a middle channel for the inflowing feed stream and a selective sodium permeable membrane (NASICON), the Sb/C electrodes exhibit an improved electrochemical performance with a discharge capacity of initially 669 mA h g^{-1} (395 mA h g^{-1} after 40 cycles) at a specific current of 200 mA g^{-1} and a voltage range of −2.0 V to +2.0 V, which results in a desalination capacity on the average of 294 mg_{Na} g_{Sb}^{-1} with a charge efficiency of about 74% in aqueous 600 mM NaCl. Future work will have to further optimize the cell design, and further reduction of the ceramic membrane thickness will allow the faster operation of the desalination battery.

Conflicts of interest

There are no conflicts to declare.

Acknowledgements

References

1 N. C. Darre and G. S. Toor, *Curr. Pollut. Rep.*, 2018, **4**, 104–111.
2 A. D. Khawaji, I. K. Kutubkhanah and J.-M. Wie, *Desalination*, 2008, **221**, 47–69.
3 A. Matin, Z. Khan, S. M. J. Zaidi and M. C. Boyce, *Desalination*, 2011, **281**, 1–16.
4 Y.-y. Lu, Y.-d. Hu, D.-m. Xu and L.-y. Wu, *J. Membr. Sci.*, 2006, **282**, 7–13.
5 A. Rich, Y. Mandri, N. Bendaoud, D. Mangin, S. Abderafi, C. Bebon, N. Semlali, J.-P. Klein, T. Bounahmidi, A. Bouhaouss and S. Veesler, *Desalin. Water Treat.*, 2010, **13**, 120–127.
6 S. Porada, R. Zhao, A. van der Wal, V. Presser and P. M. Biesheuvel, *Prog. Mater. Sci.*, 2013, **58**, 1388–1442.
7 M. E. Suss, S. Porada, X. Sun, P. M. Biesheuvel, J. Yoon and V. Presser, *Energy Environ. Sci.*, 2015, **8**, 2296–2319.
8 R. Zhao, S. Porada, P. M. Biesheuvel and A. van der Wal, *Desalination*, 2013, **330**, 35–41.
9 S. Porada, L. Zhang and J. E. Dykstra, *Desalination*, 2020, **488**, 114383.
10 P. M. Biesheuvel, S. Porada, M. Levi and M. Z. Bazant, *J. Solid State Electrochem.*, 2014, **18**, 1365–1376.
11 C. Prehal, C. Koczwara, H. Amenitsch, V. Presser and O. Paris, *Nat. Commun.*, 2018, **9**, 4145.
12 S. Bi, Y. Zhang, L. Cervini, T. Mo, J. M. Griffin, V. Presser and G. Feng, *Sustainable Energy Fuels*, 2020, **4**, 1285–1295.
13 N. Jäckel, P. Simon, Y. Gogotsi and V. Presser, *ACS Energy Lett.*, 2016, **1**, 1262–1265.
14 F. Stoeckli and T. A. Centeno, *Phys. Chem. Chem. Phys.*, 2012, **14**, 11589–11591.
15 H. Ji, X. Zhao, Z. Qiao, J. Jung, Y. Zhu, Y. Lu, L. L. Zhang, A. H. MacDonald and R. S. Ruoff, *Nat. Commun.*, 2014, **5**, 3317.
16 Z.-H. Huang, Z. Yang, F. Kang and M. Inagaki, *J. Mater. Chem. A*, 2017, **5**, 470–496.
17 M. Pasta, C. D. Wessells, Y. Cui and F. La Mantia, *Nano Lett.*, 2012, **12**, 839–843.
18 J. Lee, S. Kim, C. Kim and J. Yoon, *Energy Environ. Sci.*, 2014, **7**, 3683–3689.
19 P. Srimuk, J. Lee, Ö. Budak, J. Choi, M. Chen, G. Feng, C. Prehal and V. Presser, *Langmuir*, 2018, **34**, 13132–13143.
20 S. Porada, A. Shrivastava, P. Bukowska, P. M. Biesheuvel and K. C. Smith, *Electrochim. Acta*, 2017, **255**, 369–378.
21 P. Srimuk, J. Lee, A. Tolosa, C. Kim, M. Aslan and V. Presser, *Chem. Mater.*, 2017, **29**, 9964–9973.
22 E. Grygolowicz-Pawlak, M. Sohail, M. Pawlak, B. Neel, A. Shvarev, R. de Marco and E. Bakker, *Anal. Chem.*, 2012, **84**, 6158–6165.
23 P. Srimuk, S. Husmann and V. Presser, *RSC Adv.*, 2019, **9**, 14849–14858.
24 J. Ahn, J. Lee, S. Kim, C. Kim, J. Lee, P. M. Biesheuvel and J. Yoon, *Desalination*, 2020, **476**, 114216.

This journal is © The Royal Society of Chemistry 2021

J. Mater. Chem. A, 2021, **9**, 585–596 | **595**

181

25 D.-H. Nam and K.-S. Choi, *J. Am. Chem. Soc.*, 2017, **139**, 11055–11063.

26 F. Yu, L. Wang, Y. Wang, X. Shen, Y. Cheng and J. Ma, *J. Mater. Chem. A*, 2019, **7**, 15999–16027.

27 P. Srimuk, X. Su, J. Yoon, D. Aurbach and V. Presser, *Nat. Rev. Mater.*, 2020, **5**, 517–538.

28 S. Porada, G. Feng, M. E. Suss and V. Presser, *RSC Adv.*, 2016, **6**, 5865–5870.

29 C. Kim, P. Srimuk, J. Lee and V. Presser, *Desalination*, 2018, **443**, 56–61.

30 Y. Kim, H. Kim, S. Park, I. Seo and Y. Kim, *Electrochim. Acta*, 2016, **191**, 1–7.

31 Y. Kim, G.-T. Kim, S. Jeong, X. Dou, C. Geng, Y. Kim and S. Passerini, *Energy Storage Materials*, 2019, **16**, 56–64.

32 N. Kim, J.-S. Park, A. M. Harzandi, K. Kishor, M. Ligaray, K. H. Cho and Y. Kim, *Desalination*, 2020, **495**, 114666.

33 M. E. Suss and V. Presser, *Joule*, 2018, **2**, 10–15.

34 J. Lee, P. Srimuk, R. L. Zornitta, M. Aslan, B. L. Mehdi and V. Presser, *ACS Sustainable Chem. Eng.*, 2019, **7**, 10132–10142.

35 S. Z. Liang, Y. J. Cheng, J. Zhu, Y. G. Xia and P. Müller-Buschbaum, *Small Methods*, 2020, **4**, 2000218.

36 K. Pfeifer, S. Arnold, Ö. Budak, X. Luo, V. Presser, H. Ehrenberg and S. Dsoke, *J. Mater. Chem. A*, 2020, **8**, 6092–6104.

37 H. Tan, D. Chen, X. Rui and Y. Yu, *Adv. Funct. Mater.*, 2019, **29**, 1808745.

38 H. Hou, Y. Yang, Y. Zhu, M. Jing, C. Pan, L. Fang, W. Song, X. Yang and X. Ji, *Electrochim. Acta*, 2014, **146**, 328–334.

39 H. Park, K. Jung, M. Nezafati, C.-S. Kim and B. Kang, *ACS Appl. Mater. Interfaces*, 2016, **8**, 27814–27824.

40 M. Zeiger, N. Jäckel, M. Aslan, D. Weingarth and V. Presser, *Carbon*, 2015, **84**, 584–598.

41 D. Weingarth, M. Zeiger, N. Jäckel, M. Aslan, G. Feng and V. Presser, *Adv. Energy Mater.*, 2014, **4**, 1400316.

42 J. Qian, Y. Chen, L. Wu, Y. Cao, X. Ai and H. Yang, *Chem. Commun.*, 2012, **48**, 7070–7072.

43 Y.-X. Wang, Y.-G. Lim, M.-S. Park, S.-L. Chou, J. H. Kim, H.-K. Liu, S.-X. Dou and Y.-J. Kim, *J. Mater. Chem. A*, 2014, **2**, 529–534.

44 A. Ponrouch, D. Monti, A. Boschin, B. Steen, P. Johansson and M. R. Palacin, *J. Mater. Chem. A*, 2015, **3**, 22–42.

45 A. Ponrouch, A. R. Goñi and M. R. Palacín, *Electrochem. Commun.*, 2013, **27**, 85–88.

46 V. Simone, L. Lecarme, L. Simonin and S. Martinet, *J. Electrochem. Soc.*, 2016, **164**, A145–A150.

47 K. Xu, S. P. Ding and T. R. Jow, *J. Electrochem. Soc.*, 1999, **146**, 4172–4178.

48 J. Lee, P. Srimuk, S. Carpier, J. Choi, R. L. Zornitta, C. Kim, M. Aslan and V. Presser, *ChemSusChem*, 2018, **11**, 3460–3472.

49 S. Liu, J. Feng, X. Bian, J. Liu and H. Xu, *Energy Environ. Sci.*, 2016, **9**, 1229–1236.

50 L. Wu, X. Hu, J. Qian, F. Pei, F. Wu, R. Mao, X. Ai, H. Yang and Y. Cao, *Energy Environ. Sci.*, 2014, **7**, 323–328.

51 X. Zhou, Z. Dai, J. Bao and Y.-G. Guo, *J. Mater. Chem. A*, 2013, **1**, 13727–13731.

52 A. Darwiche, C. Marino, M. T. Sougrati, B. Fraisse, L. Stievano and L. Monconduit, *J. Am. Chem. Soc.*, 2012, **134**, 20805–20811.

53 P. R. Abel, Y.-M. Lin, T. de Souza, C.-Y. Chou, A. Gupta, J. B. Goodenough, G. S. Hwang, A. Heller and C. B. Mullins, *J. Phys. Chem. C*, 2013, **117**, 18885–18890.

54 M.-S. Balogun, Y. Luo, W. Qiu, P. Liu and Y. Tong, *Carbon*, 2016, **98**, 162–178.

55 Y. Kim, Y. Park, A. Choi, N.-S. Choi, J. Kim, J. Lee, J. H. Ryu, S. M. Oh and K. T. Lee, *Adv. Mater.*, 2013, **25**, 3045–3049.

56 M. Bahdanchyk, M. Hashempour and A. Vicenzo, *Electrochim. Acta*, 2020, **332**, 135503.

57 D. Weingarth, H. Noh, A. Foelske-Schmitz, A. Wokaun and R. Kötz, *Electrochim. Acta*, 2013, **103**, 119–124.

58 S. Narayanan, S. Reid, S. Butler and V. Thangadurai, *Solid State Ionics*, 2019, **331**, 22–29.

59 A. Jalalian-Khakshour, C. O. Phillips, L. Jackson, T. O. Dunlop, S. Margadonna and D. Deganello, *J. Mater. Sci.*, 2020, **55**, 2291–2302.

60 S. Naqash, D. Sebold, F. Tietz and O. Guillon, *J. Am. Ceram. Soc.*, 2019, **102**, 1057–1070.

61 S.-M. Lee, S.-T. Lee, D.-H. Lee, S.-H. Lee, S.-S. Han and S.-K. Lim, *Journal of Ceramic Processing Research*, 2015, **16**, 49–53.

62 H. Shao, Y. C. Wu, Z. Lin, P. L. Taberna and P. Simon, *Chem. Soc. Rev.*, 2020, **49**, 3005–3039.

63 Y. Liu, C. Y. Nie, X. J. Liu, X. T. Xu, Z. Sun and L. K. Pan, *RSC Adv.*, 2015, **5**, 15205–15225.

64 C. Kim, J. Lee, P. Srimuk, M. Aslan and V. Presser, *ChemSusChem*, 2017, **10**, 4914–4920.

65 A. Shrivastava, S. Rosenberg and M. Peery, *Desalination*, 2015, **368**, 181–192.

66 R. Semiat, *Environ. Sci. Technol.*, 2008, **42**, 8193–8201.

67 A. Al-Karaghouli and L. L. Kazmerski, *Renewable Sustainable Energy Rev.*, 2013, **24**, 343–356.

68 T. Mtombeni, J. Maree, C. Zvinowanda, J. Asante, F. Oosthuizen and W. Louw, *Int. J. Environ. Sci. Technol.*, 2013, **10**, 545–550.

69 S. Porada, L. Weinstein, R. Dash, A. van der Wal, M. Bryjak, Y. Gogotsi and P. M. Biesheuvel, *ACS Appl. Mater. Interfaces*, 2012, **4**, 1194–1199.

70 M. Aslan, M. Zeiger, N. Jäckel, I. Grobelsek, D. Weingarth and V. Presser, *J. Phys.: Condens. Matter*, 2016, **28**, 114003.

71 P. Srimuk, F. Kaasik, B. Krüner, A. Tolosa, S. Fleischmann, N. Jäckel, M. C. Tekeli, M. Aslan, M. E. Suss and V. Presser, *J. Mater. Chem. A*, 2016, **4**, 18265–18271.

72 P. Srimuk, J. Lee, S. Fleischmann, S. Choudhury, N. Jäckel, M. Zeiger, C. Kim, M. Aslan and V. Presser, *J. Mater. Chem. A*, 2017, **5**, 15640–15649.

596 | *J. Mater. Chem. A*, 2021, **9**, 585–596

This journal is © The Royal Society of Chemistry 2021

182

Supporting Information

Antimony alloying electrode for high-performance sodium removal: how to use a battery material not stable in aqueous media for saline water remediation

Stefanie Arnold,[1,2] Lei Wang,[1,2] Öznil Budak,[1,2]

Mesut Aslan,[1] Pattarachai Srimuk,[1] Volker Presser[1,2,*]

[1] INM - Leibniz Institute for New Materials, 66123 Saarbrücken, Germany

[2] Department of Materials Science and Engineering, Saarland University, 66123 Saarbrücken, Germany

* Corresponding author's E-Mail: volker.presser@leibniz-inm.de

Supporting Table

Table S1: Results of the elemental analysis (CHNS/O).

	CHNS/O elemental analysis (mass%)				
	Carbon	**Hydrogen**	**Nitrogen**	**Sulfur**	**Oxygen**
Antimony powder	0.18±0.11	*Not detected*			5.66±0.04

Supporting Material Characterization

We used a co-precipitation method to obtain the antimony nanopowder. Scanning electron micrographs, X-ray diffraction data, and Raman data are given in **Figure S1**. **Figure S1A**, the scanning electron micrograph shows partially agglomerated particles with a primary size of about 10-40 nm. The X-ray diffractogram (**Figure S1C**) is consistent with elemental antimony (space group of $R\bar{3}m$, ICSD: #55402, a=4.307 Å). Rietveld analysis yields an Sb phase content of about 97-98 mass% with a small amount of Sb_2O_3. This aligns with the small amount of oxygen found from chemical CHNS/O elemental analysis (*Supporting Information*, **Table S1**).

The Raman spectra of antimony at ambient conditions (**Figure S1D**) shows two peaks at 113 cm^{-1} and 150 cm^{-1}, which agrees with previous works on antimony.[1-3] Trigonal antimony forms stacked layers of atoms along the hexagonal axis. This structure results in two Raman active modes, the A_{1g} mode at 150 cm^{-1} and a two-fold degenerated E_g mode at 115 cm^{-1}, whereby the A_{1g} mode corresponds to the longitudinal motion of the atom planes and the E_g mode the transverse motion.[2] The Raman spectra also shows the presence of small amounts of Sb_2O_3 from the broad and low-intensity peak at around 270 cm^{-1} (Sb-O-Sb). The antimony oxide is most likely present in the form of thin skin around the antimony particles, which would act as an insulative layer between the antimony particle. This would result in high resistance of the electrode and poor electrochemical performance with a capacity close to zero.

Therefore, the use (and choice) of the conductive additive plays a central role.
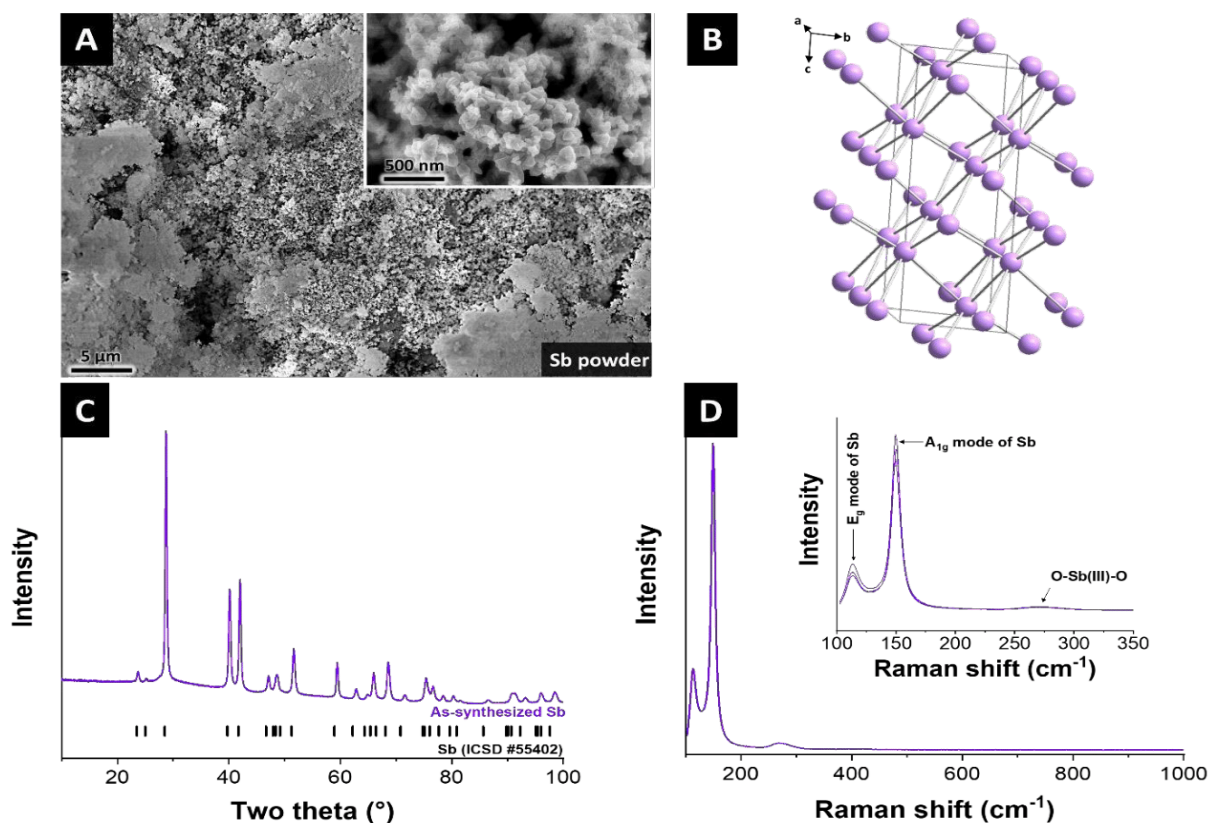
Figure S1: Material characterization of the as-synthesized antimony. (**A**) Scanning electron micrographs. (**B**) Crystal structure. (**C**) X-ray diffraction pattern. (**D**) Raman spectra (the inset shows the Raman mode assignment and three characteristic individual spectra).

We also analyzed the ceramic NASICON membrane. The XRD pattern in **Figure S2A** shows the characteristic peaks of low-NASICON (powder diffraction file, PDF 84-1184, space group C2/c; a=15.674 Å). Rietveld analysis yields a NASICON phase content of about 97-98%. There is also a second phase present, namely 2-3 mass% baddeleyite-type ZrO_2 (PDF 89-9066). The presence of ZrO_2 can potentially be due to both unreacted precursor and abrasion of the grinding balls.

The sintered material exhibits a theoretical density of 78%. This means the material still has open pores which are accessible to the electrolyte. For this reason, the pores are sealed by a post epoxy infiltration to close the pores of the membrane. The tightness of epoxy filled membranes was provided by checking the water uptake to be <1 mass%. Membranes with a diameter of 4 cm and a thickness of 300 µm were prepared for use as a membrane between the organic and the aqueous side in the desalination cell.

S3

Photographs of the NASICON discs with a thickness of 950 µm for electrochemical testing and NASICON discs with a thickness of 300 µm for desalination testing are shown in **Figure S2B**. For the electrochemical testing of the NASICON electrode, both sides of the electrode were sputtered with platinum. **Figure S2C-D** shows scanning electron micrographs of NASICON powder and NASICON membrane. The ceramic matrix is composed of sub-micrometer particles, and the interparticle pore space in the NASICON membrane is effectively filled with epoxy resin.
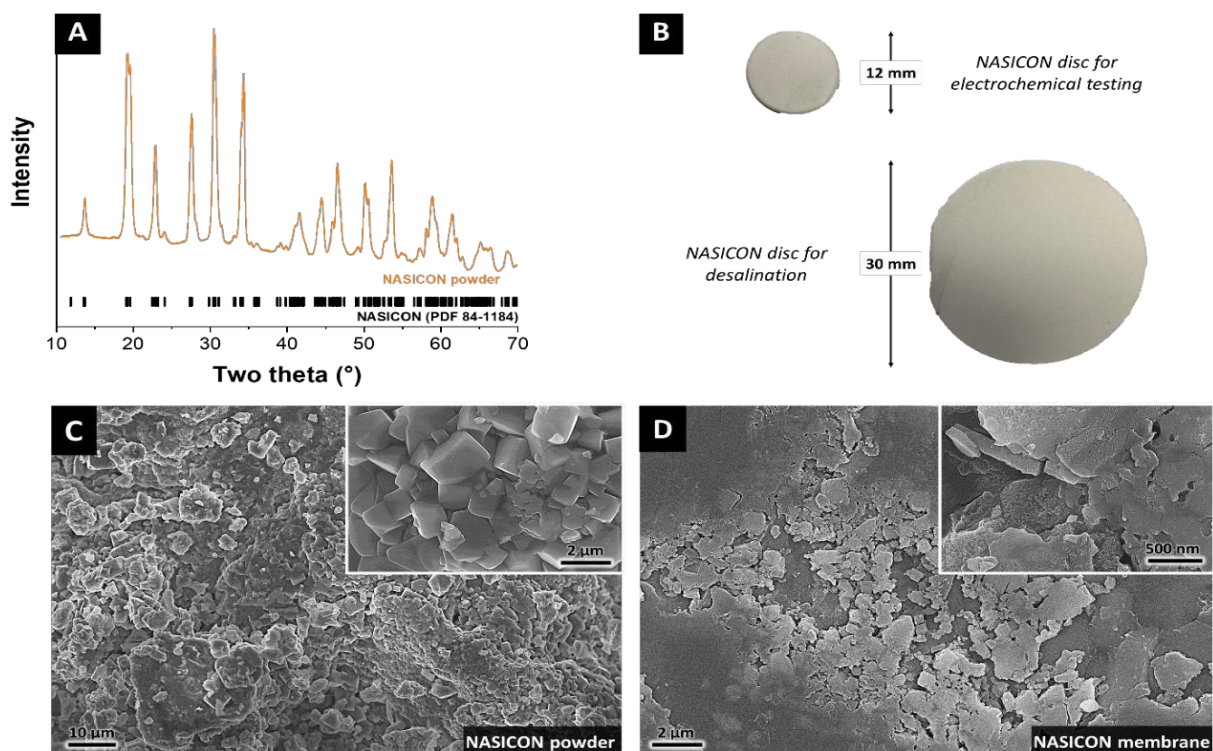
Figure S2: Material characterization of NASICON. (**A**) Diffractogram of the final NASICON powder, (**B**) photograph of NASICON discs for electrochemical characterization and desalination. (**C**) scanning electron micrographs of NASICON powder. (**D**) scanning electron micrographs of epoxy infiltrated NASICON membrane.

Supporting Electrochemical Characterization
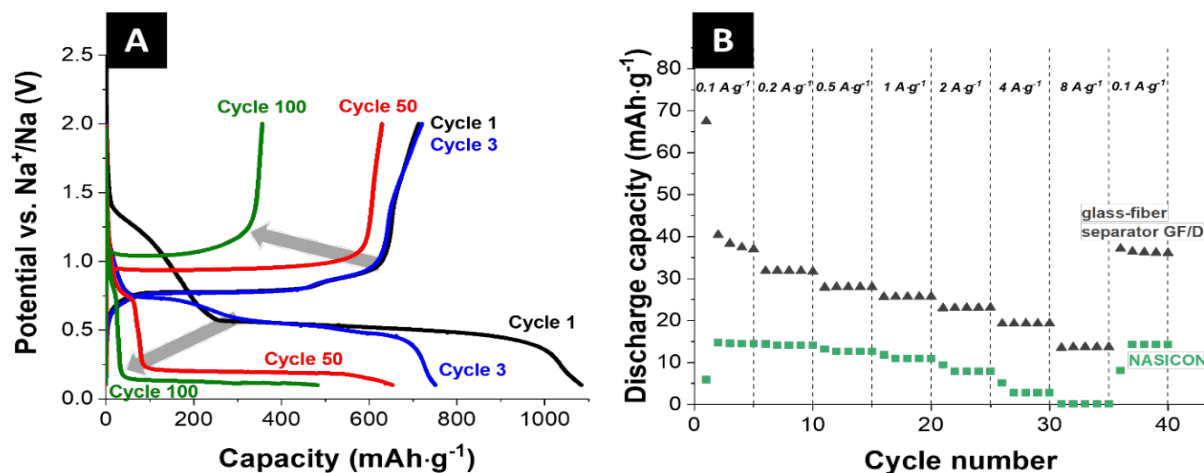
Figure S3: (**A**) Galvanostatic charge and discharge profiles of Sb/C electrode of the 1st, 3rd, 50th and 100th cycle at 200 mA·g^{-1} between 0.1 V and 2.0 V vs. Na$^+$. (**B**) Rate performance of the activated carbon cloth full-cell from galvanostatic charge/discharge cycling at different specific currents.
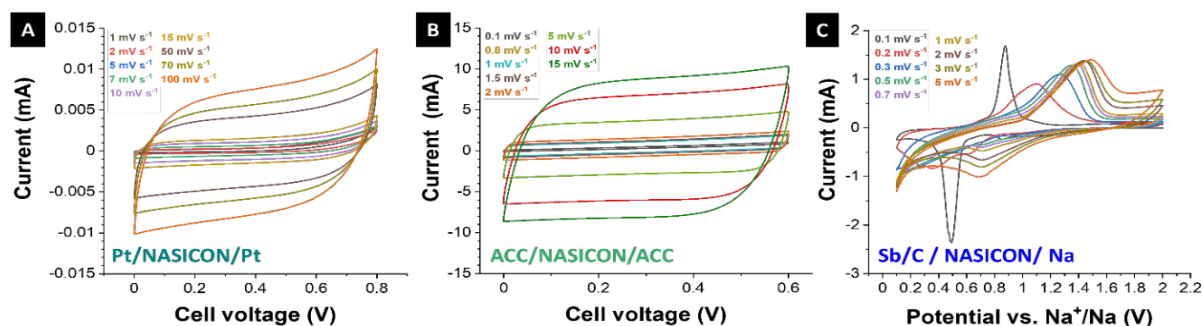
Figure S4: Cyclic voltammograms at different scan rates of (**A**) just the NASICON membrane contacted with platinum, (**B**) two activated carbon cloth electrodes separated by the NASICON membrane, and (**C**) Sb/C vs. Na separated by the NASICON membrane.

S5
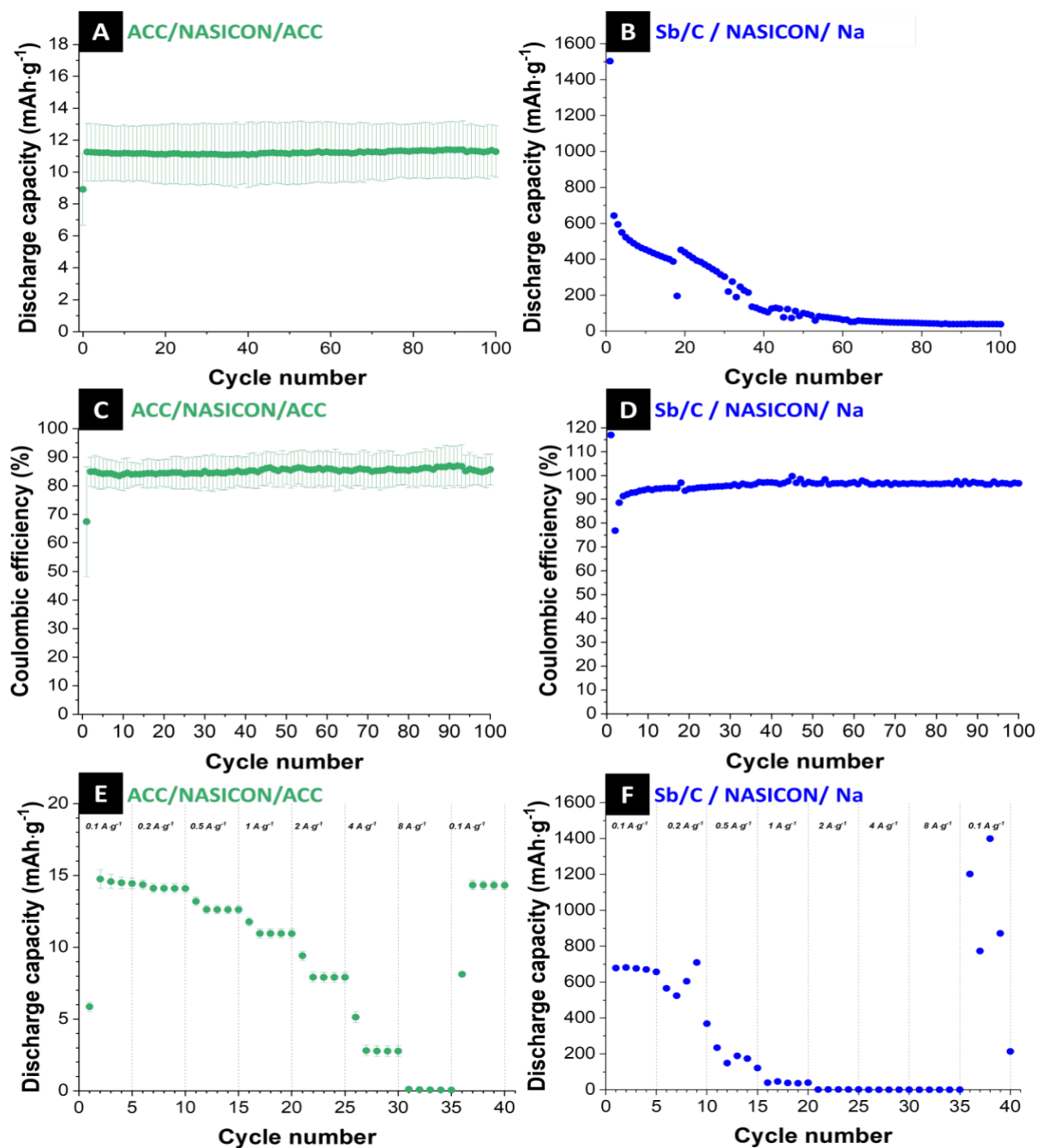
Figure S5: Electrochemical performance with NASICON as separator. (**A**) Electrochemical cycling stability at specific current of 200 mA g^{-1} of activated carbon cloth full-cell with NASICON membrane. (**B**) Electrochemical cycling stability at specific current of 200 mA g^{-1} of Sb/C vs. Na. (**C**) Coulombic efficiency at charging/discharging rates of the activated carbon cloth full-cell. (**D**) Coulombic efficiency of Sb/C electrode. (**E**) Rate performance of the activated carbon cloth full-cell from galvanostatic charge/discharge cycling at different specific currents. (**F**) Rate performance of the Sb/C electrode from galvanostatic charge/discharge cycling at different specific currents between 0.1-2.0 V vs. Na/Na$^+$.

Supporting References

1. A. Roy, M. Komatsu, K. Matsuishi and S. Onari, *Journal of Physics and Chemistry of Solids*, 1997, **58**, 741-747.
2. O. Degtyareva, V. V. Struzhkin and R. J. Hemley, *Solid State Communications*, 2007, **141**, 164-167.
3. M. L. Bansal and A. P. Roy, *Physical Review B*, 1986, **33**, 1526-1528.

4.7 Three-dimensional cobalt hydroxide hollow cube/vertical nanosheets with high desalination capacity and long-term performance stability

Yuecheng Xiong,[2,6§] Fei Yu,[1,§] Stefanie Arnold,[3,4] Lei Wang,[3,4] Volker Presser,[3,4,5]

Yifan Ren,[2,6] and Jie Ma[2,6,7*]

[1] College of Marine Ecology and Environment, Shanghai Ocean University, Shanghai 201306, P. R. China

[2] Research Center for Environmental Functional Materials, College of Environmental Science and Engineering, Tongji University, 1239 Siping Road, Shanghai 200092, P.R. China

[3] INM-Leibniz Institute for New Materials, 66123 Saarbrücken, Germany

[4] Department of Materials Science and Engineering, Saarland University, 66123 Saarbrücken, Germany

[5] Saarene-Saarland Center for Energy Materials and Sustainability, 66123 Saarbrücken, Germany

[6] State Key Laboratory of Pollution Control and Resource Reuse, College of Environmental Science and Engineering, Tongji University, Shanghai, 200092, P. R. China.

[7] Shanghai Institute of Pollution Control and Ecological Security, Shanghai, 200092, P.R. China

[§] These authors contributed equally to this work

Own Contribution:

Investigation, data curation, writing-review & editing.

Research
A SCIENCE PARTNER JOURNAL
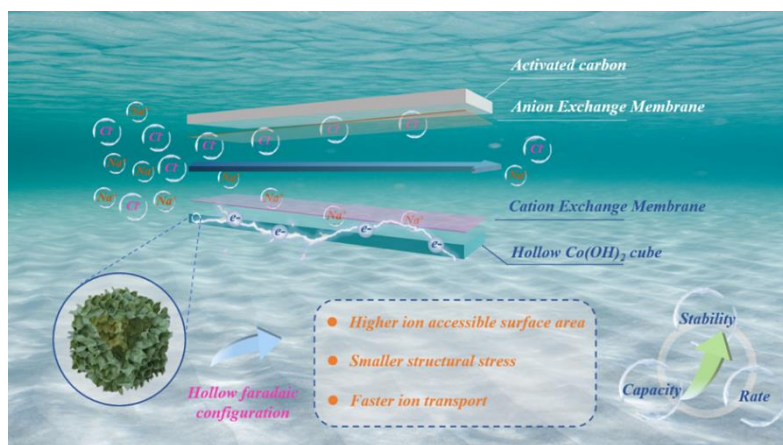
Research Article

Three-Dimensional Cobalt Hydroxide Hollow Cube/Vertical Nanosheets with High Desalination Capacity and Long-Term Performance Stability in Capacitive Deionization

Yuecheng Xiong [iD],[1,2] **Fei Yu,**[3] **Stefanie Arnold** [iD],[4,5] **Lei Wang** [iD],[4,5] **Volker Presser** [iD],[4,5,6] **Yifan Ren,**[1,2] **and Jie Ma** [iD][1,2,7]

[1]State Key Laboratory of Pollution Control and Resource Reuse, College of Environmental Science and Engineering, Tongji University, Shanghai 200092, China
[2]Research Center for Environmental Functional Materials, College of Environmental Science and Engineering, Tongji University, 1239 Siping Road, Shanghai 200092, China
[3]College of Marine Ecology and Environment, Shanghai Ocean University, Shanghai 201306, China
[4]INM-Leibniz Institute for New Materials, 66123 Saarbrücken, Germany
[5]Department of Materials Science and Engineering, Saarland University, 66123 Saarbrücken, Germany
[6]Saarene-Saarland Center for Energy Materials and Sustainability, 66123 Saarbrücken, Germany
[7]Shanghai Institute of Pollution Control and Ecological Security, Shanghai 200092, China

Correspondence should be addressed to Jie Ma; jma@tongji.edu.cn

Received 4 August 2021; Accepted 29 September 2021; Published 26 October 2021

Faradaic electrode materials have significantly improved the performance of membrane capacitive deionization, which offers an opportunity to produce freshwater from seawater or brackish water in an energy-efficient way. However, Faradaic materials hold the drawbacks of slow desalination rate due to the intrinsic low ion diffusion kinetics and inferior stability arising from the volume expansion during ion intercalation, impeding the engineering application of capacitive deionization. Herein, a pseudocapacitive material with hollow architecture was prepared *via* template-etching method, namely, cuboid cobalt hydroxide, with fast desalination rate ($3.3\,\mathrm{mg}$ $(\mathrm{NaCl}){\cdot}\mathrm{g}^{-1}$ ($\mathrm{h}\text{-}\mathrm{Co(OH)_2}){\cdot}\mathrm{min}^{-1}$ at $100\,\mathrm{mA}{\cdot}\mathrm{g}^{-1}$) and outstanding stability (90% capacity retention after 100 cycles). The hollow structure enables swift ion transport inside the material and keeps the electrode intact by alleviating the stress induced from volume expansion during the ion capture process, which is corroborated well by in situ electrochemical dilatometry and finite element simulation. Additionally, benefiting from the elimination of unreacted bulk material and vertical cobalt hydroxide nanosheets on the exterior surface, the synthesized material provides a high desalination capacity ($117 \pm 6\,\mathrm{mg}$ $(\mathrm{NaCl}){\cdot}\mathrm{g}^{-1}$ ($\mathrm{h}\text{-}\mathrm{Co(OH)_2}$) at $30\,\mathrm{mA}{\cdot}\mathrm{g}^{-1}$). This work provides a new strategy, constructing microscale hollow faradic configuration, to further boost the desalination performance of Faradaic materials.

1. Introduction

The recent two decades have witnessed soaring population growth, freshwater consumption, and global climate change, and ubiquitous pollution exacerbates freshwater deficiency [1, 2]. Therefore, scientists seek opportunities to produce usable water from inexhaustible seawater through desalination. Traditional desalination technologies, such as thermal distillation, reverse osmosis, and electrodialysis, exert heat, pressure, or electricity to extract water, which is highly energy-intensive [3]. Newly emerging processes, including capacitive deionization and membrane solar distillation, create less carbon footprint [4]. Capacitive deionization separates charged ions from saline media *via* electrosorption; the low applied cell voltage and high charge efficiency render this technique very promising regarding desalination of brackish water [5]. Distillation induced by concentrated solar radiation is intriguing because no external energy input is needed, but the freshwater production rate cannot meet large-scale production demand [6]. Therefore, capacitive deionization is attractive as an alternative energy-efficient desalination technique.

Electrodes are the core component of electrochemical desalination and ion separation. Typical electrodes can be divided into carbon electrodes and charge-transfer electrodes depending on the absence or presence of redox processes [7]. Ion intercalation or conversion reactions (charge-transfer materials) enable a much higher desalination capacity than possible for carbon-based electrodes because of the higher charge storage capacity and perm-selectivity; thereby, they enable facile desalination even at high molar strength. Currently, various charge-transfer materials for electrochemical desalination have been reported, such as transition metal oxides (MnO_2, TiO_2, V_2O_5, and $ZnFe_2O_4$) [8–11], Prussian blue analogs (nickel hexacyanoferrate) [12–14], polyanionic phosphates ($Na_3V_2(PO_4)_3$, $Na_3Ti_2(PO_4)_3$) [15–17], and two-dimensional materials (MXenes, MoS_2, and TiS_2) [18–22]. Among these materials, metal oxides or hydroxides hold the advantages of easy preparation, facile morphological manipulation, element diversity, and promising desalination performance. Yet, charge-transfer materials usually show a tradeoff between high capacity and good stability [23]. Theoretically, higher capacity means that more ions are removed, which generally causes more obvious volume changes. The performance degrades irreversibly if the material cannot relieve the accompanying stress [24]. For example, the lithiation of transition metal oxides (such as Fe_2O_3, Co_3O_4, and NiO) induces near 100% volume expansion in lithium-ion batteries, severely deteriorating the energy storage performance [25].

Stability is a vital characteristic of desalination electrodes. High stability means longer service life and more desalination cycles, which can decrease the cost of material and operation; meanwhile, less need for material signifies less solid waste produced, avoiding extra posttreatment costs. The chemical stability ensures that no toxic heavy metal ions (Mn^{2+}, V^{5+}, Co^{2+}, etc.) from electrode materials leach into treated water, which is key to safe water quality. Therefore, electrode materials with good stability and reliability are crucial for desalination application.

The critical importance of performance stability can be addressed by designing flexible three-dimensional scaffolds to support Faradaic materials. For example, interconnected carbon networks and polymer hydrogel serve as structural support and pathways for electron transport [26]. $Na_3V_2(PO_4)_3$/graphene hybrid aerogel exhibits a high capacity of about $100\,mg\cdot g^{-1}$ after 50 cycles in a dual-ion deionization system but inferior stability than pure aerogel [26]. ZIF-67/PPy hybrid materials display stable desalination performance with a capacity of $11\,mg\cdot g^{-1}$ for 200 h [27]. However, the conductive network's cushion effect cannot enhance the intrinsic stability of charge-transfer materials, and simultaneous high capacity and good stability cannot be realized because supporting materials usually have lower desalination performance. Therefore, regulating the microscale or nanoscale structure of the Faradaic electrode materials will offer opportunities to further enhance the deionization performance instead of focusing on carbon-faradaic composite materials.

Constructing a hollow structure with lightweight architecture for pseudocapacitive materials is an appealing tactic

to simultaneously achieve superior capacity and stability. A hollow configuration provides ample space for volume change, which has been widely applied in catalysis to strengthen the efficiency and cycling performance [28]. A hollow structure reduces the proportion of dead mass, which is the unreacted bulk of the material, thus improving the desalination capacity. Besides, hollow structures can ensure sufficient contact between electrode and electrolyte due to both inner and outer surfaces, providing more available active sites and enhancing the ion transport kinetics. An open graphene structure has been proposed for electrochemical desalination recently, but the inherent weakness of carbon materials restricts the performance [29]. Hollow charge-transfer electrode materials can break the tradeoff between high capacity and stable cycling, which is an appealing strategy to overcome shortcomings in capacitive deionization (low desalination capacity, low desalination rate, and poor stability) at a time.

Here, we synthesized a hollow transition hydroxide, cuboid cobalt hydroxide, with well-arranged nanosheets on its surface *via* template etching. $Co(OH)_2$ exhibits substantial pseudocapacitance, widely utilized in the energy storage field [30, 31]. Amorphous $Co(OH)_2$ nanocages or nanoboxes have also been used in batteries and catalytic water splitting, which employ similar electrochemical processes as electrochemical desalination [32, 33]. In our work, we show that cobalt hydroxide with optimized morphology provides a high desalination capacity of $117 \pm 6\,mg\ (NaCl)\cdot g^{-1}$ (h-$Co(OH)_2$) and a fast desalination rate of $3.3\,mg$ $(NaCl)\cdot g^{-1}$ (h-$Co(OH)_2$)$\cdot min^{-1}$. The cobalt hydroxide electrodes exhibit excellent stability without the coupling of three-dimensional supporting networks. This paper offers a new strategy to elevate the desalination rate and strengthen the stability through the hollow structure without sacrificing the high capacity of faradic electrodes, showing the promising application in large-scale CDI.

2. Materials and Methods

2.1. Preparation of the Cu_2O Template. All chemicals and reagents were purchased from Sinopharm Chemical Reagent Co., Ltd, and used without further purification. $CuCl_2\cdot2H_2O$ (10 mM, 100 mL) was heated in a 55°C water bath under magnetic stirring, and then, NaOH (2 M, 10 mL) was added slowly. The color of the solution changed from dusty aquamarine to dark brown. 30 min later, freshly prepared ascorbic acid (0.6 M, 10 mL) was added dropwise by a syringe, and the solution appeared brownish-black, turning into brick red in the end. After continuous agitation for 3 h, the Cu_2O template was separated by vacuum filtration and washed with deionized water and ethanol several times. The sample was acquired after 60°C of vacuum drying for 5 h.

2.2. Preparation of Hollow $Co(OH)_2$ Cube/Vertical Nanosheets. 100 mg Cu_2O powder was added into a mixed solution of 100 mL deionized water plus 100 mL ethanol, and the mixture was ultrasonicated for 1 h. The remaining steps were conducted under 500 rpm magnetic stirring. 6.6 g

polyvinylpyrrolidone K30 (PVP-K30) was added. After 30 min, 60 mg $CoCl_2 \cdot 6H_2O$ was added. Another 30 min later, $Na_2S_2O_3$ (1 M, 100 mL) was added dropwise by a peristaltic pump with a controlled rate of one drop per second. When the solution turned into jade green, the hollow cube cobalt hydroxide material was obtained after vacuum filtration, cleaning, and drying at 40°C overnight. Regarding our manuscript, we refer to hollow $Co(OH)_2$ cube as "h-$Co(OH)_2$."

2.3. Electrode Preparation. The active materials ($Co(OH)_2$ powder or activated carbon) were mixed with a conductive additive (acetylene black) and binder (polyvinylidene difluoride, PVDF) at a mass ratio of $8:1:1$. Afterward, 1-methyl-2-pyrrolidinone (NMP) was added appropriately, and the mixture was stirred overnight to form a homogeneous and viscous paste. Then, electrodes were prepared by the doctor-blade method on graphite paper with a thickness of ca. 75 μm. Next, prepared electrodes were dried at 40°C under vacuum for 12 h to remove any residual organic solvent. The electrode's mass was determined by the difference between pure graphite paper and dried electrode, and the electrode mass used for electrochemical desalination was about 4.0 mg.

2.4. Electrochemical Characterization. All electrochemical characterization, including cyclic voltammetry (CV), galvanostatic charging/discharging cycling (GCD), and electrochemical impedance spectroscopy (EIS), was conducted by the electrochemical station (CHI660D, Shanghai Chenhua Instruments Co.) in a three-electrode cell with 1 M NaCl as the electrolyte. Electrodes of $1 x 1$ cm^2 were used as the working electrode, while Pt and Ag/AgCl were employed as the counter electrode and reference electrode, respectively. Cyclic voltammetry was swept between -0.6 V and +0.6 V under various scan rates (1-50 mV$\cdot$s^{-1}), and GCD was tested under the same voltage window with different specific currents (0.1-2 A$\cdot$g^{-1}). The EIS spectra were recorded over the frequency range of 10^5 Hz to 10^{-2} Hz with an amplitude of 5 mV. Besides, CV and GCD were also carried out in a two-electrode cell with a working electrode and an oversized activated carbon powder (400 mesh, Macklin) electrode as the counter electrode in 1 M NaCl.

In situ electrochemical dilatometry was performed in an ECD-3 nanoelectrochemical dilatometer (EL-CELL) to track the volume changes during cyclic voltammetry by constructing a two-electrode cell (h-$Co(OH)_2$ versus carbon) with an oversized activated carbon (90 mass% YP-80F, 10 mass% polymer binder) as counter- and quasireference electrode in 1 M Na_2SO_4. All cell parts were dried overnight at 80°C and introduced into an argon-filled glovebox (MBraun Labmaster 130; O_2; $H_2O < 0.1$ ppm). h-$Co(OH)_2$ electrode was drop-casted on a Pt disc with a diameter of 10 mm, and the initial thickness was 65 μm. All electrochemical measurements were carried out at a climate chamber (Binder) with a constant temperature of 25 ± 1°C. Cyclic voltammetry (CV) measurements were carried out using a VMP3 multichannel potentiostat/galvanostat from Bio-Logic (France). After a resting period and stabilization time of 48 h or 72 h, cyclic

voltammograms were recorded at 1 mV s^{-1} in the range of -0.8 V to +0.3 V vs. carbon.

2.5. Electrochemical Desalination Performance. The flow-by capacitive deionization device consists of the following parts: acrylic plates, silicone gaskets, electrodes, cation/anion exchange membranes, and a chamber with the dimension of $2 \times 2 \times 1$ cm^3. The whole testing system is composed of a power source (LAND battery testing system), deionization apparatus, peristaltic pump, NaCl solution tank, and conductivity meter (Mettler Toledo S230). All deionization tests were done in constant current operation and batch mode. The NaCl solution volume was 25 mL, and the flow rate was fixed at 15 mL$\cdot$min^{-1}. Other parameters, including cutoff voltage (±0.6 V, ±0.8 V, ±1.0 V, ±1.2 V, ±1.4 V, and ±1.6 V), initial feed concentration (10 mM, 100 mM, and 600 mM), and specific current (30-100 A$\cdot$g^{-1}), were adjusted to acquire the optimized performance and investigate the desalination mechanism. The deionization capacity was calculated based on the relationship between conductivity and concentration and is presented in the following equation:

$$\text{Deionization capacity } Q = \frac{(C_i - C_f)V}{m} \left(\frac{\text{mg}_{\text{NaCl}}}{\text{g}_{\text{h-Co(OH)}_2}} \right), \quad (1)$$

where C_i and C_f (mg$\cdot$L^{-1}) are the concentration of NaCl before and after deionization, respectively; V (25 mL) is the volume of NaCl solution; and m (mg) is the total mass of $Co(OH)_2$ electrode containing conductive additive and binder.

2.6. Material Characterization. The formation process and surface morphology of hollow $Co(OH)_2$ were characterized by scanning electron microscopy (SEM, Hitachi S-4800) and transmission electron microscopy (TEM, JEOL-2010F). The crystal structure was analyzed using X-ray diffraction (XRD D8 ADVANCE, Bruker AXS) operated at 40 mA and 45 kV with Cu-Kα radiation ($\lambda = 0.154$ nm, 5°/min). X-ray photoelectron spectroscopy (XPS) analysis was carried out in a ThermoFisher ESCALAB 250Xi spectrometer using Al-Kα radiation (1486.6 eV) with a base pressure of 1×10^9 torr. The peak energies were calibrated by C1s peak at 284.8 eV. The wettability was reflected by the water contact angle (POWEREACH JC2000D2W). Raman spectra were recorded with a Renishaw inVia system using an Nd:YAG laser with an excitation wavelength of 532 nm. The spectral resolution was 1.2 cm^{-1}, and the diameter of the laser spot on the sample was around 2 μm with a total power exposure of 0.5 mW. The exposure time is 30 s with 5 accumulations. The numeric aperture was 0.75. The specific surface area and pore size distribution were calculated from the adsorption/desorption isotherms of N_2 at -196°C by the multipoint BET and BJH method using a BELSORP Max instrument (BEL), and the sample was degassed at 120°C for 6 h before the measurements. The 2D-NLDFT analysis was carried out with SAIEUS assuming finite pores with an aspect ratio of 6 and using a regularization parameter of 2.75.
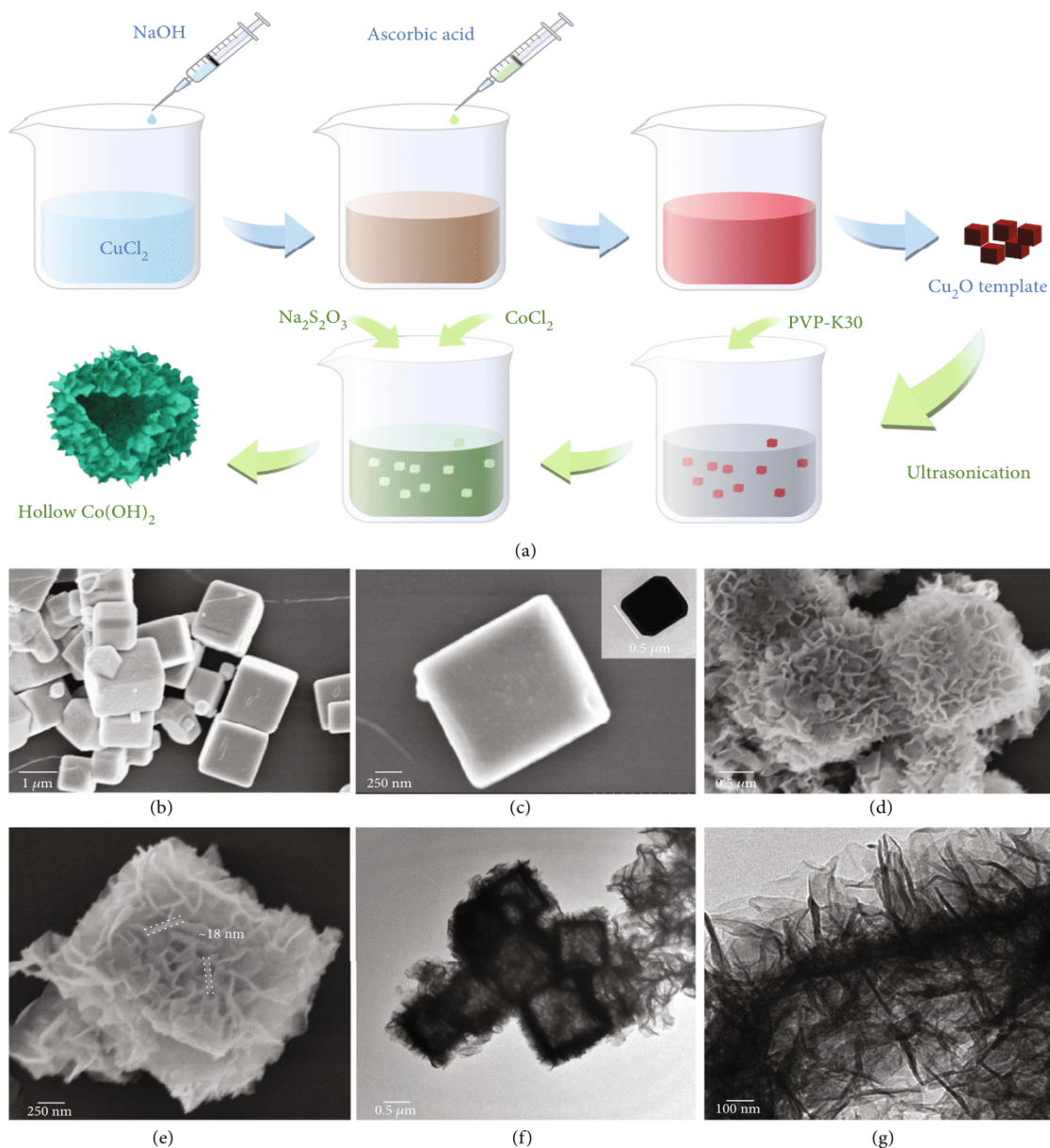
FIGURE 1: (a) Schematic illustration of the hollow $Co(OH)_2$ cube preparation. Scanning electron micrographs of the Cu_2O (b, c) (inset in (c) is the transmission electron micrograph of Cu_2O cube) and hollow $Co(OH)_2$ cube (d, e). Transmission electron micrographs of the hollow $Co(OH)_2$ cube (f, g).

3. Results and Discussion

3.1. Material Characterization. Hollow $Co(OH)_2$ cube was synthesized *via* classical coordination etching and precipitation process guided under Pearson's hard and soft acid-base principle [34, 35], with the schematic illustration shown in Figure 1(a).

First, the Cu_2O sacrificial template was prepared by precipitation and reduction reaction, exhibiting a cubic shape with a side length of 0.5 μm to 1 μm (Figure 1(b)), and the surface of the Cu_2O cube is relatively smooth (Figure 1(c)).

Afterward, $Na_2S_2O_3$ was used to etch the precursor and release OH^- to create an alkaline environment, whereby cobalt hydroxide was precipitated synchronously. The simultaneous etching and $Co(OH)_2$ growing process is verified by time-dependent TEM images (Supporting Information, Fig. S1). The appearance of cobalt hydroxide is cuboid with an apparent hollow structure (Figure 1(f)). Some individual cubes are broken, which exposes the interior surface and shortens the ion transport distance during electrochemical operation. Thin cobalt hydroxide nanosheet arrays with a thickness of around 18 nm extend from the

(a)

(b)

(c)

(d)
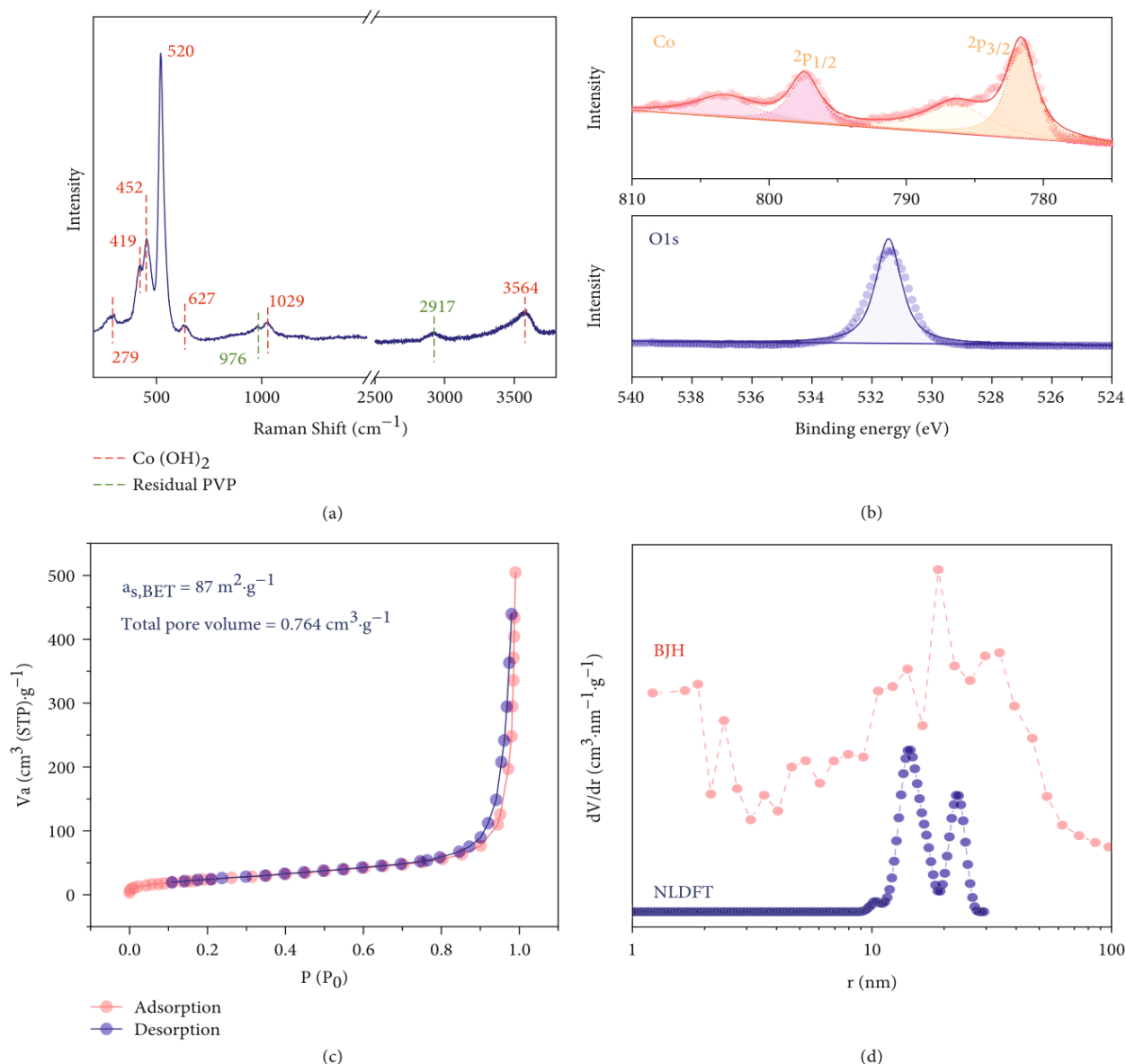
FIGURE 2: Characterization data of hollow $Co(OH)_2$ cubes: Raman spectrum (a), X-ray photoelectron spectra of Co 2p and O 1 s (b), N_2 adsorption/desorption isotherm measured at -196°C (c), and pore size distribution based on BJH and NLDFT models (d).

shell, providing abundant sites for ions to be reacted and stored (Figures 1(d), 1(e), and 1(g)).

The successful synthesis of cobalt hydroxide in the form of $Co(OH)_2$ was confirmed by Raman spectroscopy (Figure 2(a)). The peak at 279, 419, 452, 520, 1029, and 3564 cm^{-1} belongs to $Co(OH)_2$ [36, 37]; among them, the band at 520 cm^{-1} attributes to the $CoO(A_g)$ symmetric stretching mode; the bands at 452 cm^{-1} and 3564 cm^{-1} are assigned to the OCoO bending mode [37] and OH vibrational mode [38], respectively. The peak at 627 cm^{-1} corresponds to the F_{2g}^{2} of Co_3O_4 or belongs to $Co(OH)_2$ [39], while the bonds at 976 cm^{-1} and 2917 cm^{-1} possibly arise from the remaining PVP [40, 41]. Besides, none of the

characteristic reflections for CoO are found after 40°C vacuum drying. Based on the XPS results (Figure 2(b)), the prominent peak of Co $2p_{3/2}$ locates at around 781.5 eV with a satellite peak ca. 5 eV away. This spectral data verifies the existence of Co^{2+}, which is further corroborated by a single peak of O 1s spectra at approximately 531.4 eV. [42] Despite no subpeak for hydroxyls, the hydrophilicity of $Co(OH)_2$ electrode is verified by decreasing water contact angle with time. After desalination, a contact angle of 54.40° was measured (Supporting Information, Fig. S2).

N_2 adsorption/desorption isotherms show the type V curve, indicating no micropore but mesopore structure exists in h-$Co(OH)_2$, and a type H3 hysteresis loop suggests
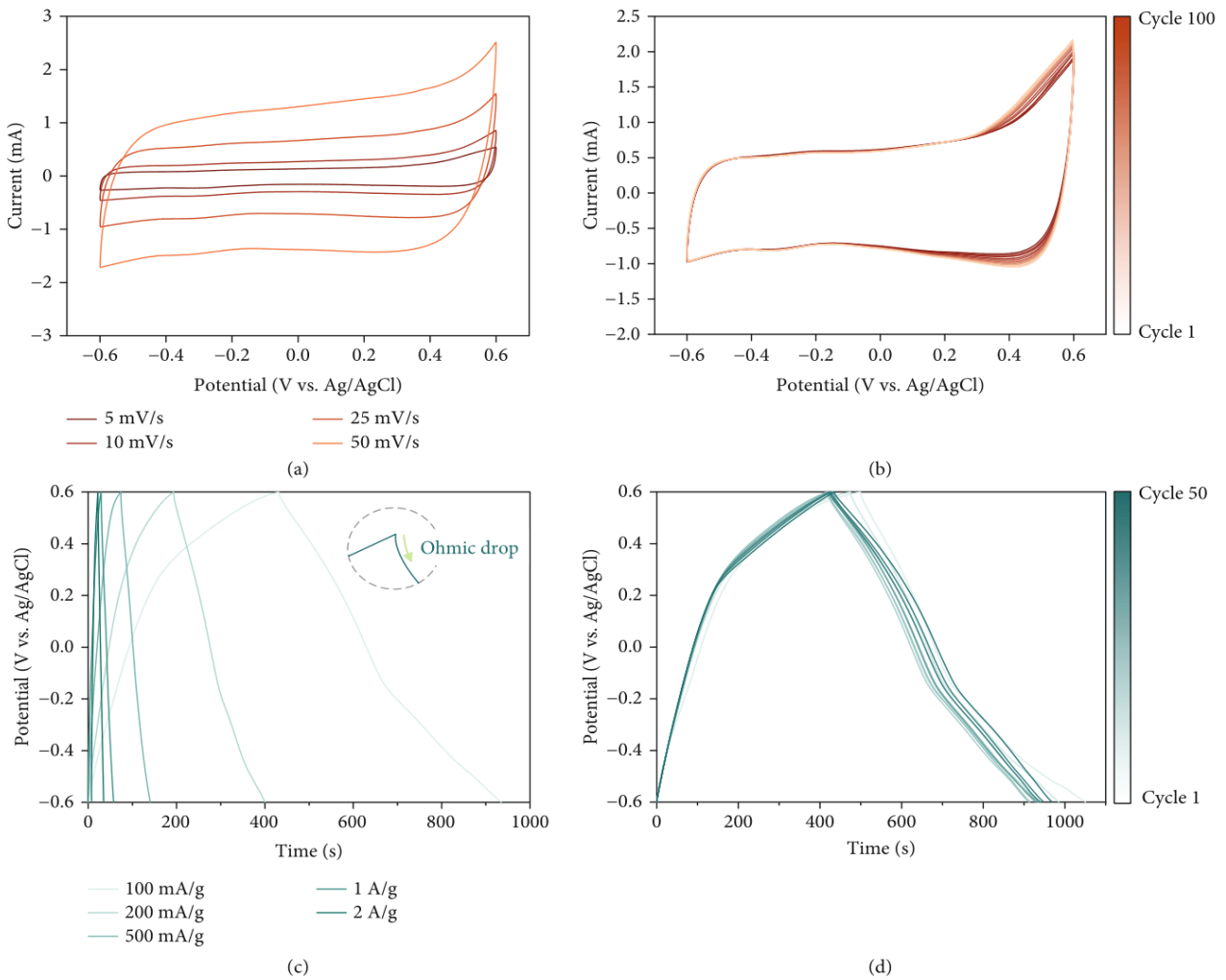
FIGURE 3: (a) Cyclic voltammograms of the hollow $Co(OH)_2$ cube at different scan rates. (b) 100 cyclic voltammetry cycling curves at $25\,mV\cdot s^{-1}$. (c) Galvanostatic charging/discharging profiles of the hollow $Co(OH)_2$ cube at different specific currents. (d) 50 galvanostatic charging/discharging cycling profiles at $100\,mA\cdot g^{-1}$.

slit pore geometry created by the stacking of flake particles (Figure 2(c)). The specific surface area of the $Co(OH)_2$ cube determined by the Brunauer-Emmett-Teller (BET) method is about $87\,m^2\cdot g^{-1}$, and the mean pore radius derived from the Barrett-Joyner-Halenda (BJH) and NLDFT (2D-NLDFT finite pores were assumed) models is about $20\,nm$. Such large mesopores are expected to yield sufficient space for ion transport pathways during electrochemical desalination (Figure 2(d)).

3.2. Electrochemical Performance.
The cyclic voltammogram of h-$Co(OH)_2$ presents a quasirectangular shape without observable redox peaks (Figure 3(a)). This specific shape indicates that h-$Co(OH)_2$ is a pseudocapacitive material like other transition metal oxides and hydroxides corroborated by GCD profiles without plateau (Figure 3(c)). A pair of shallow peaks at around $-0.3\,V$ and $-0.1\,V$ is evident at a rate of $1\,mV\cdot s^{-1}$ (Supporting Information, Fig. S3), which aligns with the pseu-

docapacitive property due to the small ΔV between redox peaks [43]. Besides, the thin-film electrode is prone to be pseudocapacitive as a result of free ion diffusion [44]. This aligns with the open (hollow) architecture and short diffusion paths within h-$Co(OH)_2$. The capacitance values calculated from different scan rates (5-$50\,mV\cdot s^{-1}$) are 32-$24\,F\cdot g^{-1}$. The slight loss of capacitance at a high scan rate demonstrates the rapid charge storage mechanism.

The h-$Co(OH)_2$ electrode shows very good performance stability, characterized by repeated cyclic voltammetry and galvanostatic charge/discharge cycling. The cyclic voltammograms' shapes display no significant change after 100 cycles except minor alteration at $+0.4\,V$ to $+0.6\,V$ (vs. Ag/AgCl). Hence, h-$Co(OH)_2$ might experience side reactions at a voltage beyond $+0.4\,V$ (Figure 3(b)). The performance from GCD profiles degrades slightly at first and returns to the original level, and the retention proportion for charging capacity is 97% after 50 cycles (Figure 3(d)).
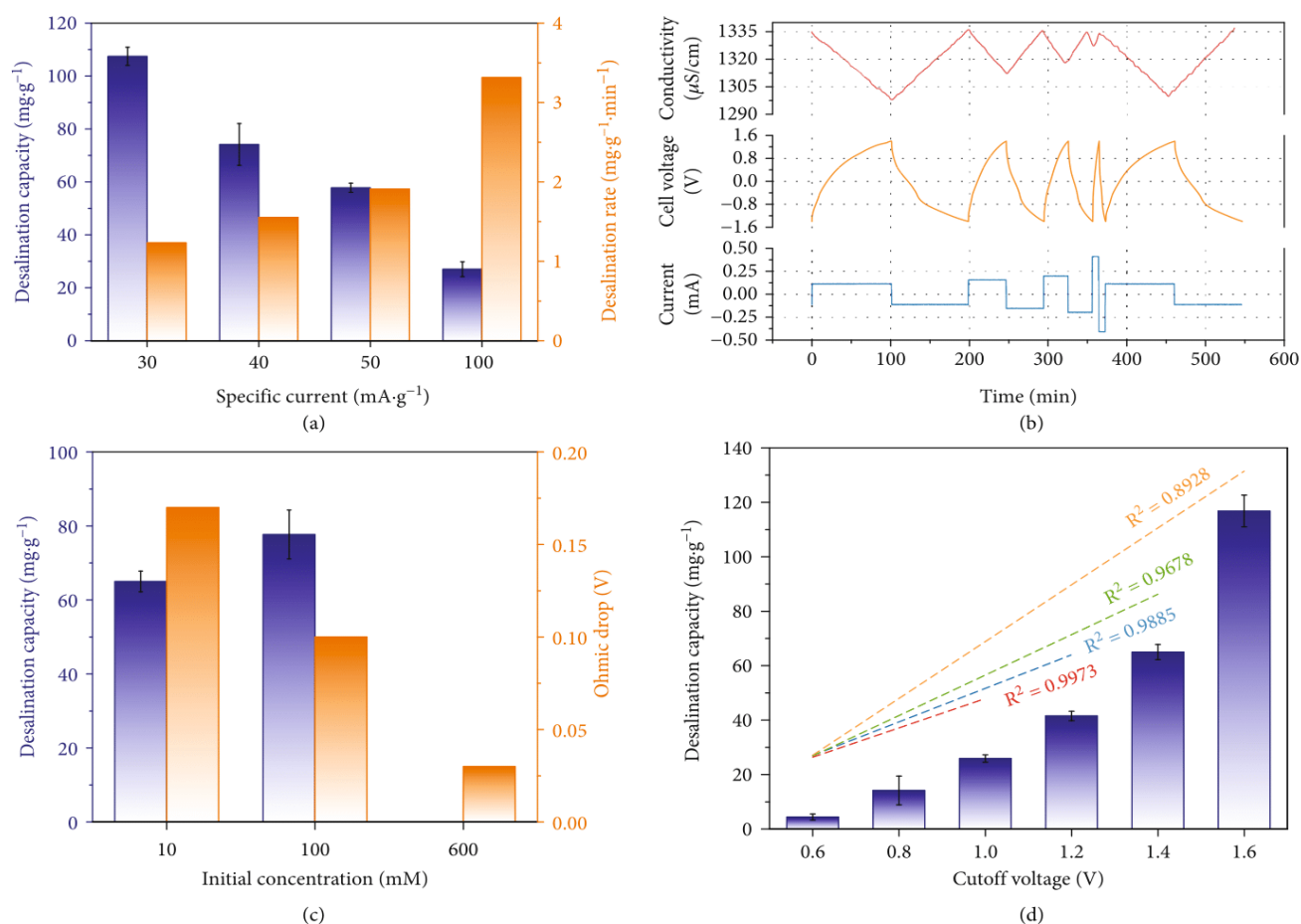
FIGURE 4: (a) Desalination capacity and desalination rate at different specific currents (initial NaCl concentration: 10 mM; cutoff voltage: ±1.4 V). (b) Recorded profiles of the conductivity, cell voltage, and current data at different rates (30/40/50/100/30 mA·g⁻¹). (c) Desalination capacity and ohmic drop at different initial NaCl concentrations (specific current: 30 mA·g⁻¹; cutoff voltage: ±1.4 V). (d) Desalination capacity with changing cutoff voltages and the correlation between capacity and cutoff voltage (initial concentration: 10 mM; specific current: 30 mA·g⁻¹).

To better predict the performance during deionization, we carried out experiments in a two-electrode configuration (Supporting Information, Fig. S4). The cyclic voltammograms show some broad redox peaks as the indicator of the valence change between Co^{2+} and Co^{3+}. The electrode polarization occurs when the cell voltage exceeds 0.8 V, which might be due to slight carbon oxidation and water hydrolysis. The charging capacity at different rates (40-1000 mA·g⁻¹) changes moderately from 35 mAh·g⁻¹ to 21 mAh·g⁻¹. This behavior is like what was observed during cyclic voltammetry. The h-Co(OH)₂ electrodes provide an excellent rate capability and stability, projecting to have relatively high deionization capacity and good durability, and the reaction equation of Na⁺ capture is stated as follows in Equations (2) and (3) [11, 31].

$$CoOOH + xe^- + xNa^+ \longrightarrow Co(OH)_2Na_x \qquad (2)$$

$$Co(OH)_2(OH)_x^- + xNa^+ \longrightarrow Co(OH)_2(OH)_xNa_x \qquad (3)$$
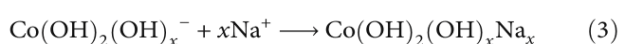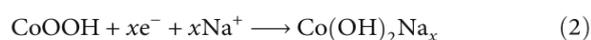
3.3. Desalination Performance. Hybrid capacitive deionization (HCDI) cell is applied to evaluate the desalination performance of h-Co(OH)₂ under various conditions, and this classical configuration adopts ion exchange membranes to strengthen the charge efficiency and oxygen penetration. The specific current is a vital operational parameter, especially for engineering practices, closely related to desalination efficiency and energy consumption. The desalination capacity is 107 ± 3 mg (NaCl)·g⁻¹ (h-Co(OH)₂) at a rate of 30 mA·g⁻¹, and the capacity declines as the specific current increases to 100 mA·g⁻¹ (Figure 4(a)). Higher values of the specific current result in a shorter charging time and greater diffusion limit, and fewer active sites are available, leading to lower capacity (Figure 4(b)). As the specific current returns to the original level, the capacity is mostly restored [45], as shown in Supporting Information, Fig. S5. A higher specific current translates to a faster charge transfer, resulting in a higher desalination rate, and this value is 3.3 mg·g⁻¹·min⁻¹ at 100 mA·g⁻¹, almost three times more than the rate at 30 mA·g⁻¹ (Figure 4(a)). The energy consumption increases

with a higher specific current, confirmed by lower charge efficiency, which drops to 93% at $100\,mA\cdot g^{-1}$ (Supporting Information, Fig. S6).

The NaCl concentration also affects the desalination capacity, increasing from $65 \pm 3\,mg\cdot g^{-1}$ to $78 \pm 7\,mg\cdot g^{-1}$ when the NaCl feedwater concentration increases from $10\,mM$ to $100\,mM$ (Figure 4(c) and Supporting Information, Fig. S7A). The positive effect of increasing NaCl concentration can be explained by declining ohmic drop, and this value derived from the voltage profile is $0.17\,V$, $0.1\,V$, and $0.03\,V$ for $10\,mM$, $100\,mM$, and $600\,mM$ NaCl, respectively (Figure 4(c)).

The desalination capacity increases from $4 \pm 1\,mg\cdot g^{-1}$ to $65 \pm 3\,mg\cdot g^{-1}$ when the voltage range expands from $-0.6\,V/+0.6\,V$ to $-1.4\,V/+1.4\,V$ (Figure 4(d) and Supporting Information, Fig. S7B). Broader voltage intervals correspond with prolonged charging times, as shown in Supporting Information, Fig. S8. Thus, more charge is accumulated at the electrode to participate in the desalination process. Some of the invested charge is consumed due to the internal cell resistance (intrinsic electrode resistance, electrode-solution contact resistance, and electrolyte resistance), and therefore, the capacity under $-0.6\,V/+0.6\,V$ is small. When the voltage is further widened to $-1.6\,V/+1.6\,V$, the desalination capacity reaches $117 \pm 6\,mg\cdot g^{-1}$. As shown in the CDI Ragone plot (known as Kim-Yoon plot; Supporting Information, Fig. S9), h-Co(OH)$_2$ shows better desalination performance than commercial Co(OH)$_2$ nanosheet, proving the positive effect of hollow configuration. Moreover, h-Co(OH)$_2$ presents higher capacity than pure Co(OH)$_2$ on graphite paper ($48\,mg\cdot g^{-1}$) and interconnected hollow graphene shell ($14\,mg\cdot g^{-1}$) proposed recently [29, 46].

A large effective surface area estimated to be around $179.8\,m^2\cdot g^{-1}$, over the value from N$_2$ adsorption, is required if all Na$^+$ is adsorbed at the external surface of h-Co(OH)$_2$ [47]. This rough deduction indicates that the subsurface also participates in deionization, underscoring the pseudocapacitive property. The relationship between average capacity and cutoff voltage is matched well by linear regression (Figure 4(d)), while the linear fit yields a larger deviation from the linear correlation at higher voltages as Faradaic side reactions intensify at $1.6\,V$ [48].

Furthermore, 100 desalination cycles were carried out to characterize the performance stability of h-Co(OH)$_2$ electrodes. The average desalination capacity is about $70\,mg\cdot g^{-1}$, with a retention of 92% (Figure 5(a)). Compared with other carbon-metal composite electrodes, h-Co(OH)$_2$ exhibits a high capacity and good stability simultaneously (Figure 5(b)). Besides, the desalination rate of h-Co(OH)$_2$ electrode is comparable to or even higher than advanced Faradic materials proposed recently (Supporting Information, Table S1). Subsequently, the electrochemical properties were also characterized after desalination. Cyclic voltammograms and galvanostatic charge/discharge profiles after desalination at different cutoff voltages and specific currents are analogous to raw electrodes except for minor peak alteration at around $-0.3\,V$. Electrochemical impedance spectra exhibit similar internal ohmic resistance and charge-transfer resistance (Supporting Information,

Fig. S10). The electrodes, after desalination at different rates, display slightly higher capacitance and smaller charge-transfer resistance. Therefore, h-Co(OH)$_2$ electrodes demonstrate good electrochemical stability. Apart from Na$^+$ removal, h-Co(OH)$_2$ is possible to intercalate Cl$^-$ by applying h-Co(OH)$_2$ as an anode, supported by its higher chlorine ion removal capacity compared with activated carbon (Supporting Information, Fig. S11-S15).

The stability of h-Co(OH)$_2$ electrodes is further illustrated by in situ electrochemical dilatometry, an indicator of volume change during sodiation/desodiation process and applied in two-dimensional Ti$_3$C$_2$-type MXene, and the schematic illustration of a dilatometer is presented in Supporting Information, Fig. S16 [27, 54, 55]. To match the voltage window vs. Ag/AgCl, the voltage range was set as $-0.8\,V$ to $+0.3\,V$ (vs. carbon), and $1\,M$ Na$_2$SO$_4$ electrolyte was used to avoid chlorine-related corrosion of the apparatus. Before testing, the cell was stabilized for $48\,h$, and over 80% of the electrode displacement occurs at the initial $4\,h$ (1st to 7th cycle), following the decay trend displayed in long-cycle desalination (Figure 5(c)). The drop in the displacement may align with the partial disintegration of hollow Co(OH)$_2$ cubes. The displacement remains almost unchanged afterward, suggesting that the h-Co(OH)$_2$ electrode has minimal volume change during salination/-desalination. Figure 5(d) displays cyclic voltammograms, which were recorded during the in situ dilatometry. The shape of the cyclic voltammogram of the h-Co(OH)$_2$ electrodes closely matched with what was recorded in a typical standard three-electrode test cell. All obtained electrochemical features are similar to those of the cyclic voltammetry results presented before, even though the current is comparably low in the dilatometry cell. Their shape remains stable after the third cycle. Correspondingly, the relative strain becomes negligible (the original data of relative strain is presented in Supporting Information, Fig. S17A), demonstrating that the hollow structure relieves the stress from volume change appropriately. To exclude the influence of the stabilization period, the system was tested after stabilizing for $72\,h$. The relative strain tends to be stable, and the relative strain becomes zero after the 10th cycle (Supporting Information, Fig. S17B). Therefore, electrochemical dilatometry proves that the hollow h-Co(OH)$_2$ structure can relieve the electrode volume change to enhance the stability after the desalination has reached equilibrium.

3.4. Desalination Mechanism. The intrinsic pseudocapacitance provides maximum synergy with the fast ion transport *via* the porous 3D architecture of the hollow Co(OH)$_2$ cubes. These beneficial electrochemical properties result in a high desalination capacity and good stability. A kinetic analysis can further investigate the charge storage and ion removal kinetics. Specifically, one can derive key information via analysis of the dependency of the measured current with the sweep rate [56], stated in equations (4) and (5).

$$i = av^b, \tag{4}$$

$$\log(i) = b\log(v) + \log(a). \tag{5}$$
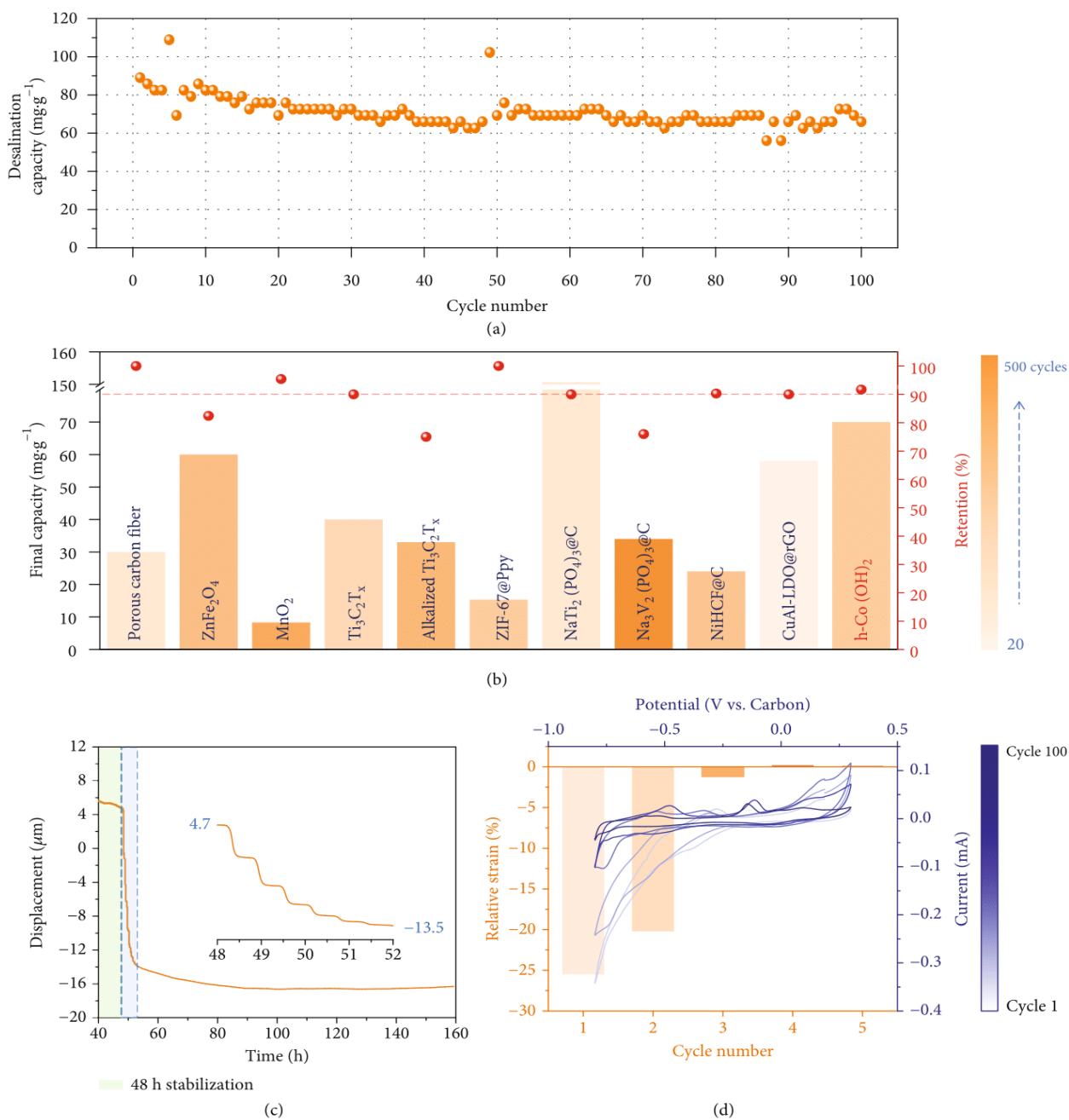
FIGURE 5: (a) Desalination capacity of HCDI cell for 100 cycles (specific current: 30 mA·g⁻¹; cutoff voltage: ±1.2 V; initial NaCl concentration: 10 mM). (b) Stability comparison of various electrode materials considering final capacity, retention rate, and cycle number (a different color represents the cycle number) [11, 16, 17, 27, 47, 49–53]. (c) h-Co(OH)$_2$ electrode displacement development during in situ electrochemical dilatometry in CV mode, and the inset is the magnified diagram for the initial 4 h. (d) Cyclic voltammograms and relative strain at the 1st, 3rd, 10th, 50th, and 100th cycle.

The b-value can be determined from the plot's slope between log (i) and log (v) and indicates the charge storage mechanism. When the b-value is 0.5, we have a system limited by diffusion, as typically found for battery-like systems via ion intercalation. In contrast, a b-value of 1.0 is found for an ideal capacitor, such as an electrical double-layer capacitor, where charge storage is enabled via ion electrosorption. According to Figure 6(a), the calculated b-values exceed 0.8 when the voltage is lower than 0.3 V. This very high value aligns with the pronounced pseudocapacitive
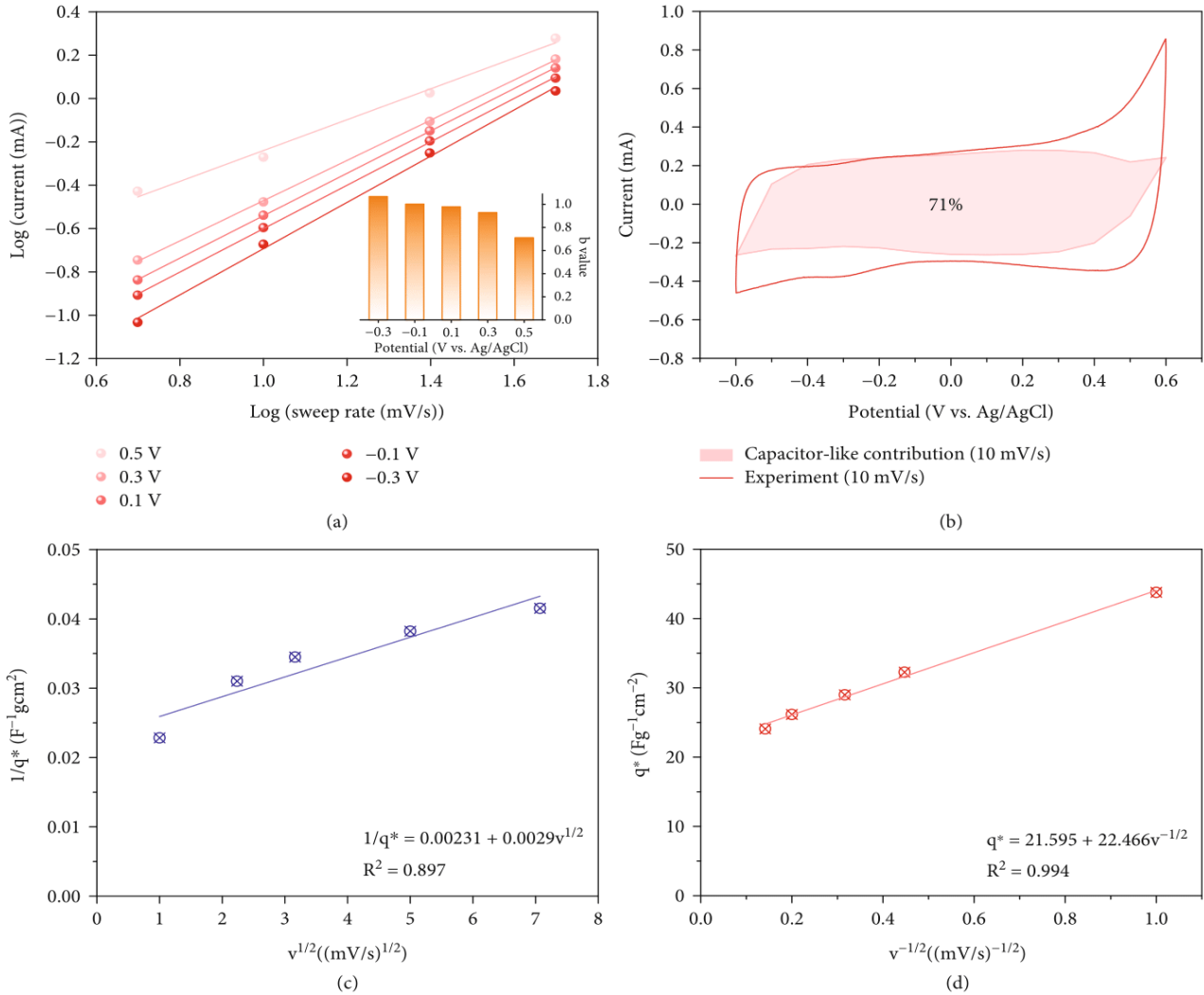
FIGURE 6: (a) Calculation of b-values based on CV curves. (b) Estimation of pseudocapacitive contribution of the cyclic voltammogram at $10\,\text{mV}\cdot\text{s}^{-1}$. (c) The relationship between $1/q^*$ and $v^{1/2}$. (d) The relationship between q^* and $v^{-1/2}$.

behavior of the electrode material. The b-value drops to about 0.7 at 0.5 V, which agrees with the more battery-like process through Na$^+$ intercalation and side reactions. This also aligns with the findings from the performance stability measurements via continued cyclic voltammetric testing.

It is also possible to quantify the percentage of surface-controlled capacitance (capacitor-like contribution) corresponding with either a perfect diffusion-limited system (b-value of 0.5) or a perfect capacitor (b-value of 1.0). The closer it is to one, the more perfect is the pseudocapacitive response. A beneficial calculation for this consideration is the use of Equation (6) which is often referred to as Dunn analysis [44]:

$$i(V) = k_1 v + k_2 v^{1/2}. \qquad (6)$$

In this equation, k_1 corresponds with an ideal (pseudo)-capacitive contribution and k_2 with a battery-like feature.

For our electrode material, k_1 represents 71% of the total capacity at the scan rate of $10\,\text{mV}\cdot\text{s}^{-1}$ (Figure 6(b)). As a comparison, this percentage for a recently reported black phosphorus composite is 59% at $5\,\text{mV}\cdot\text{s}^{-1}$ [57].

An alternative analysis is the Trasatti method. This approach differentiates an "inner" and "outer" surface-controlled capacity of h-Co(OH)$_2$ electrode [58]. To be specific, "inner" surface refers to the regions of difficult accessibility, and "outer" capacity mainly comes from the surface exposed directly to ions. The calculation is based on Equations (7) and (8) [44].

$$q^* = q_{s,out} + A_1 v^{-1/2}, \qquad (7)$$

$$q^{*-1} = q_s^{-1} + A_2 v^{1/2}. \qquad (8)$$

where q^* is the voltammetric charge, q_s is the surface-controlled capacity, and $q_{s,out}$ is the "outer" capacity. $q_{s,out}$
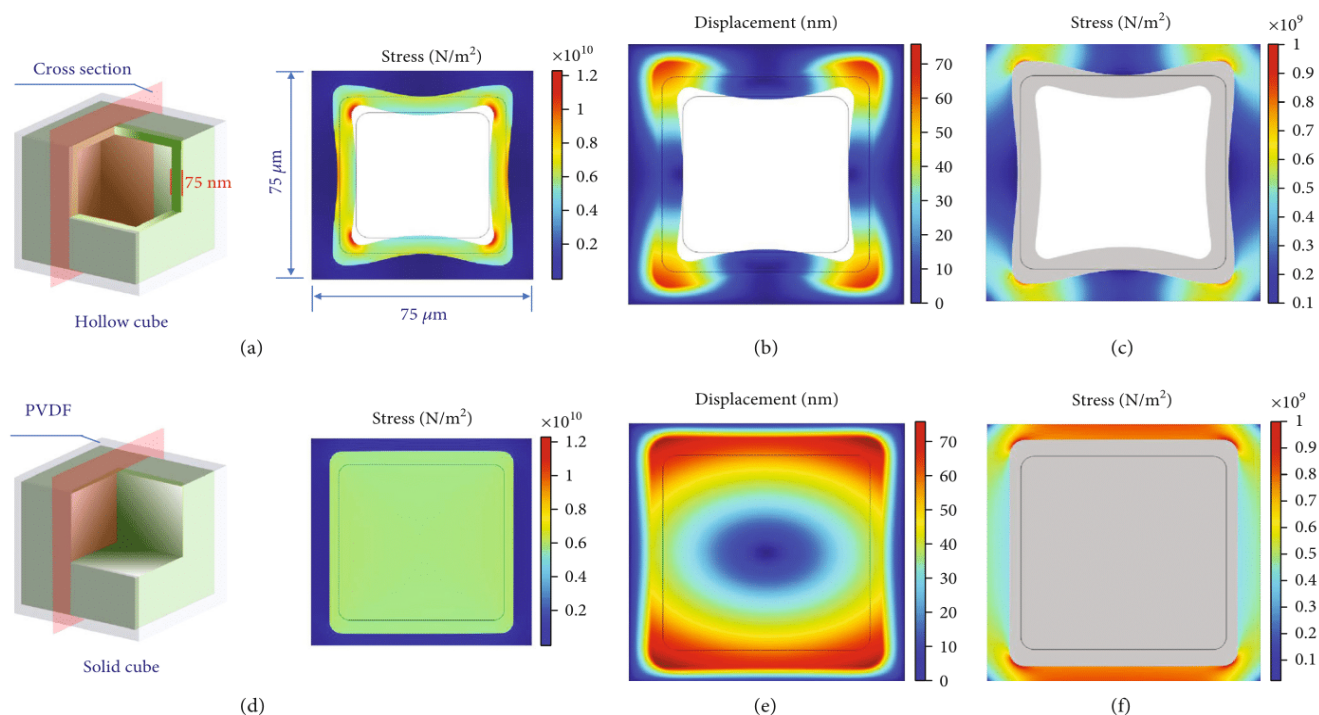
FIGURE 7: Finite element simulation results of stress and deformation displacement distribution in a hollow cube (a, b) and solid cube (d, e) at a fixed volume expansion percentage. Finite element simulation results of stress distribution in surrounding adhesive PVDF of a hollow cube (c) and solid cube (f).

is calculated to be $22 \, F \cdot g^{-1} \cdot cm^{-2}$, constituting 50% of q_s, which is comparable to modified carbon electrodes [59] and notably higher than CuAl-LDH@rGO [53]. This indicates that hollow $Co(OH)_2$ electrode provides rapid, capacitor-like charge transfer and ion removal (Figures 6(c) and 6(d)).

To further elaborate the cushion effect of hollow config-uration during ion intercalation, finite element simulation was carried out to investigate and compare the stress distri-bution in hollow and solid cubes after volume expansion; detailed simulation information is given in Supporting Information, Text S1). Finite element simulation is applied to analyze the ion concentration distribution during desalination and to demonstrate that a hollow structure is favorable for ion transport [60, 61]. Based on in situ dila-tometry, the expansion proportion is fixed at 40% for both structures. For a solid cube, the stress inside the materials is homogeneous at about $0.6 \times 10^{10} \, N/m^2$ after electrochem-ical volume expansion (Figure 7(d)), while the stress in a hollow cube is heterogeneous. Edges (especially top and bot-tom edges) of the two-dimensional hollow cross section gen-erally display more minor stress at around $0.4 \times 10^{10} \, N/m^2$. More significant stress ($1 \times 10^{10} \, N/m^2$) occurs at the corner (Figure 7(a)) due to stress from adjacent edges and induced shear stress during Na^+ intercalation. During expansion, the physical deformation of materials is expressed as displace-ment, that is, bias relative to the initial position. The displacement in a hollow cube is generally smaller, and the maximum value is approximately 60 nm (Figure 7(b)). Contrarily, half of the solid cube experiences remarkable

displacement with the maximum deformation of 70 nm (Figure 7(e)). Therefore, the hollow structure is more stable as it undergoes less distortion and stress when charging, except for higher stress at the corner.

The stress distribution of wrapped binder PVDF is stud-ied to reflect the complete working condition of the elec-trode. The PVDF around the hollow cube exhibits stress at a scale of $0.2 \times 10^9 \, N/m^2$ (Figure 7(c)), which is generally smaller than the solid cube counterpart ($0.9 \times 10^9 \, N/m^2$ at top and bottom edges; Figure 7(f)). The hollow structure exerts minor stress to surrounding binder material, condu-cive to keep the whole electrode intact during electrochemi-cal ion intercalation by relieving the accompanying stress.

4. Conclusions

In summary, a hollow pseudocapacitive cobalt hydroxide was prepared via facile synthesis conditions. The hollow $Co(OH)_2$ cube with vertical nanosheets anchored on the sur-face has a large ion accessible surface area based on electro-chemical analyses, ensuring fast ion transport. Meanwhile, this configuration can relieve the pressure during ion inter-calation to enhance the cyclability, proved by finite element simulation. Consequently, h-$Co(OH)_2$ electrode displays a high desalination rate of $3.3 \, mg \, (NaCl) \cdot g^{-1} \, (h-Co(OH)_2) \cdot min^{-1}$ at $100 \, mA \cdot g^{-1}$ and sustains over 90% of the initial capacity after 100 desalination cycles in HCDI cell. More-over, this hollow electrode holds high capacity intrinsically by avoiding "dead mass," with the maximum value of

117 ± 6 mg $(NaCl) \cdot g^{-1}$ (h-$Co(OH)_2$). The outstanding desalination performance of the hollow structure in the micro-scale navigates a new direction to the development of Faradaic electrodes for CDI.

Data Availability

The .txt or .jpeg data used to support the findings of this study are available from the corresponding author upon request.

Conflicts of Interest

The authors declare that there are no conflicts of interest regarding the publication of this article.

Authors' Contributions

Yuecheng Xiong and Fei Yu contributed equally to this work.

Acknowledgments

Supplementary Materials

Fig. S1: transmission electron micrographs of Cu_2O template etching and $Co(OH)_2$ crystal growth process. Fig. S2: water contact angle of the cobalt hydroxide electrode before (A) and after (B) desalination. Fig. S3: cyclic voltammogram of the cobalt hydroxide electrode at a rate of 1 mV·s-1. Fig. S4: (A) cyclic voltammograms of the cobalt hydroxide electrode at a rate of 10 mV·s-1 using a two electrode setup with an oversized AC electrode as counter electrode. (B) Cyclic voltammograms with different cutoff voltages. (C) Charging capacity of $Co(OH)_2$ electrode in two electrode system with changing specific current. Fig. S5: desalination capacity (A), cell voltage profiles, (B) and current profiles (C) of the HCDI cell at different specific current. Fig. S6: energy consumption (A) and charge efficiency (B) at different rates. Fig. S7: (A) desalination capacity at 100 mM initial NaCl concentration. (B) Desalination capacity of HCDI cell at different cutoff voltages. Fig. S8: voltage profiles of HCDI cell at different cutoff voltages. Fig. S9: Kim-Yoon plot of h-$Co(OH)_2$ electrode in HCDI cell. Fig. S10: electrochemical characterizations for h-$Co(OH)_2$ electrodes after desalination. Fig. S11: CV curves and capacitance of h-$Co(OH)2$ electrode at different voltage windows. Fig. S12: de-chlorination performance. Fig. S13: (A) desalination capacity of symmetric CDI cell for 100 cycles. (B) Theoretical de-chlorination capacity of asymmetric and symmetric CDI cells for 100 cycles. Fig. S14: cell voltage (A) and current profiles (B) of asymmetric cell for 100 cycles. Fig. S15: cell voltage (A) and current profiles (B) of symmetric CDI cell for 100 cycles. Fig. S16: schematic drawing of the in-situ elec-trochemical dilatometry cell. Fig. S17: (A) the original data of relative strain during electro-dilatometry in CV mode. (B) The relative strain change in the test after 72 h stabilization. Table S1: comparison of desalination rate of various advanced electrode materials. Text S1: finite element simulation. *(Supplementary Materials)*

References

[1] M. Elimelech and W. A. Phillip, "The future of seawater desalination: energy, technology, and the environment," *Science*, vol. 333, no. 6043, pp. 712–717, 2011.

[2] R. P. Schwarzenbach, B. I. Escher, K. Fenner et al., "The challenge of micropollutants in aquatic systems," *Science*, vol. 313, no. 5790, pp. 1072–1077, 2006.

[3] F. A. AlMarzooqi, A. A. Al Ghaferi, I. Saadat, and N. Hilal, "Application of capacitive deionisation in water desalination: a review," *Desalination*, vol. 342, pp. 3–15, 2014.

[4] M. Metzger, M. M. Besli, S. Kuppan et al., "Techno-economic analysis of capacitive and intercalative water deionization," *Energy & Environmental Science*, vol. 13, no. 6, pp. 1544–1560, 2020.

[5] S. Porada, R. Zhao, A. van der Wal, V. Presser, and P. M. Biesheuvel, "Review on the science and technology of water desalination by capacitive deionization," *Progress in Materials Science*, vol. 58, no. 8, pp. 1388–1442, 2013.

[6] X. Zhou, F. Zhao, Y. Guo, Y. Zhang, and G. Yu, "A hydrogel-based antifouling solar evaporator for highly efficient water desalination," *Energy & Environmental Science*, vol. 11, no. 8, pp. 1985–1992, 2018.

[7] P. Srimuk, X. Su, J. Yoon, D. Aurbach, and V. Presser, "Charge-transfer materials for electrochemical water desalination, ion separation and the recovery of elements," *Nature Reviews Materials*, vol. 5, no. 7, pp. 517–538, 2020.

[8] B. W. Byles, D. A. Cullen, K. L. More, and E. Pomerantseva, "Tunnel structured manganese oxide nanowires as redox active electrodes for hybrid capacitive deionization," *Nano Energy*, vol. 44, pp. 476–488, 2018.

[9] M. Liang, X. Bai, F. Yu, and J. Ma, "A confinement strategy to in-situ prepare a peanut-like N-doped, C-wrapped TiO_2 electrode with an enhanced desalination capacity and rate for capacitive deionization," *Nano Research*, vol. 14, no. 3, pp. 684–691, 2021.

[10] J. Lee, P. Srimuk, K. Aristizabal et al., "Pseudocapacitive desalination of brackish water and seawater with vanadium-pentoxide-decorated multiwalled carbon nanotubes," *ChemSusChem*, vol. 10, no. 18, pp. 3611–3623, 2017.

[11] J. Ma, Y. Xiong, X. Dai, and F. Yu, "Zinc spinel ferrite nanoparticles as a pseudocapacitive electrode with ultrahigh desalination capacity and long-term stability," *Environmental Science & Technology Letters*, vol. 7, no. 2, pp. 118–125, 2020.

[12] Z. Ding, X. Xu, Y. Li, K. Wang, T. Lu, and L. Pan, "Significantly improved stability of hybrid capacitive deionization using nickel hexacyanoferrate/reduced graphene oxide cathode at low voltage operation," *Desalination*, vol. 468, article 114078, 2019.

[13] S. Porada, A. Shrivastava, P. Bukowska, P. M. Biesheuvel, and K. C. Smith, "Nickel hexacyanoferrate electrodes for continuous cation intercalation desalination of brackish water," *Electrochimica Acta*, vol. 255, pp. 369–378, 2017.

[14] K. Singh, Z. Qian, P. M. Biesheuvel, H. Zuilhof, S. Porada, and L. C. P. M. de Smet, "Nickel hexacyanoferrate electrodes for

high mono/divalent ion-selectivity in capacitive deionization," *Desalination*, vol. 481, article 114346, 2020.

[15] J. Cao, Y. Wang, L. Wang, F. Yu, and J. Ma, "Na$_3$V$_2$(PO$_4$)$_3$@C as faradaic electrodes in capacitive deionization for high-performance desalination," *Nano Letters*, vol. 19, no. 2, pp. 823–828, 2019.

[16] W. Zhao, L. Guo, M. Ding, Y. Huang, and H. Y. Yang, "Ultra-high-desalination-capacity dual-ion electrochemical deionization device based on Na$_3$V$_2$(PO$_4$)$_3$@C-AgCl electrodes," *ACS Applied Materials & Interfaces*, vol. 10, no. 47, pp. 40540–40548, 2018.

[17] K. Wang, Y. Liu, Z. Ding, Y. Li, T. Lu, and L. Pan, "Metal-organic-frameworks-derived NaTi$_2$(PO$_4$)$_3$/carbon composites for efficient hybrid capacitive deionization," *Journal of Materials Chemistry A*, vol. 7, no. 19, pp. 12126–12133, 2019.

[18] P. Srimuk, F. Kaasik, B. Krüner et al., "MXene as a novel intercalation-type pseudocapacitive cathode and anode for capacitive deionization," *Journal of Materials Chemistry A*, vol. 4, no. 47, pp. 18265–18271, 2016.

[19] W. Bao, X. Tang, X. Guo et al., "Porous cryo-dried MXene for efficient capacitive deionization," *Joule*, vol. 2, no. 4, pp. 778–787, 2018.

[20] F. Xing, T. Li, J. Li, H. Zhu, N. Wang, and X. Cao, "Chemically exfoliated MoS$_2$ for capacitive deionization of saline water," *Nano Energy*, vol. 31, pp. 590–595, 2017.

[21] P. Srimuk, J. Lee, A. Tolosa, C. Kim, M. Aslan, and V. Presser, "Titanium disulfide: a promising low-dimensional electrode material for sodium ion intercalation for seawater desalination," *Chemistry of Materials*, vol. 29, no. 23, pp. 9964–9973, 2017.

[22] P. Srimuk, J. Lee, S. Fleischmann et al., "Faradaic deionization of brackish and sea water via pseudocapacitive cation and anion intercalation into few-layered molybdenum disulfide," *Journal of Materials Chemistry A*, vol. 5, no. 30, pp. 15640–15649, 2017.

[23] W. Shi, X. Liu, T. Deng et al., "Enabling superior sodium capture for efficient water desalination by a tubular polyaniline decorated with Prussian blue nanocrystals," *Advanced Materials*, vol. 32, no. 33, article e1907404, 2020.

[24] L. Xu, W. Liu, Y. Hu, and L. Luo, "Stress-resilient electrode materials for lithium-ion batteries: strategies and mechanisms," *Chemical Communications*, vol. 56, no. 87, pp. 13301–13312, 2020.

[25] M. Zheng, H. Tang, L. Li et al., "Hierarchically nanostructured transition metal oxides for lithium-ion batteries," *Advanced Science*, vol. 5, no. 3, article 1700592, 2018.

[26] W. Zhao, M. Ding, L. Guo, and H. Y. Yang, "Dual-ion electrochemical deionization system with binder-free aerogel electrodes," *Small*, vol. 15, no. 9, article 1805505, 2019.

[27] Z. Wang, X. Xu, J. Kim et al., "Nanoarchitectured metal-organic framework/polypyrrole hybrids for brackish water desalination using capacitive deionization," *Materials Horizons*, vol. 6, no. 7, pp. 1433–1437, 2019.

[28] M. Xiao, Z. Wang, M. Lyu et al., "Hollow nanostructures for photocatalysis: advantages and challenges," *Advanced Materials*, vol. 31, no. 38, article e1801369, 2019.

[29] Y. Zhu, G. Zhang, C. Xu, and L. Wang, "Interconnected graphene hollow shells for high-performance capacitive deionization," *ACS Applied Materials & Interfaces*, vol. 12, pp. 29706–29716, 2020.

[30] J. Jiang, J. Liu, R. Ding et al., "Large-scale uniform α-Co(OH)2-Long nanowire arrays grown on graphite as pseudocapacitor electrodes," *ACS Applied Materials & Interfaces*, vol. 3, no. 1, pp. 99–103, 2011.

[31] L. Wang, Z. H. Dong, Z. G. Wang, F. X. Zhang, and J. Jin, "Layered α-Co(OH)2Nanocones as electrode materials for pseudocapacitors: understanding the effect of interlayer space on electrochemical activity," *Advanced Functional Materials*, vol. 23, no. 21, pp. 2758–2764, 2013.

[32] Z. Cai, L. Li, Y. Zhang et al., "Amorphous nanocages of Cu-Ni-Fe hydr(oxy)oxide prepared by photocorrosion for highly efficient oxygen evolution," *Angewandte Chemie (International Ed. in English)*, vol. 58, no. 13, pp. 4189–4194, 2019.

[33] J. Yu, J. Xiao, A. Li et al., "Enhanced multiple anchoring and catalytic conversion of polysulfides by amorphous MoS3Na-noboxes for high-performance Li-S batteries," *Angewandte Chemie (International Ed. in English)*, vol. 59, no. 31, pp. 13071–13078, 2020.

[34] J. Nai, Y. Tian, X. Guan, and L. Guo, "Pearson's principle inspired generalized strategy for the fabrication of metal hydroxide and oxide nanocages," *Journal of the American Chemical Society*, vol. 135, no. 43, pp. 16082–16091, 2013.

[35] J. Liu, J. Nai, T. You et al., "The flexibility of an amorphous cobalt hydroxide nanomaterial promotes the electrocatalysis of oxygen evolution reaction," *Small*, vol. 14, no. 17, article e1703514, 2018.

[36] H. B. Li, P. Liu, Y. Liang, J. Xiao, and G. W. Yang, "Amorphous cobalt hydroxide nanostructures and magnetism from green electrochemistry," *RSC Advances*, vol. 3, no. 48, article 26412, 2013.

[37] J. Yang, H. Liu, W. N. Martens, and R. L. Frost, "Synthesis and characterization of cobalt hydroxide, cobalt oxyhydroxide, and cobalt oxide nanodiscs," *Journal of Physical Chemistry C*, vol. 114, no. 1, pp. 111–119, 2010.

[38] S. R. Shieh and T. S. Duffy, "Raman spectroscopy of Co(OH)$_2$ at high pressures: implications for amorphization and hydrogen repulsion," *Physical Review B*, vol. 66, no. 13, 2002.

[39] J. Liu, J. Ke, Y. Li et al., "Co$_3$O$_4$ quantum dots/TiO$_2$ nanobelt hybrids for highly efficient photocatalytic overall water splitting," *Applied Catalysis B: Environmental*, vol. 236, pp. 396–403, 2018.

[40] I. M. Alibe, K. A. Matori, H. A. A. Sidek et al., "Effects of polyvinylpyrrolidone on structural and optical properties of willemite semiconductor nanoparticles by polymer thermal treatment method," *Journal of Thermal Analysis and Calorimetry*, vol. 136, pp. 2249–2268, 2018.

[41] C. Li, C. Liu, W. Wang et al., "Towards flexible binderless anodes: silicon/carbon fabrics via double-nozzle electrospinning," *Chemical Communications*, vol. 52, no. 76, pp. 11398–11401, 2016.

[42] B. J. Tan, K. J. Klabunde, and P. M. A. Sherwood, "XPS studies of solvated metal atom dispersed (SMAD) catalysts. evidence for layered cobalt-manganese particles on alumina and silica," *Journal of the American Chemical Society*, vol. 113, no. 3, pp. 855–861, 1991.

[43] V. Augustyn, P. Simon, and B. Dunn, "Pseudocapacitive oxide materials for high-rate electrochemical energy storage," *Energy & Environmental Science*, vol. 7, no. 5, p. 1597, 2014.

[44] S. Fleischmann, J. B. Mitchell, R. Wang et al., "Pseudocapacitance: from fundamental understanding to high power energy

storage materials," *Chemical Reviews*, vol. 120, no. 14, pp. 6738–6782, 2020.

[45] M. E. Suss, S. Porada, X. Sun, P. M. Biesheuvel, J. Yoon, and V. Presser, "Water desalination via capacitive deionization: what is it and what can we expect from it?," *Energy & Environmental Science*, vol. 8, no. 8, pp. 2296–2319, 2015.

[46] X. Wen, M. Zhao, D. Zhang, X. Ma, Z. Lin, and M. Ye, "An integrated large-scale and vertically aligned Co(OH)$_2$ paper electrode for high performance capacitive deionization of saline water," *Desalination*, vol. 470, article 114117, 2019.

[47] T. Liu, J. Serrano, J. Elliott et al., "Exceptional capacitive deionization rate and capacity by block copolymer-based porous carbon fibers," *Science Advances*, vol. 6, no. 16, 2020.

[48] Y. Li, Z. Ding, K. Wang et al., "Suppressing the oxygen-related parasitic reactions in NaTi$_2$(PO$_4$)$_3$-based hybrid capacitive deionization with cation exchange membrane," *Journal of Colloid and Interface Science*, vol. 591, pp. 139–147, 2021.

[49] T. Wu, G. Wang, S. Wang et al., "Highly stable hybrid capacitive deionization with a MnO2Anode and a positively charged cathode," *Environmental Science & Technology Letters*, vol. 5, no. 2, pp. 98–102, 2018.

[50] X. Shen, Y. Xiong, R. Hai, F. Yu, and J. Ma, "All-MXene-based integrated membrane electrode constructed using Ti$_3$C$_2$T$_x$ as an intercalating agent for high-performance desalination," *Environmental Science & Technology*, vol. 54, no. 7, pp. 4554–4563, 2020.

[51] X. Shen, R. Hai, X. Wang et al., "Free-standing 3D alkalized Ti$_3$C$_2$T$_x$/Ti$_3$C$_2$T$_x$ nanosheet membrane electrode for highly efficient and stable desalination in hybrid capacitive deionization," *Journal of Materials Chemistry A*, vol. 8, no. 37, pp. 19309–19318, 2020.

[52] S. Wang, G. Wang, Y. Wang et al., "In situ formation of Prussian blue analogue nanoparticles decorated with three-dimensional carbon nanosheet networks for superior hybrid capacitive deionization performance," *ACS Applied Materials & Interfaces*, vol. 12, no. 39, pp. 44049–44057, 2020.

[53] W. Xi and H. Li, "Vertically-aligned growth of CuAl-layered double oxides on reduced graphene oxide for hybrid capacitive deionization with superior performance," *Environmental Science. Nano*, vol. 7, no. 3, pp. 764–772, 2020.

[54] D. Moreno, Y. Bootwala, W.-Y. Tsai et al., "In situ electrochemical dilatometry of phosphate anion electrosorption," *Environmental Science & Technology Letters*, vol. 5, no. 12, pp. 745–749, 2018.

[55] N. Jäckel, B. Krüner, K. L. Van Aken et al., "Electrochemical in situ tracking of volumetric changes in two-dimensional metal carbides (MXenes) in ionic liquids," *ACS Applied Materials & Interfaces*, vol. 8, no. 47, pp. 32089–32093, 2016.

[56] J. Wang, J. Polleux, J. Lim, and B. Dunn, "Pseudocapacitive contributions to electrochemical energy storage in TiO$_2$ (anatase) nanoparticles," *Journal of Physical Chemistry C*, vol. 111, no. 40, pp. 14925–14931, 2007.

[57] H. Jin, S. Xin, C. Chuang et al., "Black phosphorus composites with engineered interfaces for high-rate high-capacity lithium storage," *Science*, vol. 370, no. 6513, pp. 192–197, 2020.

[58] S. Ardizzone, G. Fregonara, and S. Trasatti, ""Inner" and "outer" active surface of RuO$_2$ electrodes," *Electrochimica Acta*, vol. 35, no. 1, pp. 263–267, 1990.

[59] R. Niu, H. Li, Y. Ma, L. He, and J. Li, "An insight into the improved capacitive deionization performance of activated carbon treated by sulfuric acid," *Electrochimica Acta*, vol. 176, pp. 755–762, 2015.

[60] X. Zang, Y. Xue, W. Ni et al., "Enhanced electrosorption ability of carbon nanocages as an advanced electrode material for capacitive deionization," *ACS Applied Materials & Interfaces*, vol. 12, no. 2, pp. 2180–2190, 2020.

[61] S. Vafakhah, G. J. Sim, M. Saeedikhani, X. Li, P. Valdivia y Alvarado, and H. Y. Yang, "3D printed electrodes for efficient membrane capacitive deionization," *Nanoscale Advances*, vol. 1, no. 12, pp. 4804–4811, 2019.

Supporting Information

Three-dimensional hollow Co(OH)₂ cube/vertical nanosheets with high desalination capacity and long-term performance stability

Yuecheng Xiong[2,6§], Fei Yu[1§], Stefanie Arnold[3,4], Lei Wang[3,4], Volker Presser[3,4,5], Yifan Ren[2,6], Jie Ma[2,6,7*]

1 College of Marine Ecology and Environment, Shanghai Ocean University, Shanghai 201306, P. R. China

2 Research Center for Environmental Functional Materials, College of Environmental Science and Engineering, Tongji University, 1239 Siping Road, Shanghai 200092, P.R. China

3 INM-Leibniz Institute for New Materials, 66123 Saarbrücken, Germany

4 Department of Materials Science and Engineering, Saarland University, 66123 Saarbrücken, Germany

5 Saarene-Saarland Center for Energy Materials and Sustainability, 66123 Saarbrücken, Germany.

6 State Key Laboratory of Pollution Control and Resource Reuse, College of Environmental Science and Engineering, Tongji University, Shanghai, 200092, P. R. China.

7 Shanghai Institute of Pollution Control and Ecological Security, Shanghai, 200092, P.R. China

§ These authors contributed equally to this work

* Corresponding author's email: jma@tongji.edu.cn

Contents

Fig. S1. Transmission electron micrographs of Cu_2O template etching and cobalt hydroxide crystal growth process.

Fig. S2. Water contact angle of the cobalt hydroxide $_2$ electrode before (A) and after (B) desalination.
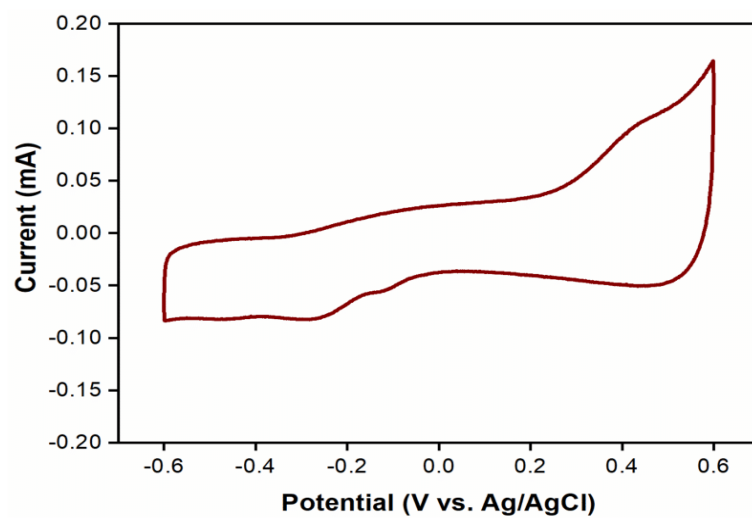
Fig. S3. Cyclic voltammogram of the cobalt hydroxide electrode at a rate of 1 mV·s⁻¹.
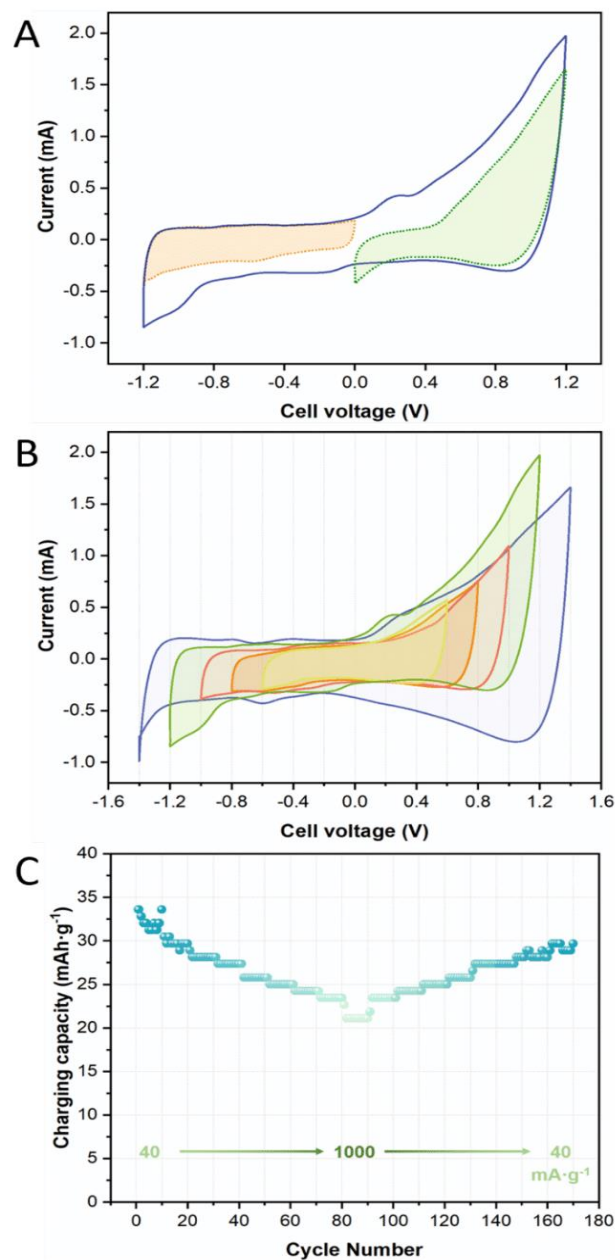
Fig. S4. (A) Cyclic voltammograms of the cobalt hydroxide electrode at a rate of 10 mV·s^{-1} using a two-electrode setup with an oversized AC electrode as counter electrode. (B) Cyclic voltammograms with different cutoff voltages. (C) Charging capacity of the cobalt hydroxide electrode in two electrode system with changing specific current.
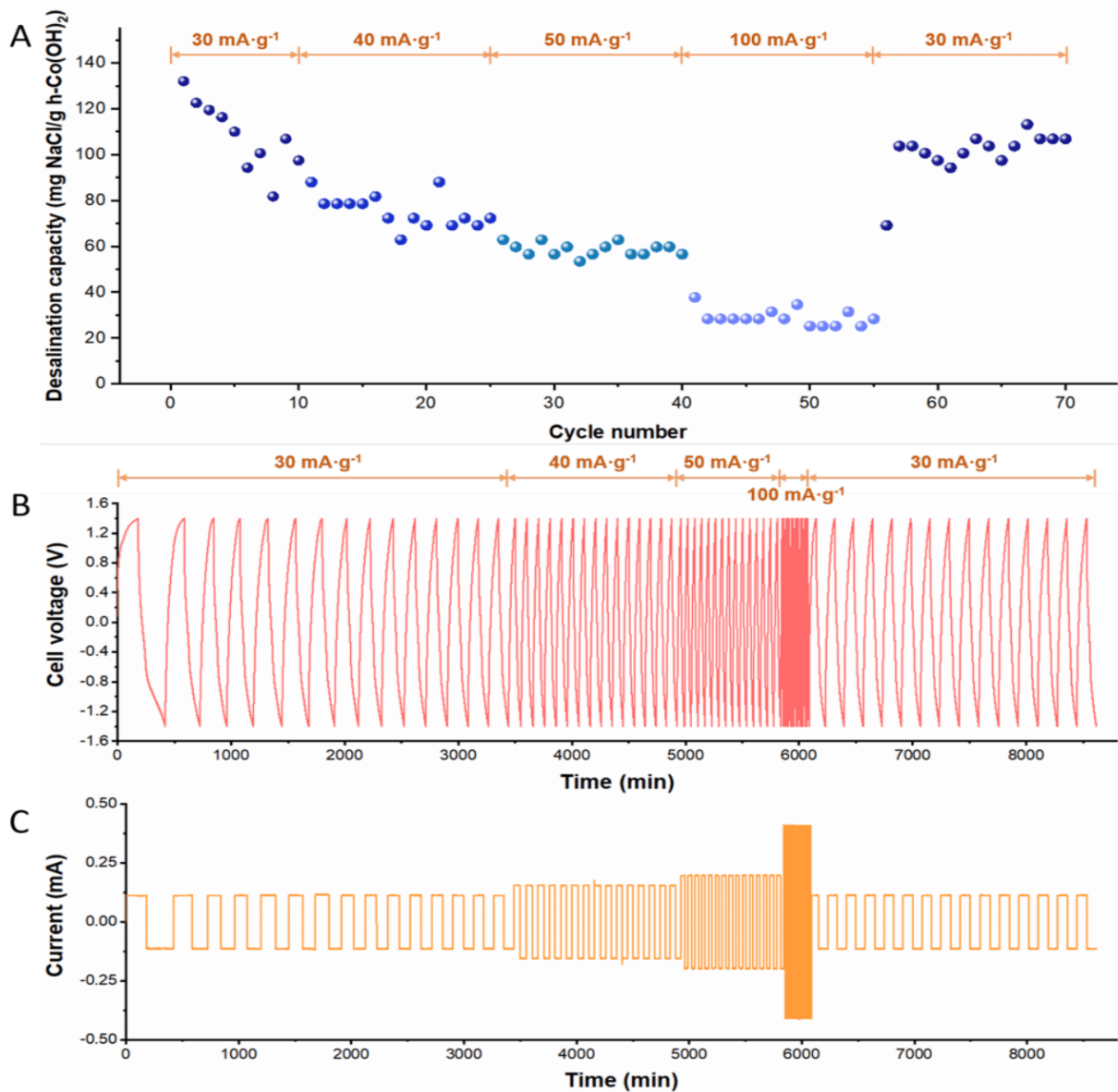
Fig. S5. Desalination capacity (A), cell voltage profiles, (B) and current profiles (C) of the HCDI cell at different specific current.
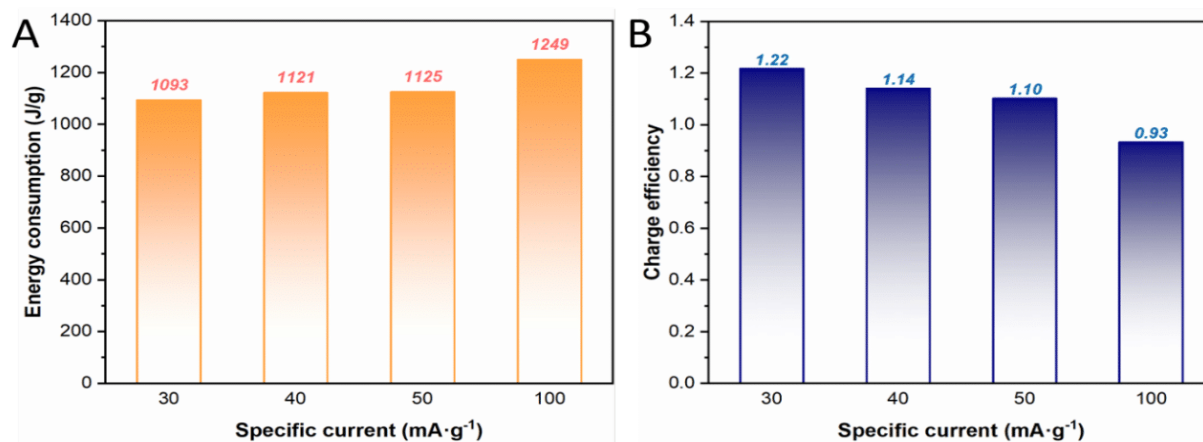
Fig. S6. Energy consumption (A) and charge efficiency (B) at different rates.
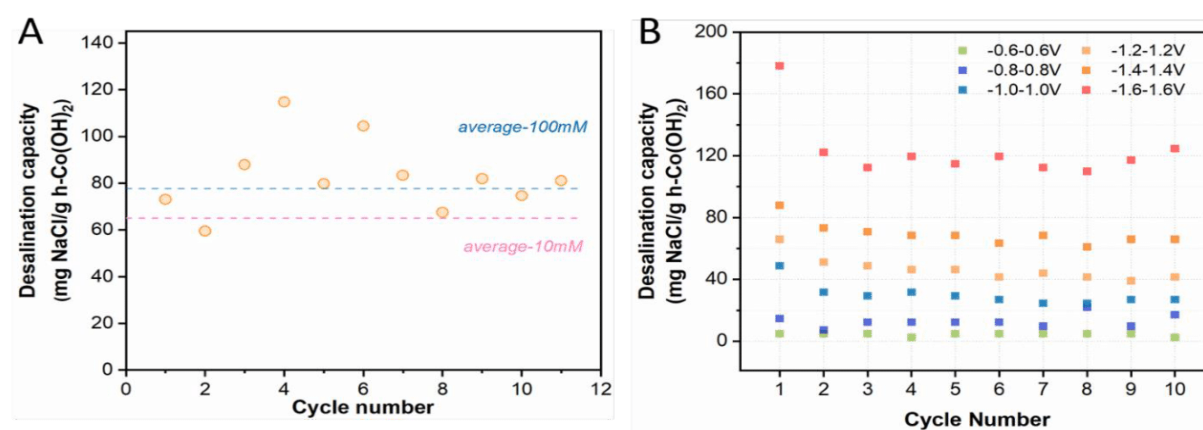
Fig. S7. (A) Desalination capacity at 100 mM initial NaCl concentration (specific current: 30 mA·g^{-1}; cutoff voltage: ±1.4 V). (B) Desalination capacity of HCDI cell at different cutoff voltages (specific current: 30 mA·g^{-1}; initial NaCl concentration: 10 mM).
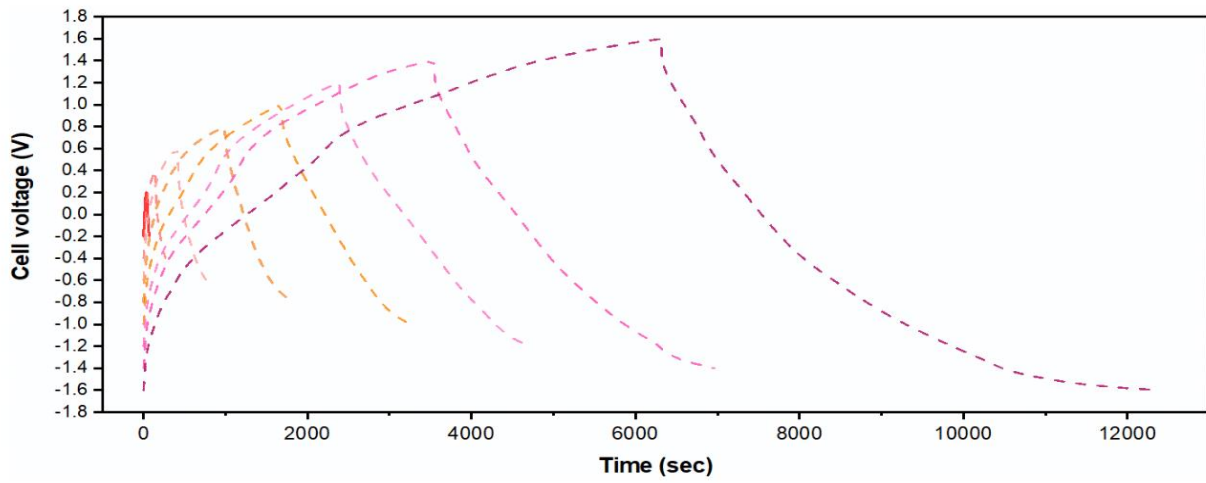
Fig. S8. Voltage profiles of the HCDI cell at different cutoff voltages.
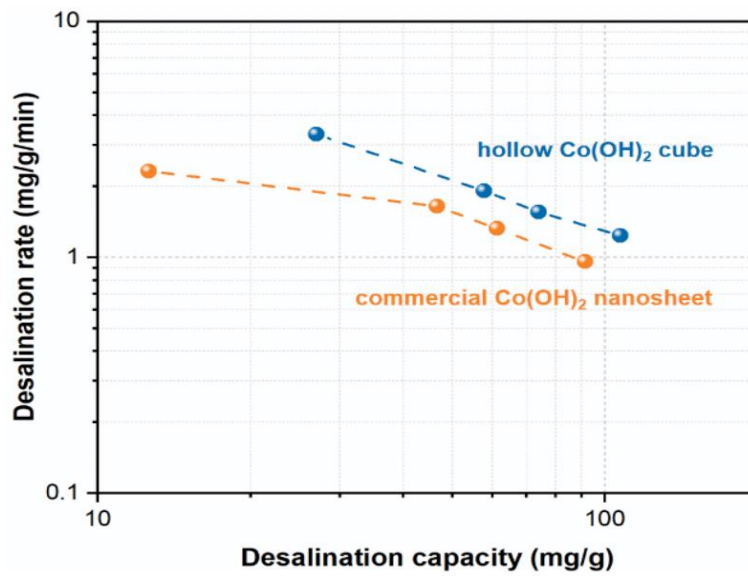
Fig. S9. Kim-Yoon plot of h-Co(OH)$_2$ and commercial Co(OH)$_2$ electrode in an HCDI cell.
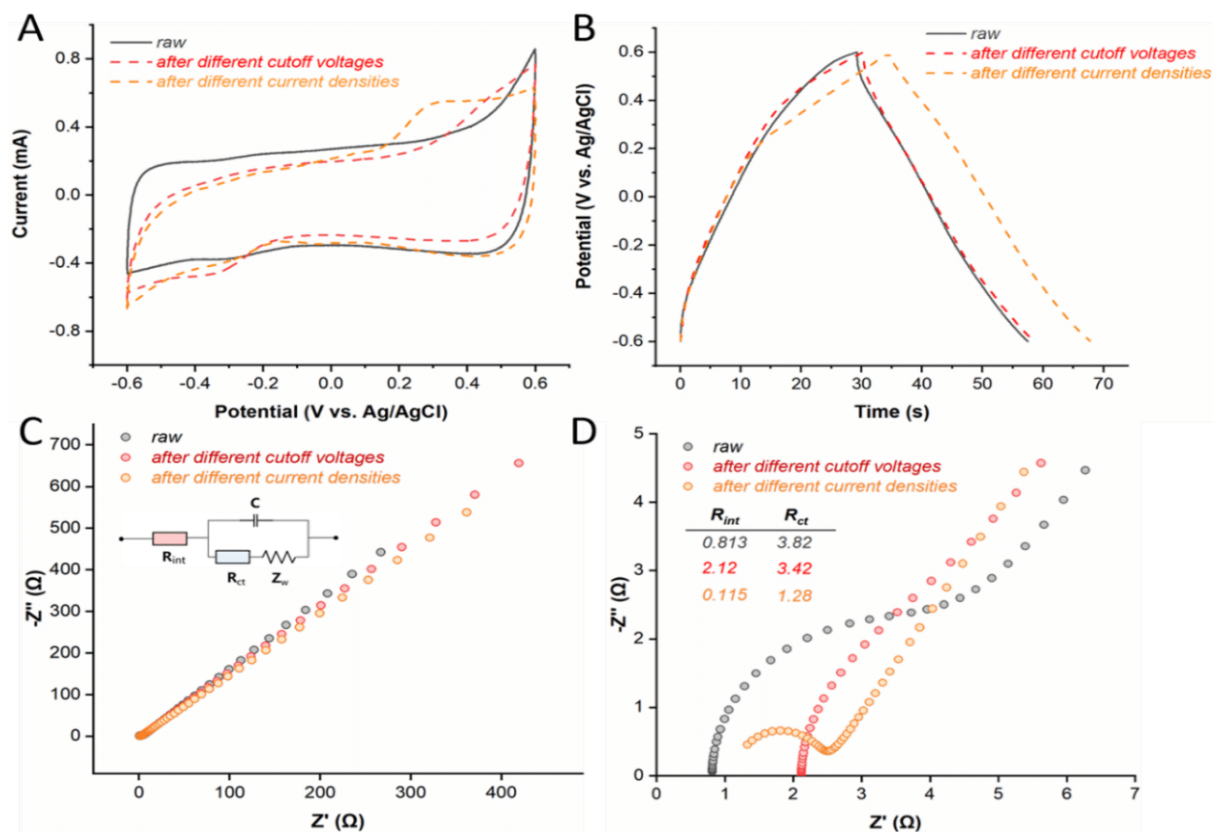
Fig. S10. Cyclic voltammograms (A), galvanostatic charge/discharge profiles (B), Nyquist plots (C) and magnified Nyquist plots at high-frequency area (D) for cobalt hydroxide electrodes before and after desalination at different cutoff voltages and values for specific current.

De-chlorination performance.

The capacitance during positive and negative polarization increases as the potential difference is increased during cyclic voltammetry (**Fig. S11**). A similar capacitance during opposite polarization indicates the ability of h-Co(OH)$_2$ electrode to serve as an electrode for the removal of either anions or cations.[1] The Cl$^-$ insertion has been proved in cobalt layered hydroxide, with the formula presented below.[2]

$$Co(OH)_2 + Cl^- \rightarrow Co(OH)_2Cl + e^-$$
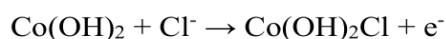
In our experiments, we further paired two h-Co(OH)$_2$ electrodes to investigate its de-chlorination potential in capacitive deionization. The average desalination capacity of the symmetric cell improves to 80 mg·g^{-1}, while the counterpart for HCDI is 70 mg·g^{-1} (**Fig. S12**). The average de-chlorination capacity based on anode mass increases slightly from 36 mg·g^{-1} to 39 mg·g^{-1}. This performance is higher than that found for conventional activated carbon, while the symmetric cell displays a higher instability with wider lower-upper limit and more outliers (**Fig. S13-S15**).
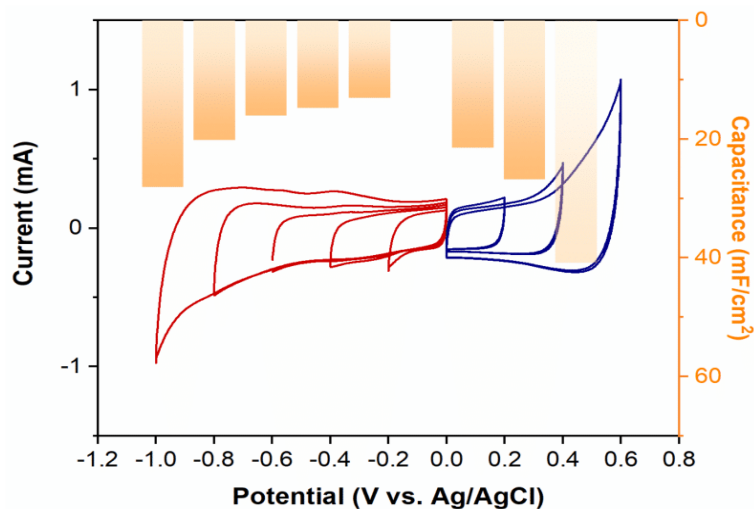
Fig. S11.　　Cyclic voltammograms and capacitance of h-Co(OH)$_2$ electrode at different voltage windows.
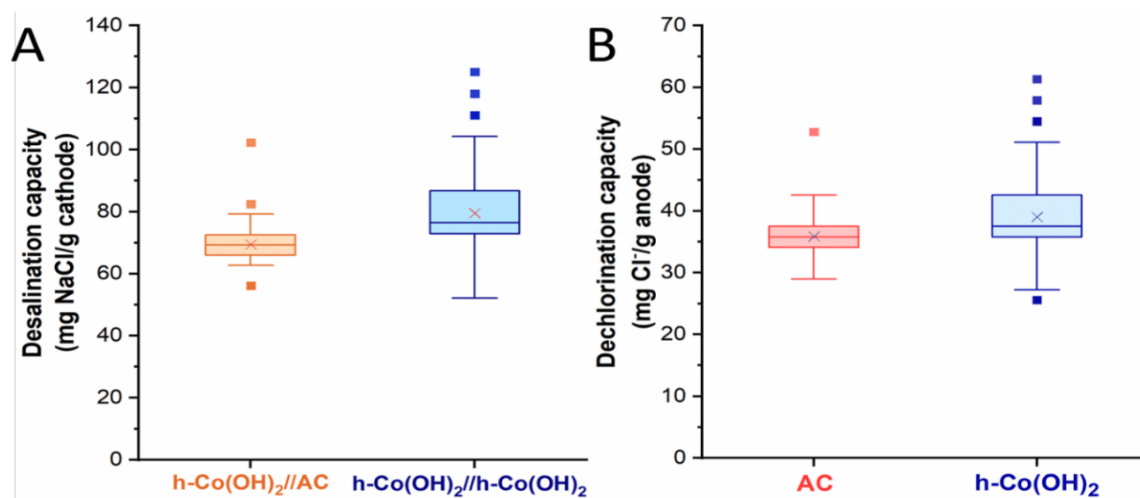
Fig. S12. De-chlorination performance. (A) Desalination capacity of asymmetric (h-Co(OH)$_2$//AC) and symmetric (h-Co(OH)$_2$//h-Co(OH)$_2$) CDI cells. (B) De-chlorination capacity of the asymmetric and symmetric CDI cells.
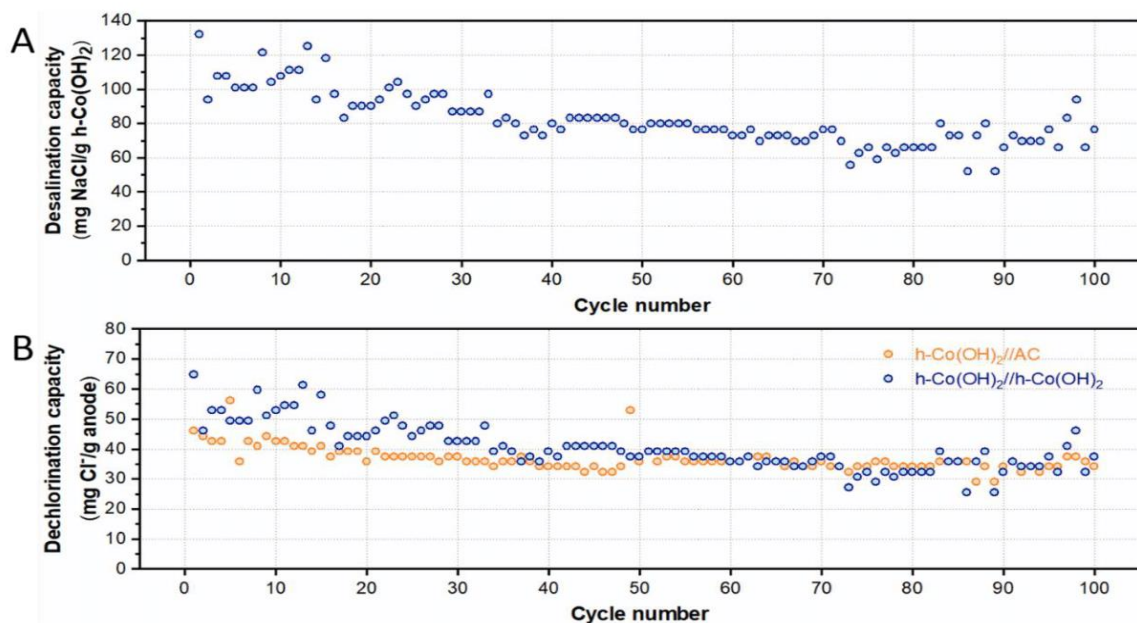
Fig. S13. (A) Desalination capacity of symmetric CDI cell for 100 cycles. (B) Theoretical dechlorination capacity of asymmetric and symmetric CDI cells for 100 cycles.

Fig. S14. Cell voltage (A) and current profiles (B) of asymmetric cell for 100 cycles.

S12

216
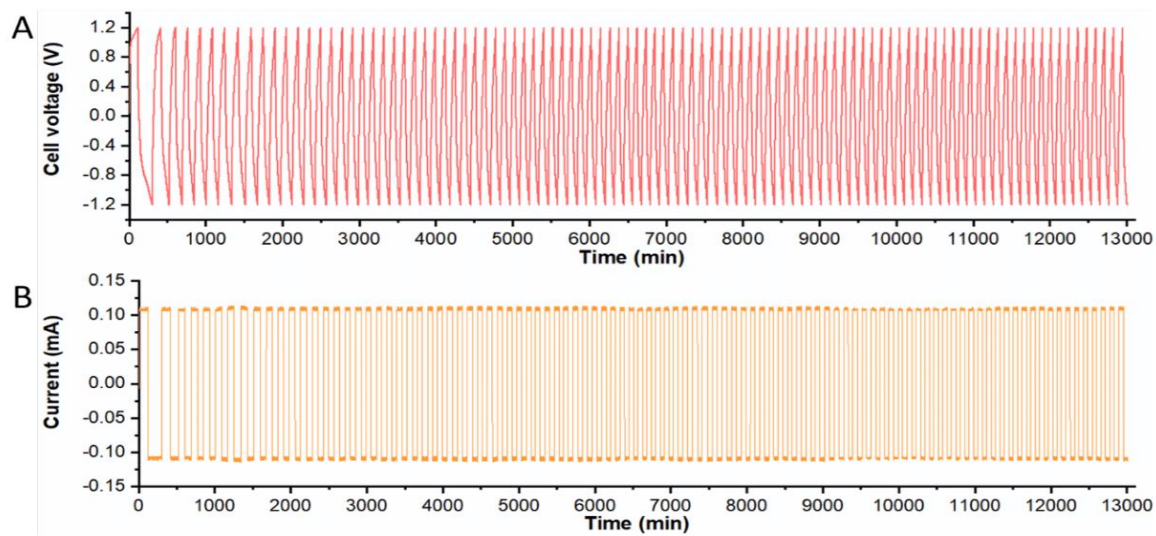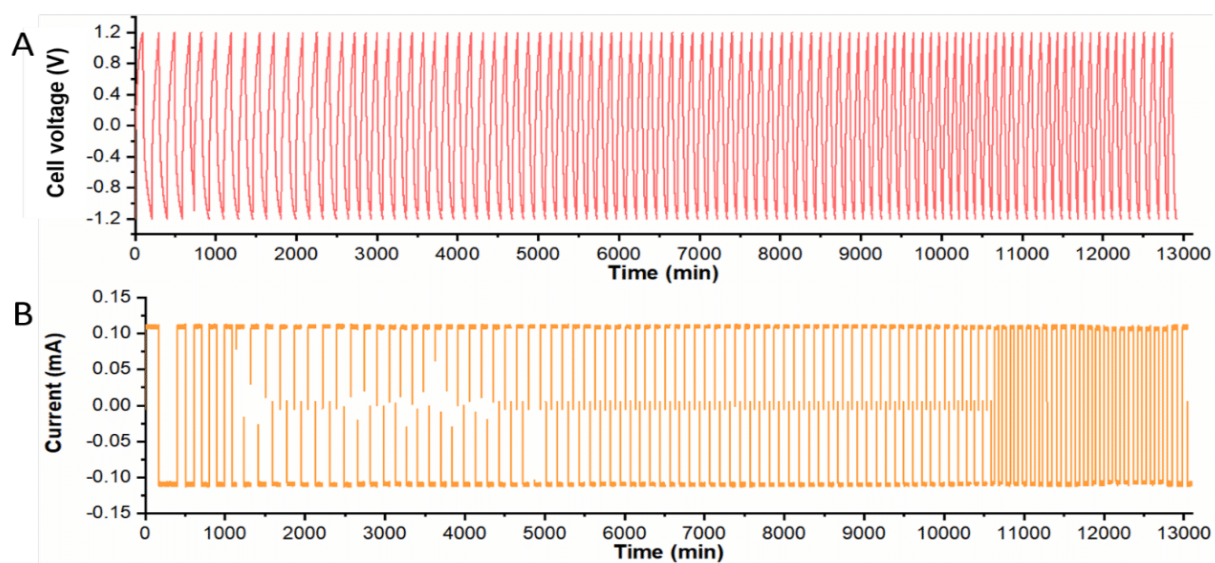
Fig. S15. Cell voltage (A) and current profiles (B) of symmetric CDI cell for 100 cycles.
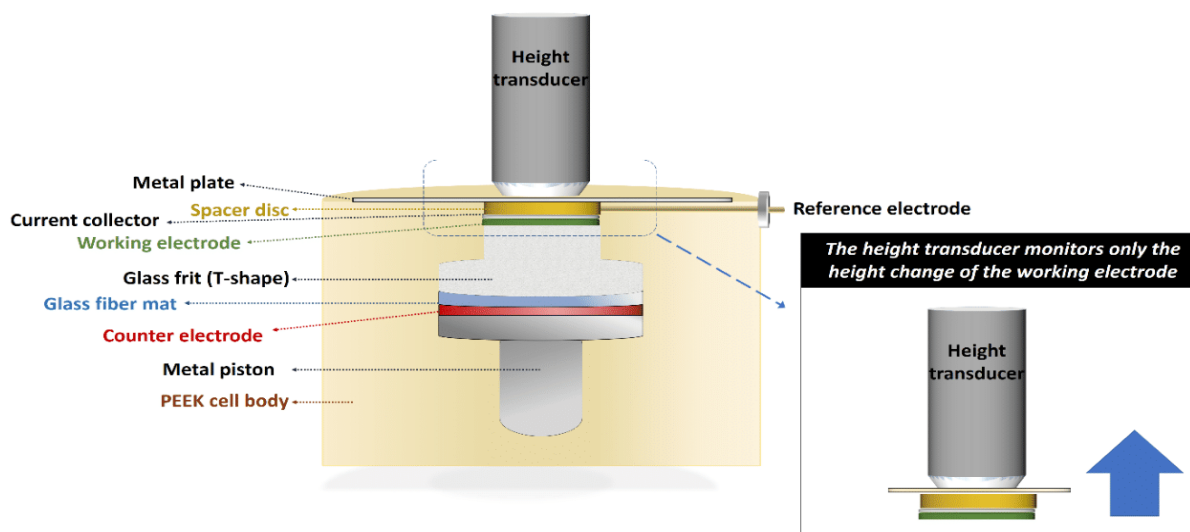
Fig. S16. Schematic drawing of the in-situ electrochemical dilatometry cell.
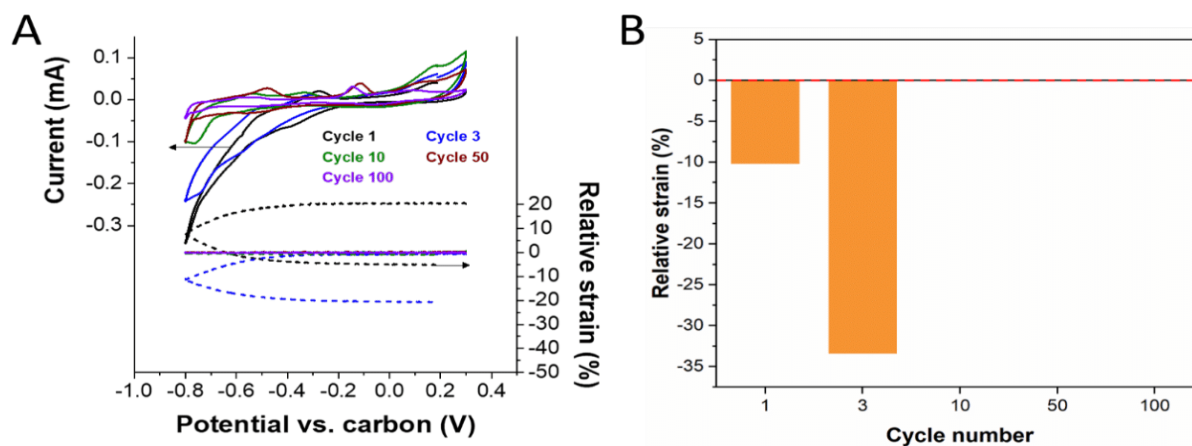
Fig. S17. (A) The original data of relative strain during electro-dilatometry during cyclic voltammetry. (B) The relative strain change in the test after 72 h stabilization.

Table S1 Comparison of desalination rate of various advanced electrode materials

Materials	Testing conditions	Desalination rate $(mg \cdot g^{-1} \cdot s^{-1})$	Ref.
PB/PANI	500 ppm, 100 mA·g^{-1}	0.03	3
h-Co(OH)$_2$	10 mM, 100 mA·g^{-1}	0.055	This work
N-Ti$_3$C$_2$T$_x$	5000 ppm, 1.2 V	0.062	4
Na$_3$V$_2$(PO$_4$)$_3$@C	10 mM, 1 V	0.04	5
K$_{0.03}$Cu[Fe(CN)$_6$]$_{0.65}$·0.43H$_2$O	500 ppm, 1.2 V	0.24	6
MnO$_2$	15 mM, 1.2 V	0.112	7
ZIF-67/PPy	10 mM, 1.2 V	0.019	8

N.B. The pink and yellow backgrounds represent the constant current and constant voltage mode, respectively. 10 mM NaCl equals to ca. 585 ppm NaCl. The estimation of the desalination rate in ref [4] and [8] takes the equilibrium time of 700 sec and 600 sec, respectively. PB, PANI, and PPy refer to Prussian blue, polyaniline and polypyrrole, respectively.

Text S1 Finite element simulation

The finite element simulation method is based on COMSOL software, combining the structural mechanics and heat transfer modules. In the heat transfer module, the thermal expansion coefficient is applied as an approximate substitution of cobalt hydroxide material expansion or contraction induced by sodium ion intercalation/deintercalation. Through the simultaneous setting of thermal expansion coefficient and the temperature K, the volume change proportion is set as 40%.

First, a hollow cube and solid cube model are constructed, with a dimension of 75 ×75 μm^2, and the wall thickness of the hollow cube is 75 nm. The density of $Co(OH)_2$ is set as 3.6 g·cm^{-3}, and $Co(OH)_2$ is an anisotropic material, which is expressed as the following elasticity matrix.

44[GPa]	12[GPa]	7[GPa]	1[GPa]	4[GPa]	1[GPa]
12[GPa]	126[GPa]	54[GPa]	-3[GPa]	1[GPa]	-21[GPa]
7[GPa]	54[GPa]	132[GPa]	0[GPa]	-2[GPa]	0[GPa]
1[GPa]	-3[GPa]	0[GPa]	41[GPa]	3[GPa]	-0[GPa]
4[GPa]	1[GPa]	-2[GPa]	3[GPa]	6[GPa]	2[GPa]
1[GPa]	-21[GPa]	0[GPa]	-0[GPa]	2[GPa]	13[GPa]

For PVDF, we assume a density of 1.77 g·cm^{-3}, the Young's modulus is 2000 MPa, Poisson's ratio is 0.3, and an isotropic behavior. The initial displacement and velocity is set as 0, and the boundary conditions are fixed, that is, the displacement is 0.

Elastic stress follows the Hook's law:

$$\varepsilon_{ij}^e = \frac{1}{E}\left[(1+v)\sigma_{ij} - v\sigma_{kk}\delta_{ij}\right]$$

where ε_{ij} is the stress fractional variable, σ_{ij} is the strain fractional variable, E is the Young's modulus, v is the Poisson's ratio, δ is the second-order unit tensor.

References

1.   Torkamanzadeh, M.; Wang, L.; Zhang, Y.; Budak, O.; Srimuk, P.; Presser, V., MXene/Activated-Carbon Hybrid Capacitive Deionization for Permselective Ion Removal at Low and High Salinity. *ACS Appl. Mater. Interfaces* **2020,** *12*, (23), 26013-26025.

2.   Young, M. J.; Kiryutina, T.; Bedford, N. M.; Woehl, T. J.; Segre, C. U., Discovery of Anion Insertion Electrochemistry in Layered Hydroxide Nanomaterials. *Sci Rep* **2019,** *9*, (1), 2462.

3.   Shi, W.; Liu, X.; Deng, T.; Huang, S.; Ding, M.; Miao, X.; Zhu, C.; Zhu, Y.; Liu, W.; Wu, F.; Gao, C.; Yang, S. W.; Yang, H. Y.; Shen, J.; Cao, X., Enabling Superior Sodium Capture for Efficient Water Desalination by a Tubular Polyaniline Decorated with Prussian Blue Nanocrystals. *Adv. Mater.* **2020,** *32*, (33), e1907404.

4.   Amiri, A.; Chen, Y.; Bee Teng, C.; Naraghi, M., Porous nitrogen-doped MXene-based electrodes for capacitive deionization. *Energy Storage Mater.* **2020,** *25*, 731-739.

5.   Cao, J.; Wang, Y.; Wang, L.; Yu, F.; Ma, J., Na3V2(PO4)3@C as Faradaic Electrodes in Capacitive Deionization for High-Performance Desalination. *Nano Lett* **2019,** *19*, (2), 823-828.

6.   Choi, S.; Chang, B.; Kim, S.; Lee, J.; Yoon, J.; Choi, J. W., Battery Electrode Materials with Omnivalent Cation Storage for Fast and Charge-Efficient Ion Removal of Asymmetric Capacitive Deionization. *Adv. Funct. Mater.* **2018,** *28*, (35), 1802665.

7.   Byles, B. W.; Cullen, D. A.; More, K. L.; Pomerantseva, E., Tunnel structured manganese oxide nanowires as redox active electrodes for hybrid capacitive deionization. *Nano Energy* **2018,** *44*, 476-488.

8.   Wang, Z.; Xu, X.; Kim, J.; Malgras, V.; Mo, R.; Li, C.; Lin, Y.; Tan, H.; Tang, J.; Pan, L.; Bando, Y.; Yang, T.; Yamauchi, Y., Nanoarchitectured metal–organic framework/polypyrrole hybrids for brackish water desalination using capacitive deionization. *Mater. Horiz.* **2019**.

4.8 Redox flow battery for continuous and energy-effective lithium recovery from aqueous solution

Lei Wang[1,2], Stefanie Arnold[1,2], Panyu Ren[1,2], Qingsong Wang[1], Jun Jin[3], Zhaoyin Wen[3,4], and Volker Presser[1,2,5]

[1] INM - Leibniz Institute for New Materials, 66123 Saarbrücken, Germany

[2] Department of Materials Science and Engineering, Saarland University, 66123 Saarbrücken, Germany

[3] CAS Key Laboratory of Materials for Energy Conversion Shanghai Institute of Ceramics, Chinese Academy of Sciences, Shanghai, 200050 P. R. China

[4] State Key Lab of High Performance Ceramics and Superfine Microstructure, Shanghai Institute of Ceramics, Chinese Academy of Sciences, Shanghai, 200050 P. R. China

[5] Saarene, Saarland Center for Energy Materials and Sustainability, Campus C4 2, 66123 Saarbrücken, Germany

Own Contribution:

Investigation, writing-review & editing.

LETTER

Redox Flow Battery for Continuous and Energy-Effective Lithium Recovery from Aqueous Solution

Lei Wang, Stefanie Arnold, Panyu Ren, Qingsong Wang, Jun Jin, Zhaoyin Wen,* and Volker Presser*

Read Online

ACCESS | 📊 Metrics & More | 📰 Article Recommendations | 🗐 Supporting Information

ABSTRACT: Lithium-ion batteries are the primary power source for electric vehicles and portable electronic devices, creating a massive demand to mine and extract lithium. So far, lithium extraction has focused on brine and geological deposits. Yet, access to the enormous amount of lithium (at low concentration) in the earth's oceans and other aqueous media remains challenging. Electrodialysis with Li-selective ceramic membranes could effectively separate lithium from seawater but at a high energy cost. Reversible electrochemical processes, like redox flow batteries, can overcome the limitation of electrodialysis-based systems. Herein we propose a system combining Li-selective ceramic membranes and a simple redox flow electrolyte to accomplish continuous lithium recovery from seawater. The lithium-extraction redox flow battery (LE-RFB) extracts dissolved lithium with a purity of 93.5% from simulated seawater, corresponding to a high Li/Mg selectivity factor of about 500.000:1. Benefiting from a low operating voltage, 1 g of lithium is extracted with only 2.5 Wh of energy consumption.
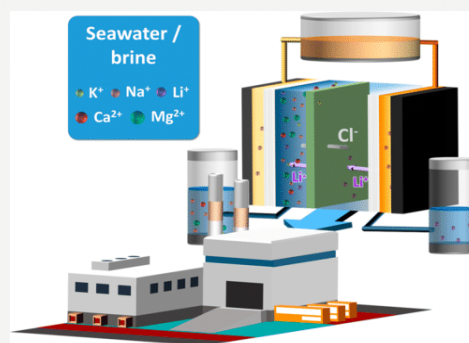
W ith the universal usage of portable electronic equipment and electric vehicles, the demand for lithium-ion batteries has increased tremendously.[1] This sharply increasing consumption would result in a complete depletion of terrestrial lithium before this century is over.[2] Thereby, it is crucial to find alternative lithium reservoirs and environmentally friendly ways for lithium extraction. Apart from recycling lithium from abandoned lithium-ion batteries, seawater is another available lithium reserve containing 230 billion tons of lithium.[3] However, the low lithium concentration (around 0.17 mg_{Li}/L on average) and high concentration of other competing cations, like Na^+ and Mg^{2+}, bring tremendous challenges to extracting lithium from seawater.[3,4] So far, several approaches, such as coprecipitation,[5] sorption,[6] liquid−liquid extraction,[7] membrane processes,[8] and electrochemical methods,[9,10] have been adapted to recover lithium from seawater.[11] However, coprecipitation, liquid−liquid extraction, and sorbent regeneration require many chemicals and are energy-costly and time-consuming.[12] In addition, while membrane-based processes can continuously extract lithium, this technology suffers from the low selectivity factor of the commercial membranes.[13]

Electrochemical methods are an energy-efficient approach with relatively high selectivity toward Li^+, as recent studies show. For example, Joo et al. used an electrode pair of λ-MnO_2

and AgCl to treat the actual desalination of concentrated seawater on a pilot scale.[14] After the enrichment, the purity of Li^+ increased from 0.0048 to 88%.[14] In another example, an electrolysis-based technique was proposed to extract lithium from seawater utilizing a solid-state lithium superionic conductor membrane (LISICON membrane).[2] On the cathode side, elemental lithium metal was formed, while the Cl_2 or O_2 was produced in the anode area. However, the electrochemical methods have not yet been able to perform continuous lithium recovery with the typical cell configuration (i.e., a lithium-capture electrode + a chloride-capture electrode or a cation-release electrode).[15,16] Kim et al. proposed a hybrid system with a redox flow battery system and lithium-selective adsorbent.[17] In this system, the water can be continuously desalinated, while the lithium recovery process is not continuous. Meanwhile, the regeneration of adsorbents consumes acid. Recently, Li et al.[18] put forward a continuous electrical pump membrane process, where a $Li_{0.33}La_{0.56}TiO_3$

223
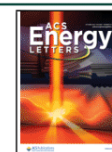
membrane accomplished the selective extraction of lithium; the catalytic reactions occurred on the cathode and anode sides formed the driven force for lithium migration. After the treatment, the lithium concentration increased from 0.2 mg/L to 9 g/L. However, due to the high voltage, the energy consumption to enrich 1 kg of lithium is about 76 kWh. With humankind striving for more sustainable technologies, there is a high demand for an economical approach with continuous operation, a high selectivity factor, and low energy consumption for the large-scale lithium extraction from the seawater.

This work reports an innovative electrochemical cell configuration for continuously recovering lithium from seawater. Our system strives toward low-cost materials and environmental friendliness. The lithium-extraction redox flow battery (LE-RFB) uses a redox pair electrolyte ($Fe[CN]_6^{4-}$/ $Fe[CN]_6^{3-}$) and operates at a low applied voltage of just 600 mV for continuous lithium extraction. The LE-RFB shows an excellent selectivity toward Li^+ with a low energy consumption of 2.5 $Wh/g_{Li-extraction}$. We also demonstrate the universal usage of this system with various lithium concentrations from seawater (ca. 0.17 mg/L) to lithium-rich brines (>1000 mg/L).

The LE-RFB cell contains four channels: one recovery-solution channel, one feedwater channel, and two redox-electrolyte channels (Figure 1A; Experimental Methods, Table S1, and Figure S1 in Supporting Information). The recovery-solution channel and the feedwater channel are each separated from the redox-electrolyte channels by a LISICON membrane. A polymer anion exchange membrane localized between the recovery-solution and feedwater channels serves to separate different compartments. During operation, the charging process results in the enrichment of lithium in the recovery-solution channel and the uptake of lithium from the feedwater channel. The ferricyanide is reduced to the ferrocyanide in the cathode area, drawing one cation (i.e., Li^+, on the basis of the selectivity of LISICON membrane) from the feedwater channel into the redox-electrolyte reservoir. At the other end, the ferrocyanide in the anode area is oxidized into ferricyanide, releasing lithium into the recovery solution through the LISICON membrane. Simultaneously, the Cl^- will migrate through the anion exchange membrane to keep the charge balanced. The reactions in the anolyte and catholyte are shown as follows. These reactions are continuously ongoing because the initial redox electrolyte contains equimolar ferricyanide and ferrocyanide, and with this continuous circulation, the uptaken Li^+ is continuously brought from the catholyte through the redox-electrolyte reservoir to the anolyte.

$$K_3[Fe(CN)_6] + Li^+ + e^- \rightarrow K_3Li[Fe(CN)_6] \quad \text{catholyte reaction}$$

$$K_3Li[Fe(CN)_6] \rightarrow K_3[Fe(CN)_6] + Li^+ + e^- \quad \text{anolyte reaction}$$
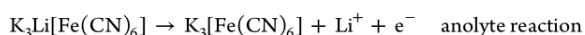
As the core component of the LE-RFB system, the LISICON membrane plays the role of selectively uptaking and releasing Li^+. The LISICON membrane used in this work consists of $Li_{1+x}Al_xGe_{2-x}(PO_4)_3$ (x = 0.5, LAGP), prepared by a solid-state-reaction method as reported previously[19,20] and as described in the Experimental Methods in the Supporting Information. Cross-sectional scanning electron micrographs confirm the presence of a dense membrane, having a thickness of about 500 μm without cracks (Figure 1B). The grain size of the particles ranges from 100 nanometers to several micro-
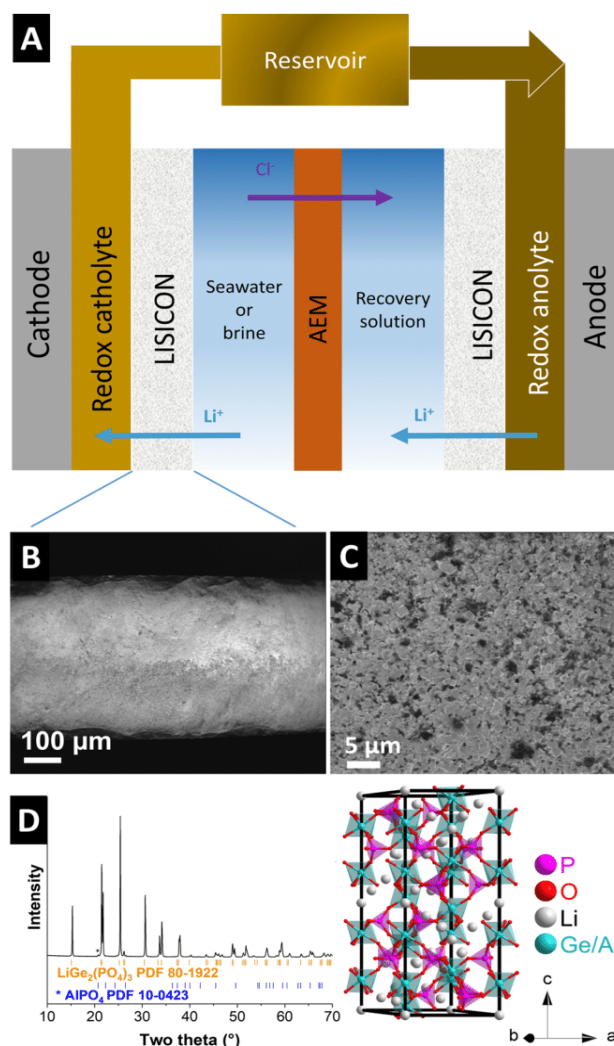
Figure 1. (A) The schematic images of a lithium-extraction redox flow battery. Cross-sectional scanning electron micrograph of the LISICON membrane at (B) low and (C) high magnification. (D) X-ray diffraction patterns of the LISICON membrane and the structure of $Li_{1+x}Al_xGe_{2-x}(PO_4)_3$; the crystal structure is based on ref 40.

meters (Figure 1C), similar to that in the reported work.[21] The energy-dispersive X-ray mapping results (Supporting Information, Figure S2) also suggest that the distribution of elements is uniform, indicating the membrane is very homogeneous. LAGP is a superionic conductor with lower energy barriers for the migration of Li^+ compared to other cations[21] and superior stability in aqueous media[22,23] (Figure 1D). The crystal structure of the membrane was verified using the XRD pattern of the LISICON membrane, which is consistent with the standard pattern of $LiGe_2(PO_4)_3$ (Figure 1D). There is a small reflection at 20.7° 2θ, which aligns with trace amounts of $AlPO_4$, the common impurity of the LAGP ceramic membrane.[24] The Li^+ conductivity of the LAGP membrane is around 1.2×10^{-4} S cm^{-1}, calculated according to the impedance results in the Supporting Information, Figure S3.

To demonstrate the feasibility and investigate the performance of the LE-RFB system, we first explored LE-RFB for Li^+
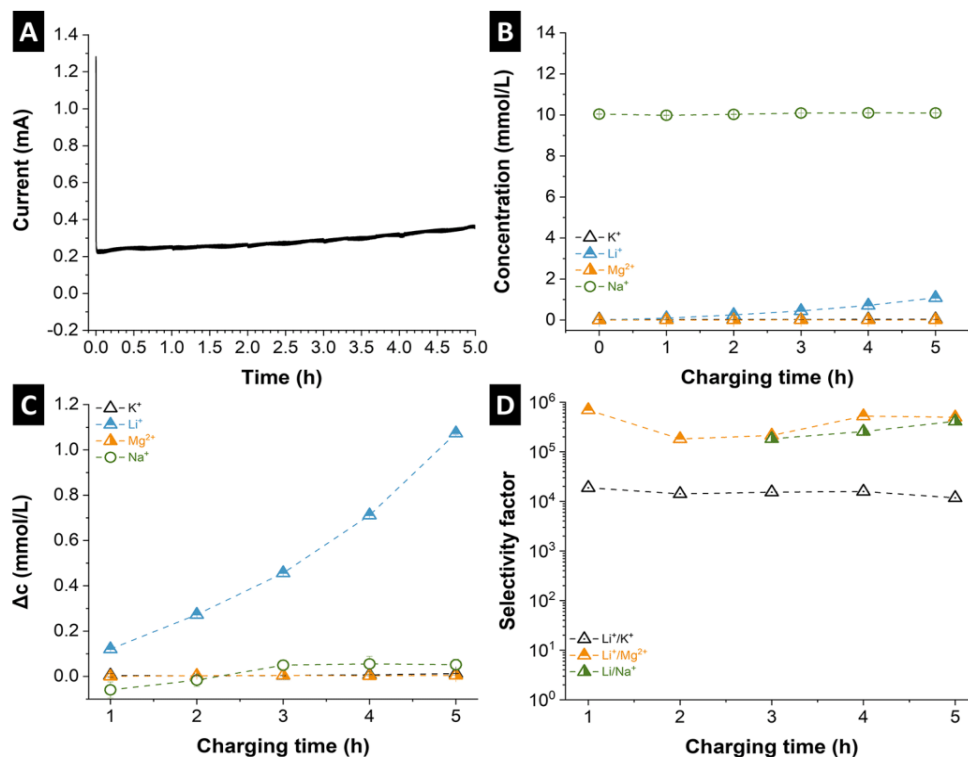
Figure 2. Lithium extraction from seawater by a lithium-extraction redox flow battery: (A) current curve, (B) concentration, (C) concentration change of cations in the recovery solution, and (D) selectivity factors between Li$^+$ and other cations at different times.

extraction in simulated seawater (24 μM Li$^+$; see Tables S1 and S2 in the Supporting Information). Figure 2A shows the trend of current change with increasing charging time. When the cell is charged at 0.6 V, the current increases from 0.22 to 0.36 mA. This is linked to the rise of the lithium-ion concentration in the recovery solution (Figure 2B), which also lowers the system resistance. In contrast to the Li$^+$ concentration, the other cations only change slightly. The concentration of Ca^{2+} is below the detection limit and is, therefore, not displayed. For better visualization of the cation concentration changes, we calculated the differences between the concentration at different charging times and the initial concentration of the recovery solution, as shown in Figure 2C. As it can be seen, the concentration of Li$^+$ increases by 1.07 $\pm$ 0.06 mM after a 5 h enrichment, while the concentrations of K$^+$, Na$^+$, and Mg^{2+} are $1.3 \times 10^{-2} \pm 1.1 \times 10^{-3}$ mM, $5.1 \times 10^{-2} \pm 2.4 \times 10^{-2}$ mM, and $5.0 \times 10^{-3} \pm 6.2 \times 10^{-5}$ mM, respectively.

To confirm that the enriched Li$^+$ originated from the feedwater and not from the Li$^+$ in the redox electrolyte, we measured the concentration of all the cations in the redox electrolyte (Supporting Information, Table S1). The Li$^+$ concentration in the redox electrolyte remains stable at a concentration of 9.35−9.37 mM, concluding that Li$^+$ in the recovery solution comes, indeed, just from the feedwater. Additionally, pH values of the redox electrolyte were continuously controlled to stay between 6 and 7 before and after the lithium recovery experiment. This is a crucial benefit for redox couples that can achieve better functioning with outstanding electrochemical stability.[25]

The LE-RFB system shows excellent selectivity of Li$^+$ toward other cations. The selectivity factors of $K_{Li/K}$, $K_{Li/Na}$, and $K_{Li/Mg}$

after the 5 h enrichment are 1.2×10^4, 4.1×10^5, and 5.0×10^5, respectively (Figure 2D). These extremely high selectivities yield a Li$^+$ purity of 93.5% in the extract. Mg^{2+}, which strongly influences the chemical precipitation of Li$^+$, is present at a ratio of 0.43% (Supporting Information, Figure S4). The absence of $K_{Li/Na}$ at 1 and 2 h is due to the concentration change at these two data points being less than the standard error.

Much higher Li$^+$ concentrations than in seawater can be found, for example, in brines. Subsequently, we used brine with a Li$^+$ concentration of 210 mM (see Table S2 in Supporting Information) to demonstrate that the LE-RFB system is suitable for lithium extraction from a low to a high concentration. When brine is used as the feedwater, the amount of Mg^{2+} (0.21%) in the extracts is similar. In contrast, more K$^+$ and Na$^+$ (accounting for 4.48 and 30.7%, respectively) migrate into the recovery solution (Supporting Information, Figure S5). This may indicate a gradual reduction in membrane selectivity over time due to the changes in structure, composition, and inhomogeneous mechanical stress.[26,27]

The lithium-extraction rate and energy consumption are other important parameters to evaluate the system's performance. The average lithium-extraction rate of LE-RFB is 0.04 mg/cm^2/h, which is comparable to other technologies for Li$^+$ extraction from seawater (Figure 3).[18,28−30] However, only 2.5 Wh is consumed for extracting 1 g of Li$^+$, which is at least 7 times lower than the electrodialysis-based technologies, which show a similar lithium purification effect (Figure 3). Considering the global average cost of the electricity fee (0.13 US$ per kWh), the energy cost of this system would at least save 2.2 US$ to extract 1 kg of lithium ions from seawater.

RESULTS AND DISCUSSION
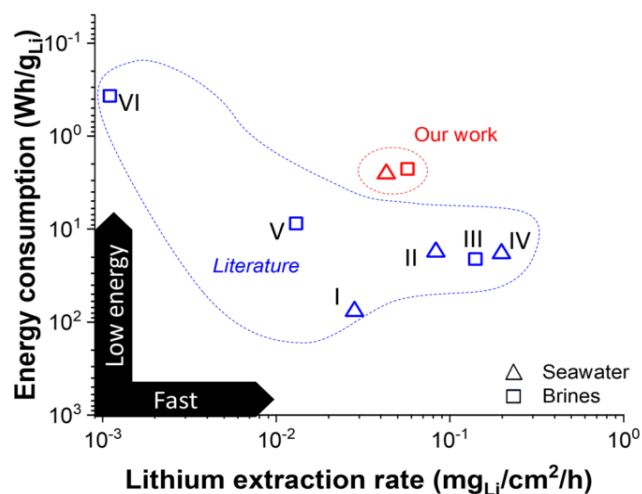
Figure 3. Comparison of lithium-extraction energy consumption and lithium-extraction rate for different extraction technologies. Data I, II, III, IV, V, and VI from refs 18, 29, 30, 28, 41, and 15, respectively.

This phenomenon is due to the low voltage of the system. Concerning lithium extraction from brines, our LE-RFB system is also energy efficient with the consumption of 2.3 Wh/g_{Li}, compared with nanofiltration (30−50 Wh/g_{Li})[13] or an electrodialysis system (2−50 Wh/g_{Li}).[31−33] The electrochemical ion pumping system is another popular electrochemical lithium-extraction system, generally utilizing $LiFePO_4$ or $LiMn_2O_4$ as the lithium-selective electrodes.[34] The energy consumption of this technology (0.1−3.0 Wh/g_{Li})[35] is lower than the LE-RFB system due to the energy recovery process. However, the ion pumping system could not accomplish continuous lithium extraction and suffers from switching between feedwater and recovery solution, which is time-consuming.

Herein, we present a brief technoeconomic analysis exploring the feasibility of LE-RFB for the industrial application (key economic price assumption shown in the Supporting Information, Table S3). Assuming an LE-RFB system with an effective area of 1 m², 18.4 kg of Li_2CO_3 could be produced per year (with a lithium-extraction rate of 0.04 mg/cm²/h), valued at 1256 US$. That means the system requires about 6 years to compensate for the initial investment cost and energy consumption (excluding the cost of the pump and electricity consumed by the pump). The key costs relate to pumping energy (1130 US$), which could be addressed by enhancing the lithium recovery rate by using thinner membranes/membranes with more rapid Li^+ transport.

Further improvements to the LE-RFB system will leverage synergetic advances in ceramic solid electrolyte technology. For example, very thin ceramic membranes of just 55 μm have been reported (meaning a higher lithium-ion extraction rate), although such thin membranes bring further requirements for an improved cell design to avoid mechanical failure.[18] Flexible hybrid organic−inorganic LAGP membranes have been synthesized, which could address the mechanical drawback of ceramic membranes, though the ion selectivity of hybrid membranes should be investigated.[36] The possible approaches for the improvement of our system could be but are not limited to optimizing the operation parameters,[37] using a LISICON membrane with higher Li^+ permeance and ionic

conductivity, optimized electrodes with high specific surface area and fluid permeability, and improved flow fields for uniform distribution of redox chemicals across the electrode surface.

In summary, we have demonstrated a continuous electrochemical lithium-extraction battery that utilizes flow redox electrolytes and LISICON membranes to mine lithium from aqueous solutions. Among the extracted ions from seawater, Li^+ predominates with a content of 93.5%. Using the redox pairs of $Fe[CN]_6^{3-}/Fe[CN]_6^{4-}$, the battery runs greenly, with no toxic byproducts, no safety concerns, and low energy consumption of 2.5 Wh/g_{Li}, which means less emission of CO_2. Furthermore, a LE-RFB system can utilize feedwater with varying chemical compositions. We see the potential of the LE-RFB system for lithium extraction from acidic leaching solution of spent lithium-ion batteries via hydrometallurgical processing.[38,39]

■ ASSOCIATED CONTENT

ⓢ Supporting Information

The Supporting Information is available free of charge at https://pubs.acs.org/doi/10.1021/acsenergylett.2c01746.

> Full description of the experimental methods, calculation methods, photographs, results from energy-dispersive X-ray spectroscopy, and supplemental lithium-extraction performance (PDF)

■ AUTHOR INFORMATION

Corresponding Authors

Zhaoyin Wen − *CAS Key Laboratory of Materials for Energy Conversion, Shanghai Institute of Ceramics, Chinese Academy of Sciences, Shanghai 200050, P. R. China; State Key Lab of High Performance Ceramics and Superfine Microstructure, Shanghai Institute of Ceramics, Chinese Academy of Sciences, Shanghai 200050, P. R. China;* ⓞ orcid.org/0000-0003-1698-7420; Email: zywen@mail.sic.ac.cn

Volker Presser − *INM - Leibniz Institute for New Materials, 66123 Saarbrücken, Germany; Department of Materials Science & Engineering, Saarland University, 66123 Saarbrücken, Germany; Saarene, Saarland Center for Energy Materials and Sustainability, 66123 Saarbrücken, Germany;* ⓞ orcid.org/0000-0003-2181-0590; Email: volker.presser@leibniz-inm.de

Authors

Lei Wang − *INM - Leibniz Institute for New Materials, 66123 Saarbrücken, Germany; Department of Materials Science & Engineering, Saarland University, 66123 Saarbrücken, Germany*

Stefanie Arnold − *INM - Leibniz Institute for New Materials, 66123 Saarbrücken, Germany; Department of Materials Science & Engineering, Saarland University, 66123 Saarbrücken, Germany*

Panyu Ren − *INM - Leibniz Institute for New Materials, 66123 Saarbrücken, Germany; Department of Materials Science & Engineering, Saarland University, 66123 Saarbrücken, Germany*

Qingsong Wang − *INM - Leibniz Institute for New Materials, 66123 Saarbrücken, Germany; Present Address: Bavarian Center for Battery Technology (BayBatt), University of Bayreuth, Universitätsstrasse 30, 95447 Bayreuth, Germany and Department of Chemistry, University of*

Bayreuth, Universitätsstrasse 30, 95447 Bayreuth, Germany; ◉ orcid.org/0000-0001-5879-8009

Jun Jin − *CAS Key Laboratory of Materials for Energy Conversion, Shanghai Institute of Ceramics, Chinese Academy of Sciences, Shanghai 200050, P. R. China*

Complete contact information is available at:
https://pubs.acs.org/10.1021/acsenergylett.2c01746

Notes

The authors declare no competing financial interest.

■ REFERENCES

(1) Greim, P.; Solomon, A. A.; Breyer, C. Assessment of lithium criticality in the global energy transition and addressing policy gaps in transportation. *Nat. Commun.* **2020**, *11* (1), 4570.

(2) Yang, S.; Zhang, F.; Ding, H.; He, P.; Zhou, H. Lithium metal extraction from seawater. *Joule* **2018**, *2* (9), 1648−1651.

(3) Diallo, M. S.; Kotte, M. R.; Cho, M. Mining critical metals and elements from seawater: Opportunities and challenges. *Environ. Sci. Technol.* **2015**, *49* (16), 9390−9399.

(4) Zhao, X.; Yang, H.; Wang, Y.; Sha, Z. Review on the electrochemical extraction of lithium from seawater/brine. *J. Electroanal. Chem.* **2019**, *850*, 113389.

(5) Um, N.; Hirato, T. Precipitation behavior of $Ca(OH)_2$, $Mg(OH)_2$, and $Mn(OH)_2$ from $CaCl_2$, $MgCl_2$, and $MnCl_2$ in $NaOH-H_2O$ solutions and study of lithium recovery from seawater via two-stage precipitation process. *Hydrometallurgy* **2014**, *146*, 142−148.

(6) Liu, C.; Tao, B.; Wang, Z.; Wang, D.; Guo, R.; Chen, L. Preparation and characterization of lithium ion sieves embedded in a hydroxyethyl cellulose cryogel for the continuous recovery of lithium from brine and seawater. *Chem. Eng. Sci.* **2021**, *229*, 115984.

(7) Harvianto, G. R.; Kim, S.-H.; Ju, C.-S. Solvent extraction and stripping of lithium ion from aqueous solution and its application to seawater. *Rare Metals* **2016**, *35* (12), 948−953.

(8) Yu, C.; Lu, J.; Dai, J.; Dong, Z.; Lin, X.; Xing, W.; Wu, Y.; Ma, Z. Bio-inspired fabrication of Ester-functionalized imprinted composite membrane for rapid and high-efficient recovery of lithium ion from seawater. *J. Colloid Interface Sci.* **2020**, *572*, 340−353.

(9) Liu, C.; Li, Y.; Lin, D.; Hsu, P.-C.; Liu, B.; Yan, G.; Wu, T.; Cui, Y.; Chu, S. Lithium extraction from seawater through pulsed electrochemical intercalation. *Joule* **2020**, *4* (7), 1459−1469.

(10) Joo, H.; Lee, J.; Yoon, J. Short review: Timeline of the electrochemical lithium recovery system using the spinel $LiMn_2O_4$ as a positive electrode. *Energies* **2020**, *13* (23), 6235.

(11) Santos, C.; La Mantia, F. Recent advances in reactor design and control for lithium recovery by means of electrochemical ion pumping. *Current Opinion in Electrochemistry* **2022**, *35*, 101089.

(12) Swain, B. Recovery and recycling of lithium: A review. *Sep. Purif. Technol.* **2017**, *172*, 388−403.

(13) Li, X.; Mo, Y.; Qing, W.; Shao, S.; Tang, C. Y.; Li, J. Membrane-based technologies for lithium recovery from water lithium resources: A review. *J. Membr. Sci.* **2019**, *591*, 117317.

(14) Joo, H.; Kim, S.; Kim, S.; Choi, M.; Kim, S.-H.; Yoon, J. Pilot-scale demonstration of an electrochemical system for lithium recovery from the desalination concentrate. *Environ. Sci.: Water Res. Technol.* **2020**, *6* (2), 290−295.

(15) Wang, L.; Frisella, K.; Srimuk, P.; Janka, O.; Kickelbick, G.; Presser, V. Electrochemical lithium recovery with lithium iron phosphate: what causes performance degradation and how can we improve the stability? *Sustainable Energy & Fuels* **2021**, *5* (12), 3124−3133.

(16) Zhang, H.; Ren, Y.; Wu, X.; Wang, N. An interface-modified solid-state electrochemical device for lithium extraction from seawater. *J. Power Sources* **2021**, *482*, 228938.

(17) Kim, N.; Su, X.; Kim, C. Electrochemical lithium recovery system through the simultaneous lithium enrichment via sustainable redox reaction. *Chemical Engineering Journal* **2021**, *420*, 127715.

(18) Li, Z.; Li, C.; Liu, X.; Cao, L.; Li, P.; Wei, R.; Li, X.; Guo, D.; Huang, K.-W.; Lai, Z. Continuous electrical pumping membrane process for seawater lithium mining. *Energy Environ. Sci.* **2021**, *14* (5), 3152−3159.

(19) Wang, Q.; Jin, J.; Wu, X.; Ma, G.; Yang, J.; Wen, Z. A shuttle effect free lithium sulfur battery based on a hybrid electrolyte. *Phys. Chem. Chem. Phys.* **2014**, *16* (39), 21225−21229.

(20) Xu, X.; Wen, Z.; Wu, X.; Yang, X.; Gu, Z. Lithium ion-conducting glass-ceramics of $Li_{1.5}Al_{0.5}Ge_{1.5}(PO_4)_3-xLi_2O$ (x = 0.0−0.20) with good electrical and electrochemical properties. *J. Am. Ceram. Soc.* **2007**, *90* (9), 2802−2806.

(21) Fu, L.; Teng, Y.; Liu, P.; Xin, W.; Qian, Y.; Yang, L.; Lin, X.; Hu, Y.; Kong, X.-Y.; Jiang, L.; et al. Electrochemical ion-pumping-assisted transfer system featuring a heterogeneous membrane for lithium recovery. *Chemical Engineering Journal* **2022**, *435*, 134955.

(22) Zhang, M.; Takahashi, K.; Uechi, I.; Takeda, Y.; Yamamoto, O.; Im, D.; Lee, D.-J.; Chi, B.; Pu, J.; Li, J.; et al. Water-stable lithium anode with $Li_{1.4}Al_{0.4}Ge_{1.6}(PO_4)_3-TiO_2$ sheet prepared by tape casting method for lithium-air batteries. *J. Power Sources* **2013**, *235*, 117−121.

(23) Zhang, P.; Wang, H.; Lee, Y.-G.; Matsui, M.; Takeda, Y.; Yamamoto, O.; Imanishi, N. Tape-cast water-stable NASICON-Type high lithium ion conducting solid electrolyte films for aqueous lithium-air batteries. *J. Electrochem. Soc.* **2015**, *162* (7), A1265−A1271.

(24) Nikodimos, Y.; Abrha, L. H.; Weldeyohannes, H. H.; Shitaw, K. N.; Temesgen, N. T.; Olbasa, B. W.; Huang, C.-J.; Jiang, S.-K.; Wang, C.-H.; Sheu, H.-S.; et al. A new high-Li^+-conductivity Mg-doped $Li_{1.5}Al_{0.5}Ge_{1.5}(PO_4)_3$ solid electrolyte with enhanced electrochemical performance for solid-state lithium metal batteries. *Journal of Materials Chemistry A* **2020**, *8* (48), 26055−26065.

(25) Luo, J.; Sam, A.; Hu, B.; DeBruler, C.; Wei, X.; Wang, W.; Liu, T. L. Unraveling pH dependent cycling stability of ferricyanide/ferrocyanide in redox flow batteries. *Nano Energy* **2017**, *42*, 215−221.

(26) Sun, Q.; He, L.; Zheng, F.; Wang, Z.; An Oh, S. J.; Sun, J.; Zhu, K.; Lu, L.; Zeng, K. Decomposition failure of $Li_{1.5}Al_{0.5}Ge_{1.5}(PO_4)_3$ solid electrolytes induced by electric field: A multi-scenario study using Scanning Probe Microscopy-based techniques. *J. Power Sources* **2020**, *471*, 228468.

(27) Paolella, A.; Zhu, W.; Xu, G.-L.; La Monaca, A.; Savoie, S.; Girard, G.; Vijh, A.; Demers, H.; Perea, A.; Delaporte, N.; et al. Understanding the reactivity of a thin $Li_{1.5}Al_{0.5}Ge_{1.5}(PO4)_3$ solid-state electrolyte toward metallic lithium anode. *Adv. Energy Mater.* **2020**, *10* (32), 2001497.

(28) Liu, G.; Zhao, Z.; He, L. Highly selective lithium recovery from high Mg/Li ratio brines. *Desalination* **2020**, *474*, 114185.

(29) Zhao, X.; Zhang, H.; Yuan, Y.; Ren, Y.; Wang, N. Ultra-fast and stable extraction of Li metal from seawater. *Chem. Commun.* **2020**, *56* (10), 1577−1580.

(30) Zhang, F.; Yang, S.; Du, Y.; Li, C.; Bao, J.; He, P.; Zhou, H. A low-cost anodic catalyst of transition metal oxides for lithium extraction from seawater. *Chem. Commun.* **2020**, *56* (47), 6396−6399.

(31) Guo, Z.-Y.; Ji, Z.-Y.; Chen, Q.-B.; Liu, J.; Zhao, Y.-Y.; Li, F.; Liu, Z.-Y.; Yuan, J.-S. Prefractionation of LiCl from concentrated seawater/salt lake brines by electrodialysis with monovalent selective ion exchange membranes. *Journal of Cleaner Production* **2018**, *193*, 338−350.

(32) Ji, P.-Y.; Ji, Z.-Y.; Chen, Q.-B.; Liu, J.; Zhao, Y.-Y.; Wang, S.-Z.; Li, F.; Yuan, J.-S. Effect of coexisting ions on recovering lithium from

RESULTS AND DISCUSSION

high Mg^{2+}/Li^+ ratio brines by selective-electrodialysis. *Sep. Purif. Technol.* **2018**, *207*, 1−11.

(33) Gmar, S.; Chagnes, A. Recent advances on electrodialysis for the recovery of lithium from primary and secondary resources. *Hydrometallurgy* **2019**, *189*, 105124.

(34) Calvo, E. J. Direct lithium recovery from aqueous electrolytes with electrochemical ion pumping and lithium intercalation. *ACS Omega* **2021**, *6* (51), 35213−35220.

(35) Battistel, A.; Palagonia, M. S.; Brogioli, D.; La Mantia, F.; Trócoli, R. Electrochemical methods for lithium recovery: A comprehensive and critical review. *Adv. Mater.* **2020**, *32* (23), 1905440.

(36) Safanama, D.; Adams, S. Flexible light-weight lithium-ion-conducting inorganic-organic composite electrolyte membrane. *ACS Energy Letters* **2017**, *2* (5), 1130−1136.

(37) Smith, K. C.; Dmello, R. Na-ion desalination (NID) enabled by Na-blocking membranes and symmetric na-intercalation: Porous-electrode modeling. *J. Electrochem. Soc.* **2016**, *163* (3), A530−A539.

(38) Kim, K.; Candeago, R.; Rim, G.; Raymond, D.; Park, A.-H. A.; Su, X. Electrochemical approaches for selective recovery of critical elements in hydrometallurgical processes of complex feedstocks. *iScience* **2021**, *24* (5), 102374.

(39) Vieceli, N.; Nogueira, C. A.; Guimarães, C.; Pereira, M. F. C.; Durão, F. O.; Margarido, F. Hydrometallurgical recycling of lithium-ion batteries by reductive leaching with sodium metabisulphite. *Waste Management* **2018**, *71*, 350−361.

(40) Weiss, M.; Weber, D. A.; Senyshyn, A.; Janek, J.; Zeier, W. G. Correlating transport and structural properties in $Li_{1+x}Al_xGe_{2-x}(PO_4)_3$ (LAGP) prepared from aqueous solution. *ACS Appl. Mater. Interfaces* **2018**, *10* (13), 10935−10944.

(41) Kim, S.; Kim, J.; Kim, S.; Lee, J.; Yoon, J. Electrochemical lithium recovery and organic pollutant removal from industrial wastewater of a battery recycling plant. *Environ. Sci.: Water Res. Technol.* **2018**, *4* (2), 175−182.

Supporting Information

Redox Flow Battery for Continuous and Energy-Effective

Lithium Recovery from Aqueous Solution

Lei Wang,[1,2] Stefanie Arnold,[1,2] Panyu Ren,[1,2]

Qingsong Wang[1,∥], Jun Jin[3], Zhaoyin Wen[3,4,*], Volker Presser,[1,2,5,*]

[1]   INM - Leibniz Institute for New Materials, D2 2, 66123, Saarbrücken, Germany

[2]   Department of Materials Science & Engineering, Saarland University, Campus D2 2, 66123, Saarbrücken, Germany

[3]   CAS Key Laboratory of Materials for Energy Conversion, Shanghai Institute of Ceramics, Chinese Academy of Sciences, Shanghai, 200050 P. R. China

[4]   State Key Lab of High Performance Ceramics and Superfine Microstructure, Shanghai Institute of Ceramics, Chinese Academy of Sciences, Shanghai, 200050 P. R. China

[5]   Saarene, Saarland Center for Energy Materials and Sustainability, Campus C4 2, 66123 Saarbrücken, Germany

*   Corresponding author's email: zywen@mail.sic.ac.cn volker.presser@leibniz-inm.de

[∥]   Current address: Bavarian Center for Battery Technology (BayBatt), University of Bayreuth, Universitätsstrasse 30, 95447 Bayreuth, Germany and Department of Chemistry, University of Bayreuth, Universitätsstrasse 30, 95447 Bayreuth, Germany

Experimental Methods

Synthesis and manufacturing of the LISICON membranes

Briefly, a mixture of precursors containing lithium carbonate Li_2CO_3, alumina Al_2O_3, germanium oxide GeO_2 (99.99%), and ammonium dihydrogen phosphate $(NH_4)H_2PO_4$ was dispersed in isopropanol and thoroughly mixed by planetary ball-milling with ZrO_2 balls for 6 h at 400 rpm. The well-mixed precursor was dried and calcinated at 800 °C for 6 h. Afterward, the synthesized powder was pressed into pellets (thickness of 0.8 mm) and sintered in a Pt crucible at 900 °C for 12 h. The obtained ceramic pellets were further polished before use.

Component and operation of the LE-RFB system

Two commercial symmetric carbon felt electrodes (discs with a diameter of 14 mm, SGL Carbon) were employed as the cathode and anode, contacting with the redox electrolyte channels. The redox electrolyte with the volume of 50 mL contained 280 mM $K_3[Fe(CN)_6]$, 280 mM $K_4[Fe(CN)_6]$, and 10 mM LiCl (to increase the lithium extraction rate), which is maintained in a brown bottle to avoid the deterioration of $K_3[Fe(CN)_6]$ when exposed to light. A 10 L tank of simulated seawater prepared according to the concentration of primary cations from the norm D1141-98 (Ref. [1]) of the American Society for Testing and Materials (**Table S2**) was applied as the feed water. The anions were chloride ions. The recovery solution consisted of 65 mL of 10 mM NaCl solution. The feed water and recovery solution were separated by an anion exchange membrane (diameter 50 mm, FAS-PET-130, Fumatech). These two solutions were separated from the redox electrolyte by the LISICON membrane (effective area 1.5 cm^2, thickness ~500 μm, geometric density 3.26 g/cm^3). All these three solutions were circulated from and back to the reservoirs through the peristaltic pump (Masterflex L/S) with a flow rate of 5 mL/min. The recovery solution and redox electrolyte reservoirs were constantly stirred at 400 rpm by magnetic stirring (Variomag, MULTIPOINT magnetic HP6). The setup of the LE-RFB system was operated in a climate chamber (Binder) at a constant temperature of 25±1 °C, shown in **Figure S1**. The LE-RFB was first charged at a constant current density of 1 mA/cm^2 limited to 0.6 V by VSP300 potentiostat/galvanostat (Bio-Logic). Subsequently, the battery was held at 0.6 V for 5 h. The concentration of all the cations in the recovery solution at various charging times was tested by an inductively coupled plasma optical emission spectrometer (ICP-OES, ARCOS FHX22, SPECTRO Analytical Instruments). The experiment of recovering lithium from brines water was complemented with the same LISICON membranes, and the other experimental conditions were the same except for the composition of the feed water (100 mL, prepared according to Ref. [2]) and the volume of recovery solution (75 mL). The chemical composition of the redox electrolyte and of the seawater and brine is provided in **Table S1** and **Table S2**, respectively.

Characterization

X-ray diffraction (XRD) analysis was carried out via a D8 Advanced diffractometer (Bruker AXS) with a copper X-ray source (Cu-K$_\alpha$, λ = 1.5406 Å; 40 kV, 40 mA). The samples were examined in the range of 10° to 70° 2θ and with 1 s per step: Scanning electron microscopy (SEM) was conducted using a ZEISS Gemini 500 system at acceleration voltages of 1-3 kV. A small piece of the LISICON membrane was vertically mounted on an aluminum sample holder and analyzed without the aid of an additional, conductive sputter coating. Energy-dispersive X-ray spectroscopy (EDX) spectra were obtained with an in-lens secondary electron (SE) detector at 15 kV employing an X-Max Silicon Detector from Oxford Instruments attached to the electron microscope.

Ionic conductivity measurement

To measure the ionic conductivity of ceramic pellets, we applied a thin layer via gold sputtering as ion conducting blocking electrode. The electrochemical impedance spectroscopy was measured in the frequency range of 100 kHz to 0.1 Hz with a perturbation voltage of 10 mV.

Calculations

The extraction ratio of all the cations is calculated according to **Equation S1**.

$$Extraction\ ratio\ (\%) = \frac{\Delta c_x}{\Delta c_{all}} \times 100 \qquad \textbf{(Eq. S1)}$$

where, Δc_x and Δc_{all} are the concentration change of x (x = Li$^+$, K$^+$, Mg^{2+} or Na$^+$) and all the cations in the recovery solution.

We also calculated the selectivity factors ($K_{Li/M}$) between Li$^+$ and other cations M (M = Na$^+$, K$^+$, Mg^{2+}), which involves the initial concentration of cations, according to the **Equation S2**

$$K_{Li/M} = \frac{\Delta c_{Li}}{\Delta c_M} \times \frac{c_{m-initial}}{c_{Li-initial}} \qquad \textbf{(Eq. S2)}$$

where, Δc_{Li} and Δc_M are the concentration change of Li$^+$ and M in the recovery solution, respectively. $c_{m-initial}$ and $c_{Li-initial}$ are the concentration of M and Li$^+$ in the initial feed water, respectively.

The lithium retraction rate and energy consumption are also important indexes to evaluate the system's performance, calculated by **Equation S3** and **Equation S4**, respectively.

$$Lithium\ extraction\ rate = \frac{\Delta c_{Li} \times V}{t \times A \times M_{Li}} \qquad \textbf{(Eq. S3)}$$

where Δc_{Li} is the concentration change of Li$^+$ in the recovery solution, V is the volume, t is the time, A the effective area of LISICON membrane, M_{Li} is the molar mass of Li.

$$Energy\ consumption = \frac{E}{V \times \Delta c_{Li} \times M_{Li}} \qquad \textbf{(Eq. S4)}$$

where E is the consumed electrical energy during the charging operation, Δc_{Li} is the concentration change of Li$^+$ in the recovery solution, V is the volume, M_{Li} is the molar mass of Li

S3

Supporting Figures
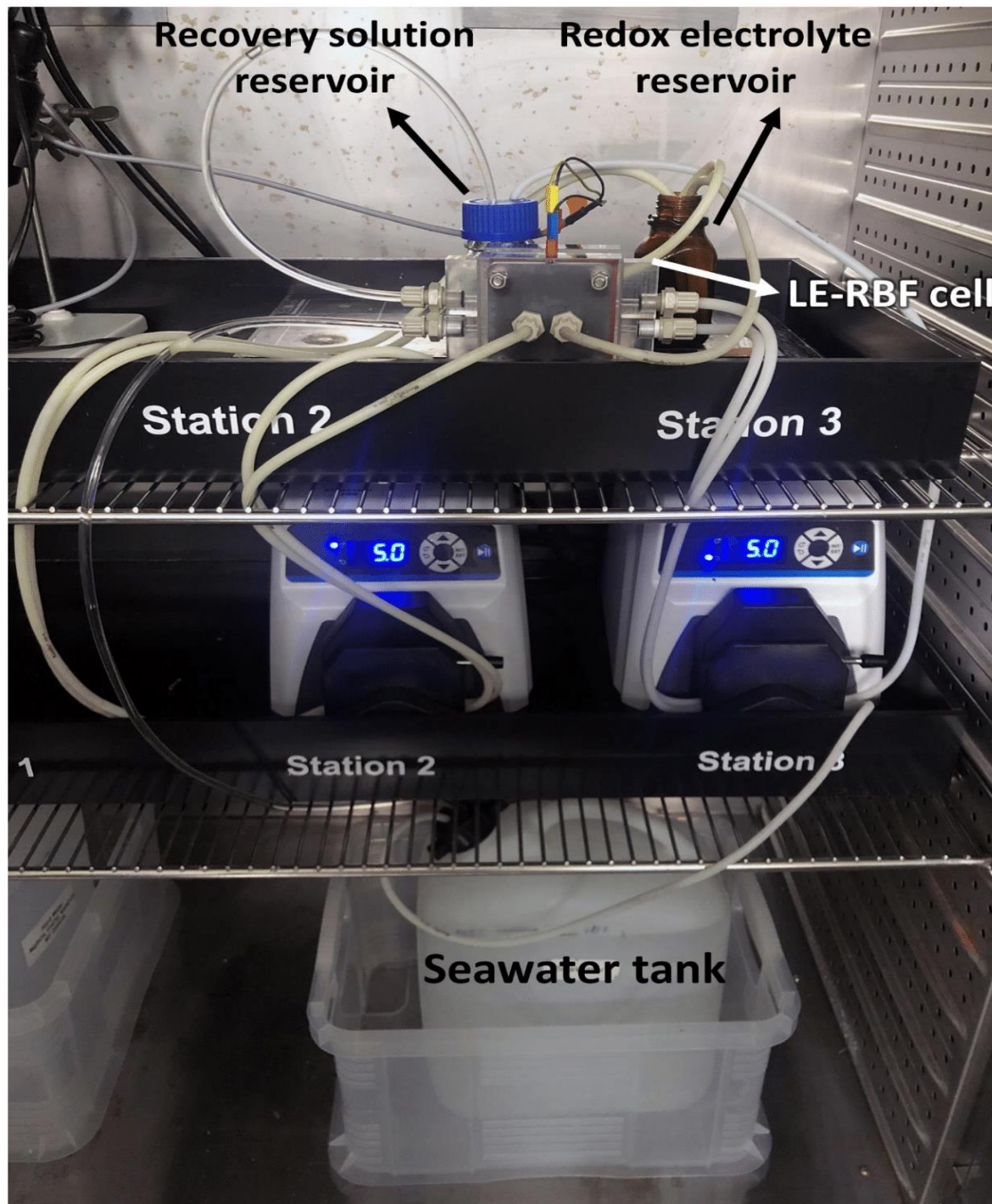
Figure S1:   Photograph of the setup of lithium-extraction redox flow battery system.
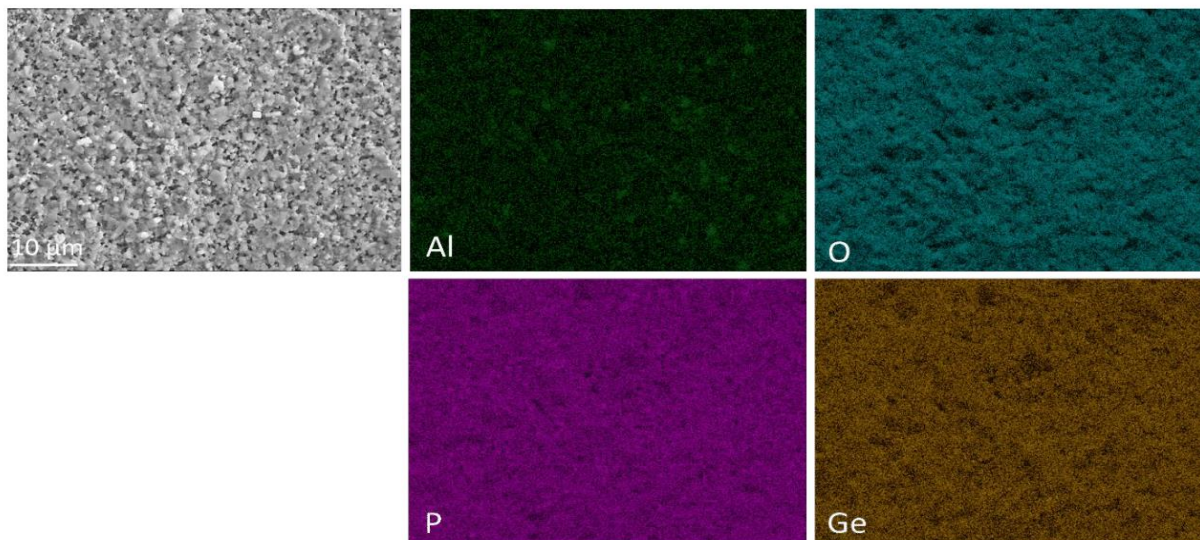
Figure S2: A cross-sectional scanning electron micrograph of the LISICON membrane and corresponding EDX mapping of Al, Ge, P, and O. All elemental maps show the same area (with same resolution) as the electron micrograph.
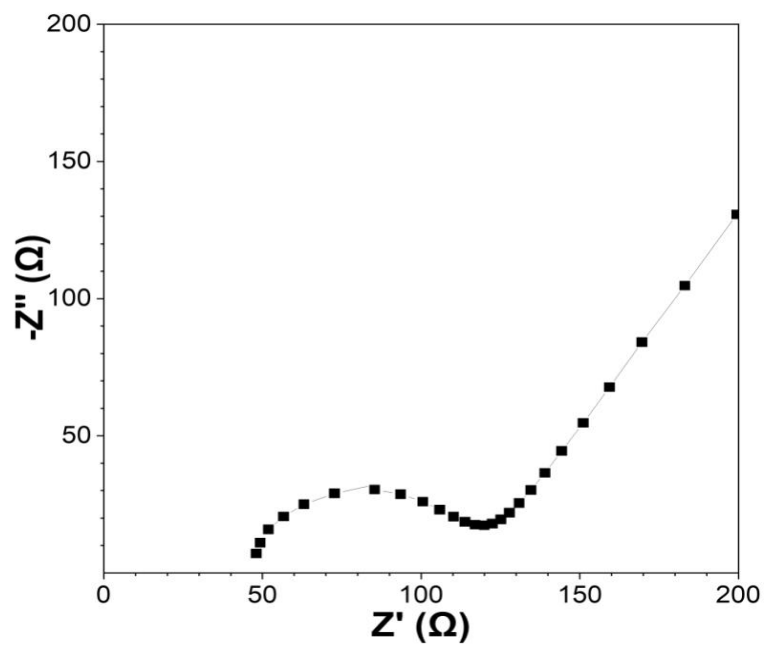
Figure S3: The electrochemical impedance spectrum of the LAGP membrane with an area of 323.5 mm^2.
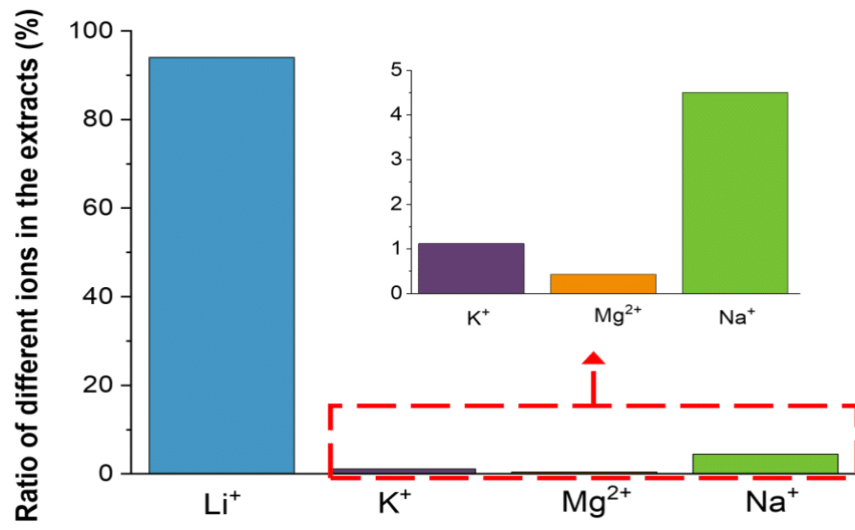
Figure S4: The percentage of all cations in the cations extracted from seawater. Insert: magnification of column graph for the K^+, Mg^{2+}, and Na^+.
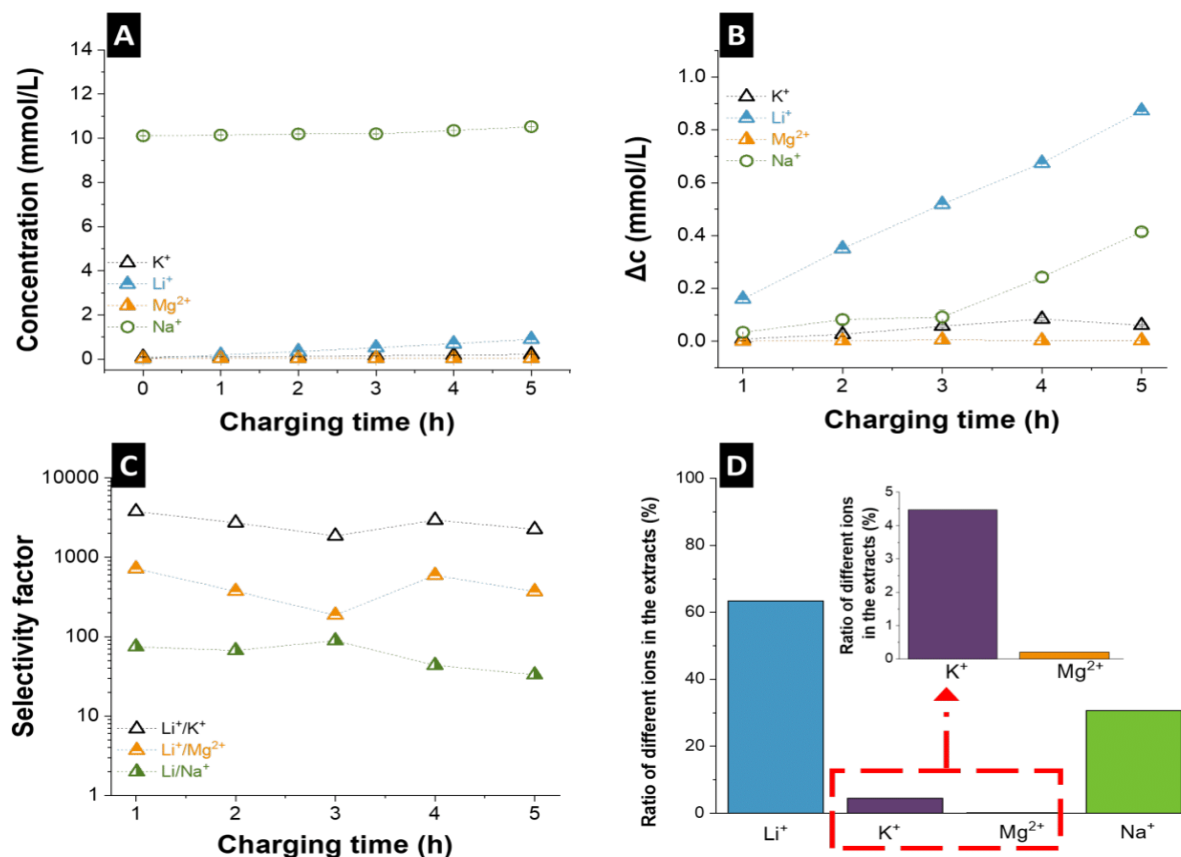
Figure S5: Lithium extraction from seawater by lithium-extraction redox flow battery: (A) the concentration and (B) concentration change of cations in the recovery solution at different times; (C) the selectivity factors between Li⁺ and other cations; (D) The percentage of all cations in the cations extracted from brine. Inset: magnification of column graph for the K⁺ and Mg²⁺.

Supporting Tables

Table S1:   The concentration of main cations and Li^+ in the redox electrolyte in the experiment for lithium extraction from seawater. No calcium was detected.

Concentration (mM)	Initial	After
Li^+	9.35±0.01	9.37±0.01
Na^+	0.95±0.01	1.13±0.01
K^+	2095.2±3.8	2119.4±2.1
Ca^{2+}	-	-
Mg^{2+}	$3.6 \cdot 10^{-3} \pm 3.3 \cdot 10^{-5}$	$1.0 \cdot 10^{-2} \pm 4.8 \cdot 10^{-5}$
Fe^{3+}	571.7±0.6	579.8±0.9
pH	6.75	6.25

Table S2:   The concentration of main cations and Li^+ in the simulated seawater (Ref. [1]) and brine water (Ref. [2]).

Concentration (mM)	Seawater	Brine water
Li^+	0.024	210
Na^+	477.5	3300
K^+	9.3	460
Ca^{2+}	10.5	7.75
Mg^{2+}	54.6	400

S8

236

Table S3: Key economic and technical price assumption for a simplified techno-economic analysis of LE-RFB system with an effective area of 1 m^2.

Price assumption		Economic assumptions		Technical assumptions
LISICON membrane ($/m^2) Ref. [3]	461	Depreciation (% yr^{-1} of fixed capital)	10	1.1 times as the effective area
Anion exchange membrane ($/m^2)	780	Depreciation (% yr^{-1} of fixed capital)	5	1.5 times as the effective area
Graphite block ($/kg)	3	Processing fee (%)	20	
PMMA ($/kg)	4	Processing fee (%)	20	
Carbon felt ($/m^2)	30			
Other components of the LE-RFB system ($)	200			Including gasket, O-rings, screws
Tax (%)	19			
Na$_2$CO$_3$ ($/kg) Ref. [3]	0.3			
Li$_2$CO$_3$ ($/kg)*	68			
Electricity ($/kWh)**	0.13			The power of the pump is 1 kW

* https://www.chemanalyst.com/Pricing-data/lithium-carbonate-1269

** https://www.globalpetrolprices.com/electricity_prices

S9

Supporting References

(1) ASTM. *D1141-98 Standard Practice for the Preparation of Substitute Ocean Water*; 2013. Access date: 14.09.2022

(2) Liu, G.; Zhao, Z.; He, L. Highly selective lithium recovery from high Mg/Li ratio brines. *Desalination* **2020**, *474*, 114185. DOI: 10.1016/j.desal.2019.114185.

(3) Hu, J.; Jiang, Y.; Li, L.; Yu, Z.; Wang, C.; Gill, G.; Xiao, J.; Cavagnaro, R. J.; Kuo, L.-J.; Asmussen, R. M.; et al. A Lithium Feedstock Pathway: Coupled Electrochemical Extraction and Direct Battery Materials Manufacturing. *ACS Energy Letters* **2022**, *7* (8), 2420-2427. DOI: 10.1021/acsenergylett.2c01216.

4.9 Recycling and second life of MXene electrodes for lithium-ion batteries and sodium-ion batteries

Yunjie Li[1,2], Stefanie Arnold[1,2], Samantha Husmann[1], and Volker Presser[1,2,3]

[1] INM - Leibniz Institute for New Materials, 66123 Saarbrücken, Germany

[2] Department of Materials Science and Engineering, Saarland University, 66123 Saarbrücken, Germany

[3] Saarene, Saarland Center for Energy Materials and Sustainability, Campus C4 2, 66123 Saarbrücken, Germany

Own Contribution:

Investigation, writing-review & editing.
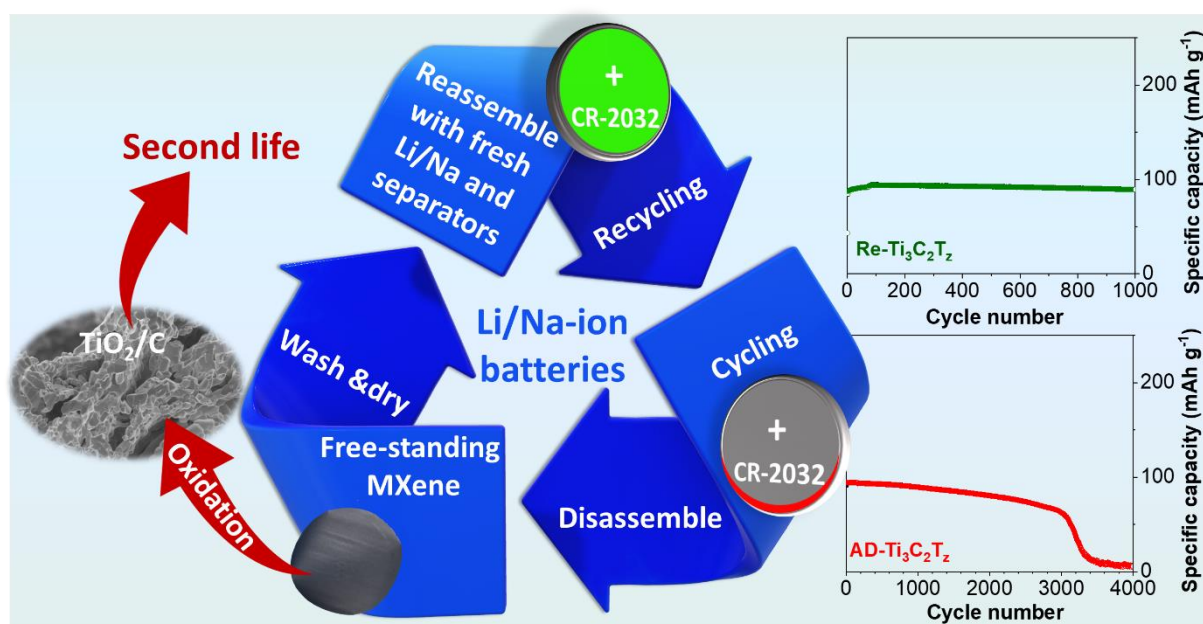
Contents lists available at ScienceDirect

Journal of Energy Storage

journal homepage: www.elsevier.com/locate/est
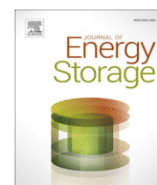
Research papers

Recycling and second life of MXene electrodes for lithium-ion batteries and sodium-ion batteries

Yunjie Li [a,b], Stefanie Arnold [a,b], Samantha Husmann [a], Volker Presser [a,b,c,*]

[a] INM - Leibniz Institute for New Materials, Campus D2.2, 66123 Saarbrücken, Germany
[b] Department of Materials Science and Engineering, Saarland University, Campus D2.2, 66123 Saarbrücken, Germany
[c] Saarene - Saarland Center for Energy Materials and Sustainability, Campus D4.2, 66123 Saarbrücken, Germany

ARTICLE INFO

ABSTRACT

The fast growth of electric vehicles and electronic devices produces a mounting number of spent batteries which have reached their end of life. Therefore, it is essential to find a sustainable and efficient approach to battery recycling. Conventional recycling via high-temperature decomposition of the active components in the electrode material into elements level has the disadvantages of cumbersome operation, environmentally unfriendly, and high cost. Herein, one type of MXene material, annealed delaminated $Ti_3C_2T_z$ (AD-$Ti_3C_2T_z$) electrodes, obtained by vacuum-assisted filtration and annealing processes, was directly used as free-standing anodes for both lithium-ion batteries and sodium-ion batteries without the use of binder or carbon additives. Electrochemical analysis showed that the non-diffusion-controlled redox reaction dominates the electrochemical behavior of the AD-$Ti_3C_2T_z$ electrode. Furthermore, the AD-$Ti_3C_2T_z$ electrode exhibits good electrochemical performance without adding conductive carbon in lithium-ion and sodium-ion batteries. For example, the lithium storage capacity was 89 mAh g^{-1} after 2000 cycles at a specific current of 1 A g^{-1}. The sodium storage capacity is 108 mAh g^{-1} and 71 mAh g^{-1} at 0.02 A g^{-1} and 2 A g^{-1}, respectively. After AD-$Ti_3C_2T_z$ electrodes reach the end of their battery life, facile direct recycling processes were employed to recover the electrodes and the capacity recovery rate is above 90 %. Besides, the cycled MXene electrodes can be easily oxidized into TiO_2/C hybrids with adjustable carbon content by changing the heat-treatment temperature in CO_2 flow. The obtained TiO_2/C could be widely applied in batteries and the electrocatalysis field, which realizes the second life of cycled MXene.

1. Introduction

Among energy storage devices, lithium-ion batteries (LIBs) dominate in electric vehicles, grid energy storage, and portable electronic devices due to their high energy and power density, long cycle life, and reduced environmental impact [1–3]. However, the limited supply of lithium and geographically uneven distribution cannot continuously meet the ever-increasing demand for energy storage devices [4]. It is necessary to develop another battery system to alleviate the excess demand for LIBs. Sodium-ion batteries (SIBs), which have similar working principles to LIBs, have recently attracted significant attention due to the high abundance and low cost of sodium [5]. In addition, sodium-ion batteries do not require copper current collectors; instead, aluminum current collectors can be used, further reducing the cost and mass of SIB devices [6]. The configuration of SIBs shares so many similarities with LIB that the industrial manufacturing line of LIBs can be adopted for SIBs with

limited modifications [7]. Due to the higher mass and larger radii size of Na$^+$ ions compared to Li$^+$ ions, SIBs deliver sluggish kinetics and lower energy density than LIBs [8]. The coordinated development and complementary cooperation of LIBs and SIBs can significantly enrich the selection of available batteries in different application scenarios. For applications that do not require high energy density but are more sensitive to cost, SIBs can be selected; for scenarios requiring high energy density, LIBs can be selected. Electrode materials, especially anodes, play essential roles in determining the electrochemical performances, like the batteries' reversible capacity, energy density, and power density [9]. Yet, SIB technology and LIB with enhanced energy storage performance mandate the development of novel electrode materials [10] that ideally also take end-of-life and recycling strategies into consideration [11,12].

MXenes, a family of two-dimensional (2D) transition metal carbides, carbonitrides, and nitrides were first obtained and developed by Naguib

et al. in 2011 [13]. $Ti_3C_2T_z$ (T_z = terminal groups, like —O, —OH, and —F), one typical MXene, shows good conductivity, high specific surface area, and abundant active sites and has been widely used in the fields of electrochemical energy storage, like LIBs, SIBs, supercapacitors, and Li—S batteries [14–18]. For example, oligolayered $Ti_3C_2T_z$ MXene obtained by delaminating multilayered $Ti_3C_2T_z$ using tetramethyl-ammonium hydroxide (TMAOH) showed a reversible lithium storage capacity of 330 mAh g^{-1} at 1.0 A g^{-1} after 800 cycles and a sodium storage capacity of 280 mAh g^{-1} at 0.5 A g^{-1} after 500 cycles [14]. Cai et al. [19] reported that controlling the surface terminal functional groups of $Ti_3C_2T_z$ via annealing could effectively improve initial Coulombic efficiency, stability, and suppress the thermal runaway process of LIBs.

After these electrode materials reach their cycle life, recycling the spent electrode materials is necessary [20]. It can reduce the environmental impact and save metal mineral resources, which is conducive to sustainable development [21]. There is also an increasing regulatory mandate on overall battery recycling and the use of recycled materials for the fabrication of new cells around the world [22]. Typically, electrodes for commercial lithium-ion batteries are prepared using the slurry casting method, in which active materials, binder, and conductive additives are mixed to form an electrode slurry. Then the slurry is cast on a metal current collector for further processing into battery cells. This fabrication technique will decrease the gravimetric energy density of the cells and introduce complicated processes to recycle the used cells. Besides, the binder and solvent used in the slurry preparation typically consist of toxic and/or costly materials, like polyvinylidene fluoride and *N*-methyl-2-pyrrolidone. To reduce the dead mass of inactive components in the battery and increase its gravimetric energy density, increase environmental friendliness, and simplify the recycling process of the battery after cycling, it is necessary to do more research on advanced free-standing electrodes without the use of binder, conductive additives, and current collectors. More and more, dry electrode processing has emerged and has become a new industry standard. This drastically reduces the energy costs in battery fabrication but still mandates the use of binder and conductive additives for common electrode materials [23].

MXene films can be obtained by vacuum-assisted filtration, spray coating, spin coating, printing, or rolling of delaminated MXene solution [24]. Among fabrication techniques of the films, vacuum-assisted filtration is widely used to prepare free-standing MXene electrodes and their hybrids with other nanomaterials with controlled thickness for batteries and capacitors [24–26]. However, to the best of our knowledge, until now, there has been no published work on the recovery and reuse of MXene electrode materials from spent batteries. We, however, see a strong contribution that MXene can play in the transition toward sustainable and circular use of electrode materials. $Ti_3C_2T_z$, the most common and widely used MXene to date, is a good model that can study the recycling and reuse of spent MXene electrodes, therefore facilitating the broad application of investigated recycling and reusing methods to other MXene materials or even 2D materials. Composed of titanium and carbon, the material does not depend on critical elements (such as nickel or cobalt), and SIB based on MXene also eliminate the dependency on lithium ore.

This work employs free-standing delaminated $Ti_3C_2T_z$ (De-$Ti_3C_2T_z$) electrodes prepared by vacuum-assisted filtration of TMAOH delaminated commercial $Ti_3C_2T_z$ MXene and annealed delaminated (AD-$Ti_3C_2T_z$) electrodes obtained by annealing at 400 °C as anode materials for LIBs and SIBs. In addition, for the first time, we investigated the structure and component change of cycled AD-$Ti_3C_2T_z$ electrodes from spent batteries. Besides, the cycling performance of recycled AD-$Ti_3C_2T_z$ electrodes could still be recovered by simply changing fresh lithium or sodium foils and separators. Finally, cycled AD-$Ti_3C_2T_z$ electrodes could also be oxidized into TiO_2/C under CO_2, and the carbon content could be modified by changing the heat treatment temperature. This work aims to give insight into the simple recycling of MXene-based free-standing electrodes and further applications by oxidizing spent MXene electrodes into transition metal oxides. Our recycling concept also avoids any

pyrometallurgical or hydrometallurgical processing as commonly used in present-day lithium-ion battery recycling and contributes toward the little explored research on sodium-ion battery recycling.

2. Experimental

2.1. Preparation of De-$Ti_3C_2T_z$ electrodes and AD-$Ti_3C_2T_z$ electrodes

200 mg of pristine $Ti_3C_2T_z$ (300 mesh, Laizhou Kai Kai Ceramic Materials), 8 mL of tetramethylammonium hydroxide aqueous solution (TMAOH, 1 M, Sigma-Aldrich), and 80 mL of Ar degassed H_2O were placed into a 100 mL bottle filled with Ar and stirred at room temperature for 40 h. After that, the mixture was centrifuged and washed with degassed H_2O three or four times until the pH value reached 7 to remove excess TMAOH. The obtained black precipitate was dispersed in H_2O named De-$Ti_3C_2T_z$ (~2 mg mL) for future use. Vacuum filtration of 25 mL of the above solution through the PVDF membrane (0.22 μm, Durapore) yielded De-$Ti_3C_2T_z$ electrodes that were easily peeled off after vacuum-drying at 80 °C overnight.

The electrodes were punched into 12 mm discs and annealed at 400 °C (heating rate of 5 °C min^{-1}) for 20 min under Ar flow (100 mL min^{-1}) to obtain AD-$Ti_3C_2T_z$ electrodes. The De-$Ti_3C_2T_z$ and AD-$Ti_3C_2T_z$ electrodes were stored in the glove box filled with Ar (MBraun Labmaster 130, O_2 < 0.1 ppm, H_2O < 0.1 ppm) for future use.

2.2. Materials characterizations

The crystal structure of obtained MXenes was studied by X-ray diffractometer (XRD, Bruker AXS, D8 Advance) using Cu-Kα (λ = 0.154 nm, 40 kV, 40 mA) as the radiation source. The samples were examined in the range of 3° to 70° 2θ and with 0.02°2θ s^{-1} per step. A Renishaw inVia Raman Microscope equipped with an Nd–YAG laser with an excitation wavelength of 532 nm, a power of 0.05 mW at the surface, using an objective lens with a numeric aperture of 0.75 within 110–2000 cm^{-1} was employed. Five different spots from each sample were recorded with 5 accumulations and 30 s acquisition time. The morphology of the samples and elemental distribution and ratio were characterized by a field emission scanning electron microscope (SEM, Zeiss GeminiSEM 500) equipped with an energy-dispersive X-ray spectrometer (EDS, Oxford MAX detectors). The accelerating voltages for SEM and EDS tests were 1 kV and 15 kV, respectively. The samples were fixed on a steel sample holder using copper adhesive tape and analyzed without an additional conductive sputter coating.

2.3. Electrochemical measurements

The electrochemical characterization of free-standing De-$Ti_3C_2T_z$ and AD-$Ti_3C_2T_z$ electrodes were investigated by assembling CR2032 coin cells. Typically, the electrodes had a thickness of 30–50 μm and a mass loading of 4.0 ± 1 mg cm^{-2} and were used as working electrodes. Discs with a diameter of 14 mm of lithium or 11 mm of sodium were used as counter and reference electrodes for LIBs and SIBs, respectively. We used one layer of glass fiber (GF/D, Whatman) cut as a disc with a diameter of 18 mm adjacent to the working electrode. Another layer adjacent to the Li or Na disc was cut with a diameter of 18 mm from either Celgard 2325 or glass fiber (GF/F, Whatman), respectively. 1 M lithium hexafluorophosphate ($LiPF_6$) in ethylene carbonate (EC) and dimethyl carbonate (DMC) (volume ratio 1:1) (Sigma Aldrich) was used as an electrolyte for LIBs and 1 M sodium perchlorate ($NaClO_4$, >99 % purity, Alfa Aesar) dissolved in the mixed solvent of EC (≥99 % purity, Sigma Aldrich), and DMC (≥99 % purity, Sigma Aldrich) in a volume ratio of 1:1 and 5 vol% fluoroethylene carbonate (FEC, 99 % purity, Sigma Aldrich) was used as an electrolyte for SIBs. $NaClO_4$ salt was dried in the vacuum oven at 80 °C for 48 h before use. The batteries were put inside a climate chamber (Binder) at a constant temperature of 25 ± 1 °C and connected to a multichannel potentiostat (Bio-Logic VMP3) for all

2

241

RESULTS AND DISCUSSION

electrochemical measurements. Cyclic voltammetry and galvanostatic charge/discharge tests were conducted in a potential window of 0.01–3 V vs. Na^+/Na and 0.01–3 V vs. Li^+/Li. Electrochemical impedance spectroscopy (EIS) was tested in a frequency range of 10 kHz to 10 mHz.

2.4. Battery recycling

After reaching the end of life (EOL-), defined as a specific capacity below 20 mAh g^{-1}, the cells were disassembled in the glove box. The cycled AD-$Ti_3C_2T_z$ MXene electrodes were removed gently, cleaned with DMC solvent to remove the remaining electrolyte salt without damaging the structure, and dried inside the glove box at room temperature for several hours. The treated cycled electrodes were named as EOL-$Ti_3C_2T_z$ and used as working electrodes again, together with fresh lithium/sodium foil and separators following the same coin cell assembling steps as depicted in *Section 2.3* to reassembly into LIBs or SIBs (named *Re*-$Ti_3C_2T_z$ batteries). The electrochemical test conditions of Re-$Ti_3C_2T_z$ batteries were the same as those of AD-$Ti_3C_2T_z$ batteries.

2.5. Battery upcycling (electrode oxidation)

The EOL-$Ti_3C_2T_z$ was oxidized in CO_2 flow (50 mL min^{-1}) with a heating rate of 180 °C min^{-1} and a holding time of 1 h at 700 °C or 900 °C. The obtained samples were named TiO$_2$/C-700 or TiO$_2$/C-900 for heat-treated at 700 °C or 900 °C, respectively.

3. Results and discussion

3.1. Structure and morphology characterization

The fabrication process of $Ti_3C_2T_z$ electrodes is shown in Fig. 1. The De-$Ti_3C_2T_z$ suspension was prepared via delaminating pristine $Ti_3C_2T_z$ MXene powder using TMAOH and subsequent vacuum filtration to obtain the De-$Ti_3C_2T_z$ electrodes. The AD-$Ti_3C_2T_z$ electrodes were obtained by annealing the De-$Ti_3C_2T_z$ electrodes at 400 °C for 20 min under an Ar atmosphere to remove some terminal groups and absorbed water. As observed in the thermogram shown in *Supporting Information* Fig. S1A, the pristine $Ti_3C_2T_z$ have no significant change in mass upon annealing in Argon. However, the delamination process leads to a significant amount of incorporated water as well as TMA^+ ions and surface groups, accounting for nearly 30 mass% of the De-$Ti_3C_2T_z$ sample. Fig. 2A demonstrates the obtained XRD patterns of pristine $Ti_3C_2T_z$ powder, De-$Ti_3C_2T_z$ electrode, and AD-$Ti_3C_2T_z$ MXene electrode. For pristine $Ti_3C_2T_z$ MXene, two intense peaks located at 8.85° 2θ (9.97 Å) and 18.12° 2θ correspond to the (002) and (004) planes, respectively. After the delamination process, the (002) peak of De-$Ti_3C_2T_z$ shifts to 6.14° 2θ, corresponding to an increased (002) spacing to 14.38 Å. The diameter of TMA^+ cations is around 5 Å, the diameter of H_2O molecule is 2.75 Å, and the thickness of $Ti_3C_2T_z$ nanosheets is about 7.5 Å,

indicating the increased interlayer spacing is due to the intercalation of TMA^+ and H_2O into $Ti_3C_2T_z$ MXene layers [27]. The interlayer spacing of the (002) plane of AD-$Ti_3C_2T_z$ decreases to 9.95 Å due to removing the physically absorbed water, some terminal functional groups, and TMA^+ cations during the annealing process [28], and the intensity of higher-order (00 *l*) peaks become stronger compared to pristine $Ti_3C_2T_z$ and De-$Ti_3C_2T_z$.

Raman spectroscopy was further used to investigate the microstructures of as-prepared $Ti_3C_2T_z$ MXene electrodes, as shown in Fig. 2B. Between 110 and 800 cm^{-1}, the Raman spectrum of all $Ti_3C_2T_z$ MXene shows several features. The sharp A_{1g}(Ti, C, O) band around 210 cm^{-1} represents the out-of-plane vibrations of titanium, carbon, and functional groups of the flake as a whole. Several broad $E_g(T_z)$ bands located between 215 cm^{-1} to 490 cm^{-1} are assigned to in-plane vibrations of functional groups. The region between 520 cm^{-1} to 660 cm^{-1} partly relates to the out-of-plane vibrations of Ti-T_z (A_{1g}(Ti-T_z)). The region 680 cm^{-1} to 800 cm^{-1} represents out-of-plane (A_{1g}(C)) vibrations of carbon [29]. For pristine $Ti_3C_2T_z$, the A_{1g}(Ti, C, O) band, A_{1g}(Ti-T_z) band, and A_{1g}(C) band are located at 213 cm^{-1}, 624 cm^{-1}, and 703 cm^{-1}, respectively [19,30]. After the TMAOH intercalant is introduced, the A_{1g}(Ti, C, O) band of De-$Ti_3C_2T_z$ shifts to lower wavenumbers (208 cm^{-1}), while the A_{1g}(C)band shifts to higher wavenumbers (741 cm^{-1}). The shifting of the A_{1g}(Ti, C, O) peak indicates the decreasing ordering of Ti and C layers and the weakening of coupling between flakes. The shifting of A_{1g}(C) relates to the increasing interlayer spacings caused by TMA^+ cations [29]. However, once the annealing process is employed after TMAOH delamination, the A_{1g}(Ti, C, O) band and A_{1g}(C) band of AD-$Ti_3C_2T_z$ shift to 212 cm^{-1} and 739 cm^{-1}, respectively. Stacking Ti and C layers and decreasing interlayer spacings can explain these shifts. For De-$Ti_3C_2T_z$ and AD-$Ti_3C_2T_z$, compared to pristine $Ti_3C_2T_z$, the A_{1g}(Ti-T_z) band shifts to lower wavenumbers due to the removal of the functional groups during the delamination and annealing process.

As shown in *Supporting Information*, Fig. S2, the broad two peaks located between 1200 cm^{-1} to 1700 cm^{-1} are attributed to the D-band and G-band of carbon (as present in the material via the X-layers in MXene) [19]. The increased intensity of carbon G-band at ca. 1600 cm^{-1} after annealing relates to the higher crystallinity of free carbon in the MXene due to thermal treatment.

As shown in Fig. 3A, pristine $Ti_3C_2T_z$ particles show an open-meshed nanolamellar structure with an average diameter of about 300 mesh. The scanning electron micrograph of De-$Ti_3C_2T_z$ in Fig. 3B shows the nanolayered structure. As shown in Fig. 3C,E, the surfaces of De-$Ti_3C_2T_z$ and AD-$Ti_3C_2T_z$ electrodes are smooth. Fig. 3D,F exhibit the side views of the De-$Ti_3C_2T_z$ and AD-$Ti_3C_2T_z$ electrodes with a thickness of ca. 40 μm and ca. 35 μm, respectively, which means the annealing process will slightly decrease the thickness of the electrodes. The atomic ratios obtained by the EDS test are shown in *Supporting Information*, Table S1. The atomic ratios of Al and F to Ti are 0.02:3 (Al/Ti) and 1.11:3 (F/Ti) in De-$Ti_3C_2T_z$ much lower than that of pristine $Ti_3C_2T_z$ (0.37:3 (Al/Ti) and
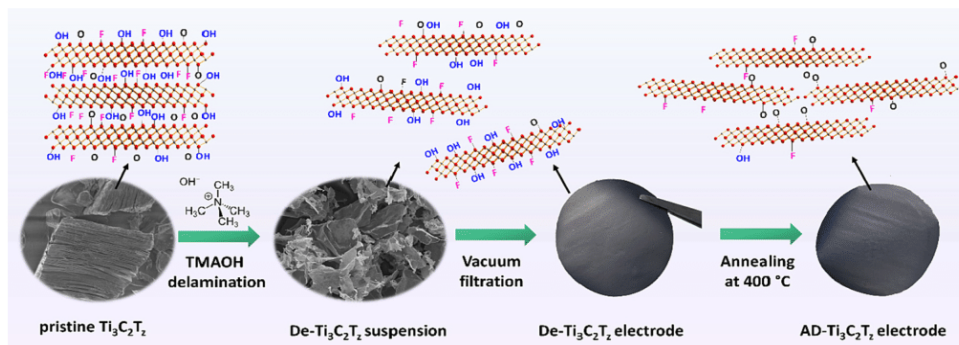
Fig. 1. Schematic illustration of the preparation process of De-$Ti_3C_2T_z$ electrodes and AD-$Ti_3C_2T_z$ electrodes.

3

242
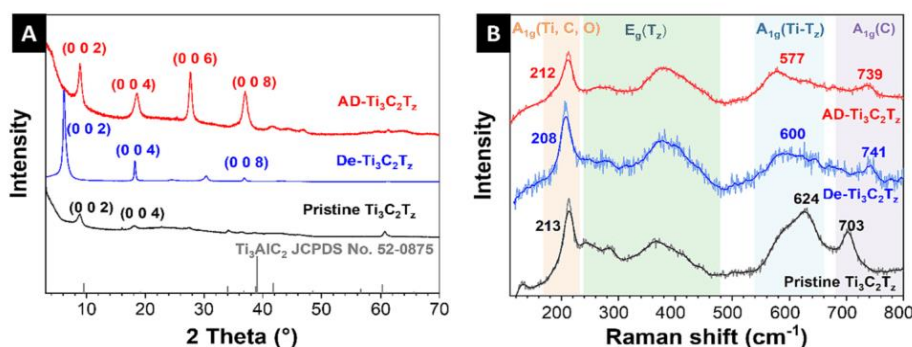
Fig. 2. (A) X-ray diffractograms and (B) Raman spectra of pristine $Ti_3C_2T_z$, De-$Ti_3C_2T_z$, and AD-$Ti_3C_2T_z$.
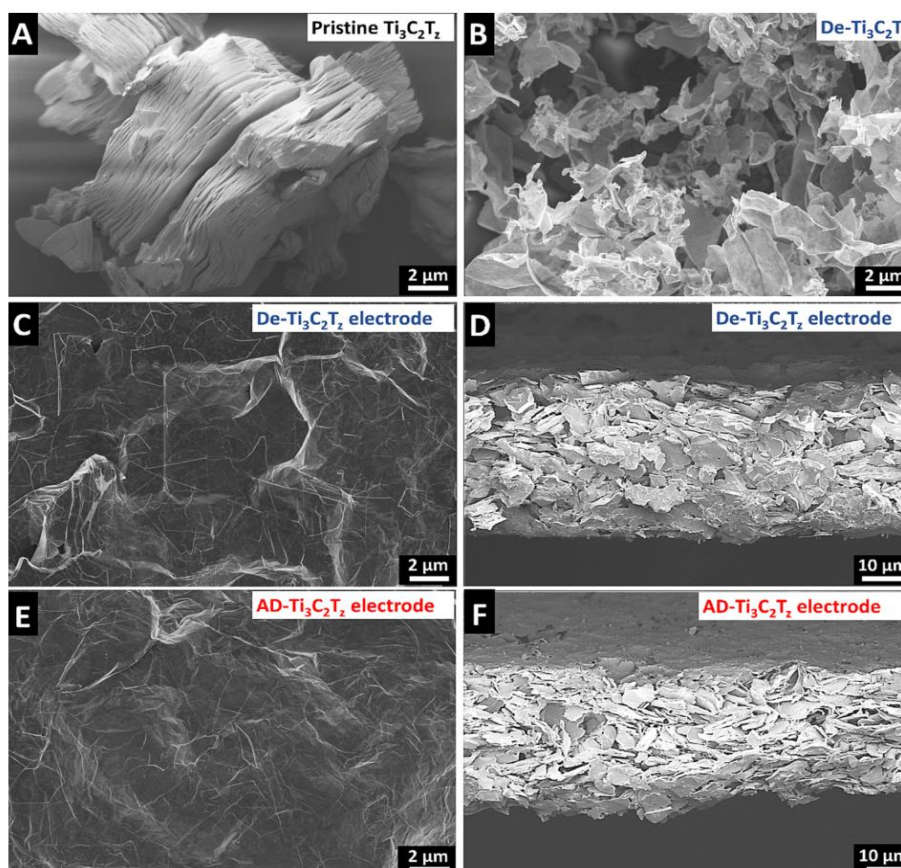
Fig. 3. Scanning electron micrographs of (A) pristine $Ti_3C_2T_z$, (B) De-$Ti_3C_2T_z$, (C) top view, and (D) side view of the De-$Ti_3C_2T_z$ electrodes, (E) top view, and (F) side view of the AD-$Ti_3C_2T_z$ electrodes.

2.66:3 (F/Ti)), which shows the delamination by TMAOH will not only enlarge the interlayer spacing but also effectively remove remaining Al species (e.g., trapped AlF_3) in pristine $Ti_3C_2T_z$ [27,31]. After the delamination process, the C/Ti atomic ratio significantly increased from 2.66:3 to 4.04:3, which attributes to the intercalation of TMA^+ cations into the interlayers of MXene. The heat treatment process at 400 °C changed the surface terminal functional groups. The atomic ratio of AD-$Ti_3C_2T_z$ decreased to 2.91:3 (C/Ti), 1.53:3(O/Ti), 0.69:3(F/Ti), and 0:3 (Al/Ti), which corresponds to the removal of physically absorbed water, the conversion of —OH and —O into H_2O, and release, and the removal of TMA^+ cations by a decomposition at 300 °C during the annealing process (*Supporting Information*, Fig. S1A) [32]. *Supporting Information*,

Fig. S3 and *Supporting Information*, Fig. S4 show the elemental mapping of De-$Ti_3C_2T_z$ and AD-$Ti_3C_2T_z$, respectively, indicating the homogeneous distribution of Ti and C.

3.2. Electrochemical performance

The lithium storage behaviors of the De-$Ti_3C_2T_z$ and AD-$Ti_3C_2T_z$ free-standing electrodes were studied by cyclic voltammetry within the potential range of 0.01–3.0 V vs. Li^+/Li. We used a scan rate of 0.2 mV s^{-1}, and the results are shown in *Supporting Information*, Fig. S5A and Fig. 4A. The cyclic voltammogram of the De-$Ti_3C_2T_z$ electrodes at the first cycle shows two cathodic peaks at around 2.28 V and 0.96 V vs. Li^+/Li,

RESULTS AND DISCUSSION
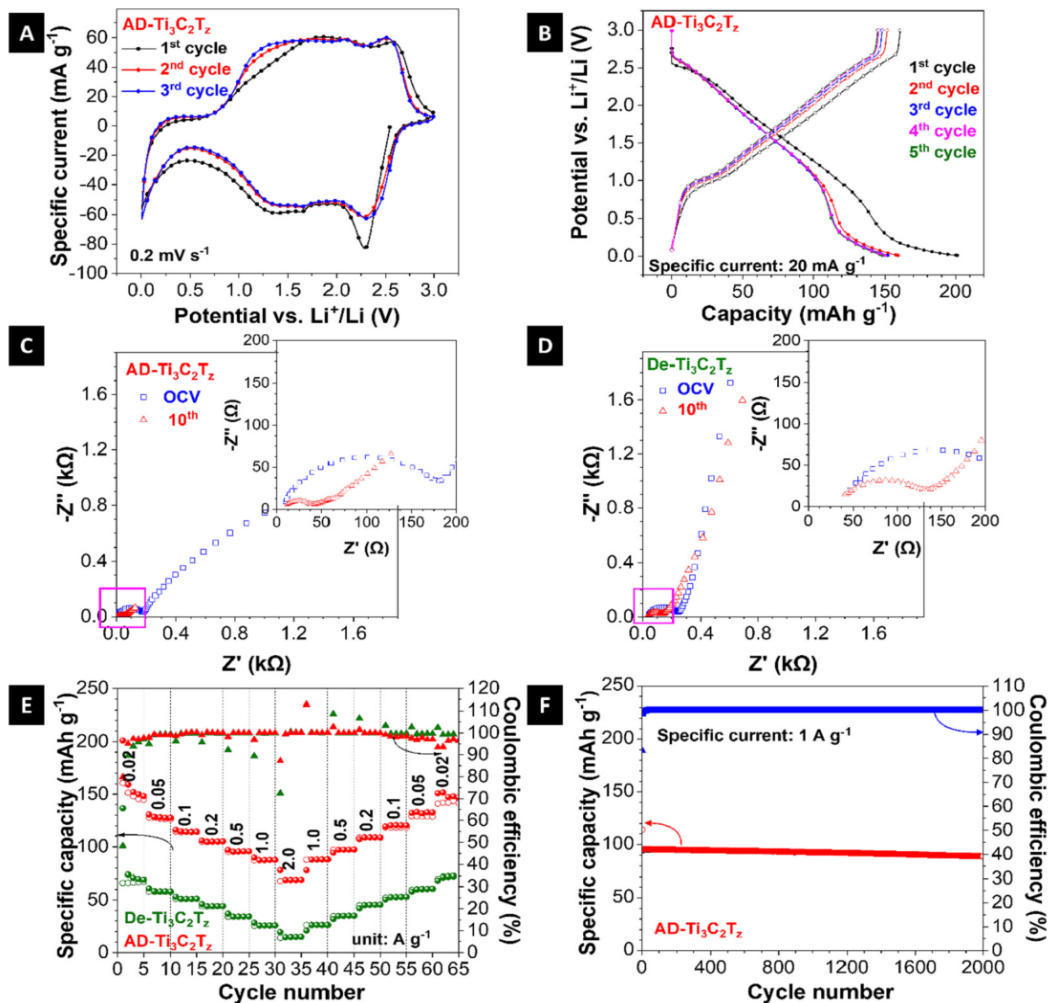
Fig. 4. Electrochemical performance tests. (A) Cyclic voltammograms and (B) galvanostatic charge/discharge profiles of AD-Ti$_3$C$_2$T$_z$ free-standing electrodes. Nyquist plots and insert images are the enlarged versions of the impedance at a high frequency of (C) AD-Ti$_3$C$_2$T$_z$, and (D) De-Ti$_3$C$_2$T$_z$ free-standing electrodes. (E) Rate capabilities of De-Ti$_3$C$_2$T$_z$ and AD-Ti$_3$C$_2$T$_z$ free-standing electrodes. (F) Long-term cycling stability at 1 A g^{-1} of AD-Ti$_3$C$_2$T$_z$.

corresponding to the intercalation and adsorption of Li$^+$ and the formation of the solid electrolyte interphase (SEI) [33,34]. The two anodic peaks at approximately 1.56 *V* and 2.46 V vs. Li$^+$/Li relate to the removal of Li$^+$ from the De-Ti$_3$C$_2$T$_z$ electrode [33]. In the subsequent cycle, two reversible cathodic peaks at 2.33 V vs. Li$^+$/Li and 1.41 V vs. Li$^+$/Li are observed, while the anodic peaks are almost unchanged. There are two redox couples near 2.29/2.59 V vs. Li$^+$/Li and 1.33/1.79 V vs. Li$^+$/Li for the first cycle, and the redox couples shift to 2.30/2.50 V vs. Li$^+$/Li and 1.35/1.00/3.10 V vs. Li$^+$/Li for the following cycles of AD-Ti$_3$C$_2$T$_z$ electrodes, as shown in Fig. 4A. *Supporting Information*, Fig. S5B shows the charge/discharge profiles of De-Ti$_3$C$_2$T$_z$ at 0.02 A g^{-1} for the first five cycles. The De-Ti$_3$C$_2$T$_z$ electrode delivers an initial lithiation capacity of 137 mAh g^{-1} and an initial Coulombic efficiency (ICE) of 48 %. The low ICE relates to the SEI layer's formation and the electrolyte's decomposition caused by the terminal groups [35,36]. The AD-Ti$_3$C$_2$T$_z$ exhibits an initial lithiation capacity of 201 mAh g^{-1} and an increased ICE of 80 % due to removing sorbed H$_2$O and part of terminal groups (Fig. 4B). Fig. 4C and D show Nyquist plots of the AD-Ti$_3$C$_2$T$_z$ electrode and De-Ti$_3$C$_2$T$_z$ electrode before and after cycling for 10 cycles, respectively. All Nyquist plots consist of a semicircle related to the SEI resistance and the charge-transfer resistance and a straight line that correlates with the ion diffusion impedance. The slope of the line in Fig. 4D is much higher than that in Fig. 4C, mainly due to the restack of

the Ti$_3$C$_2$T$_z$ layers after the annealing process. Fig. 4E shows the rate performance of AD-Ti$_3$C$_2$T$_z$ and De-Ti$_3$C$_2$T$_z$ electrodes. AD-Ti$_3$C$_2$T$_z$ electrodes exhibit much better rate capability with the delithiation capacities of 148 mAh g^{-1}, 127 mAh g^{-1}, 114 mAh g^{-1}, 105 mAh g^{-1}, 95 mAh g^{-1}, 87 mAh g^{-1}, and 69 mAh g^{-1} at 0.02 A g^{-1}, 0.05 A g^{-1}, 0.1 A g^{-1}, 0.2 A g^{-1}, 0.5 A g^{-1}, 1.0 A g^{-1}, and 2.0 A g^{-1}, respectively. The delithiation capacity recovers to 142 mAh g^{-1} when the specific current returns to 0.02 A g^{-1}. Fig. 4F exhibits the long-term cycling stability of AD-Ti$_3$C$_2$T$_z$ at 1 A g^{-1} with a capacity retention of 94 % after 2000 cycles.

Compared with reported Ti$_3$C$_2$T$_z$ MXene-based electrodes in LIBs, our AD-Ti$_3$C$_2$T$_z$ electrodes show a much longer cycle life (*Supporting Information*, Table S3). The capacity is also acceptable for the active materials without combing with carbon-based materials, doping with sulfur or nitrogen, or using conductive carbon or current collector. For example, 3D porous Ti$_3$C$_2$T$_z$/reduced graphene oxide (rGO) hybrid films show a higher specific capacity of 212 mAh g^{-1} at 1 A g^{-1} after 1000 cycles compared to our work which is not only attributed to the well-designed 3D porous structure but also because of the high content of rGO in the hybrids [37]. The kinetic process of the electrochemical behavior of Li$^+$ ions for AD-Ti$_3$C$_2$T$_z$ electrodes can be comprehensively analyzed by cyclic voltammetry at different scan rates, as shown in Fig. 5A. Whether the diffusion process or the non-diffusion process

occupies the dominant position in the charge storage process of the electrode material can be qualitatively determined based on *Eq. (1)* [14,38].

$$i = av^b \tag{1}$$

where i is the peak current at different scan rates (v), and a and b are the fitting parameters. The b values usually are determined by the slopes of the log i and log v plots. When the b values of all peaks are close to 1, the kinetic process is dominated by non-diffusion-controlled electro-chemical behavior. In contrast, when it approaches 0.5, the diffusion-controlled process will contribute more to the total stored charge [39]. As shown in Fig. 5B, the b-values calculated from the oxidation peak and the reduction peak of the AD-$Ti_3C_2T_z$ electrodes are both 0.82, which indicates a mixed behavior with a higher contribution of non-diffusion controlled kinetics. The contribution ratio of the non-diffusion-controlled process at one specific scan rate can be calculated according to *Eq. (2)* [40].

$$i = k_1v + k_2v^{1/2} \tag{2}$$

where i is the current response at one specific voltage, k_1v is the non-diffusion-controlled contribution, and $k_2v^{1/2}$ is the diffusion-controlled contribution. Fig. 5C shows the non-diffusion-controlled contribution at a scan rate of 1 mV s^{-1}. Based on the quantitative analysis, the non-diffusion-controlled contribution increases with increased scan speeds (Fig. 5D).

3.3. Recycling

For traditional electrode materials, after reaching their cycle life, complex and tedious steps are needed to disassemble the cells, separate different components and regenerate the electrode materials to recover the metal elements in the electrodes, and then use recovered metal sources as a raw material to re-synthesize the electrode material for reassembling the battery [41–44]. As shown in Fig. 6, the conventional battery recycling process is complex, time- and energy-consuming. In contrast, our AD-$Ti_3C_2T_z$ free-standing electrodes, after reaching the end of life, can be reused conveniently after the direct recycling process. As shown in the experimental part, the EOL-$Ti_3C_2T_z$ electrodes were obtained from the cycled cells and employed as working electrodes again after simply rinsing with DMC and drying processes, together with fresh Li foil and separators to reassemble into *Re*-$Ti_3C_2T_z$ batteries.

To evaluate the electrode recycling, the AD-$Ti_3C_2T_z$ was cycled at 1 A g^{-1} until cell failure. As shown in Fig. 7A, the AD-$Ti_3C_2T_z$ delivers an initial delithiation capacity of 92 mAh g^{-1} at 1.0 A g^{-1} that slowly decays until about 3000 cycles, after which it quickly drops to 5 mAh g^{-1}. The spent Li-ion batteries were then disassembled for further XRD and SEM characterizations and recycled using a direct recycling process. Fig. 7D shows the XRD patterns of the electrode materials before (AD-$Ti_3C_2T_z$) and after cycling (EOL-$Ti_3C_2T_z$), in which the diffraction peaks after cycling are mostly the same as those before cycling. As shown in Fig. 7E,F, after cycling, the AD-$Ti_3C_2T_z$ electrode material almost maintains the original morphology, with only a layer of passivated film on the electrode's surface and a few minor cracks. Both SEM images and XRD results indicate that the morphology and structure of the electrodes are well-kept during the cycling process. The TGA analysis (*Supporting Information*, Fig. S1A) of the EOL-$Ti_3C_2T_z$ electrode shows 3 mass losses, before 100 °C (−5 mass%), between 280 °C and 380 °C (−4 mass%) and a minor slope from 450 °C to 600 °C (−2 mass%). The latest two probably arise from the passivation layer and superficial modification of
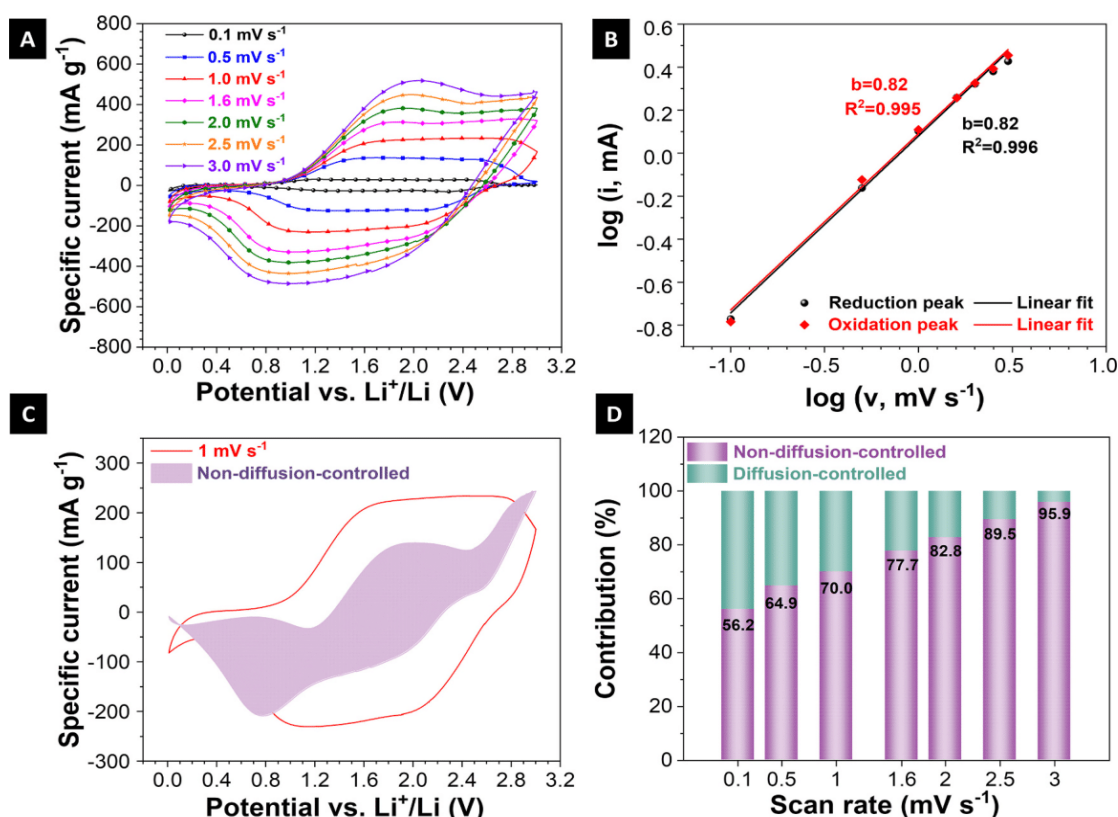
Fig. 5. Kinetics analysis of free-standing AD-$Ti_3C_2T_z$ LIB electrodes. (A) Cyclic voltammograms at different scan rates, (B) corresponding b-value calculated based on the peak current relationship to the scan rate, and (C) non-diffusion-controlled contribution at the scan rate of 1 mV s^{-1}. (D) The ratio of calculated non-diffusion-controlled contribution at different scan rates.
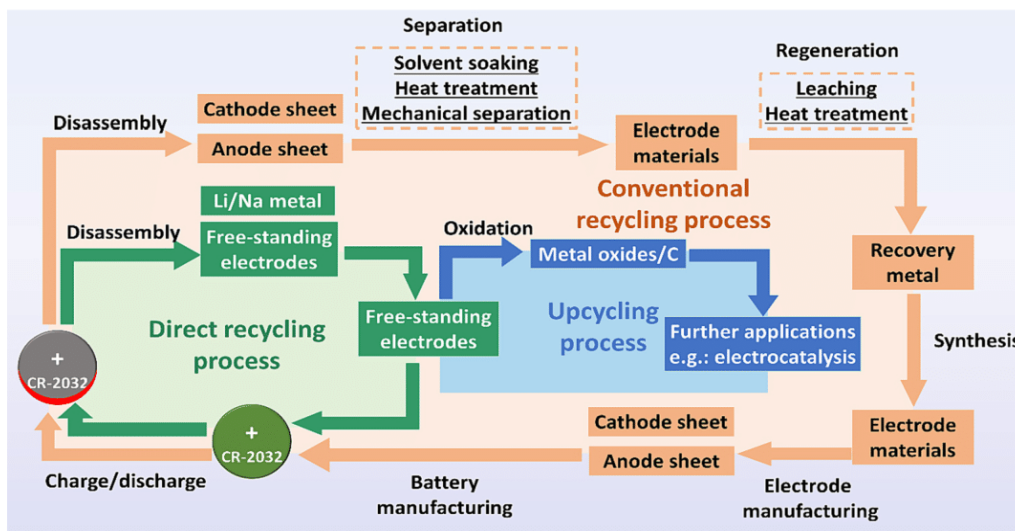
Fig. 6. Comparison of two battery recycling routes.

the material. *Supporting Information*, Fig. S6 shows photographs and SEM images of Li foil from a spent lithium-ion battery. Lithium metal is severely damaged due to the formation of lithium dendrite during the cycling process, which is the leading cause of the capacity decay of the battery. Fig. 7B shows the cycling stability of the *Re*-$Ti_3C_2T_z$ battery at 1 A g^{-1} with an initial delithiation capacity of 87 mAh g^{-1}, which is 95 % of the initial delithiation capacity of the fresh AD-$Ti_3C_2T_z$ electrode in Fig. 7A. After 1000 cycles, the delithiation capacity of the Re-$Ti_3C_2T_z$ battery can still maintain at 89 mAh g^{-1}. As shown in Fig. 7C, fresh and reassembled AD-$Ti_3C_2T_z$ electrodes reveal almost the same charge/discharge profiles at 100 cycles and 1000 cycles, confirming the excellent recyclability of AD-$Ti_3C_2T_z$ free-standing electrodes.

The electrochemical performances of AD-$Ti_3C_2T_z$ electrodes for sodium-ion batteries are depicted in Fig. 8. Fig. 8A shows the cyclic voltammogram of AD-$Ti_3C_2T_z$ electrodes of SIBs at 0.1 mV s^{-1} for the initial three cycles. For the first cycle, one sharp cathodic peak at 1.88 V vs. Na^+/Na and one broad peak below 1 V vs. Na^+/Na corresponds to the intercalation and adsorption of Na^+ ions and the formation of the SEI layer [45,46]. A broad anodic peak at 0.71 V vs. Na^+/Na and two prominent peaks at 2.37 V vs. Na^+/Na and 2.53 V vs. Na^+/Na relate to the Na^+ ions removal reactions. Fig. 8B exhibits the galvanostatic charge/discharge profiles of AD-$Ti_3C_2T_z$ electrodes for SIBs at the specific current of 0.02 A g^{-1} with an initial sodiation and desodiation capacity of 139 mAh g^{-1} and 107 mAh g^{-1}, respectively, corresponding to an ICE of 77 %. The charge/discharge profiles deliver almost the same capacity for subsequent cycles, showing good reversibility. Fig. 8C exhibits good rate capabilities with the desodiation capacities of 108 mAh g^{-1}, 104 mAh g^{-1}, 100 mAh g^{-1}, 96 mAh g^{-1}, 91 mAh g^{-1}, 85 mAh g^{-1}, and 71 mAh g^{-1} at 0.02 A g^{-1}, 0.05 A g^{-1}, 0.1 A g^{-1}, 0.2 A g^{-1}, 0.5 A g^{-1}, 1.0 A g^{-1}, and 2.0 A g^{-1}, respectively of AD-$Ti_3C_2T_z$ electrode for SIB and the desodiation capacity could recover to 110 mAh g^{-1} without any capacity loss compared to the initial state when the specific current returns to 0.02 A g^{-1}.

Cyclic voltammograms at different scan rates were used to investigate the Na^+ ion diffusion kinetics (Fig. 8D). The proportion of non-diffusion contribution increased to 98.4 % at a scan rate of 3 mV s^{-1} (Fig. 8E). High non-diffusion-controlled contribution endows good rate capability. Fig. 8F shows the Nyquist plots of AD-$Ti_3C_2T_z$ electrodes for SIBs. The impedance at a higher frequency is small, indicating the good conductivity of the electrode materials.

Similarly, the recycling performances of AD-$Ti_3C_2T_z$ electrodes for SIBs were studied. Fig. 8G presents the cycling performance of the AD-

$Ti_3C_2T_z$ electrode at 0.5 A g^{-1} with a reversible capacity of 85 mAh g^{-1} after 300 cycles. The capacity decays to almost zero after about 430 cycles. *Supporting Information*, Table S4 shows the cycling performance comparison among MXene-based electrodes in SIBs. For example, 3D macroporous MXene films deliver a sodium storage capacity of 295 mAh g^{-1} after 1000 cycles [47]. Even though the performances of our free-standing electrodes are slightly inferior compared to the elaborate MXene modified with carbon materials or doping with elements, but acceptable for battery recycling and reuse. The AD-$Ti_3C_2T_z$ electrode from spent SIBs was treated with a direct recycling process and then reassembled into a new SIB. The reassembled electrodes show a reversible capacity of 90 mAh g^{-1} after 500 cycles at 0.5 A g^{-1}. And the electrochemical processes in SIBs, as depicted in the charge/discharge curves in Fig. 8I are identical for fresh and recycled electrodes.

The cycled *Re*-$Ti_3C_2T_z$, that is, the electrode after two processes of EOL (EOL- Re-$Ti_3C_2T_z$), were characterized by XRD and SEM. *Supporting Information* Fig. S7A shows the diffractograms of the post mortem electrodes cycled as LIB and SIB compared to AD-$Ti_3C_2T_z$. The characteristic (002) peak has a pronounced shift toward lower angles from the uncycled electrode to LIB and SIB testing, indicating the intercalation of Li^+ and Na^+ ions within the MXene layers. The larger shift for the SIB electrode corroborates with the larger cation size. However, the other peaks lose intensity, corresponding to a lower degree of organization in the material. The analysis of the SEM images shows that after two sets of cycling, the surface of the electrode presents a significant amount of passivation layer at the external surface (*Supporting Information* Fig. S7B-D). Nevertheless, the free-standing layered assembly is not compromised. It is also observed that small nanoparticles start to cover the majority of the layers, characteristic of surface oxidation of Ti-based MXenes, leading to TiO_2. Such characteristics indicate that at prolonged use, the Re-$Ti_3C_2T_z$ would eventually require a second annealing process to remove impurities, or be designated to a second life application.

3.4. Upcycling

As the increase of the cycle number, the $Ti_3C_2T_z$ electrode will accumulate more and more structural collapses, or the free-standing electrodes will become damaged, eventually making it difficult to restore its electrochemical performance by simply replacing the Li/Na metal and separators. To achieve the goal of sustainable development of MXene electrode material, a facile method needs to be developed to

246
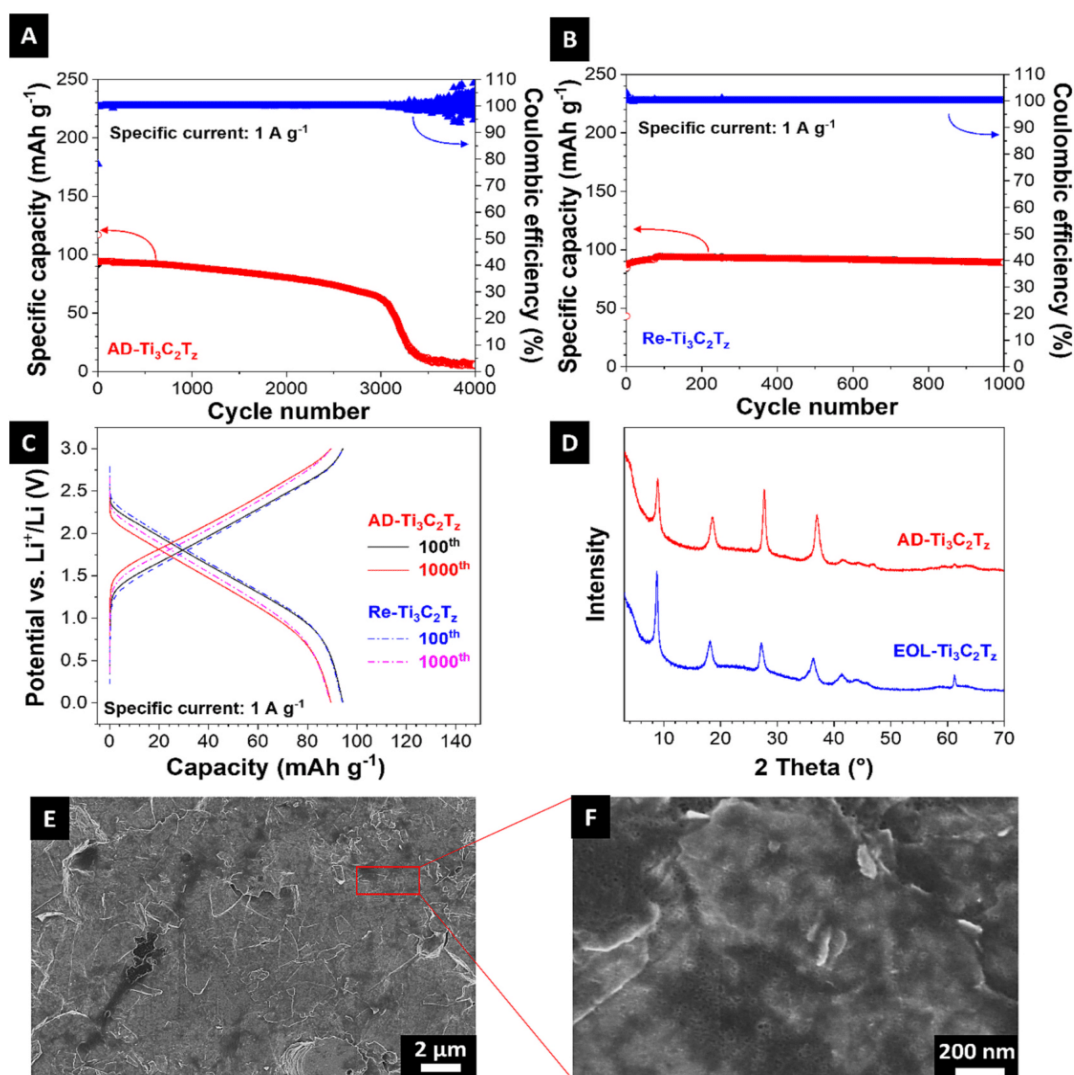
Fig. 7. Recycling of AD-Ti$_3$C$_2$T$_z$ free-standing electrodes. (A) The cycling stability of AD-Ti$_3$C$_2$T$_z$ when pushing to the end of their cycling life. (B) Cycling performance of regenerated Re-Ti$_3$C$_2$T$_z$. (C) Charge/discharge profiles of fresh and regenerated AD-Ti$_3$C$_2$T$_z$ electrodes. (D) X-ray diffractograms of AD-Ti$_3$C$_2$T$_z$ electrodes before and after the cycling test. (E-F) Scanning electron micrographs of cycled electrodes.

process the spent electrodes for further applications in other fields to realize their second life, as shown in Fig. 6. For example, the metal oxides obtained from spent electrode precursors can be applied as electrode materials for alkali-ion batteries [48], as catalysts for electrochemical oxygen revolution, photocatalytic hydrogen evolution, and microwave absorbers [49,50].

MXene is an attractive precursor for synthesizing nanoscale oxides and hybrids of oxides and carbide/carbon [51–56]. Here, we proposed a facile heat treatment method to oxidize EOL Ti$_3$C$_2$T$_z$ under CO$_2$ flow to obtain TiO$_2$/C-900 and TiO$_2$/C-700 at 900 °C and 700 °C, respectively. As shown in Fig. 9A, TiO$_2$/C-900 and TiO$_2$/C-700 show the same diffraction peaks, in which the diffraction peaks at 27.43° 2θ, 36.08° 2θ, 39.25° 2θ, 41.13° 2θ, 44.01° 2θ, 54.39° 2θ, 56.55° 2θ, 54.12° 2θ, and 69.04° 2θ are indexed to rutile TiO$_2$. The diffraction peak at 18.35° 2θ corresponds to the (004) plane of AD-Ti$_3$C$_2$T$_z$ MXene, indicating the maintenance of the layered frame of MXene after the heat treatment.

Fig. 9B displays the Raman spectra of TiO$_2$/C-900 and TiO$_2$/C-700. For TiO$_2$/C-700, the peaks at 145 cm^{-1}, 237 cm^{-1}, 444 cm^{-1}, and 611 cm^{-1}, corresponding to rutile TiO$_2$, and the two peaks at 1350 cm^{-1} and 1600 cm^{-1} can be assigned to the D-band and G-band of carbon [57]. For

TiO$_2$/C-900, there are no obvious peaks related to the formation of carbon. The amount of carbon in the samples was determined by EDS (*Supporting Information*, Table S2). The carbon content of TiO$_2$/C-700 (17.50 at.%) is much higher than that of TiO$_2$/C-900 (4.76 at.%). The thermogram of EOL-Ti$_3$C$_2$T$_z$ (*Supporting Information* Fig. S1B) shows that at 700 °C, the material is only partially oxidized, reaching a maximum mass gain only at ca. 800 °C followed by a mass decay due to loss of carbon until stabilization during holding time at 900 °C. This behavior agrees with the Boudouard reaction, where carbon consumption is strongly favored above 800 °C. These results show that the amount of carbon can be adjusted by changing the heat treatment temperature. The scanning electron micrographs in Fig. 9C show that TiO$_2$/C-900 particles with a diameter of around 2 μm aggregate together based on the frame of MXene precursors and AD-Ti$_3$C$_2$T$_z$ MXene layers cannot be seen from the scanning electron micrograph. The SEM image of TiO$_2$/C-700 in Fig. 9D exhibits a smaller particle size of ca. 1 μm and the AD-Ti$_3$C$_2$T$_z$ MXene layers can be observed. The obtained products have great potential in the field of energy and environment. For example, Zhang et al. [58] employed similar methods to oxidize MXene in the CO$_2$ atmosphere to synthesize TiO$_2$@Ti$_3$C$_2$T$_z$ hierarchical composites as anode materials
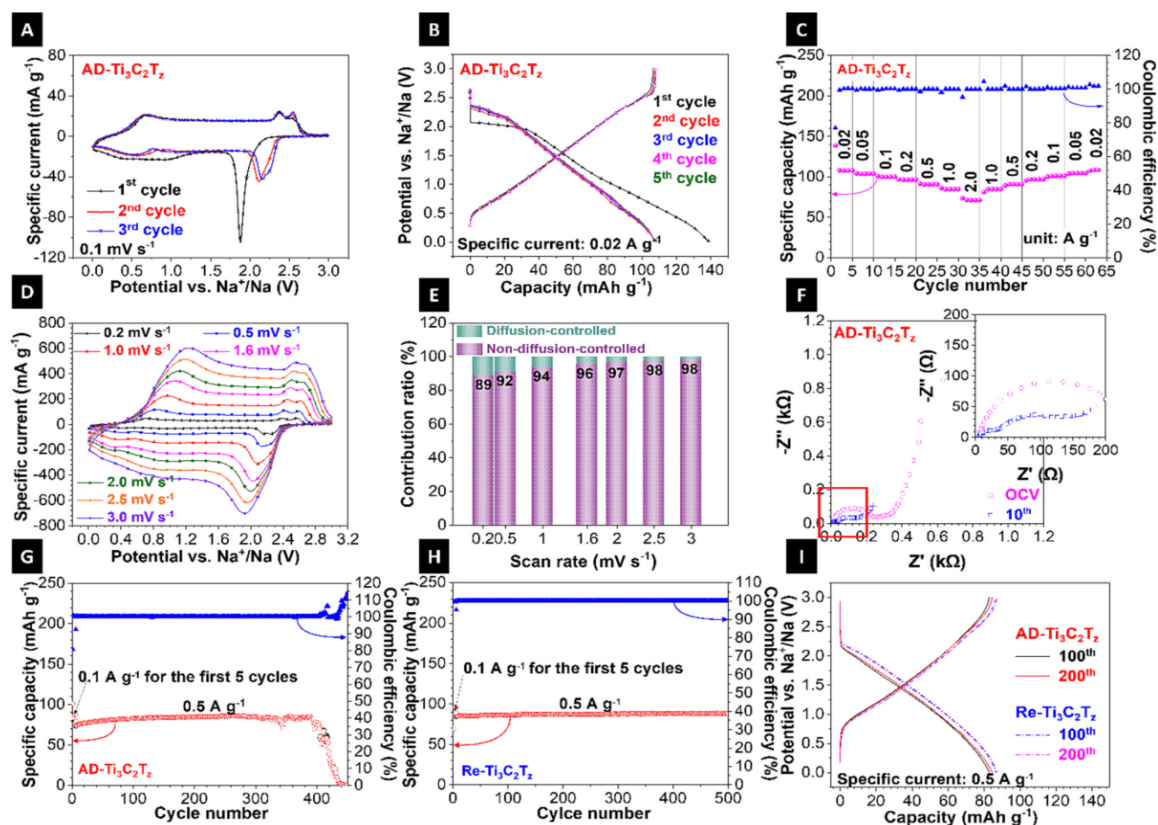
Fig. 8. Electrochemical performances and recyclability of AD-Ti$_3$C$_2$T$_z$ in SIBs. (A) Cyclic voltammograms of the first three cycles at the scan rate of 0.1 mV s^{-1}, (B) galvanostatic charge/discharge profiles at 0.02 A g^{-1}, (C) rate capabilities, (D) cyclic voltammograms at different scan rates, (E) the ratio of calculated non-diffusion contribution at different scan rates, (F) Nyquist plots before and after cycling for 10 cycles (insert: the enlarged image of the impedance at high frequency), and (G) cycling performance at 0.5 A g^{-1} of AD-Ti$_3$C$_2$T$_z$ free-standing electrodes. (H) Cycling performance at 0.5 A g^{-1} and (I) galvanostatic charge/discharge profiles at 0.5 A g^{-1} of recycled AD-Ti$_3$C$_2$T$_z$ free-standing electrodes.

for LIBs, which exhibit excellent cycling stability at 0.05 A g^{-1} (101 %) and Coulombic efficiency (100 %) after 400 cycles. Similarly, other MXene compositions can also be targeted for upcycling after their EOL as battery materials and produce different or more complex products, like the oxidation of mixed TiNb MXenes to form TNOs or sulfidation to prepare metal sulfides that have great application in catalysis and photovoltaics [59].

4. Conclusions

Our work explored the recycling of free-standing Ti$_3$C$_2$T$_z$ electrodes and their transition for second-life use. Free-standing AD-Ti$_3$C$_2$T$_z$ electrodes obtained from vacuum filtration of delaminated Ti$_3$C$_2$T$_z$ and the annealing process under the Ar atmosphere show much better electrochemical performances compared with De-Ti$_3$C$_2$T$_z$ free-standing electrodes due to the removal of surface water and part of functional groups. The AD-Ti$_3$C$_2$T$_z$ electrodes show superior cycling stability with a capacity retention of 94 % at 1 A g^{-1} after 2000 cycles for LIBs. The electrodes deliver great rate capabilities with a capacity retention of 66 % when the specific current increases from 0.02 A g^{-1} to 2 A g^{-1} for sodium-ion batteries. The spent end-of-life AD-Ti$_3$C$_2$T$_z$ free-standing electrodes (EOL-Ti$_3$C$_2$T$_z$) exhibit good recyclability after a simple direct recycling process. The capacity recovery rate is above 90 % for EOL-Ti$_3$C$_2$T$_z$ for both LIBs and SIBs. Finally, to apply EOL-Ti$_3$C$_2$T$_z$ electrodes in other fields and achieve their second life, a heat treatment method under CO$_2$ flow was used to oxidize the MXene electrodes into TiO$_2$ with controllable carbon content by changing heat temperature. The obtained TiO$_2$/C has great potential to realize its second life in the

field of batteries, electrochemical oxygen revolution, photocatalytic hydrogen evolution, or photodegradation. It is worth mentioning that this direct battery recycling method can be applied to other MXenes or 2D materials due to their easy-to-process into film properties and similar intercalation and adsorption energy storage mechanisms with little structural damage to electrode materials. Furthermore, numerous transition metal oxides can be derived from spent batteries with different MXene electrodes (e.g., Ti$_2$CT$_z$, Nb$_2$CT$_z$, Mo$_2$CT$_z$, TiVNbMoC$_3$, etc.) for further applications in the field of energy and environment.

CRediT authorship contribution statement

Yunjie Li: Conceptualization, Methodology, Investigation, Formal analysis, Validation, Writing – original draft, Visualization. **Stefanie Arnold:** Methodology, Formal analysis, Writing – review & editing. **Samantha Husmann:** Methodology, Formal analysis, Writing – review & editing. **Volker Presser:** Conceptualization, Writing – review & editing, Supervision, Funding acquisition.

Declaration of competing interest

The authors declare the following financial interests/personal relationships which may be considered as potential competing interests: Volker Presser reports financial support was provided by European Regional Development Fund.
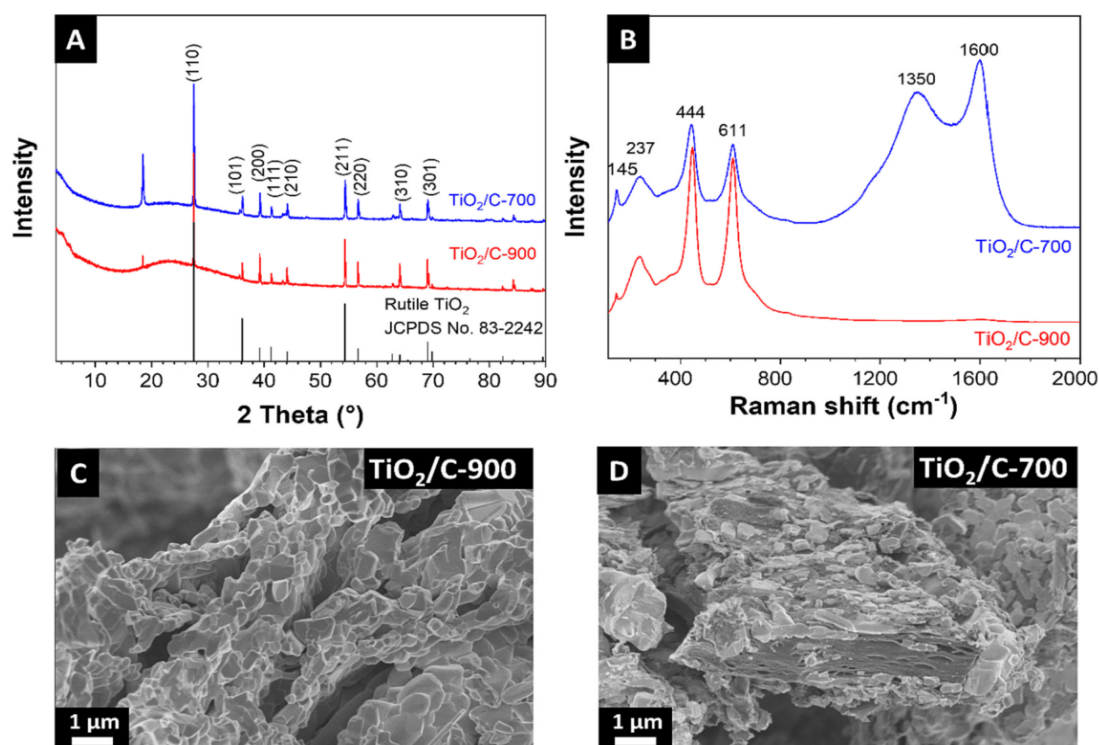
Fig. 9. (A) X-ray diffractograms and (B) Raman spectrum of TiO$_2$/C-700 and TiO$_2$/C-900. Scanning electron micrographs of (C) TiO$_2$/C-900 and (D) TiO$_2$/C-700.

Data availability

Data will be made available on request.

Acknowledgments

Appendix A. Supplementary data

Supplementary data to this article can be found online at https://doi.org/10.1016/j.est.2023.106625.

References

[1] Y. Chen, Y. Kang, Y. Zhao, L. Wang, J. Liu, Y. Li, Z. Liang, X. He, X. Li, N. Tavajohi, B. Li, A review of lithium-ion battery safety concerns: the issues, strategies, and testing standards, journal of energy, Chemistry 59 (2021) 83–99.

[2] T. Chen, Y. Jin, H. Lv, A. Yang, M. Liu, B. Chen, Y. Xie, Q. Chen, Applications of Lithium-ion batteries in grid-scale energy storage systems, Trans. Tianjin Univ. 26 (3) (2020) 208–217.

[3] Y. Yang, E.G. Okonkwo, G. Huang, S. Xu, W. Sun, Y. He, On the sustainability of lithium ion battery industry – a review and perspective, Energy Storage Mater. 36 (2021) 186–212.

[4] H. Bae, Y. Kim, Technologies of lithium recycling from waste lithium ion batteries: a review, Mater. Adv. 2 (10) (2021) 3234–3250.

[5] S. Fang, D. Bresser, S. Passerini, Transition metal oxide anodes for electrochemical energy storage in lithium- and sodium-ion batteries, Adv. Energy Mater. 10 (1) (2019) 1902485.

[6] C. Vaalma, D. Buchholz, M. Weil, S. Passerini, A cost and resource analysis of sodium-ion batteries, Nat. Rev. Mater. 3 (4) (2018) 18013.

[7] S. Roberts, E. Kendrick, The re-emergence of sodium ion batteries: testing, processing, and manufacturability, Nanotechnol. Sci. Appl. 11 (2018) 23–33.

[8] X. Pu, H. Wang, D. Zhao, H. Yang, X. Ai, S. Cao, Z. Chen, Y. Cao, Recent progress in rechargeable sodium-ion batteries: toward high-power applications, Small 15 (32) (2019), e1805427.

[9] N. Mahmood, T. Tang, Y. Hou, Nanostructured anode materials for lithium ion batteries: Progress, challenge and perspective, Adv. Energy Mater. 6 (17) (2016) 1600374.

[10] H.G. Park, K. Min, K. Park, A synergistic effect of Na+ and Al3+ dual doping on electrochemical performance and structural stability of LiNi0.88Co0.08Mn0.04O2 cathodes for Li-ion batteries, ACS Appl. Mater. Interfaces 14 (4) (2022) 5168–5176.

[11] M.-M. Titirici, Sustainable batteries - quo Vadis? Adv. Energy Mater. 11 (10) (2021) 2003700.

[12] H. Au, M. Crespo-Ribadeneyra, M.-M. Titirici, Beyond li-ion batteries: performance, materials diversification, and sustainability, One Earth 5 (3) (2022) 207–211.

[13] M. Naguib, M. Kurtoglu, V. Presser, J. Lu, J. Niu, M. Heon, L. Hultman, Y. Gogotsi, M.W. Barsoum, Two-dimensional nanocrystals produced by exfoliation of Ti3AlC2, Adv. Mater. 23 (37) (2011) 4248–4253.

[14] X. Song, H. Wang, S. Jin, M. Lv, Y. Zhang, X. Kong, H. Xu, T. Ma, X. Luo, H. Tan, D. Hu, C. Deng, X. Chang, J. Xu, Oligolayered Ti3C2Tx MXene towards high performance lithium/sodium storage, Nano Res. 13 (6) (2020) 1659–1667.

[15] X. Wang, S. Kajiyama, H. Iinuma, E. Hosono, S. Oro, I. Moriguchi, M. Okubo, A. Yamada, Pseudocapacitance of MXene nanosheets for high-power sodium-ion hybrid capacitors, Nat. Commun. 6 (2015) 6544.

[16] J. Song, D. Su, X. Xie, X. Guo, W. Bao, G. Shao, G. Wang, Immobilizing polysulfides with MXene-functionalized separators for stable lithium-sulfur batteries, ACS Appl. Mater. Interfaces 8 (43) (2016) 29427–29433.

[17] M.K. Aslam, T.S. AlGarni, M.S. Javed, S.S.A. Shah, S. Hussain, M. Xu, 2D MXene materials for sodium ion batteries: a review on energy storage, J. Energy Storage 37 (2021), 102478.

[18] W. Wu, C. Wang, C. Zhao, D. Wei, J. Zhu, Y. Xu, Facile strategy of hollow polyaniline nanotubes supported on Ti3C2-MXene nanosheets for high-performance symmetric supercapacitors, J. Colloid Interface Sci. 580 (2020) 601–613.

[19] L. Cai, Z. Li, S. Zhang, K. Prenger, M. Naguib, V.G. Pol, Safer lithium-ion battery anode based on Ti3C2Tz MXene with thermal safety mechanistic elucidation, Chem. Eng. J. 419 (2021) 129387.

[20] J. Xu, H.R. Thomas, R.W. Francis, K.R. Lum, J. Wang, B. Liang, A review of processes and technologies for the recycling of lithium-ion secondary batteries, J. Power Sources 177 (2) (2008) 512–527.

[21] S. Windisch-Kern, E. Gerold, T. Nigl, A. Jandric, M. Altendorfer, B. Rutrecht, S. Scherhaufer, H. Raupenstrauch, R. Pomberger, H. Antrekowitsch, F. Part, Recycling chains for lithium-ion batteries: a critical examination of current challenges, opportunities and process dependencies, Waste Manag. 138 (2022) 125–139.

[22] R. Bird, Z.J. Baum, X. Yu, J. Ma, The regulatory environment for lithium-ion battery recycling, ACS Energy Lett. 7 (2) (2022) 736–740.

RESULTS AND DISCUSSION

[23] Y. Lu, C.-Z. Zhao, H. Yuan, J.-K. Hu, J.-Q. Huang, Q. Zhang, Dry electrode technology, the rising star in solid-state battery industrialization, Matter 5 (3) (2022) 876–898.

[24] M. Alhabeb, K. Maleski, B. Anasori, P. Lelyukh, L. Clark, S. Sin, Y. Gogotsi, Guidelines for synthesis and processing of two-dimensional titanium carbide (Ti3C2Tx MXene), Chem. Mater. 29 (18) (2017) 7633–7644.

[25] D. Cao, M. Ren, J. Xiong, L. Pan, Y. Wang, X. Ji, T. Qiu, J. Yang, C. Zhang, Self-assembly of hierarchical Ti3C2Tx-CNT/SiNPs resilient films for high performance lithium ion battery electrodes, Electrochim. Acta 348 (2020), 136211.

[26] Z. Fan, Y. Wang, Z. Xie, X. Xu, Y. Yuan, Z. Cheng, Y. Liu, A nanoporous MXene film enables flexible supercapacitors with high energy storage, Nanoscale 10 (20) (2018) 9642–9652.

[27] M. Lu, Z. Zhang, L. Kang, X. He, Q. Li, J. Sun, R. Jiang, H. Xu, F. Shi, Z. Lei, Z.-H. Liu, Intercalation and delamination behavior of Ti3C2Tx and MnO2/Ti3C2Tx/RGO flexible fibers with high volumetric capacitance, J. Mater. Chem. A 7 (20) (2019) 12582–12592.

[28] F. Kong, X. He, Q. Liu, X. Qi, Y. Zheng, R. Wang, Y. Bai, Improving the electrochemical properties of MXene Ti3C2 multilayer for li-ion batteries by vacuum calcination, Electrochim. Acta 265 (2018) 140–150.

[29] A. Sarycheva, Y. Gogotsi, Raman spectroscopy analysis of the structure and surface chemistry of Ti3C2Tx MXene, Chem. Mater. 32 (8) (2020) 3480–3488.

[30] Y. Cao, Q. Deng, Z. Liu, D. Shen, T. Wang, Q. Huang, S. Du, N. Jiang, C.-T. Lin, J. Yu, Enhanced thermal properties of poly(vinylidene fluoride) composites with ultrathin nanosheets of MXene, RSC Adv. 7 (33) (2017) 20494–20501.

[31] J. Xuan, Z. Wang, Y. Chen, D. Liang, L. Cheng, X. Yang, Z. Liu, R. Ma, T. Sasaki, F. Geng, Organic-base-driven intercalation and delamination for the production of functionalized titanium carbide nanosheets with superior photothermal therapeutic performance, Angew. Chem. Int. Ed. 55 (47) (2016) 14569–14574.

[32] H. Tang, Y. Yang, R. Wang, J. Sun, Improving the properties of 2D titanium carbide films by thermal treatment, J. Mater. Chem. C 8 (18) (2020) 6214–6220.

[33] R. Cheng, T. Hu, H. Zhang, C. Wang, M. Hu, J. Yang, C. Cui, T. Guang, C. Li, C. Shi, P. Hou, X. Wang, Understanding the lithium storage mechanism of Ti3C2Tx MXene, J. Phys. Chem. C 123 (2) (2018) 1099–1109.

[34] J. Luo, X. Tao, J. Zhang, Y. Xia, H. Huang, L. Zhang, Y. Gan, C. Liang, W. Zhang, Sn4+ ion decorated highly conductive Ti3C2 MXene: promising lithium-ion anodes with enhanced volumetric capacity and cyclic performance, ACS Nano 10 (2) (2016) 2491–2499.

[35] M. Lu, W. Han, H. Li, W. Shi, J. Wang, B. Zhang, Y. Zhou, H. Li, W. Zhang, W. Zheng, Tent-pitching-inspired high-valence period 3-cation pre-intercalation excels for anode of 2D titanium carbide (MXene) with high Li storage capacity, Energy Storage Materials 16 (2019) 163–168.

[36] B. Zhang, J. Zhu, P. Shi, W. Wu, F. Wang, Fluoride-free synthesis and microstructure evolution of novel two-dimensional Ti3C2(OH)2 nanoribbons as high-performance anode materials for lithium-ion batteries, Ceram. Int. 45 (7) (2019) 8395–8405.

[37] Z. Ma, X. Zhou, W. Deng, D. Lei, Z. Liu, 3D porous MXene (Ti3C2)/reduced graphene oxide hybrid films for advanced lithium storage, ACS Appl. Mater. Interfaces 10 (4) (2018) 3634–3643.

[38] M. Opitz, J. Yue, J. Wallauer, B. Smarsly, B. Roling, Mechanisms of charge storage in nanoparticulate TiO2 and Li4Ti5O12 anodes: new insights from scan rate-dependent cyclic voltammetry, Electrochim. Acta 168 (2015) 125–132.

[39] Y. Wang, Y. Zheng, J. Zhao, Y. Li, Assembling free-standing and aligned tungstate/MXene fiber for flexible lithium and sodium-ion batteries with efficient pseudocapacitive energy storage, Energy Storage Mater. 33 (2020) 82–87.

[40] J. Liu, J. Wang, C. Xu, H. Jiang, C. Li, L. Zhang, J. Lin, Z.X. Shen, Advanced energy storage devices: basic principles, analytical methods, and rational materials design, Adv. Sci. 5 (1) (2018) 1700322.

[41] Y. Lu, K. Peng, L. Zhang, Sustainable recycling of electrode materials in spent Li-ion batteries through direct regeneration processes, ACS ES&T Eng. 2 (4) (2022) 586–605.

[42] L. Gaines, K. Richa, J. Spangenberger, Key issues for Li-ion battery recycling, MRS Energy Sustain. 5 (1) (2018) 12.

[43] F. Gu, P.A. Summers, P. Hall, Recovering materials from waste mobile phones: recent technological developments, J. Clean. Prod. 237 (2019), 117657.

[44] V.P. Parikh, A. Ahmadi, M.H. Parekh, F. Sadeghi, V.G. Pol, Upcycling of spent lithium cobalt oxide cathodes from discarded lithium-ion batteries as solid lubricant additive, Environ. Sci. Technol. 53 (7) (2019) 3757–3763.

[45] S. Sun, Z. Xie, Y. Yan, S. Wu, Hybrid energy storage mechanisms for sulfur-decorated Ti3C2 MXene anode material for high-rate and long-life sodium-ion batteries, Chem. Eng. J. 366 (2019) 460–467.

[46] P. Lian, Y. Dong, Z.-S. Wu, S. Zheng, X. Wang, W. Sen, C. Sun, J. Qin, X. Shi, X. Bao, Alkalized Ti3C2 MXene nanoribbons with expanded interlayer spacing for high-capacity sodium and potassium ion batteries, Nano Energy 40 (2017) 1–8.

[47] M.Q. Zhao, X. Xie, C.E. Ren, T. Makaryan, B. Anasori, G. Wang, Y. Gogotsi, Hollow MXene spheres and 3D macroporous MXene frameworks for na-ion storage, Adv. Mater. 29 (37) (2017) 1702410.

[48] Y. Fang, R. Hu, B. Liu, Y. Zhang, K. Zhu, J. Yan, K. Ye, K. Cheng, G. Wang, D. Cao, MXene-derived TiO2/reduced graphene oxide composite with an enhanced capacitive capacity for li-ion and K-ion batteries, J. Mater. Chem. A 7 (10) (2019) 5363–5372.

[49] L. Yu, B. Liu, Y. Wang, F. Yu, J. Ma, Recent progress on MXene-derived material and its' application in energy and environment, J. Power Sources 490 (2021), 229250.

[50] M. Han, X. Yin, X. Li, B. Anasori, L. Zhang, L. Cheng, Y. Gogotsi, Laminated and two-dimensional carbon-supported microwave absorbers derived from MXenes, ACS Appl. Mater. Interfaces 9 (23) (2017) 20038–20045.

[51] Y. Tian, Y. An, C. Wei, Y. Tao, Y. Zhang, H. Jiang, L. Tan, J. Feng, Y. Qian, Stable and dendrite-free lithium metal anodes enabled by carbon paper incorporated with ultrafine lithiophilic TiO2 derived from MXene and carbon dioxide, Chem. Eng. J. 406 (2021), 126836.

[52] M. Naguib, O. Mashtalir, M.R. Lukatskaya, B. Dyatkin, C. Zhang, V. Presser, Y. Gogotsi, M.W. Barsoum, One-step synthesis of nanocrystalline transition metal oxides on thin sheets of disordered graphitic carbon by oxidation of MXenes, Chem. Commun. 50 (56) (2014) 7420–7423.

[53] S. Husmann, M. Besch, B.X. Ying, A. Tabassum, M. Naguib, V. Presser, Layered titanium niobium oxides derived from solid-solution ti-nb carbides (MXene) as anode material for Li-ion batteries, ACS Appl. Energy Mater. 5 (7) (2022) 8132–8142.

[54] T. Ke, S. Shen, K. Rajavel, K. Yang, D. Lin, In situ growth of TiO2 nanoparticles on nitrogen-doped Ti3C2 with isopropyl amine toward enhanced photocatalytic activity, J. Hazard. Mater. 402 (2021), 124066.

[55] Z. Miao, G. Wang, X. Zhang, X. Dong, Oxygen vacancies modified TiO2/Ti3C2 derived from MXenes for enhanced photocatalytic degradation of organic pollutants: the crucial role of oxygen vacancy to Schottky junction, Appl. Surf. Sci. 528 (2020), 146929.

[56] H. Tang, S. Zhuang, Z. Bao, C. Lao, Y. Mei, Two-step oxidation of MXene in the synthesis of layer-stacked anatase titania with enhanced lithium-storage performance, ChemElectroChem 3 (6) (2016) 871–876.

[57] G.S. Zakharova, A. Ottmann, L. Möller, E.I. Andreikov, Z.A. Fattakhova, I.S. Puzyrev, Q. Zhu, E. Thauer, R. Klingeler, TiO2/C nanocomposites prepared by thermal annealing of titanium glycerolate as anode materials for lithium-ion batteries, J. Mater. Sci. 53 (17) (2018) 12244–12253.

[58] C.J. Zhang, S.J. Kim, M. Ghidiu, M.-Q. Zhao, M.W. Barsoum, V. Nicolosi, Y. Gogotsi, Layered orthorhombic Nb2O5@Nb4C3Tx and TiO2@Ti3C2Tx hierarchical composites for high performance Li-ion batteries, Adv. Funct. Mater. 26 (23) (2016) 4143–4151.

[59] S. Husmann, M. Torkamanzadeh, K. Liang, A. Majed, C. Dun, J.J. Urban, M. Naguib, V. Presser, Layered nano-mosaic of niobium disulfide heterostructures by direct sulfidation of niobium carbide MXenes for hydrogen evolution, Adv. Mater. Interfaces 9 (14) (2022) 2102185.

250

Supporting Information

Recycling and second life of MXene electrodes

for lithium-ion and sodium-ion batteries

Yunjie Li,[1,2] Stefanie Arnold,[1,2] Samantha Husmann,[1] Volker Presser[1,2,3*]

[1]   INM - Leibniz Institute for New Materials, Campus D2.2, 66123 Saarbrücken, Germany

[2]   Department of Materials Science and Engineering, Saarland University, Campus D2.266123 Saarbrücken, Germany

[3]   Saarene - Saarland Center for Energy Materials and Sustainability, Campus D4.2, 66123 Saarbrücken, Germany

*   Corresponding author's E-Mail: volker.presser@leibniz-inm.de

Supporting Tables

Table S1. The composition of pristine $Ti_3C_2T_z$, De-$Ti_3C_2T_z$, and AD-$Ti_3C_2T_z$. All values in at%.

	Ti	C	O	F	Al
pristine $Ti_3C_2T_z$	28.26±9.66	25.10±4.73	18.10±3.79	25.06±6.93	3.48±1.41
De-$Ti_3C_2T_z$	29.67±4.04	39.95±2.52	19.18±1.47	11.02±0.85	0.19±0.16
AD-$Ti_3C_2T_z$	36.90±5.00	35.84±2.70	18.80±1.97	8.45±0.69	0.02±0.03

Table S2. The composition of TiO_2/C-900 and TiO_2/C-700. All values in at%.

	Ti	C	O
TiO_2/C-900	29.36±9.51	4.76±1.03	65.88±8.52
TiO_2/C-700	31.38±14.59	17.50±5.88	51.12±10.05

S2

252

Table S3. Comparison of the cycling performances of $Ti_3C_2T_z$ MXene-based anodes in LIBs

Active materials (AM)	Morphology of materials	Composition of AM Mass ratio /%	Total electrode composition /%	Potential V vs. Li^+/Li	Specific current /A g^{-1}	Initial capacity /mAh g^{-1}	100th cycle capacity /mAh g^{-1}	Capacity (n^{th} cycles) /mAh g^{-1}	Reference
AE-$Ti_3C_2T_z$	**Multilayer/films**	**100% AE-$Ti_3C_2T_z$**	**100% AM**	**0.01-3.0**	**1**	**95**	**95**	**89 (2000th)**	**This work**
$Ti_3C_2T_z$ nanosheets	Ultrathin oligolayer	100% $Ti_3C_2T_z$	AM: Super P:PVdF 80:10:10	0.01-2.5	1	340	326	300 (1000th)	[1]
$Ti_3C_2T_z$−rGO hybrid	3D porous films	$Ti_3C_2T_z$:GO 50:50	100% AM	0.005-3.0	1	182	176	212 (1000th)	[2]
Porous $Ti_3C_2T_z$/CNTs	Films	$Ti_3C_2T_z$:CNTs 90:10	100% AM	0.01-3.0	0.16	794	500	500 (100th)	[3]
RGO/porous $Ti_3C_2T_z$-cellulose	Nanofibers	$Ti_3C_2T_z$:GO:cellulose 25:25:50	100% AM	0.01-3.0	1	148	140	120 (1000th)	[4]
$Ti_3C_2T_z$	Multilayer	100% $Ti_3C_2T_z$	AM:Super P:PVdF 80:10:10	0.01-3.0	0.02	502	97	97 (100th)	[5]
NH_3-$Ti_3C_2T_z$	Multilayer	N-doping	AM:Super P:PVdF 80:10:10	0.05-3.0	0.3	173	184	171 (500th)	[6]

S3

253

Table S4. Comparison of the cycling performances of $Ti_3C_2T_z$ MXene-based anodes in SIBs.

Active materials (AM)	Morphology of materials	Composition of AM Mass ratio/%	Total electrode composition/%	Potential/ V vs. Na^+/Na	Specific current/ A g^{-1}	Initial capacity/ mAh g^{-1}	100th cycle capacity /mAh g^{-1}	Capacity (XXth cycles) /mAh g^{-1}	Reference
AE-$Ti_3C_2T_z$	**Multilayer/films**	**100% AE-$Ti_3C_2T_z$**	**100% AM**	**0.01-3.0**	**0.5**	**73**	**83**	**85 (300th)**	**This work**
$Ti_3C_2T_z$ nanosheets	Ultrathin oligolayer	100% $Ti_3C_2T_z$	AM:Super P:PVdF 80:10:10	0.01-2.5	0.5	284	261	280 (800th)	[1]
$Ti_3C_2T_z$	3D microporous film	100% $Ti_3C_2T_z$	100% AM	0.01-3.0	0.5	210	195	295 (1,000th)	[7]
$Ti_3C_2T_z$	Multilayer	100% $Ti_3C_2T_z$	AM:multiwall carbon nanotube:sodium alginate 80:10:10	0.01-2.5	0.2	84	72	68 (1,000th)	[8]
$Ti_3C_2T_z$	Few-layered nanosheets	S-doping	AM:acetylene black:CMC 80:10:10	0.01-2.5	1	141	130	76 (1,500th)	[9]
Alkalized Ti_3C_2 MXene	Nanoribbons	100% Ti_3C_2	AM:carbon black:PVdF 70:20:10	0.01-3.0	0.2	96	65	50 (500th)	[10]
$Ti_3C_2T_z$	Multilayered nanosheets	100% $Ti_3C_2T_z$	AM:acetylene black:PVdF 80:10:10	0.1-3.0	0.02	150	100	100 (100th)	[11]

Supporting Figures
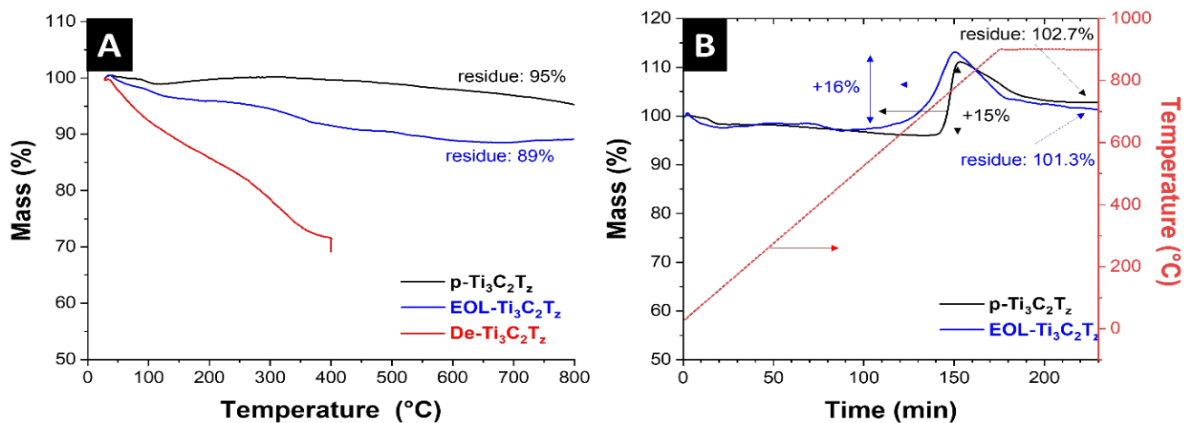
Figure S1. Thermogravimetric behavior of $Ti_3C_2T_z$ Mxene pristine (p-), delaminated (De-) and cycled to end-of-life as LIB electrode (EOL-) in (**A**) argon and (**B**) CO_2 atmosphere. Heating rate: 5 °C min^{-1}.
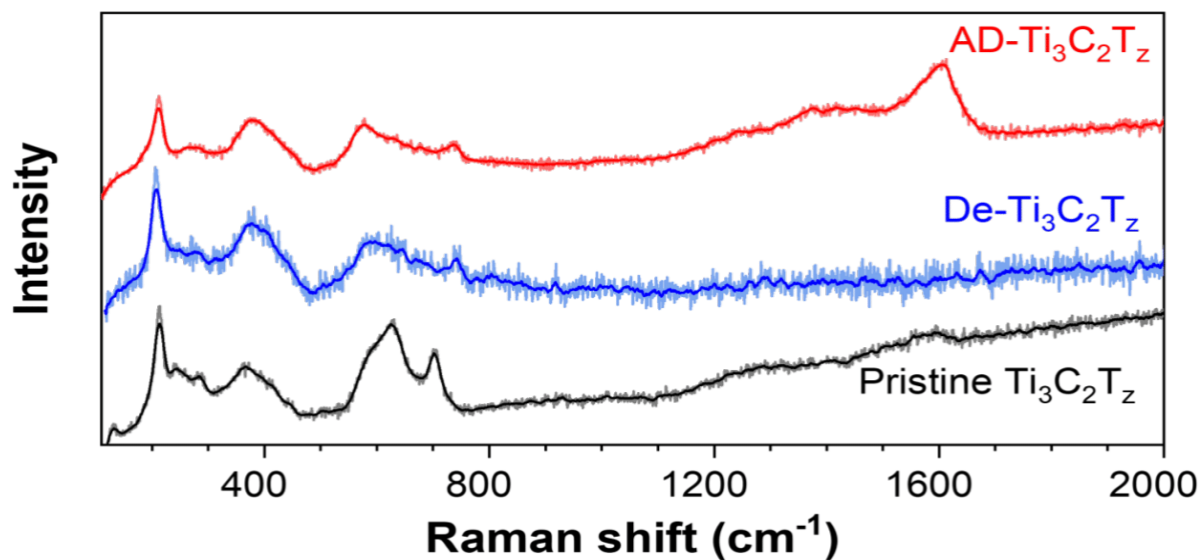
Figure S2. Raman spectra of $AD\text{-}Ti_3C_2T_z$, $De\text{-}Ti_3C_2T_z$, and pristine-$Ti_3C_2T_z$.
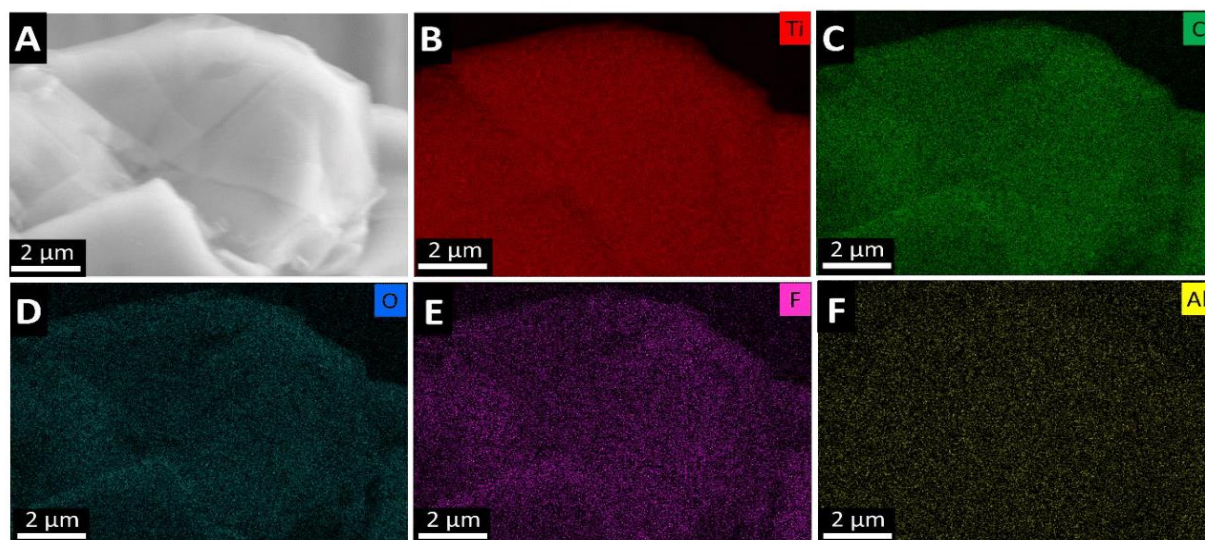
Figure S3. Elemental mapping of De-Ti$_3$C$_2$T$_z$ free-standing electrodes.
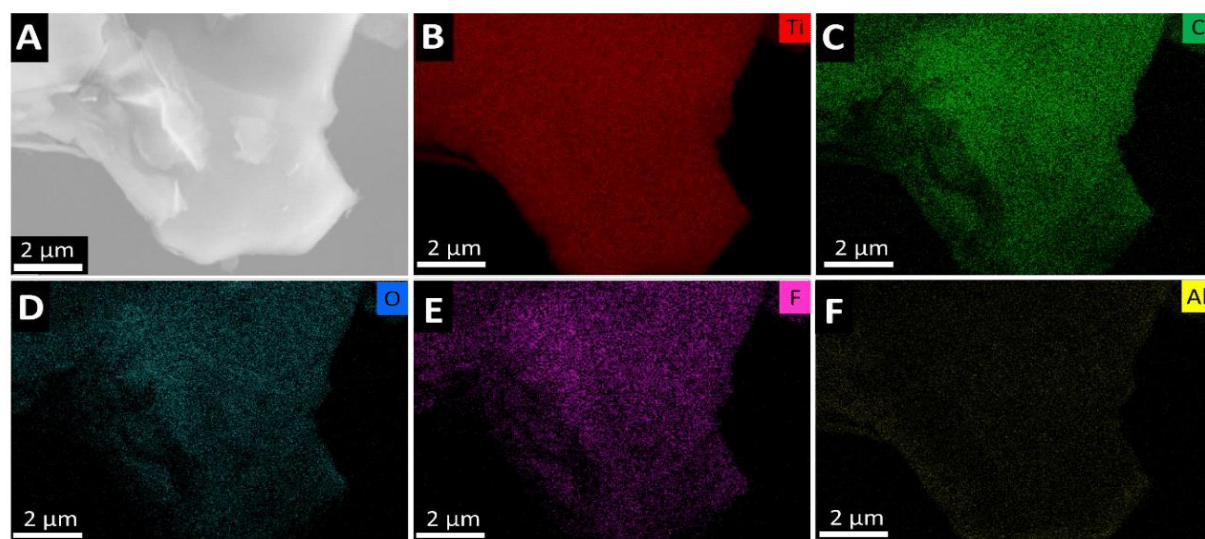
Figure S4. Elemental mapping of AD-Ti$_3$C$_2$T$_z$ free-standing electrodes.

256
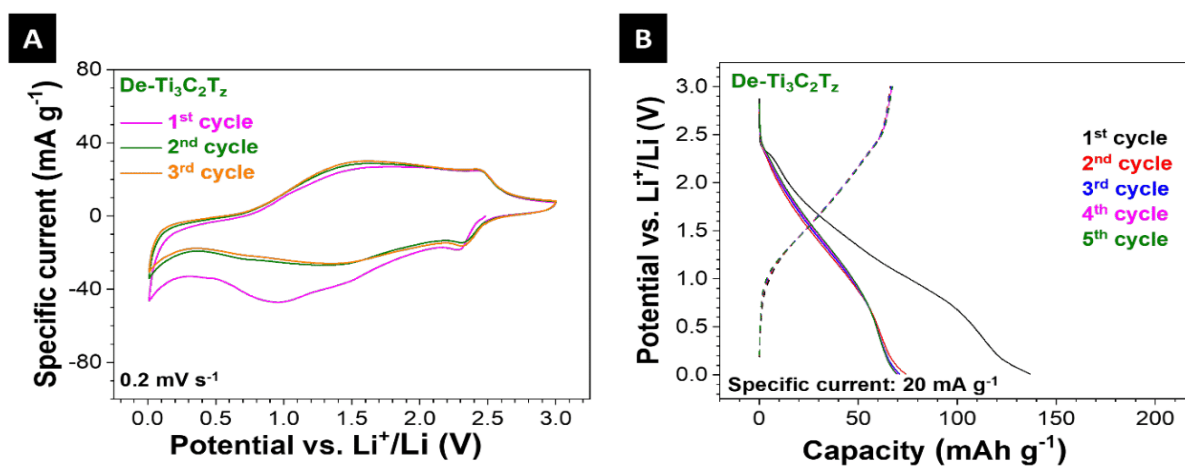
Figure S5. (**A**) Cyclic voltammograms, and (**B**) galvanostatic charge/discharge profiles of De-$Ti_3C_2T_z$ free-standing electrodes.
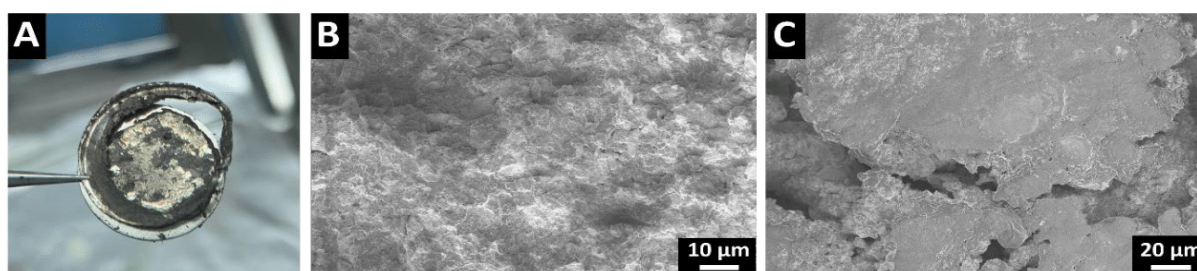
Figure S6. (A) Photograph, and **(B-C)** scanning electron micrographs of the Li electrodes after 4,000 cycles.
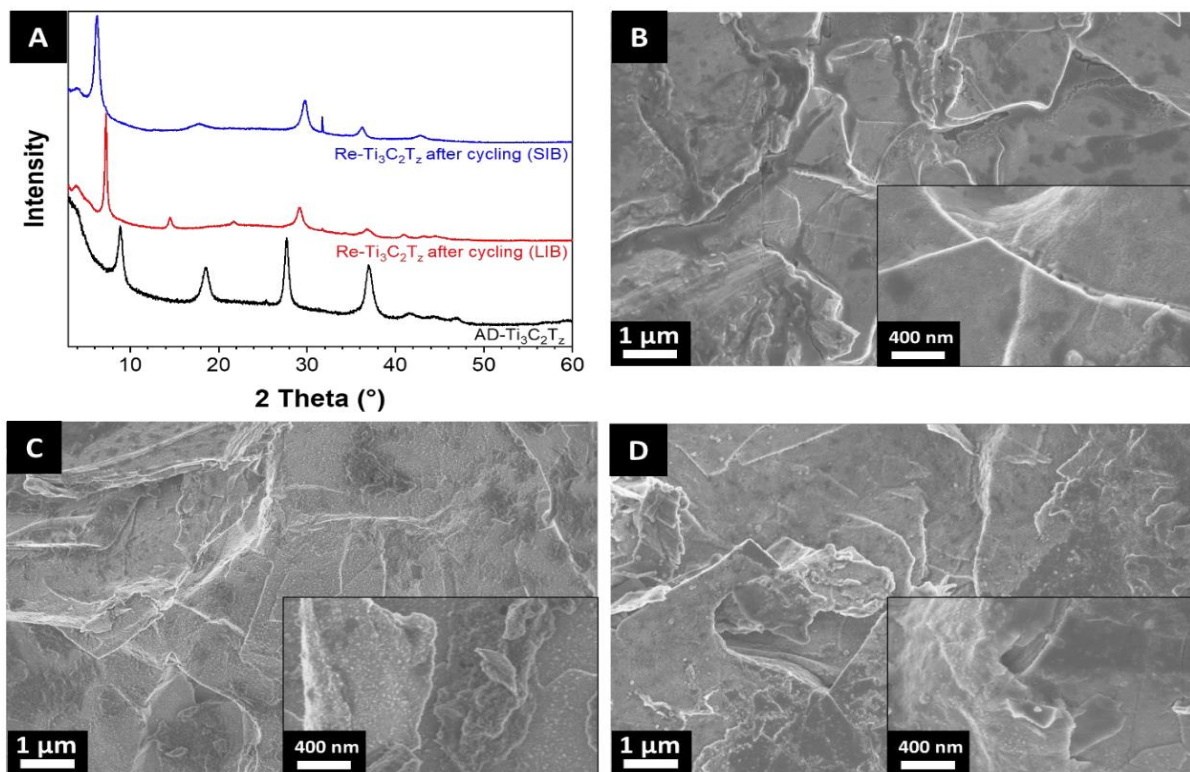
Figure S7. (**A**) X-ray diffractograms of AD-Ti$_3$C$_2$T$_z$ prior to cycling and Re-Ti$_3$C$_2$T$_z$ after being cycled (AD-Ti$_3$C$_2$T$_z$ cycled twice) as LIB and SIB electrode. Scanning electron micrographs of (**B**) EOL-Ti$_3$C$_2$T$_z$ (AD-Ti$_3$C$_2$T$_z$ cycled once) and cycled Re-Ti$_3$C$_2$T$_z$ (AD-Ti$_3$C$_2$T$_z$ cycled twice) as LIB (**C**) and SIB (**D**) electrode.

Supporting references

[1] X. Song, H. Wang, S. Jin, M. Lv, Y. Zhang, X. Kong, H. Xu, T. Ma, X. Luo, H. Tan, D. Hu, C. Deng, X. Chang, J. Xu, Oligolayered $Ti_3C_2T_x$ MXene towards high performance lithium/sodium storage, Nano Research 13(6) (2020) 1659-1667.

[2] Z. Ma, X. Zhou, W. Deng, D. Lei, Z. Liu, 3D Porous MXene (Ti_3C_2)/reduced graphene oxide hybrid films for advanced Lithium storage, ACS Applied Materials & Interfaces 10(4) (2018) 3634-3643.

[3] C.E. Ren, M.Q. Zhao, T. Makaryan, J. Halim, M. Boota, S. Kota, B. Anasori, M.W. Barsoum, Y. Gogotsi, Porous two-dimensional transition metal carbide (MXene) flakes for high-performance Li-ion storage, ChemElectroChem 3(5) (2016) 689-693.

[4] W. Zhang, Z.-Z. Pan, W. Lv, R. Lv, W. Shen, F. Kang, Q.-H. Yang, Y. Weng, Z.-H. Huang, Wasp nest-imitated assembly of elastic rGO/p-$Ti_3C_2T_x$ MXene-cellulose nanofibers for high-performance sodium-ion batteries, Carbon 153 (2019) 625-633.

[5] N. Sun, B.-y. Yang, J.-c. Zheng, Z.-j. He, H. Tong, L.-b. Tang, C.-s. An, B. Xiao, Effect of synthesis temperature on the phase structure, morphology and electrochemical performance of Ti_3C_2 as an anode material for Li-ion batteries, Ceramics International 44(14) (2018) 16214-16218.

[6] R. Cheng, T. Hu, H. Zhang, C. Wang, M. Hu, J. Yang, C. Cui, T. Guang, C. Li, C. Shi, P. Hou, X. Wang, Understanding the Lithium storage mechanism of $Ti_3C_2T_x$ MXene, The Journal of Physical Chemistry C 123(2) (2018) 1099-1109.

[7] M.Q. Zhao, X. Xie, C.E. Ren, T. Makaryan, B. Anasori, G. Wang, Y. Gogotsi, Hollow MXene spheres and 3D macroporous MXene frameworks for Na-Ion Storage, Advanced Materials 29(37) (2017) 1702410.

[8] X. Wang, X. Shen, Y. Gao, Z. Wang, R. Yu, L. Chen, Atomic-scale recognition of surface structure and intercalation mechanism of $Ti_3C_2T_x$, Journal of the American Chemical Society 137(7) (2015) 2715-21.

[9] Y. Wu, P. Nie, J. Wang, H. Dou, X. Zhang, Few-Layer MXenes delaminated via high-energy mechanical milling for enhanced Sodium-ion batteries performance, ACS Applied Materials & Interfaces 9(45) (2017) 39610-39617.

[10] P. Lian, Y. Dong, Z.-S. Wu, S. Zheng, X. Wang, W. Sen, C. Sun, J. Qin, X. Shi, X. Bao, Alkalized Ti_3C_2 MXene nanoribbons with expanded interlayer spacing for high-capacity sodium and potassium ion batteries, Nano Energy 40 (2017) 1-8.

[11] S. Kajiyama, L. Szabova, K. Sodeyama, H. Iinuma, R. Morita, K. Gotoh, Y. Tateyama, M. Okubo, A. Yamada, Sodium-ion intercalation mechanism in MXene nanosheets, ACS Nano 10(3) (2016) 3334-41.

5 CONCLUSION AND OUTLOOK

The global drive towards an environmentally friendly society and the associated steady growth of the renewable energy sector requires the continuous further development and optimization of a wide range of energy storage systems. In order to be able to guarantee the supply of energy independent of environmental influences, energy-efficient and safe energy storage technologies must be applied. In this context, there is an extreme need for technologies that exceed the performance characteristics of today's commercial storage modules in terms of energy and power density while at the same time conserving critical material resources and being highly recyclable. Improving established systems such as LIBs plays just as important a role as advancing equivalent alternatives that conserve diminished resources, like the NIB technology. In addition, electrochemical processes explored in this context offer an attractive opportunity to develop energy-efficient water treatment technologies that can address water scarcity resulting from global climate change and the ever-growing world population. At the end of the lifetime of successfully deployed electrochemical modules is the successful return to the economic process, which must be realized concerning highly depleted resources such as lithium.

This thesis explores the (hybrid) electrode materials at the intersection of the energy/water/recycling nexus and their continuous optimization and reorientation. It is widely recognized that the carbon substrate plays a critical role in determining the homogenous distribution and physical properties of electrodes, which can strongly impact energy storage performance. To improve performance, carbon onions - with their small size and graphitic order - were used in combination with the well-studied LTO material as a hybrid electrode material in the initial stage of the experiment. After manufacturing two different types of carbon onion, one obtained from annealing in argon at 1300 °C (with a lower degree of graphitic ordering, and which is constructed of both carbon onions and graphene nanoribbons), and one from annealing under vacuum conditions at 1700 °C (with a higher degree of graphitic ordering) their electrochemical performance in combination with synthesized nano-sized LTO was investigated as anode material in LIBs and NIBs. The best performance was yielded with the LTO hybridized with carbon onions treated under argon atmosphere which resulted in a specific capacity of 188 mAh g^{-1} with a capacity retention of 95.8% after 400 cycles. When applied as NIB anode material, the performance demonstrated an excellent longevity of 96% capacity retention after 500 cycles. The selection of the right carbon substrate plays a vital role in the electrochemical performance. The carbon structure seems less relevant compared to the nanoscale distribution and homogeneity within the hybrid and the electrode.

MXene, a powerful 2D material class in different parts applications, is also widely explored in electrochemical energy storage devices such as alkali-ion batteries. With multilayered stacked MXene lacking high rate capabilities and cycling stabilities in addition to the limited uptake capacity, further improvements have increased the focus on open architectures. Therefore, in this work, silica-pillared

$Ti_3C_2T_z$ MXene was synthesized using tetraethylortho silicate as the silica source and dodecylamine (DDA) as the co-pillar amine. Obtained improved MXene structure with enlarged interlayer spacing significantly enhanced performance as anode material of LIB. Thereby at a specific current of 1 A g^{-1} the silica silica-pillared MXene achieved over 4 times the capacity of the non-pillared material (<150 mAh g^{-1}) while showing capacity retention of 71% after 500 consecutive cycles. Subsequent in situ dilatometry, in combination with XRD data, revealed that during lithiation, a constant relative expansion of 3-4% occurred while the non-pillared MXene expanded continuously with increasing cycle number. This work provides key insights into the design of MXene electrodes, demonstrating that significantly enhanced electrochemical performance along with consistent volume changes can be achieved by a simple pillaring method. This makes MXenes become increasingly important for different energy storage systems.

Also benefiting from the excellent properties of the MXene material class, including their high electrical conductivity and accessible interlayer space, can be conversion or alloying type materials which suffer extremely from volume expansion and subsequent electrode pulverization resulting in poor cycling stability. Based on only the intercalation process, the specific capacity of pure MXene remains limited, but the exploration of combinations with other materials makes it a promising additive. Antimony, an alloying material with a high theoretical capacity of 660 mAh g^{-1} suffers from a volume expansion of up to 300% when alloying with sodium to form Na_3Sb. By synthesizing different antimony MXene hybrid materials, the influence of different MXenes, and different hybrid synthesis routes, resulting in different morphologies and electrode compositions, were explored by the electrochemical performance in NIB half cells. Thereof an initial expansion of the MXene layers to allow for the subsequent antimony intercalation during the synthesis seems not advantageous since parts of the active materials lose their electrochemical accessibility. Optimized synthesis conditions with a ratio of 60 mass% antimony and 40 mass% MXene accommodate volume expansion while delivering a specific capacity of 450 mAh g^{-1} at 0.1 A g^{-1} and 365 mAh g^{-1} at 4 A g^{-1}, with a capacity retention of around 96% after 100 cycles.

Overall, the best performance is not triggered by the smallest nanoparticles, the largest interlayer distance of the MXene, or the highest amount of antimony particles but by the most homogeneous distribution of antimony and MXene while both components remain electrochemically addressable. While confirming via in situ XRD that the alloying mechanism is not to be changed, this work gives inside into a promising combination exploiting positive features of different material classes resulting in synergistic electrochemical performance improvement.

In the adjacent work, a conversion material, which exhibits a promising high theoretical capacity of 1493 mAh g^{-1} and benefits from a relatively large natural occurrence, was also investigated in more detail in the hybrid with MXene. After successfully fabricating the SnO_2 nanoparticles in the presence

of $Ti_3C_2T_z$ MXene in a composition of 50/50 mass%, the obtained hybrid was used as an anode in a LIB half-cell, and the performance was evaluated in detail. Stable high specific capacities of 525 mAh g^{-1} were obtained for more than 700 cycles. Promising kinetic properties were also achieved, showing a capacity of 340 mAh g^{-1} at a specific current of high 8 A g^{-1}. Through various XPS and STEM investigations, the electrode reaction, which finally turned out to be $Sn+Li_2O \rightleftarrows SnO + 2e^- + 2\ Li^+$, was established. The obtained reversible and kinetically preferred electrochemical performance results from the synergistic interaction between tin oxide and MXene. In contrast, tin oxide provides the main charge storage property, and MXene is a buffer for the volume change during the electrochemical reaction as well as to improve the charge transport properties of the electrode.

In general, hybrid materials also exhibit additional benefits for alkali-ion batteries in addition to improving electrical conductivities, exhibiting highly efficient ion-electron transport properties, and faster charge/discharge rates. Thereby carbon hybrid materials, the most popular combined materials for electrodes, deliver a variety of possible combinations and designs while being cost-efficient, abundant, and supporting short diffusion paths for ions and electrolytes. When extending the possibilities of composite materials to the class of 2D materials, such as MXenes, further promising materials for use in the energy storage sector could be obtained, which can be used both as pure materials and in combination with other material classes. In addition, MXenes provide outstanding conductivity and offer the possibility of buffering the volume changes of alloys and conversion reactions. Thus, outstanding electrochemical performances could be obtained for both the LIB technology and the NIB application, giving a booster to applying high-performance alloying and conversion-type materials.

A bridge between the energy storage sector and water treatment is built by the seawater battery, which introduces the direct use of seawater as a source for converting electrical energy and chemical energy, providing an option for sustainable renewable energy storage. State-of-the-art seawater batteries are still challenged by technological drawbacks like a shortened lifetime, unsafe battery operation, low efficiencies, and low stabilities, which hinder the commercial application. However, the advantages of seawater batteries offer a perspective for sustainable, environmentally friendly, performance-oriented, and cost-efficient applications at the interface between energy and water. Expanding the concept of hybrid materials to the application as an electrode in water remediation offers the possibility for energy-efficient drinking water processing.

Antimony as a lithium/sodium alloy material, a promising and high-performance electrode for NIBs, can, for example, provide stable desalination performance at a more extended cell voltage than conventional capacitive deionization technology allows (1.0-1.2 V) using a bi-electrolyte system (organic and aqueous part). The Sb/C electrode in a combination of a selective sodium permeable membrane (NASICON) provides discharge capacities of initially 669 mAh g^{-1} (395 mAh g^{-1} after 40

cycles) at a specific current of 200 mA g^{-1} and a cut-off cell voltage of ±2.0 V. Therefore, operation in hybrid CDI cell provides a desalination capacity of an average of 294 mg$_{Na}$ g$_{Sb}^{-1}$ (748 mg$_{NaCl}$ g$_{Sb}^{-1}$) with a charge efficiency of about 74% in a 600 mM NaCl. Future work on optimizing the cell design and reducing the thickness of the ceramic membrane, can provide a promising technology for water desalination.

Another promising Faradaic material for effective desalination to generate fresh water is the three-dimensional cobalt hydroxide hollow cube, which can be prepared under simple synthesis conditions via template etching. By allowing fast ion transport, large surface area, and mitigation of volume expansion during cycling, a high desalination rate of 3.3 mg$_{NaCl}$ g$_{(Co(OH)2)}^{-1}$ min^{-1} with a corresponding desalination capacity of 1176 mg$_{NaCl}$ g$_{(Co(OH)2)}^{-1}$ can be obtained.

Faradaic materials in the context of water desalination deliver a promising approach for future developments for energy-efficient and high-performance ion removal providing the chance to offer the majority of the population access to clean drinking water. Approaches have been delivered by using aqueous solutions in combination with Faradaic materials, while also battery materials, which electrochemical potential window would not be suitable with the electrochemical stable voltage window of water, can be deployed in the context of water desalination by simply using a bi-electrolyte cell set up in combination with a selective ion exchange membrane.

The use of a selective membrane can also play an indispensable role in another application. Lithium, for example, is currently one of the most sought-after raw materials, and its demand will continue to rise in the foreseeable future. The development from combustion engines to electric drives for vehicles alone will make lithium a scarce resource. The development of further lithium sources, such as seawater, mine waters, or recycling solutions for old batteries, is thus inevitable. Regional lithium sources are ideal, as the CO_2 footprint of lithium technologies can be significantly improved by shortening transport distances. However, the problem of relatively low concentrations, usually present, is still a major challenge. One approach to counteract this could be a redox flow battery for continuous and energy-efficient recovery from aqueous solutions. Using a green redox battery and a LISICON membrane for selective uptake and release of Li$^+$-ions, a technology was proposed to recover dissolved lithium with a purity of 93.5% from simulated seawater.

When more and more batteries reach the end of their life in the future, multi-layered recycling approaches will be required in order to be able to return a large part of the resources directly to the economic cycle in an energy-efficient way. In addition to the threateningly depleted Li resources, many other metals, such as cobalt and nickel, which are used in many commercial battery cells, play a major role. As a case study, it has even been demonstrated that electrode materials can deliver near-initial capacities at the end of their life by simply washing the electrode and replacing the separator and lithium or sodium counter electrode. MXene (Ti$_3$C$_2$T$_z$) was employed as a pure electrode without

additional conductive additive to evaluate the recycling performance of LIBs and NIBs. Freestanding delaminated and annealed MXene electrodes deliver superior stability with a capacity retention of 94 % at 1 A g^{-1} after 2000 cycles when applied as negative electrodes in LIBs. For NIBs, capacities of 108 mAh g^{-1} and 71 mAh g^{-1} at 0.02 A g^{-1} and 2 A g^{-1} could be obtained, respectively. After the MXene electrode reached the end of its battery life, simple direct recycling processes were used to recover the electrodes, and the capacity recovery rate exceeded 90%. After reaching two times the end of life, the material was transformed into a metal oxide/carbon/carbide nanohybrid for alternative use, delivering a promising second-life application.

This study focused on developing (hybrid) electrode materials for various applications in energy storage, water treatment, and recycling. Different intercalation, conversion, and alloying materials were synthesized and incorporated into hybrid materials, and their electrochemical performance was tested and optimized in LIB and NIB. Optimized electrode materials with sodium ion storage performance were used in water desalination in a unique cell configuration to realize high-performance sodium removal. Other Faradaic materials were applied in the aqueous medium for capacitive deionization with high desalination capacity and long-term performance stability. Various recycling processes were also investigated, starting from electrode material, which could be reused after reaching the end of life by simple reprocessing steps, as well as finding an alternative application as converted material after finally reaching the end of life. For example, heavily depleted lithium resources can be relieved using an environmentally friendly redox flow battery for continuous and energy-efficient lithium recovery from aqueous solution by recovering lithium from low-concentration sources such as seawater, mine water, or dissolved spent battery.

Easy synthesis methods towards more sustainability could guide designing more hybrid materials for different energy storage applications at the energy/water/recycling nexus. For next-generation energy storage technology, it should be considered to improve all aspects of electrode material design and electrolyte choice while improving energy and power density next to recyclability. Applying battery electrode materials in water desalination could open more opportunities for further high-capacity developments, even in flow-electrode CDI. Essential for all aspects will be the possibility to recycle different cell parts. Approaches for electrode material recycling and element recovery show this topic's relatively simple handling. Further progress can be achieved through further simplification and research on suitable free-standing electrodes, which can be returned to the economic cycle. In addition, lithium recovery can be extended to other key elements of the energy storage sector that do not neglect future-oriented technologies such as NIB.

6 REFERENCES

1. P. D. B. Burger, *Öffentliche Nettostromerzeugung in Deutschland im Jahr 2022*, Frauenhofer ISE, www.energy-charts.info, 2023.
2. K. Petr and B. Petr, in *Energy Storage*, ed. Z. Ahmed Faheem, IntechOpen, Rijeka, 2013, DOI: 10.5772/52222, p. Ch. 3.
3. M. Li, J. Lu, Z. Chen and K. Amine, *Advanced Materials*, 2018, **30**, 1800561.
4. F. Wu, J. Maier and Y. Yu, *Chemical Society Reviews*, 2020, **49**, 1569-1614.
5. J.-M. Tarascon, *Nature Chemistry*, 2010, **2**, 510-510.
6. D. Kundu, E. Talaie, V. Duffort and L. F. Nazar, *Angewandte Chemie International Edition*, 2015, **54**, 3431-3448.
7. C. Vaalma, D. Buchholz, M. Weil and S. Passerini, *Nature reviews materials*, 2018, **3**, 1-11.
8. P. K. Nayak, L. Yang, W. Brehm and P. Adelhelm, *Angewandte Chemie International Edition*, 2018, **57**, 102-120.
9. H. Zhang, I. Hasa and S. Passerini, *Advanced Energy Materials*, 2018, **8**, 1702582.
10. M. T. McDowell, S. W. Lee, W. D. Nix and Y. Cui, *Advanced Materials*, 2013, **25**, 4966-4985.
11. Y. Wu, X. Huang, L. Huang and J. Chen, *energy & environmental materials*, 2021, **4**, 19-45.
12. S. Wilke, B. Schweitzer, S. Khateeb and S. Al-Hallaj, *Journal of Power Sources*, 2017, **340**, 51-59.
13. J. M. Lee, G. Singh, W. Cha, S. Kim, J. Yi, S.-J. Hwang and A. Vinu, *ACS Energy Letters*, 2020, **5**, 1939-1966.
14. Y. Chen, X. Li, K. Park, J. Song, J. Hong, L. Zhou, Y.-W. Mai, H. Huang and J. B. Goodenough, *Journal of the American Chemical Society*, 2013, **135**, 16280-16283.
15. S. Arnold, L. Wang and V. Presser, *Small*, 2022, **18**, 2107913.
16. M. A. Shannon, P. W. Bohn, M. Elimelech, J. G. Georgiadis, B. J. Marinas and A. M. Mayes, *Nature*, 2008, **452**, 301-310.
17. A. Alkaisi, R. Mossad and A. Sharifian-Barforoush, *Energy Procedia*, 2017, **110**, 268-274.
18. T. Welgemoed and C. F. Schutte, *Desalination*, 2005, **183**, 327-340.
19. Y. Oren, *Desalination*, 2008, **228**, 10-29.
20. E. Martinez-Laserna, I. Gandiaga, E. Sarasketa-Zabala, J. Badeda, D.-I. Stroe, M. Swierczynski and A. Goikoetxea, *Renewable and Sustainable Energy Reviews*, 2018, **93**, 701-718.
21. Y. Zhao, O. Pohl, A. I. Bhatt, G. E. Collis, P. J. Mahon, T. Rüther and A. F. Hollenkamp, *Sustainable Chemistry*, 2021, **2**, 167-205.
22. J. Kondoh, I. Ishii, H. Yamaguchi, A. Murata, K. Otani, K. Sakuta, N. Higuchi, S. Sekine and M. Kamimoto, *Energy Conversion and Management*, 2000, **41**, 1863-1874.
23. H. Chen, T. N. Cong, W. Yang, C. Tan, Y. Li and Y. Ding, *Progress in Natural Science*, 2009, **19**, 291-312.
24. S. Hameer and J. L. van Niekerk, *International Journal of Energy Research*, 2015, **39**, 1179-1195.
25. Y. Shao, M. F. El-Kady, J. Sun, Y. Li, Q. Zhang, M. Zhu, H. Wang, B. Dunn and R. B. Kaner, *Chemical reviews*, 2018, **118**, 9233-9280.
26. L. Zhang, X. Hu, Z. Wang, F. Sun and D. G. Dorrell, *Renewable and Sustainable Energy Reviews*, 2018, **81**, 1868-1878.
27. V. V. Jadhav, R. S. Mane, P. V. Shinde, V. V. Jadhav, R. S. Mane and P. V. Shinde, *Bismuth-Ferrite-Based Electrochemical Supercapacitors*, 2020, 11-36.
28. S. Wang, T. Wei and Z. Qi, 2009.
29. S. Mekhilef, R. Saidur and A. Safari, *Renewable and Sustainable Energy Reviews*, 2012, **16**, 981-989.
30. T. Placke, R. Kloepsch, S. Dühnen and M. Winter, *Journal of Solid State Electrochemistry*, 2017, **21**, 1939-1964.
31. A. Volta, *Philosophical transactions of the Royal Society of London*, 1800, 403-431.
32. T. P. Crompton and T. R. Crompton, *Battery reference book*, Newnes, 2000.

REFERENCES

33. K. Kordesch and W. Taucher-Mautner, in *Encyclopedia of Electrochemical Power Sources*, ed. J. Garche, Elsevier, Amsterdam, 2009, DOI: https://doi.org/10.1016/B978-044452745-5.00003-4, pp. 555-564.
34. M. Broussely, P. Biensan and B. Simon, *Electrochimica Acta*, 1999, **45**, 3-22.
35. J. Broadhead, D. Murphy and B. Steele, *Materials for advanced batteries*, Plenum Press, 1980.
36. K. Mizushima, P. Jones, P. Wiseman and J. B. Goodenough, *Materials Research Bulletin*, 1980, **15**, 783-789.
37. R. Korthauer, *Handbuch lithium-ionen-batterien*, Springer, 2013.
38. P. Kurzweil and O. K. Dietlmeier, *Elektrochemische Speicher: Superkondensatoren, Batterien, Elektrolyse-Wasserstoff, Rechtliche Rahmenbedingungen*, Springer-Verlag, 2018.
39. M. Lazzari and B. Scrosati, *Journal of The Electrochemical Society*, 1980, **127**, 773.
40. R. Van Noorden, *Nature*, 2014, **507**, 26.
41. F. Meng, J. McNeice, S. S. Zadeh and A. Ghahreman, *Mineral Processing and Extractive Metallurgy Review*, 2021, **42**, 123-141.
42. J.-Y. Hwang, S.-T. Myung and Y.-K. Sun, *Chemical Society Reviews*, 2017, **46**, 3529-3614.
43. N. Yabuuchi, K. Kubota, M. Dahbi and S. Komaba, *Chemical reviews*, 2014, **114**, 11636-11682.
44. M. Slater, D. Kim, E. Lee and C. Johnson, *Adv Funct Mater*, 2013, 947-958.
45. E. Comission, Critical raw materials, https://single-market-economy.ec.europa.eu/sectors/raw-materials/areas-specific-interest/critical-raw-materials_en, (accessed 07.03.2023).
46. J. F. Peters and M. Weil, *Resources*, 2016, **5**, 46.
47. G. G. Eshetu, S. Grugeon, H. Kim, S. Jeong, L. Wu, G. Gachot, S. Laruelle, M. Armand and S. Passerini, *ChemSusChem*, 2016, **9**, 462-471.
48. I. Hasa, S. Mariyappan, D. Saurel, P. Adelhelm, A. Y. Koposov, C. Masquelier, L. Croguennec and M. Casas-Cabanas, *Journal of Power Sources*, 2021, **482**, 228872.
49. M. Sarkar, A. R. M. H. Rashid and M. Hasanuzzaman, in *Reference Module in Materials Science and Materials Engineering*, Elsevier, 2022, DOI: https://doi.org/10.1016/B978-0-12-819728-8.00005-X.
50. Y.-X. Wang, Y.-G. Lim, M.-S. Park, S.-L. Chou, J. H. Kim, H.-K. Liu, S.-X. Dou and Y.-J. Kim, *Journal of Materials Chemistry A*, 2014, **2**, 529-534.
51. Faradion, First Faradion battery installed in Australia, https://faradion.co.uk/first-faradion-battery-installed-in-australia/, (accessed 06.03.2023).
52. CATL, CATL Unveils Its Latest Breakthrough Technology by Releasing Its First Generation of Sodium-ion Batteries, https://www.catl.com/en/news/665.html, (accessed 12.12.2022).
53. S. Gourang Patnaik, I. Escher, G. A. Ferrero and P. Adelhelm, *Batteries & Supercaps*, 2022, **5**, e202200043.
54. F. Nobili and R. Marassi, *Batteries: Present and Future Energy Storage Challenges*, 2020, 13.
55. H. Hou, X. Qiu, W. Wei, Y. Zhang and X. Ji, *Advanced energy materials*, 2017, **7**, 1602898.
56. H. Wendt and G. Kreysa, *Electrochemical engineering: science and technology in chemical and other industries*, Springer Science & Business Media, 1999.
57. W. Liu, P. Liu and D. Mitlin, *Advanced Energy Materials*, 2020, **10**, 2002297.
58. G. C. Chung, H. J. Kim, S. I. Yu, S. H. Jun, J. w. Choi and M. H. Kim, *Journal of The Electrochemical Society*, 2000, **147**, 4391.
59. S. J. An, J. Li, C. Daniel, D. Mohanty, S. Nagpure and D. L. Wood III, *Carbon*, 2016, **105**, 52-76.
60. P. Verma, P. Maire and P. Novák, *Electrochimica Acta*, 2010, **55**, 6332-6341.
61. D. Aurbach, M. D. Levi, E. Levi and A. Schechter, *The Journal of Physical Chemistry B*, 1997, **101**, 2195-2206.
62. E. Peled, *Journal of The Electrochemical Society*, 1979, **126**, 2047.
63. E. Peled and S. Menkin, *Journal of The Electrochemical Society*, 2017, **164**, A1703.
64. H. Adenusi, G. A. Chass, S. Passerini, K. V. Tian and G. Chen, *Advanced Energy Materials*, **n/a**, 2203307.
65. A. Jana and R. E. García, *Nano Energy*, 2017, **41**, 552-565.
66. J. Steiger, 2015.

266

67. J. Lee, J. Kim, S. Kim, C. Jo and J. Lee, *Materials Advances*, 2020, **1**, 3143-3166.
68. M. S. Whittingham, *Chemical reviews*, 2004, **104**, 4271-4302.
69. C. Liu, F. Li, L.-P. Ma and H.-M. Cheng, *Advanced Materials*, 2010, **22**, E28-E62.
70. M. S. E. Houache, C.-H. Yim, Z. Karkar and Y. Abu-Lebdeh, *Batteries*, 2022, **8**, 70.
71. S. W. Kim, D. H. Seo, X. Ma, G. Ceder and K. Kang, *Advanced Energy Materials*, 2012, **2**, 710-721.
72. S.-M. Oh, S.-T. Myung, J. Hassoun, B. Scrosati and Y.-K. Sun, *Electrochemistry communications*, 2012, **22**, 149-152.
73. R. Marom, S. F. Amalraj, N. Leifer, D. Jacob and D. Aurbach, *Journal of Materials Chemistry*, 2011, **21**, 9938-9954.
74. Y. Zhu, Y. Xu, Y. Liu, C. Luo and C. Wang, *Nanoscale*, 2013, **5**, 780-787.
75. M. Chen, W. Hua, J. Xiao, D. Cortie, W. Chen, E. Wang, Z. Hu, Q. Gu, X. Wang and S. Indris, *Nature communications*, 2019, **10**, 1-11.
76. S. Chen, C. Wu, L. Shen, C. Zhu, Y. Huang, K. Xi, J. Maier and Y. Yu, *Advanced Materials*, 2017, **29**, 1700431.
77. Q. Ni, Y. Bai, F. Wu and C. Wu, *Advanced Science*, 2017, **4**, 1600275.
78. C. Li, R. Zang, P. Li, Z. Man, S. Wang, X. Li, Y. Wu, S. Liu and G. Wang, *Chemistry–An Asian Journal*, 2018, **13**, 342-349.
79. C. Q. Lim and Z.-K. Tan, *ACS Applied Energy Materials*, 2021, **4**, 6214-6220.
80. D. O. Ojwang, M. Svensson, C. Njel, R. Mogensen, A. S. Menon, T. Ericsson, L. Häggström, J. Maibach and W. R. Brant, *ACS applied materials & interfaces*, 2021, **13**, 10054-10063.
81. Z. Shen, S. Guo, C. Liu, Y. Sun, Z. Chen, J. Tu, S. Liu, J. Cheng, J. Xie and G. Cao, *ACS Sustainable Chemistry & Engineering*, 2018, **6**, 16121-16129.
82. K. Abraham, *Electrochimica Acta*, 1993, **38**, 1233-1248.
83. T. Ohzuku, A. Ueda and N. Yamamoto, *Journal of the Electrochemical Society*, 1995, **142**, 1431.
84. X. Han, M. Ouyang, L. Lu and J. Li, *Energies*, 2014, **7**, 4895-4909.
85. G. Wang, J. Gao, L. Fu, N. Zhao, Y. Wu and T. Takamura, *Journal of Power Sources*, 2007, **174**, 1109-1112.
86. C.-H. Yim, S. Niketic, N. Salem, O. Naboka and Y. Abu-Lebdeh, *Journal of The Electrochemical Society*, 2016, **164**, A6294.
87. Y. Okamoto, *The Journal of Physical Chemistry C*, 2014, **118**, 16-19.
88. H. Moriwake, A. Kuwabara, C. Fisher and Y. Ikuhara, *Journal*, 2017.
89. D. Bresser, K. Hosoi, D. Howell, H. Li, H. Zeisel, K. Amine and S. Passerini, *Journal of Power Sources*, 2018, **382**, 176-178.
90. D. Stevens and J. Dahn, *Journal of the Electrochemical Society*, 2000, **147**, 1271.
91. M. D. Slater, D. Kim, E. Lee and C. S. Johnson, *Advanced Functional Materials*, 2013, **23**, 947-958.
92. M. Winter, J. O. Besenhard, M. E. Spahr and P. Novak, *Advanced materials*, 1998, **10**, 725-763.
93. G. Qin, X. Zhang and C. Wang, *Journal of Materials Chemistry A*, 2014, **2**, 12449-12458.
94. Y. Jin, B. Zhu, Z. Lu, N. Liu and J. Zhu, *Advanced Energy Materials*, 2017, **7**, 1700715.
95. K. Feng, M. Li, W. Liu, A. G. Kashkooli, X. Xiao, M. Cai and Z. Chen, *Small*, 2018, **14**, 1702737.
96. T. Kennedy, M. Brandon and K. M. Ryan, *Advanced Materials*, 2016, **28**, 5696-5704.
97. S. Y. Hong, Y. Kim, Y. Park, A. Choi, N.-S. Choi and K. T. Lee, *Energy & Environmental Science*, 2013, **6**, 2067-2081.
98. S. Mukherjee, Z. Ren and G. Singh, *Nano-Micro Letters*, 2018, **10**, 70.
99. Y. Han, N. Lin, T. Xu, T. Li, J. Tian, Y. Zhu and Y. Qian, *Nanoscale*, 2018, **10**, 3153-3158.
100. C. Nithya and S. Gopukumar, *WIREs Energy and Environment*, 2015, **4**, 253-278.
101. G.-L. Xu, R. Amine, A. Abouimrane, H. Che, M. Dahbi, Z.-F. Ma, I. Saadoune, J. Alami, W. L. Mattis, F. Pan, Z. Chen and K. Amine, *Advanced Energy Materials*, 2018, **8**, 1702403.
102. M. Wang, F. Zhang, C. S. Lee and Y. Tang, *Advanced Energy Materials*, 2017, **7**, 1700536.
103. Y. Kim, K.-H. Ha, S. M. Oh and K. T. Lee, *Chemistry – A European Journal*, 2014, **20**, 11980-11992.

104. A. Darwiche, L. Bodenes, L. Madec, L. Monconduit and H. Martinez, *Electrochimica Acta*, 2016, **207**, 284-292.
105. L. Bodenes, A. Darwiche, L. Monconduit and H. Martinez, *Journal of Power Sources*, 2015, **273**, 14-24.
106. W. Luo, F. Shen, C. Bommier, H. Zhu, X. Ji and L. Hu, *Accounts of Chemical Research*, 2016, **49**, 231-240.
107. Y. Zhang, H. Wang, Z. Luo, H. T. Tan, B. Li, S. Sun, Z. Li, Y. Zong, Z. J. Xu, Y. Yang, K. A. Khor and Q. Yan, *Advanced Energy Materials*, 2016, **6**, 1600453.
108. M. R. Palacin, *Chemical Society Reviews*, 2009, **38**, 2565-2575.
109. C. Fang, Y. Huang, W. Zhang, J. Han, Z. Deng, Y. Cao and H. Yang, *Advanced Energy Materials*, 2016, **6**, 1501727.
110. F. Klein, B. Jache, A. Bhide and P. Adelhelm, *Physical Chemistry Chemical Physics*, 2013, **15**, 15876-15887.
111. S.-H. Yu, X. Feng, N. Zhang, J. Seok and H. D. Abruña, *Accounts of Chemical Research*, 2018, **51**, 273-281.
112. L. Wang, J. Światowska, S. Dai, M. Cao, Z. Zhong, Y. Shen and M. Wang, *Materials Today Energy*, 2019, **11**, 46-60.
113. P. Kuang, J. Low, B. Cheng, J. Yu and J. Fan, *Journal of Materials Science & Technology*, 2020, **56**, 18-44.
114. Q. Zhong, Y. Li and G. Zhang, *Chemical Engineering Journal*, 2021, **409**, 128099.
115. J. K. Im, E. J. Sohn, S. Kim, M. Jang, A. Son, K.-D. Zoh and Y. Yoon, *Chemosphere*, 2021, **270**, 129478.
116. H. Wang and J.-M. Lee, *Journal of Materials Chemistry A*, 2020, **8**, 10604-10624.
117. A. Liu, X. Liang, X. Ren, W. Guan, M. Gao, Y. Yang, Q. Yang, L. Gao, Y. Li and T. Ma, *Advanced Functional Materials*, 2020, **30**, 2003437.
118. Z. W. Seh, K. D. Fredrickson, B. Anasori, J. Kibsgaard, A. L. Strickler, M. R. Lukatskaya, Y. Gogotsi, T. F. Jaramillo and A. Vojvodic, *ACS Energy Letters*, 2016, **1**, 589-594.
119. K. Rasool, M. Helal, A. Ali, C. E. Ren, Y. Gogotsi and K. A. Mahmoud, *ACS Nano*, 2016, **10**, 3674-3684.
120. G. Liu, J. Zou, Q. Tang, X. Yang, Y. Zhang, Q. Zhang, W. Huang, P. Chen, J. Shao and X. Dong, *ACS applied materials & interfaces*, 2017, **9**, 40077-40086.
121. C. Xing, S. Chen, X. Liang, Q. Liu, M. Qu, Q. Zou, J. Li, H. Tan, L. Liu and D. Fan, *ACS applied materials & interfaces*, 2018, **10**, 27631-27643.
122. S. Yu, H. Tang, D. Zhang, S. Wang, M. Qiu, G. Song, D. Fu, B. Hu and X. Wang, *Science of The Total Environment*, 2021, 152280.
123. K. Rasool, R. P. Pandey, P. A. Rasheed, S. Buczek, Y. Gogotsi and K. A. Mahmoud, *Materials Today*, 2019, **30**, 80-102.
124. D. Xiong, X. Li, Z. Bai and S. Lu, *Small*, 2018, **14**, 1703419.
125. X. Zhang, Z. Zhang and Z. Zhou, *Journal of energy chemistry*, 2018, **27**, 73-85.
126. J. Nan, X. Guo, J. Xiao, X. Li, W. Chen, W. Wu, H. Liu, Y. Wang, M. Wu and G. Wang, *Small*, 2021, **17**, 1902085.
127. M. Naguib, M. Kurtoglu, V. Presser, J. Lu, J. Niu, M. Heon, L. Hultman, Y. Gogotsi and M. W. Barsoum, *Advanced Materials*, 2011, **23**, 4248-4253.
128. G. Deysher, C. E. Shuck, K. Hantanasirisakul, N. C. Frey, A. C. Foucher, K. Maleski, A. Sarycheva, V. B. Shenoy, E. A. Stach, B. Anasori and Y. Gogotsi, *ACS Nano*, 2020, **14**, 204-217.
129. K. Deshmukh, A. Muzaffar, T. Kovářík, M. B. Ahamed and S. K. K. Pasha, in *Mxenes and their Composites*, eds. K. K. Sadasivuni, K. Deshmukh, S. K. K. Pasha and T. Kovářík, Elsevier, 2022, DOI: https://doi.org/10.1016/B978-0-12-823361-0.00009-5, pp. 1-47.
130. L. E. Toth, W. Jeitschko and C. M. Yen, *Journal of the Less Common Metals*, 1966, **10**, 29-32.
131. B. Anasori, M. R. Lukatskaya and Y. Gogotsi, *Nature Reviews Materials*, 2017, **2**, 1-17.
132. Y. Bai, K. Zhou, N. Srikanth, J. H. Pang, X. He and R. Wang, *RSC advances*, 2016, **6**, 35731-35739.
133. D. Magne, V. Mauchamp, S. Célérier, P. Chartier and T. Cabioc'h, *Physical Review B*, 2015, **91**, 201409.

134. A. S. Zeraati, S. A. Mirkhani, P. Sun, M. Naguib, P. V. Braun and U. Sundararaj, *Nanoscale*, 2021, **13**, 3572-3580.

135. K. R. G. Lim, M. Shekhirev, B. C. Wyatt, B. Anasori, Y. Gogotsi and Z. W. Seh, *Nature Synthesis*, 2022, **1**, 601-614.

136. V. Kamysbayev, A. S. Filatov, H. Hu, X. Rui, F. Lagunas, D. Wang, R. F. Klie and D. V. Talapin, *Science*, 2020, **369**, 979-983.

137. R. Zhao, M. Wang, D. Zhao, H. Li, C. Wang and L. Yin, *ACS Energy Letters*, 2017, **3**, 132-140.

138. Q. Guo, X. Zhang, F. Zhao, Q. Song, G. Su, Y. Tan, Q. Tao, T. Zhou, Y. Yu and Z. Zhou, *ACS nano*, 2020, **14**, 2788-2797.

139. L. Jiang, D. Zhou, J. Yang, S. Zhou, H. Wang, X. Yuan, J. Liang, X. Li, Y. Chen and H. Li, *Journal of Materials Chemistry A*, 2022, **10**, 13651-13672.

140. M. D. Levi, M. R. Lukatskaya, S. Sigalov, M. Beidaghi, N. Shpigel, L. Daikhin, D. Aurbach, M. W. Barsoum and Y. Gogotsi, *Advanced Energy Materials*, 2015, **5**, 1400815.

141. J. Come, J. M. Black, M. R. Lukatskaya, M. Naguib, M. Beidaghi, A. J. Rondinone, S. V. Kalinin, D. J. Wesolowski, Y. Gogotsi and N. Balke, *Nano Energy*, 2015, **17**, 27-35.

142. Z. Lin, D. Barbara, P.-L. Taberna, K. L. Van Aken, B. Anasori, Y. Gogotsi and P. Simon, *Journal of Power Sources*, 2016, **326**, 575-579.

143. P. Srimuk, F. Kaasik, B. Krüner, A. Tolosa, S. Fleischmann, N. Jäckel, M. C. Tekeli, M. Aslan, M. E. Suss and V. Presser, *Journal of Materials Chemistry A*, 2016, **4**, 18265-18271.

144. F. Dixit, K. Zimmermann, R. Dutta, N. J. Prakash, B. Barbeau, M. Mohseni and B. Kandasubramanian, *Journal of Hazardous Materials*, 2022, **423**, 127050.

145. M. Liang, L. Wang, V. Presser, X. Dai, F. Yu and J. Ma, *Advanced Science*, 2020, **7**, 2000621.

146. J. Ma, Y. Cheng, L. Wang, X. Dai and F. Yu, *Chemical Engineering Journal*, 2020, **384**, 123329.

147. L. Chen, X. Xu, L. Wan, G. Zhu, Y. Li, T. Lu, M. D. Albaqami, L. Pan and Y. Yamauchi, *Materials Chemistry Frontiers*, 2021, **5**, 3480-3488.

148. M. R. Lukatskaya, O. Mashtalir, C. E. Ren, Y. Dall'Agnese, P. Rozier, P. L. Taberna, M. Naguib, P. Simon, M. W. Barsoum and Y. Gogotsi, *Science*, 2013, **341**, 1502-1505.

149. M. Ghidiu, M. R. Lukatskaya, M.-Q. Zhao, Y. Gogotsi and M. W. Barsoum, *Nature*, 2014, **516**, 78-81.

150. O. Mashtalir, M. R. Lukatskaya, A. I. Kolesnikov, E. Raymundo-Pinero, M. Naguib, M. Barsoum and Y. Gogotsi, *Nanoscale*, 2016, **8**, 9128-9133.

151. T. Li, L. Yao, Q. Liu, J. Gu, R. Luo, J. Li, X. Yan, W. Wang, P. Liu, B. Chen, W. Zhang, W. Abbas, R. Naz and D. Zhang, *Angewandte Chemie International Edition*, 2018, **57**, 6115-6119.

152. M. R. Lukatskaya, S. Kota, Z. Lin, M.-Q. Zhao, N. Shpigel, M. D. Levi, J. Halim, P.-L. Taberna, M. W. Barsoum, P. Simon and Y. Gogotsi, *Nature Energy*, 2017, **2**, 17105.

153. K. Prenger, Y. Sun, K. Ganeshan, A. Al-Temimy, K. Liang, C. Dun, J. J. Urban, J. Xiao, T. Petit, A. C. T. van Duin, D.-e. Jiang and M. Naguib, *ACS Applied Energy Materials*, 2022, **5**, 9373-9382.

154. Y. Dall'Agnese, P. Rozier, P.-L. Taberna, Y. Gogotsi and P. Simon, *Journal of Power Sources*, 2016, **306**, 510-515.

155. K. Liang, R. A. Matsumoto, W. Zhao, N. C. Osti, I. Popov, B. P. Thapaliya, S. Fleischmann, S. Misra, K. Prenger, M. Tyagi, E. Mamontov, V. Augustyn, R. R. Unocic, A. P. Sokolov, S. Dai, P. T. Cummings and M. Naguib, *Advanced Functional Materials*, 2021, **31**, 2104007.

156. M. Naguib, J. Come, B. Dyatkin, V. Presser, P.-L. Taberna, P. Simon, M. W. Barsoum and Y. Gogotsi, *Electrochemistry Communications*, 2012, **16**, 61-64.

157. D. Sun, M. Wang, Z. Li, G. Fan, L.-Z. Fan and A. Zhou, *Electrochemistry communications*, 2014, **47**, 80-83.

158. X. Wang, X. Shen, Y. Gao, Z. Wang, R. Yu and L. Chen, *Journal of the American Chemical Society*, 2015, **137**, 2715-2721.

159. M. K. Aslam, T. S. AlGarni, M. S. Javed, S. S. A. Shah, S. Hussain and M. Xu, *Journal of Energy Storage*, 2021, **37**, 102478.

160. M. K. Aslam, Y. Niu and M. Xu, *Advanced Energy Materials*, 2021, **11**, 2000681.

161. J. Meng, F. Zhang, L. Zhang, L. Liu, J. Chen, B. Yang and X. Yan, *Journal of Energy Chemistry*, 2020, **46**, 256-263.

REFERENCES

162. H. Zhang, P. Zhang, W. Zheng, W. Tian, J. Chen, Y. Zhang and Z. Sun, *Electrochimica Acta*, 2018, **285**, 94-102.
163. Y. Liu, W. Wang, Y. Ying, Y. Wang and X. Peng, *Dalton transactions*, 2015, **44**, 7123-7126.
164. Y. An, Y. Tian, H. Wei, B. Xi, S. Xiong, J. Feng and Y. Qian, *Advanced Functional Materials*, 2020, **30**, 1908721.
165. J. Huang, R. Meng, L. Zu, Z. Wang, N. Feng, Z. Yang, Y. Yu and J. Yang, *Nano Energy*, 2018, **46**, 20-28.
166. P. Wang, Y. Yan, C. Cheng, W. Zhang, D. Zhou, L. Li, X. Yang, X.-Z. Liao, Z.-F. Ma and Y.-S. He, *CrystEngComm*, 2021, **23**, 368-377.
167. S. Zhang, H. Ying, R. Guo, W. Yang and W.-Q. Han, *The Journal of Physical Chemistry Letters*, 2019, **10**, 6446-6454.
168. Y. Chen, Y. Sun, M. Geng, W. Shao, Y. Chen, X. Liu and M. Ou, *Materials Letters*, 2021, **304**, 130704.
169. R. Meng, J. Huang, Y. Feng, L. Zu, C. Peng, L. Zheng, L. Zheng, Z. Chen, G. Liu, B. Chen, Y. Mi and J. Yang, *Advanced Energy Materials*, 2018, **8**, 1801514.
170. S. Arnold, A. Gentile, Y. Li, Q. Wang, S. Marchionna, R. Ruffo and V. Presser, *Journal of Materials Chemistry A*, 2022, **10**, 10569-10585.
171. H. Hou, M. Jing, Y. Yang, Y. Zhang, W. Song, X. Yang, J. Chen, Q. Chen and X. Ji, *Journal of Power Sources*, 2015, **284**, 227-235.
172. J. Zheng, Y. Yang, X. Fan, G. Ji, X. Ji, H. Wang, S. Hou, M. R. Zachariah and C. Wang, *Energy & Environmental Science*, 2019, **12**, 615-623.
173. J. He, Y. Wei, T. Zhai and H. Li, *Materials Chemistry Frontiers*, 2018, **2**, 437-455.
174. A. Darwiche, C. Marino, M. T. Sougrati, B. Fraisse, L. Stievano and L. Monconduit, *Journal of the American Chemical Society*, 2012, **134**, 20805-20811.
175. K. Pfeifer, S. Arnold, Ö. Budak, X. Luo, V. Presser, H. Ehrenberg and S. Dsoke, *Journal of Materials Chemistry A*, 2020, **8**, 6092-6104.
176. W. Wang, J. Xu, Z. Xu, W. Zheng, Y. Wang, Y. Jia, J. Ma, C. Wang and W. Xie, *Nanotechnology*, 2020, **31**, 215403.
177. J. Qian, Y. Xiong, Y. Cao, X. Ai and H. Yang, *Nano letters*, 2014, **14**, 1865-1869.
178. Y. G. Guo, J. S. Hu and L. J. Wan, *Advanced Materials*, 2008, **20**, 2878-2887.
179. P. G. Bruce, B. Scrosati and J. M. Tarascon, *Angewandte Chemie International Edition*, 2008, **47**, 2930-2946.
180. L. Hu, X. Zhu, Y. Du, Y. Li, X. Zhou and J. Bao, *Chemistry of Materials*, 2015, **27**, 8138-8145.
181. H. Lv, S. Qiu, G. Lu, Y. Fu, X. Li, C. Hu and J. Liu, *Electrochimica Acta*, 2015, **151**, 214-221.
182. W. Luo, J. Ren, W. Feng, X. Chen, Y. Yan and N. Zahir, *Coatings*, 2021, **11**, 1233.
183. M. Morcrette, D. Larcher, J. Tarascon, K. Edström, J. Vaughey and M. Thackeray, *Electrochimica acta*, 2007, **52**, 5339-5345.
184. L. M. Fransson, J. Vaughey, R. Benedek, K. Edström, J. O. Thomas and M. Thackeray, *Electrochemistry Communications*, 2001, **3**, 317-323.
185. X. Li, S. Xiao, X. Niu, J. S. Chen and Y. Yu, *Advanced Functional Materials*, 2021, **31**, 2104798.
186. Y. He and W. Sun, *Journal of Alloys and Compounds*, 2018, **753**, 371-377.
187. M. Hu, Y. Jiang, W. Sun, H. Wang, C. Jin and M. Yan, *ACS applied materials & interfaces*, 2014, **6**, 19449-19455.
188. X. Xie, D. Su, J. Zhang, S. Chen, A. K. Mondal and G. Wang, *Nanoscale*, 2015, **7**, 3164-3172.
189. Y. Zhao and A. Manthiram, *Chemical Communications*, 2015, **51**, 13205-13208.
190. Y. Lin, W. Feng, Z. Li, T. Xu and H. Fei, *Ionics*, 2017, **23**, 3197-3202.
191. J. Xie, Y. Pei, L. Liu, S. Guo, J. Xia, M. Li, Y. Ouyang, X. Zhang and X. Wang, *Electrochimica Acta*, 2017, **254**, 246-254.
192. K. P. Lakshmi, K. J. Janas and M. M. Shaijumon, *Carbon*, 2018, **131**, 86-93.
193. S. Huang, Z. Wen, J. Zhang, Z. Gu and X. Xu, *Solid State Ionics*, 2006, **177**, 851-855.
194. S. Fleischmann, A. Tolosa and V. Presser, *Chemistry–A European Journal*, 2018, **24**, 12143-12153.

195. K. Naoi, S. Ishimoto, J.-i. Miyamoto and W. Naoi, *Energy & Environmental Science*, 2012, **5**, 9363-9373.
196. G. Kickelbick, *Hybrid materials*, 2007, **1**, 2.
197. W. L. Wang, B.-Y. Oh, J.-Y. Park, H. Ki, J. Jang, G.-Y. Lee, H.-B. Gu and M.-H. Ham, *Journal of Power Sources*, 2015, **300**, 272-278.
198. M. Walter, R. Erni and M. V. Kovalenko, *Scientific Reports*, 2015, **5**, 8418.
199. Z. Hai and S. Zhuiykov, *Advanced Materials Interfaces*, 2018, **5**, 1701385.
200. Q. Yun, L. Li, Z. Hu, Q. Lu, B. Chen and H. Zhang, *Advanced Materials*, 2020, **32**, 1903826.
201. S. Schweidler, L. de Biasi, A. Schiele, P. Hartmann, T. Brezesinski and J. r. Janek, *The Journal of Physical Chemistry C*, 2018, **122**, 8829-8835.
202. M. Naguib, M. W. Barsoum and Y. Gogotsi, *Advanced Materials*, 2021, **33**, 2103393.
203. M. R. Lukatskaya, S.-M. Bak, X. Yu, X.-Q. Yang, M. W. Barsoum and Y. Gogotsi, *Advanced Energy Materials*, 2015, **10**.
204. Y. Li, H. Shao, Z. Lin, J. Lu, L. Liu, B. Duployer, P. O. Persson, P. Eklund, L. Hultman and M. Li, *Nature Materials*, 2020, **19**, 894-899.
205. E. Yang, H. Ji, J. Kim, H. Kim and Y. Jung, *Physical Chemistry Chemical Physics*, 2015, **17**, 5000-5005.
206. D. Er, J. Li, M. Naguib, Y. Gogotsi and V. B. Shenoy, *ACS applied materials & interfaces*, 2014, **6**, 11173-11179.
207. M. Widmaier, N. Jäckel, M. Zeiger, M. Abuzarli, C. Engel, L. Bommer and V. Presser, *Electrochimica Acta*, 2017, **247**, 1006-1018.
208. M. E. Spahr, D. Goers, A. Leone, S. Stallone and E. Grivei, *Journal of Power Sources*, 2011, **196**, 3404-3413.
209. Q. Zhang, Z. Yu, P. Du and C. Su, *Recent Patents on Nanotechnology*, 2010, **4**, 100-110.
210. M. Lao, Y. Zhang, W. Luo, Q. Yan, W. Sun and S. X. Dou, *Advanced Materials*, 2017, **29**, 1700622.
211. C. Li, A. Sarapulova, K. Pfeifer and S. Dsoke, *ChemSusChem*, 2020, **13**, 986-995.
212. A. Saal, T. Hagemann and U. S. Schubert, *Advanced Energy Materials*, 2021, **11**, 2001984.
213. R. W. Nunes, J. R. Martin and J. F. Johnson, *Polymer Engineering & Science*, 1982, **22**, 205-228.
214. G. Ceder, A. Van der Ven and M. K. Aydinol, *JOM*, 1998, **50**, 35-40.
215. H. Zheng, R. Yang, G. Liu, X. Song and V. S. Battaglia, *The Journal of Physical Chemistry C*, 2012, **116**, 4875-4882.
216. S.-L. Chou, J.-Z. Wang, H.-K. Liu and S.-X. Dou, *The Journal of Physical Chemistry C*, 2011, **115**, 16220-16227.
217. T. Nakajima and H. Groult, *Fluorinated materials for energy conversion*, Elsevier, 2005.
218. C. C. Nguyen, T. Yoon, D. M. Seo, P. Guduru and B. L. Lucht, *ACS applied materials & interfaces*, 2016, **8**, 12211-12220.
219. K. Lee, N. Chromey, R. Culik, J. Barnes and P. Schneider, *Fundamental and Applied Toxicology*, 1987, **9**, 222-235.
220. D. L. Wood, J. D. Quass, J. Li, S. Ahmed, D. Ventola and C. Daniel, *Drying Technology*, 2018, **36**, 234-244.
221. J. Li, Y. Lu, T. Yang, D. Ge, D. L. Wood and Z. Li, *IScience*, 2020, **23**.
222. M. Wang, X. Dong, I. C. Escobar and Y.-T. Cheng, *ACS Sustainable Chemistry & Engineering*, 2020, **8**, 11046-11051.
223. O. Chernysh, V. Khomenko, I. Makyeyeva and V. Barsukov, *Materials Today: Proceedings*, 2019, **6**, 42-47.
224. H. Chen, M. Ling, L. Hencz, H. Y. Ling, G. Li, Z. Lin, G. Liu and S. Zhang, *Chemical reviews*, 2018, **118**, 8936-8982.
225. W. B. Hawley and J. Li, *Journal of Energy Storage*, 2019, **25**, 100862.
226. H. Liu, X. Cheng, Y. Chong, H. Yuan, J.-Q. Huang and Q. Zhang, *Particuology*, 2021, **57**, 56-71.
227. B. Ludwig, Z. Zheng, W. Shou, Y. Wang and H. Pan, *Scientific reports*, 2016, **6**, 1-10.
228. J. B. Goodenough and Y. Kim, *Chemistry of Materials*, 2010, **22**, 587-603.
229. K. Xu, *Chemical Reviews*, 2004, **104**, 4303-4418.

REFERENCES

230. D. Aurbach, Y. Talyosef, B. Markovsky, E. Markevich, E. Zinigrad, L. Asraf, J. S. Gnanaraj and H.-J. Kim, *Electrochimica Acta*, 2004, **50**, 247-254.
231. V. Aravindan, J. Gnanaraj, S. Madhavi and H.-K. Liu, *Chemistry – A European Journal*, 2011, **17**, 14326-14346.
232. A. Ponrouch, D. Monti, A. Boschin, B. Steen, P. Johansson and M. R. Palacín, *Journal of Materials Chemistry A*, 2015, **3**, 22-42.
233. C. Bommier and X. Ji, *Small*, 2018, **14**, 1703576.
234. A. Ponrouch, E. Marchante, M. Courty, J.-M. Tarascon and M. R. Palacin, *Energy & Environmental Science*, 2012, **5**, 8572-8583.
235. A. Ponrouch, R. Dedryvère, D. Monti, A. E. Demet, J. M. A. Mba, L. Croguennec, C. Masquelier, P. Johansson and M. R. Palacín, *Energy & Environmental Science*, 2013, **6**, 2361-2369.
236. C. Hamann and W. Vielstich, 1998.
237. K. X. T. Richard Jow, Oleg Borodin, Makoto Ue, *Electrolytes for Lithium and Lithium-Ion Batteries*, Springer New York, NY, Springer New York, NY, 2014.
238. J. Qian, X. Wu, Y. Cao, X. Ai and H. Yang, *Angewandte Chemie*, 2013, **125**, 4731-4734.
239. S. Komaba, W. Murata, T. Ishikawa, N. Yabuuchi, T. Ozeki, T. Nakayama, A. Ogata, K. Gotoh and K. Fujiwara, *Advanced Functional Materials*, 2011, **21**, 3859-3867.
240. T. M. Knoche, *Elektrolytbefüllung prismatischer Lithium-Ionen-Zellen*, Herbert Utz Verlag, 2018.
241. D. Di Lecce, V. Marangon, H.-G. Jung, Y. Tominaga, S. Greenbaum and J. Hassoun, *Green Chemistry*, 2022, **24**, 1021-1048.
242. K. Li, J. Zhang, D. Lin, D.-W. Wang, B. Li, W. Lv, S. Sun, Y.-B. He, F. Kang and Q.-H. Yang, *Nature communications*, 2019, **10**, 1-10.
243. K. Westman, R. Dugas, P. Jankowski, W. Wieczorek, G. Gachot, M. Morcrette, E. Irisarri, A. Ponrouch, M. R. Palacín and J.-M. Tarascon, *ACS Applied Energy Materials*, 2018, **1**, 2671-2680.
244. M. S. Park, S. B. Ma, D. J. Lee, D. Im, S.-G. Doo and O. Yamamoto, *Scientific reports*, 2014, **4**, 1-8.
245. X. Ren, S. Chen, H. Lee, D. Mei, M. H. Engelhard, S. D. Burton, W. Zhao, J. Zheng, Q. Li and M. S. Ding, *Chem*, 2018, **4**, 1877-1892.
246. G. Yang, S. Frisco, R. Tao, N. Philip, T. H. Bennett, C. Stetson, J.-G. Zhang, S.-D. Han, G. Teeter, S. P. Harvey, Y. Zhang, G. M. Veith and J. Nanda, *ACS Energy Letters*, 2021, **6**, 1684-1693.
247. N. Takami, T. Ohsaki, H. Hasebe and M. Yamamoto, *Journal of the Electrochemical Society*, 2001, **149**, A9.
248. A. Chagnes, B. Carré, P. Willmann, R. Dedryvère, D. Gonbeau and D. Lemordant, *Journal of The Electrochemical Society*, 2003, **150**, A1255.
249. S.-c. Kinoshita, M. Kotato, Y. Sakata, M. Ue, Y. Watanabe, H. Morimoto and S.-i. Tobishima, *Journal of Power Sources*, 2008, **183**, 755-760.
250. Y. Gu, S. Fang, L. Yang and S.-i. Hirano, *Journal of Materials Chemistry A*, 2021, **9**, 15363-15372.
251. D. Aurbach, *Journal of the Electrochemical Society*, 1989, **136**, 1606.
252. R. Mogensen, S. Colbin and R. Younesi, *Batteries & Supercaps*, 2021, **4**, 791-814.
253. S. Hess, M. Wohlfahrt-Mehrens and M. Wachtler, *Journal of The Electrochemical Society*, 2015, **162**, A3084.
254. P. Jankowski, N. Lindahl, J. Weidow, W. Wieczorek and P. Johansson, *ACS Applied Energy Materials*, 2018, **1**, 2582-2591.
255. K. Abe, in *Electrolytes for Lithium and Lithium-Ion Batteries*, Springer, 2014, pp. 167-207.
256. P. Bai, X. Han, Y. He, P. Xiong, Y. Zhao, J. Sun and Y. Xu, *Energy Storage Materials*, 2020, **25**, 324-333.
257. J. Qian, Y. Chen, L. Wu, Y. Cao, X. Ai and H. Yang, *Chemical Communications*, 2012, **48**, 7070-7072.
258. A. Ponrouch, A. Goñi and M. R. Palacín, *Electrochemistry communications*, 2013, **27**, 85-88.
259. V. Simone, L. Lecarme, L. Simonin and S. Martinet, *Journal of The Electrochemical Society*, 2016, **164**, A145.

260. R. Jung, M. Metzger, D. Haering, S. Solchenbach, C. Marino, N. Tsiouvaras, C. Stinner and H. A. Gasteiger, *Journal of The Electrochemical Society*, 2016, **163**, A1705.

261. V. Etacheri, O. Haik, Y. Goffer, G. A. Roberts, I. C. Stefan, R. Fasching and D. Aurbach, *Langmuir*, 2012, **28**, 965-976.

262. H. Lu, L. Wu, L. Xiao, X. Ai, H. Yang and Y. Cao, *Electrochimica Acta*, 2016, **190**, 402-408.

263. Y. Lee, J. Lee, J. Lee, K. Kim, A. Cha, S. Kang, T. Wi, S. J. Kang, H.-W. Lee and N.-S. Choi, *ACS applied materials & interfaces*, 2018, **10**, 15270-15280.

264. X. Zhao, Q.-C. Zhuang, S.-D. Xu, Y.-X. Xu, Y.-L. Shi and X.-X. Zhang, *Int. J. Electrochem. Sci*, 2015, **10**, 2515-2534.

265. Z. Yang, A. A. Gewirth and L. Trahey, *ACS Applied Materials & Interfaces*, 2015, **7**, 6557-6566.

266. K. U. Schwenke, S. Solchenbach, J. Demeaux, B. L. Lucht and H. A. Gasteiger, *Journal of The Electrochemical Society*, 2019, **166**, A2035.

267. S. Klein, P. Harte, S. van Wickeren, K. Borzutzki, S. Röser, P. Bärmann, S. Nowak, M. Winter, T. Placke and J. Kasnatscheew, *Cell Reports Physical Science*, 2021, **2**, 100521.

268. L. Ma, L. Ellis, S. Glazier, X. Ma, Q. Liu, J. Li and J. Dahn, *Journal of the electrochemical society*, 2018, **165**, A891.

269. S. Hong, B. Hong, W. Song, Z. Qin, B. Duan, Y. Lai and F. Jiang, *Journal of The Electrochemical Society*, 2018, **165**, A368.

270. X. Ma, R. Young, L. Ellis, L. Ma, J. Li and J. Dahn, *Journal of The Electrochemical Society*, 2019, **166**, A2665.

271. S. Wang, H. Hu, P. Yu, H. Yang, X. Cai and X. Wang, *Journal of Applied Electrochemistry*, 2018, **48**, 1221-1230.

272. Z. Wu, S. Li, Y. Zheng, Z. Zhang, E. Umesh, B. Zheng, X. Zheng and Y. Yang, *Journal of The Electrochemical Society*, 2018, **165**, A2792.

273. L. Xia, S. Lee, Y. Jiang, S. Li, Z. Liu, L. Yu, D. Hu, S. Wang, Y. Liu and G. Z. Chen, *ChemElectroChem*, 2019, **6**, 3747-3755.

274. Y. Yang, J. Xiong, S. Lai, R. Zhou, M. Zhao, H. Geng, Y. Zhang, Y. Fang, C. Li and J. Zhao, *ACS applied materials & interfaces*, 2019, **11**, 6118-6125.

275. B. Mosallanejad, S. S. Malek, M. Ershadi, A. A. Daryakenari, Q. Cao, F. Boorboor Ajdari and S. Ramakrishna, *Journal of Electroanalytical Chemistry*, 2021, **895**, 115505.

276. D.-H. Kim, B. Kang and H. Lee, *Journal of Power Sources*, 2019, **423**, 137-143.

277. H. Che, X. Yang, H. Wang, X.-Z. Liao, S. S. Zhang, C. Wang and Z.-F. Ma, *Journal of Power Sources*, 2018, **407**, 173-179.

278. Y.-K. Han, J. Yoo and T. Yim, *Journal of Materials Chemistry A*, 2015, **3**, 10900-10909.

279. J. Feng, Y. An, L. Ci and S. Xiong, *Journal of Materials Chemistry A*, 2015, **3**, 14539-14544.

280. X. Yuan, H. Liu and J. Zhang, *Lithium-ion batteries: advanced materials and technologies*, CRC press, 2011.

281. P. Kritzer and J. A. Cook, *Journal of the Electrochemical Society*, 2007, **154**, A481.

282. X. Huang, *Journal of Solid State Electrochemistry*, 2011, **15**, 649-662.

283. J. Kim, S. Choi, S. Jo, W. Lee and B. Kim, *Journal of the Electrochemical Society*, 2004, **152**, A295.

284. S. S. Zhang, *Journal of power sources*, 2007, **164**, 351-364.

285. J. Zhu, M. Yanilmaz, K. Fu, C. Chen, Y. Lu, Y. Ge, D. Kim and X. Zhang, *Journal of membrane science*, 2016, **504**, 89-96.

286. P. Zhu, D. Gastol, J. Marshall, R. Sommerville, V. Goodship and E. Kendrick, *Journal of Power Sources*, 2021, **485**, 229321.

287. J. Busom, A. Schreiber, A. Tolosa, N. Jäckel, I. Grobelsek, N. J. Peter and V. Presser, *Journal of Power Sources*, 2016, **329**, 432-440.

288. S.-T. Myung, Y. Hitoshi and Y.-K. Sun, *Journal of Materials Chemistry*, 2011, **21**, 9891-9911.

289. P. W. Atkins and J. De Paula, *Physikalische chemie*, John Wiley & Sons, 2013.

290. M. Winter and R. J. Brodd, *Chemical reviews*, 2004, **104**, 4245-4270.

291. J. O. Besenhard, *Handbook of battery materials*, John Wiley & Sons, 2008.

292. V. S. Bagotsky, A. M. Skundin and Y. M. Volfkovich, *Electrochemical power sources: batteries, fuel cells, and supercapacitors*, John Wiley & Sons, 2015.

REFERENCES

293. H.-G. Schweiger, M. Multerer, M. Schweizer-Berberich and H. Gores, *International Journal of Electrochemical Science*, 2008, **3**, 427-443.
294. A. Tornheim and D. C. O'Hanlon, *Journal of The Electrochemical Society*, 2020, **167**, 110520.
295. N. Elgrishi, K. J. Rountree, B. D. McCarthy, E. S. Rountree, T. T. Eisenhart and J. L. Dempsey, *Journal of chemical education*, 2018, **95**, 197-206.
296. J. Heinze, *Angewandte Chemie*, 1984, **96**, 823-840.
297. K. G. Cassman and P. Grassini, *Nature Sustainability*, 2020, **3**, 262-268.
298. S. Mitchell, R. Qin, N. Zheng and J. Pérez-Ramírez, *Nature Nanotechnology*, 2021, **16**, 129-139.
299. G. Crabtree, E. Kócs and L. Trahey, *Mrs Bulletin*, 2015, **40**, 1067-1078.
300. M. M. Thackeray, C. Wolverton and E. D. Isaacs, *Energy & Environmental Science*, 2012, **5**, 7854-7863.
301. A. Luntz, *Journal*, 2015, **6**, 300-301.
302. J. Sun, T. Wang, Y. Gao, Z. Pan, R. Hu and J. Wang, *InfoMat*, 2022, **4**, e12359.
303. S. M. Hwang, J. S. Park, Y. Kim, W. Go, J. Han, Y. Kim and Y. Kim, *Advanced Materials*, 2019, **31**, 1804936.
304. I. C. Blake, *Journal of The Electrochemical Society*, 1952, **99**, 202C.
305. S. Senthilkumar, W. Go, J. Han, L. P. T. Thuy, K. Kishor, Y. Kim and Y. Kim, *Journal of Materials Chemistry A*, 2019, **7**, 22803-22825.
306. J. K. Kim, E. Lee, H. Kim, C. Johnson, J. Cho and Y. Kim, *ChemElectroChem*, 2015, **2**, 328-332.
307. N. C. Darre and G. S. Toor, *Current Pollution Reports*, 2018, **4**, 104-111.
308. Y. J. Lim, K. Goh, M. Kurihara and R. Wang, *Journal of Membrane Science*, 2021, **629**, 119292.
309. M. Al-Obaidi, G. Filippini, F. Manenti and I. M. Mujtaba, *Desalination*, 2019, **456**, 136-149.
310. O. A. Hamed, M. A. Al-Sofi, M. Imam, G. M. Mustafa, K. B. Mardouf and H. Al-Washmi, *Desalination*, 2000, **128**, 281-292.
311. F. A. AlMarzooqi, A. A. Al Ghaferi, I. Saadat and N. Hilal, *Desalination*, 2014, **342**, 3-15.
312. H. Nassrullah, S. F. Anis, R. Hashaikeh and N. Hilal, *Desalination*, 2020, **491**, 114569.
313. M. Sadrzadeh and T. Mohammadi, *Desalination*, 2008, **221**, 440-447.
314. M. E. Suss, Y. Zhang, I. Atlas, Y. Gendel, E. Ruck and V. Presser, *Electrochemistry Communications*, 2022, **136**, 107211.
315. Y. Zhang, L. Wang and V. Presser, *Cell Reports Physical Science*, 2021, **2**, 100416.
316. P. Srimuk, X. Su, J. Yoon, D. Aurbach and V. Presser, *Nature Reviews Materials*, 2020, **5**, 517-538.
317. M. Pasta, C. D. Wessells, Y. Cui and F. La Mantia, *Nano letters*, 2012, **12**, 839-843.
318. M. E. Suss, S. Porada, X. Sun, P. M. Biesheuvel, J. Yoon and V. Presser, *Energy & Environmental Science*, 2015, **8**, 2296-2319.
319. Y. Mandri, A. Rich, D. Mangin, S. Abderafi, C. Bebon, N. Semlali, J.-P. Klein, T. Bounahmidi and A. Bouhaouss, *Desalination*, 2011, **269**, 142-147.
320. L. Wang, J. E. Dykstra and S. Lin, *Environmental Science & Technology*, 2019, **53**, 3366-3378.
321. S. Porada, R. Zhao, A. van der Wal, V. Presser and P. M. Biesheuvel, *Progress in Materials Science*, 2013, **58**, 1388-1442.
322. G. Amy, N. Ghaffour, Z. Li, L. Francis, R. V. Linares, T. Missimer and S. Lattemann, *Desalination*, 2017, **401**, 16-21.
323. B. B. Arnold and G. W. Murphy, *The Journal of Physical Chemistry*, 1961, **65**, 135-138.
324. G. Murphy and D. Caudle, *Electrochimica Acta*, 1967, **12**, 1655-1664.
325. J. Ma, D. He, W. Tang, P. Kovalsky, C. He, C. Zhang and T. D. Waite, *Environmental Science & Technology*, 2016, **50**, 13495-13501.
326. S. Porada, L. Weinstein, R. Dash, A. van der Wal, M. Bryjak, Y. Gogotsi and P. M. Biesheuvel, *ACS Applied Materials & Interfaces*, 2012, **4**, 1194-1199.
327. B. Krüner, P. Srimuk, S. Fleischmann, M. Zeiger, A. Schreiber, M. Aslan, A. Quade and V. Presser, *Carbon*, 2017, **117**, 46-54.
328. P. Srimuk, J. Lee, S. Fleischmann, S. Choudhury, N. Jäckel, M. Zeiger, C. Kim, M. Aslan and V. Presser, *Journal of Materials Chemistry A*, 2017, **5**, 15640-15649.

329. C. Tsouris, R. Mayes, J. Kiggans, K. Sharma, S. Yiacoumi, D. DePaoli and S. Dai, *Environmental Science & Technology*, 2011, **45**, 10243-10249.

330. S. Ahualli, G. R. Iglesias, M. M. Fernández, M. L. Jiménez and Á. V. Delgado, *Environmental Science & Technology*, 2017, **51**, 5326-5333.

331. S. Porada, D. Weingarth, H. V. M. Hamelers, M. Bryjak, V. Presser and P. M. Biesheuvel, *Journal of Materials Chemistry A*, 2014, **2**, 9313-9321.

332. K. B. Hatzell, L. Fan, M. Beidaghi, M. Boota, E. Pomerantseva, E. C. Kumbur and Y. Gogotsi, *ACS Applied Materials & Interfaces*, 2014, **6**, 8886-8893.

333. M. E. Suss, T. F. Baumann, W. L. Bourcier, C. M. Spadaccini, K. A. Rose, J. G. Santiago and M. Stadermann, *Energy & Environmental Science*, 2012, **5**, 9511-9519.

334. E. García-Quismondo, C. Santos, J. Soria, J. Palma and M. A. Anderson, *Environmental Science & Technology*, 2016, **50**, 6053-6060.

335. C. Kim, P. Srimuk, J. Lee, M. Aslan and V. Presser, *Desalination*, 2018, **425**, 104-110.

336. B. Lian, Y. Zhu, D. Branchaud, Y. Wang, C. Bales, T. Bednarz and T. D. Waite, *Desalination*, 2022, **525**, 115482.

337. T. D. Hasseler, A. Ramachandran, W. A. Tarpeh, M. Stadermann and J. G. Santiago, *Water Research*, 2020, **183**, 116034.

338. J.-H. Ryu, T.-J. Kim, T.-Y. Lee and I.-B. Lee, *Journal of the Taiwan Institute of Chemical Engineers*, 2010, **41**, 506-511.

339. R. Zhao, S. Porada, P. M. Biesheuvel and A. van der Wal, *Desalination*, 2013, **330**, 35-41.

340. S. Porada, L. Zhang and J. E. Dykstra, *Desalination*, 2020, **488**, 114383.

341. P. M. Biesheuvel, S. Porada, M. Levi and M. Z. Bazant, *Journal of Solid State Electrochemistry*, 2014, **18**, 1365-1376.

342. C. Prehal, C. Koczwara, H. Amenitsch, V. Presser and O. Paris, *Nature Communications*, 2018, **9**, 4145.

343. S. Bi, Y. Zhang, L. Cervini, T. Mo, J. M. Griffin, V. Presser and G. Feng, *Sustainable Energy & Fuels*, 2020, **4**, 1285-1295.

344. Y. Zhang, C. Prehal, H. Jiang, Y. Liu, G. Feng and V. Presser, *Cell Reports Physical Science*, 2022, **3**, 100689.

345. N. Jäckel, P. Simon, Y. Gogotsi and V. Presser, *ACS Energy Letters*, 2016, **1**, 1262-1265.

346. F. Stoeckli and T. A. Centeno, *Physical Chemistry Chemical Physics*, 2012, **14**, 11589-11591.

347. Z.-H. Huang, Z. Yang, F. Kang and M. Inagaki, *Journal of Materials Chemistry A*, 2017, **5**, 470-496.

348. C. Zhang, D. He, J. Ma, W. Tang and T. D. Waite, *Water Research*, 2018, **128**, 314-330.

349. J. Lee, S. Kim, C. Kim and J. Yoon, *Energy & Environmental Science*, 2014, **7**, 3683-3689.

350. P. Srimuk, J. Lee, Ö. Budak, J. Choi, M. Chen, G. Feng, C. Prehal and V. Presser, *Langmuir*, 2018, **34**, 13132-13143.

351. S. Porada, A. Shrivastava, P. Bukowska, P. M. Biesheuvel and K. C. Smith, *Electrochimica Acta*, 2017, **255**, 369-378.

352. P. Srimuk, J. Lee, A. Tolosa, C. Kim, M. Aslan and V. Presser, *Chemistry of Materials*, 2017, **29**, 9964-9973.

353. P. Srimuk, S. Husmann and V. Presser, *RSC Advances*, 2019, **9**, 14849-14858.

354. D.-H. Nam and K.-S. Choi, *Journal of the American Chemical Society*, 2017, **139**, 11055-11063.

355. E. Grygolowicz-Pawlak, M. Sohail, M. Pawlak, B. Neel, A. Shvarev, R. de Marco and E. Bakker, *Analytical Chemistry*, 2012, **84**, 6158-6165.

356. J. Ahn, J. Lee, S. Kim, C. Kim, J. Lee, P. M. Biesheuvel and J. Yoon, *Desalination*, 2020, **476**, 114216.

357. F. Yu, L. Wang, Y. Wang, X. Shen, Y. Cheng and J. Ma, *Journal of Materials Chemistry A*, 2019, **7**, 15999-16027.

358. P. M. Biesheuvel and A. van der Wal, *Journal of Membrane Science*, 2010, **346**, 256-262.

359. M. D. Andelman and G. S. Walker, *Journal*, 2004.

360. J.-B. Lee, K.-K. Park, H.-M. Eum and C.-W. Lee, *Desalination*, 2006, **196**, 125-134.

361. Y. Zhao, Y. Wang, R. Wang, Y. Wu, S. Xu and J. Wang, *Desalination*, 2013, **324**, 127-133.

362. B. M. Asquith, J. Meier-Haack and B. P. Ladewig, *Desalination*, 2014, **345**, 94-100.
363. R. Zhao, P. M. Biesheuvel and A. van der Wal, *Energy & Environmental Science*, 2012, **5**, 9520-9527.
364. P. M. Biesheuvel, R. Zhao, S. Porada and A. van der Wal, *Journal of Colloid and Interface Science*, 2011, **360**, 239-248.
365. P. Długołecki and A. van der Wal, *Environmental science & technology*, 2013, **47**, 4904-4910.
366. K. Mitko, A. Rosiński and M. Turek, *Desalin. Water Treat*, 2021, **214**, 294-301.
367. J. Zhou, P. Zuo, Y. Liu, Z. Yang and T. Xu, *Science China Chemistry*, 2018, **61**, 1062-1087.
368. J. Ran, L. Wu, Y. He, Z. Yang, Y. Wang, C. Jiang, L. Ge, E. Bakangura and T. Xu, *Journal of Membrane Science*, 2017, **522**, 267-291.
369. J. Kamcev, D. R. Paul and B. D. Freeman, *Journal of Materials Chemistry A*, 2017, **5**, 4638-4650.
370. J. Kamcev and B. D. Freeman, *Annual review of chemical and biomolecular engineering*, 2016, **7**, 111-133.
371. G. M. Geise, D. R. Paul and B. D. Freeman, *Progress in Polymer Science*, 2014, **39**, 1-42.
372. W. D. Richards, T. Tsujimura, L. J. Miara, Y. Wang, J. C. Kim, S. P. Ong, I. Uechi, N. Suzuki and G. Ceder, *Nature communications*, 2016, **7**, 1-8.
373. J. Janek and W. G. Zeier, *Nature Energy*, 2016, **1**, 1-4.
374. X. He, Y. Zhu and Y. Mo, *Nature communications*, 2017, **8**, 1-7.
375. N. Anantharamulu, K. Koteswara Rao, G. Rambabu, B. Vijaya Kumar, V. Radha and M. Vithal, *Journal of materials science*, 2011, **46**, 2821-2837.
376. H.-P. Hong, *Materials Research Bulletin*, 1976, **11**, 173-182.
377. U. Von Alpen, M. Bell and H. Höfer, *Solid State Ionics*, 1981, **3**, 215-218.
378. W. Go, J. Kim, J. Pyo, J. B. Wolfenstine and Y. Kim, *ACS Applied Materials & Interfaces*, 2021, **13**, 52727-52735.
379. M. Avdeev, V. B. Nalbandyan and I. L. Shukaev, in *Solid State Electrochemistry I*, 2009, DOI: https://doi.org/10.1002/9783527627868.ch7, pp. 227-278.
380. H. Y. P. Hong, *Materials Research Bulletin*, 1978, **13**, 117-124.
381. F. Zheng, M. Kotobuki, S. Song, M. O. Lai and L. Lu, *Journal of Power Sources*, 2018, **389**, 198-213.
382. U. v. Alpen, M. F. Bell, W. Wichelhaus, K. Y. Cheung and G. J. Dudley, *Electrochimica Acta*, 1978, **23**, 1395-1397.
383. D. Mazumdar, D. N. Bose and M. L. Mukherjee, *Solid State Ionics*, 1984, **14**, 143-147.
384. J. Kuwano and A. R. West, *Materials Research Bulletin*, 1980, **15**, 1661-1667.
385. Y. W. Hu, I. D. Raistrick and R. A. Huggins, *Journal of The Electrochemical Society*, 1977, **124**, 1240.
386. S. Song, J. Lu, F. Zheng, H. M. Duong and L. Lu, *RSC Advances*, 2015, **5**, 6588-6594.
387. P. Knauth, *Solid State Ionics*, 2009, **180**, 911-916.
388. L. Wang, S. Arnold, P. Ren, Q. Wang, J. Jin, Z. Wen and V. Presser, *ACS Energy Letters*, 2022, DOI: 10.1021/acsenergylett.2c01746, 3539-3544.
389. S. Porada, G. Feng, M. E. Suss and V. Presser, *RSC Advances*, 2016, **6**, 5865-5870.
390. C. Kim, P. Srimuk, J. Lee and V. Presser, *Desalination*, 2018, **443**, 56-61.
391. S. Arnold, L. Wang, Ö. Budak, M. Aslan, P. Srimuk and V. Presser, *Journal of Materials Chemistry A*, 2021, **9**, 585-596.
392. E. Parliament, New EU rules for more sustainable and ethical batteries https://www.europarl.europa.eu/news/en/headlines/economy/20220228STO24218/new-eu-rules-for-more-sustainable-and-ethical-batteries, (accessed 08.12.2022).
393. E. Comission, Green Deal: EU agrees new law on more sustainable and circular batteries to support EU's energy transition and competitive industry, https://ec.europa.eu/commission/presscorner/detail/en/ip_22_7588, (accessed 02.01.2023).
394. J. Spangenberger, *ReCell Center, USD o. E., Ed*, 2019.
395. J. Yu, X. Wang, M. Zhou and Q. Wang, *Energy & Environmental Science*, 2019, **12**, 2672-2677.
396. X. Chen, C. Luo, J. Zhang, J. Kong and T. Zhou, *ACS Sustainable Chemistry & Engineering*, 2015, **3**, 3104-3113.

397. B. Makuza, Q. Tian, X. Guo, K. Chattopadhyay and D. Yu, *Journal of Power Sources*, 2021, **491**, 229622.
398. A. Porvali, M. Aaltonen, S. Ojanen, O. Velazquez-Martinez, E. Eronen, F. Liu, B. P. Wilson, R. Serna-Guerrero and M. Lundström, *Resources, Conservation and Recycling*, 2019, **142**, 257-266.
399. S. Virolainen, T. Wesselborg, A. Kaukinen and T. Sainio, *Hydrometallurgy*, 2021, **202**, 105602.
400. W. Wang, W. Chen and H. Liu, *Hydrometallurgy*, 2019, **185**, 88-92.
401. X. Zheng, Z. Zhu, X. Lin, Y. Zhang, Y. He, H. Cao and Z. Sun, *Engineering*, 2018, **4**, 361-370.
402. V. Goodship, A. Stevels and J. Huisman, *Waste electrical and electronic equipment (WEEE) handbook*, Woodhead Publishing, 2019.
403. J. Jegan Roy, M. Srinivasan and B. Cao, *ACS Sustainable Chemistry & Engineering*, 2021, **9**, 3060-3069.
404. N. B. Horeh, S. Mousavi and S. Shojaosadati, *Journal of power sources*, 2016, **320**, 257-266.
405. Y. Xin, X. Guo, S. Chen, J. Wang, F. Wu and B. Xin, *Journal of cleaner production*, 2016, **116**, 249-258.
406. M. Pasta, A. Battistel and F. La Mantia, *Energy & Environmental Science*, 2012, **5**, 9487-9491.
407. Y. Liu, R. Zhang, J. Wang and Y. Wang, *iScience*, 2021, **24**, 102332.
408. E. Karden, in *Lead-Acid Batteries for Future Automobiles*, eds. J. Garche, E. Karden, P. T. Moseley and D. A. J. Rand, Elsevier, Amsterdam, 2017, DOI: https://doi.org/10.1016/B978-0-444-63700-0.00001-5, pp. 3-25.
409. M. Fichtner, K. Edström, E. Ayerbe, M. Berecibar, A. Bhowmik, I. E. Castelli, S. Clark, R. Dominko, M. Erakca, A. A. Franco, A. Grimaud, B. Horstmann, A. Latz, H. Lorrmann, M. Meeus, R. Narayan, F. Pammer, J. Ruhland, H. Stein, T. Vegge and M. Weil, *Advanced Energy Materials*, 2022, **12**, 2102904.
410. U. S. G. Survey, *Journal*, 2020.
411. S. v. d. Brink, R. Kleijn, B. Sprecher, N. Mancheri and A. Tukker, *Resources, Conservation and Recycling*, 2022, **186**, 106586.
412. U. S. G. Survey, *Journal*, 2020.

7 ABBREVIATIONS

A.1. Abbreviations

AEM	anion exchange membrane
CDI	capacitive deionization
CE	Coulombic efficiency
CEI	cathode electrolyte interphase
CEM	cation exchange membrane
CMC	carboxymethyl cellulose
CV	cyclic voltammetry
CV	cyclic voltammetry
DEC	diethyl carbonate
DMC	dimethyl carbonate
DMC	dimethylcarbonate
DMSO	dimethyl sulfoxide
DTD	1,3,2-dioxathiolane-2,2-dioxide
e.g.	exempli gratia → for example
EC	ethylene carbonate
EES	electrochemical energy storage
EFPN	ethoxy(pentafluoro)cyclotriphosphazene
EMC	ethylmethyl carbonate
ESR	equivalent series resistance
et al.	et alii → and others
FEC	fluoroethylene carbonate
GBL	γ-butyrolactone
GCPL	galvanostatic cycling with potential limitation
GVL	γ-valerolactone
i.e.	id est → for example
LCO	lithium cobalt oxide
LFP	lithium iron phosphate
LIB	lithium-ion battery
LiDFOB	lithium difluoro(oxalato)borate
LiDFP	lithium difluorophosphate
LISICON	lithium superionic conductor
LMO	lithium manganese oxide
LTO	lithium titanoxide ($Li_4Ti_5O_{12}$)
MCDI	membrane-based capacitive deionization
Na	sodium
NASICON	sodium superionic conductors
NaTFSI	sodium trifluoromethanesulfonimide
NIB	sodium-ion battery
NMC	lithium nickel manganese cobalt oxide
NMP	N-methyl-2-pyrrolidone
ODTO	1,2,6-oxadithiane 2,2,6,6-tetraoxide
OER	oxygen evolution reaction
OLC	onion-like carbon
ORR	oxygen reduction reaction
PAA	poly acrylic acid
PC	propylene carbonate
PC	propylene carbonate
PE	polyethylene

PP	polypropylene
PST	propene sulfone
PVdF	polyvinylidenefluoride
SA	sodium alginate
SA	succinic anhydride
Sb	antimony
SEI	solid electrolyte Interphase
SEM	scanning electron microscope
SHE	standard hydrogen electrode
TMSP	tris(trimethylsilyl) phosphite
TTE	1,1,2,2-tetrafluoroethyl 2,2,3,3-tetrafluoropropyl ether
VC	vinylene carbonate
XRD	X-ray diffraction

A.2. Symbols and Constants

%	percent
°C	degree Celsius
A	Ampere
A g^{-1}	Ampere per gram
C	C-rate
cm^2	square centimeter
e$_0$	elementary charge
Eo	redox potential
F	Farad
F	Faraday constant
g	gram
g	gram
h	hours
I	electric current
kt	kiloton
M	molar
M	molar mass
m	mass
m^2 g^{-1}	square meter per gram
mAh g^{-1}	milli-ampere-hour per gram
min	minutes
mm	millimeter
n	amount of substance (mol)
N$_A$	Avogadro constant
nm	nanometer
Q	charge
t	time
TWh	terawatt hour
U	Voltage in volt
V	Volt
Wh g^{-1}	Watt-hour per gram
µm	micrometers